

Exploring the
Photophysics and
Reactivity of
Nickel–Bipyridine
Cross-Coupling Catalysts

Thesis by
David A. Cagan

In Partial Fulfillment of the Requirements for
the degree of
Doctor of Philosophy

The logo for the California Institute of Technology (Caltech), featuring the word "Caltech" in a bold, orange, sans-serif font.

CALIFORNIA INSTITUTE OF TECHNOLOGY
Pasadena, California

2024
(Defended May 29, 2024)

© 2024

David A. Cagan
ORCID: 0000-0002-4719-2789

ACKNOWLEDGEMENTS

The journey to earn my doctorate in chemistry has been transformative. I have found chemistry to be an empowering mechanism to express my creativity and individuality while trying to understand the world. This scientific method was given to me by my professors, my mentors, my friends, and my family. I am deeply indebted to each of them, and I would like to take this time to thank them.

Thank you to my Pasadena City College professors. Professor Castro, you taught me the history of chemical discovery from alchemy to Bohr. Your lectures contextualized and humanized science. Thank you for your passion and your representation. Professor Harman, you showed me that chemistry and art are not so separate. Your discussions allowed me to see science as a creative process. Thank you for encouraging my individuality. Professor Ansari, you taught me to join math and chemistry together for the first time. Your notes on reaction kinetics carried me into my subdiscipline. Thank you for showing me the value of organization and structure in my learning. Professor Sweimeh, you not only uncovered my love for organic chemistry, but you also demonstrated the value of mentorship. Your hands-on approach to teaching and mentoring has made a tremendous impact in my own goals as an educator. Thank you for believing in me before I did. Professor Ganapathi, you presented an enthusiastic and logical approach to organic mechanisms. Your lectures gave me an intuition for reactivity that has been vital for my research. Thank you for showing me the joy in a mechanistic puzzle. Professor Jaramillo, you hosted the STEM study center. Your willingness to maintain our study space gave me a second home. Thank you for supporting my all-hours education. Professor Socrates, you taught me the artistry of linear algebra. Your teaching became the seed for my love of inorganic chemistry. Thank you for showing me the value of an interdisciplinary understanding. Professor Riley, you expanded my appreciation of reaction kinetics by teaching me differential equations. Your support of my project modeling the Belousov–Zhabotinsky reaction solidified physical chemistry as a subdiscipline of mine. Thank you for always having time for your students. Professor Underwood, you expanded my horizon of understanding to the intersection of hermeneutics and science. Your lectures fostered my love for academic writing and challenged my critical

thinking skills. Thank you for teaching me that a methodological scientific undertaking is still a human endeavor, and as such, should be conducted with openness and an awareness of my own biases.

Thank you to my Cal State LA professors. Professor Foster, you furthered my understanding of physical chemistry. Your discussion of statistical thermodynamics was very helpful; I have used your notes several times throughout my research. Thank you for making these complicated subjects intelligible to me. Professor Liu, you taught me the fundamentals of inorganic chemistry and group theory. Your lectures have carried me throughout my advanced studies. Thank you for teaching me the importance of a rigorous scientific foundation. Professor Yap, you demonstrated advanced synthetic methods with an infectious casual demeanor. Your laboratory tutelage encouraged my appreciation for inorganic synthesis. Thank you for making inorganic chemistry colorful. Professor Tunstad, you ran the research programs while I was at Cal State LA. Your grant writing gave me funding for my research, allowing me to not have to hold another job. Thank you for letting research be a priority for me and for showing me what opportunities could lie ahead. Professor Selke, you taught me how to conduct research. Your mentorship, friendship, and instruction have been invaluable to me. Thank you for teaching me how to begin, lead, and finish a project. Thank you for your willingness to discuss with me until well into the evening. Thank you for teaching me the value of a well-thought-out failure. Thank you for showing me how to recover detailed information from simple experiments. Thank you for exemplifying an excellent PI.

Thank you to my Caltech professors (who I will call by first name as is customary at Caltech). Theo, you expanded my understanding of inorganic chemistry. Your lecture notes have been a valuable resource; I keep them printed out in my desk drawer for reference. Thank you for your enthusiastic instruction and thank you for your leadership of FUTURE Ignited. It was a pleasure to work with you on it for two years. Greg, you took an interest in my research and supported me in collaboration. Your knowledge of catalysis is seemingly endless, and you took the time to share your thoughts with me to guide my research plans. Thank you for

hosting me at your subgroups. Jay, thank you for your many discussions on photophysics and spectroscopy. I have the utmost respect for your understanding of kinetics. Thank you for sharing your thoughts with me and for allowing me to bounce ideas off of you. Doug, thank you for leading DICI and for being a mentor to me in DEI work. I am always happy to see you on campus and catch up. Harry, you took a chance on me as a summer WAVE student. Your mentorship allowed me to grow in understanding and in confidence. Thank you for teaching me the value of humility in research. Thank you for championing me on into graduate school. Thank you for teaching me advanced ligand field theory and for having me as a TA for the same class. You will find that I have used your lectures in all of my papers.

Thank you to my dissertation committee. Jonas, you have always asked the tough questions. Thank you for maintaining a strict academic standard. Thank you for teaching me the importance of each statement or claim I make. Thank you for serving as the chair of my committee. Brian, you also took a chance on me as a summer WAVE student, for which I am very grateful. Thank you for being a mentor to me, both academically and professionally. Your leadership of the CCE DEI Committee is outstanding; thank you for making Caltech a welcoming place. Thank you for serving on my committee. Sarah, you have inspired me as a leader in your field. Your ability to tackle complex organic chemistry and present it with clarity and enthusiasm is a goal of mine. Thank you for challenging me to think beyond my field. Thank you for serving on my committee.

Thank you to my thesis advisor. Ryan, you have been a mentor, counselor, and friend. Thank you for your guidance as I navigated my research. Thank you for your openness to my ideas. It has been a privilege to work with you and under your leadership. Joining your group at its early stages has been hugely educational for me. Thank you for your transparency in discussing some of the challenges associated with being a new PI. Thank you for trusting me to lead Team Nickel. Thank you for your willingness to try a risky new project and for being “all about the science”. Thank you for our many one-on-one meetings and countless hours

of discussion. Thank you for supporting me in my DEI work and for being vital to the start of Rising Tide. Thank you for believing in me.

Thank you to the many administrators and staff who have supported me. Candace, Maria, and Carol, the three queens of the Student-Faculty Programs Office, thank you for supporting my time as a WAVE student, for making Rising Tide more than just a dream of mine, and for hosting key programs like the GSRI. You three are core to what makes Caltech a great place for research. Paul, your expertise in EPR has made my detailed mechanistic inquiries possible. Thank you for being open to collaboration, for running my many (sadly) EPR silent Ni samples, and for being a friend to me.

Thank you to my coworkers. Ruben, thank you for being the first one to welcome me into the lab. I have enjoyed chatting science with you and playing basketball together. Gautam, thank you for teaching me my first bit of computational chemistry. I wish you the best at U Chicago. Daniel, Brendon, and Erica, thank you for being incredibly supportive postdocs and research teammates. It has been a pleasure working with you and learning from you. Katie, thank you for being a bright presence in the group. Your expertise in physical chemistry has been very valuable to me. Thank you for entertaining my random questions and for proofreading my emails. Thank you for teaching me your synthetic inorganic techniques and for being co-lab managers with me. Nathanael, isn't it time you start your own lab? Thank you for your patience in teaching me MATLAB, collaborating with me on many projects, your openness to discussing science and philosophy, and your general supportiveness of my research. Chris (Goose), thank you for answering all my chemical biology questions and for being such a good sport. Stephen, thank you for teaching me about your approach to quantum yields and rate constants. It has been fun working with you. Kay, Thais, Edwin, and Stefan, although we have spent less time together in the group, I am grateful for all our discussions. Maria and Keon Ha, you are doing fantastic. Thank you for bringing such good energy and research enthusiasm to the group. I am excited to read your future published projects.

Thank you to my research friends. Nick, Robert, and Brian, thank you for being such good friends to me. Even though our cohort suffered due to the pandemic, I have enjoyed sharing meals together and discussing science/general research frustrations. I look forward to our friendship beyond Caltech. Robert, I am also thankful for all your helpful discussions about nickel with myself and Maria. The DICl team, including Trixia, Javier, Mary, Joel, Karen, Kim, Levi, Melinda, Marva, Cami, Jacob, and so many others. Thank you for making DICl a successful program. Thank you for working to make Caltech a more equitable place. You have each played a key role in my time at Caltech. Julian, thank you for mentoring me when I was a WAVE student. I am confident that your review of my graduate application was a significant contributor to my entrance into doctoral programs. Arman, thank you for being a friend for these many years. I am thrilled to hear of your successes at U of O, and I look forward to your independent career. You have made my time at Caltech more enjoyable.

Thank you to my family. John, you are first-class. Thank you for carrying me through all these years. I could not have done it without you. I respect you deeply. Thank you for being such an outstanding brother to me. It was all not for nothing. To my parents, Mama and Papa, thank you for supporting me all these years. Thank you for understanding my busyness, for being patient as I figured out my plans, and for being excited to learn of my research. I also could not have gotten here without your support.

Thank you to my partner. Lizette, you have taught me a great deal about myself. I owe you so much of my mindset. Thank you for being understanding of me and for listening to me. You are my best friend. Thank you for giving me the stability I needed to pursue my research. Thank you for supporting me, for keeping me grounded, and for inspiring me to be my best self. You were there when I started this journey, and you have carried me through. You are my home.

ABSTRACT

Ni(II)–bipyridine (bpy) aryl halide complexes have been prized for nearly a decade for their catalytic potency to facilitate cross-coupling reactions. To achieve these transformations, the energy from light is leveraged to drive the key catalytic processes. Thus, Ni-mediated photoredox catalysis provides an attractive and sustainable means to replace precious metal catalysts. However, precise mechanistic information regarding how these transformations occur is limited. This thesis thus focuses on a dual experimental and computational analysis of Ni(II)–bpy aryl halide complexes and their photoproducts to provide insight into the specific photophysical and chemical pathways that these catalysts undertake for cross-coupling reactions. The first chapter is a review of the proposed mechanisms presented for Ni-mediated photoredox catalysis and serves as an introduction to this work. Therein, certain portions of this work are also summarized. The second chapter provides a computational description of the Ni(II) excited states. The third chapter expands on this analysis with experiment, elucidating the photophysical pathway that grants entry into dark Ni(I)/Ni(III) catalytic cycles. Together, chapters two and three show that Ni(II)–bpy aryl halide complexes form low-valent Ni(I)–bpy halide species by an aryl-to-Ni ligand-to-metal charge transfer. Chapter four outlines a method to generate and study these reactive Ni(I)–bpy halide intermediates, identifying their mechanism of C(sp²)–Cl bond activation as nucleophilic aromatic substitution, tunable via the energies of the 3*d*-orbitals and the effective nuclear charge of Ni. The final chapter finds that these low-valent Ni species are competitive light-absorbers, and it presents a study into their ultrafast photophysics, marking the first of its kind on any Ni(I) complex. The excited-state relaxation dynamics of Ni(I)–bpy halide complexes are well described by vibronic Marcus theory, spanning the normal and inverted regions as a result of simple changes to the bpy substituents. Altogether, these studies have provided a framework to gain electronic structural control over Ni-mediated photoredox catalysis and, thus, guides the use of photonic energy as a sustainable alternative to precious metal catalysis.

PUBLISHED CONTENT AND CONTRIBUTIONS

1. Multireference Description of Nickel–Aryl Bond Dissociation Processes in Photoredox Catalysis. **Cagan, D.A.**;[†] Stroschio, G.D.;[†] Cusumano, A.Q.; Hadt, R.G. *J. Phys. Chem. A* **2020**, *124*(48), 9915–9922. DOI: 10.1021/acs.jpca.0c08646.
◇ Contribution: Co-first authorship with Gautam Stroschio. We both performed the computational work, conducted the data analysis, and contributed to the writing of the publication.
2. Elucidating the Mechanism of Excited-State Bond Homolysis in Nickel–Bipyridine Photoredox Catalysts. **Cagan, D. A.**; Bím, D.; Silva, B.; Kazmierczak, N. P.; McNicholas, B. J.; Hadt, R. G. *J. Am. Chem. Soc.* **2022**, *144*(14), 6516–6531. DOI: 10.1021/jacs.2c01356.
◇ Contribution: As first author, I performed the experimental work and some of the initial computations. I also conducted the data analysis and contributed to the writing of the publication.
3. Photogenerated Ni(I)–Bipyridine Halide Complexes: Structure–Function Relationships for Competitive C(sp²)–Cl Oxidative Addition and Dimerization Reactivity Pathways. **Cagan, D. A.**;[†] Bím, D.;[†] McNicholas, B. J.; Kazmierczak, N. P.; Oyala, P. H.; Hadt, R. G. *Inorg. Chem.* **2023**, *62*(24), 9538–9551. DOI: 10.1021/acs.inorgchem.3c00917.
◇ Contribution: Co-first authorship with Daniel Bím. I conceptualized the project, performed experimental work, and conducted the data analysis. D.B. assisted with the experimental work and performed the computational analysis. We both contributed to the writing of the publication.
4. Mechanisms of Photoredox Catalysis Featuring Nickel–Bipyridine Complexes. **Cagan, D. A.**; Bím, D.; Kazmierczak, N. P.; Hadt, R. G. *ACS Catalysis*, **2024**, Accepted.
◇ Contribution: As first author, I performed the bulk of the literature review, organized its structure, and contributed to the writing of the manuscript.
5. Ultrafast Photophysics of Ni(I)–Bipyridine Halide Complexes: Spanning the Marcus Normal and Inverted Regimes. Sutcliffe, E.;[†] **Cagan, D. A.**;[†] Hadt, R. G. *J. Am. Chem. Soc.* **2024**, Accepted.
◇ Contribution: Co-first authorship with Erica Sutcliffe. I conceptualized the project, performed the synthetic work, and conducted the computational analysis. E.S. performed the ultrafast spectroscopy and data analysis. We both contributed to the writing of the manuscript.

TABLE OF CONTENTS

Acknowledgements	iii
Abstract	viii
Published Content and Contributions.....	ix
Table of Contents.....	x
List of Figures, Schemes, and Tables.....	xii
Nomenclature and Abbreviations	xvi
Chapter 1. Mechanisms of Photoredox Catalysis Featuring Nickel–Bipyridine Complexes..	1
§1-1. Introduction	2
§1-2. Nickel Electronic Structure Primer.....	4
§1-3. Summary and Comparisons of Proposed Photoredox Mechanisms	10
§1-3.1. Photosensitization.....	10
§1-3.1.1. Reductive SET.....	10
§1-3.1.1.2. Key Considerations for the Reductive SET Mechanism	12
§1-3.1.3. Oxidative SET	14
§1-3.1.4. Key Considerations for the Oxidative SET Mechanism.....	15
§1-3.1.5. Photosensitization for Homolysis (SET vs. ³ EnT).....	17
§1-3.1.6. Key points of the Photosensitization for Homolysis Mechanisms.....	19
§1-3.1.7. Triplet Energy Transfer (³ EnT).....	22
§1-3.1.8. Key Components of the ³ EnT Mechanism	23
§1-3.1.9. SET for Active Ni(I)	25
§1-3.1.10. Key Components of the SET for Active Ni(I) Mechanism.....	29
§1-3.2. Direct Excitation	32
§1-3.2.1. Direct Excitation for Dark Cycle Initiation	32
§1-3.2.2. Direct Excitation for Reductive Elimination.....	39
§1-3.2.3. Key Components of Direct Excitation	40
§1-4. Conclusions and Outlook.....	45
§1-5. References.....	47
Chapter 2. Multireference Description of Nickel–Aryl Homolytic Bond Dissociation Processes in Photoredox Catalysis	63
§2-1. Introduction	64
§2-2. Computational Methods	66
§2-3. Results and Discussion.....	68
§2-4. Conclusions	75
§2-5. References.....	76
Chapter 3. Elucidating the Mechanism of Excited-State Bond Homolysis in Nickel– Bipyridine Photoredox Catalysts	82
§3-1. Introduction	83
§3-1.1 Ni(II)–bpy Photoredox Catalysis	83
§3-1.2. Mechanistic Hypotheses for Excited-State Ni(II)–C Bond Homolysis	85
§3-2. Results and Analysis.....	87
§3-2.1. Experimental Studies.....	87
§3-2.1.2. Steady-State UV–Vis Spectroscopy.....	88
§3-2.1.3. Photochemical Investigations.....	90

§3-2.1.4. Preliminary Investigations of the Photochemically Generated Species.....	95
§3-2.1.5. Further Examination of the Mechanism of Excited-State Bond Homolysis .	98
§3-2.2. Computational Studies	101
§3-2.2.1. DFT versus CASSCF/QD-NEVPT2 Ground and Excited States	101
§3-2.2.3. Investigating the Mechanism of Excited-State Ni(II)–C Bond Homolysis..	104
§3-3. Discussion.....	110
§3-4. Conclusions	116
§3-5. References.....	118
Chapter 4. Photogenerated Ni(I)–Bipyridine Halide Complexes: Structure-Function Relationships for Competitive C(sp ²)–Cl Oxidative Addition and Dimerization Reactivity Pathways.....	127
§4-1. Introduction	128
§4-2. Results and Analysis.....	131
§4-2.1 Photochemical Synthesis and Spectroscopic Characterization of Ni(I)–bpy Halide Complexes	131
§4-2.2. Oxidative Addition Kinetics with 2-Chloro-toluene.....	135
§4-2.3. Oxidative Addition Mechanistic Investigations	139
§4-2.4. Thermodynamics of the Dimerization of Ni(I)–bpy Halides.....	144
§4-2.5. Dimerization Mechanistic Investigations	147
§4-3. Discussion.....	149
§4-4. Conclusions	154
§4-5. References.....	156
Chapter 5. Ultrafast Photophysics of Ni(I)–Bipyridine Halide Complexes: Spanning the Marcus Normal and Inverted Regimes.....	164
§5-1. Introduction	165
§5-2. Results.....	168
2.1. Steady State and Ultrafast UV-vis-NIR Spectroscopy.....	168
§5-2.2. Isolation and Characterization of Ni(I)(^{MeO₂C} bpy)Cl, 5'.....	172
§5-3. Discussion.....	174
§5-4. Conclusions	179
§5-5. References.....	180
Appendix 1. Supporting Information for Chapter 2: Multireference Description Of Nickel–Aryl Homolytic Bond Dissociation Processes in Photoredox Catalysis.....	187
Appendix 2. Supporting Information for Chapter 3: Elucidating The Mechanism of Excited-State Bond Homolysis in Nickel–Bipyridine Photoredox Catalysts.....	188
Appendix 3. Supporting Information for Chapter 4: Photogenerated Ni(I)–Bipyridine Halide Complexes: Structure-Function Relationships for Competitive C(sp ²)–Cl Oxidative Addition and Dimerization Reactivity Pathways	189
Appendix 4. Supporting Information for Chapter 5: Ultrafast Photophysics of Ni(I)– Bipyridine Halide Complexes: Spanning the Marcus Normal and Inverted Regimes..	190

LIST OF FIGURES, SCHEMES, AND TABLES

<i>Item</i>	<i>Page</i>
Figure 1.1. Qualitative molecular orbital correlation diagram of four Ni(II)–bpy species of potential relevance in photocatalytic pathways.....	6
Figure 1.2. UV-vis absorption spectra of a common Ir(III) photosensitizer and various Ni complexes.....	8
Figure 1.3. Proposed Reductive SET mechanism.....	11
Figure 1.4. Proposed Oxidative SET mechanism.....	15
Figure 1.5. Proposed Photosensitization for Homolysis Mechanism (Doyle, Shields).....	18
Figure 1.6. Proposed Photosensitization for Homolysis Mechanism (Molander).....	18
Figure 1.7. Proposed ³ EnT Mechanism.....	23
Figure 1.8. Proposed SET for Active Ni(I) Mechanism for C(sp ²)–S coupling.....	27
Figure 1.9. Proposed SET for Active Ni(I) Mechanism.....	28
Figure 1.10. Proposed direct excitation for photohalogen elimination from five-coordinate Ni complexes.....	34
Figure 1.11. Proposed direct excitation for Ni(II)–C(aryl) bond homolysis and C(sp ²)–O product formation mechanism.....	37
Figure 2.1. Mechanistic hypotheses related to Ni–bpy photoredox catalysis.....	65
Figure 2.2. Simplified MO diagram of 1 calculated by CASSCF/QD-NEVPT2.....	69
Figure 2.3. Ni(II)–C bond dissociation from the lowest energy singlet and triplet states in 1	71
Figure 2.4. DFT vs. CASSCF/QD-NEVPT2 description of the formal Ni(I) species formed upon homolytic Ni–C bond cleavage.....	72

Figure 2.5. CASSCF/QD-NEVPT2 relaxed ground- and excited-state PESs along the Ni–C coordinate of 1	74
Figure 3.1. Plausible photocatalytic approaches to Ni(II)–bpy-mediated C–O bond formation, direct excitation energy diagram, and summary of work Chapter 3.....	85
Figure 3.2. Matrix of Ni(^R bpy)(^{R'} Ph)Cl (R = MeO, <i>t</i> -Bu, H, and MeOOC; R' = <i>ortho</i> -CH ₃ , H, OMe, F, and CF ₃) complexes examined in Chapter 3.....	88
Figure 3.3. UV–vis spectra in THF of complexes studied and correlation between λ _{max} and the Hammett parameter.....	89
Figure 3.4. Photolysis profiles of 1A–1D in THF for 390 nm excitation.....	92
Table 3.1. Summary of UV-vis λ _{max} and first-order rate constants.....	93
Figure 3.5. Correlation between normalized rate constants (390 nm excitation) of excited-state bond homolysis and specific Hammett σ parameters of the bpy and aryl ligands.....	95
Figure 3.6. Photolysis profile of 1B–Br in THF, comparison between long-time UV–vis spectra of five compounds, and comparison between UV–vis spectra for 1B–Br in THF and DMF before and after irradiation.....	96
Figure 3.7. Eyring analysis of the temperature-dependent photolysis rates.....	99
Figure 3.8. Wavelength-dependent photolysis for 1B , 1D , and 5D	99
Figure 3.9. Correlation between the calculated ¹ MLCT transition energies and the specific Hammett σ parameters.....	103
Figure 3.10. Two plausible excited-state mechanisms of Ni(II)–C bond homolysis...	106
Figure 3.11. Computed excited-state activation energies plotted against experimental ln(<i>k</i> _{obs,1}).....	109
Figure 3.12. Comparison between the change in energy of the MLCT energy and experimental ln(<i>k</i> _{obs,1}) and energetic barrier for photolysis; PES diagram illustrating how the barrier for photolysis is dependent on both the ¹ MLCT and repulsive ³ (MLCT+LMCT) surfaces.....	113

Figure 4.1. Catalytic cycle displaying the photochemical activation of Ni(II)–bpy aryl halide complexes and two competing pathways for the Ni(I) complexes.....	131
Figure 4.2. Spectroscopic characterization of the Ni(I)–bpy halides examined in Chapter 4.....	133
Table 4.1. Experimental <i>g</i> values for the Ni(I)–bpy halide complexes in 2-MeTHF at 5 K.....	134
Scheme 4.1. Oxidative addition reaction conducted with photogenerated Ni(I)–bpy halide.....	136
Figure 4.3. Experimental kinetic analysis of the oxidative addition reaction for 1-Cl , 2-Cl , and 3-Cl	138
Table 4.2. Rate constants for room temperature oxidative addition for the reaction between 2- <i>chloro</i> -toluene and various Ni(I)(^R bpy)X species.....	139
Figure 4.4. Hammett analysis for the reaction of 1-Cl with 4-substituted aryl chlorides.....	140
Figure 4.5. Computational analysis of the oxidative addition process of Ni(I)(^R bpy)X with 2- <i>chloro</i> -toluene.....	142
Figure 4.6. Experimental thermodynamic analysis of the dimerization reaction for 1-Cl , 2-Cl , and 3-Cl	146
Table 4.3. Thermodynamic parameters for dimerization of Ni(I)–bpy halide complexes.....	147
Figure 4.7. Computational analysis of the dimerization of Ni(I)–bpy halides.....	148
Figure 4.8. Reaction coordinate and state energy diagrams for the Ni(I)–bpy halide complexes.....	152
Figure 5.1. Photogeneration and cross-coupling reactivity of Ni(I)–bipyridine halides, the overlapping absorption of Ni(I)–bpy with Ni(II)–bpy, and schematic of pump-probe transient absorption spectroscopy.....	167
Figure 5.2. Structures and UV-vis-NIR absorption spectra of the photochemically generated Ni(I)–bpy halides in THF.....	169

Figure 5.3. Cascaded difference spectra of 1 and 5	170
Table 5.1. Lowest-energy MLCT absorption positions and relaxation time constants for all compounds studied in Chapter 5.....	172
Figure 5.4. Photochemical generation and isolation of 5'	173
Figure 5.5. Modeling excited state relaxation dynamics of Ni(I) compounds.....	177

NOMENCLATURE AND ABBREVIATIONS

2-MeTHF	2-methyltetrahydrofuran
³EnT	Triplet energy transfer
Å	Angstrom
Ac	Acetate
Ar	Aryl
BDE	Bond dissociation energy
BDFE	Bond dissociation free energy
bpy	2,2'-bipyridine
BSS	Broken-symmetry singlet
CASSCF	Complete active space self-consistent field theory
CI	Configuration interaction
COD	Cyclooctadiene
CPCM	Conductor-like polarizable continuum model
CSS	Closed-shell singlet
CW	Continuous wave
DABCO	1,4-diazabicyclo[2.2. 2]octane
d-d	Refers to a ligand field electronic transition
DFT	Density functional theory
DMF	Dimethylformamide
<i>E</i>^o	Reduction potential
EnT	Energy transfer
EPR	Electron paramagnetic resonance
<i>E</i>_s	Taft's steric parameter
ESA	Excited-state absorption
Et	Ethyl
Fc	Ferrocene
GC-MS	Gas chromatography with mass spectrometry
GSB	Ground-state bleach

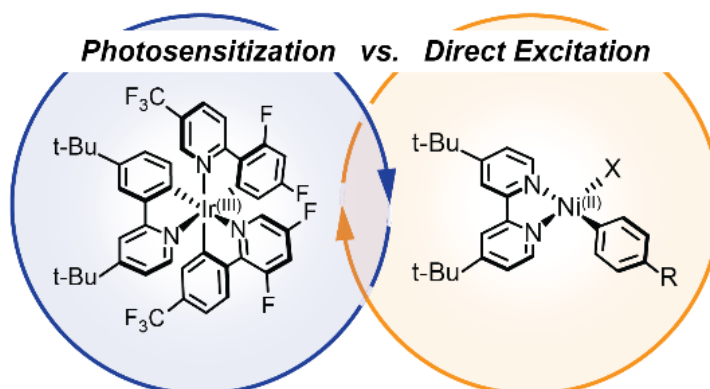
IR	Infrared
<i>k</i>	Rate constant
LMCT	Ligand-to-metal charge transfer
LUMO	Lowest unoccupied molecular orbital
MCD	Magnetic circular dichroism
Me	Methyl
MLCT	Metal-to-ligand charge transfer
NIR	Near infrared
NMR	Nuclear magnetic resonance
OAc	Acetate
PES	Potential energy surface
Ph	Phenyl
ppy	2-phenylpyridine
<i>Q</i>	Nuclear coordinate
QD-NEVPT2	Quasi-degenerate N-electron valence second-order perturbation theory
RAMO	Redox-active molecular orbital
RI	Resolution of identities approximation
RI	Resolution of identities
RIXS	Resonant inelastic X-ray scattering
RKS	Restricted Kohn-Sham formalism
RKS	Restricted Kohn-Sham formalism
<i>S</i>	Spin quantum number
SCE	Saturated calomel electrode
SCF	Self-consistent field
SET	Single electron transfer
<i>S_NAr</i>	Nucleophilic aromatic substitution
SOMO	Singly occupied molecular orbital
TA	Transient absorption
TBA	Tetrabutyl ammonium
<i>t</i>-Bu	<i>Tert</i> -butyl

TDDFT	Time-dependent density functional theory
THF	Tetrahydrofuran
TMEDA	<i>N,N,N',N'</i> -tetramethylethylenediamine
UKS	Unrestricted Kohn-Sham formalism
UV-Vis	Ultraviolet-visible
V	Volt
VT	Variable temperature
X	Halide
XRD	X-ray diffraction
Z_{eff}	Effective nuclear charge
Δ	Contextual: ligand field splitting energy or "change in"
ϵ	Molar extinction coefficient
$\langle \hbar\omega \rangle$	Average vibrational energy
λ	Contextual: wavelength in nanometers or total reorganization energy
λ_{max}	Wavelength at which the absorbance is maximized
λ_s	Solvent contribution to λ
λ_v	Vibrational contribution to λ
μ_{eff}	Effective magnetic moment
ν	Frequency (energy) in inverse centimeters
ν_{max}	Wavenumber at which the absorbance is maximized
ρ	Hammett reaction rate constant
σ_{F}	Taft's field parameter
σ_{m}	Meta-Hammett parameter
σ_{p}	Para-Hammett parameter
τ	Excited-state lifetime
Φ	Quantum yield

Chapter 1

Mechanisms of Photoredox Catalysis Featuring Nickel–Bipyridine Complexes

Review of Mechanisms of Photoredox Catalysis with Ni–bpy



▪ *Electronic Structure* ▪ *Key Considerations* ▪ *Implications*

Adapted with permission from:

Cagan, D. A.; Bím, D.; Kazmierczak, N. P.; Hadt, R. G. Mechanisms of Photoredox Catalysis Featuring Nickel–Bipyridine Complexes. *ACS Catalysis*, **2024**, Accepted.

Copyright 2024 American Chemical Society.

§1-1. Introduction

Pd-catalyzed cross-coupling reactions have transformed organic chemistry with their synthetic contributions to drug discovery and development.¹⁻³ Although subtle differences emerge between reactions, the majority of Pd-catalyzed couplings leverage a mechanism featuring dominantly two-electron processes: oxidative addition, transmetalation, and reductive elimination.⁴ Going beyond Pd, a precious metal and limited resource, significant strides have been made toward more sustainable approaches to catalysis. These advances feature critical contributions from methodology-driven research into homogenous cross-coupling catalysis by first-row transition metal complexes, which are becoming more widely adopted for enabling the construction of new C–X (X = C, O, N, F, etc.) bonds.⁵⁻⁷ Mechanistic studies highlight the complexities of these ground-state cross-coupling reactions, but also bring to light new possibilities stemming from one-electron redox processes and the variety of intermediates involved in the underlying bond-formation and bond-rupture processes.⁸

Ni-mediated catalysis has emerged as a key alternative to Pd, as it can access a range of formal oxidation and/or spin states (**Figure 1.1**) and facilitate numerous complex substrate transformations.⁹⁻¹¹ In addition to metal redox, ligand-based redox (i.e., ligand non-innocence and potential multireference character)¹²⁻¹⁵ further increases reaction complexity by providing important, yet poorly understood, electronic structure contributions. These can result in noble-metal-like reactivity in base-metal catalysts and provide a basis for transformative structure/function relationships.⁷

Metallaphotoredox catalysis has had a profound influence on many areas of organic chemistry, including cross-coupling reactions. This approach uses photosensitizers to generate metal-based intermediates that can be active in dark cycles.¹⁶⁻²² These intermediates often form due to their propensity for single electron transfer (SET).²³ Photosensitizers can additionally transfer energy to metal complexes to form reactive excited states.^{24,25} The merger of photoredox catalysis with Ni–bipyridine (bpy) complexes has claimed a prominent place in the organic, inorganic, and physical chemistry communities owing to its wide synthetic utility and rich photophysical aspects.^{20,26-32} In addition to light absorption by the

photosensitizers present in reaction mixtures (often cyclometalated Ir(III) heteroleptic complexes^{33–35}), these Ni–bpy co-catalysts also absorb strongly across the UV–vis region and can directly harvest light to access key excited states.^{22,36–40} In principle, ultrafast spectroscopic methods should be critical to studying the photophysical processes that undergird the overall chemical bond transformations.⁴¹ However, as discussed below, there are often strongly competing intramolecular excited-state relaxation pathways, and care needs to be taken to account for low quantum yield processes that can be difficult to probe directly using time-resolved spectral methods. Overall, the elucidation of mechanistic routes requires the knowledge of both light- and thermally-driven components and the interplay between them. As discussed below, this has proven to be a difficult task for light-driven, Ni-mediated catalytic cycles, and our overall understanding of how photon energy drives organic transformations is still superficial.

The aforementioned progress motivates further efforts to elucidate the geometric and electronic structures of critical inorganic species and photoinduced states that are involved in metallaphotoredox cross-coupling reactions. We believe these knowledge gaps can be addressed by a synergistic combination of synthesis, spectroscopy, and computation to define electronic structure contributions to reactivity, and we hold that there is significant general potential linked to leveraging these complexities for cross-coupling catalysis. To do so, however, significant strides need to be made toward detailed and fundamental studies of discrete light and dark reaction steps that constitute photoredox catalytic cycles. Ultimately, in concert with additional methodological studies, this understanding will help inform chemists how to leverage the inherent properties of first-row transition metals and, thus, guide academic and industrial research toward sustainable approaches for bond constructions in organic synthesis.

While previous reviews have highlighted the tremendous advancements made in the development of new photoredox-enabled transformations,^{19,20,31} this review seeks to compare and evaluate mechanisms that have been proposed in the literature, with a focus on Ni–bpy complexes. We note that additives can influence the catalytic pathway. However, mechanistic analysis of their contributions is quite limited. Thus, while potentially important

to consider, this review does not provide a complete picture of their potential mechanistic roles. Given the growing importance of ground- and excited-state processes in metallaphotoredox catalysis, the review first features a brief electronic structure primer, which discusses key aspects of different electronic states of Ni at a broadly accessible level. We subsequently provide a summary and comparison of proposed photoredox mechanisms. Divided into two main sections, we firstly summarize mechanisms featuring key photosensitization steps. Secondly, we discuss mechanisms that feature direct excitation of Ni-based species for bond-homolysis-driven dark cycle initiation or excited-state bond-formation reactions. The mechanistic summaries are further bolstered by “Key Consideration” sections designed to highlight the importance of Ni-based intermediates and their electronic structures. By doing so, we hope to 1) demonstrate the importance and need for further mechanistic studies of metallaphotoredox reactions, even beyond Ni, and 2) highlight the interdisciplinary nature of this growing area, hopefully motivating future synergistic contributions that will span the physical, organic, and inorganic chemistry communities.

§1-2. Nickel Electronic Structure Primer

Prior to embarking on our review of light-activated catalytic cycles featuring Ni complexes, it is valuable to consider the distinct electronic structures of the commonly invoked Ni intermediates. Even within a given oxidation state, such as Ni(II), disparate geometries, spin states, and ligand field strengths can lead to unique properties for different species.²² These changes have direct implications for evaluating the plausibility of ground- and excited-state reactivity, including mechanistic steps such as light harvesting, energy/electron transfer, and electrophile activation.

Nickel is most stable in the 2+ oxidation state with a d^8 electron configuration.⁴² Many stable four-coordinate Ni(II) species are known, and several feature prominent roles in the mechanisms outlined below. Given the importance of these species and their reactivity, we consider their geometric and electronic structures at length. As this review focuses on Ni–

bpy complexes, we assume that two of the four coordination sites are occupied by the bpy ligand. Charge balance requires the remaining two ligands be anionic. Common options in the context of cross-coupling include aryl and halide ligands, which could potentially be arranged in either a square planar (D_{4h}) or a pseudo-tetrahedral (T_d) geometry (**Figure 1.1**). These options are not independent of the ligand character, as described below.

In the square planar geometry, the vast majority of the σ^* character is concentrated in the $3d(x^2-y^2)$ orbital, resulting in a large ligand field splitting energy, Δ (**Figure 1.1**).⁴³ This splitting is greater than the electron-electron repulsion (i.e., spin pairing energy) incurred by having the seventh and eighth electrons occupying the same orbital (the $3d(z^2)$ orbital here). Thus, it is more energetically favorable to adopt a low-spin, $S = 0$ configuration with a doubly unoccupied $3d(x^2-y^2)$ orbital. If the ligands are rotated into a pseudo- T_d geometry, multiple nearly degenerate orbitals share the σ^* character, leading to a small Δ relative to the square planar case and a high-spin, $S = 1$ d^8 configuration. (Note that calculations of molecular orbital energies for related pseudo- T_d Ni(II) complexes suggest two main σ^* orbitals, as opposed to the three σ^* -orbitals found in a perfect tetrahedron.)^{44,45} Accordingly, population of the strongly antibonding $3d(x^2-y^2)$ orbital in the D_{4h} geometry (such as through metal-centered photoexcitation) induces a geometric rotation to the pseudo- T_d geometry to minimize the σ^* overlap.

The choice between a square planar and pseudo- T_d geometry can thus be understood as a competition between electron repulsion (spin pairing energy) and the ligand field splitting energy.⁴⁶ The D_{4h} $S = 0$ state pays the energetic penalty for pairing electrons, but it avoids populating the high-lying $3d(x^2-y^2)$ orbital and is therefore unaffected by larger values of Δ (**Figure 1.1, A and D**). On the other hand, the pseudo- T_d $S = 1$ state avoids the energetic penalty for pairing electrons in the same orbital, yet it populates both the $3d(z^2)$ and $3d(x^2-y^2)$ orbitals, which each experience an energetic disadvantage according to the magnitude of Δ (**Figure 1.1, B and C**). Accordingly, strong-field ligands favor the square planar geometry, while weak-field ligands favor the pseudo- T_d geometry.⁴⁷

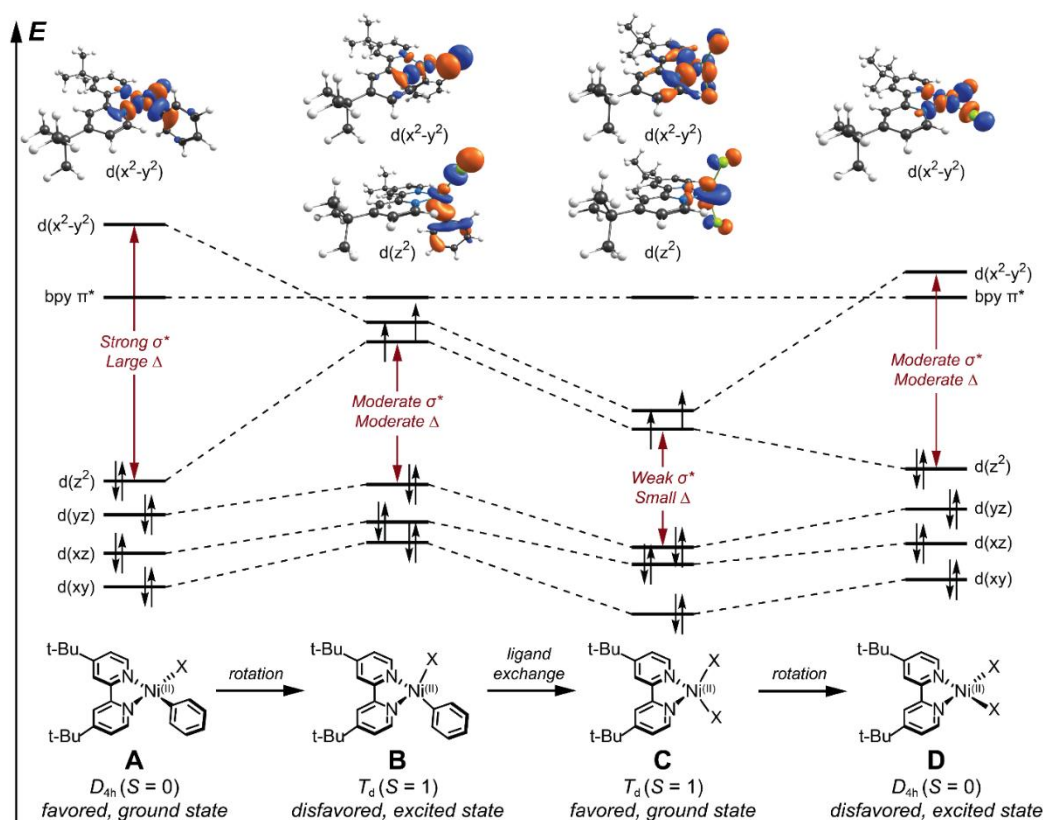


Figure 1.1. Qualitative molecular orbital correlation diagram of four Ni(II)–bpy species of potential relevance in photocatalytic pathways; each feature distinct geometric and electronic structures, ligand field splitting energies (Δ), and σ^* effects. The Ni(II)–bpy aryl halide (A) adopts a square planar (D_{4h}) geometry, leading to a diamagnetic $S = 0$ ground state. The high spin $S = 1$ geometry (B) is observed as a relaxed excited-state intermediate; population of the $3d(x^2-y^2)$ orbital induces a rotation into a pseudo- T_d geometry. Ni(II)–bpy dihalide (C) is stable as a T_d triplet ground state. For completeness, we also show this complex in a square planar geometry (D). This singlet state is energetically disfavored and yet-to-be identified to date. Select molecular orbitals (computed with density functional theory at the B3LYP/def2-TZVP^{48–50} level) are depicted at the top of the figure for illustration of σ^* effects.

Herein arises the essential difference between aryl and halide ligands. From the perspective of ligand field theory, the aryl is considered a strong-field ligand, while halides are weak-field ligands.⁵¹ As such, the gap between the σ^* orbital(s) and the remaining, lower-lying $3d$ -

orbitals will be large for a Ni(II)–bpy aryl halide species, but comparatively small for Ni(II)–bpy dihalides. For this reason, Ni(II)–bpy aryl halides feature singlet, square planar ground states, while Ni(II)–bpy dihalides feature pseudo- T_d triplet ground states. Note that pseudo-halide ligands (such as alcohols or acetates) result in similar electronic structures as halides; alkyl ligands behave as aryls, but with larger values for Δ , as they are stronger σ -donors.

For Ni(II)–bpy aryl halides vs. Ni(II)–bpy dihalides, their distinct geometries and spin states have significant implications for electron transfer in catalysis owing to the divergent energies of the redox-active molecular orbital (RAMO). For the ground-state Ni(II)–bpy aryl halide, the lowest unoccupied molecular orbital (LUMO) is not metal-based. The strong σ^* overlap of $3d(x^2-y^2)$ orbital raises its energy above the bpy π^* orbital manifold. As such, the first reduction event for Ni(II)–bpy aryl halide is observed on the bpy ligand rather than the metal.^{52,54} Reduction of the complex results in an anionic [Ni(II)–bpy⁻ aryl halide]⁻, which slowly decomposes to a three-coordinate Ni(I)–bpy aryl species.^{52,53} When the aryl ligand is replaced by a halide, the reduction in σ -donation strength and associated antibonding character leads to a significant decrease in the $3d(x^2-y^2)$ orbital energy. Furthermore, as the ground-state Ni(II)–bpy dihalide adopts a pseudo- T_d geometry, an additional stabilization in the Ni-based RAMO is expected. One-electron reduction of this complex affords a doubly occupied σ^* $3d(z^2)$ orbital, resulting in ejection of a halide to give a Ni(I)–bpy halide complex.^{55,56}

The reduction potential of the complex trends with the energy of the LUMO. In Ni(II)(^{*t*}-Bu₃bpy)(*o*-tolyl)Cl, the first reduction event is found to be -1.6 V vs. SCE, corresponding to electrochemically reversible bpy reduction. Irreversible Ni-based reduction appears at \sim -1.8 V vs. SCE⁵⁷. By contrast, the first reduction event for Ni(II)(^{*t*}-Bu₃bpy)Cl₂ is at -1.3 V vs. SCE (Ni-based and irreversible).^{55,56,58} The activity of a Ni(II) complex toward reductive steps in a catalytic cycle is dramatically influenced by ligand field strength and coordination geometry;^{54,59,60} similar considerations were also demonstrated for $S = 1$ chiral enantioselective Ni(II)–diimine dihalide cross-coupling catalysts.^{44,61,62} Ligand field analysis

of molecular orbital energies indicates the relative plausibility of various catalytic reduction events.

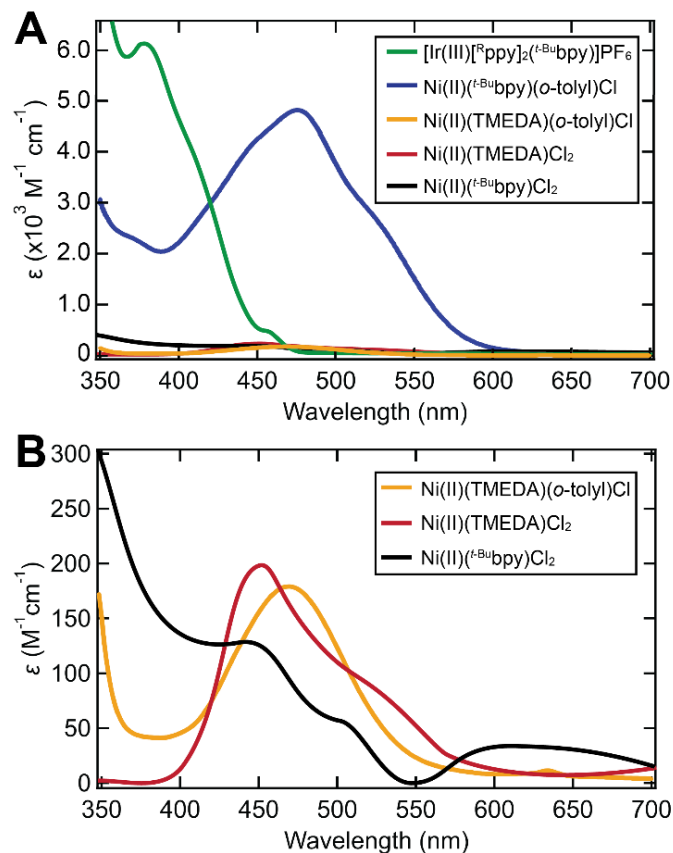


Figure 1.2. UV-vis absorption spectra of a common Ir(III) photosensitizer and various Ni complexes. (A) Strongly absorbing complexes with charge transfer bands, $[\text{Ir(III)}][^{\text{R}}\text{ppy}]_2(^{\text{t-Bu}}\text{bpy})\text{PF}_6$ (green line, R = 2-(2,4-difluorophenyl)-5-trifluoromethyl), and $\text{Ni(II)}(^{\text{t-Bu}}\text{bpy})(o\text{-tolyl})\text{Cl}$ ($S = 0$, blue line), are highlighted. (B) An expanded view of complexes with only ligand field transitions in the visible region, $\text{Ni(II)}(\text{TMEDA})(o\text{-tolyl})\text{Cl}$ ($S = 0$, orange line), $\text{Ni(II)}(\text{TMEDA})\text{Cl}_2$ ($S = 1$, red line), and $\text{Ni(II)}(^{\text{t-Bu}}\text{bpy})\text{Cl}_2$ ($S = 1$, black line). Solvent = THF. Spectra were digitized and scaled with permission from references 36, (Copyright 2018 American Chemical Society) 38 (Copyright 2022 American Chemical Society), 65 (available under a CC-BY NC 3.0 Deed license, copyright 2024 Bryden and Zysman-Colman), 66 (Copyright 2016 John Wiley and Sons) and 67 (Copyright 2020 American Chemical Society).

In addition to redox potentials, the geometric and electronic structures of Ni–bpy complexes determine their light-harvesting ability through the molar absorption coefficients of the UV–vis transitions. As a ligand with a significant π -conjugation, the bpy possesses low-lying π^* -orbitals capable of backbonding with the metal center. These bpy orbitals serve as acceptors for metal-to-ligand charge transfer (MLCT) transitions in the visible absorption spectrum and possess significant electron delocalization, leading to a large transition dipole moment. Replacement of the bpy ligand for aliphatic *N,N,N',N'*-tetramethylethylenediamine (TMEDA) exemplifies this point, where only ligand field bands become possible, leading to reduced values of ϵ (Figure 2).^{38,63,64,66} Ni(II)–bpy aryl halide complexes exhibit MLCT transitions (350 nm–550 nm) that possess molar extinction coefficients of comparable magnitude as iridium photosensitizers ($\epsilon = 10^3$ – 10^4 M⁻¹ cm⁻¹),^{36,38,65,67} rendering these Ni(II) species competitive for photocatalytic light harvesting. Ni(II)–bpy dihalide complexes show orbitally-forbidden ligand field transitions in the visible to near-infrared region with $\epsilon = 10^1$ – 10^2 M⁻¹ cm⁻¹ (Figure 1.2).³⁶

Similar analyses may be conducted for other oxidation states. Three-coordinate Ni(I) complexes adopt an approximately planar geometry; while the $3d(x^2-y^2)$ σ^* interaction is somewhat lessened due to the loss of fourfold symmetry and consequent orbital overlap, there nonetheless remains a large energetic separation between the $3d(x^2-y^2)$ orbital and the remainder of the $3d$ -manifold due to σ^* interactions with the bpy and π^* interactions with the halide. The d^9 Ni(I) configuration implies single occupation of the high-energy σ^* -orbital; however, this is tolerated, and such Ni(I) compounds have been characterized.^{54,56,68} However, further reduction of Ni(I) to Ni(0) requires the introduction of an additional electron into the destabilized σ^* $3d(x^2-y^2)$ orbital. The reduction potentials for such an event are thought to be high, and it is unclear whether Ni(0) is catalytically accessible^{69,70} (see Reductive SET mechanism below). Indeed, Ni(0)–bpy cyclooctadiene (COD) exhibits a large degree of bpy ligand redox non-innocence and is proposed to exist as Ni(I)(bpy⁻)(COD).⁷¹ Interestingly, Ni(I)–bpy halide complexes exhibit MLCT transitions across a wide wavelength range (350 nm–1400 nm) and have molar extinction coefficients

of equal or greater magnitude than Ni(II)–bpy aryl halides, marking yet another competitive light-harvesting species in photocatalytic cycles.⁵⁶

§1-3. Summary and Comparisons of Proposed Photoredox Mechanisms

Key consideration sections are provided for each of the mechanisms summarized herein, with the goal of connecting these considerations to experimental observations that are emphasized across all Ni–bpy-based photoredox mechanisms, both in terms of direct excitation and photosensitization.

§1-3.1. Photosensitization

§1-3.1.1. Reductive SET

The first metallaphotoredox reactions using light-activated nickel were reported independently in 2014 by the groups of Molander²⁹ and Doyle and MacMillan,³⁰ where C(sp²)–C(sp³) cross-couplings were discovered in reactions combining Ni(0)–bpy, an Ir(III) photosensitizer, and organic coupling partners. The reaction scope was further extended to C(sp²)–C(sp²) and C(sp³)–C(sp³) couplings in 2015 and 2016, respectively,^{72–74} then for the activation of aliphatic C–H bonds in 2018,⁷⁵ and to alkyl chloride substrates in 2019⁷⁶ and 2020;⁷⁷ enantioselective cross-coupling was seen a year later.⁷⁸ Based on a thermodynamic redox potential argument, it was speculated that the iridium excited state, *Ir(III), carried out two separate SET events. This mechanism is termed “Reductive SET” herein, as the first (and only) proposed interaction between iridium and nickel is a reduction of Ni(I) to Ni(0) (**Figure 1.3**).

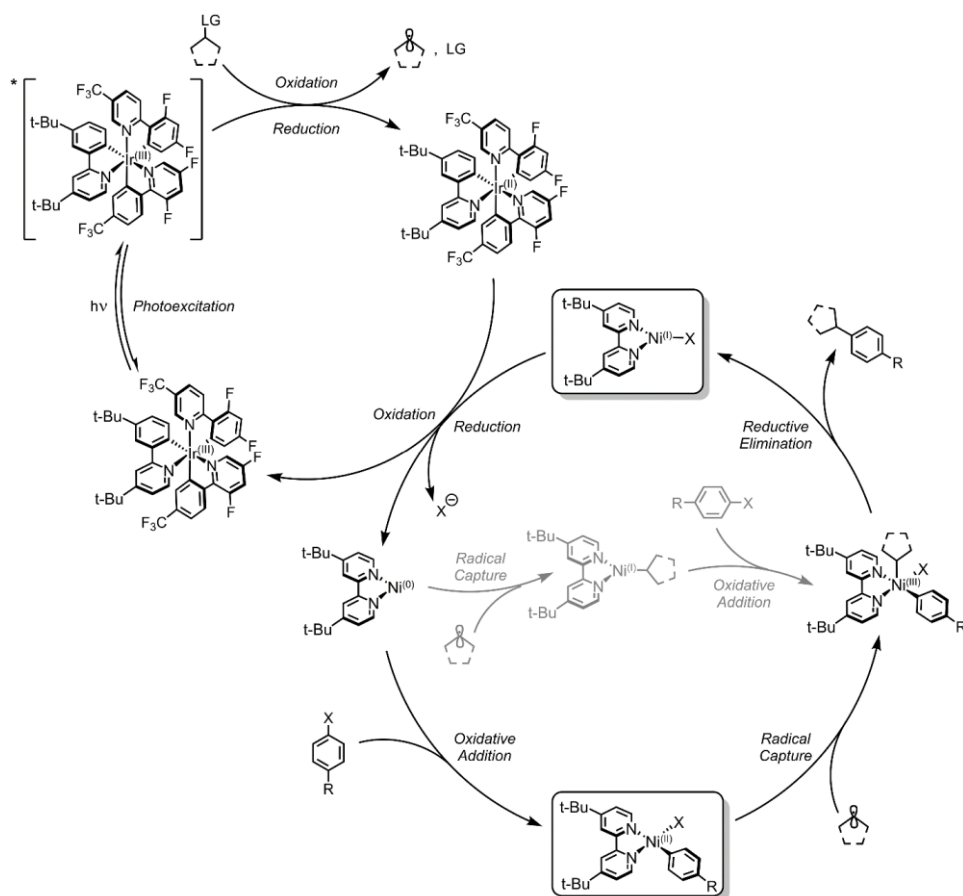


Figure 1.3. Proposed Reductive SET mechanism. C(sp²)-C(sp³) coupling is presented as a representative example. LG = leaving group.

In the Reductive SET mechanism, the Ir(III) photosensitizer is the sole excited-state active species. In one SET, $^*Ir(III)$ oxidizes the alkyl coupling partner, affording C(alkyl) $^{\bullet}$ and Ir(II). In another SET, Ir(II) reduces a Ni(I)-bpy halide complex (top box, **Figure 1.3**) to Ni(0)-bpy, which can undergo oxidative addition with an aryl halide to generate a square-planar ($S = 0$) Ni(II)-bpy aryl halide complex (bottom box, **Figure 1.3**). This Ni(II) complex captures the $^*Ir(III)$ -generated alkyl radical, and the resultant pentacoordinate Ni(III) species undergoes reductive elimination to form a Ni(I)-bpy halide and the C(sp²)-C(sp³) cross-coupled product. The cycle continues upon further reduction of Ni(I)-bpy halide by Ir(II) to Ni(0)-bpy and Ir(III).

§1-3.1.2. Key Considerations for the Reductive SET Mechanism

1. Ir(III) acts as the sole light-harvesting species. This is a critical point for any photoredox cycle featuring multiple intermediates that could absorb photons with energies matching those of the irradiation source. For example, Ni(II)–bpy aryl halide complexes (bottom box, **Figure 1.3**) are now known to be photoactive in C(sp²)–C(sp³) cross-coupling upon direct excitation via a Ni(II)–C(aryl) to Ni(I) + C(aryl)^{*} bond homolysis step.^{36–38,79} Even a small amount of photogenerated Ni(I) through this alternative step may be sufficient to catalyze the reaction. These examples are discussed in **Section §1-3.1.9**. Importantly, both the Ir photosensitizer and the Ni(II)–bpy aryl halide complexes absorb light in the visible region with molar extinction coefficients of 10³ M⁻¹ cm⁻¹ (**Figure 1.2**). The molar absorptivities of the various Ni intermediates possible in the reaction cycle are largely unknown.

2. *Ir(III) is sufficiently oxidizing to react with alkyl substrates, doing so preferentially. Redox interactions between *Ir(III) and substrate can be probed through electrochemical measurements and the oxidation state of the Ir complex tracked by absorption spectroscopy. Interactions between *Ir(III) and species in solution other than the organic substrate, including any Ni complexes in the putative cycle, are possible and should be evaluated. For example, the alkyl substrates used in the abovementioned work have accessible oxidation potentials of ~ 1 V versus SCE,^{29,30,80} but these neighbor the oxidation potential of Ni(II)–bpy aryl halide (~ 0.8–0.9 V versus SCE). As will be seen below, related interactions between *Ir(III) and Ni complexes are invoked in the Oxidative SET mechanism (**Section §1-3.1.3**). Furthermore, both SET and triplet energy transfer (³EnT) are possible from *Ir(III) to Ni(II),⁸¹ further complicating analyses (see **Sections §1-3.1.3** and **§1-3.1.7**).

3. Ni(0)–bpy undergoes oxidative addition, while Ni(I)–bpy halide does not. Both Ni(0) and Ni(I) can undergo oxidative addition with aryl halides. However, Ni(I)–Ni(III) oxidative addition would divert the proposed Reductive SET mechanism from Ni(0)–Ni(II) oxidative addition. The reactivity of Ni(0) and Ni(II) vs. Ni(I) and Ni(III) are distinct. Furthermore, the presence of Ni(I) and Ni(III) can lead to facile comproportionation to *S* = 0 Ni(II)–bpy aryl halide and *S* = 1 Ni(II)–bpy dihalide,⁸² another chemically distinct species that is not

considered in this mechanism but is important for others (**Section §1-3.1.9**). Additionally, Oderinde, Johannes, and coworkers noted the reduction potential of Ir(II) is scarcely able to reduce various Ni(I) complexes, finding their potentials to be similar ($[\text{Ir}^{\text{III}}/\text{Ir}^{\text{II}}] = -1.37 \text{ V vs. SCE}$, $[\text{Ni}^{\text{I}}/\text{Ni}^{\text{0}}] = -1.41 \text{ V vs. SCE}$), and that Ni(0) is ineffective to turn over the cycle.⁶⁹ Further disfavoring Ni(0), Gutierrez, Martin and coworkers found that Ni(II)–bpy dihalide complexes engage in rapid, facile comproportionation with Ni(0)–bpy species in solution, affording Ni(I)–bpy halide species.⁸³ However, Plasson, Fensterbank, Grimaud and coworkers argued that Ni(0) is indeed a vital source of Ni(II)–bpy aryl halide,⁸⁴ and Bahamonde and coworkers argued that oxidative addition to Ni(0) outcompeted the comproportionation reaction, supporting an Oxidative SET mechanism, though ³EnT pathways were not discarded⁸⁵ (see **Section §1-3.1.7**). Altogether, the requirement of Ni(0) for catalytic cycle turnover is still debated.

4. Alkyl radicals are preferentially captured by Ni(II), not Ni(0). Given that Ni(0) and Ni(II) complexes are present in the proposed mechanism, a comparison between the relative rates of radical capture by both of these species would help confirm the Ni(II) to Ni(III)–alkyl hypothesis. Computations by Molander, Kozlowski, and coworkers suggest both oxidation states should be productive toward radical capture.⁸⁶ While kinetic analysis for radical capture at Ni(II) was recently reported ($k = 10^6\text{--}10^7 \text{ M}^{-1} \text{ s}^{-1}$)⁸⁷, we are unaware of studies for C(alkyl)• capture by Ni(0).

5. Ir(II) is sufficiently reducing to regenerate Ni(0) and Ir(III). The presence of Ir(II) presupposes that Reductive SET is indeed operative (see point 2 above). Given the highly reducing nature of Ir(II), one must also consider its potential interaction with Ni(II) and Ni(III). Reduction of Ni(II) to Ni(I) would present an alternative mechanistic route, potentially favoring a Ni(I/III) catalytic cycle (see point 3). Additionally, Neurock, Minter, Baran, and coworkers reported that pentacoordinate Ni(III) complexes are readily reduced to Ni(II) via Ni–X heterolysis.⁵⁵ It is possible the Ni(III) species could be intercepted by Ir(II) prior to reductive elimination and thereby be diverted from the cycle making C(sp²)–C(sp³) bonds. Again, relative reactivity rates between Ir(II) and the relevant Ni species would prove invaluable for mechanistic insight.

There have been limited experimental mechanistic studies conducted on this reaction, but one notable example is the work by Lloyd-Jones and coworkers in 2022.⁸⁸ Careful kinetic analysis using radiolabeled substrates and ¹³C NMR identified the Ni(II)–bpy aryl halide as a genuine intermediate. From the kinetic modeling, three plausible mechanisms were proposed for the reaction, including one which is akin to the Reductive SET mechanism illustrated above. Interestingly, this mechanistic possibility was the only one of the three the researchers were able to rule out. The remaining two mechanisms proposed by Lloyd-Jones and coworkers centered around *Ir(III) promoting a photoinduced Ni–halide bond homolysis step, referred to here as “Photosensitization for Homolysis” (see **Section §1-3.1.5**). However, the three mechanisms considered therein are not an exhaustive list, as noted by the authors.⁸⁸ *Nonetheless, based on these considerations and the recent kinetics study, the initially proposed Reductive SET mechanism is unlikely operative.* Additional detailed experimental studies are necessary, however, particularly addressing the five points outlined above.

§1-3.1.3. Oxidative SET

The expansion of dual Ni/Ir metallaphotoredox reactions to C(sp²)–X coupling led to an additional mechanistic hypothesis, Oxidative SET, as proposed for C(sp²)–N coupling by Jamison and coworkers in 2015⁸⁹ and C(sp²)–O/N coupling by MacMillan and Buchwald and coworkers^{28,90} in 2015 and 2016, respectively. In the Reductive SET mechanism for C–C bond coupling, Ir(II) interacted with a Ni(I)–bpy halide complex, reducing it by one electron in a dark reaction. Keeping with the naming convention adopted herein, the Oxidative SET mechanism features a SET wherein *Ir(III) oxidizes a Ni(II)–bpy aryl alkoxide complex (right box, **Figure 1.4**), leading to a Ni(III) species and Ir(II). As in Reductive SET, the Ir(III) complex acts as the sole excited-state active species in Oxidative SET. Ir(II) reduces a Ni(I)–bpy halide species to generate Ni(0)–bpy, which undergoes oxidative addition of an aryl halide coupling partner to form a Ni(II)–bpy aryl halide species (bottom box, **Figure 1.4**). Ligand substitution of the alcohol (or amine) via the assistance of exogenous base generates the aforementioned four-coordinate, square-planar Ni(II)–bpy aryl

alkoxide (right box, **Figure 1.4**). The critical chemical impetus behind this mechanism is the Ni(III)-promoted reductive elimination of the C–X product, akin to the one-electron oxidation chemistry developed by Hillhouse and coworkers.^{91,92} Initial reports founded this reaction scheme on the basis of redox potentials and reductive elimination thermodynamics for Ni(II) vs. Ni(III).

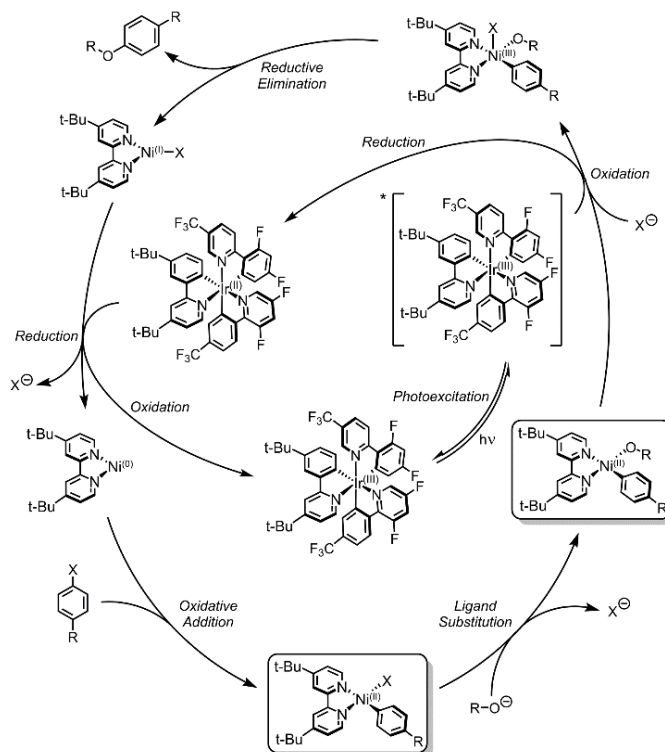


Figure 1.4. Proposed Oxidative SET mechanism. C(sp²)-O coupling (alcohols) is shown as a representative example.

§1-3.1.4. Key Considerations for the Oxidative SET Mechanism

1. Ni(II)-bpy aryl alkoxide is the SET partner with *Ir(III). While oxidation of the Ni(II)-bpy aryl alkoxide species to formal Ni(III) may be necessary to drive reductive elimination, there are additional Ni species present, including the Ni(II)-bpy aryl halide complex. It is currently unclear why *Ir(III) would preferentially oxidize one and not the other. Additionally, if Ir(II) is competent for the reduction of Ni(I) to Ni(0), why either of

these Ni(II) species is not also reduced presents an open question. As demonstrated by Diao and coworkers, electrochemical reduction of Ni(II)–bpy aryl halide to Ni(I)–bpy aryl represents an important step in alternative cross-coupling mechanisms.⁵² Indeed, through electrochemical and computational mechanistic analysis, Oderinde and coworkers presented an alternative mechanism wherein Ni(II)–bpy aryl halide is reduced by Ir(II) to form Ni(I)–bpy aryl.⁵³ This reduction was also suggested to be important through computations by Molander, Gutierrez, and coworkers.⁹³ Thus, there may be additional, alternative routes aiding in or solely responsible for the production of cross-coupled product. Mechanistic analyses of these discrete steps, particularly those involving key interactions between Ir and Ni, are needed.

2. The proposed cycle rests on Ni(0)–bpy/Ni(II)–bpy aryl halide as the starting source of nickel. While Oxidative SET features Ni(0)–bpy to Ni(II)–bpy aryl halide oxidative addition, Buchwald, MacMillan, and co-workers also find that beginning with high-spin ($S = 1$) Ni(II)–bpy dichloride is suitable for the transformation.⁹⁰ Indeed, the substrate scope and product yields are all achieved using this NiCl₂ starting species, not Ni(0). *This switch in Ni precursor presents a dilemma, namely that the electronic structure, redox potential, and behavior of high-spin Ni(II)–bpy dihalide vary considerably compared to the low-spin Ni(II)–bpy aryl halide that arises from Ni(0).* Little-to-no experimental mechanistic analysis on this reaction beginning with Ni(0) has been reported.⁹⁴

Detailed follow-up work was done on this reaction by Nocera and coworkers⁹⁵ to interrogate the cycle beginning with Ni(II)–bpy dihalide, and their analysis argued against the Oxidative SET mechanism (see SET for Active Ni(I)). Furthermore, in the closely related C(sp²)–O cross-coupling of aryl–acetate substrates,⁹⁶ a ³EnT mechanism was favored over Oxidative SET by experimental mechanistic work.⁹⁷ We therefore find it plausible that either the Oxidative SET mechanism is not operative for C(sp²)–X coupling, or it is only operative when beginning with a Ni(0)–bpy/Ni(II)–bpy aryl halide precursor combination—a pathway still underexplored mechanistically. The electronic structure of the Ni precursor is non-trivial for dictating the mechanistic pathway for catalysis (see **Section §1-2**).

§1-3.1.5. Photosensitization for Homolysis (SET vs. ^3EnT)

Two versions of the Photosensitization for Homolysis mechanism were invoked by concurrent works in 2016, one by Doyle, Shields and coworkers⁵⁷ and another by Molander and coworkers.⁹⁸ The two studies identified a simplified version of a $\text{C}(\text{sp}^2)\text{--C}(\text{sp}^3)$ coupling reaction that no longer required an easily oxidized alkyl coupling partner for C^\bullet generation. Instead, the groups found ethereal solvent (THF) to be a suitable $\text{C}(\text{sp}^3)$ source. The two versions of the Photosensitization for Homolysis mechanism are shown below, one involving SET (**Figure 1.5**), another ^3EnT (**Figure 1.6**).

The original SET mechanism of Doyle, Shields, and coworkers⁵⁷ involves oxidative addition of an aryl halide coupling partner to $\text{Ni}(0)\text{--bpy}$, affording $\text{Ni}(\text{II})\text{--bpy}$ aryl halide. Rather than engaging an organic substrate, $^*\text{Ir}(\text{III})$ oxidizes this $\text{Ni}(\text{II})$ complex to a four-coordinate, cationic $[\text{Ni}(\text{III})\text{--bpy aryl halide}]^+$ species and $\text{Ir}(\text{II})$. $\text{Ir}(\text{III})$ is no longer the primary light-absorber in this mechanism. Here the $\text{Ni}(\text{III})$ intermediate must undergo photon absorption as well, which promotes halide-to- $\text{Ni}(\text{III})$ ligand to metal charge transfer (LMCT). This electron excitation populates a $\text{Ni}(\text{III})\text{--X}$ antibonding orbital, resulting in an excited-state bond homolysis, ejection of an in-cage X^\bullet , and formation of a three-coordinate $\text{Ni}(\text{II})\text{--bpy}$ aryl species. Note this step is analogous to the excited-state bond homolysis for isolable $\text{Ni}(\text{III})$ trihalide species,^{99,100} wherein the apical $\text{Ni}(\text{III})\text{--X}$ bond cleaves due to a dissociative LMCT excited-state potential energy surface (PES). The X^\bullet abstracts a hydrogen atom from neighboring ethereal solvent (THF in this case), generating an in-cage C^\bullet and HCl . The C^\bullet is captured by the three-coordinate $\text{Ni}(\text{II})\text{--bpy}$ aryl species, resulting in the formation of the cationic $[\text{Ni}(\text{III})\text{--bpy aryl alkyl}]^+$ complex (upper left box, **Figure 1.5**). Rapid reductive elimination follows, affording $\text{C}(\text{sp}^2)\text{--C}(\text{sp}^3)$ coupled product and $\text{Ni}(\text{I})\text{--bpy}$. $\text{Ir}(\text{II})$ reduces this $\text{Ni}(\text{I})$ species to $\text{Ni}(0)\text{--bpy}$, returning $\text{Ir}(\text{III})$.

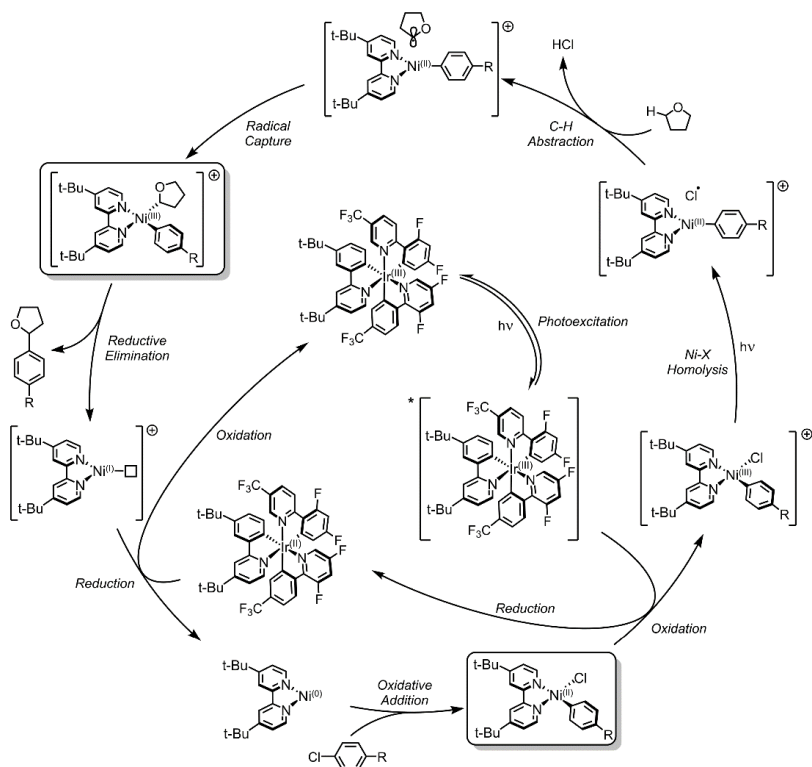


Figure 1.5. Proposed Photosensitization for Homolysis Mechanism (Doyle, Shields).⁵⁷

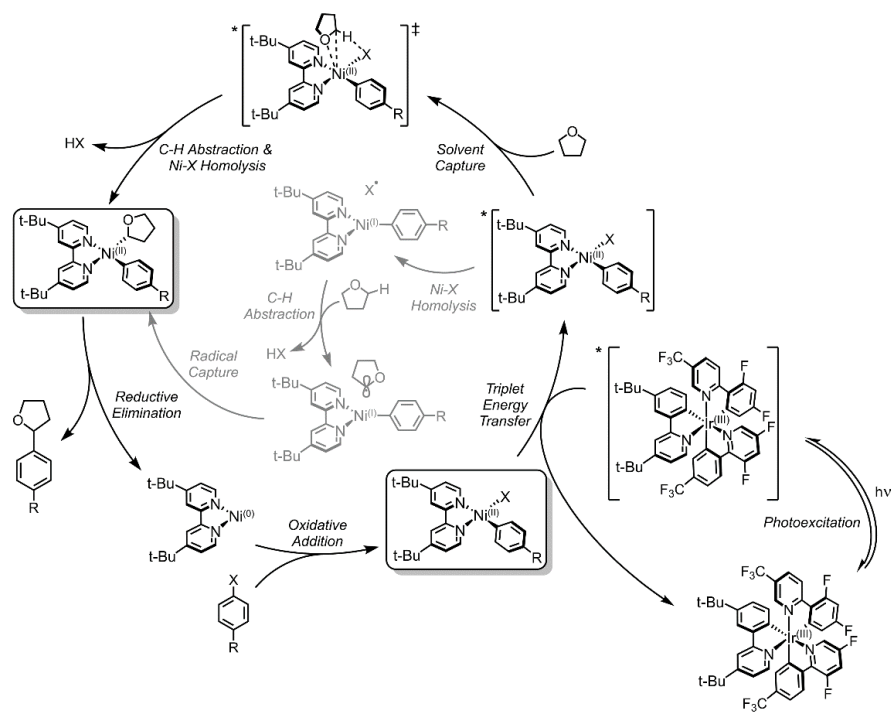


Figure 1.6. Proposed Photosensitization for Homolysis Mechanism (Molander).⁹⁸

Molander and coworkers⁹⁸ proposed a related catalytic cycle featuring the same Ni(0) to Ni(II) oxidative addition (bottom of **Figure 1.6**). However, instead of undergoing subsequent SET, the Ni(II)–bpy aryl halide acts as a ³EnT acceptor from *Ir(III). Thus, in this mechanism, Ir(III) is again the sole light-harvesting species. Upon photosensitization, excited *[Ni(II)–bpy aryl halide] can follow either stepwise out-of-cage or concerted in-cage Ni–X bond homolysis and alkyl solvent capture. The product of either process is a Ni(II)–bpy aryl alkyl species (left box, **Figure 1.6**), which undergoes thermal reductive elimination to yield the aryl–alkyl coupled product and Ni(0).

§1-3.1.6. Key points of the Photosensitization for Homolysis Mechanisms

1. In addition to Ir(III), a Ni–bpy aryl halide species also absorbs light. While the cycle in **Figure 1.6** requires photon absorption by Ir(III), additional mechanistic analysis has found that direct irradiation of the reaction mixture with high-energy light (290–315 nm) without the Ir(III) complex also yields the desired cross-coupled product.⁹⁸ Relatedly, the cycle in **Figure 5** necessitates additional photon absorption by a Ni(III) complex in the cycle. As such, identifying 1) the relative absorption cross-sections and 2) the resulting quantum yields of ensuing processes for the Ir(III), Ni(II)–bpy aryl halide, and cationic [Ni(III)–bpy aryl halide]⁺ species is imperative for evaluating these potential mechanistic pathways. Furthermore, oxidation of Ni(II)–bpy aryl halide has been demonstrated to rapidly afford the aryl halide substrate.³⁶ The proposed intermediacy of a [Ni(III)–bpy aryl halide]⁺ species is therefore critical. In order for this species to avoid reduction by iridium or aryl halide reductive elimination, it must 1) remain stable in room-temperature solution long enough to outcompete Ir(III) as a light-harvesting species and 2) have an LMCT within the energy range of the excitation source. The Ir(III) complex has a near unity quantum yield ($\Phi = 1$) for *Ir(III) formation,^{34,67,101} which can react through near-diffusion-controlled quenching with Ni(II)–bpy aryl halide ($k_q = 10^9 \text{ M}^{-1} \text{ s}^{-1}$)^{57,95} to regenerate ground-state Ir(III); both *Ir(III) and Ir(II) are thermodynamically suitable reductants for Ni(III).

2. *Ir(III) can undergo SET or ³EnT with Ni(II)–bpy aryl halides. Determination of whether *Ir(III) facilitates SET, ³EnT, or both when combined with Ni(II)–bpy aryl halide is

at the core of the Photosensitization for Homolysis mechanisms shown in **Figures 1.5-1.6**.

It is evident from Stern–Volmer analysis that Ni(II)–bpy aryl halide complexes do quench $^3\text{Ir(III)}$ excited states (*vide supra*), but the mechanism of quenching is still undetermined.

Reports by MacMillan, Scholes, and coworkers on Ni(II)–bpy aryl acetate complexes favor ^3EnT over reductive SET,⁹⁷ but it is possible that halide to acetate ligand exchange sufficiently alters the electronic structure of the compound to favor one mechanism vs. another. Mechanism switches have been reported for Ni(II)–polypyridyl complexes upon halide to acetate ligand substitution.⁸³ Moreover, reduced reactivity was observed by Molander and coworkers when employing strongly oxidizing photocatalysts that were unproductive for ^3EnT ,⁹⁸ a result that contrasts the good product yields observed by MacMillan and coworkers when using an external chemical oxidant in place of the photosensitizer.⁹⁷ Beginning with Ni(0) and aryl halide, Rueping and coworkers¹⁰² proposed a similar mechanism to that proposed by Molander and coworkers (**Figure 1.6**). In this case, strongly oxidizing photocatalysts also did not provide good product yields, but neither did direct excitation of the independently synthesized Ni(II)–bpy alkyl bromide complex. Notably, no direct evidence for Ni–X homolysis was provided in this work.

In related reports, Ni(II)–bpy acyl chlorides were examined by Shibasaki and coworkers¹⁰³ in 2017; they found photosensitizers with high triplet energies and low oxidizing power alone gave good product yields (favoring ^3EnT Photosensitization for Homolysis). However, Paixão, König and coworkers¹⁰⁴ surmised that beginning with a high-spin Ni(II)–bpy dihalide precursor gave entry via SET into the Photosensitization for Homolysis mechanism (**Figure 1.5**) and not the ^3EnT pathway (**Figure 1.6**). Notably, alternative routes have been demonstrated for the combination of Ni(II)–bpy dihalide and photocatalyst. *Therefore, the electronic structure of the receiving low-spin Ni(II)–bpy complex is susceptible to changes by both ligands, the aryl and the halide, and it is possible that high-spin Ni(II)–bpy dihalide precursors can enter into a variety of pathways upon photosensitization.* One should take care when extending mechanistic analysis of one Ni complex to even seemingly similar ones. Careful experimental electronic structure-centered analysis on the mechanism of excited-state quenching between Ni(II)–bpy aryl halide and $^*\text{Ir(III)}$ is still needed.

3. Halide radicals are photogenerated. Mechanisms outlined in **Figure 1.5-1.6** both rest on a critical Ni–X bond homolysis induced via the photosensitizer, either through SET or ^3EnT . Kinetic isotope effect measurements supported the generation of radicals, with halide radicals being favored over aryl radicals by Doyle, Shields, and coworkers.^{57,105} Evidence of aryl radical generation upon direct excitation of Ni(II)–bpy aryl halide complexes has also been provided on numerous accounts (pathway discussed in **Section §1-3.2.1**). Evans–Polanyi analysis conducted on the Photosensitization for Homolysis pathway by Doyle and coworkers in 2018 determined an α -value of 0.44,¹⁰⁶ near that for the proposed Cl^\bullet ($\alpha_{\text{Cl}} = 0.45$), but also near CH_3^\bullet ($\alpha_{\text{CH}_3} = 0.45$), and H^\bullet ($\alpha_{\text{H}} = 0.43$)¹⁰⁷; the $\alpha_{\text{C}_6\text{H}_5}$ value is unknown. Discrete experiments using Ni(II)–bpy aryl halide in conjunction with chemical oxidant and light source found that 1) the dehalogenated arene, Ar–H, is produced in 40% yield, 2) the direct reductive elimination product, Ar–X, is produced in 12% yield, 3) the solvent-aryl cross-coupled product is produced in 7% yield, and 4) the bis-aryl is produced 2% yield.³⁶ These values, in particular the large amounts of Ar–H, are suggestive of aryl radical generation, not halide radicals. These disparate conclusions call for more detailed work to evaluate these proposed mechanisms.

4. Reductive elimination proceeds from a Ni–bpy aryl alkyl species. In **Figure 1.5**, cross-coupled product is the result of reductive elimination from an oxidized $[\text{Ni(III)–bpy aryl alkyl}]^+$ complex. Indeed, reductive elimination from more highly oxidized Ni complexes is well established.^{91,92} However, the direct Ni(II)–Ni(0) reductive elimination in **Figure 1.6** is less common. Stable Ni(II)–bpy aryl alkyl complexes have been synthesized and isolated by Park and coworkers; reductive elimination does not proceed under irradiation or at elevated temperatures (75 °C).^{108,109} Thus, it remains unclear whether Ni(II)–Ni(0) $\text{C}(\text{sp}^2)\text{–C}(\text{sp}^3)$ reductive elimination is thermodynamically feasible near room temperature.

We note that, shortly before finalizing this Review, a mechanistic study by Doyle and coworkers¹¹⁰ was deposited to the ChemRxiv preprint server. In this detailed work, the authors revisit the abovementioned 2016 proposals, finding that 1) ^3EnT from $^*\text{Ir(III)}$ to Ni(II)–bpy aryl halide promotes reductive elimination of the aryl halide. 2) Direct light absorption by a Ni(II)–bpy aryl halide complex affords an aryl radical and Ni(I)–bpy halide;

photohalogen elimination from the Ni(II) complex is not favored. 3) In addition to aryl radical generation, excitation of the Ni(II) complex likely also facilitates excited-state reductive elimination of the aryl halide to afford Ni(0)–bpy. 4) *In situ* oxidation to [Ni(III)–bpy aryl halide]⁺ immediately releases the aryl halide at room temperature. However, at cryogenic temperatures, the Ni(III) species persists long enough to absorb an additional photon, again ejecting an aryl radical and not the halogen, in agreement with previous computational work.¹⁴ 5) C(sp²)–C(sp³) reductive elimination from a Ni(II)–bpy aryl alkyl species is faced with a substantial room temperature barrier of ~25 kcal mol⁻¹. However, absorption of high energy light (390–470 nm) by this complex promotes the formation of aryl–alkyl product. This mechanistic work illustrates the importance of thorough experimental consideration of each step in proposed mechanistic cycles, such as those presented in the Key Points highlighted above.

§1-3.1.7. Triplet Energy Transfer (³EnT)

In 2017, McCusker, MacMillan and coworkers demonstrated C(sp²)–O cross-coupling of aryls and carboxylic acids;⁹⁶ product yields correlated with the ³EnT ability of the photocatalyst, not its oxidizing potential, a result that argued against the Oxidative SET mechanism outlined in **Figure 1.4**. Rather, a ³EnT mechanism was proposed (**Figure 1.7**).

The ³EnT mechanism also features oxidative addition of the aryl halide to Ni(0)–bpy to form a Ni(II)–bpy aryl halide species (left box, **Figure 1.7**). Base assisted ligand substitution generates a Ni(II)–bpy aryl acetate species (bottom box, **Figure 1.7**). The Ir(III) complex acts as the primary light-absorbing species to form *Ir(III). This excited state is quenched by the Ni(II)–bpy aryl acetate complex through Dexter EnT ($k_q = 10^9 \text{ M}^{-1} \text{ s}^{-1}$ by Stern–Volmer analysis)^{95,98} affording ground-state Ir(III) and an excited-state Ni(II) complex, *[Ni(II)–bpy aryl acetate]. Reductive elimination was proposed to occur from a Ni(II)-based ligand field excited state, resulting in C(sp²)–O cross-coupled product and Ni(0)–bpy.

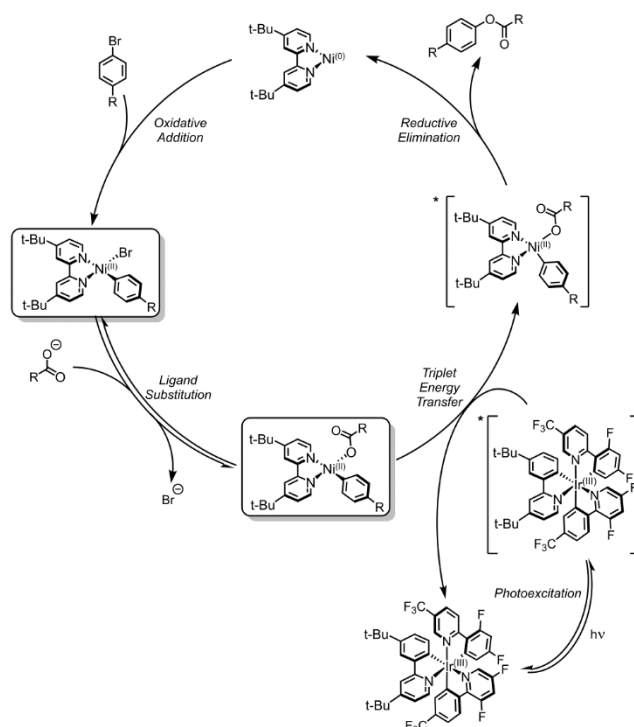


Figure 1.7. Proposed ^3EnT Mechanism. $\text{C}(\text{sp}^2)\text{-O}$ coupling (carboxylic acids) coupling is shown as a representative example.

§1-3.1.8. Key Components of the ^3EnT Mechanism

1. Ir(III) is the primary light-harvesting species, but potentially not the only one. While it is clear from Stern–Volmer analysis that the Ni(II)–bpy aryl acetate quenches $^*\text{Ir(III)}$, excitation without the photosensitizer also results in cross-coupled product (albeit with slower kinetics under the given conditions).⁹⁶ Furthermore, the precursor Ni(II)–bpy aryl halide species also absorbs light;³⁷ direct excitation of Ni(II)–bpy aryl halide in the presence of cross-coupling partners is productive for C–O bond formation (discussed in **Section §1-3.2.2**),^{36,79} marking at least three distinct light-harvesting species present in the reaction mixture (**Figure 1.2**). It is unclear if one or more mechanisms are operative. However, given the photosensitizer’s high absorption cross-section and quantum yield for $^3\text{Ir(III)}$ formation,¹⁰¹ its excitation may be dominant.

2. ^3EnT , not SET, is the dominant mechanism promoting photosensitized cross-coupling reactions. The proposed divergence away from SET to favor ^3EnT for $\text{C}(\text{sp}^2)\text{-O}$

coupling seems contingent upon the presence of the Ni(II)–bpy aryl acetate species.¹¹¹ Previous reports favored SET to the Ni(II)–bpy aryl halide precursor (*vide supra*, **Section §1-3.1.3**). However, several observations support ³EnT from *Ir(III) to the Ni(II)–bpy aryl acetate species: 1) the lack of reactivity with a chemical reductant, 2) a ³EnT threshold for product yield of ~40 kcal mol⁻¹, 3) product generation upon direct excitation of the Ni complex alone, and 4) an inverse correlation between product and oxidizing power of the photocatalyst.⁹⁶ Furthermore, computational analysis by Chen and coworkers¹³ and follow-up ns transient absorption studies on C(sp²)–O coupling reactivity by MacMillan, Scholes, and coworkers⁹⁷ demonstrated additional support for the ³EnT mechanism, although in the latter, chemical oxidant was still effective for product yield. Recent work by Oderinde, Hudson, and coworkers finds that a series of organic ³EnT photosensitizers are also competent photocatalysts for C(sp²)–O esterification reactions when used in combination with Ni(II)–bpy aryl acetate species.¹¹² *It may be the case that both the aryl halide and aryl acetate complexes undergo ³EnT with *Ir(III), but only in the case of the aryl acetate is it irreversible and productive for catalysis.*

The aryl halide coupling partner has also been implicated as redox non-innocent. Pieber, Seeberger, and coworkers¹¹³ conducted a kinetic analysis of the aryl–acetate C(sp²)–O coupling presented by McCusker, MacMillan and coworkers in 2017, but they began with Ar–I instead of the Ar–Br substrates. Evidence supported rapid SET from *Ir(III) to Ar–I; this off-cycle electron transfer, which resulted in a dehalogenated Ar–H product, was said to be involved in turnover-limiting oxidative addition of the substrate to Ni(0). However, the Ni precursor used was Ni(II)–bpy dihalide, not Ni(0), making the presence of Ni(0) somewhat speculative (see Point 3 below). Nonetheless, the authors cited previous work to propose that ³EnT between *Ir(III) and Ni(II)–bpy aryl acetate was the active mechanism for C–O coupled product formation.¹¹³

3. The proposed cycle rests on the Ni(0)–bpy/Ni(II)–bpy aryl halide combination as the starting source of nickel. As in the Oxidative SET Mechanism, the reaction was initiated with a Ni(0) source to give the Ni(II)–bpy aryl halide precatalyst. However, optimized reaction conditions utilized high-spin Ni(II)–bpy dihalide as the precursor nickel source.⁹⁶

The same complication is then introduced in this ^3EnT proposal. It is unclear if the experimental mechanistic analysis conducted between the Ir photosensitizer and the Ni(II)–bpy aryl acetate complex holds true for the Ir and Ni(II)–bpy dihalide combination. Important and complementary analysis was conducted by Li, Huang, Zhang and coworkers¹¹⁴ in 2018 on the aryl–acetate coupling reaction but using organic photosensitizers in place of the Ir(III) and beginning with Ni(II)–bpy dihalide. Under these conditions, strongly oxidizing photocatalysts gave an undesired dehalogenation of the aryl halide and no cross-coupled product, consistent with the 2017 study.⁹⁶ Transitioning to ^3EnT -active photosensitizers with lowered oxidation potentials gave some product yield, but still saw ~20% dehalogenation product. Thus, it was reasoned that when using Ni(II)–bpy dihalide as the precursor species, SET is favored over ^3EnT and proceeds prior to energy transfer.¹¹⁴ Only careful and deliberate suppression of oxidation allows for ^3EnT to become the major pathway. Under standard conditions (i.e., with Ir(III)), SET is therefore likely the sole or dominant mechanism, but it is unclear from these studies if the oxidation occurs with Ni, with the substrate coupling partners, or with the exogenous amine base. This electron transfer event is explicitly considered in the SET for Active Ni(I) Mechanism (**Section §1-3.1.9**), a proposal that appears to be the principal pathway when combining Ir(III) and Ni(II)–bpy dihalide, thereby marking a critical mechanistic switch when using high- vs. low-spin Ni(II) precursors.

It is clear from these studies that the highly potent and versatile $^* \text{Ir(III)}$ may engage in multiple pathways at once, including ^3EnT and SET. Diversion from one route to another depends on the Ni catalyst precursor, substrate coupling partners, exogenous base, and even photon intensity.^{58,115}

§1-3.1.9. SET for Active Ni(I)

Dual Ir/Ni cross-coupling reactions beginning with Ni(II)–bpy dihalide precursors have seen wide use, largely due to their incredible substrate scope potential. In 2016, Oderinde, Johannes, and coworkers uncovered C(sp²)–S coupling reactivity by combining an aryl

halide and thiol with Ni(II)–bpy dichloride and Ir(III).⁶⁹ Interestingly, it was found through Stern–Volmer analysis and radical traps that the thiol appreciably quenches $^*Ir(III)$ ($k = 10^5 M^{-1} s^{-1}$) to generate thiyl radicals and Ir(II). Ir(II) reduces the high-spin Ni(II)–bpy dihalide complex, affording Ni(I)–bpy halide and Ir(III) (**Figure 1.8**). The Ni(I)–bpy halide is at the core of the catalytic cycle turnover. First, it is intercepted by the thiyl radical to make a Ni(II)–bpy halide sulfide complex, which is reduced by a second equivalent of Ir(II) to Ni(I)–bpy sulfide. This Ni(I) undergoes oxidative addition with aryl halide to form a Ni(III)–bpy aryl halide sulfide species. This complex undergoes rapid reductive elimination to return Ni(I)–bpy halide and the C(sp²)–S coupled product (**Figure 1.8**).¹¹⁶ The generalizability of the reaction became evident by the extension to C(sp²)–N coupling of aryls and amines.¹¹⁷

Inspired by the 2018 work of Miyake and coworkers,¹¹⁸ which demonstrated the formation of arylamines upon direct excitation of a nickel–amine complex formed in situ from Ni(II)Br₂, Neurock, Minter, Baran, and coworkers⁵⁵ eliminated the photocatalyst, demonstrating that the Ni(II)–Ni(I) initiation step could be achieved through applied electrochemical potential. As discussed in the Ni Electronic Structure Primer (**Section 2**), the high-spin Ni(II)–bpy dihalide has a less-negative (more accessible) reduction potential than a Ni(II)–bpy aryl halide species, an additional species formed in the catalytic cycle. By controlling the applied potential, the researchers ruled out Oxidative SET; electrochemical oxidation of Ni(II)–bpy aryl halide did not occur within the solvent window. Ni(I)–bpy halide intermediates were observed spectroelectrochemically and were demonstrated to be active toward oxidative addition, thereby facilitating reaction turnover.⁵⁵

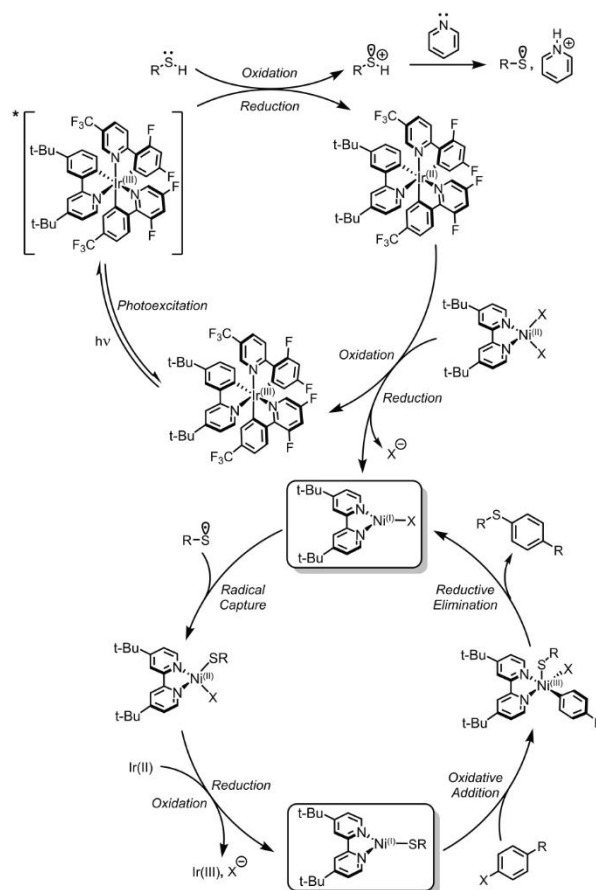


Figure 1.8. Proposed SET for Active Ni(I) Mechanism for C(sp²)-S coupling.⁶⁹

While examining the C(sp²)-O coupling of aryl halide and alcohol coupling partners pioneered by MacMillan and coworkers²⁸ in 2015 (see Oxidative SET, **Figure 1.4**, above), Nocera and coworkers⁹⁵ instead found support for the SET for Active Ni(I) mechanism (**Figure 1.9**). Again, Ir(III) is the sole light-harvesting species, being promoted to *Ir(III). Like in the case of aryl thiolate formation, the exogenous base used for the ligand substitution step (i.e., quinuclidine), was found to quench *Ir(III) with ease, generating Ir(II) and amine cation radicals. Ir(II) reduces the Ni(II)-bpy dihalide to Ni(I)-bpy halide and Ir(III). This Ni(I) species undergoes oxidative addition to form a Ni(III)-bpy aryl dihalide species, followed by ligand substitution of the halide by the alcohol/alkoxide and subsequent reductive elimination of the C(sp²)-O product. However, it was also proposed that the Ni(I)-bpy halide species can be diverted via comproportionation with the Ni(III)-bpy aryl dihalide species to regenerate the *S* = 1 Ni(II)-bpy dihalide complex and the *S* = 0 Ni(II)-bpy aryl

halide species. The former acts to regenerate the cycle, while the latter presents an off-pathway sink for diminished catalysis. Indeed, the Ni(II)–bpy aryl halide itself can aggregate with the Ni(I)–bpy halide, as observed by Nocera and coworkers⁹⁵ (using X-ray crystallography and electron paramagnetic resonance), as well as Hadt and coworkers⁵⁶ (using temperature-dependent spectroscopic methods).

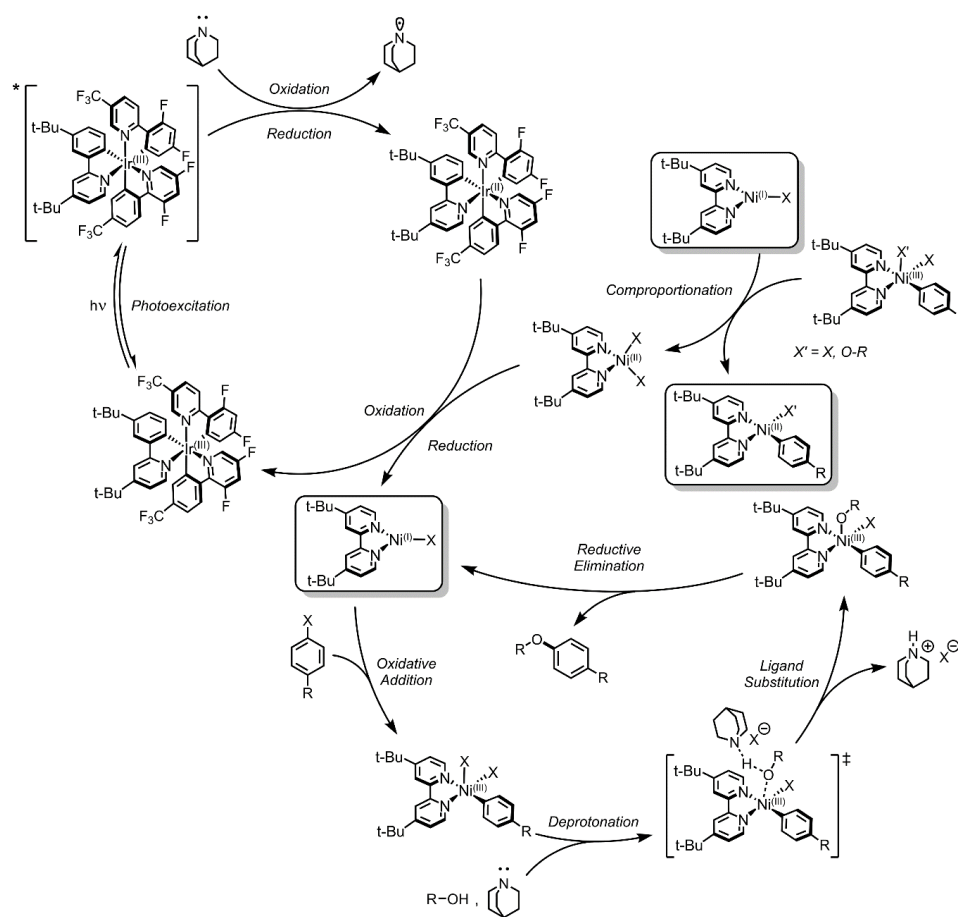


Figure 1.9. Proposed SET for Active Ni(I) Mechanism. $C(sp^2)$ –O coupling (alcohols) is shown as a representative example.

Following these three studies, researchers began to revisit previous mechanistic proposals. In 2020, MacMillan and coworkers⁶⁷ conducted a detailed study on the mechanism proposed in 2016 for $C(sp^2)$ –N coupling⁹⁰ (see Oxidative SET, **Figure 1.4**) and found the SET for Active Ni(I) Mechanism was better supported by their data, despite using the amine base DABCO (1,4-diazabicyclo[2.2.2]octane) instead of quinuclidine. DABCO quenches *Ir(III)

with a quantum yield near unity ($\Phi > 0.99$) and near-diffusion-controlled kinetics ($k = 10^9 \text{ M}^{-1} \text{ s}^{-1}$), affording amine⁺ and Ir(II). This initial quenching step was confirmed using spectroelectrochemistry and transient absorption spectroscopy and was not found to be sensitive to the addition of either aryl halide or high-spin Ni(II)–bpy dihalide. When varying the photosensitizer, the data further indicated that SET from Ir(II) to Ni(II) was involved in the rate-determining step of the overall catalytic cycle.⁶⁷

§1-3.1.10. Key Components of the SET for Active Ni(I) Mechanism

1. Ir(III) is the sole light-harvesting species, and its excited state is quenched by exogenous organic base (e.g., amine or thiol in solution) to generate Ir(II). *Ir(III) is quenched by the amine or thiol in solution (Figures 8-9); this fact has been verified by numerous sources via Stern–Volmer analysis.^{67,95,118–120} In the case of C(sp²)–S coupling, twelve discrete rate constants have been elucidated, altogether pointing to a self-sustained Ni(I)/(III) cycle with product $\Phi > 1$.¹¹⁹ Nocera and coworkers also demonstrated that Ni(II)–bpy dihalide is an effective quencher of *Ir(III), but with a quenching rate constant ~six times smaller than that of quinuclidine.⁹⁵ Interestingly, the Ni(II)–bpy aryl alkoxide complex generated by comproportionation of Ni(I) and Ni(III) also quenches *Ir(III), but with a rate constant twice as large as that of quinuclidine.⁹⁵ *It is therefore possible that the cross-coupling reaction begins with the SET for Active Ni(I) Mechanism, but once sufficient concentration of the Ni(II)–bpy aryl alkoxide species is generated, the mechanism diverts to one in which the S = 0 Ni(II) species is the dominant quencher (e.g., the ³EnT mechanism discussed above).* Computational evidence by Liu, Tlili, and by Zhu and Guan and their coworkers lends preliminary support to this hypothesis.^{121,122}

A switch in mechanism, or multiple, simultaneous kinetically competing mechanisms occurring in dual Ir/Ni(II)–bpy dihalide catalysis is likely. MacMillan found that C(sp²)–N coupling for arylamines proceeded rapidly with DABCO present, but it was not switched off with DABCO absent; the reaction rate decreased by ~nine times as a function of decreasing DABCO concentration, but 14% product yield was still obtained without DABCO.⁶⁷ Thus, the more kinetically active mechanism involves the quenching of the amine, but *Ir(III) is

also quenched by other species present in solution (including high-spin Ni(II)–bpy dihalide). Discrete reactivity pathways with $^*Ir(III)$ and Ni(II)–bpy dihalide in the absence of other quenchers were also examined, finding that no Ir(II) spectral features were observed without the organic quencher and, thus, invoking another cycle that does not involve the reduced Ir(II) species as an intermediate.⁶⁷ This analysis was computationally extended by Su, Guan, and coworkers,¹²³ then experimentally by Escobar, Thordarson, Johannes, Miyake, and coworkers.¹²⁴ It was proposed through ns transient absorption spectroscopy and oxidative spectroelectrochemistry that $^*Ir(III)$ is oxidatively quenched by high-spin Ni(II)–bpy dihalide to give Ni(I)–bpy halide and Ir(IV);¹²⁴ computations by Su in 2018 also favor this pathway.¹²⁵ The Ir(IV) is reduced downstream to return the starting Ir(III) by SET from a redox non-innocent aryl halide substrate.¹²⁴

2. Ni(II)–bpy dihalide is the precursor source of Ni and is reduced by Ir(II) to Ni(I)–bpy halide. The reduction of Ni(II) to Ni(I) by Ir(II) has been demonstrated multiple times (*vide supra*). Additionally, the importance of Ni(I) for product yields was established through a photosensitizer screen by MacMillan and coworkers.⁶⁷ Analysis of a library of Ir(III) photocatalysts demonstrated that product yields and reaction rates trend with Ir(II) reduction potential. However, the Ir(II) reduction potential also trends well with 3EnT capability. The first non-functioning photosensitizer has an emission energy of ~ 45 kcal mol⁻¹ and a reduction potential of -0.77 V vs. SCE. This energy transfer threshold is similar to that used to support 3EnT ,⁹⁶ which makes these trends alone a poor distinction between mechanisms. However, the first functioning photosensitizer (albeit with low product yields of $\sim 3\%$) makes a notable exception to this trend. It has an emission energy of ~ 62 kcal mol⁻¹ and reduction potential of -1.23 V vs. SCE. The best performing Ir photocatalyst (100% yield) has a 3EnT potential of 61 kcal mol⁻¹ but reduction potential of -1.91 V vs. SCE, confirming that reduction potential, not 3EnT energy, is a good predictor of productive catalysis.⁶⁷ In accord, Rovis and coworkers utilized a red light-absorbing Os(II) photocatalyst with a highly reducing potential to successfully achieve C(sp²)–N coupling.¹²⁶ Therefore, Ni(I) formation is on-pathway and required for product formation. This result was further supported by Nocera and coworkers, who found an induction period when organic quenchers were not

present to transform $^*Ir(III)$ to $Ir(II)$, the preferred species for $Ni(II)$ to $Ni(I)$ reduction,¹¹⁹ and by Liu, Tlili, and coworkers who leveraged active $Ni(I)$ for $C(sp^2)$ –N coupling with CO_2 as electrophile.¹²¹

3. $Ni(I)$ –bpy halide supports a dark $Ni(I)/(III)$ cycle. The reactivity of $Ni(I)$ –bpy halide toward oxidative addition and subsequent reductive elimination is well established.^{70,127} Recent mechanistic studies have identified rate constants for the reaction between $Ni(I)$ –bpy halide and aryl iodides, bromides, and chlorides.^{56,60,82,105} The immediate product of this reaction has been confirmed as $Ni(III)$ by comparison to model complexes.^{82,128} Importantly, $Ni(I)$ –bpy halide species undergo dimerization or oligomerization to binuclear or polynuclear Ni species, respectively, representing significant off-cycle deactivation pathways.^{56,82,95,129} Because of the exponential rate law dependence on the $Ni(I)$ concentration in these reactions, maintaining lower $Ni(I)$ concentration leads to improved cross-coupling yields. Indeed, by modulating the flux of the incident light to minimize the rate of $^*Ir(III)$ formation (and therefore the downstream concentration of $Ni(I)$ at a given time), the quantum yield for product formation could be increased ~15 times (from $\Phi = 1.6$ to $\Phi = 25$).⁹⁵ The observation of a quantum yield greater than one at even high flux levels supported a dark $Ni(I)/(III)$ cycle. A similar observation was made for aryl thiolate formation.¹¹⁹

The prevalence of the SET for Active $Ni(I)$ Mechanism cannot be overstated. König reports a general reaction beginning with high-spin $Ni(II)$ –bpy dihalide that is competent for $C(sp^2)$ –X (X = $C(sp, sp^2, sp^3)$, S, Se, N, O, P, B, Si, Cl) coupling.¹³⁰ *Mechanistic work is needed on a case-by-case basis, but the authors propose that this dramatic substrate scope is largely, if not fully, dominated by a $Ni(I)/(III)$ self-sustaining cycle, even when alternative mechanisms are possible.*

§1-3.2. Direct Excitation

This section, divided into two parts, describes research invoking direct photon absorption by specific Ni-based species involved in catalytic cycles. The first part considers cases where direct photoexcitation generates Ni-based intermediates for dark reactions that mediate cross-coupling. The second considers cases in which the cross-coupling events occur directly from transient excited states.

§1-3.2.1. Direct Excitation for Dark Cycle Initiation

1. Photoinduced Ni–X Bond Homolysis

Photoinduced Ni–X bond homolysis has been proposed as an initiation step that generates reactive species involved in key dark reactions. Often drawing comparisons to photohalogen elimination from five-coordinate Ni complexes, researchers have proposed pathways for metal–halide bond homolysis from four-coordinate Ni (**Figure 1.10**). These include the generation of triplet excited states of Ni(II)–bpy aryl halide species, photohalogen elimination from a Ni(III)–bpy aryl halide intermediate, the generation of intraligand charge transfer excited states that relax to dissociative metal-based excited states, and the direct generation of photoactive triplet metal-centered excited states of Ni(II) complexes with triplet ground states.

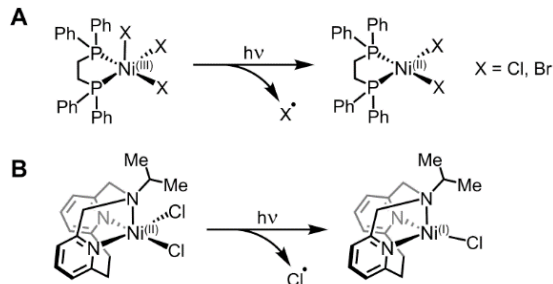
In 2016, Molander and coworkers reported C(sp³)–H arylation using a Ni(II)–bpy aryl bromide catalyst⁹⁸ (**Section §1-3.1.5, Figure 1.4; Figure 1.10C**). Arylated product was observed when the reaction was carried out with an Ir(III) photosensitizer, as discussed above. However, it was noted that aryated product could be detected when the reaction mixture was irradiated at specific wavelengths without the Ir(III) photosensitizer. Visible-light excitation (~400–600 nm) did not lead to product, while UV-B irradiation (290–315 nm) did. Based on these results and additional control photosensitization experiments, a catalytic mechanism was proposed that included a triplet excited state responsible for Ni reactivity. Mechanistic scenarios were presented for the generation of reactive Ni intermediates, all of which involved Ni(II)–Br bond homolysis. In the case of direct UV-B

excitation, a high-energy singlet excited state was proposed to relax via nonradiative intersystem crossing to a triplet excited state from which the Ni(II)–Br homolysis could occur.⁹⁸ As discussed above, the resultant bromine radicals were suggested to activate THF through hydrogen atom abstraction, and coupling to the aryl ligand could occur via reductive elimination from Ni(II) in an overall Ni(0)/Ni(II) cycle (see **Figure 1.4**).

Also in 2016, Doyle and coworkers reported a C(sp³)–H cross-coupling platform with Ni(II)–bpy aryl chloride and an Ir(III) photocatalyst⁵⁷ (**Section §1-3.1.5, Figure 1.4; Figure 1.10D**). As discussed above, the Ir(III) photocatalyst is proposed to carry out reductive SET to generate Ni(0) species for oxidative addition with the aryl chloride, as well as oxidative SET to oxidize the Ni(II)–bpy aryl chloride. The resulting cationic [Ni(III)–bpy aryl chloride]⁺ intermediate was proposed to undergo direct photon absorption to drive excited-state Ni(III)–Cl bond homolysis via an LMCT state in a manner analogous to an isolable pentacoordinate Ni(III) species^{99,100} (**Figure 1.10A**).

Ni(II)–X bond homolysis was further proposed in a Ni(II)–bpy dihalide *S* = 1 system that featured a dicarbazoyl functionalized bpy ligand (**Figure 1.10E**).¹³¹ The extended ligand alters the bpy orbital energies levels such that intra-ligand charge transfer (ILCT) states are present in the visible region. Combining transient absorption with computational analysis, the mechanism of Ni(II)–Cl bond homolysis was proposed to involve an initial excitation into a ³ILCT state, followed by relaxation into an optically dark square-planar metal-centered state. This state was proposed to feature antibonding character along the Ni–halide bond, thereby facilitating Ni(II)–X bond homolysis and formation of catalytically relevant Ni(I) species.

Photohalogen Elimination from 5-Coordinate Ni Complexes



Photohalogen Elimination from 4-Coordinate Ni Complexes

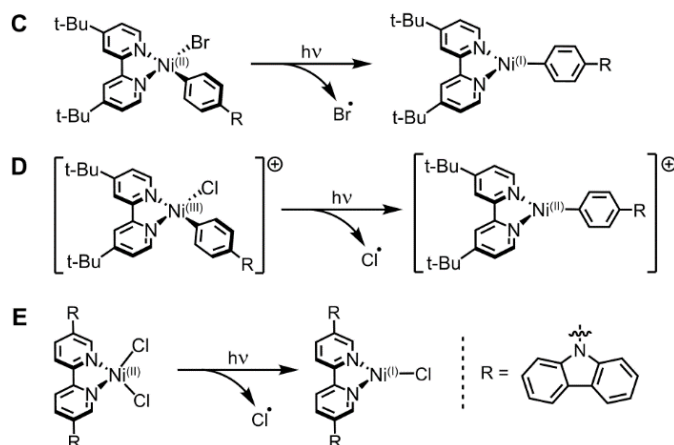


Figure 1.10. Proposed direct excitation for photohalogen elimination from five-coordinate Ni complexes studied by (A) Nocera^{95,96} and (B) Mirica,¹²² and from four-coordinate Ni complexes studied by (C) Molander,⁹⁴ (D) Doyle, Shields,⁵⁶ and (E) van der Veen, Thomas, and Pieber.¹²⁵

2. Photoinduced Ni–C Bond Homolysis.

In addition to excited-state Ni–X bond homolysis, recent studies have invoked analogous Ni–C bond homolysis.^{36–38} For Ni(II)–bpy complexes, after photoexcitation and carbon radical formation, the resultant Ni(I)–bpy halides mediate dark chemistry leading to the cross-coupled products (including C(sp²)–C(sp³), O, N, S coupling)^{36,79,109,132,133} via the proposed mechanism outlined in **Figure 1.11**.

In 2018, Doyle and coworkers utilized transient absorption spectroscopy to study the excited-state dynamics of isolable Ni(II)–bpy aryl halide compounds.³⁶ It was proposed that the

excitation of the complex resulted in $^3\text{MLCT}$ excited states that could undergo bimolecular electron transfer with a ground-state Ni(II)-bpy aryl halide species. The downstream result of this photochemical process was aryl ligand loss and the generation of a three-coordinate Ni(I)-bpy halide that would engage in Ni(I)/Ni(III) oxidative addition/reductive elimination cycles for C(sp²)-O cross-coupled product formation. However, later studies conducted by MacMillan, Scholes, and coworkers⁹⁷ indicated that this bimolecular photoinduced disproportionation pathway is not operative, as Stern-Volmer studies did not find appreciable Ni(II) excited-state quenching by ground-state Ni(II)-bpy aryl halide.

In a subsequent 2020 study, Doyle and coworkers expanded on their earlier transient absorption analysis and proposed an alternative excited-state relaxation pathway that could lead to Ni(II)-C(aryl) bond homolysis via a triplet ligand field ($^3\text{d-d}$) excited state of Ni(II)-bpy aryl halides.³⁷ Transient spectroscopic measurements carried out with either a 530–590 nm (for transient absorption) or 610 nm (time-resolved IR) laser pump demonstrated that initial excitation dominantly populates a $^1\text{MLCT}$ excited-state manifold, which can relax through additional MLCT states to ultimately form the $^3\text{d-d}$ state. By correlating density functional theory (DFT) calculations to transient absorption and 2D exchange NMR experiments, it was proposed that the $^3\text{d-d}$ state features a pseudo- T_d geometry (see **Figure 1.1B**) that can be accessed photochemically or thermally at room temperature. This pseudo- T_d geometry featured electron population of a σ^* orbital, reducing the Ni-aryl bond order to one half, thereby activating it for thermally driven homolysis. In support of that, DFT predicted a significantly weaker Ni(II)-Cl bond in the $^3\text{d-d}$ excited state ($\sim 24 \text{ kcal mol}^{-1}$) vs. the ground state ($\sim 35 \text{ kcal mol}^{-1}$). Both ^1H NMR and electron paramagnetic resonance (EPR) spectroscopy confirmed the generation of aryl radicals; no chlorine radicals were trapped, arguing against photoinduced Ni(II)-Cl homolysis.³⁷

Also in 2020, Hadt and coworkers explored mechanistic aspects of excited-state Ni(II)-C(aryl) bond homolysis from Ni(II)-bpy aryl halides using quantum chemical calculations of both ground- and excited-state PESs.¹² Multireference/multiconfigurational calculations suggested intractable energies for thermal bond dissociation from the lowest-energy $^3\text{d-d}$ state, with calculated bond strengths differing significantly from those predicted by DFT.

This study also suggested an alternative mechanism of excited-state Ni(II)–C(aryl) bond homolysis that featured 1) initial ¹MLCT formation and 2) intersystem crossing and aryl-to-Ni LMCT to form repulsive triplet excited-state PESs.¹² These MLCT/LMCT surfaces featured a Ni(II)–C(aryl) $\sigma \rightarrow \sigma^*$ electron excitation, which reduces the bond order to zero, hence the repulsive excited-state PESs. Notably, such description of dissociative excited-state bond homolysis conceptually resembles the isolable pentacoordinate Ni(III) photochemistry,⁹⁹ as well as the mixed MLCT/ $\sigma\pi^*$ (σ bond to ligand charge transfer) photoinduced radical formation in Re(I) and Ru(II) complexes.^{136–138}

In 2021, Park and coworkers proposed an analogous mechanism, utilizing Ni(II) complexes with cyclic ligands inherently predisposed to facile photochemical reductive elimination.¹⁰⁹ Regardless of the bidentate backbone ligand (diimine, diamine, or diphosphine), all studied complexes exhibited photoactivity under irradiation.

The ³LMCT excited-state PES was suggested to initiate carbon radical generation. This could occur through pathways from a preferred ¹MLCT state in aromatic diimine complexes or from a ¹d-d state in aliphatic diamine or diphosphine complexes lacking low-lying unoccupied ligand-based orbitals. Additionally, both ¹d-d and ¹MLCT excited states may operate simultaneously, with their ratio depending on the ground-state complexes' electronic structure and molar absorptivities. Importantly, charge transfer excitations exhibit orders of magnitude higher molar absorptivity than ligand field transitions, but vibronic coupling with a weakly absorbing, dissociative triplet state can potentially mediate intersystem crossing and Ni–C bond homolysis.

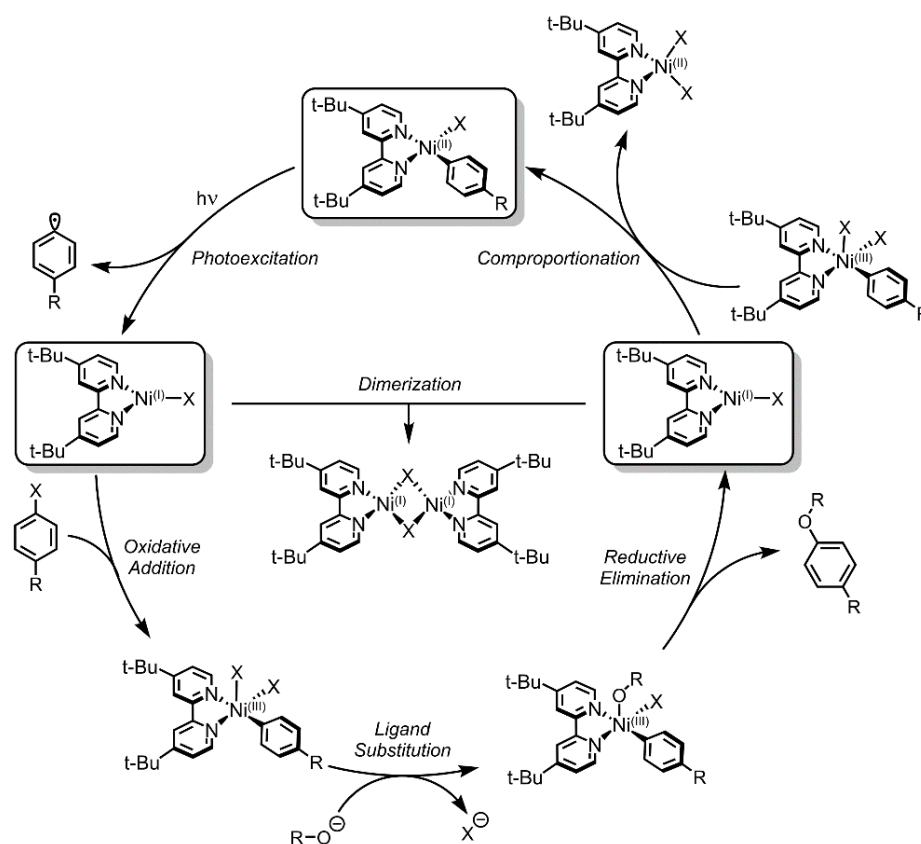


Figure 1.11. Proposed direct excitation for Ni(II)–C(aryl) bond homolysis and C(sp²)–O product formation mechanism (as a representative example). Following light-initiation, Ni(I)–bpy halide participates in “dark” substrate turnover but can be deactivated via off-cycle dimerization.

Following their earlier work, Hadt and coworkers provided further exploration of the excited-state bond homolysis mechanism.³⁸ In 2022, experimental analysis of a library of Ni(II)–bpy aryl halides found that 1) Ni(II)–C(aryl) bond homolysis was dependent on the bpy (MLCT acceptor) and aryl (LMCT donor) ligand substituents. A linear relationship was found for bpy/aryl Hammett parameters¹³⁹ and the rate constants and quantum yields for photochemical aryl radical generation; switching the halide from Cl to Br to I increased the rate of Ni–C bond homolysis. Notably, the quantum yields were very low ($\Phi = 10^{-3}$ – 10^{-4} at 390 nm for Ni(II)–bpy aryl halides). 2) Temperature-dependent rate analysis revealed that there existed a modest barrier for excited-state Ni(II)–C(aryl) bond homolysis (~ 4 kcal mol⁻¹); this barrier was well below the predicted values for thermal dissociation from the ³d-d

excited state. 3) Quantum yields and rate constants for excited-state bond homolysis were highly wavelength-dependent; excitation into the lowest-energy MLCT (which relaxes to the ^3d-d state) was unproductive. Only high-energy light (>525 nm, ~ 55 kcal mol $^{-1}$) afforded aryl radicals. These experiments, alongside an expanded computational analysis, supported a dissociative MLCT/LMCT excited state for C(aryl) $^{\bullet}$ generation.³⁸ Experiments further supported that Ni(I)–bpy halide species were the products of the unimolecular excited-state bond homolysis.⁵⁶

In 2024, Hadt and coworkers expanded their photochemical analysis of Ni(II)–bpy aryl halides to a Ni(II)–^{Ph}bpy chloride complex that features a covalent bond between the aryl ligand and the bpy backbone.¹⁴⁰ This geometrically constrained complex demonstrated apparent photochemical stability over a broad wavelength range. However, evidence for Ni(I) generation upon irradiation was demonstrated through a reaction with an introduced aryl bromide, wherein substrate activation outcompeted radical recombination of the tethered aryl group. From transient absorption experiments, the structural constraint of the ligand prevented access to a ^3d-d state by prohibiting the formation of a pseudo- T_d geometry (see **Section §1-2** for electronic structure implications). The retention of light-promoted activation of an electrophile in this tethered complex again suggested that the triplet charge transfer dissociative pathway (MLCT/LMCT) likely facilitates excited-state Ni–C bond homolysis. As noted above, due to the small quantum yields for Ni(II)–C(aryl) homolysis, transient spectroscopies largely probe unproductive background excited-state relaxation processes that do not lead to the formation of Ni(I) intermediates and organic radicals, making the assignment of the photochemical pathway challenging and inconclusive.⁴¹

We briefly note that in addition to Ni(II)–C(aryl) bond homolysis, Ni(II)–C(alkyl) homolysis has been observed. For example, Park prepared Ni(II)–bpy methyl thiolate complexes to corroborate the possibility of carbon radical formation (see above).¹⁰⁹ These complexes were designed to prefer irreversible Ni(II)–C(alkyl) bond homolysis and yielded ethane as the dominant photoproduct, thereby confirming methyl radical generation. Furthermore, aliphatic nickellacycles generated β -hydride elimination products under 390 nm irradiation. Similarly, Oderinde and coworkers questioned if Ni(II)–bpy dimethyl catalysts could

mediate C(sp²)-C(sp³) cross-coupling reactions under visible-light irradiation.¹⁴¹ Indeed, stoichiometric cross-coupled products were observed upon irradiation of the Ni(II) complex alongside 5-bromophthalide substrate using blue or violet light. Methyl radicals were confirmed via EPR radical-trap experiments followed by GC-MS analysis. These results reveal that alkyl radical formation through a Ni(II)-C(alkyl) bond homolysis pathway can be photoinduced with a variety of ligand backbones, including sulfur-ligated systems, an aromatic ligand (such as bpy), an aliphatic ligand (such as TMEDA), and occurs in both cyclic and acyclic compounds.

§1-3.2.2. Direct Excitation for Reductive Elimination

Excited states that serve to either 1) oxidize Ni via Ni-to-ligand charge transfer transitions or 2) populate Ni-ligand antibonding orbitals via ligand field or ligand-to-Ni transitions have been suggested to promote direct intramolecular reductive elimination of organic substrates. In either case, experimental mechanistic analysis is lacking, marking an opportunity for interdisciplinary follow-up analysis.

Absorption of a photon by Ni(II)-bpy complexes has been suggested to drive excited-state reductive elimination. Originally conceptualized by the McCusker and MacMillan groups in 2017,⁹⁶ it was proposed that direct excitation of a Ni(II)-bpy aryl acetate complex ultimately resulted in the population of a low-energy triplet ligand field state, from which intramolecular reductive elimination could afford an aryl-acetate product with new C(sp²)-O bond and a reduced Ni(0)-bpy complex. Follow-up ns transient absorption on a mixture of Ir(III) photosensitizer and Ni(II)-bpy aryl acetate was conducted in 2020, wherein it was surmised that *Ir(III) underwent Dexter EnT to a ground-state Ni(II) complex (see **Section §1-3.1.7** above), populating a long-lived triplet excited state. The nature of this state, i.e., charge transfer vs. metal centered, was not described. It was proposed, however, that this excited state was active for reductive elimination. Notably, ultrafast transient absorption on the independent excited-state dynamics of the Ni(II)-bpy aryl acetate was not presented. Computational assessment of the excited-state relaxation pathways of a Ni(II)-bpy aryl acetate was undertaken by Ma and coworkers that same year.¹³ Therein, it was proposed that

direct excitation of the Ni(II) complex into a high-energy, anti-Kasha^{142,143} Ni(III)–bpy^{•-} MLCT state was responsible for intramolecular reductive elimination, where the oxidation of the Ni(II) center serves as the driving force for substrate formation.^{91,92,144}

Excited-state-driven reductive elimination was also seen by Lloyd-Jones and coworkers on Ni(II)–bpy aryl halides.⁸⁸ Energy transfer from *Ir(III) to generate a triplet excited-state Ni(II) complex resulted in the formation of an aryl halide substrate and Ni(0)—a reversible process as oxidative addition from Ni(0) is readily accessible at room temperature. Following these results, the Lin and Doyle groups noted that direct excitation of the Ni complex is also productive for the same reductive elimination/oxidative addition equilibrium.^{110,145} Indeed, this reversible light-driven chemistry was utilized for ligand exchange, promoting a (*retro*-)Finkelstein reaction. The long-lived excited state of Ni(II)–bpy aryl halides is a ³d-d state, which is populated after relaxation from higher-energy MLCT states.³⁷ It is unclear if a charge transfer or metal-centered excited state is productive for reductive elimination; further experimental mechanistic work is still needed to elucidate the photophysics of this process.

Direct aryl–alkyl C(sp²)–C(sp³) reductive elimination from excited-state, high-valent Ni(III/IV)–bpy complexes was demonstrated by Park in 2020.¹⁰⁸ In this case, a LMCT promoted the cross-coupled product via the population of a Ni–C σ*-orbital, increasing the rate of substrate formation by up to a factor 10⁵ when compared to thermal, dark reactivity. Interestingly, these complexes were penta-coordinate, suggesting similarities to the light-driven Ni–X homolysis reactivity seen by Nocera, Mirica, and coworkers.^{99,100,128} A recent report by the Doyle group finds evidence for excited-state intramolecular C(sp²)–C(sp³) reductive elimination from Ni(II)–bpy aryl alkyl complexes;¹¹⁰ the mechanism for this process is presently unknown.

§1-3.2.3. Key Components of Direct Excitation

1. Ni(II)–bpy aryl halides are light-harvesting species. The absorptive nature of Ni(II)–bpy aryl halide complexes is well described. The primary absorption features in the visible-light region are Ni(II)-to-bpy MLCT in nature, with molar absorptivities in the range of 10³–10⁴ M⁻¹ cm⁻¹.^{37,38} Hadt and coworkers found that these transitions can be further

separated into low- and high-energy MLCTs, with the various bpy π^* acceptor orbitals marking the difference between the two.^{12,38} The low-energy bands are typically ~ 415–580 nm, while the high-energy bands are found between ~ 340–400 nm, with additional transitions extending into the higher-energy region. If present, d-d bands are likely obscured by MLCT transitions due to their relatively low molar absorptivities (10^1 – 10^2 M⁻¹ cm⁻¹) (**Figure 1.2**). While low-temperature magnetic circular dichroism (MCD) can enhance ligand field transitions relative to charge transfer due to different selection rules relative to UV–vis, the greatest utility involves *C*-term intensity, which requires a paramagnetic ground state.¹⁴⁶ The ground states of Ni(II)–bpy aryl halide compounds are diamagnetic, however, which would lead to an absence of *C*-term intensity. Thus, additional spectroscopic methods may be required to locate and assign ligand field excited states in these compounds. 2p3d resonant inelastic X-ray scattering (RIXS) may be a viable technique due to its ability to resonantly excite metal-based states.^{147–149} Higher-energy incident wavelengths (< 330 nm) populate ILCT (bpy $\pi \rightarrow \pi^*$) transitions. These have been found to relax into the MLCT manifold via transient absorption spectroscopy.^{36,131} Similarly, the MLCT transitions relax into d-d excited states before ultimately returning to the ground state.^{37,150}

2. Ni(I)–bpy halide is produced via direct excitation, not Ni(I)–bpy aryl. Although the very low quantum yields for photoinduced Ni–ligand homolysis from Ni(II)–bpy aryl halides have made them challenging to study by transient spectroscopies, steady-state methods including UV–vis, NMR, EPR, and GC-MS have verified the formation of aryl radicals, not halogen radicals, upon light absorption (*vide supra*). Indeed, to the best of our knowledge, no direct experimental evidence of halogen radical production upon irradiation of Ni(II)–bpy aryl halide complexes has been provided. The exclusive observation of aryl radicals is in contrast to the early mechanistic proposals by Molander, Doyle, and Shields.^{57,98}

These 2016 reports featuring key Ni(II/III)–X bond homolysis refer to the work by Nocera and coworkers developed in the context of HX splitting for solar energy storage.^{99,100} It is important to highlight the distinctions in the photohalogen elimination chemistry between these systems. In HX splitting, the Ni(III) species is an isolable, penta-coordinate Ni(III)–dppe trichloride complex (dppe = bis(diphenylphosphino)ethane). Here, a common

dissociative excited-state surface is accessed upon 370 and 434 nm irradiation and was proposed to be responsible for the photoelimination of the apical chlorine ligand (**Figure 1.10A**). Based on time-dependent DFT calculations (TDDFT), the Ni(III)–Cl bond cleavage was attributed to a LMCT excitation into the unoccupied $p(z)/d(z^2)$ antibonding Ni-based hole, reducing the bond order between Ni(III) and the apical Cl to zero. The resulting photoproduct, Ni(II)(dppe)Cl₂, exhibited a square-planar structure with a singlet ground state; no further halogen photoelimination occurred.

In 2022, Mirica and Na reported a study¹²⁸ with a similar isolable, five-coordinate Ni(II) complex that featured a tridentate pyridinophane ligand (**Figure 1.10B**). Their proposed mechanism also featured chlorine photoelimination, both Ir(III)-facilitated via SET and under direct light excitation of the $S = 1$ Ni(II) complex. The latter displayed accessible triplet Ni-to-ligand charge transfer states. Excitation into one of these triplet states promoted an electron from the Ni 3*d*-orbital manifold, thus generating a transient Ni(III) complex. It was proposed that subsequent relaxation gave rise to a ³d-d state with significant σ^* character along the Ni–Cl bond, triggering homolysis. Although chlorine radical trapping experiments were not presented, the lability of the Ni–Cl bonds was demonstrated in the chemically oxidized cationic Ni(III) complex.

Thus, photohalogen elimination is possible with penta-coordinate Ni(II/III) di- or trihalide complexes, but it is disfavored when using four-coordinate Ni(II/III) aryl halide complexes. The MLCT/LMCT process seen in Ni(II)–bpy aryl halide complexes is akin to that considered using time-dependent density functional theory (TDDFT) in the Ni(III)–Cl photohalogen elimination chemistry, but with the distinct difference that the LMCT originates from an aryl donor, not the halide. This is unsurprising, as the DFT predicted bond dissociation energy for Ni(II)–X homolysis is roughly twice that of Ni(II)–C(aryl).³⁷ Interestingly, the Ni(II)–C(aryl) homolysis pathway is promiscuous with respect to the backbone ligand, as demonstrated by Park and coworkers and by Hadt and coworkers for aliphatic TMEDA ligands.^{38,109} *It is therefore the presence of the aryl group that governs the selectivity for radical generation.*

This notion has been corroborated experimentally. Xue and coworkers¹³³ demonstrated that even when replacing the halide with a stronger field ligand, as in the Ni(II)–bpy aryl cyanide complex, aryl radicals are still preferentially generated upon light absorption. Here, the starting Ni(II) complex was initially presented as a potential reactive intermediate in C(sp²)–N coupling reactions, with the authors suggesting that reductive elimination from a Ni(III) state would yield C(sp²)–N coupled products. Reductive elimination was indeed observed after single-electron oxidation via an excited photosensitizer. However, in the absence of photosensitizer, no reductive elimination occurred; the reaction instead resulted in biphenyl product formation, suggesting photochemical Ni(II)–C(aryl) bond homolysis (which was later confirmed by EPR). The formation of the d⁹ Ni(I)–bpy cyanide intermediate upon irradiation of the parent Ni(II) structure was also confirmed by EPR.¹³³ Furthermore, recent work suggests that high-spin ($S = 1$) Ni(II)–bpy dihalide (and Ni(II)–TMEDA dihalide) engage in photohalogen elimination upon direct excitation with high-energy light, thereby recovering the photohalogen elimination pathway by removing the aryl group from the parent Ni(II) complex.^{110,151–153} Similarly, photo-pseudo-halogen elimination from Ni(II)–bpy diacetate has been proposed by Xue and coworkers when using purple light.^{154–}

156

3. Ni(I)–bpy halide is the active species for oxidative addition, but also suffers from off-cycle dimerization. The potency of Ni(I)–bpy halide for the oxidative addition of aryl halide substrates has been demonstrated experimentally. Hammett analysis by the groups of Bird and MacMillan, Sigman, and Doyle suggested that aryl iodides and bromides are activated via a concerted, two-electron oxidative addition mechanism.^{60,82,157} When studying reactivity of Ni(I)–bpy halides with aryl chlorides, Hadt and coworkers found a relatively higher ρ value from Hammett analysis, which suggested the activation step is characterized by a concerted, two-electron nucleophilic substitution mechanism (S_NAr).⁵⁶ For this, the nucleophilic site is the doubly occupied $3d(z^2)$ orbital, which carries out a two-electron transfer into the C(sp²)–Cl σ^* orbital. It was found that the reactivity of the Ni(I)–bpy halide species can be tuned via the energy of this orbital; bpy ligand modifications alter the effective nuclear charge (Z_{eff}) of the Ni(I) and serve to increase (via electron-donating groups) or

decrease (via electron-withdrawing groups) the reactivity of the complex toward substrate activation.

Although one might speculate that cross-coupling reactions would be accelerated by increased Ni(I) concentration in solution, Nocera and coworkers found that doing so (by increasing the photon flux of the irradiation source) was actually detrimental to productive catalysis.⁹⁵ At a high concentration of Ni(I), the low-valent species is prone to either direct dimerization to yield formal [Ni(I)–bpy halide]₂ complexes (**Figure 1.11**) or to aggregation with the parent Ni(II)–bpy aryl halide species—both of which are off-cycle products. On the basis of X-ray photoelectron spectroscopy on a synthesized [Ni(I)–bpy halide]₂ complexes, Hazari and coworkers described this species as a dimeric Ni(II)–bpy^{•-} halide.¹²⁹ It was also found to be inert toward aryl halide substrates.^{129,157} Importantly, the same electronic structure effects that govern the reactivity of Ni(I)–bpy halide species also dictate their tendency toward this dimerization pathway; electron-rich ligands promote dimerization, while electron-deficient ligands slow or fully inhibit room temperature dimerization ($\Delta G^\ddagger \sim 25 \text{ kcal mol}^{-1}$).⁵⁶ *Therefore, the relative rates of Ni(I)–bpy halide formation, substrate activation, and off-cycle dimerization should be considered when optimizing catalytic cycles.*

4. Penta-coordinate Ni(III) undergoes reductive elimination and/or comproportionation to close the cycle. As has been discussed above, Ni(III) is prone to rapid reductive elimination. Indeed, mechanistic work by Mirica and Doyle and coworkers found that reductive elimination is facile, even at low temperatures.^{110,128} In good agreement with these experimental observations, DFT calculations by Hadt and coworkers suggest that reductive elimination of an aryl halide from a Ni(III)(bpy)(aryl)X₂ species is effectively barrierless.⁵⁶ Nonetheless, under continuous irradiation and formation of both Ni(I) and Ni(III) species, there exists a non-negligible resting state concentration of Ni(III) in solution that can undergo comproportionation with Ni(I) to afford *S* = 0 Ni(II)–bpy aryl halide and *S* = 1 Ni(II)–bpy dihalide.^{158,159} This has been experimentally demonstrated by Doyle and coworkers in 2022⁸⁴ and 2024¹¹⁰ and by Hadt and coworkers in 2023⁵⁶ by NMR analysis. The low-spin Ni(II)–bpy aryl halide is thereby returned to the catalytic cycle, where it can absorb a photon and be transformed anew to Ni(I)–bpy halide (**Figure 1.11**). However, *S* =

1 Ni(II)–bpy dihalide accumulates following comproportionation over multiple turnovers, potentially diverting the cycle to one beginning at the high spin species. Detailed mechanistic work on the photophysical pathway upon direct excitation of Ni(II)–bpy dihalide complexes is still needed.

§1-4. Conclusions and Outlook

In this Review, we have provided a summary of the various mechanisms presented for metallaphotoredox reactions featuring Ni(II)–bpy catalysts. A few common mechanistic observations have arisen:

- 1) Commonly employed photosensitizers such as cyclometalated Ir(III) heteroleptic complexes can engage in numerous excited-state quenching pathways, including ^3EnT and reductive/oxidative SET, complicating mechanistic analysis. Furthermore, in metallaphotoredox cycles there are often numerous species capable of quenching the photosensitizer excited state, organic and inorganic alike. The precise mechanism of quenching, and the quenching species, are still largely debated. Detailed experimental mechanistic work (including Stern–Volmer analysis) is needed for individual steps in Ir/Ni dual photocatalytic cycles.
- 2) The electronic structure of the Ni(II)–bpy species present in the reaction governs the specific mechanistic pathway it follows; this electronic structure is highly sensitive to both ligands and the surrounding environment. To highlight a few key structures, Ni(II)–bpy aryl halides and Ni(II)–bpy aryl acetates are both photosensitized species and direct light-harvesters. Ni(II)–bpy aryl halides undergo photochemical Ni(II)–C(aryl) bond homolysis, a key step for initiation into Ni(I)/Ni(III) dark cycles, while Ni(II)–bpy aryl acetates have been proposed to follow an excited-state intramolecular reductive elimination path. Ni(II)–bpy dihalide species are primarily photosensitized complexes, typically resulting in a reduced Ni(I)–bpy halide. However, with high-energy light, these complexes have been proposed to also engage in direct $^*\text{Ni(II)–X}$ bond homolysis to form the same Ni(I) intermediate.

3) Regardless of the Ni(I)–bpy halide photochemical generation mechanism, a consistent Ni(I)/Ni(III) cycle has been proposed for most cross-coupling reactions. The key catalytic steps consist of an oxidative addition of electrophile (such as aryl halide) to Ni(I) to form a reactive Ni(III)(bpy)(Ar)X₂ intermediate. This Ni(III) can undergo X ligand exchange with a nucleophile (presumably facilitated by a base), followed by reductive elimination to form the cross-coupled product and regenerate Ni(I)–bpy halide. Continuous irradiation is often necessary, likely due to the formation of off-cycle, catalytically inactive Ni(II)–bpy dihalide via Ni(I)/Ni(III) comproportionation. However, continuous high photon flux leads to an accumulation of Ni(I)–bpy halide, resulting in aggregation with other Ni species in solution or dimerization to [Ni(I)/Ni(I)] off-cycle products.

Viewing these light-driven mechanisms from an electronic structure perspective has granted key considerations for the steps in each cycle, particularly pertaining to Ni-based intermediates. Although tremendous advancements have been made in reaction development in this field, unified, experimentally supported mechanisms are still lacking for many of the reactions. Due to the inherent complexity in these cycles, care should be taken to evaluate individual steps independently. We hope that presenting this Review from the standpoint of the outlined key considerations has provided a model logic from which to conduct such analyses. Finally, thermally driven enantioselective cross-coupling catalysis, often utilizing metal-based reductants instead of photochemical processes, feature similar complementary mechanistic considerations.^{6,10,61,62,160,161} As such, mechanistic studies in this field are of direct relevance for designing future studies. We hope research groups from the physical, organic, and inorganic fields will take on interdisciplinary research to elucidate the precise mechanisms of Ni-mediated cross-coupling catalysis, providing rationale to improve product scope and reaction efficiency and laying a foundation to extend catalyst activity to other transition metals.

§1-5. References

- (1) Chen, X.; Engle, K. M.; Wang, D.-H.; Yu, J.-Q. Palladium(II)-Catalyzed C–H Activation/C–C Cross-Coupling Reactions: Versatility and Practicality. *Angew. Chem. Int. Ed.* **2009**, *48* (28), 5094–5115. <https://doi.org/10.1002/anie.200806273>.
- (2) Torborg, C.; Beller, M. Recent Applications of Palladium-Catalyzed Coupling Reactions in the Pharmaceutical, Agrochemical, and Fine Chemical Industries. *Adv. Synth. Catal.* **2009**, *351* (18), 3027–3043. <https://doi.org/10.1002/adsc.200900587>.
- (3) Nicolaou, K. C.; Bulger, P. G.; Sarlah, D. Palladium-Catalyzed Cross-Coupling Reactions in Total Synthesis. *Angew. Chem. Int. Ed.* **2005**, *44* (29), 4442–4489. <https://doi.org/10.1002/anie.200500368>.
- (4) Jiang, L.; Buchwald, S. L. Palladium-Catalyzed Aromatic Carbon-Nitrogen Bond Formation. In *Metal-Catalyzed Cross-Coupling Reactions*; John Wiley & Sons, Ltd, 2004; pp 699–760. <https://doi.org/10.1002/9783527619535.ch13>.
- (5) Tasker, S. Z.; Standley, E. A.; Jamison, T. F. Recent Advances in Homogeneous Nickel Catalysis. *Nature* **2014**, *509* (7500), 299–309. <https://doi.org/10.1038/nature13274>.
- (6) Cherney, A. H.; Kadunce, N. T.; Reisman, S. E. Enantioselective and Enantiospecific Transition-Metal-Catalyzed Cross-Coupling Reactions of Organometallic Reagents To Construct C–C Bonds. *Chem. Rev.* **2015**, *115* (17), 9587–9652. <https://doi.org/10.1021/acs.chemrev.5b00162>.
- (7) Fu, G. C. Transition-Metal Catalysis of Nucleophilic Substitution Reactions: A Radical Alternative to SN1 and SN2 Processes. *ACS Cent. Sci.* **2017**, *3* (7), 692–700. <https://doi.org/10.1021/acscentsci.7b00212>.
- (8) Crabtree, R. H. Deactivation in Homogeneous Transition Metal Catalysis: Causes, Avoidance, and Cure. *Chem. Rev.* **2015**, *115* (1), 127–150. <https://doi.org/10.1021/cr5004375>.
- (9) Ananikov, V. P. Nickel: The “Spirited Horse” of Transition Metal Catalysis. *ACS Catal.* **2015**, *5* (3), 1964–1971. <https://doi.org/10.1021/acscatal.5b00072>.
- (10) Diccianni, J. B.; Diao, T. Mechanisms of Nickel-Catalyzed Cross-Coupling Reactions. *Trends Chem.* **2019**, *1* (9), 830–844. <https://doi.org/10.1016/j.trechm.2019.08.004>.
- (11) Gesmundo, N. J.; Rago, A. J.; Young, J. M.; Keess, S.; Wang, Y. At the Speed of Light: The Systematic Implementation of Photoredox Cross-Coupling Reactions for Medicinal Chemistry Research. *J. Org. Chem.* **2024**. <https://doi.org/10.1021/acs.joc.3c02351>.

- (12) Cagan, D. A.; Strocio, G. D.; Cusumano, A. Q.; Hadt, R. G. Multireference Description of Nickel–Aryl Homolytic Bond Dissociation Processes in Photoredox Catalysis. *J. Phys. Chem. A* **2020**, *124* (48), 9915–9922. <https://doi.org/10.1021/acs.jpca.0c08646>.
- (13) Ma, P.; Wang, S.; Chen, H. Reactivity of Transition-Metal Complexes in Excited States: C–O Bond Coupling Reductive Elimination of a Ni(II) Complex Is Elicited by the Metal-to-Ligand Charge Transfer State. *ACS Catal.* **2020**, *10* (1), 1–6. <https://doi.org/10.1021/acscatal.9b03827>.
- (14) Maity, B.; Scott, T. R.; Strocio, G. D.; Gagliardi, L.; Cavallo, L. The Role of Excited States of $\text{LNi}^{\text{II/III}}(\text{Aryl})(\text{Halide})$ Complexes in Ni–Halide Bond Homolysis in the Arylation of $\text{Csp}^3\text{–H}$ Bonds. *ACS Catal.* **2022**, *12* (21), 13215–13224. <https://doi.org/10.1021/acscatal.2c04284>.
- (15) Dawson, G. A.; Spielvogel, E. H.; Diao, T. Nickel-Catalyzed Radical Mechanisms: Informing Cross-Coupling for Synthesizing Non-Canonical Biomolecules. *Acc. Chem. Res.* **2023**, *56* (24), 3640–3653. <https://doi.org/10.1021/acs.accounts.3c00588>.
- (16) Nicewicz, D. A.; MacMillan, D. W. C. Merging Photoredox Catalysis with Organocatalysis: The Direct Asymmetric Alkylation of Aldehydes. *Science* **2008**, *322* (5898), 77–80. <https://doi.org/10.1126/science.1161976>.
- (17) Yoon, T. P.; Ischay, M. A.; Du, J. Visible Light Photocatalysis as a Greener Approach to Photochemical Synthesis. *Nat. Chem.* **2010**, *2* (7), 527–532. <https://doi.org/10.1038/nchem.687>.
- (18) Prier, C. K.; Rankic, D. A.; MacMillan, D. W. C. Visible Light Photoredox Catalysis with Transition Metal Complexes: Applications in Organic Synthesis. *Chem. Rev.* **2013**, *113* (7), 5322–5363. <https://doi.org/10.1021/cr300503r>.
- (19) Twilton, J.; Le, C.; Zhang, P.; Shaw, M. H.; Evans, R. W.; MacMillan, D. W. C. The Merger of Transition Metal and Photocatalysis. *Nat. Rev. Chem.* **2017**, *1* (7), 0052. <https://doi.org/10.1038/s41570-017-0052>.
- (20) Chan, A. Y.; Perry, I. B.; Bissonnette, N. B.; Buksh, B. F.; Edwards, G. A.; Frye, L. I.; Garry, O. L.; Lavagnino, M. N.; Li, B. X.; Liang, Y.; Mao, E.; Millet, A.; Oakley, J. V.; Reed, N. L.; Sakai, H. A.; Seath, C. P.; MacMillan, D. W. C. Metallaphotoredox: The Merger of Photoredox and Transition Metal Catalysis. *Chem. Rev.* **2022**, *122* (2), 1485–1542. <https://doi.org/10.1021/acs.chemrev.1c00383>.
- (21) McAtee, R. C.; McClain, E. J.; Stephenson, C. R. J. Illuminating Photoredox Catalysis. *Trends Chem.* **2019**, *1* (1), 111–125. <https://doi.org/10.1016/j.trechm.2019.01.008>.
- (22) Wenger, O. S. Photoactive Nickel Complexes in Cross-Coupling Catalysis. *Chem. Eur. J.* **2021**, *27* (7), 2270–2278. <https://doi.org/10.1002/chem.202003974>.

- (23) Arias-Rotondo, D. M.; McCusker, J. K. The Photophysics of Photoredox Catalysis: A Roadmap for Catalyst Design. *Chem. Soc. Rev.* **2016**, *45* (21), 5803–5820. <https://doi.org/10.1039/C6CS00526H>.
- (24) Strieth-Kalthoff, F.; J. James, M.; Teders, M.; Pitzer, L.; Glorius, F. Energy Transfer Catalysis Mediated by Visible Light: Principles, Applications, Directions. *Chem. Soc. Rev.* **2018**, *47* (19), 7190–7202. <https://doi.org/10.1039/C8CS00054A>.
- (25) Strieth-Kalthoff, F.; Glorius, F. Triplet Energy Transfer Photocatalysis: Unlocking the Next Level. *Chem* **2020**, *6* (8), 1888–1903. <https://doi.org/10.1016/j.chempr.2020.07.010>.
- (26) Yuan, M.; Gutierrez, O. Mechanisms, Challenges, and Opportunities of Dual Ni/Photoredox-Catalyzed C(sp²)–C(sp³) Cross-Couplings. *WIREs Comput. Mol. Sci.* **2022**, *12* (3), e1573. <https://doi.org/10.1002/wcms.1573>.
- (27) Millet, A.; Cesana, P. T.; Sedillo, K.; Bird, M. J.; Schlau-Cohen, G. S.; Doyle, A. G.; MacMillan, D. W. C.; Scholes, G. D. Bioinspired Supercharging of Photoredox Catalysis for Applications in Energy and Chemical Manufacturing. *Acc. Chem. Res.* **2022**, *55* (10), 1423–1434. <https://doi.org/10.1021/acs.accounts.2c00083>.
- (28) Terrett, J. A.; Cuthbertson, J. D.; Shurtleff, V. W.; MacMillan, D. W. C. Switching on Elusive Organometallic Mechanisms with Photoredox Catalysis. *Nature* **2015**, *524* (7565), 330–334. <https://doi.org/10.1038/nature14875>.
- (29) Tellis, J. C.; Primer, D. N.; Molander, G. A. Single-Electron Transmetalation in Organoboron Cross-Coupling by Photoredox/Nickel Dual Catalysis. *Science* **2014**, *345* (6195), 433–436. <https://doi.org/10.1126/science.1253647>.
- (30) Zuo, Z.; Ahneman, D. T.; Chu, L.; Terrett, J. A.; Doyle, A. G.; MacMillan, D. W. C. Merging Photoredox with Nickel Catalysis: Coupling of α -Carboxyl sp³-Carbons with Aryl Halides. *Science* **2014**, *345* (6195), 437–440. <https://doi.org/10.1126/science.1255525>.
- (31) Palkowitz, M. D.; Emmanuel, M. A.; Oderinde, M. S. A Paradigm Shift in Catalysis: Electro- and Photomediated Nickel-Catalyzed Cross-Coupling Reactions. *Acc. Chem. Res.* **2023**, *56* (20), 2851–2865. <https://doi.org/10.1021/acs.accounts.3c00479>.
- (32) Cavalcanti, L. N.; Molander, G. A. Photoredox Catalysis in Nickel-Catalyzed Cross-Coupling. *Top. Curr. Chem.* **2016**, *374* (4), 39. <https://doi.org/10.1007/s41061-016-0037-z>.
- (33) Lowry, M. S.; Bernhard, S. Synthetically Tailored Excited States: Phosphorescent, Cyclometalated Iridium(III) Complexes and Their Applications. *Chem. Eur. J.* **2006**, *12* (31), 7970–7977. <https://doi.org/10.1002/chem.200600618>.
- (34) Monti, F.; Baschieri, A.; Sambri, L.; Armaroli, N. Excited-State Engineering in Heteroleptic Ionic Iridium(III) Complexes. *Acc. Chem. Res.* **2021**, *54* (6), 1492–1505. <https://doi.org/10.1021/acs.accounts.0c00825>.

- (35) DiLuzio, S.; Connell, T. U.; Mdluli, V.; Kowalewski, J. F.; Bernhard, S. Understanding Ir(III) Photocatalyst Structure-Activity Relationships: A Highly Parallelized Study of Light-Driven Metal Reduction Processes. *J. Am. Chem. Soc.* **2022**, *144* (3), 1431–1444. <https://doi.org/10.1021/jacs.1c12059>.
- (36) Shields, B. J.; Kudisch, B.; Scholes, G. D.; Doyle, A. G. Long-Lived Charge-Transfer States of Nickel(II) Aryl Halide Complexes Facilitate Bimolecular Photoinduced Electron Transfer. *J. Am. Chem. Soc.* **2018**, *140* (8), 3035–3039. <https://doi.org/10.1021/jacs.7b13281>.
- (37) Ting, S. I.; Garakyaraghi, S.; Taliaferro, C. M.; Shields, B. J.; Scholes, G. D.; Castellano, F. N.; Doyle, A. G. ³d-d Excited States of Ni(II) Complexes Relevant to Photoredox Catalysis: Spectroscopic Identification and Mechanistic Implications. *J. Am. Chem. Soc.* **2020**, *142* (12), 5800–5810. <https://doi.org/10.1021/jacs.0c00781>.
- (38) Cagan, D. A.; Bím, D.; Silva, B.; Kazmierczak, N. P.; McNicholas, B. J.; Hadt, R. G. Elucidating the Mechanism of Excited-State Bond Homolysis in Nickel–Bipyridine Photoredox Catalysts. *J. Am. Chem. Soc.* **2022**, *144* (14), 6516–6531. <https://doi.org/10.1021/jacs.2c01356>.
- (39) Abderrazak, Y.; Bhattacharyya, A.; Reiser, O. Visible-Light-Induced Homolysis of Earth-Abundant Metal-Substrate Complexes: A Complementary Activation Strategy in Photoredox Catalysis. *Angew. Chem. Int. Ed.* **2021**, *60* (39), 21100–21115. <https://doi.org/10.1002/anie.202100270>.
- (40) Zhu, C.; Yue, H.; Jia, J.; Rueping, M. Nickel-Catalyzed C–Heteroatom Cross-Coupling Reactions under Mild Conditions via Facilitated Reductive Elimination. *Angew. Chem. Int. Ed.* **2021**, *60* (33), 17810–17831. <https://doi.org/10.1002/anie.202013852>.
- (41) Kandoth, N.; Hernández, J. P.; Palomares, E.; Lloret-Fillol, J. Mechanisms of Photoredox Catalysts: The Role of Optical Spectroscopy. *Sustain. Energy Fuels* **2021**, *5* (3), 638–665. <https://doi.org/10.1039/D0SE01454K>.
- (42) Venkataraman, D.; Du, Y.; Wilson, S. R.; Hirsch, K. A.; Zhang, P.; Moore, J. S. A Coordination Geometry Table of the D-Block Elements and Their Ions. *J. Chem. Educ.* **1997**, *74* (8), 915. <https://doi.org/10.1021/ed074p915>.
- (43) Gray, H. B.; Ballhausen, C. J. A Molecular Orbital Theory for Square Planar Metal Complexes. *J. Am. Chem. Soc.* **1963**, *85* (3), 260–265. <https://doi.org/10.1021/ja00886a002>.
- (44) McNicholas, B. J.; Tong, Z. J.; Bím, D.; Turro, R. F.; Kazmierczak, N. P.; Chalupský, J.; Reisman, S. E.; Hadt, R. G. Electronic Structures of Nickel(II)-Bis(Indanyloxazoline)-Dihalide Catalysts: Understanding Ligand Field Contributions That Promote C(sp²)–C(sp³) Cross-Coupling. *Inorg. Chem.* **2023**, *62* (34), 14010–14027. <https://doi.org/10.1021/acs.inorgchem.3c02048>.

- (45) Zuckerman, J. J. Crystal Field Splitting Diagrams. *J. Chem. Educ.* **1965**, *42* (6), 315. <https://doi.org/10.1021/ed042p315>.
- (46) Eaton, D. R.; Zaw, K. Geometry of Nickel(II) Complexes. *J. Am. Chem. Soc.* **1972**, *94* (12), 4394–4395. <https://doi.org/10.1021/ja00767a087>.
- (47) Lundgren, R. J.; Stradiotto, M. Key Concepts in Ligand Design. In *Ligand Design in Metal Chemistry*; John Wiley & Sons, Ltd, 2016; pp 1–14. <https://doi.org/10.1002/9781118839621.ch1>.
- (48) Lee, C.; Yang, W.; Parr, R. G. Development of the Colle-Salvetti Correlation-Energy Formula into a Functional of the Electron Density. *Phys. Rev. B* **1988**, *37* (2), 785–789. <https://doi.org/10.1103/PhysRevB.37.785>.
- (49) Becke, A. D. Density-functional Thermochemistry. III. The Role of Exact Exchange. *J. Chem. Phys.* **1993**, *98* (7), 5648–5652. <https://doi.org/10.1063/1.464913>.
- (50) Weigend, F.; Ahlrichs, R. Balanced Basis Sets of Split Valence, Triple Zeta Valence and Quadruple Zeta Valence Quality for H to Rn: Design and Assessment of Accuracy. *Phys. Chem. Chem. Phys.* **2005**, *7* (18), 3297–3305. <https://doi.org/10.1039/B508541A>.
- (51) Chatt, J.; Hayter, R. G. 167. Ligand Field Strengths of the Halide, Methyl, Phenyl, and Hydride Anions. *J. Chem. Soc. Resumed* **1961**, No. 0, 772–774. <https://doi.org/10.1039/JR9610000772>.
- (52) Lin, Q.; Fu, Y.; Liu, P.; Diao, T. Monovalent Nickel-Mediated Radical Formation: A Concerted Halogen-Atom Dissociation Pathway Determined by Electroanalytical Studies. *J. Am. Chem. Soc.* **2021**, *143* (35), 14196–14206. <https://doi.org/10.1021/jacs.1c05255>.
- (53) Pitchai, M.; Ramirez, A.; Mayder, D. M.; Ulaganathan, S.; Kumar, H.; Aulakh, D.; Gupta, A.; Mathur, A.; Kempson, J.; Meanwell, N.; Hudson, Z. M.; Oderinde, M. S. Metallaphotoredox Decarboxylative Arylation of Natural Amino Acids via an Elusive Mechanistic Pathway. *ACS Catal.* **2023**, *13* (1), 647–658. <https://doi.org/10.1021/acscatal.2c05554>.
- (54) Dawson, G. A.; Lin, Q.; Neary, M. C.; Diao, T. Ligand Redox Activity of Organonickel Radical Complexes Governed by the Geometry. *J. Am. Chem. Soc.* **2023**, *145* (37), 20551–20561. <https://doi.org/10.1021/jacs.3c07031>.
- (55) Kawamata, Y.; Vantourout, J. C.; Hickey, D. P.; Bai, P.; Chen, L.; Hou, Q.; Qiao, W.; Barman, K.; Edwards, M. A.; Garrido-Castro, A. F.; deGruyter, J. N.; Nakamura, H.; Knouse, K.; Qin, C.; Clay, K. J.; Bao, D.; Li, C.; Starr, J. T.; Garcia-Irizarry, C.; Sach, N.; White, H. S.; Neurock, M.; Minter, S. D.; Baran, P. S. Electrochemically Driven, Ni-Catalyzed Aryl Amination: Scope, Mechanism, and Applications. *J. Am. Chem. Soc.* **2019**, *141* (15), 6392–6402. <https://doi.org/10.1021/jacs.9b01886>.

- (56) Cagan, D. A.; Bím, D.; McNicholas, B. J.; Kazmierczak, N. P.; Oyala, P. H.; Hadt, R. G. Photogenerated Ni(I)–Bipyridine Halide Complexes: Structure-Function Relationships for Competitive C(sp²)–Cl Oxidative Addition and Dimerization Reactivity Pathways. *Inorg. Chem.* **2023**, *62* (24), 9538–9551. <https://doi.org/10.1021/acs.inorgchem.3c00917>.
- (57) Shields, B. J.; Doyle, A. G. Direct C(sp³)–H Cross Coupling Enabled by Catalytic Generation of Chlorine Radicals. *J. Am. Chem. Soc.* **2016**, *138* (39), 12719–12722. <https://doi.org/10.1021/jacs.6b08397>.
- (58) Deng, H.-P.; Fan, X.-Z.; Chen, Z.-H.; Xu, Q.-H.; Wu, J. Photoinduced Nickel-Catalyzed Chemo- and Regioselective Hydroalkylation of Internal Alkynes with Ether and Amide α -Hetero C(sp³)–H Bonds. *J. Am. Chem. Soc.* **2017**, *139* (38), 13579–13584. <https://doi.org/10.1021/jacs.7b08158>.
- (59) Tang, T.; Jones, E.; Wild, T.; Hazra, A.; Minter, S. D.; Sigman, M. S. Investigating Oxidative Addition Mechanisms of Allylic Electrophiles with Low-Valent Ni/Co Catalysts Using Electroanalytical and Data Science Techniques. *J. Am. Chem. Soc.* **2022**, *144* (43), 20056–20066. <https://doi.org/10.1021/jacs.2c09120>.
- (60) Tang, T.; Hazra, A.; Min, D. S.; Williams, W. L.; Jones, E.; Doyle, A. G.; Sigman, M. S. Interrogating the Mechanistic Features of Ni(I)-Mediated Aryl Iodide Oxidative Addition Using Electroanalytical and Statistical Modeling Techniques. *J. Am. Chem. Soc.* **2023**, *145* (15), 8689–8699. <https://doi.org/10.1021/jacs.3c01726>.
- (61) Turro, R. F.; Wahlman, J. L. H.; Tong, Z. J.; Chen, X.; Yang, M.; Chen, E. P.; Hong, X.; Hadt, R. G.; Houk, K. N.; Yang, Y.-F.; Reisman, S. E. Mechanistic Investigation of Ni-Catalyzed Reductive Cross-Coupling of Alkenyl and Benzyl Electrophiles. *J. Am. Chem. Soc.* **2023**, *145* (27), 14705–14715. <https://doi.org/10.1021/jacs.3c02649>.
- (62) Chen, L.-M.; Reisman, S. E. Enantioselective C(sp²)–C(sp³) Bond Construction by Ni Catalysis. *Acc. Chem. Res.* **2024**, *57* (5), 751–762. <https://doi.org/10.1021/acs.accounts.3c00775>.
- (63) Hoshino, N.; Fukuda, Y.; Sone, K. Studies on Mixed Chelates. XI. Syntheses and Comparative Study of a New Series of Mixed Nickel(II) Chelates with Halide and Pseudohalide Ligands. *Bull. Chem. Soc. Jpn.* **1981**, *54* (2), 420–427. <https://doi.org/10.1246/bcsj.54.420>.
- (64) Sacconi, L.; Bertini, I. Nickel(II) Complexes with N,N'-Tetramethylalkylenediamines. *Inorg. Nucl. Chem. Lett.* **1966**, *2* (1), 29–32. [https://doi.org/10.1016/0020-1650\(66\)80086-7](https://doi.org/10.1016/0020-1650(66)80086-7).
- (65) Bryden, M. A.; Millward, F.; Lee, O. S.; Cork, L.; Gather, M. C.; Steffen, A.; Zysman-Colman, E. Lessons Learnt in Photocatalysis—the Influence of Solvent Polarity and the Photostability of the Photocatalyst. *Chem. Sci.* **2024**, *15* (10), 3741–3757. <https://doi.org/10.1039/D3SC06499A>.

- (66) Buslov, I.; Song, F.; Hu, X. An Easily Accessed Nickel Nanoparticle Catalyst for Alkene Hydrosilylation with Tertiary Silanes. *Angew. Chem. Int. Ed.* **2016**, *55* (40), 12295–12299. <https://doi.org/10.1002/anie.201606832>.
- (67) Till, N. A.; Tian, L.; Dong, Z.; Scholes, G. D.; MacMillan, D. W. C. Mechanistic Analysis of Metallaphotoredox C–N Coupling: Photocatalysis Initiates and Perpetuates Ni(I)/Ni(III) Coupling Activity. *J. Am. Chem. Soc.* **2020**, *142* (37), 15830–15841. <https://doi.org/10.1021/jacs.0c05901>.
- (68) Newman-Stonebraker, S. H.; Raab, T. J.; Roshandel, H.; Doyle, A. G. Synthesis of Nickel(I)–Bromide Complexes via Oxidation and Ligand Displacement: Evaluation of Ligand Effects on Speciation and Reactivity. *J. Am. Chem. Soc.* **2023**, *145* (35), 19368–19377. <https://doi.org/10.1021/jacs.3c06233>.
- (69) Oderinde, M. S.; Frenette, M.; Robbins, D. W.; Aquila, B.; Johannes, J. W. Photoredox Mediated Nickel Catalyzed Cross-Coupling of Thiols With Aryl and Heteroaryl Iodides via Thiyl Radicals. *J. Am. Chem. Soc.* **2016**, *138* (6), 1760–1763. <https://doi.org/10.1021/jacs.5b11244>.
- (70) Lin, C.-Y.; Power, P. P. Complexes of Ni(I): A “Rare” Oxidation State of Growing Importance. *Chem. Soc. Rev.* **2017**, *46* (17), 5347–5399. <https://doi.org/10.1039/C7CS00216E>.
- (71) King, A. E.; Stieber, S. C. E.; Henson, N. J.; Kozimor, S. A.; Scott, B. L.; Smythe, N. C.; Sutton, A. D.; Gordon, J. C. Ni(bpy)(COD): A Convenient Entryway into the Efficient Hydroboration of Ketones, Aldehydes, and Imines. *Eur. J. Inorg. Chem.* **2016**, *2016* (11), 1635–1640. <https://doi.org/10.1002/ejic.201600143>.
- (72) Chu, L.; Lipshultz, J. M.; MacMillan, D. W. C. Merging Photoredox and Nickel Catalysis: The Direct Synthesis of Ketones by the Decarboxylative Arylation of α -Oxo Acids. *Angew. Chem. Int. Ed.* **2015**, *54* (27), 7929–7933. <https://doi.org/10.1002/anie.201501908>.
- (73) Johnston, C. P.; Smith, R. T.; Allmendinger, S.; MacMillan, D. W. C. Metallaphotoredox-Catalysed sp^3 – sp^3 Cross-Coupling of Carboxylic Acids with Alkyl Halides. *Nature* **2016**, *536* (7616), 322–325. <https://doi.org/10.1038/nature19056>.
- (74) Zhang, P.; Le, C. “Chip”; MacMillan, D. W. C. Silyl Radical Activation of Alkyl Halides in Metallaphotoredox Catalysis: A Unique Pathway for Cross-Electrophile Coupling. *J. Am. Chem. Soc.* **2016**, *138* (26), 8084–8087. <https://doi.org/10.1021/jacs.6b04818>.
- (75) Perry, I. B.; Brewer, T. F.; Sarver, P. J.; Schultz, D. M.; DiRocco, D. A.; MacMillan, D. W. C. Direct Arylation of Strong Aliphatic C–H Bonds. *Nature* **2018**, *560* (7716), 70–75. <https://doi.org/10.1038/s41586-018-0366-x>.

- (76) Chen, T. Q.; MacMillan, D. W. C. A Metallaphotoredox Strategy for the Cross-Electrophile Coupling of α -Chloro Carbonyls with Aryl Halides. *Angew. Chem. Int. Ed.* **2019**, *58* (41), 14584–14588. <https://doi.org/10.1002/anie.201909072>.
- (77) Sakai, H. A.; Liu, W.; Le, C. “Chip”; MacMillan, D. W. C. Cross-Electrophile Coupling of Unactivated Alkyl Chlorides. *J. Am. Chem. Soc.* **2020**, *142* (27), 11691–11697. <https://doi.org/10.1021/jacs.0c04812>.
- (78) Lau, S. H.; Borden, M. A.; Steiman, T. J.; Wang, L. S.; Parasram, M.; Doyle, A. G. Ni/Photoredox-Catalyzed Enantioselective Cross-Electrophile Coupling of Styrene Oxides with Aryl Iodides. *J. Am. Chem. Soc.* **2021**, *143* (38), 15873–15881. <https://doi.org/10.1021/jacs.1c08105>.
- (79) Yang, L.; Lu, H.-H.; Lai, C.-H.; Li, G.; Zhang, W.; Cao, R.; Liu, F.; Wang, C.; Xiao, J.; Xue, D. Light-Promoted Nickel Catalysis: Etherification of Aryl Electrophiles with Alcohols Catalyzed by a Ni^{II}-Aryl Complex. *Angew. Chem. Int. Ed.* **2020**, *59* (31), 12714–12719. <https://doi.org/10.1002/anie.202003359>.
- (80) Roth, H. G.; Romero, N. A.; Nicewicz, D. A. Experimental and Calculated Electrochemical Potentials of Common Organic Molecules for Applications to Single-Electron Redox Chemistry. *Synlett* **2016**, *27* (5), 714–723. <https://doi.org/10.1055/s-0035-1561297>.
- (81) Tay, N. E. S.; Lehnerr, D.; Rovis, T. Photons or Electrons? A Critical Comparison of Electrochemistry and Photoredox Catalysis for Organic Synthesis. *Chem. Rev.* **2022**, *122* (2), 2487–2649. <https://doi.org/10.1021/acs.chemrev.1c00384>.
- (82) Ting, S. I.; Williams, W. L.; Doyle, A. G. Oxidative Addition of Aryl Halides to a Ni(I)-Bipyridine Complex. *J. Am. Chem. Soc.* **2022**, *144* (12), 5575–5582. <https://doi.org/10.1021/jacs.2c00462>.
- (83) Day, C. S.; Rentería-Gómez, Á.; Ton, S. J.; Gogoi, A. R.; Gutierrez, O.; Martin, R. Elucidating Electron-Transfer Events in Polypyridine Nickel Complexes for Reductive Coupling Reactions. *Nat. Catal.* **2023**, *6* (3), 244–253. <https://doi.org/10.1038/s41929-023-00925-4>.
- (84) Jaouadi, K.; Abdellaoui, M.; Levernier, E.; Payard, P.-A.; Derat, E.; Le Saux, T.; Ollivier, C.; Torelli, S.; Jullien, L.; Plasson, R.; Fensterbank, L.; Grimaud, L. Regime Switch in the Dual-Catalyzed Coupling of Alkyl Silicates with Aryl Bromides. *Chem. Eur. J.* **2023**, *29* (59), e202301780. <https://doi.org/10.1002/chem.202301780>.
- (85) Bradley, R. D.; McManus, B. D.; Yam, J. G.; Carta, V.; Bahamonde, A. Mechanistic Evidence of a Ni(0/II/III) Cycle for Nickel Photoredox Amide Arylation. *Angew. Chem. Int. Ed.* **2023**, *62* (43), e202310753. <https://doi.org/10.1002/anie.202310753>.

- (86) Gutierrez, O.; Tellis, J. C.; Primer, D. N.; Molander, G. A.; Kozlowski, M. C. Nickel-Catalyzed Cross-Coupling of Photoredox-Generated Radicals: Uncovering a General Manifold for Stereoconvergence in Nickel-Catalyzed Cross-Couplings. *J. Am. Chem. Soc.* **2015**, *137* (15), 4896–4899. <https://doi.org/10.1021/ja513079r>.
- (87) Lin, Q.; Spielvogel, E. H.; Diao, T. Carbon-Centered Radical Capture at Nickel(II) Complexes: Spectroscopic Evidence, Rates, and Selectivity. *Chem* **2023**, *9* (5), 1295–1308. <https://doi.org/10.1016/j.chempr.2023.02.010>.
- (88) Ben-Tal, Y.; Lloyd-Jones, G. C. Kinetics of a Ni/Ir-Photocatalyzed Coupling of ArBr with RBr: Intermediacy of ArNi^{II}(L)Br and Rate/Selectivity Factors. *J. Am. Chem. Soc.* **2022**, *144* (33), 15372–15382. <https://doi.org/10.1021/jacs.2c06831>.
- (89) Tasker, S. Z.; Jamison, T. F. Highly Regioselective Indoline Synthesis under Nickel/Photoredox Dual Catalysis. *J. Am. Chem. Soc.* **2015**, *137* (30), 9531–9534. <https://doi.org/10.1021/jacs.5b05597>.
- (90) Corcoran, E. B.; Pirnot, M. T.; Lin, S.; Dreher, S. D.; DiRocco, D. A.; Davies, I. W.; Buchwald, S. L.; MacMillan, D. W. C. Aryl Amination Using Ligand-Free Ni(II) Salts and Photoredox Catalysis. *Science* **2016**, *353* (6296), 279–283. <https://doi.org/10.1126/science.aag0209>.
- (91) Koo, K.; Hillhouse, G. L. Carbon-Nitrogen Bond Formation by Reductive Elimination from Nickel(II) Amido Alkyl Complexes. *Organometallics* **1995**, *14* (9), 4421–4423. <https://doi.org/10.1021/om00009a054>.
- (92) Han, R.; Hillhouse, G. L. Carbon–Oxygen Reductive-Elimination from Nickel(II) Oxametallacycles and Factors That Control Formation of Ether, Aldehyde, Alcohol, or Ester Products. *J. Am. Chem. Soc.* **1997**, *119* (34), 8135–8136. <https://doi.org/10.1021/ja9714999>.
- (93) Yuan, M.; Song, Z.; Badir, S. O.; Molander, G. A.; Gutierrez, O. On the Nature of C(sp³)–C(sp²) Bond Formation in Nickel-Catalyzed Tertiary Radical Cross-Couplings: A Case Study of Ni/Photoredox Catalytic Cross-Coupling of Alkyl Radicals and Aryl Halides. *J. Am. Chem. Soc.* **2020**, *142* (15), 7225–7234. <https://doi.org/10.1021/jacs.0c02355>.
- (94) Qi, Z.-H.; Ma, J. Dual Role of a Photocatalyst: Generation of Ni(0) Catalyst and Promotion of Catalytic C–N Bond Formation. *ACS Catal.* **2018**, *8* (2), 1456–1463. <https://doi.org/10.1021/acscatal.7b03024>.
- (95) Sun, R.; Qin, Y.; Rucolo, S.; Schnedermann, C.; Costentin, C.; Daniel G. Nocera. Elucidation of a Redox-Mediated Reaction Cycle for Nickel-Catalyzed Cross Coupling. *J. Am. Chem. Soc.* **2019**, *141* (1), 89–93. <https://doi.org/10.1021/jacs.8b11262>.
- (96) Welin, E. R.; Le, C.; Arias-Rotondo, D. M.; McCusker, J. K.; MacMillan, D. W. C. Photosensitized, Energy Transfer-Mediated Organometallic Catalysis through Electronically

- Excited Nickel(II). *Science* **2017**, *355* (6323), 380–385. <https://doi.org/10.1126/science.aal2490>.
- (97) Tian, L.; Till, N. A.; Kudisch, B.; MacMillan, D. W. C.; Scholes, G. D. Transient Absorption Spectroscopy Offers Mechanistic Insights for an Iridium/Nickel-Catalyzed C–O Coupling. *J. Am. Chem. Soc.* **2020**, *142* (10), 4555–4559. <https://doi.org/10.1021/jacs.9b12835>.
- (98) Heitz, D. R.; Tellis, J. C.; Molander, G. A. Photochemical Nickel-Catalyzed C–H Arylation: Synthetic Scope and Mechanistic Investigations. *J. Am. Chem. Soc.* **2016**, *138* (39), 12715–12718. <https://doi.org/10.1021/jacs.6b04789>.
- (99) Hwang, S. J.; Powers, D. C.; Maher, A. G.; Anderson, B. L.; Hadt, R. G.; Zheng, S.-L.; Chen, Y.-S.; Nocera, D. G. Trap-Free Halogen Photoelimination from Mononuclear Ni(III) Complexes. *J. Am. Chem. Soc.* **2015**, *137* (20), 6472–6475. <https://doi.org/10.1021/jacs.5b03192>.
- (100) Hwang, S. J.; Anderson, B. L.; Powers, D. C.; Maher, A. G.; Hadt, R. G.; Nocera, D. G. Halogen Photoelimination from Monomeric Nickel(III) Complexes Enabled by the Secondary Coordination Sphere. *Organometallics* **2015**, *34* (19), 4766–4774. <https://doi.org/10.1021/acs.organomet.5b00568>.
- (101) Hofbeck, T.; Yersin, H. The Triplet State of *fac*-Ir(ppy)₃. *Inorg. Chem.* **2010**, *49* (20), 9290–9299. <https://doi.org/10.1021/ic100872w>.
- (102) Kancherla, R.; Muralirajan, K.; Maity, B.; Karuthedath, S.; Kumar, G. S.; Laquai, F.; Cavallo, L.; Rueping, M. Mechanistic Insights into Photochemical Nickel-Catalyzed Cross-Couplings Enabled by Energy Transfer. *Nat. Commun.* **2022**, *13* (1), 2737. <https://doi.org/10.1038/s41467-022-30278-8>.
- (103) Sun, Z.; Kumagai, N.; Shibasaki, M. Photocatalytic α -Acylation of Ethers. *Org. Lett.* **2017**, *19* (14), 3727–3730. <https://doi.org/10.1021/acs.orglett.7b01552>.
- (104) Santos, M. S.; Corrêa, A. G.; Paixão, M. W.; König, B. C(sp³)–C(sp³) Cross-Coupling of Alkyl Bromides and Ethers Mediated by Metal and Visible Light Photoredox Catalysis. *Adv. Synth. Catal.* **2020**, *362* (12), 2367–2372. <https://doi.org/10.1002/adsc.202000167>.
- (105) Kariofillis, S. K.; Doyle, A. G. Synthetic and Mechanistic Implications of Chlorine Photoelimination in Nickel/Photoredox C(sp³)–H Cross-Coupling. *Acc. Chem. Res.* **2021**, *54* (4), 988–1000. <https://doi.org/10.1021/acs.accounts.0c00694>.
- (106) Ackerman, L. K. G.; Martinez Alvarado, J. I.; Doyle, A. G. Direct C–C Bond Formation from Alkanes Using Ni-Photoredox Catalysis. *J. Am. Chem. Soc.* **2018**, *140* (43), 14059–14063. <https://doi.org/10.1021/jacs.8b09191>.

- (107) Afanas'ev, I. B. Correlation Equations in Free-Radical Reactions. *Russ. Chem. Rev.* **1971**, *40* (3), 216. <https://doi.org/10.1070/RC1971v040n03ABEH001914>.
- (108) Shin, J.; Gwon, S.; Kim, S.; Lee, J.; Park, K. Correlation between the C–C Cross-Coupling Activity and C-to-Ni Charge Transfer Transition of High-Valent Ni Complexes. *J. Am. Chem. Soc.* **2020**, *142* (9), 4173–4183. <https://doi.org/10.1021/jacs.9b10405>.
- (109) Shin, J.; Lee, J.; Suh, J.-M.; Park, K. Ligand-Field Transition-Induced C–S Bond Formation from Nickelacycles. *Chem. Sci.* **2021**, *12* (48), 15908–15915. <https://doi.org/10.1039/D1SC05113J>.
- (110) Cusumano, A.; Chaffin, B.; Doyle, A. Mechanism of Ni-Catalyzed Photochemical Halogen Atom-Mediated C(sp³)–H Arylation. *ChemRxiv* March 4, 2024. <https://doi.org/10.26434/chemrxiv-2024-lmg7f>.
- (111) Zhu, D.-L.; Li, H.-X.; Xu, Z.-M.; Li, H.-Y.; Young, D. J.; Lang, J.-P. Visible Light Driven, Nickel-Catalyzed Aryl Esterification Using a Triplet Photosensitizer Thioxanthene-9-One. *Org. Chem. Front.* **2019**, *6* (14), 2353–2359. <https://doi.org/10.1039/C9QO00536F>.
- (112) Hojo, R.; Bergmann, K.; Elgadi, S. A.; Mayder, D. M.; Emmanuel, M. A.; Oderinde, M. S.; Hudson, Z. M. Imidazophenothiazine-Based Thermally Activated Delayed Fluorescence Materials with Ultra-Long-Lived Excited States for Energy Transfer Photocatalysis. *J. Am. Chem. Soc.* **2023**, *145* (33), 18366–18381. <https://doi.org/10.1021/jacs.3c04132>.
- (113) Malik, J. A.; Madani, A.; Pieber, B.; Seeberger, P. H. Evidence for Photocatalyst Involvement in Oxidative Additions of Nickel-Catalyzed Carboxylate O-Arylations. *J. Am. Chem. Soc.* **2020**, *142* (25), 11042–11049. <https://doi.org/10.1021/jacs.0c02848>.
- (114) Lu, J.; Pattengale, B.; Liu, Q.; Yang, S.; Shi, W.; Li, S.; Huang, J.; Zhang, J. Donor–Acceptor Fluorophores for Energy-Transfer-Mediated Photocatalysis. *J. Am. Chem. Soc.* **2018**, *140* (42), 13719–13725. <https://doi.org/10.1021/jacs.8b07271>.
- (115) Du, Y.; Pearson, R. M.; Lim, C.-H.; Sartor, S. M.; Ryan, M. D.; Yang, H.; Damrauer, N. H.; Miyake, G. M. Strongly Reducing, Visible-Light Organic Photoredox Catalysts as Sustainable Alternatives to Precious Metals. *Chem. Eur. J.* **2017**, *23* (46), 10962–10968. <https://doi.org/10.1002/chem.201702926>.
- (116) Jouffroy, M.; Kelly, C. B.; Molander, G. A. Thioetherification via Photoredox/Nickel Dual Catalysis. *Org. Lett.* **2016**, *18* (4), 876–879. <https://doi.org/10.1021/acs.orglett.6b00208>.
- (117) Oderinde, M. S.; Jones, N. H.; Juneau, A.; Frenette, M.; Aquila, B.; Tentarelli, S.; Robbins, D. W.; Johannes, J. W. Highly Chemoselective Iridium Photoredox and Nickel Catalysis for the Cross-Coupling of Primary Aryl Amines with Aryl Halides. *Angew. Chem. Int. Ed.* **2016**, *55* (42), 13219–13223. <https://doi.org/10.1002/anie.201604429>.

- (118) Lim, C.-H.; Kudisch, M.; Liu, B.; Miyake, G. M. C–N Cross-Coupling via Photoexcitation of Nickel–Amine Complexes. *J. Am. Chem. Soc.* **2018**, *140* (24), 7667–7673. <https://doi.org/10.1021/jacs.8b03744>.
- (119) Qin, Y.; Sun, R.; Gianoulis, N. P.; Nocera, D. G. Photoredox Nickel-Catalyzed C–S Cross-Coupling: Mechanism, Kinetics, and Generalization. *J. Am. Chem. Soc.* **2021**, *143* (4), 2005–2015. <https://doi.org/10.1021/jacs.0c11937>.
- (120) Kudisch, M.; Lim, C.-H.; Thordarson, P.; Miyake, G. M. Energy Transfer to Ni–Amine Complexes in Dual Catalytic, Light-Driven C–N Cross-Coupling Reactions. *J. Am. Chem. Soc.* **2019**, *141* (49), 19479–19486. <https://doi.org/10.1021/jacs.9b11049>.
- (121) Abid, S.; Quirion, K. P.; Yang, Y.; Tang, R.; Mai, B. K.; Liu, P.; Tlili, A. Photochemically Driven Nickel-Catalyzed Carboxylative C–N Coupling: Scope and Mechanism. *Chem. Eur. J.* **2023**, *29* (44), e202301271. <https://doi.org/10.1002/chem.202301271>.
- (122) Dong, Y.-J.; Zhao, Z.-W.; Geng, Y.; Su, Z.-M.; Zhu, B.; Guan, W. Theoretical Insight on the High Reactivity of Reductive Elimination of Ni^{III} Based on Energy- and Electron-Transfer Mechanisms. *Inorg. Chem.* **2023**, *62* (3), 1156–1164. <https://doi.org/10.1021/acs.inorgchem.2c03502>.
- (123) Ren, H.; Li, G.-F.; Zhu, B.; Lv, X.-D.; Yao, L.-S.; Wang, X.-L.; Su, Z.-M.; Guan, W. How Does Iridium(III) Photocatalyst Regulate Nickel(II) Catalyst in Metallaphotoredox-Catalyzed C–S Cross-Coupling? Theoretical and Experimental Insights. *ACS Catal.* **2019**, *9* (5), 3858–3865. <https://doi.org/10.1021/acscatal.9b00375>.
- (124) Chrisman, C. H.; Kudisch, M.; Puffer, K. O.; Stewart, T. K.; Lamb, Y. M. L.; Lim, C.-H.; Escobar, R.; Thordarson, P.; Johannes, J. W.; Miyake, G. M. Halide Noninnocence and Direct Photoreduction of Ni(II) Enables Coupling of Aryl Chlorides in Dual Catalytic, Carbon–Heteroatom Bond-Forming Reactions. *J. Am. Chem. Soc.* **2023**, *145* (22), 12293–12304. <https://doi.org/10.1021/jacs.3c02784>.
- (125) Zhu, B.; Yan, L.-K.; Geng, Y.; Ren, H.; Guan, W.; Su, Z.-M. Ir^{III}/Ni^{II}-Metallaphotoredox Catalysis: The Oxidation State Modulation Mechanism versus the Radical Mechanism. *Chem. Commun.* **2018**, *54* (47), 5968–5971. <https://doi.org/10.1039/C8CC03550D>.
- (126) Goldschmid, S. L.; Soon Tay, N. E.; Joe, C. L.; Lainhart, B. C.; Sherwood, T. C.; Simmons, E. M.; Sezen-Edmonds, M.; Rovis, T. Overcoming Photochemical Limitations in Metallaphotoredox Catalysis: Red-Light-Driven C–N Cross-Coupling. *J. Am. Chem. Soc.* **2022**, *144* (49), 22409–22415. <https://doi.org/10.1021/jacs.2c09745>.
- (127) Sun, R.; Qin, Y.; Nocera, D. G. General Paradigm in Photoredox Nickel-Catalyzed Cross-Coupling Allows for Light-Free Access to Reactivity. *Angew. Chem. Int. Ed.* **2020**, *59* (24), 9527–9533. <https://doi.org/10.1002/anie.201916398>.

- (128) Na, H.; Mirica, L. M. Deciphering the Mechanism of the Ni-Photocatalyzed C–O Cross-Coupling Reaction Using a Tridentate Pyridinophane Ligand. *Nat. Commun.* **2022**, *13* (1), 1313. <https://doi.org/10.1038/s41467-022-28948-8>.
- (129) Mohadjer Beromi, M.; Brudvig, G. W.; Hazari, N.; Lant, H. M. C.; Mercado, B. Q. Synthesis and Reactivity of Paramagnetic Nickel Polypyridyl Complexes Relevant to C(sp²)–C(sp³) Coupling Reactions. *Angew. Chem. Int. Ed.* **2019**, *58* (18), 6094–6098. <https://doi.org/10.1002/anie.201901866>.
- (130) Ghosh, I.; Shlapakov, N.; Karl, T. A.; Düker, J.; Nikitin, M.; Burykina, J. V.; Ananikov, V. P.; König, B. General Cross-Coupling Reactions with Adaptive Dynamic Homogeneous Catalysis. *Nature* **2023**, *619* (7968), 87–93. <https://doi.org/10.1038/s41586-023-06087-4>.
- (131) Cavedon, C.; Gisbertz, S.; Reischauer, S.; Vogl, S.; Sperlich, E.; Burke, J. H.; Wallick, R. F.; Schrottke, S.; Hsu, W.-H.; Anghileri, L.; Pfeifer, Y.; Richter, N.; Teutloff, C.; Müller-Werkmeister, H.; Cambié, D.; Seeberger, P. H.; Vura-Weis, J.; van der Veen, R. M.; Thomas, A.; Pieber, B. Intraligand Charge Transfer Enables Visible-Light-Mediated Nickel-Catalyzed Cross-Coupling Reactions. *Angew. Chem. Int. Ed.* **2022**, *61* (46), e202211433. <https://doi.org/10.1002/anie.202211433>.
- (132) Li, G.; Yang, L.; Liu, J.-J.; Zhang, W.; Cao, R.; Wang, C.; Zhang, Z.; Xiao, J.; Xue, D. Light-Promoted C–N Coupling of Aryl Halides with Nitroarenes. *Angew. Chem. Int. Ed.* **2021**, *60* (10), 5230–5234. <https://doi.org/10.1002/anie.202012877>.
- (133) Yan, Y.; Sun, J.; Li, G.; Yang, L.; Zhang, W.; Cao, R.; Wang, C.; Xiao, J.; Xue, D. Photochemically Enabled, Ni-Catalyzed Cyanation of Aryl Halides. *Org. Lett.* **2022**, *24* (12), 2271–2275. <https://doi.org/10.1021/acs.orglett.2c00203>.
- (134) Rossenaar, B. D.; George, M. W.; Johnson, F. P. A.; Stufkens, D. J.; Turner, J. J.; Vlček, A. Jr. First Direct Structural Information on a Reactive $\sigma\pi^*$ Excited State: Time-Resolved UV–Vis and IR Spectroscopic Study of Re(benzyl)(CO)₃(iPr-DAB). *J. Am. Chem. Soc.* **1995**, *117* (46), 11582–11583. <https://doi.org/10.1021/ja00151a025>.
- (135) Stufkens, D. J.; Vlček, A. Ligand-Dependent Excited State Behaviour of Re(I) and Ru(II) Carbonyl–Diimine Complexes. *Coord. Chem. Rev.* **1998**, *177* (1), 127–179. [https://doi.org/10.1016/S0010-8545\(98\)00132-5](https://doi.org/10.1016/S0010-8545(98)00132-5).
- (136) Rossenaar, B. D.; Kleverlaan, C. J.; Stufkens, D. J.; Oskam, A. Photochemistry of ReR(CO)₃(Prⁱ-dab)(R = Me, Et, Bn; dab = 1,4-Diazabuta-1,3-Diene): Homolysis of the Re–R Bond, Its Dependence on R and Evidence for the Reactive $\sigma_b\pi^*$ State from Transient Absorption Spectra. *J. Chem. Soc. Chem. Commun.* **1994**, No. 1, 63–64. <https://doi.org/10.1039/C39940000063>.
- (137) Vlček, A.; Vichová, J.; Hartl, F. Bond Activation by MLCT Excitation of Organometallic Compounds: Prompt CO-Photodissociation from [Cr(CO)₄bpy]. *Coord. Chem. Rev.* **1994**, *132*, 167–174. [https://doi.org/10.1016/0010-8545\(94\)80037-5](https://doi.org/10.1016/0010-8545(94)80037-5).

- (138) Rossenaar, B. D.; Kleverlaan, C. J.; Van De Ven, M. C. E.; Stufkens, D. J.; Vlček, Jr., A. Mechanism of an Alkyl-Dependent Photochemical Homolysis of the Re–Alkyl Bond in $[\text{Re}(\text{R})(\text{CO})_3(\alpha\text{-diimine})]$ Complexes via a Reactive $\sigma\pi^*$ Excited State. *Chem. Eur. J.* **1996**, *2* (2), 228–237. <https://doi.org/10.1002/chem.19960020216>.
- (139) Hansch, Corwin.; Leo, A.; Taft, R. W. A Survey of Hammett Substituent Constants and Resonance and Field Parameters. *Chem. Rev.* **1991**, *91* (2), 165–195. <https://doi.org/10.1021/cr00002a004>.
- (140) Bím, D.; Luedecke, K. M.; Cagan, D. A.; Hadt, R. G. Light Activation and Photophysics of a Structurally Constrained Nickel(II)–Bipyridine Aryl Halide Complex. *Inorg. Chem.* **2024**, *63* (9), 4120–4131. <https://doi.org/10.1021/acs.inorgchem.3c03822>.
- (141) Oderinde, M. S.; Jin, S.; Das, J.; Jorge, C.; Yip, S.; Ramirez, A.; Wu, D.-R.; Li, Y.; Kempson, J.; Meanwell, N. A.; Mathur, A.; Dhar, T. G. M. Photo-Initiated Nickel Catalysis (PiNiC): Unmasking Dimethylnickel with Light. *ACS Catal.* **2022**, *12* (20), 12511–12520. <https://doi.org/10.1021/acscatal.2c04213>.
- (142) Kasha, M. Characterization of Electronic Transitions in Complex Molecules. *Discuss. Faraday Soc.* **1950**, *9* (0), 14–19. <https://doi.org/10.1039/DF9500900014>.
- (143) Demchenko, A. P.; Tomin, V. I.; Chou, P.-T. Breaking the Kasha Rule for More Efficient Photochemistry. *Chem. Rev.* **2017**, *117* (21), 13353–13381. <https://doi.org/10.1021/acs.chemrev.7b00110>.
- (144) Estrada, J. G.; Williams, W. L.; Ting, S. I.; Doyle, A. G. Role of Electron-Deficient Olefin Ligands in a Ni-Catalyzed Aziridine Cross-Coupling To Generate Quaternary Carbons. *J. Am. Chem. Soc.* **2020**, *142* (19), 8928–8937. <https://doi.org/10.1021/jacs.0c02237>.
- (145) Feng, Y.; Luo, H.; Zheng, W.; Matsunaga, S.; Lin, L. Light-Promoted Nickel-Catalyzed Aromatic Halogen Exchange. *ACS Catal.* **2022**, *12* (18), 11089–11096. <https://doi.org/10.1021/acscatal.2c03354>.
- (146) Neese, F.; Solomon, E. I. MCD C-Term Signs, Saturation Behavior, and Determination of Band Polarizations in Randomly Oriented Systems with Spin $S \geq 1/2$. Applications to $S = 1/2$ and $S = 5/2$. *Inorg. Chem.* **1999**, *38* (8), 1847–1865. <https://doi.org/10.1021/ic981264d>.
- (147) Hahn, A. W.; Van Kuiken, B. E.; al Samarai, M.; Atanasov, M.; Weyhermüller, T.; Cui, Y.-T.; Miyawaki, J.; Harada, Y.; Nicolaou, A.; DeBeer, S. Measurement of the Ligand Field Spectra of Ferrous and Ferric Iron Chlorides Using 2p3d RIXS. *Inorg. Chem.* **2017**, *56* (14), 8203–8211. <https://doi.org/10.1021/acs.inorgchem.7b00940>.
- (148) Hahn, A. W.; Van Kuiken, B. E.; Chilkuri, V. G.; Levin, N.; Bill, E.; Weyhermüller, T.; Nicolaou, A.; Miyawaki, J.; Harada, Y.; DeBeer, S. Probing the Valence Electronic Structure of Low-Spin Ferrous and Ferric Complexes Using 2p3d Resonant Inelastic X-Ray Scattering

- (RIXS). *Inorg. Chem.* **2018**, *57* (15), 9515–9530. <https://doi.org/10.1021/acs.inorgchem.8b01550>.
- (149) Van Kuiken, B. E.; Hahn, A. W.; Maganas, D.; DeBeer, S. Measuring Spin-Allowed and Spin-Forbidden d–d Excitations in Vanadium Complexes with 2p3d Resonant Inelastic X-Ray Scattering. *Inorg. Chem.* **2016**, *55* (21), 11497–11501. <https://doi.org/10.1021/acs.inorgchem.6b02053>.
- (150) Ogawa, T.; Sinha, N.; Pfund, B.; Prescimone, A.; Wenger, O. S. Molecular Design Principles to Elongate the Metal-to-Ligand Charge Transfer Excited-State Lifetimes of Square-Planar Nickel(II) Complexes. *J. Am. Chem. Soc.* **2022**, *144* (48), 21948–21960. <https://doi.org/10.1021/jacs.2c08838>.
- (151) Song, G.; Li, Q.; Nong, D.-Z.; Song, J.; Li, G.; Wang, C.; Xiao, J.; Xue, D. Ni-Catalyzed Photochemical C–N Coupling of Amides with (Hetero)Aryl Chlorides. *Chem. Eur. J.* **2023**, *29* (37), e202300458. <https://doi.org/10.1002/chem.202300458>.
- (152) Zieleniewska, A.; Earley, J.; Yu, J.; Kudisch, M.; DiLuzio, S.; Cordones-Hahn, A.; Sayre, H.; Zhang, X.; Rumbles, G.; Reid, O. Tetrahedral to Octahedral Nickel(II) as an Initiation Step in Metallaphotoredox Catalysis. *ChemRxiv* August 24, 2023. <https://doi.org/10.26434/chemrxiv-2023-wptwr-v2>.
- (153) Li, R.; Yang, C.-X.; Niu, B.-H.; Li, L.-J.; Ma, J.-M.; Li, Z.-L.; Jiang, H.; Cheng, W.-M. Visible Light-Induced Ni-Catalyzed C–Heteroatom Cross-Coupling of Aryl Halides via LMCT with DBU to Access a Ni(I)/Ni(III) Cycle. *Org. Chem. Front.* **2022**, *9* (14), 3847–3853. <https://doi.org/10.1039/D2QO00607C>.
- (154) Song, G.; Yang, L.; Li, J.-S.; Tang, W.-J.; Zhang, W.; Cao, R.; Wang, C.; Xiao, J.; Xue, D. Chiral Arylated Amines via C–N Coupling of Chiral Amines with Aryl Bromides Promoted by Light. *Angew. Chem. Int. Ed.* **2021**, *60* (39), 21536–21542. <https://doi.org/10.1002/anie.202108587>.
- (155) Song, G.; Nong, D.-Z.; Li, J.-S.; Li, G.; Zhang, W.; Cao, R.; Wang, C.; Xiao, J.; Xue, D. General Method for the Amination of Aryl Halides with Primary and Secondary Alkyl Amines via Nickel Photocatalysis. *J. Org. Chem.* **2022**, *87* (15), 10285–10297. <https://doi.org/10.1021/acs.joc.2c01284>.
- (156) Song, G.; Nong, D.-Z.; Li, Q.; Yan, Y.; Li, G.; Fan, J.; Zhang, W.; Cao, R.; Wang, C.; Xiao, J.; Xue, D. Photochemical Synthesis of Anilines via Ni-Catalyzed Coupling of Aryl Halides with Ammonium Salts. *ACS Catal.* **2022**, *12* (24), 15590–15599. <https://doi.org/10.1021/acscatal.2c04959>.
- (157) Till, N. A.; Oh, S.; MacMillan, D. W. C.; Bird, M. J. The Application of Pulse Radiolysis to the Study of Ni(I) Intermediates in Ni-Catalyzed Cross-Coupling Reactions. *J. Am. Chem. Soc.* **2021**, *143* (25), 9332–9337. <https://doi.org/10.1021/jacs.1c04652>.

(158) Day, C. S.; Martin, R. Comproportionation and Disproportionation in Nickel and Copper Complexes. *Chem. Soc. Rev.* **2023**, *52* (19), 6601–6616. <https://doi.org/10.1039/D2CS00494A>.

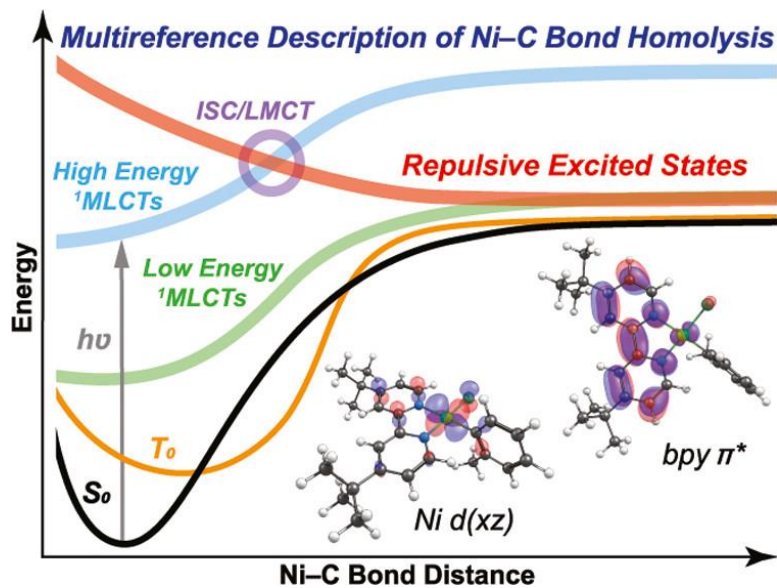
(159) Day, C. S. Advances in Understanding Comproportionation and Disproportionation in Nickel Catalysis. *Pure Appl. Chem.* **2024**. <https://doi.org/10.1515/pac-2024-0106>.

(160) Li, Z.; Li, C.; Ding, Y.; Huo, H. Photoinduced Nickel-Catalyzed Enantioselective Coupling Reactions. *Coord. Chem. Rev.* **2022**, *460*, 214479. <https://doi.org/10.1016/j.ccr.2022.214479>.

(161) Poremba, K. E.; Dibrell, S. E.; Reisman, S. E. Nickel-Catalyzed Enantioselective Reductive Cross-Coupling Reactions. *ACS Catal.* **2020**, *10* (15), 8237–8246. <https://doi.org/10.1021/acscatal.0c01842>.

Chapter 2

Multireference Description of Nickel–Aryl Homolytic Bond Dissociation Processes in Photoredox Catalysis



Adapted with permission from:

Cagan, D.A.;[†] Stroschio, G.D.;[†] Cusumano, A.Q.; Hadt, R.G. Multireference Description of Nickel–Aryl Bond Dissociation Processes in Photoredox Catalysis. *J. Phys. Chem. A.* **2020**, *124*(48), 9915–9922. DOI: 10.1021/acs.jpca.0c08646. [†]Co-first author.
Copyright 2020 American Chemical Society.

§2-1. Introduction

Merging thermal catalysis with photochemistry (i.e., photoredox catalysis) has provided new, more sustainable routes to bond activations and coupling reactions in organic synthesis.¹⁻¹⁰ An extension of solar energy conversion, photoredox catalysis utilizes photosensitizers to harvest photon energy and transform it into chemical potential to drive single electron transfer (SET) processes to generate reactive high- and/or low-valent species and important organic radicals. However, photoredox reactions feature complex mechanisms that are challenging to elucidate, and our understanding of how photon energy drives organic transformations is therefore still growing.

Beyond SET, photosensitizer energy transfer can form photocatalyst excited states that can be uniquely reactive relative to ground states.¹¹⁻¹⁶ The photocatalyst can also potentially act as both the light-absorbing and catalytic unit through direct excitation.^{17,18} In direct excitation and energy-transfer-mediated catalysis, the ultrafast photophysical processes of transition metal excited-state relaxation can also contribute to reactivity.⁹ Notably, Ni(II) complexes of 2,2'-bipyridine (bpy) exhibit photocatalytic activity for coupling reactions using either energy transfer^{11,19} or direct excitation.²⁰ Several mechanistic hypotheses have been discussed and are summarized in Figure 1. In one scenario, energy transfer to a Ni(II)-bpy aryl acetate complex induces reductive elimination from a triplet excited state of Ni(II) (**Figure 2.1A**, bottom), originally proposed to be ligand field in nature.¹¹ Ni(II)-to-bpy metal-to-ligand charge transfer (MLCT) excited states have also been suggested to: 1) mediate bimolecular electron transfer to generate Ni(I) and Ni(III) species for catalysis,¹⁷ or 2) directly mediate reductive elimination.²¹ The latter consideration encompasses the one-electron oxidatively induced ground state formal Ni(III) reactivity discovered by Hillhouse and co-workers.^{22,23}

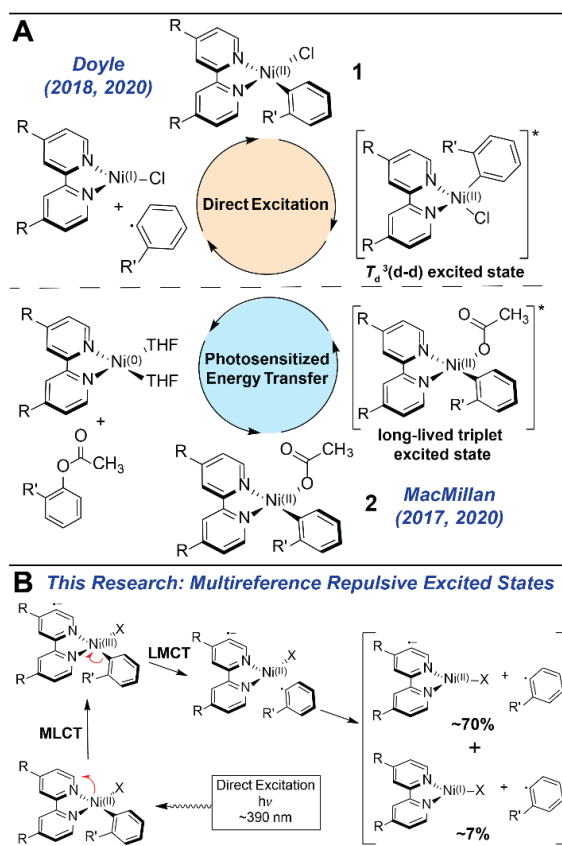


Figure 2.1. (A) Two previous mechanistic hypotheses related to Ni–bpy photoredox catalysis and (B) findings in this study. Complex **1** = Ni(II)(*t*-Bu^{bpy})(*o*-tolyl)Cl; Complex **2** = Ni(II)(bpy)(ph)(ac) (ph = phenyl, ac = acetate).

Thermally assisted homolytic Ni(II)–C bond dissociation from photochemically formed triplet ligand field excited states in Ni(II)–bpy aryl halide complexes has also been proposed. This process results in the formation of formal Ni(I) and aryl radicals (**Figure 2.1A**, top).¹⁸ While it is unclear whether these species initiate a subsequent Ni(I)/Ni(III) catalytic cycle, this represents an intriguing means to photochemically generate reduced Ni species and organic radicals for ground-state thermal catalysis.^{18,20} Overall, more detailed experimental and theoretical descriptions of the ground-state bonding and excited-state relaxation processes in Ni–bpy complexes (and other Ni heteroaromatic complexes²⁴) are critical for developing synthetic applications.

Here we describe a new electronic structural framework to interpret experimental data on Ni(II)–bpy complexes of relevance to photoredox catalysis. Of particular importance is the multireference description (relative to DFT), which manifests in mixed ground and excited-state wave functions and potential energy surfaces (PESs) in Ni(II)–C homolytic bond dissociation. Intractable barriers are found for thermal bond dissociation from the lowest-energy triplet ligand field excited state within the multireference framework. However, higher-energy repulsive triplet excited states are found here and are proposed to be responsible for homolytic bond dissociation. These triplet excited states feature a high-spin Ni(II) coupled to anionic bpy and neutral aryl radicals and can be generated from initial ¹MLCT excitation (Ni(II)-to-bpy) followed by intersystem crossing and intramolecular charge transfer (aryl-to-Ni(III)) (**Figure 2.1B**).

§2-2. Computational Methods

Calculations were performed using ORCA^{25,26} version 4.2.1. The BP86²⁷⁻²⁹ functional was used for geometry optimizations and frequency calculations, including both full geometry optimizations and constrained optimizations where the Ni–C bond length was systematically varied. The 6-311G(d)³⁰ basis set was used on all atoms, and AutoAux³¹ was used as the auxiliary basis set. Split-RI-J, the default and recommended version of resolution of identities³²⁻³⁵ (RI) approximation was used. The finest available DFT grids were used (GRID7 NOFINALGRID). Very tight SCF convergence criteria, which has a convergence tolerance of 10⁻⁹ Hartrees, was applied for all DFT calculations. The restricted Kohn–Sham formalism (RKS) was used for the singlet ground-state optimizations; the unrestricted Kohn–Sham formalism (UKS) was used for the triplet optimizations. Additional single point calculations using the B3LYP^{28,36} functional, the def2-TZVP³⁷ basis, and implicit solvation by tetrahydrofuran (THF) modeled by the conductor-like polarizable continuum model³⁸ (CPCM) were performed on optimized structures. Here the RIJCOX³⁹ approximation was used with fine DFT grids (GRID7 NOFINALGRID GRIDX9). At this level of theory, broken-symmetry singlet (BSS) and unrestricted triplet single point calculations were performed on the $S = 0$ and $S = 1$ optimized geometries, respectively. Likewise, TDDFT calculations were performed using these same settings. Applying a Yamaguchi spin

correction^{40,41} did not significantly affect the BSS dissociations energies of **1** and **2**. It lowered the dissociation energy of **1** from 43.3 kcal mol⁻¹ to 41.7 kcal mol⁻¹ (Table S1P); it barely changed the dissociation energy of **2** from 44.9 kcal mol⁻¹ to 45.1 kcal mol⁻¹ (Table S2L). Sample input DFT and TDDFT parameters are given on page S3.

Quasidegenerate N-electron valence second-order perturbation theory⁴² (QD-NEVPT2) corrected complete active space self-consistent field (CASSCF) single point calculations were performed on DFT-optimized geometries. As suggested in the documentation for ORCA CASSCF-based calculations, tight SCF convergence criteria with an energy tolerance of 10⁻⁷ Hartrees were applied. The def2-TZVP basis set was used on all atoms, and the RIJCOSX approximation was employed. Note that the number of states averaged was varied (see Table S1G-1–S1G-3), and it was found that a state-averaging with fifteen singlets and twenty-five triplets yielded a thorough description of the ground and excited states of interest while maintaining reasonable computational costs. Therefore, state-averaged CASSCF/QD-NEVPT2 single point calculations utilized fifteen singlets and twenty-five triplets throughout. The recommended Nakano formalism was used, and the corresponding CI vectors are tabulated below. A comparison between gas phase and solvent corrected CASSCF/QD-NEVPT2 single point calculations yielded qualitatively similar results at both the singlet equilibrium geometry and at longer Ni–C distances (3.2 Å for **1** and 3.1 Å for **2**); therefore, gas phase calculations were conducted on all structures (comparisons are tabulated below). Sample input files for CASSCF/QD-NEVPT2 calculations are given on page S3.

The size of the active space was varied until a thorough description of **1** and **2** was reached (comparisons between active space sizes are tabulated below). Active spaces are shown in Figures S1C and S1E for **1** ($S = 0$ and $S = 1$) and Figure S2C and S2E for **2** ($S = 0$ and $S = 1$). The first 10-20 lowest-energy roots, CI vectors, transitions, and oscillator strengths are tabulated below. An active space consisting of nine orbitals filled with ten electrons (9o/10e): $d(xy)$, $d(z^2)$, $d(xz)$, $d(yz)$, a pair of bonding and antibonding orbitals from the $d(x^2-y^2)$ and the C(sp²) orbital on the dissociating phenyl group, and three π^* orbitals on the bipyridine ligand, were found to be thorough descriptors of the $S=0$ equilibrium geometry of **1**, while

an additional orbital was added for **2**. The additional orbital in **2** is a bonding $d(xy)/C(\pi)$ orbital (see Figure S2C), which was kept in the active space due to its partially unfilled occupancy of 1.93 (for compound **1**, this orbital has occupancy of ~ 2 (1.99), and thus was not needed to generate a complete active space). However, as can be seen in Table S2C1-3, the additional orbital in **2** was not involved in any critical transitions. At all other Ni–C bond lengths, the third bpy π^* orbital exhibited very low occupancy and was removed to aid convergence. For example, the ten electrons in nine orbitals CASSCF calculation using the 3.6 Å geometry of **1**, the third π^* orbital had an extremely low active space occupancy value of 0.00004.

As the Ni–C bond was elongated and eventually cleaved, the molecular geometry along the singlet surface approached that of the optimized triplet surface. This observation is particularly clear for **2**. Geometry coordinates along the Ni–C scan are listed in the Appendix portion of the Supporting Information. The active space for the triplet scan of **1** again consisted of the ten electrons in eight orbitals (active space with the third π^* removed, Figure S1E). Here the third bpy π^* again had very low active space occupancy values (~ 0.0001). This was true in geometries ranging from 2.0 Å to 3.6 Å. For triplet structures of **1** with a short Ni–C bond (between 1.6–2.0 Å), the second π^* orbital was similarly removed to aid convergence. For the triplet scan of **2**, it was possible to use an active space of ten electrons in nine orbitals active space for the entire scan (Figure S2E).

§2-3. Results and Discussion

Homolytic bond dissociation is an inherently multireference process that can pose difficulties for DFT.^{43,44} Analyses therefore began by comparing the ground-state wave functions of Ni(II)(*t*-Bu₃bpy)(*o*-tolyl)Cl (**1**) and Ni(II)(bpy)(ph)(ac) (ph = phenyl, ac = acetate) (**2**), as well as their lowest-energy singlet and triplet bond dissociation energies (BDEs) using both DFT and multireference ab initio calculations (i.e., CASSCF and quasidegenerate N-electron valence state second-order perturbation theory (QD-NEVPT2⁴²)) within ORCA^{25,26} (see Supporting Information for computational details).

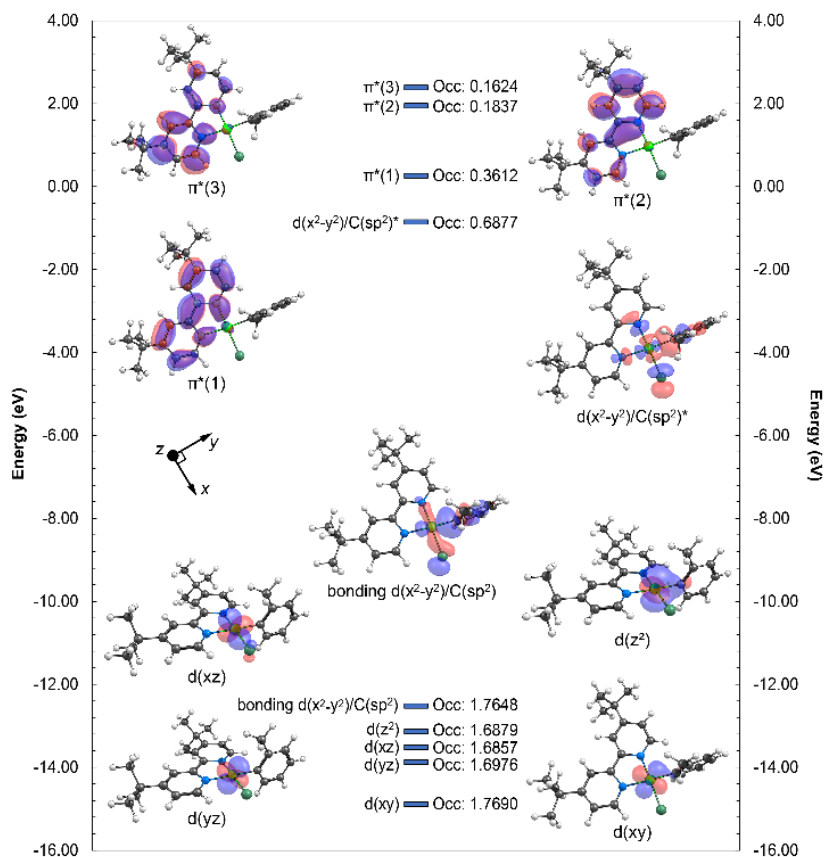


Figure 2.2. Simplified MO diagram of **1** as calculated by CASSCF/QD-NEVPT2 using a nine orbital, ten electron active space. Natural orbitals energies are plotted; orbital occupancies are labeled.

CASSCF/QD-NEVPT2 calculations on **1** and **2** exhibit appreciable ground-state multiconfigurational character (S1C/S2C and Tables S1C/S2C-1). Using a nine orbital, ten electron active space (**Figure 2.2**, S1C), the dominant contributions to the configuration interaction (CI) vector of the singlet ground state of **1** are ~58 % low-spin d^8 (closed-shell singlet, CSS) and ~22 % 1MLCT (Table S1E). Similar values are obtained for **2** (~57% CSS and ~23 % 1MLCT) (Table S2D-2). With only an eight electron, five 3d-orbital active space, the low-spin d^8 character increases to ~95 % in both **1** and **2** (Table S1A-2/S2B-2). Thus, the unoccupied π^* orbitals, which have high active space occupancies, play a critical role in the degree of multiconfigurational ground-state bonding.

It is interesting to consider the multireference data in the context of the DFT bonding description. The low-spin $d(x^2-y^2)$ ground states of **1** and **2** are highly covalent (~56/57 % Ni(II) and ~11/13 % bpy character), with some back-bonding (~7-8 % occupied Ni(II) character in the bpy-based unoccupied π^* orbitals of both **1** and **2**) (Figure S1B/S2B). This highly covalent bonding framework is not particularly amenable to formal redox state assignment and is more consistent with a multiconfigurational bonding description.^{45,46}

PESs for Ni(II)–C bond dissociations from **1** and **2** are given in **Figures 2.3A** and S2G, respectively. The DFT BDEs are ~43 kcal mol⁻¹ and ~31 kcal mol⁻¹ starting from the relaxed, lowest-energy singlet and triplet structures of **1**, respectively, consistent with the ~32 kcal mol⁻¹ from a study invoking thermal homolysis on the triplet PES.¹⁸ Values for **2** are similar (~45 kcal mol⁻¹ and ~38 kcal mol⁻¹). The multireference bond dissociation is fundamentally different than DFT, with significantly higher BDEs (~87/65 kcal mol⁻¹ and 73/70 kcal mol⁻¹ from the lowest-energy singlet and triplet states of **1/2**), suggesting the Ni(II)–C bonds are stronger than in DFT and will not be thermally cleaved, even upon formation of the relaxed lowest-energy triplet ligand field excited state. This difference is important, as the ~30 kcal mol⁻¹ barrier was used to rationalize photochemical formation of radicals and reduced Ni species from **1**.¹⁸

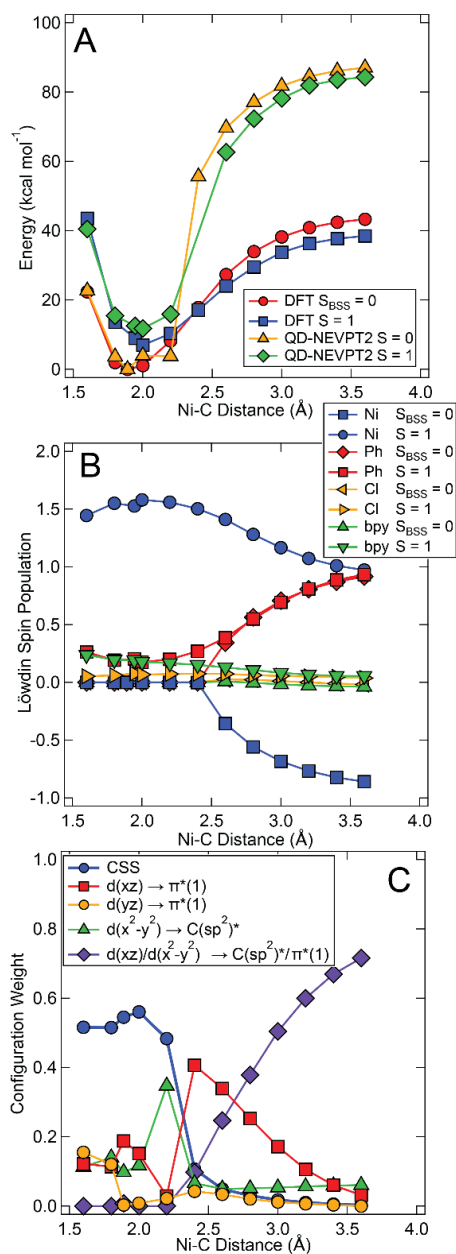


Figure 2.3. Ni(II)–C bond dissociation from the lowest-energy singlet and triplet states in **1**. (A) Relaxed DFT vs. CASSCF/QD-NEVPT2 PESs and (B) DFT Löwdin spin densities for both the singlet (BSS) and triplet states and (C) the CASSCF/QD-NEVPT2 lowest-energy singlet CI vector.

From Löwdin spin density plots in **Figures 2.3B** and S2H, the DFT-based homolytic bond dissociation results in the formation of Ni(I) and neutral aryl radicals for **1** and **2**. The

compositions of the multiconfigurational ground-state CI vectors of **1** and **2** upon bond dissociation from the singlet ground state are given in **Figures 2.3C** and S2I, respectively, and describe the nature of bond homolysis. Upon initial elongation of the Ni–C bond, the amount of low-spin d^8 character (CSS) decreases significantly, with a concomitant increase in the weighting of $^1\text{MLCT}$ character at 2.4 Å, beyond which the CI vector becomes dominantly $d(xz)/d(x^2-y^2) \rightarrow C(\text{sp}^2)^*/\pi^*$, formally corresponding to a high-spin Ni(II) coupled to anionic bpy and neutral aryl radicals. Some additional formal Ni(I) character is also present (~7 %). Independent DFT vs. multireference calculations on the formal Ni(I) species after homolytic bond dissociation (**Figure 2.4**) further support this description. Notably, similar ligand redox has been observed for reduced formal Ni(I) species in ground-state cross-coupling reactions.^{24,47}

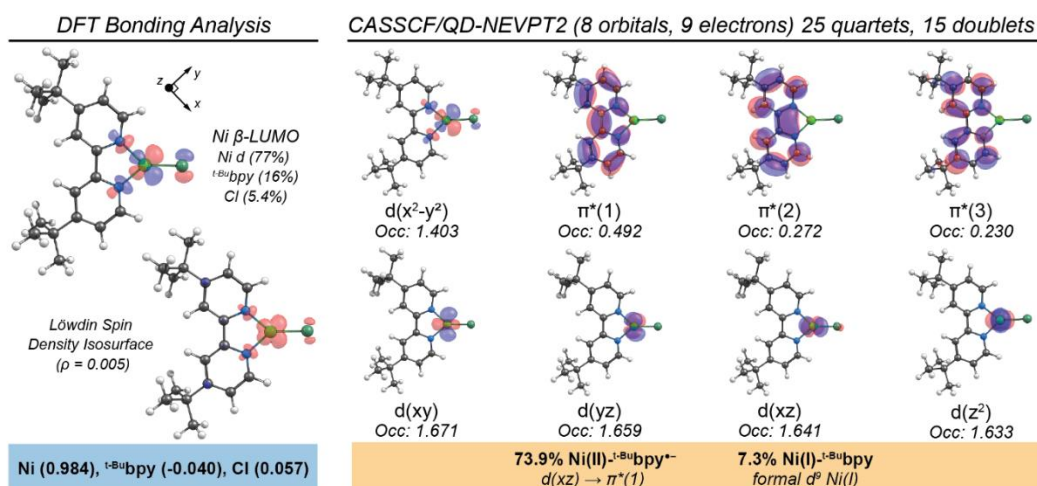


Figure 2.4. DFT (left) vs. CASSCF/QD-NEVPT2 (right) description of the formal Ni(I) species formed upon homolytic Ni–C bond cleavage.

Given the intractability of thermally assisted Ni(II)–C homolysis and radical formation from the lowest-energy triplet ligand field excited states, we now further describe the excited-state PESs/manifolds of **1** and **2** to develop new understanding of the mechanism of homolytic bond dissociation. TDDFT and CASSCF/QD-NEVPT2 calculated excited-state manifolds at the ground-state singlet relaxed structures of **1** and **2** are given in Figure S1G and Tables S1I–K, S2A, and S2C. Both methods predict a set of lower and higher-energy $^1,^3\text{MLCTs}$.

However, their relative oscillator strengths differ somewhat from one another and, for **1**, the experimental spectrum.

The CASSCF/QD-NEVPT2 ground and excited-state PESs along the Ni(II)–C coordinate of **1** and **2** are given in **Figure 2.5** and S2J, respectively, while the analogous TDDFT PESs are given in Figure S1F and S2K, respectively. From **Figure 2.5**, repulsive excited states are present (left panel: black, red, and yellow lines). The higher-energy MLCT excited states (**A** in **Figure 2.5**, left) cross the repulsive surfaces at Ni–C bond distances of ~ 2.3 – 2.4 Å (circled in **Figure 2.5**) in both **1** and **2** with an activation energy from the Franck-Condon point of ~ 25 kcal mol⁻¹. Thus, the multireference approach predicts homolytic bond dissociation occurs via population of a ¹MLCT excited state (Ni(II)-to-bpy) followed by an intersystem crossing and intramolecular charge transfer (aryl-to-Ni(III)) (**Figure 2.1B**). The resulting multiconfigurational species can be described as a high-spin Ni(II) with antiferromagnetically coupled electrons on the bpy and phenyl ligands (see Supporting Information Tables S1Q–R and S2M–N for more details). Interestingly, this description is conceptually similar to that given for the mixed MLCT/ $\sigma\pi^*$ (sigma bond to ligand charge transfer) photoinduced radical formation in Re(I) and Ru(II) complexes.⁴⁸⁻⁵⁷ Here, the intersystem crossing could occur between the ^{1,3}MLCT states or the ¹MLCT and dissociative triplet state. Overall, this represents a novel homolytic bond dissociation mechanism in nickel catalysis, which we propose derives from the redox noninnocent and multiconfigurational ground and excited-state bonding in Ni(II)–bpy complexes.

Experimentally, the lowest-energy triplet ligand field excited states of Ni(II)–bpy aryl halide complexes are populated in ~ 5 - 10 ps.¹⁸ Given an estimated Ni(II)–C frequency of ~ 250 cm⁻¹, ~ 40 - 80 vibrational periods could occur to drive intersystem and surface crossings that could compete with population of the lowest-energy triplet ligand field state. A higher-energy aryl vibration (~ 650 cm⁻¹; Figures S1I/S2L for **1** and **2**, respectively) exhibiting significant changes in Ni–C bond distance may also provide ~ 100 - 200 vibrational periods to drive these processes.

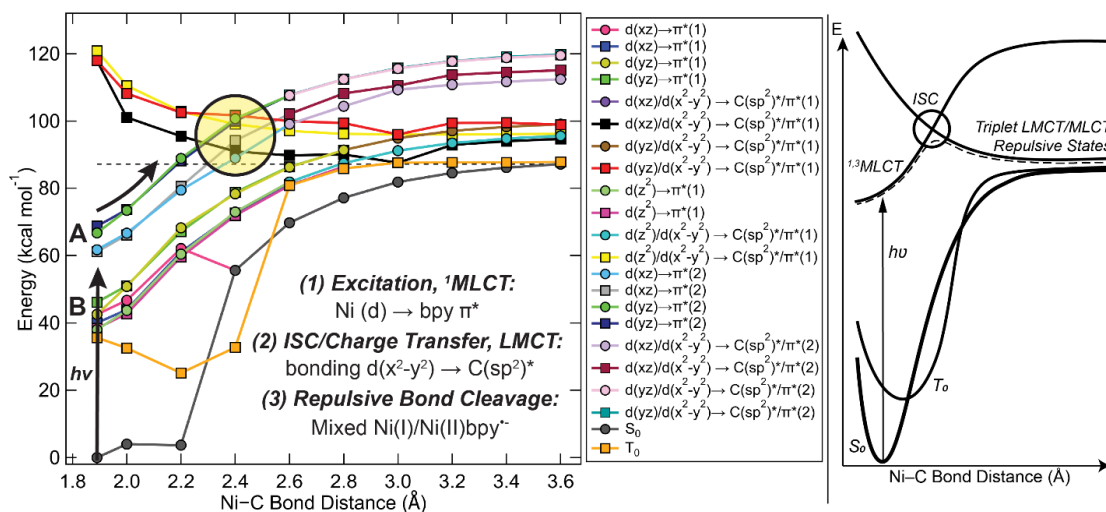


Figure 2.5. CASSCF/QD-NEVPT2 relaxed ground- and excited-state PESs along the Ni–C coordinate of **1**. *Left*: Vertical excitation (black vertical arrow), the higher (A) and lower-energy (B) manifolds of MLCTs, and the crossings between the higher-energy MLCTs and repulsive triplets (circled) are depicted. Singlet states, circles; triplets, squares. *Right*: Simplified depiction of the UV light photoinduced Ni–C bond homolysis process.

The yield of cross-coupled product obtained from direct excitation of **1** is incident light dependent; high yields are only observed with UV light (390–395 nm or ~ 70 kcal mol⁻¹),²⁰ corresponding to excitation into the higher-energy manifold of MLCT states (**Figure 2.5**). Of particular relevance to compound **2**, variations in the energy of the photosensitizer triplet state demonstrated C–O coupling occurs when ~ 40 – 45 kcal mol⁻¹ is transferred to the Ni catalyst.¹¹ This energy would excite complexes to the lower-energy manifold of MLCT states (**Figure 2.5**, S2J), resulting in thermodynamically unfavorable radical formation (~ 45 kcal mol⁻¹) for both **1** and **2**. Thus, an alternative relaxation pathway and mechanism may exist for photosensitized cross-coupling. In fact, triplet ligand field excited-state formation, reductive elimination, and homolytic bond dissociation may all be possible for a given Ni(II)–bpy complex. We believe the ligands in addition to bpy will be of particular importance in determining the relative propensity for specific relaxation pathways. For example, reductive elimination is disfavored for the aryl halide (**1**) relative to the aryl carboxylate (**2**). This may preferentially lead to excited-state processes that favor the

formation of radicals and ligand field excited states over an intractable photosensitized or direct excitation induced reductive elimination. A future study will aim to elucidate and analyze these potentially competitive pathways.

§2-4. Conclusions

In summary, we have provided a new electronic structural framework to interpret UV light-induced homolytic bond dissociation in Ni(II)–bpy complexes of relevance for photoredox catalysis. Compared to DFT, multireference ab initio calculations predict: 1) thermal homolysis from the lowest-energy triplet ligand field excited state is not energetically favorable (barriers: DFT ~ 30 kcal mol⁻¹, CASSCF/QD-NEVPT2 ~ 70 kcal mol⁻¹), 2) initial population of a Ni(II)-to-bpy ¹MLCT excited state can be followed by intersystem crossing and aryl-to-Ni(III) intramolecular charge transfer, resulting in the formation of repulsive triplet excited states described as a high-spin Ni(II) coupled to anionic bpy and neutral aryl radicals. Formally, this represents an overall two-electron transfer process driven by a single photon. The formation of repulsive excited states likely also competes with relaxation to the experimentally observed triplet ligand field excited state, which further relaxes to the ground state without radical formation. 3) The immediate products of homolytic bond dissociation are not Ni(I)–bpy and an aryl radical as described by DFT, but rather, a multiconfigurational species with a dominantly high-spin Ni(II) coupled to a redox-active bpy anion radical ligand, similar to descriptions for formal Ni(I) intermediates in ground-state thermal cross-coupling catalysis.^{24,47}

§2-5. References

- (1) Nicewicz, D. A.; MacMillan, D. W. C. Merging Photoredox Catalysis with Organocatalysis: The Direct Asymmetric Alkylation of Aldehydes. *Science* **2008**, *322*, 77–80.
- (2) Prier, C. K.; Rankic, D. A.; MacMillan, D. W. C. Visible Light Photoredox Catalysis with Transition Metal Complexes: Applications in Organic Synthesis. *Chem. Rev.* **2013**, *113*, 5322–5363.
- (3) Shaw, M. H.; Twilton, J.; MacMillan, D. W. C. Photoredox Catalysis in Organic Chemistry. *J. Org. Chem.* **2016**, *81*, 6898–6926.
- (4) Twilton, J.; Le, C. (Chip); Zhang, P.; Shaw, M. H.; Evans, R. W.; MacMillan, D. W. C. The Merger of Transition Metal and Photocatalysis. *Nat. Rev. Chem.* **2017**, *1*, 0052.
- (5) Cavalcanti, L. N.; Molander, G. A. Photoredox Catalysis in Nickel-Catalyzed Cross-Coupling. *Top. Curr. Chem.* **2016**, *374*, 39.
- (6) Milligan, J. A.; Phelan, J. P.; Badir, S. O.; Molander, G. A. Alkyl Carbon–Carbon Bond Formation by Nickel/Photoredox Cross-Coupling. *Angew. Chem. Int. Ed.* **2019**, *58*, 6152–6163.
- (7) Larsen, C. B.; Wenger, O. S. Photoredox Catalysis with Metal Complexes Made from Earth-Abundant Elements. *Chem. Eur. J.* **2018**, *24*, 2039–2058.
- (8) Schultz, D. M.; Yoon, T. P. Solar Synthesis: Prospects in Visible Light Photocatalysis. *Science* **2014**, *343*, 1239176.
- (9) Arias-Rotondo, D. M.; McCusker, J. K. The Photophysics of Photoredox Catalysis: A Roadmap for Catalyst Design. *Chem. Soc. Rev.* **2016**, *45*, 5803–5820.
- (10) Yoon, T. P.; Ischay, M. A.; Du, J. Visible Light Photocatalysis as a Greener Approach to Photochemical Synthesis. *Nat. Chem.* **2010**, *2*, 527–532.
- (11) Welin, E. R.; Le, C.; Arias-Rotondo, D. M.; McCusker, J. K.; MacMillan, D. W. C. Photosensitized, Energy Transfer-Mediated Organometallic Catalysis through Electronically Excited Nickel(II). *Science* **2017**, *355*, 380–385.
- (12) Ischay, M. A.; Anzovino, M. E.; Du, J.; Yoon, T. P. Efficient Visible Light Photocatalysis of [2+2] Enone Cycloadditions. *J. Am. Chem. Soc.* **2008**, *130*, 12886–12887.

- (13) Lu, Z.; Yoon, T. P. Visible Light Photocatalysis of [2+2] Styrene Cycloadditions by Energy Transfer. *Angew. Chem. Int. Ed.* **2012**, *51*, 10329–10332.
- (14) Zhang, Z.; Rogers, C. R.; Weiss, E. A. Energy Transfer from CdS QDs to a Photogenerated Pd Complex Enhances the Rate and Selectivity of a Pd-Photocatalyzed Heck Reaction. *J. Am. Chem. Soc.* **2020**, *142*, 495–501.
- (15) Strieth-Kalthoff, F.; Glorius, F. Triplet Energy Transfer Photocatalysis: Unlocking the Next Level. *Chem* **2020**, *6*, 1888–1903.
- (16) Strieth-Kalthoff, F.; J. James, M.; Teders, M.; Pitzer, L.; Glorius, F. Energy Transfer Catalysis Mediated by Visible Light: Principles, Applications, Directions. *Chem. Soc. Rev.* **2018**, *47*, 7190–7202.
- (17) Shields, B. J.; Kudisch, B.; Scholes, G. D.; Doyle, A. G. Long-Lived Charge-Transfer States of Nickel(II) Aryl Halide Complexes Facilitate Bimolecular Photoinduced Electron Transfer. *J. Am. Chem. Soc.* **2018**, *140*, 3035–3039.
- (18) Ting, S. I.; Garakyaraghi, S.; Taliaferro, C. M.; Shields, B. J.; Scholes, G. D.; Castellano, F. N.; Doyle, A. G. 3d-d Excited States of Ni(II) Complexes Relevant to Photoredox Catalysis: Spectroscopic Identification and Mechanistic Implications. *J. Am. Chem. Soc.* **2020**, *142*, 5800–5810.
- (19) Kim, T.; McCarver, S. J.; Lee, C.; MacMillan, D. W. C. Sulfonamidation of Aryl and Heteroaryl Halides through Photosensitized Nickel Catalysis. *Angew. Chem. Int. Ed.* **2018**, *57*, 3488–3492.
- (20) Yang, L.; Lu, H.-H.; Lai, C.-H.; Li, G.; Zhang, W.; Cao, R.; Liu, F.; Wang, C.; Xiao, J.; Xue, D. Light-Promoted Nickel Catalysis: Etherification of Aryl Electrophiles with Alcohols Catalyzed by a Ni(II)-Aryl Complex. *Angew. Chem. Int. Ed.* **2020**, *59*, 12714–12719.
- (21) Ma, P.; Wang, S.; Chen, H. Reactivity of Transition-Metal Complexes in Excited States: C–O Bond Coupling Reductive Elimination of a Ni(II) Complex Is Elicited by the Metal-to-Ligand Charge Transfer State. *ACS Catal.* **2020**, *10*, 1–6.
- (22) Koo, K.; Hillhouse, G. L. Carbon-Nitrogen Bond Formation by Reductive Elimination from Nickel(II) Amido Alkyl Complexes. *Organometallics* **1995**, *14*, 4421–4423.

- (23) Han, R.; Hillhouse, G. L. Carbon–Oxygen Reductive-Elimination from Nickel(II) Oxametallacycles and Factors That Control Formation of Ether, Aldehyde, Alcohol, or Ester Products. *J. Am. Chem. Soc.* **1997**, *119*, 8135–8136.
- (24) Jones, G. D.; Martin, J. L.; McFarland, C.; Allen, O. R.; Hall, R. E.; Haley, A. D.; Brandon, R. J.; Konovalova, T.; Desrochers, P. J.; Pulay, P.; Vivic, D. A. Ligand Redox Effects in the Synthesis, Electronic Structure, and Reactivity of an Alkyl–Alkyl Cross-Coupling Catalyst. *J. Am. Chem. Soc.* **2006**, *128*, 13175–13183.
- (25) Neese, F. The ORCA Program System. *Wiley Interdiscip. Rev. Comput. Mol. Sci.* **2012**, *2*, 73–78.
- (26) Neese, F. Software Update: The ORCA Program System, Version 4.0. *Wiley Interdiscip. Rev. Comput. Mol. Sci.* **2018**, *8*, e1327.
- (27) Perdew, J. P. Density-Functional Approximation for the Correlation Energy of the Inhomogeneous Electron Gas. *Phys. Rev. B* **1986**, *33*, 8822–8824.
- (28) Becke, A. D. Density-Functional Exchange-Energy Approximation with Correct Asymptotic Behavior. *Phys. Rev. A* **1988**, *38*, 3098–3100.
- (29) Becke, A. D. Density-functional Thermochemistry. III. The Role of Exact Exchange. *J. Chem. Phys.* **1993**, *98*, 5648–5652.
- (30) Curtiss, L. A.; McGrath, M. P.; Blaudeau, J.; Davis, N. E.; Binning, R. C.; Radom, L. Extension of Gaussian-2 Theory to Molecules Containing Third-row Atoms Ga–Kr. *J. Chem. Phys.* **1995**, *103*, 6104–6113.
- (31) Stoychev, G. L.; Auer, A. A.; Neese, F. Automatic Generation of Auxiliary Basis Sets. *J. Chem. Theory Comput.* **2017**, *13*, 554–562.
- (32) Neese, F. An Improvement of the Resolution of the Identity Approximation for the Formation of the Coulomb Matrix. *J. Comput. Chem.* **2003**, *24*, 1740–1747.
- (33) Kossmann, S.; Neese, F. Comparison of Two Efficient Approximate Hartree–Fock Approaches. *Chem. Phys. Lett.* **2009**, *481*, 240–243.
- (34) Izsák, R.; Neese, F. An Overlap Fitted Chain of Spheres Exchange Method. *J. Chem. Phys.* **2011**, *135*, 144105.

- (35) Izsák, R.; Neese, F. Speeding up Spin-Component-Scaled Third-Order Perturbation Theory with the Chain of Spheres Approximation: The COSX-SCS-MP3 Method. *Mol. Phys.* **2013**, *111*, 1190–1195.
- (36) Lee, C.; Yang, W.; Parr, R. G. Development of the Colle-Salvetti Correlation-Energy Formula into a Functional of the Electron Density. *Phys. Rev. B* **1988**, *37*, 785–789.
- (37) Weigend, F.; Ahlrichs, R. Balanced Basis Sets of Split Valence, Triple Zeta Valence and Quadruple Zeta Valence Quality for H to Rn: Design and Assessment of Accuracy. *Phys Chem Chem Phys* **2005**, *7*, 3297–3305.
- (38) Barone, V.; Cossi, M. Quantum Calculation of Molecular Energies and Energy Gradients in Solution by a Conductor Solvent Model. *J. Phys. Chem. A* **1998**, *102*, 1995–2001.
- (39) Kossmann, S.; Neese, F. Efficient Structure Optimization with Second-Order Many-Body Perturbation Theory: The RIJCOSX-MP2 Method. *J. Chem. Theory Comput.* **2010**, *6*, 2325–2338.
- (40) Yamaguchi, K.; Takahara, Y.; Fueno, T.; Houk, K. N. Extended Hartree–Fock (EHF) Theory of Chemical Reactions. *Theor. Chim. Acta* **1988**, *73*, 337–364.
- (41) Kitagawa, Y.; Saito, T.; Nakanishi, Y.; Kataoka, Y.; Matsui, T.; Kawakami, T.; Okumura, M.; Yamaguchi, K. Spin Contamination Error in Optimized Geometry of Singlet Carbene (1A_1) by Broken-Symmetry Method. *J. Phys. Chem. A* **2009**, *113*, 15041–15046.
- (42) Angeli, C.; Borini, S.; Cestari, M.; Cimiraglia, R. A Quasidegenerate Formulation of the Second Order N-Electron Valence State Perturbation Theory Approach. *J. Chem. Phys.* **2004**, *121*, 4043–4049.
- (43) Bao, J. L.; Odoh, S. O.; Gagliardi, L.; Truhlar, D. G. Predicting Bond Dissociation Energies of Transition-Metal Compounds by Multiconfiguration Pair-Density Functional Theory and Second-Order Perturbation Theory Based on Correlated Participating Orbitals and Separated Pairs. *J. Chem. Theory Comput.* **2017**, *13*, 616–626.
- (44) Cramer, C. J.; Truhlar, D. G. Density Functional Theory for Transition Metals and Transition Metal Chemistry. *Phys. Chem. Chem. Phys.* **2009**, *11*, 10757–10816.
- (45) Wilson, S. A.; Kroll, T.; Decréau, R. A.; Hocking, R. K.; Lundberg, M.; Hedman, B.; Hodgson, K. O.; Solomon, E. I. Iron L-Edge X-Ray Absorption Spectroscopy of Oxy-

Picket Fence Porphyrin: Experimental Insight into Fe–O₂ Bonding. *J. Am. Chem. Soc.* **2013**, *135*, 1124–1136.

(46) Yan, J. J.; Kroll, T.; Baker, M. L.; Wilson, S. A.; Decréau, R.; Lundberg, M.; Sokaras, D.; Glatzel, P.; Hedman, B.; Hodgson, K. O.; Solomon, E. I. Resonant Inelastic X-Ray Scattering Determination of the Electronic Structure of Oxyhemoglobin and Its Model Complex. *Proc. Natl. Acad. Sci.* **2019**, *116*, 2854–2859.

(47) Diccianni, J. B.; Diao, T. Mechanisms of Nickel-Catalyzed Cross-Coupling Reactions. *Trends Chem.* **2019**, *1*, 830–844.

(48) Rossenaar, B. D.; Kleverlaan, C. J.; Stufkens, D. J.; Oskam, A. Photochemistry of ReR(CO)₃(Prⁱ-dab)(R=Me, Et, Bn; dab=1,4-diazabuta-1,3-diene): Homolysis of the Re–R bond, its Dependence on R and Evidence for the Reactive $\sigma_b\pi^*$ State from Transient Absorption Spectra. *J. Chem. Soc., Chem. Commun.* **1994**, 63–64.

(49) Nieuwenhuis, H. A.; van de Ven, M. C. E.; Stufkens, D. J.; Oskam, A.; Goubitz, K. Photochemistry of [Ru(I)(iPr)(CO)₂(iPr-DAB)] (iPr-DAB = *N,N'*-diisopropyl-1,4-diaza-1,3-butadiene): Homolysis of the Metal-Alkyl Bond from the $\sigma_b(\text{Ru-iPr})\pi^*$ State. Crystal Structure of the Photoproduct [Ru(I)₂(CO)₂(iPr-DAB)]. *Organometallics* **1995**, *14*, 780–788.

(50) Rossenaar, B. D.; George, M. W.; Johnson, F. P. A.; Stufkens, D. J.; Turner, J. J.; Vlček, A., Jr. First Direct Structural Information on a Reactive $\sigma\pi^*$ Excited State: Time-Resolved UV–Vis and IR Spectroscopic Study of Re(benzyl)(CO)₃(iPr-DAB). *J. Am. Chem. Soc.* **1995**, *117*, 11582–11583.

(51) Rossenaar, B. D.; Lindsay, E.; Stufkens, D. J.; Vlček, A., Jr. Properties and Dynamics of the $\sigma(\text{M}'\text{-Re})\pi^*$ Excited State of Photoreactive Dinuclear L_nM'–Re(CO)₃(α -diimine) (L_nM' = Ph₃Sn, (CO)₅Mn, (CO)₅Re; α -diimine = bpy', iPr-PyCa, iPr-DAB) Complexes Studied by Time-Resolved Emission and Absorption Spectroscopies. *Inorg. Chim. Acta* **1996**, *250*, 5–14.

(52) Aarnts, M. P.; Wilms, M. P.; Stufkens, D. J.; Baerends, E. J.; Vlček, A., Jr. $\sigma\text{-}\pi^*$ Electronic Transition of the Di- and Trinuclear Complexes Ru(E)(E')(CO)₂(iPr-DAB): Resonance Raman, Electronic Absorption, Emission, and Density Functional Study (E = Me, SnPh₃, M(CO)₅; E' = M(CO)₅; M = Mn, Re; iPr-DAB = *N,N'*-Diisopropyl-1,4-diaza-1,3-butadiene). *Organometallics* **1997**, *16*, 2055–2062.

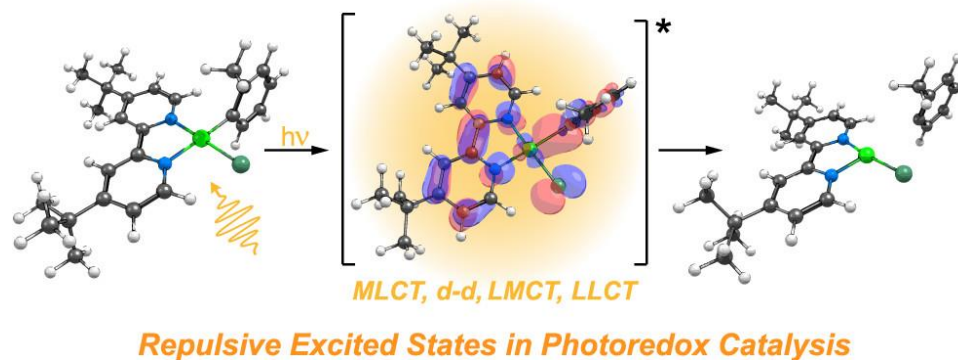
(53) Stufkens, D. J.; Aarnts, M. P.; Rossenaar, B. D.; Vlček, A., Jr. A New Series of Re- and Ru-Complexes Having a Lowest $\sigma\pi^*$ Excited State That Varies from Reactive to Stable and Long Lived. *Pure Appl. Chem.* **1997**, *69*, 831–835.

- (54) Kleverlaan, C. J.; Martino, D. M.; van Slageren, J.; van Willigen, H.; Stufkens, D. J.; Oskam, A. FT-EPR Study of Alkyl Radicals Formed in the Photochemical Reaction of Re(alkyl)(α -diimine) and Ru(alkyl)(α -diimine) Complexes. *Appl. Magn. Reson.* **1998**, *15*, 203-214.
- (55) Kleverlaan, C. J.; Stufkens, D. J.; Clark, I. P.; George, M. W.; Turner, J. J.; Martino, D. M.; van Willigen, H.; Vlček, A., Jr. Photoinduced Radical Formation from the Complexes [Re(R)(CO)₃(4,4'-Me₂-bpy)] (R = CH₃, CD₃, Et, ⁱPr, Bz): A Nanosecond Time-Resolved Emission, UV-Vis and IR Absorption, and FT-EPR Study. *J. Am. Chem. Soc.* **1998**, *120*, 10871-10879.
- (56) Weinstein, J. A.; van Slageren, J.; Stufkens, D. J.; Zálíš, S.; George, M. W. A Time-Resolved Infrared Spectroscopic Study of [M(SnR₃)₂(CO)₂(α -diimine)] (M = Ru, Os; R = Ph, Me): Evidence of Charge Redistribution in the Lowest-Excited State. *J. Chem. Soc., Dalton Trans.* **2001**, 2587-2592.
- (57) Stufkens, D. J.; Vlček, A., Jr., Ligand-dependent Excited State Behaviour of Re(I) and Ru(II) Carbonyl-Diimine Complexes. *Coord. Chem. Rev.* **1998**, *177*, 127-179.

Chapter 3

Elucidating the Mechanism of Excited-State Bond Homolysis in Nickel–Bipyridine Photoredox Catalysts

Ni(II)–C Bond Homolysis Rates, Barriers, Mechanistic Implications



Adapted with permission from:

Cagan, D. A.; Bím, D.; Silva, B.; Kazmierczak, N. P.; McNicholas, B. J.; Hadt, R. G. Elucidating the Mechanism of Excited-State Bond Homolysis in Nickel–Bipyridine Photoredox Catalysts. *J. Am. Chem. Soc.* **2022**, 144(14), 6516-6531. DOI: 10.1021/jacs.2c01356.

Copyright 2022 American Chemical Society.

§3-1. Introduction

§3-1.1 Ni(II)–bpy Photoredox Catalysis

Merging thermal catalysis with photochemistry (i.e., photoredox catalysis) has had a profound influence within organic chemistry, including coupling reactions forging sp^2 – sp^3 and sp^3 – sp^3 C–C or C–X bonds and their applications to medicinal chemistry.^{1–9} By leveraging photonic energy to drive key catalytic processes and utilizing earth-abundant transition metals, photoredox catalysis provides an attractive and sustainable means to replace precious metal catalysts.^{10–14} The disparate electron-transfer properties of first-row transition-metal catalysts can also provide pathways to new reactive intermediates and/or excited-state avenues that can unlock synthetic possibilities for drug development and discovery. However, while methodological studies have demonstrated the power of photoredox approaches in achieving bond-forming reactivity, the mechanisms that underlie these processes are largely unknown. In response, recent research has taken key steps toward a deeper mechanistic understanding, utilizing a combination of experiment and theory.^{4,5,15–19}

Mechanistic survey of photoredox catalysts requires thorough exploration due to the numerous possible photophysical pathways present. For example, reactive molecular excited states can be generated photochemically through photosensitized energy transfer^{17,20–22} or direct excitation.^{16,23,24} In either case, the ensuing transition-metal photophysics will strongly influence the overall catalytic efficacy by directing the photonic energy to specific pathways, only some of which may be productive to the target reaction. This complexity motivates highly detailed studies of the excited-state PESs that govern the important photophysics underlying photoredox catalysis.

Being catalytically active via photosensitization or direct excitation, Ni(II) complexes featuring the bidentate 2,2'–bipyridine (bpy) ligand have received a great deal of attention due to their many applications in photoredox catalysis. For example, MacMillan et al. demonstrated a photosensitized, energy-transfer-mediated approach to enable Ni(II)–bpy-catalyzed coupling of aryl halides with carboxylic acids.²⁰ In particular, an Ir(III)

photosensitizer enabled triplet energy transfer to a ground-state Ni(II)–bpy aryl acetate complex (formed *in situ* from a Ni(II)–bpy aryl halide). Energy transfer from the Ir(III) complex generates a long-lived triplet excited state of the Ni(II)–bpy complex, which can subsequently undergo reductive elimination of the aryl and acetate ligands, forming a new C–O bond (**Figure 3.1A**, top).²⁵ The mechanism of this photosensitized, energy-transfer-mediated reaction is still being investigated. However, *ab initio* calculations have suggested that a triplet metal-to-ligand charge-transfer (³MLCT) state may be active for excited-state C–O bond formation.²⁶ Furthermore, the chemical oxidation of the ground-state Ni(II)–bpy complex also facilitates reductive elimination.²⁵ These ground- and excited-state pathways are consistent with earlier research from the Hillhouse group demonstrating that the ground-state chemical oxidation of Ni(II) complexes to Ni(III) can trigger reductive elimination and the formation of new C–X bonds.^{27,28} In addition to energy-transfer pathways, photocatalytic cross-couplings can also be driven by direct excitation and can circumvent the need for external photosensitizers, which often contain precious metals.

For example, irradiation of the Ni(II)–bpy aryl halide complex in the presence of ancillary ligands enables the downstream formation of new C–O bonds (**Figure 3.1A**, bottom).^{23,24} Previous research has noted that the direct excitation of the Ni(II)–bpy complex homolytically cleaves the Ni(II)–C(aryl) bond, generating aryl radicals and a formal Ni(I) species. This reduced Ni species may allow access to catalytically active Ni(I)/Ni(III) cycles.^{16,23,24} While the use of light-induced homolysis to generate reactive Ni species has broad implications for photoredox catalysis, the precise mechanism of this critical bond-rupture step is not yet well understood and is the main subject of this study.

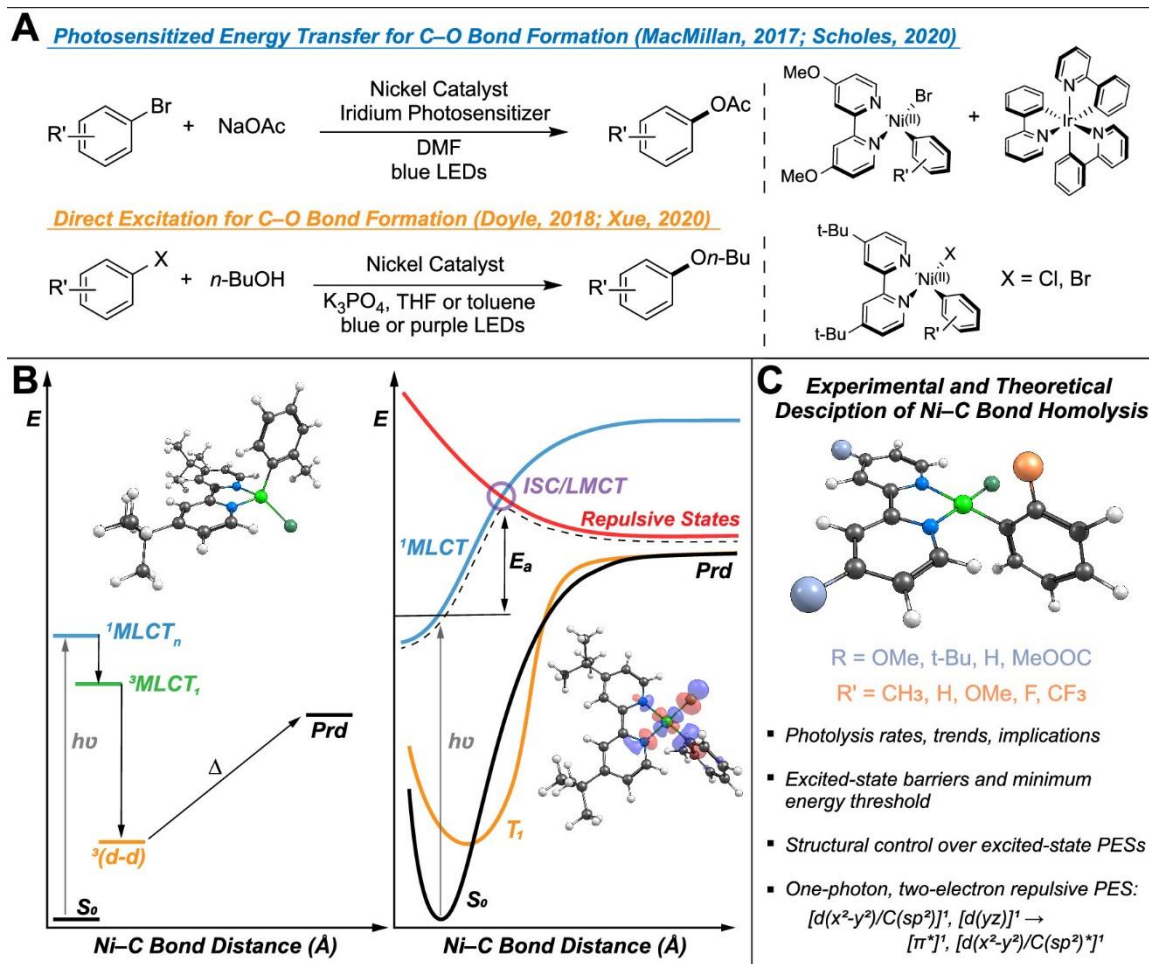


Figure 3.1. (A) Two possible photocatalytic approaches to Ni(II)–bpy-mediated C–O bond formation. (B) Left: energy diagram showing the direct excitation mechanistic pathway proposed in ref (16). The structure of the tetrahedral triplet ligand field excited state $^3(d-d)$ is shown. Right: PESs as described in ref (29) with *ab initio* calculations showing the 3LMCT -based repulsive surface (in red) responsible for Ni–C bond homolysis. Note that T_1 is the $^3(d-d)$ state. The antibonding $d(x^2-y^2)/C(sp^2)^*$ orbital is depicted. (C) Summary of this research.

§3-1.2. Mechanistic Hypotheses for Excited-State Ni(II)–C Bond Homolysis

There are two proposed excited-state Ni(II)–C bond homolysis mechanisms in Ni(II)–bpy aryl halide complexes. Using a combination of transient optical and IR spectroscopies, Doyle et al. demonstrated that the excitation of Ni(II)–bpy singlet metal-to-ligand charge

transfer ($^1\text{MLCT}$) ($\lambda_{\text{pump}} = 530 \text{ nm}$) resulted in the formation of triplet Ni(II) ligand field excited states ($^3(\text{d-d})$).¹⁶ Intersystem crossing occurs in ~ 5 to 10 ps , and the $^3(\text{d-d})$ state has a lifetime of $\sim 4 \text{ ns}$. Subsequent correlation to DFT calculations led to the proposal that Ni(II)–C homolysis occurs thermally from this photochemically formed Ni(II) $^3(\text{d-d})$ state (**Figure 3.1B**), which features a tetrahedral coordination geometry and a weakened Ni(II)–C bond. With DFT, the calculated homolytic BDE is $\sim 25 \text{ kcal mol}^{-1}$. However, no direct experimental evidence was provided to demonstrate homolysis from the $^3(\text{d-d})$ state.

Ab initio multiconfigurational/multireference calculations suggested an alternative mechanism of excited-state Ni(II)–C bond homolysis that is also consistent with the experimental data provided by Doyle et al. (**Figure 3.1B**).²⁹ This approach yielded larger homolytic BDEs ($\sim 90 \text{ kcal mol}^{-1}$ from the $S = 0$ geometry, $\sim 70 \text{ kcal mol}^{-1}$ from $S = 1$ geometry) than DFT and highlighted a putative one-photon, two-electron process leading to Ni(II)–C bond homolysis. In this mechanism, the initial excitation of the $S = 0$ complex forms a $^1\text{MLCT}$ state (Ni(II)-to-bpy). From this PES (blue curve in **Figure 3.1B**), a ligand-to-metal (aryl-to-Ni(III)) charge-transfer (LMCT) PES can be accessed. Critically, this LMCT results in the population of the antibonding $d(x^2-y^2)/C(\text{sp}^2)^*$ orbital (**Figure 3.1B**, right), which reduces the bond order and results in a repulsive triplet PES, leading to homolytic bond rupture (red curve in **Figure 1B**, right).²⁹ Notably, the energy difference between the MLCT/repulsive triplet crossing point (purple circle in **Figure 3.1B**, right) and the Frank–Condon point of the MLCT state constitutes the energy barrier (E_a) for bond rupture. Thus, it was reasoned that the structural and electronic control over the key MLCT/LMCT PESs, and, consequently, the barrier for photolysis, will result in variable rates of excited-state Ni(II)–C bond homolysis (**Figure 3.1C**), but new experimental data are required to further elucidate the overall mechanism.

Indeed, we demonstrate a direct correlation between experimental rate constants at given excitation wavelengths and the energies of both of these excited-state PESs. Furthermore, we provide an experimental measure of the excited-state energetic barrier for homolysis in Ni(II)–bpy aryl halide complexes utilized as photoredox catalysts. The homolysis rate

constants are wavelength-dependent, and we have demonstrated a minimum energy threshold for photochemical activation. Coupled to extensive computational analyses, these data provide experimental evidence implicating high-energy, repulsive aryl-to-Ni LMCT PESs as being vital to homolytically cleaving the Ni(II)–C bond, a critical process in the photocatalytic C–X cross-coupling catalysis. The dynamics of the excited states of these Ni(II) complexes resemble those previously associated with third-row transition-metal catalysts (e.g., Re complexes),^{30–39} unveiling underexplored reactivity pathways in these earth-abundant transition-metal catalysts. Beyond fundamental interest, demonstrating structural and electronic control over the key PESs in photoredox catalysis will, for example, allow chemists to tune the rates of formation of novel reactive intermediates and guide the discovery of new photon-driven organic methodological approaches to coupling reactions.

§3-2. Results and Analysis

§3-2.1. Experimental Studies

In **Sections §3-2.1.1–§3-2.1.5**, we detail the syntheses and spectroscopic/photochemical characterizations of a matrix of Ni(II)–bpy aryl halide complexes (**Figure 3.2**). We demonstrate direct correlations between ligand-based electronic perturbations, observable MLCT transition energies, and rate constants of excited-state bond homolysis. Temperature- and wavelength-dependent studies provide experimental barriers and energetic thresholds for excited-state Ni(II)–C bond homolysis, respectively.

§3-2.1.1. Synthetic Approach

To probe the mechanism of excited-state Ni(II)–C bond homolysis, we targeted the matrix of Ni(II)(^Rbpy)(^{R'}Ph)Cl complexes (R = CH₃O, *t*-Bu, H, CH₃OOC; R' = *ortho*-CH₃, H, CH₃O, F, CF₃), **1A–5D**, shown in **Figure 3.2**. Two primary synthetic approaches were utilized: (1) oxidative addition and (2) ligand substitution (Scheme S1). In the former, bis-(1,5-cyclooctadiene) nickel(0) was prestirred with a given bpy ligand; subsequent reaction with the specific aryl halide resulted in the target complex.

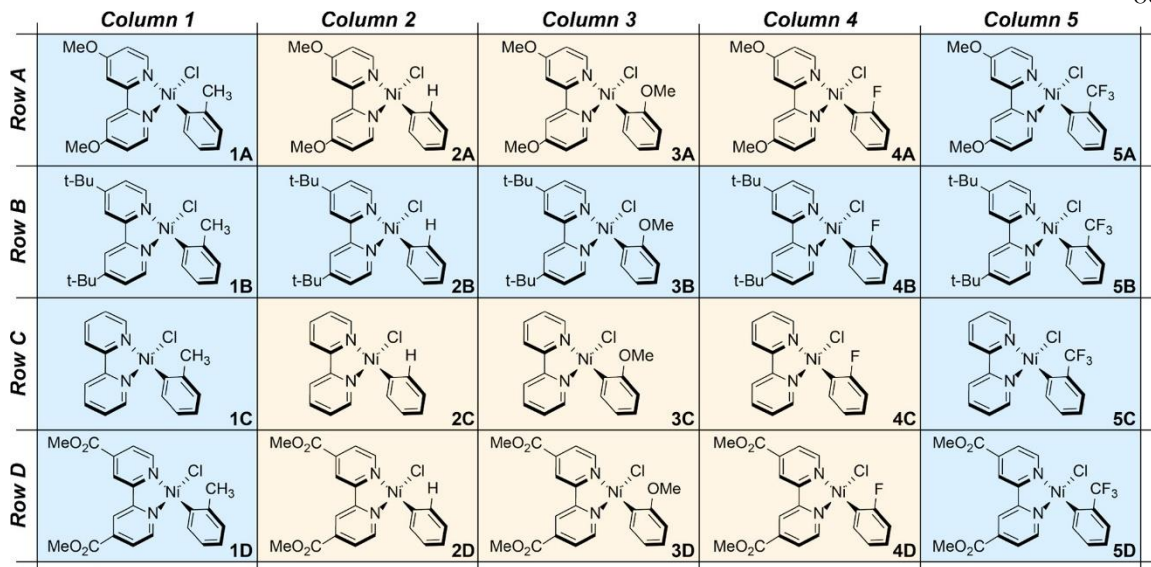


Figure 3.2. Matrix of Ni(^Rbpy)(^{R'}Ph)Cl (R = MeO, *t*-Bu, H, and MeOOC; R' = *ortho*-CH₃, H, OMe, F, and CF₃) complexes examined in this study. The bpy ligand varies down a column, while the aryl ligand varies across a row. Complexes shaded in blue were synthesized and examined both experimentally and computationally, while those in orange were examined only computationally.

The latter method called for either bis(triphenylphosphino)(2-methylphenyl)chloronickel(II) or the independent preparation of a precatalyst complex, Ni(TMEDA)(^{R'}Ph)Cl, R' = CH₃ or CF₃, TMEDA = *N,N,N',N'*-tetramethyl ethylenediamine.⁴⁰ These TMEDA compounds afforded a more labile ligand that could be substituted by bpy.⁴¹ The precatalyst complexes themselves were prepared by oxidative addition. Ligand substitution was used in cases where oxidative addition proved slow, yielded inconsistent results, or would not produce the desired product. Full synthetic details for both previously prepared¹⁶ and novel compounds are available in Supporting Information Section S1.3.

§3-2.1.2. Steady-State UV–Vis Spectroscopy

The steady-state UV–vis spectra of the Ni(II)–bpy aryl halide series in tetrahydrofuran (THF) are given in **Figure 3.3A**. Molar absorptivity plots in both THF and toluene are

given in Figures S5 and S6 and are consistent with previous spectral assignments of dominantly MLCT intensity across the UV–vis range (Table S1).

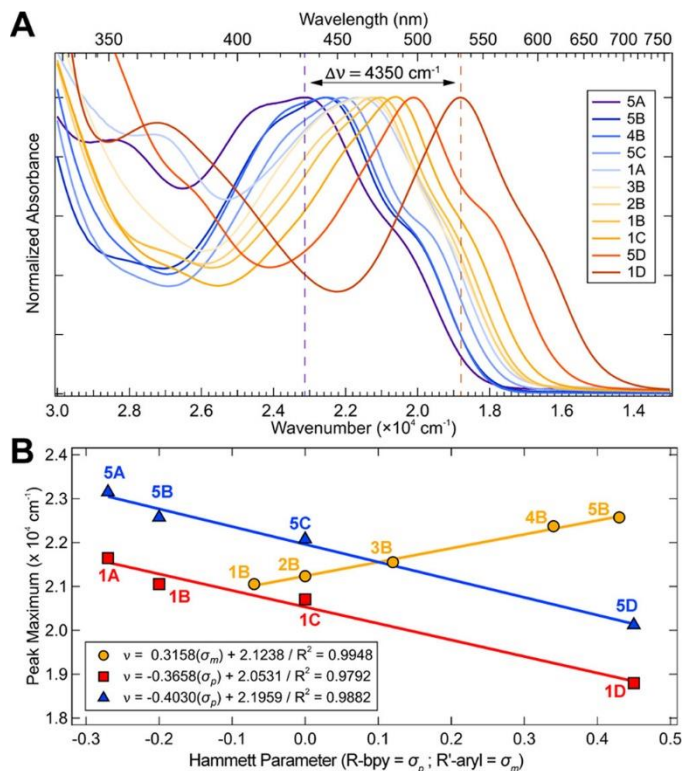


Figure 3.3. (A) Normalized UV–vis spectra in THF of complexes studied here (overall $\Delta\nu_{\text{max}} = 4350 \text{ cm}^{-1}$). (B) Correlation between λ_{max} (dashed lines in panel A given for the extrema) in THF and the Hammett parameter (σ_p) for each bpy substituent or (σ_m) for each aryl substituent. Analogous plots are given in Figure S6 for toluene; molar extinction coefficient data are summarized in Table S1. The legend code used hereafter references the matrix of complexes in **Figure 3.2**: red, squares = column 1; blue, triangles = column 5, orange, circles = row B.

The spectral assignments are discussed further in Section §3-2.2.1 and given explicitly in Table S10. It is also noted that the MLCT transition energies are generally solvatochromic, with transition energies being lower in toluene relative to THF (Figures S5 and S6).

Increasing the electron-withdrawing effect of the bpy substituents (proceeding down the columns in **Figure 3.2**) generally decreases the energies of the ¹MLCT transitions. The MLCT λ_{max} for spectra in **Figure 3.3A** (extrema denoted by dashed lines) correlates linearly with the Hammett parameter⁴² (σ_{p}) for each bpy substituent (blue and red curves in **Figure 3.3B**; $\Delta\nu_{\text{max}} = 3000 \text{ cm}^{-1}$). Similar Hammett relationships have been shown for Cu and Re bipyridine complexes.^{43,44}

Variation in the aryl ligand (rows in **Figure 3.2**) also modulates λ_{max} (**Figure 3.3A**) ($\Delta\nu_{\text{max}} = 1500 \text{ cm}^{-1}$), with increases in the electron-withdrawing group strength leading to increases in the energy of the ¹MLCT transitions. While the aryl ligands are all modified at the *ortho*-position with respect to the Ni(II)–C bond, the MLCT λ_{max} correlates with the corresponding *meta*-Hammett parameter (σ_{m}) (orange line in **Figure 3.3B**). This demonstrates a larger contribution of electrostatic and inductive effects over resonance effects upon variation of the aryl substituent relative to bpy.^{45–50} Accordingly, this series (**1B–5B**) also trends with Taft's field parameter, σ_{F} (Figure S7);⁴² for consistency, we use σ_{m} in the main text of this manuscript. No linear trend was observed when using Taft's steric (E_{s}) parameter,⁴² as the aryl ligand and its substituent are rotated orthogonal to the plane of the molecule (Figures S7 and S55).^{45,50}

§3-2.1.3. Photochemical Investigations

We first sought to confirm the formation of aryl radicals upon irradiation (see Supporting Information S1.2 for experimental setup). Irradiating well-characterized **1B** and analogous **5B** at 390 nm results in distinctive ¹H NMR peaks assigned to aryl radical products, 2-(*o*-tolyl)tetrahydrofuran, and 2,2'-dimethyl-1,1'-biphenyl (Figures S11 and S12).²³ Using ¹⁹F NMR, **5B** revealed new peaks associated with the free aryl ligand, concomitant with a loss of aryl peaks in the ¹H NMR after 390 nm irradiation (Figure S14). As demonstrated previously, homolysis does not occur in the absence of light; only minor degradation is observed when the complex is heated to 55 °C for 60 min (Figure S13), but no radical products are observed.^{23,24} We also noted the formation of radical products upon extended irradiation of the analogous precatalyst complexes, Ni(TMEDA)(^{R'}Ph)Cl ($R' =$

CH₃, CF₃), implicating ligand field excited states as operative for photolysis in the diamine complexes.⁵¹ More detailed discussion regarding this result relative to the photochemistry of Ni(II)–bpy complexes is available in Supporting Information Section S1.6.

Time-dependent absorption spectra were obtained during photolyses (390 nm) in THF of all complexes **1A–5D**. Photolysis kinetics were monitored at two wavelengths (arrows in **Figure 3.4** and Figures S19 and S20). From these kinetics, the observed rate constant ($k_{\text{obs},1}$) of the excited-state Ni(II)–C bond homolysis can be obtained. For a representative compound, **1B**, concentration dependence studies found a negligible change in $k_{\text{obs},1}$ across the absorbance window tested (Figure S44). The data for series **1A–1D**, which varies only the bpy substituent, are provided in **Figure 3.4**. Note that this series of complexes (**1A–1D**) has previously been investigated using transient absorption spectroscopy (the only difference being EtOOC versus MeOOC in **1D** here).¹⁶ *Clear rate constant changes are observed upon variation of the bpy ligand (Figure 3.4 and Table 3.1).* The largest rate constant was found for **1D**, which underwent photolysis with an observed rate constant of $k_{\text{obs},1} = (17.0 \pm 0.7) \times 10^{-2} \text{ min}^{-1}$. Compounds **1A–1C** presented smaller, but noticeable, differences in their decay rate constants (**Table 3.1**). For **1A**, background scattering from precipitation precluded a clear observation of the decay of the starting material.

Excited-state homolysis of the Ni(II)–C bond yielded a new product with absorbance in the visible region for each compound. Isosbestic points are observed in the photolysis data for all compounds studied here except **1A**, where light scattering contributes to the time-dependent spectra. While the general absorption profiles of these new species are similar, the primary low-energy features shift from ~650 nm in **1A** to 805 nm for **1D** (**Figure 3.4**). The spectral shift over this series suggests that the bpy ligand is present in the new species.

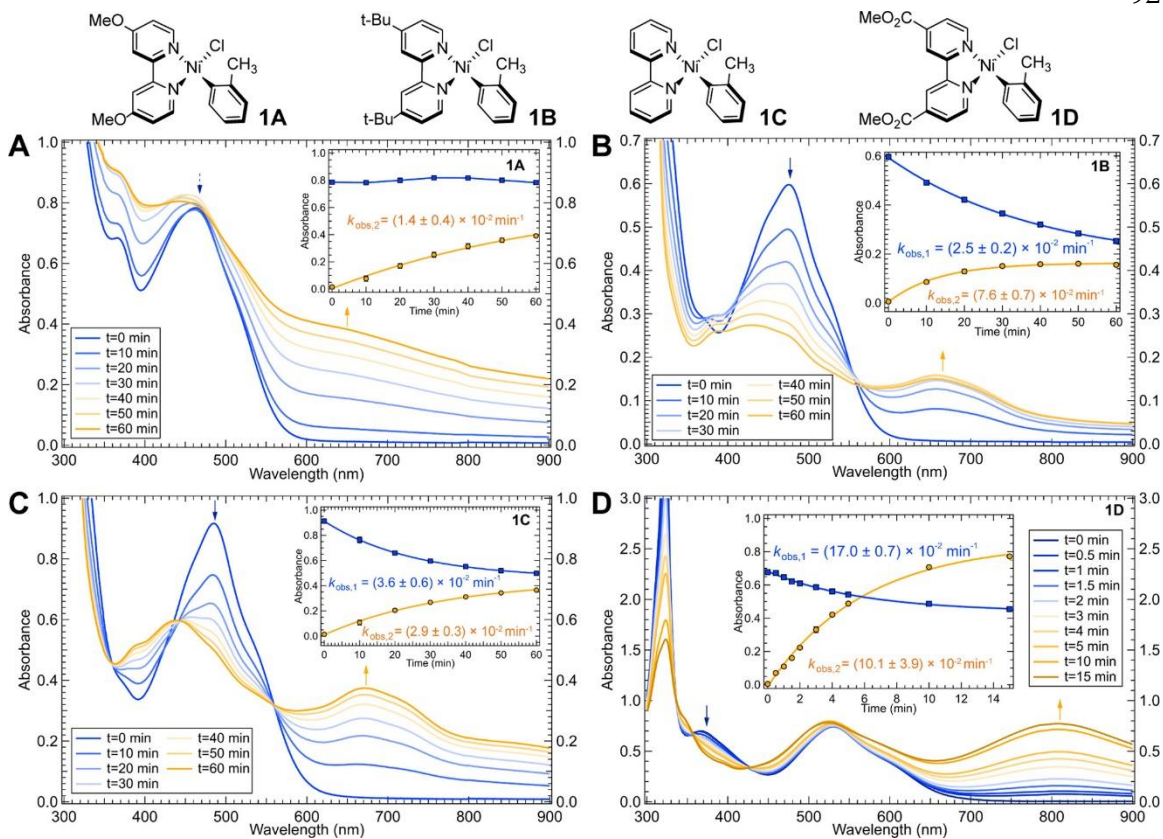


Figure 3.4. Photolysis profiles of **1A–1D** in THF for 390 nm excitation. Photolysis kinetics were monitored at two wavelengths indicated by the blue and orange arrows in each panel. The insets correspond to the fitted kinetic data (blue curve for the decay of the starting material, orange curve for the formation of the new species). Data were fit using a single exponential; error bars are 1 standard deviation. For **1A**, background scattering from precipitation precluded a clear observation of the decay of the starting material. This scattering also contributes to the kinetics measured at longer wavelengths for **1A**. Photolysis profiles of **5A–5D** and **2B–4B** are given in Figures S19 and S20.

The analogous time-dependent UV–vis spectra for compounds **5A–5D** are given in Figure S19. There are significant changes in the rate constants of excited-state Ni(II)–C bond homolysis across these compounds, with $k_{\text{obs},1}$ varying over an order of magnitude (Figure S19 and **Table 3.1**). However, these compounds generally exhibit much smaller rate constants than the complementary **1A–1D** series. Thus, the electron-withdrawing effect of the aryl ligand also impacts the rate. The growth of a new species was also observed for

these complexes (~650 nm in **5A** to 805 nm in **5D**), albeit at significantly lower quantities. To further investigate the dependence of $k_{\text{obs},1}$ on the variation of the aryl ligand, analogous time-dependent UV-vis data were obtained for complexes **2B–4B** (Figure S20). From these data, the full trend is revealed: increasing the electron-withdrawing nature of the aryl ligand (left to right in the row of **Figure 3.2**) again resulted in smaller rate constants across the series.

Table 3.1. Summary of UV-vis λ_{max} and first-order rate constants.^c

Compound	λ_{MLCT} (nm)	ν_{MLCT} (cm^{-1})	$k_{\text{obs},1}$ ($\times 10^{-2} \text{ min}^{-1}$)	k_{p} ($\times 10^{-2} \text{ min}^{-1}$)	$k_{\text{obs},2}$ ($\times 10^{-2} \text{ min}^{-1}$)
1A	462	21645	<i>n.d.</i> ^a	0.9 ± 0.1	1.4 ± 0.4
1B	475	21053	2.5 ± 0.2	4.1 ± 0.4	7.6 ± 0.7
1C	483	20704	3.6 ± 0.6	3.3 ± 0.5	2.9 ± 0.3
1D	532	18797	17.0 ± 0.7	15.0 ± 0.8	10.1 ± 3.9
2B	471	21231	2.6 ± 0.1	4.4 ± 0.1	6.5 ± 0.4
3B	464	21552	0.55 ± 0.02	1.6 ± 0.1	2.3 ± 0.2
4B	447	22371	0.219 ± 0.002	0.14 ± 0.18	10.4 ± 5.2
5A	432	23148	0.13 ± 0.01	0.08 ± 0.03	0.40 ± 0.15
5B	443	22573	0.16 ± 0.03	<i>n.d.</i> ^b	2.3 ± 1.1
5C	453	22075	0.19 ± 0.05	0.16 ± 0.01	1.4 ± 0.4
5D	497	20121	1.39 ± 0.02	3.0 ± 0.5	5.1 ± 1.0
1B-Br	479	20877	6.9 ± 0.4	8.1 ± 0.8	9.2 ± 0.7

^aBecause the new species formed upon Ni(II)–C bond homolysis has absorption underneath that of the starting material, we were unable to obtain $k_{1,\text{obs}}$ for this compound. The rate is approximated by $k_{2,\text{obs}}$. ^bComplex **5B** was omitted owing to poor convergence of the global kinetics model. ^cSolvent, THF. Errors are listed as one standard deviation over three trials.

This behavior is opposite to that observed for variations in the electron-withdrawing effect of the bpy ligand, hence the opposite slopes in **Figure 3.3B**. Note also that the primary low-energy absorption feature of the new species is not dependent on the aryl ligand ($\lambda = 660 \text{ nm}$ for **1B–5B**; Figures S41–S43).

We note that in certain regions, the absorption spectrum of the photolysis product overlaps with that of the starting material, including where decay kinetics are measured (blue arrows in **Figures 3.4** and S19 and S20). Furthermore, $k_{\text{obs},1}$ is in most cases less than $k_{\text{obs},2}$. To deconvolute the spectral overlap and rationalize these differences, global kinetics modeling was carried out (full discussion and details of the kinetic modeling are available in Supporting Information Section S1.9). Good agreement is seen between the observed rate constants and those obtained from the global fits, and the kinetic trends across the matrix of compounds are preserved (Figure S40). Comparison between $k_{\text{obs},1}$ and rate constants from global fitting (k_p) is also given in Table 1. Additionally, using the method developed by Gescheidt et al.,⁵² we calculated the quantum yields for each complex to account for differential absorbance at the 390 nm excitation wavelength (see Supporting Information Section S1.11 for complete details). We found good linear agreement between the observed photolysis rates and the calculated quantum yields ($R^2 = 0.9730$; Figure S53), further supporting our kinetic analysis. Furthermore, the rate constants of excited-state Ni(II)–C bond homolysis correlate linearly with specific Hammett parameters of the bpy and aryl ligands. As shown in **Figure 3.5**, linear relationships are observed upon plotting $\log(k_{\text{obs},1}/k_{\text{obs},1}(\text{H}))$ versus σ_p or σ_m (for ^Rbpy or ^RPh, respectively) ($R^2 \geq 0.95$) ($\rho = \sim 1.4$ for ^Rbpy and $\rho = \sim -2.6$ for ^RPh). *Thus, the rate of excited-state Ni(II)–C homolysis is sensitive to electronic structure perturbations from both the bpy and aryl ligands.*

Electronically stabilizing the Ni(II)-to-bpy MLCT transition energies by increasing the bpy-based electron-withdrawing effect accelerated the rate of photolysis. Conversely, increasing the aryl-based electron-withdrawing effect resulted in increased MLCT transition energies and slower rates of photolysis (see the oppositely signed slopes in **Figure 3.3B**). These data reflect competing effects on the excited-state PESs involved in homolysis and are further described in Section 2.2.

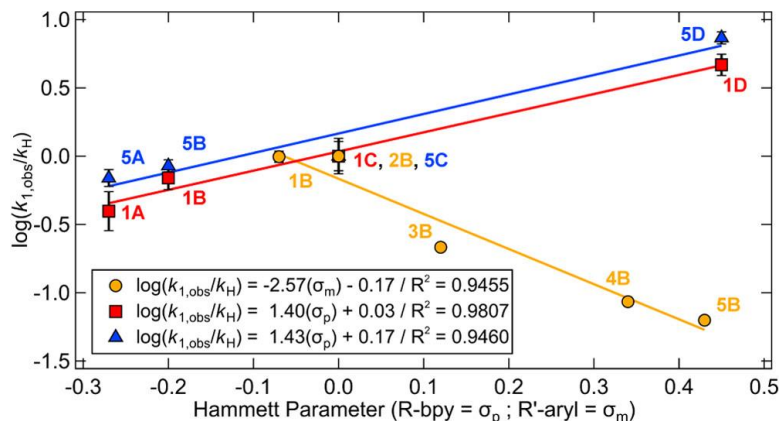


Figure 3.5. Correlation between normalized rate constants (390 nm excitation) of excited-state bond homolysis and specific Hammett σ parameters of the bpy and aryl ligands. Note that in **1A**, the rate is approximated by $k_{2,obs}$. Analogous plot of the relative quantum yields versus specific Hammett σ parameters is given in Figure S54.

§3-2.1.4. Preliminary Investigations of the Photochemically Generated Species

The immediate product of Ni(II)–C bond homolysis has been proposed to be a three-coordinate Ni(I)(^Rbpy)Cl complex. A recent study by Bird et al. on the related Ni(I)(^t-Bu₃bpy)Br reported its UV–vis spectrum as generated by pulse radiolysis or electrolysis.⁵³ For direct comparison, we synthesized Ni(^t-Bu₃bpy)(CH₃Ph)Br, **1B–Br**, and subjected it to the same photolysis conditions as above.

We found a roughly threefold enhancement in the rate constant of photolysis for **1B–Br** ($k_{obs,1} = (6.9 \pm 0.4) \times 10^{-2} \text{ min}^{-1}$) relative to **1B** ($k_{obs,1} = (2.5 \pm 0.2) \times 10^{-2} \text{ min}^{-1}$) and a change in the absorption spectrum of the product species (**Figure 3.6A**). The primary low-energy absorption feature of the product appears at higher energy when produced from the *bromo*-complex (653 nm) versus the *chloro*-complex (660 nm). Thus, there is a halide dependence on the absorption spectrum of the product compound. A comparison between the long-time spectra of the photoproducts from compounds **1B–Br**, **1B**, **3B**, **1C**, and **1D** is given in **Figure 3.6B**, illustrating a change in peak maxima when changing the bpy or halide ligands, but not the aryl ligand.

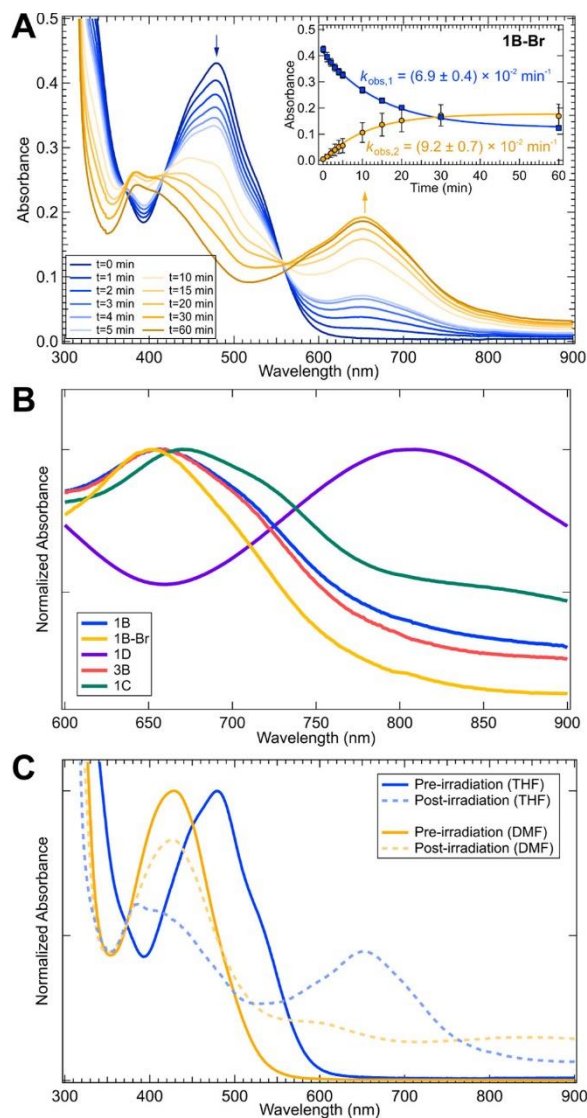


Figure 3.6. (A) Photolysis profile of **1B-Br** in THF (390 nm excitation) monitored at two wavelengths indicated by the blue and orange arrows in each panel. The inset corresponds to the first-order kinetics data (blue curve for the decay of the starting material, and orange curve for the formation of the new species). Error bars are 1 standard deviation. (B) Comparison between long-time UV-vis spectra for **1B-Br** ($\lambda_{\text{max}} = 653 \text{ nm}$), **1B** ($\lambda_{\text{max}} = 660 \text{ nm}$), **3B** ($\lambda_{\text{max}} = 660 \text{ nm}$), **1C** ($\lambda_{\text{max}} = 673 \text{ nm}$), and **1D** ($\lambda_{\text{max}} = 805 \text{ nm}$). (C) Comparison between UV-vis spectra for **1B-Br** in THF and DMF before and after irradiation with 390 nm light.

We also followed the photolysis of **1B–Br** in dimethylformamide (DMF), the same solvent used by Bird et al. (Figure S51).⁵³ We first note that the steady-state UV–vis data are solvatochromic, with the main MLCT bands being lower in energy in THF relative to DMF (**Figure 3.6C**, blue versus orange lines, respectively). The homolysis product UV–vis spectra are also solvatochromic (**Figure 3.6C**, dashed lines). In particular, DMF solutions exhibit the same characteristic UV–vis features for the three-coordinate monomeric species (430, 620, and 860 nm), as observed by Bird et al. (**Figure 3.6C**, orange dashed line). We further note that the rate constant of excited-state Ni(II)–C bond homolysis is smaller in DMF relative to THF. We tentatively ascribe these differences in rate constants to changes in the MLCT energies and overall excited-state PESs (*vide infra*). These interesting solvent effects on the excited-state PESs and, thus, rates of homolysis are currently under more detailed investigation.

Monomeric Ni(I)(*t*-Bu₃bpy)X, X = Cl, Br has been shown to be active toward the oxidative addition of aryl iodides, while the dimeric form, [Ni(*t*-Bu₃bpy)X]₂, is unreactive with the same.^{53,54} We irradiated a sample of **1B–Br** in THF, generating the photoproduct. Addition of 2-iodotoluene to this solution revealed rapid reactivity and complete removal of the characteristic absorption feature at 653 nm (Figure S52). Furthermore, the absorption spectrum of the dimeric species shows peaks only in the UV region, further implicating the monomeric form as the photoproduct.⁵⁴

Therefore, we postulate that the new species formed here upon excited-state Ni(II)–C homolysis are three-coordinate Ni(I)(^Rbpy)X complexes (R = MeO, *t*-Bu, H, and MeOOC, X = Cl or Br), as they have been shown by steady-state UV–vis spectroscopy to (1) contain the bpy ligand, (2) not contain the aryl ligand, (3) contain the halide and, in the case of **1B–Br**, (4) exhibit the same absorption profile as Ni(I)(*t*-Bu₃bpy)Br, and (5) exhibit oxidative addition reactivity with iodotoluene. A detailed comparative study of the reactivities and further spectroscopic characterizations of these species is currently underway.

§3-2.1.5. Further Examination of the Mechanism of Excited-State Bond Homolysis

To further investigate the mechanism of excited-state Ni(II)–C bond homolysis, we carried out temperature-dependent photolyses of **1B** and **1B–Br**. Among the matrix of complexes studied here, these two are most often utilized for synthetic applications, giving their analyses direct implications for photoredox catalysis.²⁴

Eyring plots of temperature-dependent rate constants for these complexes are given in **Figure 3.7**. From these data, the enthalpy and entropy of activation for the excited-state Ni(II)–C bond homolysis in **1B** are $\Delta H^\ddagger = 4.4 \pm 0.6 \text{ kcal mol}^{-1}$ and $\Delta S^\ddagger = -45.3 \pm 1.8 \text{ cal mol}^{-1} \text{ K}^{-1}$, with $\Delta G^\ddagger(298 \text{ K}) = 17.9 \pm 0.8 \text{ kcal mol}^{-1}$. Similar analysis of **1B–Br** gives $\Delta H^\ddagger = 2.1 \pm 0.1 \text{ kcal mol}^{-1}$ and $\Delta S^\ddagger = -49.3 \pm 0.4 \text{ cal mol}^{-1} \text{ K}^{-1}$, with $\Delta G^\ddagger(298 \text{ K}) = 16.8 \pm 0.2 \text{ kcal mol}^{-1}$. At high temperatures (328 K), thermal decay of the starting material occurs for **1B–Br**, resulting in a downturn in the temperature-dependent rate constants (dashed yellow line; **Figure 3.7**). Because of this, the linear fit utilized a room temperature point. As expected, the barrier for excited-state Ni(II)–C bond homolysis is lower in **1B–Br** than in **1B**, consistent with its larger rate constant.

In addition to being dependent on temperature, the rate constant of excited-state bond homolysis in **1B** is also highly dependent on the excitation wavelength (**Figure 3.8A**). Varying incident wavelengths (390, 427, 456, and 525 nm; Figure S21) revealed a minimum energy threshold for the excited-state Ni(II)–C bond homolysis of $\sim 55 \text{ kcal mol}^{-1}$ (525 nm, $19,050 \text{ cm}^{-1}$) in **1B**; below this incident energy, no homolysis is observed (Figure S22).

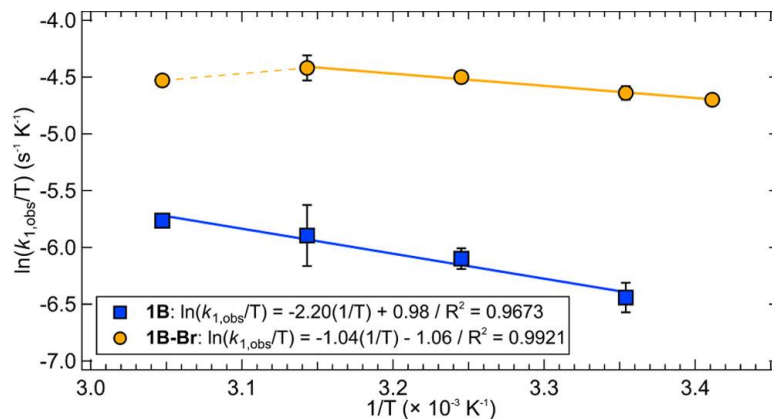


Figure 3.7. Eyring analysis of the temperature-dependent photolysis rates of **1B** (blue, squares) and **1B-Br** (orange, circles); error bars are one standard deviation over three trials.

Previous optical transient absorption measurements on **1B** were carried out using $\lambda_{pump} = 530$ nm.¹⁶ Laser excitation at this wavelength results in the formation of a Ni(II)-based triplet ligand field excited state, from which homolysis was proposed on the basis of DFT calculations. Notably, however, very limited photolysis occurs here using a 525 nm excitation light source. *These results demonstrate that the lower-energy ligand field state is not responsible for excited-state Ni(II)-C bond homolysis but rather indicate the involvement of higher-energy excited states.*

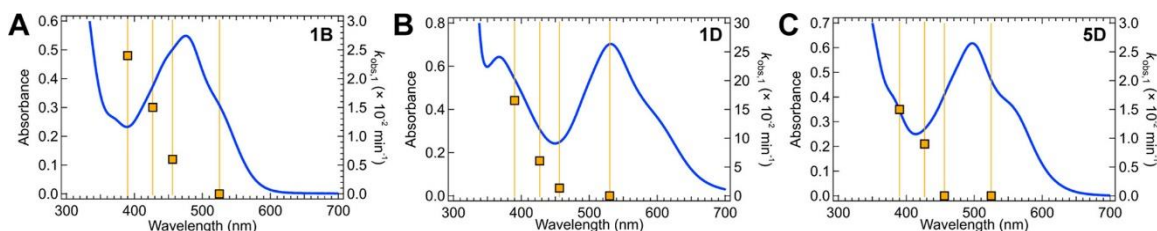


Figure 3.8. Wavelength-dependent photolysis for **1B**, **1D**, and **5D**. The absorbance spectra are shown in blue; the observed photolysis rate constants (squares) and incident wavelengths are given in orange. Analogous plot of wavelength dependency of quantum yields is given in Figure S25.

To search for general trends across compounds considered here, we also conducted wavelength-dependent studies on **1D** and **5D** (**Figure 3.8B,C**). Altogether, these complexes

span a wide range of photolysis rate constants, have varying MLCT transition energies, and feature electronic structure differences provided by the bpy and aryl ligands. In each case, a clear wavelength dependence was observed, and high-energy incident light was required for homolysis. No appreciable decay was observed using low-energy light (Figures S23 and S24), again implicating high-energy excited states in the mechanism of light-induced homolysis. We also evaluated the wavelength dependency of quantum yields for each complex, accounting for variable LED power and complex absorbance at each wavelength, and found that their behavior mirrors the photolysis kinetics (Figure S25). In summary, through experimental analyses of a matrix of Ni(II)–bpy aryl halide complexes, we have demonstrated the following:

- (1) a dependence between the MLCT λ_{max} and the Hammett parameters of the bpy and aryl substituents over the **1A–5D** series (**Figure 3.3B**),
- (2) linear correlations between the Hammett parameters of the bpy and aryl substituents and the rate constants of excited-state Ni(II)–C bond homolysis over the **1A–5D** series, interestingly with oppositely signed slopes (**Figure 3.5**),
- (3) the barrier for excited-state bond homolysis is moderate (e.g., $\Delta H^\ddagger = 4.4 \pm 0.6$ kcal mol⁻¹ in **1B** using 390 nm excitation; **Figure 3.7**), and
- (4) excited-state bond homolysis is distinctly wavelength-dependent (**Figure 3.8**); e.g., in **1B**, requiring a minimum of ~ 55 kcal mol⁻¹ (525 nm, 19,050 cm⁻¹).

These experimental observations are discussed below in the context of computational studies, which further aid in the elucidation of the mechanism of excited-state Ni(II)–C bond homolysis.

§3-2.2. Computational Studies

In the following computational **Sections §3-2.2.1–§3-2.2.3**, we first compare the ground- and excited-state properties of **1A–5D** computed at different levels of theory. We discuss the possible photoactivation pathways that are accessible in the energy range of the external light sources used in the photolysis experiments, as well as those pathways that are consistent with the experimental barrier. Notably, the incident light energy required for photolysis (as determined from wavelength-dependent kinetic experiments) is substantially greater than the energy of the ³(d–d) bands in **1A–5D**, and the calculated barriers for homolysis from these states are significantly larger than the experiment. These points indicate that the thermally driven excited-state Ni(II)–C bond homolysis from a spin-forbidden ligand field state is not the operative mechanism. Instead, we focus on the possible photolysis pathways that exploit triplet excited-state LMCT-based repulsive PESs. We propose a working mechanism that can ultimately be described as ¹MLCT [Ni *d* → bpy $\pi^*(2)$] excitation followed by surface hopping to a repulsive ³LMCT (aryl-to-Ni) PES (³MLCT + LMCT). This mechanism is in agreement with the experimentally derived reaction rates and thermodynamic barriers determined herein.

§3-2.2.1. DFT versus CASSCF/QD-NEVPT2 Ground and Excited States

To evaluate the geometric and electronic structures of **1A–5D**, we compared their ground- and excited-state properties calculated with either DFT/TD-DFT or *ab initio* complete active space self-consistent field theory with the quasidegenerate *N*-electron valence state perturbation theory correction (CASSCF/QD-NEVPT2);^{55–58} full computational details are available in Supporting Information Section S2.1.

With DFT (B3LYP),^{59–61} all Ni(II) complexes are predicted to have low-spin, singlet (*S* = 0) ground states with square-planar geometries (note that the x-axis is directed along the Ni–halide bond and the y-axis is along the Ni–aryl bond). The fully optimized triplet (*S* = 1) ligand field excited states are in all cases ~10 kcal mol⁻¹ higher in energy with pseudo-tetrahedral geometries. The valence electronic configuration of the d⁸ ground state is $[d(xy)]^2[d(yz)]^2[d(xz)]^2[d(z^2)]^2$, with three unoccupied bpy-based π^* orbitals and a highly

covalent antibonding $[d(x^2-y^2)/C(sp^2)^*]^0$ orbital (see Figure S59 for an example molecular orbital diagram for **1D**). The orbital energies are modulated by the bpy substituents; increasing the electron-withdrawing effect of the bpy ligand (columns in **Figure 3.2**) decreases the energies of the bpy π^* orbitals, reducing the Ni(II)-to-bpy MLCT energy (Figure S60), consistent with the red-shifted experimental λ_{\max} features in **Figure 3.3**. On the other hand, the HOMO and the bpy π^* orbital energies remain essentially unchanged when modulating the aryl substituent (rows in **Figure 3.2**), contrasting with the blue shift in **Figure 3.3**. The correct behavior can be recovered at the TD-DFT level, which accounts for orbital mixing in the excited states (Figure S62). Interestingly, the changes in orbital energies are not translated into changes in the covalencies of the ground states, which remain ~ 51 to 54% Ni d and ~ 11 to 13% bpy characters for **1A–5D** (Table S9).

The calculated TD-DFT absorption spectra agree well with the experimental UV–vis data (see overlaid spectra in Figure S62) and also demonstrate a similar linear relationship with the substituent-specific Hammett σ parameters (**Figure 3.9**, top). The broad feature at longer wavelengths (~ 400 to 600 nm, $\sim 25,000$ to $16,500$ cm^{-1}) encompasses all of the “low-energy” $^1\text{MLCT}$ transitions $[\text{Ni } d \rightarrow \text{bpy } \pi^*(1)]$, with $[d(yz) \rightarrow \text{bpy } \pi^*(1)]$ having the highest calculated oscillator strength. The shoulder at ~ 350 to 370 nm ($\sim 28,500$ to $27,000$ cm^{-1}) apparent in most of the experimental UV–vis spectra of **1A–5D** can be similarly assigned to a $[d(yz) \rightarrow \text{bpy } \pi^*(2)]$ transition; other “high-energy” $^1\text{MLCT}$ $[\text{Ni } d \rightarrow \text{bpy } \pi^*(2)]$ transitions are predicted to fall in the ~ 300 to 450 nm ($\sim 33,000$ to $22,000$ cm^{-1}) range. The $^1(d-d)$ transitions are calculated to be comparable in energy to the “low-energy” $^1\text{MLCT}$ bands (~ 400 to 500 nm, $25,000$ to $20,000$ cm^{-1}) and are not visible in the experimental UV–vis spectra of **1A–5D**. This assignment is also consistent with the energy of the observable $^1(d-d)$ band $[d(yz) \rightarrow d(x^2-y^2)/C(sp^2)^*]$ in the Ni(II)(TMEDA)(CH₃Ph)Cl complex that is detected in the visible range (found at ~ 470 nm, $21,280$ cm^{-1} ; calculated at 533 nm, $18,760$ cm^{-1}); the less-intense bands observed near ~ 635 nm ($15,750$ cm^{-1}) can be assigned to the spin-forbidden triplet transitions. For example, the $[d(xy) \rightarrow d(x^2-y^2)/C(sp^2)^*]$ triplet transition is calculated at 642 nm ($15,580$ cm^{-1}). Others, including $[d(xz) \rightarrow d(x^2-y^2)/C(sp^2)^*]$ and $[d(yz) \rightarrow d(x^2-y^2)/C(sp^2)^*]$, are calculated at 847 nm ($11,810$

cm^{-1}) and 945 nm ($10,580 \text{ cm}^{-1}$), respectively. All relevant TD-DFT electronic transition energies are given in Table S10.

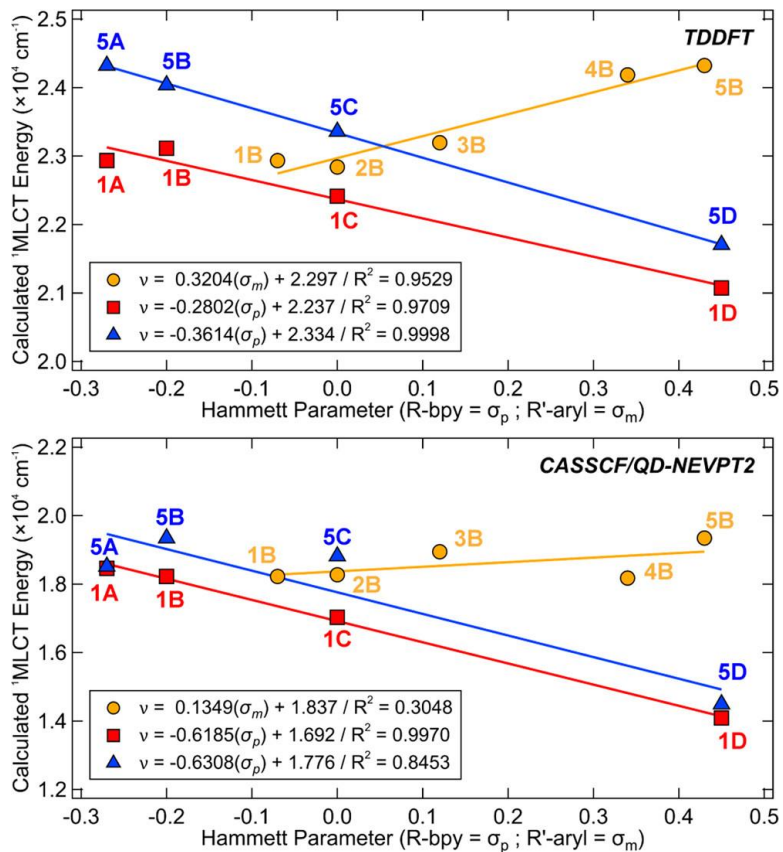


Figure 3.9. Correlation between the calculated $^1\text{MLCT}$ [$d(yz) \rightarrow \pi^*(1)$] transition energies (CPCM solvation model, THF) and the specific Hammett σ parameters using both TD-DFT (top) and CASSCF/QD-NEVPT2 (bottom) methods.

Therefore, the light sources exhibiting most appreciable excited-state Ni(II)–C bond homolysis (i.e., 390 nm, $25,640 \text{ cm}^{-1}$ and 427 nm, $23,420 \text{ cm}^{-1}$) in **1A–5D** favor initial excitation into high-energy $^1\text{MLCT}$ bands, [Ni $d \rightarrow$ bpy $\pi^*(2)$], while longer-wavelength light sources from the wavelength dependence study in **Figure 3.8** (456 nm, $21,930 \text{ cm}^{-1}$ and 525 nm, $19,050 \text{ cm}^{-1}$) are in the range of the low-energy $^1\text{MLCT}$ bands, [Ni $d \rightarrow$ bpy $\pi^*(1)$]. The minimum energy threshold of $\sim 525 \text{ nm}$, below which no photolysis is observed, is not consistent with the previous DFT-based assignment of bond rupture from a low-lying triplet

ligand field state (**Figure 3.1B**, left).¹⁶ The lack of bond homolysis from the low-lying MLCTs is likely the result of an increased barrier for homolysis (discussed further in **Section §3-2.2.3**).

Multiconfigurational/multireference CASSCF/QD-NEVPT2 calculations were conducted using the DFT-optimized singlet geometries. State-averaged CASSCF calculations (15 singlets, 25 triplets) were performed with an active space of ten electrons in nine orbitals (10e, 9o): $d(yz)$, $d(z^2)$, $d(xy)$, $d(xz)$, a pair of bonding and antibonding Ni $d(x^2-y^2)$ /aryl C(sp²) orbitals, and three bpy π^* orbitals (Figure S56). The method and active space follow our previous study on **1B**.²⁹ For **1A–5D**, the ground-state wave functions exhibit a substantial multiconfigurational character. While the CI vectors (Figure S57 and Table S9) are primarily comprised of the CSS configuration (i.e., the configuration also acquired with DFT), both the MLCT and LMCT configurations contribute significantly to the character of the ground-state wave function.

The calculated CASSCF/QD-NEVPT2 absorption spectra generally agree with the observed bands in the experimental UV–vis data (Figure S63; tabulated in Table S11). However, the λ_{\max} is notably red-shifted ($\sim 5000\text{ cm}^{-1}$) as compared with TD-DFT (Figure S62 and Table S10). The composition of the ground-state CI vector, particularly the total ¹MLCT contribution, also closely correlates with the transition energy in the calculated UV–vis spectra. As the ¹MLCT [Ni $d(xz) \rightarrow$ bpy $\pi^*(1)$] weight increases, the calculated energy of λ_{\max} in the absorption spectrum decreases (Figure S65). The multiconfigurational/multireference calculations also demonstrate a similar linear relationship with the substituent-specific Hammett σ parameters (**Figure 3.9**, bottom).

§3-2.2.3. Investigating the Mechanism of Excited-State Ni(II)–C Bond Homolysis

DFT-relaxed PES scans along the Ni(II)–C bond coordinates of **1A–5D** revealed a singlet/triplet degenerate homolytic dissociation product of $\sim 40\text{ kcal mol}^{-1}$ above the singlet equilibrium geometry. Thermal dissociation barriers of $\sim 30\text{ kcal mol}^{-1}$ were calculated from the triplet equilibrium geometries, consistent with a previous study.¹⁶ Given the large

differences in BDEs between DFT and CASSCF/QD-NEVPT2 observed previously for **1B**,²⁷ we have also evaluated the BDEs using different levels of theory. Referencing to the experimental energy of the ³(d-d) state found by Doyle et al. (12 kcal mol⁻¹),¹⁶ we find BDEs of ~40 kcal mol⁻¹ (SCS-MP2/QZ), ~41 kcal mol⁻¹ (DLPNO-CCSD(T)/QZ), and ~76 kcal mol⁻¹ (CASSCF/QD-NEVPT2; 10e, 8o) (Tables S6 and S7), suggesting that the DFT BDE of ~30 kcal mol⁻¹ represents the lower limit for thermally driven, excited-state Ni(II)–C bond homolysis from the triplet ligand field equilibrium geometry. These calculated barriers are all significantly higher than the experimental value of ~5 kcal mol⁻¹ demonstrated above. Therefore, we again find that *thermal dissociation from the lowest-energy triplet ligand field state is not consistent with the experimental data provided here and, thus, is not a viable mechanism for excited-state Ni(II)–C bond homolysis.*

Instead of thermally driven excited-state Ni(II)–C bond homolysis from ligand field states, we propose that the mechanism of bond homolysis exploits excited-state triplet repulsive aryl-to-Ni LMCT PESs (outlined in **Figure 3.10**). Critically, in these scenarios, the transfer of an electron between the bonding and antibonding $d(x^2-y^2)/C(sp^2)$ orbitals significantly lowers the overall bond order, facilitating bond rupture.

We have found two pathways utilizing either ¹(d-d) (blue panel in **Figure 3.10**) or ¹MLCT (orange panel in Figure 10) transitions as the initial entrance to the excited-state mechanism. In both cases, these initial excitations are followed by intersystem crossing (ISC) and formation of an aryl-to-Ni ³LMCT state. Accordingly, two principally different triplet repulsive surfaces are viable for homolysis: a “one-photon, one-electron” excited state $^3[d(x^2-y^2)/C(sp^2) \rightarrow d(x^2-y^2)/C(sp^2)^*]$ and a “one-photon, two-electron” excited state $^3[d(x^2-y^2)/C(sp^2) + d(yz) \rightarrow d(x^2-y^2)/C(sp^2)^* + \pi^*(1)]$ (green and red surfaces in Figure 10 (right), respectively). This former pathway expands our initially delineated mechanism in reference,²⁹ wherein the probability for population of the ¹(d-d) excited states versus the ¹MLCT upon irradiation would contribute to determining the excited-state surface-mediating homolysis. Indeed, it is likely that this “one-photon, one-electron” repulsive surface facilitates Ni(II)–C bond homolysis in the Ni(TMEDA) aryl halide complexes, as

described in **Section §3-2.1.3**; a recent report by Park et al. implicated the corresponding surface in the homolysis of related Ni(II) complexes.⁵¹

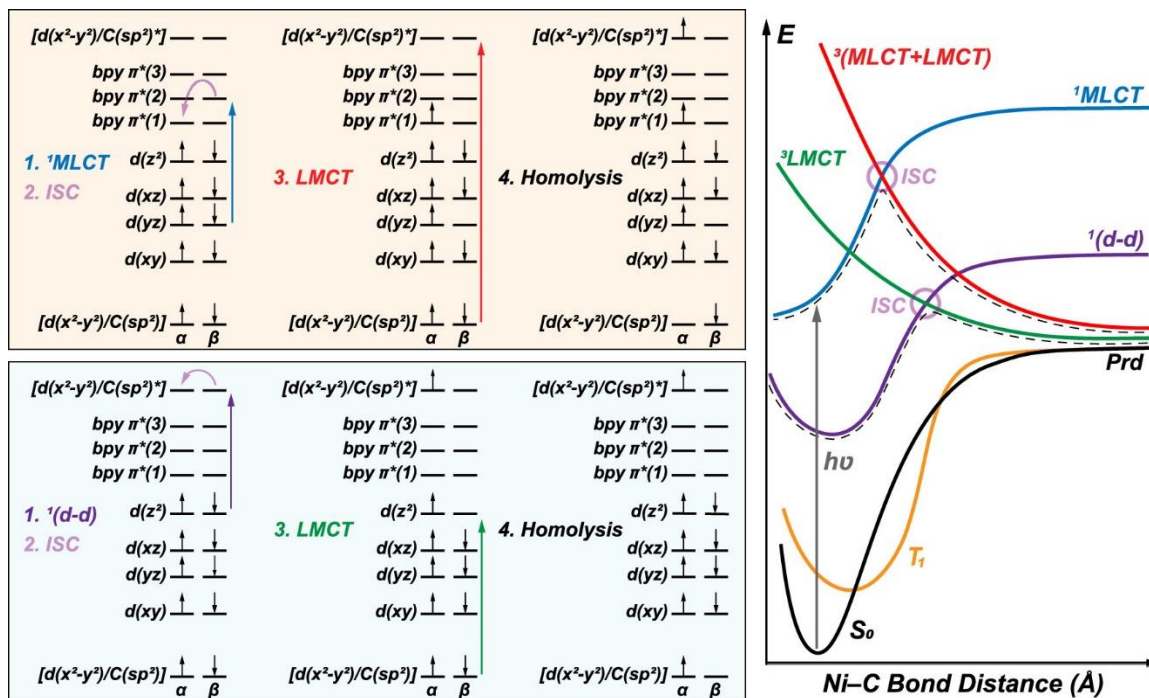


Figure 3.10. Two plausible excited-state mechanisms of Ni(II)–C bond homolysis. Initial $^1(d-d)$ or 1MLCT excitation (blue or orange boxes, respectively) is followed by ISC and 3LMCT formation. On the right, this surface hopping mechanism is exemplified with the shaded purple circles connecting the $^1(d-d)$ excited-state surface (purple line) to the one-electron triplet repulsive 3LMCT surface (green line) or 1MLCT excited-state surface (blue line) to the two-electron triplet repulsive $^3(MLCT + LMCT)$ surface (red line). Corresponding plots computed at the TD-DFT and CASSCF/QD-NEVPT2 levels are provided in Figures S68 and S69. For clarity, exchange splitting between α and β orbitals is neglected. Illustrative orbital energies and ordering on the left are provided from the ground state and are held constant through steps 1–4; the right panel gives a more accurate depiction of relative state energies, reflecting a small thermal barrier relative to the excitation energy.

From the singlet ground state, the standard TD-DFT approach (i.e., single-electron excitations) cannot access the two-electron nature of the red surface in **Figure 3.10** (right).

Also, the spin-flipped α -to- β excitations (needed for description of the green surface in **Figure 3.10**, right) are only available from the singlet ground state using the restricted Kohn–Sham orbitals, which are inadequate for producing the accurate excited-state charge-transfer states, especially for out-of-equilibrium geometries with increased charge separation. Nevertheless, we were able to identify both of these triplet repulsive PESs using TD-DFT from the high-spin ($S = 1$) triplet reference state (i.e., the electronic configuration of the middle structure in the blue panel of **Figure 3.10**). From this configuration, the one-electron or two-electron triplet repulsive surfaces can be obtained via β -to- β [$d(x^2-y^2)/C(sp^2) \rightarrow d(z^2)$] or [$d(x^2-y^2)/C(sp^2) \rightarrow \text{bpy } \pi^*(1)$] excitations.

However, we note that, due to the triplet reference state containing the singly occupied Ni $d(z^2)$ orbital configuration, our description of the $^3\text{MLCT}$ surfaces and two-electron triplet repulsive surface is restricted to those with [$\text{Ni } d(z^2) \rightarrow \text{bpy } \pi^*$] MLCT transitions. Detailed discussion on the limitations of this approach is given in Supporting Information Section S2.2.

Despite these limitations, we were able to obtain an excellent energetic correlation between the “one-photon, two-electron” triplet repulsive surface at the equilibrium geometry and both the experimental $\ln(k_{\text{obs},1})$ and Hammett σ parameters (Figures S66 and S67), suggesting that this surface (or an analogous surface with another singly occupied Ni d -orbital) is involved in the mechanism of excited-state bond homolysis. In contrast, a significantly poorer correlation was found for the energy of the “one-photon, one-electron” $^3[d(x^2-y^2)/C(sp^2) \rightarrow d(x^2-y^2)/C(sp^2)^*]$ repulsive surface (Figure S66). Furthermore, when considering that the calculated $^{1/3}(d-d)$ transitions are near or below the minimum excitation energy threshold obtained from the wavelength-dependent experiments in **Figure 3.8**, it appears that the one-electron triplet repulsive surface is not likely operative for the excited-state Ni(II)–C bond homolysis in **1A–5D**.

The activation energies derived from the high-energy $^1\text{MLCT}$ excited states (as defined by the crossing of the MLCT/triplet repulsive surface and the Frank–Condon point of the MLCT

state) agree qualitatively well with those of $\Delta H^\ddagger = 4.4 \pm 0.6$ and 2.1 ± 0.3 kcal mol⁻¹ measured for **1B** and **1B-Br** (**Figure 3.11**). The best fit between the calculated activation energies and the experimental $\ln(k_{\text{obs},1})$ was observed for the ¹MLCT [$d(yz) \rightarrow \pi^*(2)$] excited surface hopping to the two-electron repulsive surface, ³[$d(x^2-y^2)/C(sp^2) + d(z^2) \rightarrow d(x^2-y^2)/C(sp^2)^* + \pi^*(1)$] (**Figure 3.11**). It should also be noted that the MLCT transitions from the donor $d(yz)$ orbitals correspond to the absorption bands with greatest oscillator strengths, making the [$d(yz) \rightarrow \pi^*(2)$] surface most likely to be populated from the initial photon absorption. However, due to the aforementioned limitations of the TD-DFT approach (Section S2.2), we cannot exclude an equal or better correlation for the same pathway utilizing another ³(MLCT + LMCT) excited state instead.

The CASSCF/QD-NEVPT2 computations provide the same photolysis mechanism for **1A-5D** as that obtained from TD-DFT (**Figure 3.10**, left). However, the predicted activation energy is increased by ~20 to 25 kcal mol⁻¹ (**Figure 3.11**). This increase is likely the result of the higher Ni(II)-C BDEs found by CASSCF/QD-NEVPT2, as increasing the overall BDE also increases the energies of the crossing point between the initial ¹MLCT and the repulsive two-electron excited-state surfaces. As discussed in detail in Supporting Information Section S2.2, we believe that the higher BDEs for these calculations originate from a potentially incomplete description of the CASSCF reference wave function.

From the initial ¹MLCT [$d(yz) \rightarrow \pi^*(2)$] excitation, we have evaluated the activation energies for this surface crossing from all of the accessible ³(MLCT + LMCT) repulsive states. Although the correlation is satisfactory with the same ³[$d(x^2-y^2)/C(sp^2) + d(z^2) \rightarrow d(x^2-y^2)/C(sp^2)^* + \pi^*(1)$] surface as explored by TD-DFT (with $R^2 = 0.79$), an even better correlation was observed for surface hopping to the ³[$d(x^2-y^2)/C(sp^2) + d(yz) \rightarrow d(x^2-y^2)/C(sp^2)^* + \pi^*(1)$], characterized by $R^2 = 0.91$ (**Figure 3.11**, bottom).

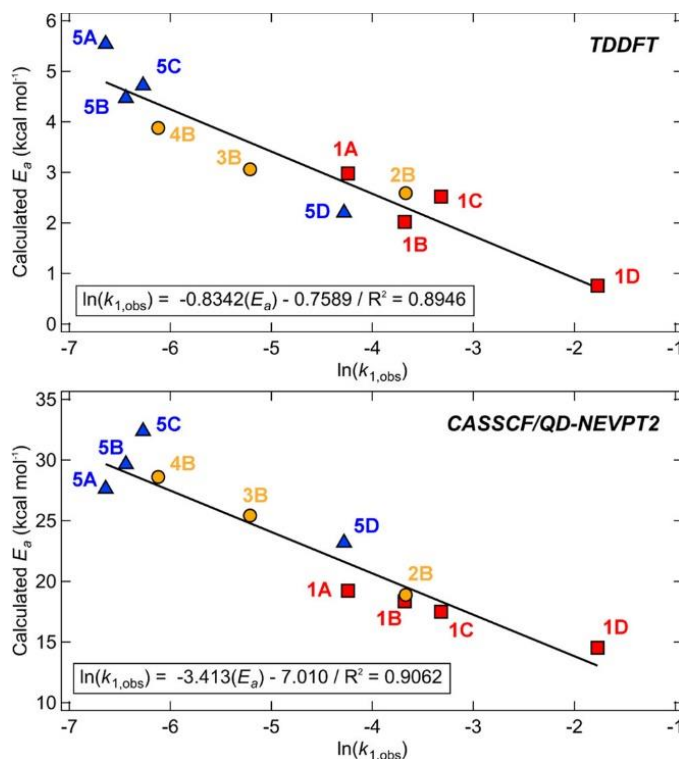


Figure 3.11. Computed excited-state activation energies (TD-DFT, top; CASSCF/QD-NEVPT2, bottom) for **1A–5D** plotted against experimental $\ln(k_{obs,1})$ obtained using 390 nm excitation. Note that for **1A**, $k_{1,obs}$ is approximated by $k_{2,obs}$. The activation energies are estimated from the surface crossing between the high-energy ¹MLCT [$d(yz) \rightarrow \pi^*(2)$] PES and the “one-photon, two-electron” triplet repulsive surface, ³(MLCT + LMCT) (more details can be found in Supporting Information Section S2.2; see Figure S66 for an analogous plot with the “one-photon, one-electron” triplet repulsive surface). Additionally, we have found an activation energy of ~ 2.2 kcal mol⁻¹ for the **1B–Br** complex, which is in excellent agreement with the experimental ΔH^\ddagger .

Overall, both TD-DFT and CASSCF/QD-NEVPT2 methods predict analogous photolysis mechanisms that exploit triplet repulsive “one-photon, two-electron” excited-state PESs, and the calculations further capture the critical aspects that lead to geometric and electronic structural control over the excited-state PES manifold that ultimately governs the photochemical behavior. However, each method is associated with its own limitations, precluding a definitive assignment of which ^{1/3}MLCT is initially operative or at which

stage ISC occurs (i.e., before or after the surface hopping between MLCT and MLCT + LMCT surfaces). We also speculate that this mechanism may not be identical for all Ni complexes used in photoredox catalysis. Additional possibilities, including the “one-photon, one-electron” $^1/3(d-d) \rightarrow ^3LMCT$ pathway, might be operative depending on the energetics of the individual excited states, the probability of the initial light-induced transitions, and/or the probability of the surface hopping to the triplet repulsive PESs.

§3-3. Discussion

Light-induced homolysis provides a powerful means to activate ligand–metal bonds for the generation of reactive radical species involved in targeted catalytic bond transformations.^{5,62,63} Defining the photophysical processes underlying the mechanisms of light-induced homolysis will therefore aid chemists in elucidating the role(s) of photogenerated intermediates in currently established photoredox catalytic cycles, as well as further guide the development of novel bond-formation reactions in organic chemistry. Here, we have provided new combined experimental and computational insights that have aided in the elucidation of the mechanism of excited-state Ni(II)–C bond homolysis in commonly employed Ni(II)–bpy aryl halide photoredox catalysts.

In particular, rate constants of excited-state homolysis depend on the temperature (**Figure 3.7**) and the wavelength of light excitation (**Figure 3.8**). From these observations, we conclude that there exists an energy barrier between the light-absorbing and homolytically dissociative excited states. For **1B**, $\Delta H^\ddagger = 4.4 \pm 0.6$ kcal mol⁻¹ using 390 nm excitation. Note that ΔH^\ddagger is the energy parameter that is most relevant for comparisons to calculated excited-state PESs. From the wavelength dependence on the rate constants, it is also clear that the lower-energy ¹MLCTs near ~525 nm (19,050 cm⁻¹, 55 kcal/mol) are not productive for excited-state homolysis. Rather, higher-energy excitation is required. Overall, these observations are not consistent with thermally driven Ni(II)–C bond homolysis from excited ligand field states. We further note that similar wavelength dependence trends have been demonstrated for Ni(II)–bpy-mediated C–O cross-coupling product yields, directly implicating these high-energy ¹MLCT states in photoredox

catalysis.²⁴ Substituent-driven modulation of the critical PESs and bond homolysis rates may provide a synthetic handle to promote (or discourage) radical formation during catalysis.

In addition to the temperature and wavelength dependence, we have found that the rate constants of homolysis in Ni(II)–bpy aryl halide complexes are also sensitive to variations in both the solvent and the nature of all three ligands. For example, the rate constants of excited-state Ni(II)–C bond homolysis for **1B** and **1B–Br** are slower in toluene and DMF (Figures S48–S51) relative to THF, suggesting a solvent influence on the excited-state PESs. Solvent dependence has been observed for other light-induced homolysis reactions that feature activation energies, and similar arguments regarding perturbations to the barrier have been made.^{30,31} Furthermore, exchanging chloride with bromide (**1B** versus **1B–Br**) increases the observed rate of homolysis from 2.5 ± 0.2 to $6.9 \pm 0.4 \times 10^{-2} \text{ min}^{-1}$. The calculated barriers and excited-state PESs for these two compounds are similar (Figure S70). However, changing Cl to Br increases the ligand-based spin-orbit coupling constant.⁶⁴ This increased spin-orbit coupling may increase the rate of surface crossing and suggests that spin-vibronic effects may be important to consider (*vide infra*).^{65–67}

Furthermore, light-induced homolysis results in the production of an additional visible-light absorbing species (**Section §3-2.1.4**). Based on the correlation between the UV–vis spectrum of the intermediate formed from **1B–Br** via photolysis to that identified recently by Bird et al.,⁵³ we tentatively assign this species as a three-coordinate, formal Ni(I)(^t-Bu₃bpy)(Br) complex. While further study of this intermediate is outside the scope of this study, it is worth noting that, under controlled air- and moisture-free conditions, excited-state homolysis provides a means to generate and isolate putative reactive intermediates for detailed studies of their spectroscopic properties and reactivity patterns. Thus, the rate of formation of these intermediates is tunable via structural and electronic control over key PESs, affording chemists new photon-driven synthetic possibilities in photoredox catalysis.⁶⁸

Variation of the bpy ligand (columns in **Figure 3.2**) modifies the MLCT λ_{\max} (**Figure 3.3B**) and the rate constant of homolysis at a given excitation wavelength; there is in fact a linear correlation between the normalized logarithm of the rate constant and the σ_p of the bpy substituent (**Figure 3.5**). Increased electron-withdrawing strength of the bpy lowers the energies of the MLCT excited-state PES manifold (e.g., the MLCT of **1D** is 8.1 kcal mol⁻¹ lower relative to **1A**; see **Figure 3.12A**). If the MLCT surface was the only excited-state PES involved in the bond-rupture mechanism, one would expect an increased barrier and an accordingly slower rate for homolysis in **1D** than for **1A**. However, when considering the barrier as governed by the crossing point between the MLCT and ³(MLCT + LMCT) states, the correct rate trend is recovered. Increasing the electron-withdrawing strength of the bpy enables more facile aryl-to-Ni(III) charge transfer, lowering the LMCT energies. Furthermore, from the Hammett trends/slopes (**Figure 3.5**), we see a greater impact on the rate constant when modulating the aryl substituent (i.e., the LMCT component) versus the bpy substituent.

Thus, while the energetic shifts of the ¹MLCT and ³(MLCT+LMCT) PESs are of the same sign, they shift at different rates as a function of ligand perturbation. The ligand-based effects on the ³(MLCT + LMCT) repulsive excited state outweigh the drop in the initial MLCT energy. Ultimately, these effects result in a lower barrier for homolysis (e.g., **1D** has a barrier of 1.4 kcal mol⁻¹ lower than that for **1A**; **Figure 3.12B**) and, thus, a larger rate constant.

The ligand-based perturbations to the excited-state PESs described in **Figure 3.12C** demonstrate that the coupled changes to the overall excited-state PES manifold, including surface intersections and barriers, govern the barriers and rates of Ni(II)–C bond homolysis.

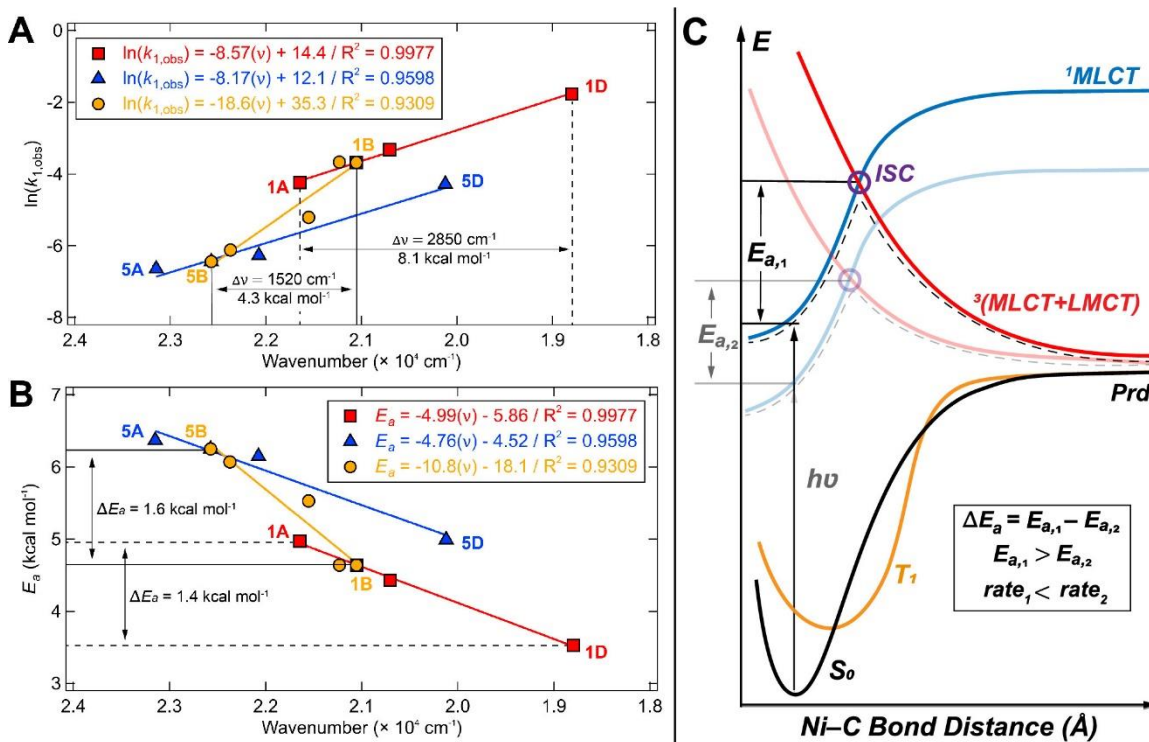


Figure 3.12. Comparison between the change in energy of the MLCT λ_{max} and (A) the experimental $\ln(k_{obs,1})$ obtained with 390 nm excitation and (B) the energetic barrier for photolysis for **1A–1D** and **1B–5B**. Barriers are estimated using the Arrhenius equation (assuming a uniform pre-exponential factor) and are normalized to the experimental value obtained for **1B**. (C) PES diagram illustrating how the barrier for photolysis is dependent on both the $^1\text{MLCT}$ and repulsive $^3(\text{MLCT}+\text{LMCT})$ surfaces. Full detailed PESs for **1A–5D** are given in Figures S68 and S69.

Electronic structure calculations have provided further insights into these experimental observations, successfully correlating the calculated PES features to the experimental rate constants by capturing the critical aspects that lead to geometric and electronic structure control over the excited-state PES manifolds (**Figure 3.9**). Also, both TD-DFT and CASSCF/QD-NEVPT2 methods predict analogous mechanisms that exploit “one-photon, two-electron” repulsive $^3(\text{MLCT} + \text{LMCT})$ excited-state PESs. In particular, **Figure 3.11** demonstrates a strong correlation between the computed excited-state activation energies and the experimental $\ln(k_{obs,1})$ obtained using 390 nm excitation. The activation

energies are predicted to arise from the surface crossing between the high-energy $^1\text{MLCT}$ [$d(yz) \rightarrow \pi^*(2)$] PES and the two-electron triplet repulsive surface, $^3(\text{MLCT} + \text{LMCT})$. Thus, the calculations are consistent with the overall experimental data and mechanism presented in **Figure 3.12C**.

Further comment on the specific mode of entry into the repulsive $^3(\text{MLCT} + \text{LMCT})$ state is warranted. Given that the UV-vis electronic absorption spectra of Ni(II)-bpy compounds exhibit dominantly MLCT intensity, there is a minimum energy threshold for homolysis, and the calculated ligand field transitions are lower than photochemically active higher-energy MLCT excited states, we posit that MLCT surfaces provide an entry into the $^3(\text{MLCT} + \text{LMCT})$ state. However, we do not know if ISC occurs between $^1,^3\text{MLCT}$ states or the $^3(\text{MLCT} + \text{LMCT})$ states. It may also be the case that vibronic coupling between charge-transfer and ligand field states may be an important component of the mechanism (*vide infra*).⁶⁷ Therefore, experimental determination of the energies of the ligand field transitions across these Ni(II)-bpy aryl halide complexes would be informative. If the $^1(d-d)$ transitions are indeed experimentally obscured by the dominant, photochemically active MLCT intensity, electronic absorption will not be appropriate. Due to the *C*-term intensity mechanism, low-temperature optical MCD would be ideal for this. However, the diamagnetic ground states of these complexes will also likely complicate ligand field assignments. As an alternative, $2p3d$ RIXS is a less commonly employed, but powerful, methodology to obtain spectroscopic insights into the spin-allowed and forbidden ligand field excited-state manifolds.⁶⁹⁻⁷⁴ This technique represents a potential approach to observe the ligand field excited-state manifold in the presence of charge-transfer bands, which will provide important insight into potential $^1(d-d)$ states as a mode of entry to a dissociative $^3\text{LMCT}$ state.⁵¹

Ni(II)-bpy aryl halide complexes feature a high density of excited states (Figure S68 and Tables S10 and S11), many vibrational degrees of freedom, and large spin-orbit coupling. The combination of these factors can complicate mechanistic analyses that feature discrete processes of vibrational relaxation, internal conversion, and ISC, especially when they

occur on the time scale of molecular vibrations (i.e., sub-picosecond time scale).^{39,67} Thus, the ultrafast spectroscopic characterization of the homolytically active state in Ni(II)–bpy aryl halide complexes may be hampered by the nature of the excited-state homolysis mechanism. That is, the spectral dynamics will be dominated by MLCT and ligand field states, and there may be little-to-no dynamics detectable for the repulsive ³(MLCT + LMCT) surfaces proposed here, unless they can be accessed in sufficient amounts, perhaps with high-energy excitation. Additionally, it may be that the TD-DFT and multiconfigurational/multireference mechanistic pictures provided by the calculated PESs need to be further supplemented to account for more complex aspects of spin-vibronic coupling.⁶⁷ Further experimental characterization of aspects such as the specific state that provides entry to the repulsive ³(MLCT + LMCT) states, as well as more detailed experimental characterization of potential spin-vibronic coupling effects, will be useful for better understanding how they manifest in the mechanism of excited-state bond homolysis.

Finally, it is instructive to note that findings reported here resemble results from detailed photochemical investigations of d⁶ Re-complexes, Re(R)(CO)₃(α -diimine), where R = Me, Et, Bz.^{30–38} For these complexes, it was found that the excited-state Re–R bond homolysis is a result of the formation of a repulsive $\sigma\pi^*$ excited state. In the case of the Re systems, the $\sigma\pi^*$ excited state refers to an electronic configuration in which one electron is added to a π^* orbital of the α -diimine ligand (¹MLCT) and one electron is depleted from the Re–R bond (LMCT). The final dissociative state is not accessible via direct excitation but is instead accessed from excitation of the ¹MLCT state followed by the LMCT. Moreover, excited-state homolysis in the Re(Me)(CO)₃(α -diimine) complex occurs on the sub-picosecond time scale with a small quantum yield, is dependent on temperature and excitation wavelengths, and has activation energies between ~ 1.8 and $5.5 \text{ kcal mol}^{-1}$ using 458–502 nm excitation ($\sim 21,830$ to $19,920 \text{ cm}^{-1}$).³¹ These photophysical properties and excited-state barriers are in the range of those determined for the Ni(II)–bpy aryl halide complexes studied here and are indicative of a dissociative excited state that is higher in energy than the ¹MLCT excited state, creating a barrier and surface crossing (**Figure**

3.12A,B). It was further noted in the Re complex that enhanced quantum yields correlated with increasing energy of excitation; this behavior mirrors the rate accelerations we observed herein upon increased excitation energy (Figure S25). This observation was interpreted as arising from excitation into higher-energy vibronic levels of the $^1\text{MLCT}$ state, which promotes the $^1\text{MLCT} \rightarrow \sigma\pi^*$ surface hopping.^{30,36} Based on these similarities, in particular, the increased homolysis rate constants with increasing energy of excitation into the higher-energy MLCT transitions (**Figure 3.8**), we hypothesize that the mechanism of excited-state homolysis in Ni(II)–bpy aryl halide complexes may indeed feature a similar vibronically mediated component, wherein the optically excited $^1\text{MLCT}$ is vibronically coupled to dissociative $^3(\text{MLCT} + \text{LMCT})$ states or even potentially to weakly absorbing ligand field excited states, as observed by Park et al.⁵¹ Overall, we highlight Re-like reactivity in Ni-catalysts, adapting the excited-state dynamics of third-row transition-metal complexes to first-row, earth-abundant metal-based systems.

§3-4. Conclusions

In summary, we have demonstrated that rate constants of excited-state Ni(II)–C bond homolysis are temperature- and wavelength-dependent. Both of these experimental observations point to a thermal barrier involved in the photophysical mechanism. The barrier is moderate and inconsistent with thermally driven homolysis from a low-energy ligand field excited state. Additionally, we have demonstrated a linear correlation between bpy and aryl perturbations and the observed rate constants of homolysis using a consistent energy of irradiation. In this way, pinning the excitation wavelength reveals the ligand-induced electronic perturbations to the energetic barrier for Ni(II)–C bond homolysis by controlling the key excited-state MLCT/LMCT surfaces. In accordance with this, electronic structure calculations predict a mechanism that exploits “one-photon, two-electron” repulsive $^3(\text{MLCT} + \text{LMCT})$ excited-state PESs and reveal a strong correlation between the computed excited-state activation energies and the experimental $\ln(k_{\text{obs},1})$ obtained using 390 nm excitation. The activation energies are predicted to arise from the surface crossing between the high-energy $^1\text{MLCT} [d(yz) \rightarrow \pi^*(2)]$ and the two-electron triplet repulsive surfaces, highlighting the specific excited-state PESs that contribute to

Ni(II)–bpy-mediated photoredox catalysis. This study provides insights into the electronic structural control over light-induced homolysis and, thus, guides the use of photonic energy as a sustainable alternative to coupling catalysis as carried out by precious metals.

§3-5. References

- (1) Nicewicz, D. A.; MacMillan, D. W. C. Merging Photoredox Catalysis with Organocatalysis: The Direct Asymmetric Alkylation of Aldehydes. *Science* **2008**, *322* (5898), 77–80. <https://doi.org/10.1126/science.1161976>.
- (2) Shaw, M. H.; Twilton, J.; MacMillan, D. W. C. Photoredox Catalysis in Organic Chemistry. *J. Org. Chem.* **2016**, *81* (16), 6898–6926. <https://doi.org/10.1021/acs.joc.6b01449>.
- (3) Cavalcanti, L. N.; Molander, G. A. Photoredox Catalysis in Nickel-Catalyzed Cross-Coupling. *Top. Curr. Chem.* **2016**, *374* (4), 39. <https://doi.org/10.1007/s41061-016-0037-z>.
- (4) Till, N. A.; Tian, L.; Dong, Z.; Scholes, G. D.; MacMillan, D. W. C. Mechanistic Analysis of Metallaphotoredox C–N Coupling: Photocatalysis Initiates and Perpetuates Ni(I)/Ni(III) Coupling Activity. *J. Am. Chem. Soc.* **2020**, *142* (37), 15830–15841. <https://doi.org/10.1021/jacs.0c05901>.
- (5) Qin, Y.; Sun, R.; Gianoulis, N. P.; Nocera, D. G. Photoredox Nickel-Catalyzed C–S Cross-Coupling: Mechanism, Kinetics, and Generalization. *J. Am. Chem. Soc.* **2021**, *143* (4), 2005–2015. <https://doi.org/10.1021/jacs.0c11937>.
- (6) Huang, L.; Ji, T.; Rueping, M. Remote Nickel-Catalyzed Cross-Coupling Arylation via Proton-Coupled Electron Transfer-Enabled C–C Bond Cleavage. *J. Am. Chem. Soc.* **2020**, *142* (7), 3532–3539. <https://doi.org/10.1021/jacs.9b12490>.
- (7) Ackerman, L. K. G.; Martinez Alvarado, J. I.; Doyle, A. G. Direct C–C Bond Formation from Alkanes Using Ni-Photoredox Catalysis. *J. Am. Chem. Soc.* **2018**, *140* (43), 14059–14063. <https://doi.org/10.1021/jacs.8b09191>.
- (8) Kim, T.; McCarver, S. J.; Lee, C.; MacMillan, D. W. C. Sulfonamidation of Aryl and Heteroaryl Halides through Photosensitized Nickel Catalysis. *Angew. Chem. Int. Ed.* **2018**, *57* (13), 3488–3492. <https://doi.org/10.1002/anie.201800699>.
- (9) Zhang, R.; Li, G.; Wismer, M.; Vachal, P.; Colletti, S. L.; Shi, Z.-C. Profiling and Application of Photoredox C(sp³)–C(sp²) Cross-Coupling in Medicinal Chemistry. *ACS Med. Chem. Lett.* **2018**, *9* (7), 773–777. <https://doi.org/10.1021/acsmchemlett.8b00183>.
- (10) Schultz, D. M.; Yoon, T. P. Solar Synthesis: Prospects in Visible Light Photocatalysis. *Science* **2014**, *343* (6174), 1239176. <https://doi.org/10.1126/science.1239176>.

- (11) M. Arias-Rotondo, D.; K. McCusker, J. The Photophysics of Photoredox Catalysis: A Roadmap for Catalyst Design. *Chem. Soc. Rev.* **2016**, *45* (21), 5803–5820. <https://doi.org/10.1039/C6CS00526H>.
- (12) Larsen, C. B.; Wenger, O. S. Photoredox Catalysis with Metal Complexes Made from Earth-Abundant Elements. *Chem. Eur. J.* **2018**, *24* (9), 2039–2058. <https://doi.org/10.1002/chem.201703602>.
- (13) Yoon, T. P.; Ischay, M. A.; Du, J. Visible Light Photocatalysis as a Greener Approach to Photochemical Synthesis. *Nat. Chem.* **2010**, *2* (7), 527–532. <https://doi.org/10.1038/nchem.687>.
- (14) Chan, A. Y.; Perry, I. B.; Bissonnette, N. B.; Buksh, B. F.; Edwards, G. A.; Frye, L. I.; Garry, O. L.; Lavagnino, M. N.; Li, B. X.; Liang, Y.; Mao, E.; Millet, A.; Oakley, J. V.; Reed, N. L.; Sakai, H. A.; Seath, C. P.; MacMillan, D. W. C. Metallaphotoredox: The Merger of Photoredox and Transition Metal Catalysis. *Chem. Rev.* **2021**. <https://doi.org/10.1021/acs.chemrev.1c00383>.
- (15) Diccianni, J. B.; Diao, T. Mechanisms of Nickel-Catalyzed Cross-Coupling Reactions. *Trends Chem.* **2019**, *1* (9), 830–844. <https://doi.org/10.1016/j.trechm.2019.08.004>.
- (16) Ting, S. I.; Garakyaraghi, S.; Taliaferro, C. M.; Shields, B. J.; Scholes, G. D.; Castellano, F. N.; Doyle, A. G. ³d-d Excited States of Ni(II) Complexes Relevant to Photoredox Catalysis: Spectroscopic Identification and Mechanistic Implications. *J. Am. Chem. Soc.* **2020**, *142* (12), 5800–5810. <https://doi.org/10.1021/jacs.0c00781>.
- (17) Yuan, M.; Song, Z.; Badir, S. O.; Molander, G. A.; Gutierrez, O. On the Nature of C(sp³)–C(sp²) Bond Formation in Nickel-Catalyzed Tertiary Radical Cross-Couplings: A Case Study of Ni/Photoredox Catalytic Cross-Coupling of Alkyl Radicals and Aryl Halides. *J. Am. Chem. Soc.* **2020**, *142* (15), 7225–7234. <https://doi.org/10.1021/jacs.0c02355>.
- (18) Gonzalez, M. I.; Gygi, D.; Qin, Y.; Zhu, Q.; Johnson, E. J.; Chen, Y.-S.; Nocera, D. G. Taming the Chlorine Radical: Enforcing Steric Control over Chlorine-Radical-Mediated C–H Activation. *J. Am. Chem. Soc.* **2022**, *144* (3), 1464–1472. <https://doi.org/10.1021/jacs.1c13333>.
- (19) Treacy, S. M.; Rovis, T. Copper Catalyzed C(sp³)–H Bond Alkylation via Photoinduced Ligand-to-Metal Charge Transfer. *J. Am. Chem. Soc.* **2021**, *143* (7), 2729–2735. <https://doi.org/10.1021/jacs.1c00687>.

- (20) Welin, E. R.; Le, C.; Arias-Rotondo, D. M.; McCusker, J. K.; MacMillan, D. W. C. Photosensitized, Energy Transfer-Mediated Organometallic Catalysis through Electronically Excited Nickel(II). *Science* **2017**, *355* (6323), 380–385. <https://doi.org/10.1126/science.aal2490>.
- (21) Strieth-Kalthoff, F.; Glorius, F. Triplet Energy Transfer Photocatalysis: Unlocking the Next Level. *Chem* **2020**, *6* (8), 1888–1903. <https://doi.org/10.1016/j.chempr.2020.07.010>.
- (22) Sun, R.; Qin, Y.; Rucolo, S.; Schnedermann, C.; Costentin, C.; Nocera, D. G. Elucidation of a Redox-Mediated Reaction Cycle for Nickel-Catalyzed Cross Coupling. *J. Am. Chem. Soc.* **2019**, *141* (1), 89–93. <https://doi.org/10.1021/jacs.8b11262>.
- (23) Shields, B. J.; Kudisch, B.; Scholes, G. D.; Doyle, A. G. Long-Lived Charge-Transfer States of Nickel(II) Aryl Halide Complexes Facilitate Bimolecular Photoinduced Electron Transfer. *J. Am. Chem. Soc.* **2018**, *140* (8), 3035–3039. <https://doi.org/10.1021/jacs.7b13281>.
- (24) Yang, L.; Lu, H.-H.; Lai, C.-H.; Li, G.; Zhang, W.; Cao, R.; Liu, F.; Wang, C.; Xiao, J.; Xue, D. Light-Promoted Nickel Catalysis: Etherification of Aryl Electrophiles with Alcohols Catalyzed by a Ni^{II}-Aryl Complex. *Angew. Chem. Int. Ed.* **2020**, *59* (31), 12714–12719. <https://doi.org/10.1002/anie.202003359>.
- (25) Tian, L.; Till, N. A.; Kudisch, B.; MacMillan, D. W. C.; Scholes, G. D. Transient Absorption Spectroscopy Offers Mechanistic Insights for an Iridium/Nickel-Catalyzed C–O Coupling. *J. Am. Chem. Soc.* **2020**, *142* (10), 4555–4559. <https://doi.org/10.1021/jacs.9b12835>.
- (26) Ma, P.; Wang, S.; Chen, H. Reactivity of Transition-Metal Complexes in Excited States: C–O Bond Coupling Reductive Elimination of a Ni(II) Complex Is Elicited by the Metal-to-Ligand Charge Transfer State. *ACS Catal.* **2020**, *10* (1), 1–6. <https://doi.org/10.1021/acscatal.9b03827>.
- (27) Han, R.; Hillhouse, G. L. Carbon–Oxygen Reductive-Elimination from Nickel(II) Oxametallacycles and Factors That Control Formation of Ether, Aldehyde, Alcohol, or Ester Products. *J. Am. Chem. Soc.* **1997**, *119* (34), 8135–8136. <https://doi.org/10.1021/ja9714999>.
- (28) Koo, K.; Hillhouse, G. L. Carbon-Nitrogen Bond Formation by Reductive Elimination from Nickel(II) Amido Alkyl Complexes. *Organometallics* **1995**, *14* (9), 4421–4423. <https://doi.org/10.1021/om00009a054>.

- (29) Cagan, D. A.; Strocio, G. D.; Cusumano, A. Q.; Hadt, R. G. Multireference Description of Nickel–Aryl Homolytic Bond Dissociation Processes in Photoredox Catalysis. *J. Phys. Chem. A* **2020**, *124* (48), 9915–9922. <https://doi.org/10.1021/acs.jpca.0c08646>.
- (30) Kleverlaan, C. J.; Stufkens, D. J.; Clark, I. P.; George, M. W.; Turner, J. J.; Martino, D. M.; van Willigen, H.; Vlček, A. Photoinduced Radical Formation from the Complexes $[\text{Re}(\text{R})(\text{CO})_3(4,4'\text{-Me}_2\text{-bpy})]$ ($\text{R} = \text{CH}_3, \text{CD}_3, \text{Et}, \text{}^i\text{Pr}, \text{Bz}$): A Nanosecond Time-Resolved Emission, UV–Vis and IR Absorption, and FT-EPR Study. *J. Am. Chem. Soc.* **1998**, *120* (42), 10871–10879. <https://doi.org/10.1021/ja980540k>.
- (31) Rossenaar, B. D.; Kleverlaan, C. J.; Van De Ven, M. C. E.; Stufkens, D. J.; Vlček, Jr., A. Mechanism of an Alkyl-Dependent Photochemical Homolysis of the Re–Alkyl Bond in $[\text{Re}(\text{R})(\text{CO})_3(\alpha\text{-diimine})]$ Complexes via a Reactive $\sigma\pi^*$ Excited State. *Chem. Eur. J.* **1996**, *2*(2), 228–237. <https://doi.org/10.1002/chem.19960020216>.
- (32) Rossenaar, B. D.; Kleverlaan, C. J.; Stufkens, D. J.; Oskam, A. Photochemistry of $\text{ReR}(\text{CO})_3(\text{Pr}^i\text{-Dab})$ ($\text{R} = \text{Me}, \text{Et}, \text{Bn}$; $\text{Dab} = 1,4\text{-Diazabuta-1,3-Diene}$): Homolysis of the Re–R Bond, Its Dependence on R and Evidence for the Reactive $\sigma_b\pi^*$ State from Transient Absorption Spectra. *J. Chem. Soc. Chem. Commun.* **1994**, No. 1, 63–64. <https://doi.org/10.1039/C39940000063>.
- (33) Stufkens, D. J.; Vlček, A. Ligand-Dependent Excited State Behaviour of Re(I) and Ru(II) Carbonyl–Diimine Complexes. *Coord. Chem. Rev.* **1998**, *177* (1), 127–179. [https://doi.org/10.1016/S0010-8545\(98\)00132-5](https://doi.org/10.1016/S0010-8545(98)00132-5).
- (34) A. Weinstein, J.; van Slageren, J.; J. Stufkens, D.; Záliš, S.; W. George, M. A Time-Resolved Infrared Spectroscopic Study of $[\text{M}(\text{SnR}_3)_2(\text{CO})_2(\alpha\text{-Diimine})]$ ($\text{M} = \text{Ru}, \text{Os}$; $\text{R} = \text{Ph}, \text{Me}$): Evidence of Charge Redistribution in the Lowest-Excited State. *J. Chem. Soc. Dalton Trans.* **2001**, *18*, 2587–2592. <https://doi.org/10.1039/B102450G>.
- (35) Stufkens, D. J.; Aarnts, M. P.; Rossenaar, B. D.; Vlček, A. A new series of Re- and Ru-complexes having a lowest $\sigma\pi^*$ excited state that varies from reactive to stable and long lived. *Pure Appl. Chem.* **1997**, *69* (4), 831–836. <https://doi.org/10.1351/pac199769040831>.
- (36) Aarnts, M. P.; Wilms, M. P.; Stufkens, D. J.; Baerends, E. J.; Vlček, A. $\sigma\text{-}\pi^*$ Electronic Transition of the Di- and Trinuclear Complexes $\text{Ru}(\text{E})(\text{E}')(\text{CO})_2(\text{}^i\text{Pr-DAB})$: Resonance Raman, Electronic Absorption, Emission, and Density Functional Study ($\text{E} = \text{Me}, \text{SnPh}_3, \text{M}(\text{CO})_5$; $\text{E}' = \text{M}(\text{CO})_5$; $\text{M} = \text{Mn}, \text{Re}$; $\text{}^i\text{Pr-DAB} = \text{N,N}'\text{-Diisopropyl-1,4-Diaza-}$

1,3-Butadiene). *Organometallics* **1997**, *16* (10), 2055–2062. <https://doi.org/10.1021/om9608667>.

(37) Nieuwenhuis, H. A.; van de Ven, M. C. E.; Stufkens, D. J.; Oskam, A.; Goubitz, K. Photochemistry of [Ru(I)(*i*Pr)(CO)₂(*i*Pr-DAB)] (*i*Pr-DAB = N,N'-Diisopropyl-1,4-Diaza-1,3-Butadiene): Homolysis of the Metal-Alkyl Bond from the $\sigma_b(\text{Ru-}i\text{Pr})\pi^*$ State. Crystal Structure of the Photoproduct [Ru(I)₂(CO)₂(*i*Pr-DAB)]. *Organometallics* **1995**, *14* (2), 780–788. <https://doi.org/10.1021/om00002a027>.

(38) Rossenaar, B. D.; George, M. W.; Johnson, F. P. A.; Stufkens, D. J.; Turner, J. J.; Vlček, A. First Direct Structural Information on a Reactive $\sigma\pi^*$ Excited State: Time-Resolved UV–Vis and IR Spectroscopic Study of Re(Benzyl)(CO)₃(*i*Pr-DAB). *J. Am. Chem. Soc.* **1995**, *117* (46), 11582–11583. <https://doi.org/10.1021/ja00151a025>.

(39) Vlček, A.; Vichová, J.; Hartl, F. Bond Activation by MLCT Excitation of Organometallic Compounds: Prompt CO-Photodissociation from [Cr(CO)₄bpy]. *Coord. Chem. Rev.* **1994**, *132*, 167–174. [https://doi.org/10.1016/0010-8545\(94\)80037-5](https://doi.org/10.1016/0010-8545(94)80037-5).

(40) Shields, J. D.; Gray, E. E.; Doyle, A. G. A Modular, Air-Stable Nickel Precatalyst. *Org. Lett.* **2015**, *17* (9), 2166–2169. <https://doi.org/10.1021/acs.orglett.5b00766>.

(41) Marshall, W. J.; Grushin, V. V. Activation of Chlorobenzene with Ni(0) N,N-Chelates—A Remarkably Profound Effect of a Minuscule Change in Ligand Structure. *Can. J. Chem.* **2005**, *83* (6–7), 640–645. <https://doi.org/10.1139/v05-022>.

(42) Hansch, Corwin.; Leo, A.; Taft, R. W. A Survey of Hammett Substituent Constants and Resonance and Field Parameters. *Chem. Rev.* **1991**, *91* (2), 165–195. <https://doi.org/10.1021/cr00002a004>.

(43) Magenau, A. J. D.; Kwak, Y.; Schröder, K.; Matyjaszewski, K. Highly Active Bipyridine-Based Ligands for Atom Transfer Radical Polymerization. *ACS Macro Lett.* **2012**, *1* (4), 508–512. <https://doi.org/10.1021/mz3000489>.

(44) Clark, M. L.; Cheung, P. L.; Lessio, M.; Carter, E. A.; Kubiak, C. P. Kinetic and Mechanistic Effects of Bipyridine (Bpy) Substituent, Labile Ligand, and Brønsted Acid on Electrocatalytic CO₂ Reduction by Re(bpy) Complexes. *ACS Catal.* **2018**, *8* (3), 2021–2029. <https://doi.org/10.1021/acscatal.7b03971>.

(45) Sinnokrot, M. O.; Sherrill, C. D. Substituent Effects in Π – π Interactions: Sandwich and T-Shaped Configurations. *J. Am. Chem. Soc.* **2004**, *126* (24), 7690–7697. <https://doi.org/10.1021/ja049434a>.

- (46) Ringer, A. L.; Sinnokrot, M. O.; Lively, R. P.; Sherrill, C. D. The Effect of Multiple Substituents on Sandwich and T-Shaped π - π Interactions. *Chem. Eur. J.* **2006**, *12* (14), 3821–3828. <https://doi.org/10.1002/chem.200501316>.
- (47) Gung, B. W.; Patel, M.; Xue, X. A Threshold for Charge Transfer in Aromatic Interactions? A Quantitative Study of π -Stacking Interactions. *J. Org. Chem.* **2005**, *70* (25), 10532–10537. <https://doi.org/10.1021/jo051808a>.
- (48) Wheeler, S. E.; Houk, K. N. Substituent Effects in the Benzene Dimer Are Due to Direct Interactions of the Substituents with the Unsubstituted Benzene. *J. Am. Chem. Soc.* **2008**, *130* (33), 10854–10855. <https://doi.org/10.1021/ja802849j>.
- (49) Santiago, C. B.; Milo, A.; Sigman, M. S. Developing a Modern Approach To Account for Steric Effects in Hammett-Type Correlations. *J. Am. Chem. Soc.* **2016**, *138* (40), 13424–13430. <https://doi.org/10.1021/jacs.6b08799>.
- (50) Lewis, M.; Bagwill, C.; Hardebeck, L. K. E.; Wireduah, S. The Use of Hammett Constants to Understand the Non-Covalent Binding of Aromatics. *Comput. Struct. Biotechnol. J.* **2012**, *1*, e201204004. <https://doi.org/10.5936/csbj.201204004>.
- (51) Shin, J.; Lee, J.; Suh, J.-M.; Park, K. Ligand-Field Transition-Induced C–S Bond Formation from Nickelacycles. *Chem. Sci.* **2021**, *12* (48), 15908–15915. <https://doi.org/10.1039/D1SC05113J>.
- (52) Stadler, E.; Eibel, A.; Fast, D.; Freißmuth, H.; Holly, C.; Wiech, M.; Moszner, N.; Gescheidt, G. A Versatile Method for the Determination of Photochemical Quantum Yields via Online UV–Vis Spectroscopy. *Photochem. Photobiol. Sci.* **2018**, *17* (5), 660–669. <https://doi.org/10.1039/C7PP00401J>.
- (53) Till, N. A.; Oh, S.; MacMillan, D. W. C.; Bird, M. J. The Application of Pulse Radiolysis to the Study of Ni(I) Intermediates in Ni-Catalyzed Cross-Coupling Reactions. *J. Am. Chem. Soc.* **2021**, *143* (25), 9332–9337. <https://doi.org/10.1021/jacs.1c04652>.
- (54) Mohadjer Beromi, M.; Brudvig, G. W.; Hazari, N.; Lant, H. M. C.; Mercado, B. Q. Synthesis and Reactivity of Paramagnetic Nickel Polypyridyl Complexes Relevant to C(sp²)-C(sp³) Coupling Reactions. *Angew. Chem. Int. Ed.* **2019**, *58* (18), 6094–6098. <https://doi.org/10.1002/anie.201901866>.
- (55) Roos, B. O.; Taylor, P. R.; Sigbahn, P. E. M. A Complete Active Space SCF Method (CASSCF) Using a Density Matrix Formulated Super-CI Approach. *Chem. Phys.* **1980**, *48* (2), 157–173. [https://doi.org/10.1016/0301-0104\(80\)80045-0](https://doi.org/10.1016/0301-0104(80)80045-0).

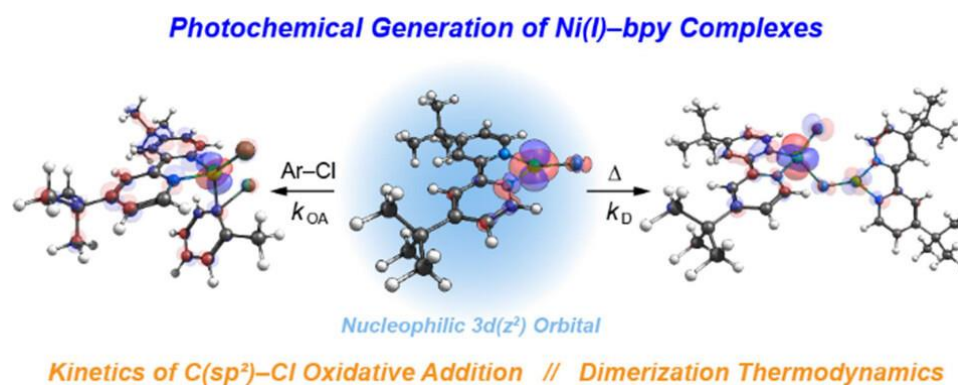
- (56) Siegbahn, P. E. M.; Almlöf, J.; Heiberg, A.; Roos, B. O. The Complete Active Space SCF (CASSCF) Method in a Newton–Raphson Formulation with Application to the HNO Molecule. *J. Chem. Phys.* **1981**, *74* (4), 2384–2396. <https://doi.org/10.1063/1.441359>.
- (57) Angeli, C.; Borini, S.; Cestari, M.; Cimiraglia, R. A Quasidegenerate Formulation of the Second Order N-Electron Valence State Perturbation Theory Approach. *J. Chem. Phys.* **2004**, *121* (9), 4043–4049. <https://doi.org/10.1063/1.1778711>.
- (58) Lang, L.; Sivalingam, K.; Neese, F. The Combination of Multipartitioning of the Hamiltonian with Canonical Van Vleck Perturbation Theory Leads to a Hermitian Variant of Quasidegenerate N-Electron Valence Perturbation Theory. *J. Chem. Phys.* **2020**, *152* (1), 014109. <https://doi.org/10.1063/1.5133746>.
- (59) Becke, A. D. Density-functional Thermochemistry. III. The Role of Exact Exchange. *J. Chem. Phys.* **1993**, *98* (7), 5648–5652. <https://doi.org/10.1063/1.464913>.
- (60) Lee, C.; Yang, W.; Parr, R. G. Development of the Colle-Salvetti Correlation-Energy Formula into a Functional of the Electron Density. *Phys. Rev. B* **1988**, *37* (2), 785–789. <https://doi.org/10.1103/PhysRevB.37.785>.
- (61) Becke, A. D. Density-Functional Exchange-Energy Approximation with Correct Asymptotic Behavior. *Phys. Rev. A* **1988**, *38* (6), 3098–3100. <https://doi.org/10.1103/PhysRevA.38.3098>.
- (62) Abderrazak, Y.; Bhattacharyya, A.; Reiser, O. Visible-Light-Induced Homolysis of Earth-Abundant Metal-Substrate Complexes: A Complementary Activation Strategy in Photoredox Catalysis. *Angew. Chem. Int. Ed.* **2021**, *60* (39), 21100–21115. <https://doi.org/10.1002/anie.202100270>.
- (63) Hwang, S. J.; Powers, D. C.; Maher, A. G.; Anderson, B. L.; Hadt, R. G.; Zheng, S.-L.; Chen, Y.-S.; Nocera, D. G. Trap-Free Halogen Photoelimination from Mononuclear Ni(III) Complexes. *J. Am. Chem. Soc.* **2015**, *137* (20), 6472–6475. <https://doi.org/10.1021/jacs.5b03192>.
- (64) Richards, W. G.; Trivedi, H. P.; Cooper, D. L. *Spin-Orbit Coupling in Molecules*. In The International series of monographs on chemistry, Clarendon Press, **1981**, pp 17.
- (65) Harvey, J. N. Understanding the Kinetics of Spin-Forbidden Chemical Reactions. *Phys. Chem. Chem. Phys.* **2007**, *9* (3), 331–343. <https://doi.org/10.1039/B614390C>.

- (66) Harvey, J. N. Spin-Forbidden Reactions: Computational Insight into Mechanisms and Kinetics. *WIREs Comput. Mol. Sci.* **2014**, *4* (1), 1–14. <https://doi.org/10.1002/wcms.1154>.
- (67) Penfold, T. J.; Gindensperger, E.; Daniel, C.; Marian, C. M. Spin-Vibronic Mechanism for Intersystem Crossing. *Chem. Rev.* **2018**, *118* (15), 6975–7025. <https://doi.org/10.1021/acs.chemrev.7b00617>.
- (68) Gisbertz, S.; Reischauer, S.; Pieber, B. Overcoming Limitations in Dual Photoredox/Nickel-Catalysed C–N Cross-Couplings Due to Catalyst Deactivation. *Nat. Catal.* **2020**, *3* (8), 611–620. <https://doi.org/10.1038/s41929-020-0473-6>.
- (69) Wang, R.-P.; Liu, B.; Green, R. J.; Delgado-Jaime, M. U.; Ghiasi, M.; Schmitt, T.; van Schooneveld, M. M.; de Groot, F. M. F. Charge-Transfer Analysis of 2p3d Resonant Inelastic X-Ray Scattering of Cobalt Sulfide and Halides. *J. Phys. Chem. C* **2017**, *121* (45), 24919–24928. <https://doi.org/10.1021/acs.jpcc.7b06882>.
- (70) Al Samarai, M.; Hahn, A. W.; Beheshti Askari, A.; Cui, Y.-T.; Yamazoe, K.; Miyawaki, J.; Harada, Y.; Rüdiger, O.; DeBeer, S. Elucidation of Structure-Activity Correlations in a Nickel Manganese Oxide Oxygen Evolution Reaction Catalyst by Operando Ni L-Edge X-Ray Absorption Spectroscopy and 2p3d Resonant Inelastic X-Ray Scattering. *ACS Appl. Mater. Interfaces* **2019**, *11* (42), 38595–38605. <https://doi.org/10.1021/acsami.9b06752>.
- (71) de Groot, F. M. F.; Fuggle, J. C.; Thole, B. T.; Sawatzky, G. A. 2p X-Ray Absorption of 3d Transition-Metal Compounds: An Atomic Multiplet Description Including the Crystal Field. *Phys. Rev. B* **1990**, *42* (9), 5459–5468. <https://doi.org/10.1103/PhysRevB.42.5459>.
- (72) Van Kuiken, B. E.; Hahn, A. W.; Maganas, D.; DeBeer, S. Measuring Spin-Allowed and Spin-Forbidden d–d Excitations in Vanadium Complexes with 2p3d Resonant Inelastic X-Ray Scattering. *Inorg. Chem.* **2016**, *55* (21), 11497–11501. <https://doi.org/10.1021/acs.inorgchem.6b02053>.
- (73) Hahn, A. W.; Van Kuiken, B. E.; Chilkuri, V. G.; Levin, N.; Bill, E.; Weyhermüller, T.; Nicolaou, A.; Miyawaki, J.; Harada, Y.; DeBeer, S. Probing the Valence Electronic Structure of Low-Spin Ferrous and Ferric Complexes Using 2p3d Resonant Inelastic X-Ray Scattering (RIXS). *Inorg. Chem.* **2018**, *57* (15), 9515–9530. <https://doi.org/10.1021/acs.inorgchem.8b01550>.

(74) Hahn, A. W.; Van Kuiken, B. E.; al Samarai, M.; Atanasov, M.; Weyhermüller, T.; Cui, Y.-T.; Miyawaki, J.; Harada, Y.; Nicolaou, A.; DeBeer, S. Measurement of the Ligand Field Spectra of Ferrous and Ferric Iron Chlorides Using 2p3d RIXS. *Inorg. Chem.* **2017**, *56* (14), 8203–8211. <https://doi.org/10.1021/acs.inorgchem.7b00940>.

Chapter 4

Photogenerated Ni(I)–Bipyridine Halide Complexes: Structure-Function Relationships for Competitive C(sp²)–Cl Oxidative Addition and Dimerization Reactivity Pathways



Adapted with permission from:

Cagan, D. A.;[†] Bím, D.;[†] McNicholas, B. J.; Kazmierczak, N. P.; Oyala, P. H.; Hadt, R. G. Photogenerated Ni(I)–Bipyridine Halide Complexes: Structure-Function Relationships for Competitive C(sp²)–Cl Oxidative Addition and Dimerization Reactivity Pathways. *Inorg. Chem.* **2023**, 62(24), 9538–9551. DOI: 10.1021/acs.inorgchem.3c00917. [†]Co-first author. Copyright 2023 American Chemical Society.

§4-1. Introduction

Photoredox catalysis has captivated the fields of organic and inorganic chemistry, with nickel(II)–bipyridine (bpy) aryl halide complexes retaining a prominent place as the metal–ligand scaffold of choice for numerous cross-coupling reactivity pathways.^{1–11} Among these, C–C and C–heteroatom couplings have been facilitated by Ni(II)–bpy complexes through either the use of an external photosensitizer (e.g., Ir(ppy)₃) or via direct excitation of the Ni(II)–bpy aryl halide complex.^{12–18} Due to the diverse reactivity and intriguing photophysics of these complexes, much interest has been placed on understanding the underlying photophysical and thermal processes involved in photoredox mediated cross-coupling reactivity.^{19–28}

While originally thought to proceed through a Ni(0)/Ni(II) cycle,⁶ recent work has instead supported a Ni(I)/Ni(III) cycle in the direct excitation pathway (**Figure 4.1A**).^{23,29,30} Through analysis of a library of Ni(II)–bpy aryl halide complexes, we have revealed that excited-state Ni(II)–C_{aryl} bond homolysis from the $S = 0$ square planar Ni(II) ground state features a key ligand-to-metal charge transfer (LMCT) process. This LMCT results in electron excitation between the Ni–aryl σ and σ^* orbitals, which lowers the bond order from one to zero, resulting in repulsive homolytic bond cleavage and the generation of an aryl radical and a three-coordinate Ni(I)–bpy halide species.²⁷

Related Ni(I)–bpy halide complexes have been prepared by alternate methods, including pulse radiolysis, electrolysis, and independent synthesis.^{30–33} Importantly, these compounds have demonstrated potency for the activation of aryl halide substrates. Following the work by Vicic *et al.* on Ni(I)–terpyridine complexes,^{34–36} Bird and MacMillan *et al.* reported a nickel(I)(4,4'-di-*tert*-butyl bipyridine)bromide complex (Ni(I)(*t*-Bu₂bpy)Br) that exhibited rapid reactivity toward aryl iodides with second-order rate constants of $\sim 10^4 \text{ M}^{-1} \text{ s}^{-1}$.³¹ The activation of C(sp²)–Br substrates was demonstrated by Doyle *et al.* using a nickel(I)(diethyl-2,2'-bipyridine-4,4'-dicarboxylate)chloride complex, Ni(I)(^{EtOOC}bpy)Cl. Activation of the stronger aryl bromide bond proceeded with slower, but still catalytically relevant, rate

constants of $\sim 10^{-2}$ – $10^1 \text{ M}^{-1} \text{ s}^{-1}$.³⁰ Notably, $\text{C}(\text{sp}^2)\text{--Cl}$ bonds could not be activated by this Ni(I) complex.

Careful kinetic analysis has been employed to understand the mechanism of this reactivity;^{30,37} the Ni(I) species has been suggested to undergo two-electron oxidative addition to form a short-lived five-coordinate Ni(III)–bpy aryl dihalide complex. This Ni(III) intermediate rapidly decays by comproportionation with another equivalent of Ni(I), forming Ni(II)–bpy aryl halide and Ni(II)–bpy dihalide complexes (**Figure 4.1A**).³⁰ Using three-coordinate pyridinophane Ni(I) model complexes, Mirica *et al.* have also provided evidence for this Ni(I)/Ni(III) oxidative addition pathway.²⁹ Therefore, these and related studies have argued for the importance of three-coordinate Ni(I)–bpy halide complexes to facilitate the oxidative addition step, without which the cross-coupling catalytic cycle would not close.^{21,23,38,39}

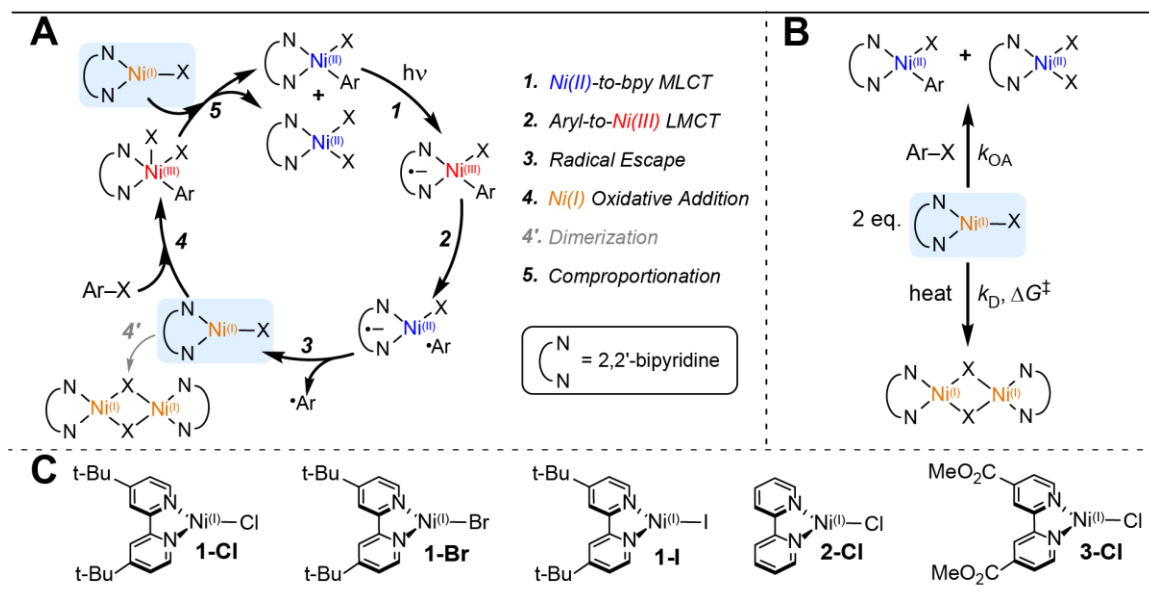


Figure 4.1. (A) Catalytic cycle displaying the photochemical activation of Ni(II)–bpy aryl halide complexes proposed in ref. 27 for the generation of Ni(I) and Ni(III) intermediates. (B) Two competing pathways for the Ni(I) complexes investigated here: oxidative addition and dimerization. (C) Photogenerated Ni(I)(^Rbpy)X structures examined in this work (R = *t*-Bu, H, MeOOC; X = Cl, Br, I).

While the reactivity of Ni(I)–bpy complexes has proven desirable for organic synthesis, their solution-phase stabilities vary widely, limiting their scope. Numerous Ni(I) dimerization products have been characterized, and the resultant polypyridyl species are no longer reactive toward oxidative addition with aryl halides.^{30,32,40,41} Dimerization thereby acts as an off-cycle sink with diminished catalytic activity (**Figure 4.1A**). Hazari *et al.* independently synthesized and characterized the dimeric [Ni(I)(*t*-Bu₂bpy)Cl]₂ complex. Once formed, the compound was stable in solution and exhibited no oxidative addition reactivity even with weak C(sp²)–I bonds.³² The related [Ni(I)(*t*-Bu₂bpy)Br]₂ complex was studied by Bird and MacMillan *et al.* and similarly showed no oxidative addition reactivity with aryl iodides.³¹ Additionally, tetrameric [Ni(I)(^{Et}OOCbpy)Cl]₄ and dimeric [Ni(I)(^{Et}OOCbpy)Cl]₂ complexes were studied by Doyle *et al.*³⁰ In solution, both species can dissociate to form the monomeric Ni(I)(^{Et}OOCbpy)Cl complex mentioned above. This three-coordinate species was reported to exist in solution-phase equilibria with Ni(II)Cl₂ and Ni(0)(^{Et}OOCbpy)₂. However, the oxidative addition reactivity was favored from the Ni(I) complex, not the Ni(0) species, and no reactivity was found for the dimeric or tetrameric species.

Understanding the interplay between the oxidative addition and dimerization/oligomerization pathways available to three-coordinate Ni(I)–bpy halide complexes is critical for optimized ground-state and metallaphotoredox catalysis and reaction development (**Figure 4.1B**). There is also a fundamental knowledge gap related to specific structure-function relationships underlying the elementary oxidative addition step in Ni(I)–bpy complexes, a key component of the scope of bond activations that can be achieved. To the best of our knowledge, no systematic study has either compared the oxidative addition reactivity and solution-phase stability of Ni(I)–bpy complexes or rationalized the relative rates of oxidative addition upon structural perturbation.

Here we accomplish both of these aims through the facile photogeneration of a series of Ni(I)(^Rbpy)X species (R = *t*-Bu, H, MeOOC; X = Cl, Br, I; **Figure 4.1C**). We provide direct evidence for C(sp²)–Cl bond activation with Ni(I)–bpy complexes, which thus far has only been implied as part of catalytic cycles.^{33,42} Furthermore, we broadly detail the kinetics and

mechanisms of their oxidative addition reactivity toward $C(sp^2)-X$ ($X = Cl, Br, I$) bonds, and their thermal barriers for dimerization. Results reported herein implicate key ligand effects on the electronic structure of the Ni(I)–bpy halide complexes that result in tunable reactivity and variable solution-phase lifetimes. Ultimately, the ability of Ni(I)–bpy complexes to activate challenging $C(sp^2)-Cl$ bonds stems from bpy-induced modulation of the effective nuclear charge (Z_{eff}) of the Ni(I) center. Related analyses reported here have afforded a molecular orbital-based picture of oxidative addition reactivity, which provides specific electronic structure benchmarks that need to be achieved to activate strong $C(sp^2)-X$ bonds and opens the door for the targeted synthesis of next-generation cross-coupling catalysts.

§4-2. Results and Analysis

§4-2.1 Photochemical Synthesis and Spectroscopic Characterization of Ni(I)–bpy Halide Complexes

Parent four-coordinate Ni(II)(^Rbpy)(*o*-tolyl)X ($R = tert\text{-butyl, H, MeOOC}$; $X = Cl, Br, I$) complexes were synthesized according to a previous report.²⁷ Three-coordinate Ni(I)(^Rbpy)X species, which are important reaction intermediates in photoredox cross-coupling catalysis, can be accessed directly from these precursors by air- and moisture-free irradiation at 370 nm using purple LEDs. Light excitation drives a key LMCT process that results in Ni(II)–C_{aryl} excited-state bond homolysis; this shorter wavelength enhances the quantum yield of Ni(I)(^Rbpy)X generation relative to more commonly used, longer wavelength blue light sources (Table S2). Typical irradiation times were ~30–60 minutes; irradiation time variations among complexes depended on the rate of photo-driven decay of the starting Ni(II) complex and the rate of Ni(I) decomposition. Global kinetic analysis provides strong support for a first-order process in which the Ni(II)–bpy aryl halide parent complex is cleanly photolyzed to the Ni(I)–bpy halide (for more details, see Supporting Information Section S1.5, including Figures S6-S10).

To systematically probe the reactivity and stability of the photochemically generated Ni(I) complexes, the bpy ligand was varied with electron donating *tert*-butyl groups

(Ni(I)(^t-Bu**bpy**)Cl, **1-Cl**), electronically neutral H-atoms (Ni(I)(^Hbpy)Cl, **2-Cl**), and electron-withdrawing methyl ester groups (Ni(I)(^{MeOOC}bpy)Cl, **3-Cl**). The halide was also varied by first synthesizing Ni(II)(^t-Bu**bpy**)(*o*-tolyl)Br and Ni(II)(^t-Bu**bpy**)(*o*-tolyl)I parent complexes, followed by irradiation to form Ni(I)(^t-Bu**bpy**)Br (**1-Br**) and Ni(I)(^t-Bu**bpy**)I (**1-I**), respectively. Note that **1-Br** is the same as that examined by Bird and MacMillan *et al.* by pulse radiolysis,³¹ while **3-Cl** is similar to that studied by Doyle *et al.*,³⁰ the only difference being the appended methyl ester vs. ethyl ester substituents, following our previous study.²⁷

Having direct access to the Ni(I)–bpy halide complexes via photolysis allows for their characterization using UV–vis electronic absorption and EPR spectroscopies (**Figure 4.2A** and **Figure 4.2C**, respectively). Irradiation of Ni(II) parent compounds and spectral analysis were done in tetrahydrofuran (THF). The primary UV–vis absorption band in the ~550 nm–900 nm region of the three-coordinate Ni(I)(^Rbpy)X species shifts strongly with changes to the bpy ligand from 660 nm (**1-Cl**) to 805 nm (**3-Cl**). Moderate shifts are also observed when changing the halide (640 nm for **1-I** to 660 nm for **1-Cl**, **Figure 4.2A**). To further corroborate the spectral assignment of UV–vis peak to the Ni(I)–bpy halides, we conducted reductive spectroelectrochemistry on Ni(^t-Bu**bpy**)Cl₂ to form Ni(^t-Bu**bpy**)Cl; the resultant spectrum is identical to that of photogenerated **1-Cl** (**Figure 4.2B**).

From TD-DFT calculated spectra (bottom of **Figure 4.2A**; see Computational Details in Supporting Information Section S2.1), the intensity of the primary absorption band is attributed to Ni(I)-to-bpy MLCT transitions ($3d(xz/yz) \rightarrow \pi^*(1)$; note these orbitals are labeled according to their parallel (\parallel) or perpendicular (\perp) orientation to Ni–halide bond—see details in Supporting Information Section S2.4). Consistent with the experimental spectra, smaller shifts are observed for variations in the halide; the MLCT energies are more sensitive to bpy variation, with an energy trend of **1-Cl** > **2-Cl** > **3-Cl**. Through analyses of the molecular orbital energy diagrams for these complexes (Figures S40-S44 and Table S7), the MLCT energy shift arises mainly from the stabilization of the bpy π^* acceptor orbitals as a function of electron-withdrawing substituents.

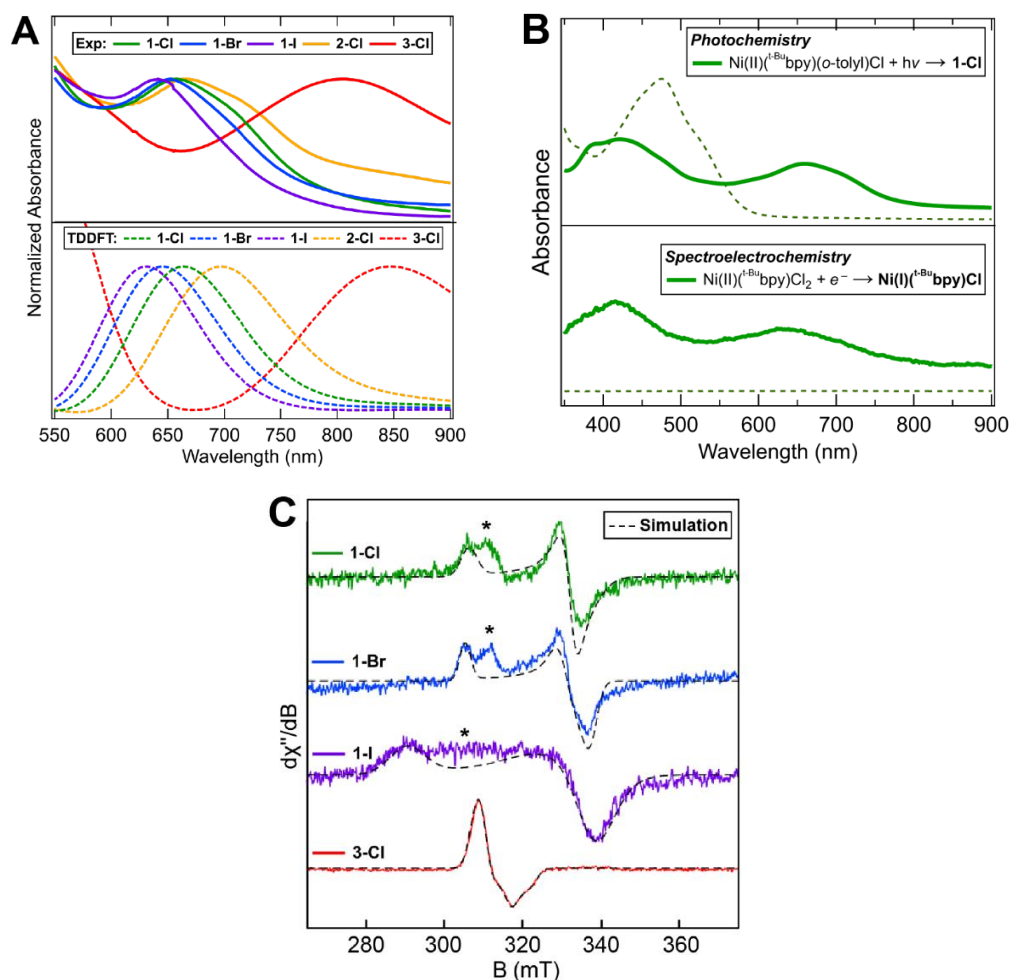


Figure 4.2. Spectroscopic characterization of the Ni(I)-bpy halides examined in this study. (A) UV-vis absorption spectra (THF) of the three-coordinate Ni(I)-bpy halide complexes, highlighting the Ni(I)-to-bpy MLCT transitions and the excellent spectral agreement between experiment and TDDFT calculations (dashed lines). (B) *Top*: UV-vis spectrum for the photochemical preparation of **1-Cl** (solid line) from its Ni(II)-bpy aryl halide parent (dashed lines) using 370 nm LEDs. *Bottom*: Spectroelectrochemistry of Ni(II)(*t*-Bu)bpyCl₂ (dashed lines) forming Ni(I)(*t*-Bu)bpyCl (solid line) in THF with TBAPF₆ electrolyte. For more details, see Figure S13. (C) Frozen-glass X-band CW-EPR spectra for the S = 1/2 Ni(I) region (T = 5 K; solvent = 2-MeTHF; frequency for **1-Cl**, **1-Br**, **3-Cl** = 9.637 GHz, for **1-I** = 9.646 GHz; power = 2.2 mW; modulation amplitude = 8 G). Corresponding g values are given in **Table 4.1**. Starred peaks may correspond to THF coordination.

Table 4.1. Experimental g values for the Ni(I)–bpy halide complexes in 2-MeTHF at 5 K. DFT computed g values are given in parentheses.

Compound	$g_{z,\text{exp.}}$ ($g_{z,\text{calc.}}$)	$g_{x,\text{exp.}}$ ($g_{x,\text{calc.}}$)	$g_{y,\text{exp.}}$ ($g_{y,\text{calc.}}$)	$g_{\text{iso,exp.}}$ ($g_{\text{iso,calc.}}$)
1-Cl	2.248 (2.238)	2.050 (2.070)	2.070 (2.174)	2.123 (2.161)
1-Br	2.255 (2.246)	2.042 (2.080)	2.079 (2.166)	2.125 (2.164)
1-I	2.370 (2.262)	2.044 (2.094)	2.075 (2.161)	2.163 (2.172)
2-Cl^a	— (2.238)	— (2.066)	— (2.190)	— (2.165)
3-Cl	2.217 (2.252)	2.171 (2.057)	2.195 (2.251)	2.194 (2.187)

^aSufficiently high concentration samples of **2-Cl** were precluded due to precipitation. As such, no EPR signal could be resolved experimentally. ¹⁴N hyperfine values of $A_x = 146$ MHz, $A_y = 91$ MHz, and $A_z = 64$ MHz were fit for **3-Cl** and required to model the line shape. Computational details are given in Supporting Information Section S2.1.

While room temperature EPR analysis provided no resolvable signals, likely due to rapid spin relaxation times (Figure S31), spectra taken at 5 K in 2-methyl tetrahydrofuran (2-MeTHF) after irradiation provided signals characteristic of $S = 1/2$ Ni(I) species (**Figure 4.2C**), with g values in the range of $g_z = \sim 2.22\text{--}2.37$, $g_x = \sim 2.04\text{--}2.17$, $g_y = \sim 2.07\text{--}2.20$, and $g_{\text{iso}} = \sim 2.12\text{--}2.19$ (**Figure 4.2C**; **Table 4.1**). The axial g tensor values are overall consistent with a single unpaired electron in the Ni(I) $3d(x^2-y^2)$ orbital. The EPR spectra and g values of compounds **1-Cl/Br** and **3-Cl** are congruent with previous reports for Ni(I) halide species with aromatic ligand backbones (e.g., phenanthroline, bipyridine, and bis(pyrazolyl)pyridines).^{30,39,42–45} The ¹⁴N hyperfine values employed in the **3-Cl** simulation are of comparable magnitude to those previously reported for Ni(I)-neocuproine complexes (0, 50, and 170 MHz).³² Sufficiently high concentration samples of **2-Cl** were precluded due to a precipitation (dimerization) pathway (*vide infra*, **Section §4-2.4**); as such, no EPR signal could be detected. The intermediate peak at ~ 310 mT in **1-Cl/Br/I** is likely attributable to THF solvent coordination (see Supporting Information Section 2.7), as it does not appear in previous spectra recorded in toluene but does appear in toluene:THF solvent mixtures and in neat 2-MeTHF.^{42,43} These published data share excellent agreement with the spectra collected and presented in **Figure 4.2C**. Importantly, the relative intensities of the g_z and

intermediate peaks remain approximately constant with variations in photolysis time, indicating there is not a second Ni(I) species with a distinct kinetic profile (Figures S33–S35). The DFT calculated g values are in general agreement with the experimental data, with the exception of the g_z value for **1-I** and significantly more predicted rhombicity throughout (computed g_x and g_y in **Table 4.1**).

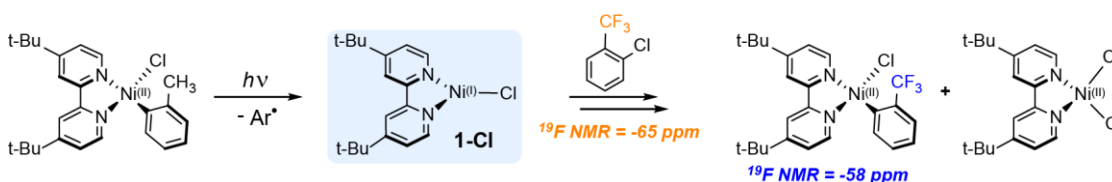
We also note the presence of additional complex signals in the half-field region of the concentrated samples of **1-Cl** in the low-temperature (5 K) EPR (Figures S33–S35). Variable-temperature (VT) UV–vis experiments indicate that these are attributable to a reversible concentration- and temperature-dependent speciation (see Supporting Information Section S1.9). That is, these additional species form rapidly upon freezing the EPR samples. Future studies should consider speciation changes that can occur upon freezing samples for low-temperature spectroscopic characterization. That said, under standard catalysis conditions (~0.2 mM, room temperature) studied herein, the Ni(I)–bpy halide complexes corresponding to the $S = 1/2$ signals are the dominant species after irradiation is terminated (~95% Ni(I) by VT UV–vis analysis), with the additional species (~5%) being the starting Ni(II)–bpy aryl halide complex.

§4-2.2. Oxidative Addition Kinetics with 2-Chloro-toluene

Having demonstrated near quantitative conversion of parent Ni(II) complexes to the three-coordinate Ni(I) complexes, we sought to gauge their relative reactivity toward oxidative addition. As expected, room temperature addition of excess *2-bromo*-toluene or *2-iodo*-toluene (0.2 mL) to all photogenerated Ni(I) complexes studied herein resulted in immediate color changes, with loss of the Ni(I)–bpy MLCT features observed in the UV–vis spectra (Figures S14–S15). The diagnostic $S = 1/2$ Ni(I) EPR signal is also quenched upon addition of aryl halide (Figure S36). Again, reactivity with $C(sp^2)$ –I and $C(sp^2)$ –Br bonds is consistent with previous reports.^{30,31} However, interestingly, many of the Ni(I) intermediates studied herein also react with *2-chloro*-toluene—the exception being **3-Cl**. As a control, addition of 0.2 mL of toluene did not result in UV–vis spectral changes, further implicating the reactivity

of the Ni(I) species with the C(sp²)–Cl bond. The lack of reactivity of **3-Cl** is also significant and is directly related to the bpy ligand, as discussed further in **Section §4-2.3**.

Taking **1-Cl** as a representative compound, we sought to confirm the C(sp²)–Cl reactivity by stoichiometric ¹H NMR studies in *d*₈-THF. However, to facilitate reaction turnover at a rate greater than the decay of the Ni(I) intermediate, a large excess of *2-chloro*-toluene is necessary, which overwhelms the ¹H NMR analysis. Using fewer equivalents of aryl halide, the reaction between *2-chloro*-toluene and the photogenerated Ni(I) species is too slow and precludes definitive product speciation assignments (Supporting information Section S1.7). This can be circumvented using a fluorinated aryl halide and ¹⁹F NMR analysis. As depicted in **Scheme 4.1**, addition of 20 μL of *2-chloro-α,α,α*-trifluorotoluene (~200-fold excess, ¹⁹F NMR peak at –63 ppm) to a solution of **1-Cl** afforded a new peak in the ¹⁹F NMR spectrum at –58 ppm. Independent synthesis²⁷ confirms this peak originates from the four-coordinate complex, Ni(II)(^t-Bu₃bpy)(CF₃Ph)Cl (Figure S18). Thus, this experiment provides direct evidence of a Ni(I)–bpy halide complex activating an aryl chloride substrate. We now describe the relative reactivity of the Ni(I)–bpy complexes toward C(sp²)–Cl oxidative addition.



Scheme 4.1. Oxidative addition reaction conducted with the photogenerated Ni(I)–bpy halide, **1-Cl**. Incident wavelength = 370 nm; solvent = *d*₈-THF. Formation of Ni(II)(^t-Bu₃bpy)(CF₃Ph)Cl was verified by ¹⁹F NMR; the high spin Ni(II)–bpy dihalide is paramagnetic and not observed, but is invoked to account for the mass balance on the basis of previous work.³⁰

Pseudo-first-order kinetics investigations with quantitative addition of excess *2-chloro*-toluene to the photogenerated Ni(I) complexes were carried out by monitoring the fast decay

of the primary MLCT absorption feature via UV–vis spectroscopy (**Figure 4.3A** and Figure S20A). The natural logarithm of the normalized peak absorbance varies linearly with time for ~3-5 half-lives, depending on the magnitude of starting Ni(I) absorption (**Figure 4.3B** and Figure S20B). The slope of this correlation provides k_{obs} values that vary linearly with 2-chloro-toluene concentration (**Figure 4.3C** and Figure S20C), yielding second-order rate constants for oxidative addition, k_{OA} ($\text{M}^{-1} \text{s}^{-1}$) (**Table 4.2**). The bimolecular rate constants are on the order of $10^{-2} \text{M}^{-1} \text{s}^{-1}$, six orders of magnitude slower than the reaction of **1-Br** with aryl iodides and two orders of magnitude slower than the reaction of Ni(I)(^{Ei}OOCbpy)Cl with aryl bromides.^{30,31} This reduction in rate constant for the activation of 2-chloro-toluene is attributable to the increased bond dissociation free energy (BDFE) of the carbon–halogen bond (BDFE of $\text{C}(\text{sp}^2)\text{--Cl} > \text{C}(\text{sp}^2)\text{--Br} > \text{C}(\text{sp}^2)\text{--I}$, Table S15) and a steric effect of the *ortho*-methyl group (**Figure 4.4**).

Analysis of ligand effects reveals that changes to the halide manifest in minor changes in k_{OA} (**Figure S20**). These results agree well with the electronic effects of the halide as predicted by the Hammett parameters ($\sigma_{\text{p}} = 0.23$ for Cl and Br, and 0.18 for I).⁴⁶ More pronounced effects are observed upon variation of the bpy substituent. Substitution of the electron-donating *tert*-butyl groups ($\sigma_{\text{p}} = -0.20$) for hydrogens ($\sigma_{\text{p}} = 0.0$) in going from **1-Cl** to **2-Cl** results in a twofold decrease in k_{OA} from $7.2 \pm 0.2 \times 10^{-2} \text{M}^{-1} \text{s}^{-1}$ to $3.2 \pm 0.2 \times 10^{-2} \text{M}^{-1} \text{s}^{-1}$. Furthermore, introduction of the electron-withdrawing methyl ester groups ($\sigma_{\text{p}} = 0.45$) eliminates $\text{C}(\text{sp}^2)\text{--Cl}$ oxidative addition reactivity altogether. As described further below in **Section §4-2.3**, these differences in oxidative addition reactivity can be traced directly to ligand-induced differences in Z_{eff} on the metal, as changes in Z_{eff} tune the energy of the RAMO involved in the oxidative addition reaction. Follow-up work is currently underway to push the limits of Ni(I)-facilitated oxidative addition reactivity by substituent-based modulation of Z_{eff} .

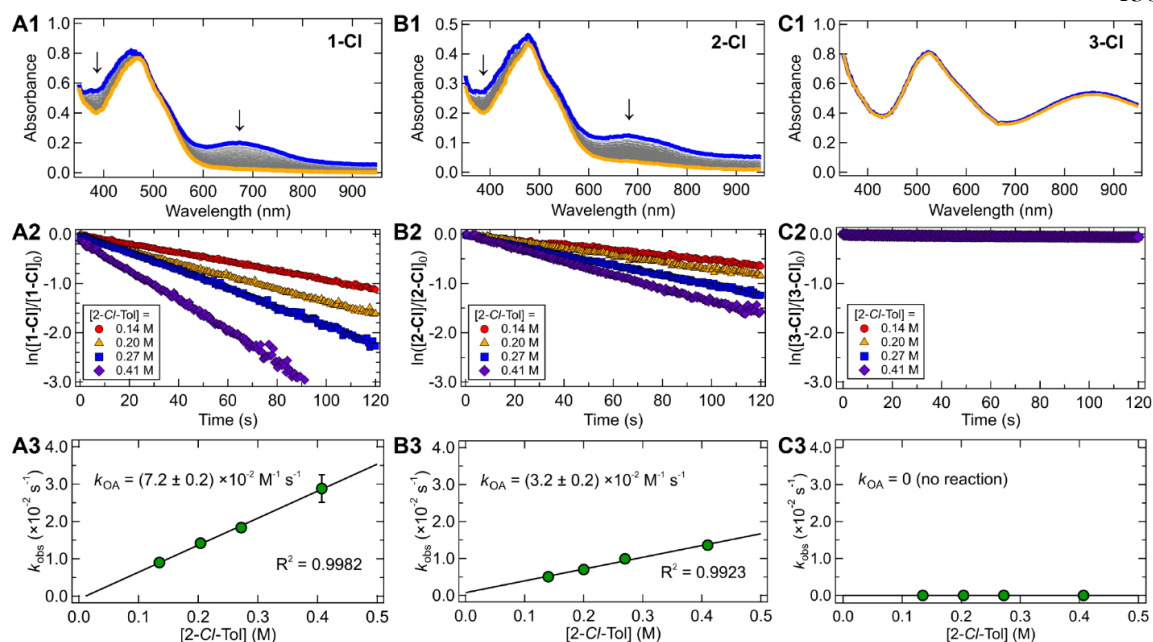


Figure 4.3. Experimental kinetic analysis of the oxidative addition reaction for **1-Cl**, **2-Cl**, and **3-Cl**. (A1, B1, C1) UV-vis absorption plots in THF showing the addition of *2-chloro*-toluene to photochemically generated Ni(I)-bpy halides (initial spectrum of Ni(I)-bpy halide, blue line ($\sim 10^{-4}$ M); after *2-chloro*-toluene addition, orange line). Note the orange spectra depict unreacted and newly generated parent four-coordinate Ni(II)-bpy aryl halide (Figure S1-S2). (A2, B2, C2) Linear plots of $\ln([\text{Ni(I)}]/[\text{Ni(I)}]_0)$ vs. time showing the pseudo-first-order nature of the oxidative addition reaction over several half-lives; $[\text{2-Cl-Tol}] = 0.14$ M (red circles), 0.20 M (orange triangles), 0.27 M (blue squares), and 0.41 M (purple diamonds). (A3, B3, C3) Plots of k_{obs} vs. $[\text{2-Cl-Tol}]$. Error bars are one standard deviation of three trials. Slope of the fitted line gives second-order rate constants, k_{OA} ($\text{M}^{-1} \text{s}^{-1}$). Complex **3-Cl** showed no reaction with *2-chloro*-toluene. Analogous data for **1-Cl**, **1-Br**, and **1-I** are given in Figure S20.

Table 4.2. Rate constants for room temperature oxidative addition for the reaction between 2-chloro-toluene and various Ni(I)(^Rbpy)X species (R = *t*-Bu, H, MeOOC; X = Cl, Br, I).^a

Compound	σ_p (R)	σ_p (X)	k_{OA} ($\times 10^{-2} \text{ M}^{-1} \text{ s}^{-1}$)
1-Cl	-0.20	0.23	7.2 ± 0.2
1-Br	-0.20	0.23	7.0 ± 0.4
1-I	-0.20	0.18	6.5 ± 0.6
2-Cl	0.00	0.23	3.2 ± 0.2
3-Cl	0.45	0.23	no reaction

^aReactions were done under inert atmosphere in anhydrous THF and followed by UV-vis spectroscopy. Reported errors are one standard deviation of three trials. Hammett σ_p values taken from ref. 46.

§4-2.3. Oxidative Addition Mechanistic Investigations

Having examined the effect of the substituents on the Ni(I)-bpy halides toward the C(sp²)-Cl oxidative addition reactivity, we next turned to the kinetic dependence of the substituents on the aryl chloride substrates. We performed a Hammett analysis on the reactivity of series of para-substituted aryl chlorides with **1-Cl**. The rate constants (k_{OA}) of the formal Ni(I)/Ni(III) oxidative addition process increased by two orders of magnitude when switching from electron-donating to electron-withdrawing substituents ($\sigma_p = -0.27$ to 0.50, **Figure 4.4**). We further found the slope (ρ) of the plot of $\ln(k_x/k_H)$ vs. σ_p was ~ 5 , indicative of an S_NAr-type activation⁴⁷ of the C(sp²)-Cl bond, wherein the Ni(I) metal center acts as a nucleophile, attacking the polarized C(sp²)-Cl bond at the electron-deficient carbon. While an activation pathway that proceeds by single electron transfer (SET) also has a fairly large ρ value (~ 4),⁴⁸ the reduction potentials of the aryl chlorides are too negative (experimentally found to be less than -3.2 V vs. Fc⁺/Fc, calculated as -3.5 V vs. Fc⁺/Fc; for more details see Supporting Information Sections S1.6 and S2.6) to be accessed by the Ni(I)-bpy halides (calculated Ni(II)/Ni(I) potential of 0.2 V vs. Fc⁺/Fc).⁴⁹

Interestingly, we note that $\rho \sim 5$ represents a change in the specific mechanism of C(sp²)-X bond activation by Ni(I) halides. Aryl bromides and aryl iodides exhibit Hammett slope values of $\rho \sim 2-3$, typical of a concerted oxidative addition pathway,^{30,31,50,51} but the activation of the stronger, more polarized C(sp²)-Cl bond is better described as nucleophilic aromatic substitution.

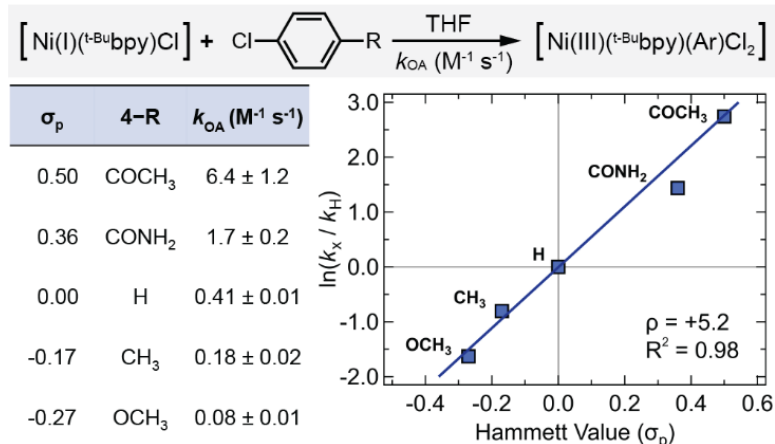


Figure 4.4. Hammett analysis for the reaction of **1-Cl** with 4-substituted aryl chlorides. Recall that the reaction of **1-Cl** with sterically hindered 2-chloro-toluene has $k_{\text{OA}} = 0.072 \text{ M}^{-1} \text{ s}^{-1}$. We note that Hammett analysis is commonly presented with base 10 log instead of the natural log, but we present the latter here for direct comparison to literature values for ρ .^{30,31,50,51} Hammett σ_p values taken from ref. 46. Reported standard errors are propagated from the linear least-squares analysis (Figures S21-S25).

DFT calculations were used to further detail the mechanism of oxidative addition (i.e., step-wise vs. concerted two-electron nucleophilic attack by Ni) and to identify the key frontier molecular orbitals involved in this elementary reaction step. Oxidative addition of 2-chloro-toluene to a three-coordinate Ni(I)(^Rbpy)X species yields a five-coordinate Ni(III)(^Rbpy)(*o*-tolyl)(Cl)(X) intermediate. Following the initial oxidative addition step, comproportionation of the Ni(III) complex with an additional Ni(I)(^Rbpy)X species can take place with a calculated Gibbs free energy of $\sim -23 \text{ kcal mol}^{-1}$, which produces a considerable driving force for the overall reaction. Comproportionation can occur via transfer of a halide from the five-

coordinate intermediate, which is readily accessible through a barrierless transition state (**Figure 4.5A**). This step therefore results in the regeneration of a parent Ni(II)–bpy aryl halide complex and the formation of a Ni(II) dihalide (i.e., the speciation determined experimentally by Diao et al. and Doyle et al. and ^{19}F NMR and UV–vis studies presented herein (*vide supra*, Section 4.2.2)).^{30,39}

The rate-determining step of the overall reaction is found to be oxidative addition, with calculated Gibbs free-energy barriers of $\sim 21\text{--}23$ kcal mol $^{-1}$, consistent with the slow reaction rates at room temperature and the requirement of a large excess of 2-*chloro*-toluene (**Figure 4.5A**). The computed free energy barriers vary by only ~ 1.3 kcal mol $^{-1}$ for **1-Cl**, **1-Br**, **1-I**, and **2-Cl** (i.e., within the general accuracy obtainable with DFT calculations).^{55,56} However, this observation is still in accord with the differences in k_{OA} for the compounds observed experimentally (**Table 4.2**). Furthermore, the highest computed activation free energy is observed for **3-Cl** (~ 23 kcal mol $^{-1}$, red in **Figure 4.5A**), consistent with its lack of reactivity with 2-*chloro*-toluene.

We have also computationally reproduced the Hammett analysis for the reaction of **1-Cl** with 4-substituted aryl chlorides and have found excellent agreement with experiment (calculated $\rho \sim 5.8$; see Supporting Information Section S2.6). Furthermore, the calculated bond lengths in the transition state show that the new Ni–Cl bond is ~ 0.3 Å longer than the new Ni–C bond (potentially implying the Ni–C bond is formed prior to the Ni–Cl bond and corroborating an $\text{S}_{\text{N}}\text{Ar}$ -type mechanism, **Figure 4.5B**). Additionally, we observe that the experimental rate constants trend linearly and positively with the Löwdin atomic charges, the Mulliken atomic charges, and the natural population analysis (NPA) charges at the carbon in the Ar–Cl bond, but they do not trend well with the energy of the LUMO of the aryl chlorides (Figure S66). This observation is also indicative of an $\text{S}_{\text{N}}\text{Ar}$ mechanism as the electrophilicity of this carbon is related to the rate and not the reduction potential of the aryl chlorides (as would be expected for SET).⁵⁷

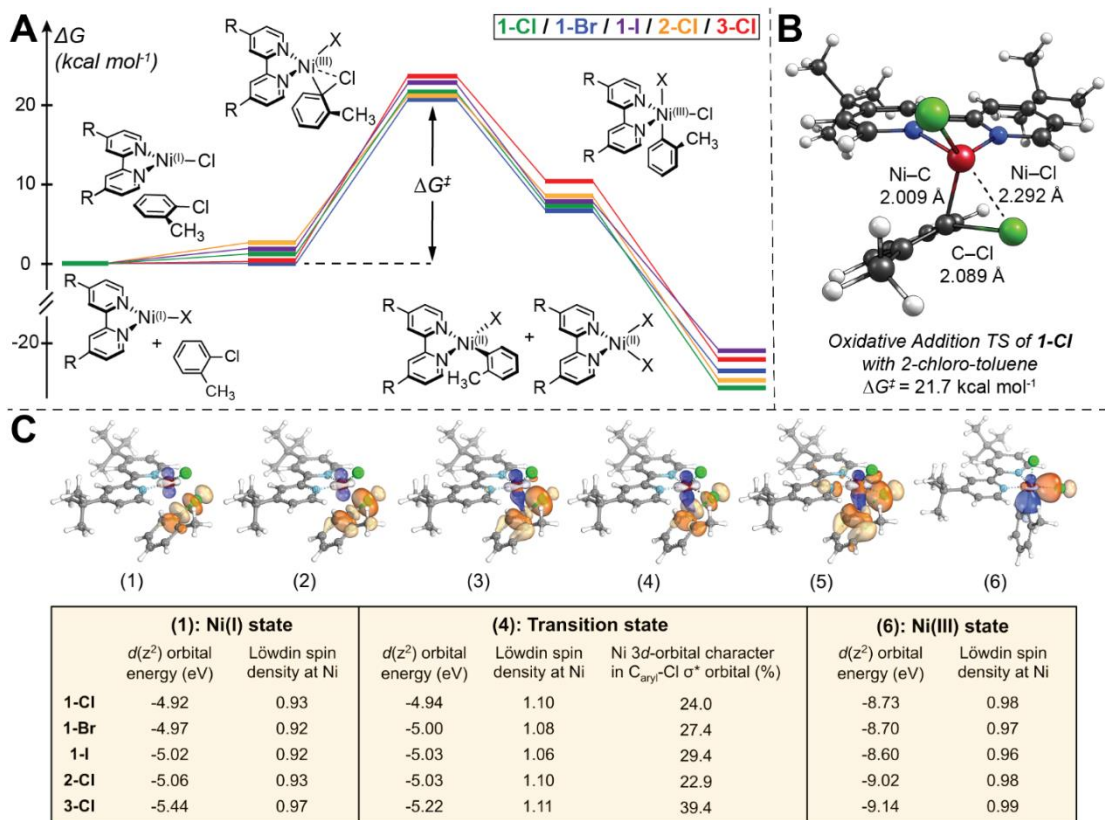


Figure 4.5. (A) DFT energetics of the oxidative addition reactions of Ni(I)(^Rbpy)X with 2-chloro-toluene and (B) the transition state structure of **1-Cl** with 2-chloro-toluene. Relative Gibbs free energy values were computed at the B3LYP-D3/def2-TZVP(CPCM)//BP86-D3/def2-TZVP(CPCM) level.^{52–54} Computed free energies are provided in Table S13. A related plot showing the DFT energetics of the oxidative addition with 2-bromo-toluene and 2-iodo-toluene is given in Figure S65. (C) Computational analysis of the oxidative addition process. The doubly occupied Ni 3d(z^2) orbital transforms into a new Ni–C_{aryl} σ -bond (blue), transferring electrons into the C_{aryl}–Cl σ^* orbital (orange). This breaks the C_{aryl}–Cl σ bond, affording a new Ni–Cl σ -bond. Tabulated are the energies of the β Ni 3d(z^2) orbital for several steps along the intrinsic reaction coordinate (IRC), the Ni 3d character in the C_{aryl}–Cl σ^* orbital at the transition state, and the Löwdin spin density at the Ni center. Note energies of Ni 3d(z^2) orbitals trend with the Ni(I) reactivity (see **Table 4.2**), while the other tabulated properties uncover the two-electron nature of the nucleophilic attack by the Ni(I) at the C_{aryl} site. See Supporting Information Section S2.3 for more detailed intrinsic bond orbital (IBO) analysis.

To further elucidate the origin of the different reactivity profiles for the different Ni(I) species, we analyzed the initial oxidative addition step in the context of intrinsic bond orbital (IBO) progression.^{58,59} IBO analysis allowed for the identification of orbital changes (δ -orb) along the intrinsic reaction coordinate (IRC), wherein the separated Ni(I) and aryl halide reactants come together to form the five-coordinate Ni(III) adduct. Although the unpaired electron is located in the Ni $3d(x^2-y^2)$ orbital (*cf.* EPR analysis in **Section §4-2.1**), the largest δ -orb effects are observed in the doubly occupied Ni $3d(z^2)$ orbital and $C_{\text{aryl}}\text{-Cl}$ σ orbital. These are transformed into new Ni- C_{aryl} and Ni-Cl σ bonds, respectively (Figure S39). This change in bonding is the outcome of two-electron transfer from the occupied Ni $3d(z^2)$ orbital into the virtual $C_{\text{aryl}}\text{-Cl}$ σ^* orbital (**Figure 4.5C**). Direct observation of Ni-to-($C_{\text{aryl}}\text{-Cl}$) σ^* backbonding at the transition state is evidenced by significant mixing of filled $3d$ orbital character into the unoccupied $C_{\text{aryl}}\text{-Cl}$ σ^* orbital along the IRC (**Figure 4.5C**, middle). For example, from **1-Cl** to **2-Cl** to **3-Cl**, the Löwdin Ni $3d$ character varies from 24.0 to 29.4 to 39.4. Previous analysis on Pd-catalyzed aryl chloride activation found that the increase in Pd backbonding to the $C_{\text{aryl}}\text{-Cl}$ σ^* orbital was related to an increase in the barrier for the reaction.⁶⁰ This same trend is seen in our Ni-based $C(\text{sp}^2)\text{-Cl}$ bond activation. Thus, backbonding in the transition state may play an important role in activating stronger $C(\text{sp}^2)\text{-Cl}$ bonds by Ni(I) species. As discussed further below, this backbonding will increase with less-negative electron binding energies on the metal.

At the transition state, the α - and β -type orbitals are transformed in conjunction, suggesting a two-electron nucleophilic attack by the Ni(I) $3d(z^2)$ orbital on the C_{aryl} atom, yielding a Ni(III) intermediate. This concerted two-electron transfer is supported by a small change of Löwdin spin density on the Ni center throughout the reaction (~ 1 unpaired electron throughout; see inset table in **Figure 4.5C**); one-electron transfer or stepwise two-electron transfer would reveal more substantial metal-based spin density changes along the IRC. The small increase in the spin density at the transition state arises from the slightly misaligned attack initiated by β Ni $3d(z^2)$ orbital, which is ~ 0.8 eV higher in energy than the α Ni $3d(z^2)$ orbital due to spin polarization arising from the presence of five vs. four $3d$ electrons in α and β manifolds, respectively (Table S7). That $C_{\text{aryl}}\text{-Cl}$ bond-breaking is rate determining is

consistent with the more facile oxidative addition activation of *2-bromo*-toluene and *2-iodo*-toluene substrates (e.g., their reactivity is observed even with **3-Cl** due to their weaker $C_{\text{aryl}}\text{-halogen}$ σ bonds and lower-energy $C_{\text{aryl}}\text{-Cl}$ σ^* orbitals, which facilitates backbonding from the metal).

From the preceding analysis, the reactivity of individual Ni(I) complexes should correlate with the energies of the Ni $3d(z^2)$ orbitals. Indeed, the calculated Ni(I)-bpy $3d(z^2)$ orbital energies trend with the k_{OA} rate constants (**Figure 4.5C** and **Table 4.2**). For example, the most- and least-reactive complexes, **1-Cl** and **3-Cl**, have β $3d(z^2)$ orbital energies of -4.92 eV and -5.44 eV, respectively ($\Delta = -0.52$ eV). There is also a linear trend between the energy of the $3d(z^2)$ orbital and the bpy σ_p Hammett parameters for **1-Cl**, **2-Cl**, and **3-Cl** (Figure S45). The less-negative electron binding energies of **1-Cl** will increase nucleophilicity and propensity for a two-electron reduction. As discussed below, this effect on the $3d$ orbital energies is not necessarily specific to $3d(z^2)$ alone, specifically because the bpy-based σ interaction only involves the torus of the $3d(z^2)$ orbital. Rather, the bpy ligand ultimately tunes the entire $3d$ orbital manifold via changes in Z_{eff} of the metal, making the ligand substitution effects a key predictor of reactivity. In further support of these changes, the calculated Ni(I) $1s$ and $2p(x,y,z)$ orbital energies of **1-Cl**, **2-Cl**, and **3-Cl** all trend linearly with bpy-based Hammett parameters and oxidative addition rate constants, with slopes similar to the $3d$ orbitals (Figure S45-S46). Moving forward, the calculated $3d$ orbital energies of three-coordinate Ni(I) intermediates will be a useful predictor for oxidative addition reactivity and will bracket relative reactivity for specific $C(\text{sp}^3)\text{-X}$ and $C(\text{sp}^2)\text{-X}$ bonds.

§4-2.4. Thermodynamics of the Dimerization of Ni(I)-bpy Halides

Having established the reactivity of the Ni(I) complexes toward oxidative addition, we sought to better understand their general stability in solution. Their stability is of particular interest, as unreactive halide-bridged dimers have been proposed to form in bpy and related systems.^{30-32,40} Photogeneration of the Ni(I) compounds was again achieved using 370 nm LEDs in THF. Even in the absence of aryl halide, the characteristic MLCT band of the Ni(I)-

bpy halide complexes decayed over time; this decay was accelerated by increased temperature. In all cases, this decomposition results in the formation of a precipitate. However, we found that the precipitate of complexes **1-Cl/Br** exhibited slight solubility in THF, likely owing to the bulky, non-polar *tert*-butyl substituents on the bipyridine. Taking **1-Cl** as a representative complex, we thus collected the precipitation product and analyzed it by UV-vis, ¹H NMR, and EPR (in THF, *d*₈-THF, and 2-MeTHF, respectively; Figures S28–S30). We found that its spectra matched that of independently synthesized [Ni(I)(*t*-Bu**bpy**)Cl]₂, suggesting that the primary thermal decomposition product of the Ni(I)–bpy halides is their halide-bridged dimers (see Supporting Information Section S1.8). Furthermore, this thermal decay pathway of the Ni(I)–bpy halides can be monitored by the decrease of their characteristic UV-vis spectra over time (**Figure 4.6**, top). Linear fits were obtained when plotting the reciprocal of the absorbance change vs. time (**Figure 4.6**, middle), consistent with a decay process that is second-order in nickel concentration. Together with the comparison to independent synthesis, this pathway is therefore assigned to Ni(I)–bpy halide dimerization.

The slope of the linear fit yielded second-order dimerization rate constants, k_D , which were observed to be temperature-dependent (**Figure 4.6**, bottom and **Table 4.3**). Eyring analysis of the temperature-dependent rate constants afforded enthalpic and entropic thermodynamic parameters, ΔH^\ddagger and ΔS^\ddagger (**Table 4.3**).^{61–63} Rather large enthalpic barriers are observed for all compounds, ranging from ~11 kcal mol⁻¹ to 19 kcal mol⁻¹. The most significant trend follows ΔH^\ddagger of **3-Cl** > **2-Cl** > **1-Cl**. ΔS^\ddagger values ranged from ~–15 cal mol⁻¹ K⁻¹ to –38 cal mol⁻¹ K⁻¹. The fairly large, negative values of ΔS^\ddagger are consistent with an associative (i.e., bimolecular) transition state. $\Delta G^\ddagger(298\text{ K})$ values yielded small overall differences, however, falling in the range of ~22 kcal mol⁻¹ to 25 kcal mol⁻¹. The largest $\Delta G^\ddagger(298\text{ K})$ is observed for **3-Cl**; at ~25 kcal mol⁻¹, this barrier is consistent with very slow decomposition at room temperature and is in agreement with the overall stability of the related Ni(I)(^EtOOC**bpy**)Cl complex.³⁰ We note, however, that dimer precipitation can offset the chemical equilibrium, acting as a thermodynamic sink and driving the Ni(I) monomer to dimer conversion.

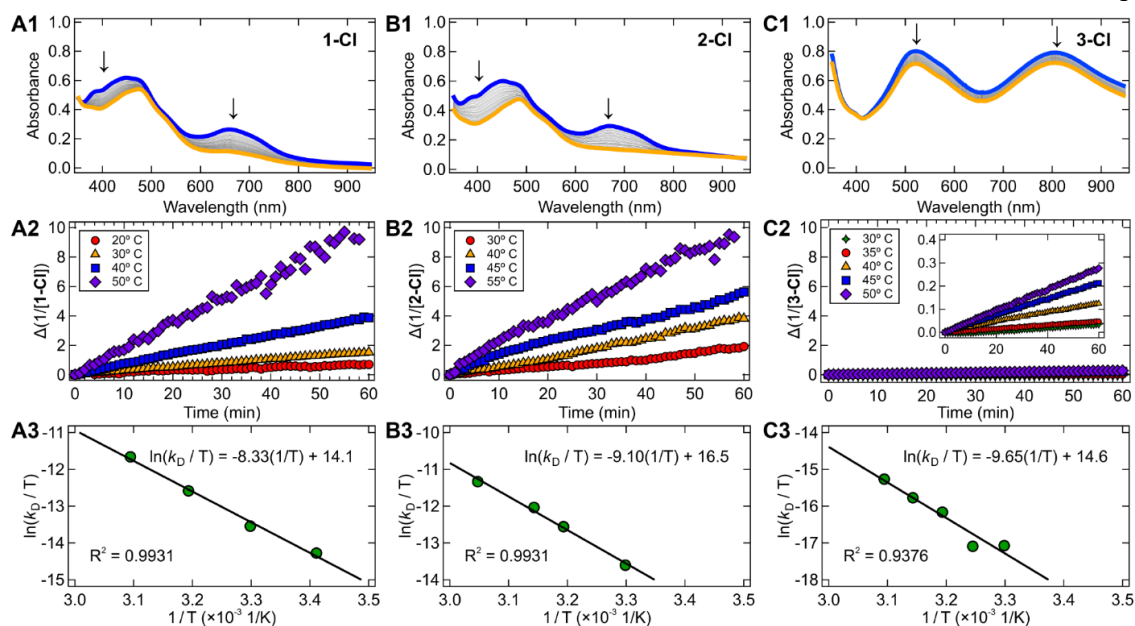


Figure 4.6. Experimental thermodynamic analysis of the dimerization reaction for **1-Cl**, **2-Cl**, and **3-Cl**. (*A1*, *B1*, *C1*) UV-vis absorption plots in THF showing the starting spectra of the Ni(I)-bpy halide generated by irradiation with 370 nm light (blue line) and the final spectra after thermally induced dimerization (orange line). Note that in the orange spectra, there remains some unreacted parent four-coordinate Ni(II)-bpy aryl halide (Figure S1-S2). (*A2*, *B2*, *C2*) Linear plots of $1/([\text{Ni(I)}]-[\text{Ni(I)}]_0)$ vs. time showing the second-order nature of the dimerization; temperatures between 20 °C and 55 °C were chosen. (*A3*, *B3*, *C3*) Eyring plots of $\ln(k_D/T)$ vs. $1/T$ giving thermodynamics data. Prohibitively slow dimerization made low-temperature data collection challenging for **3-Cl**, so an intermediate temperature point was added. Analogous data for **1-Cl**, **1-Br**, and **1-I** are given in Figure S27.

We again turn to substituent-based electronic effects to rationalize the changes in dimerization rate constants and thermodynamics. The ΔH^\ddagger for dimerization is lowest for **1-Cl/Br/I** and higher for **2-Cl/3-Cl**, a trend similar to that observed for oxidative addition (*vide supra*, **Section §4-2.2**). Electron-withdrawing effects weaken the nucleophilicity of the Ni(I) center, lowering the propensity for dimerization. Conversely, electron donation from the ligands enhances the reactivity of the Ni(I) center for both oxidative addition and dimerization. The halide appears to have a lesser effect on the dimerization thermodynamics

than the bpy, with **1-Br** exhibiting the lowest enthalpic barrier of the three halide variants (Figure S27).

Table 4.3. Thermodynamic parameters for dimerization of Ni(I)–bpy halide complexes.^a

Compound	k_D ($\times 10^{-5} \text{ M}^{-1} \text{ s}^{-1}$) ^b	ΔH^\ddagger (kcal mol^{-1})	ΔS^\ddagger ($\text{cal mol}^{-1} \text{ K}^{-1}$)	$\Delta G^\ddagger(298 \text{ K})$ (kcal mol^{-1})
1-Cl	4.0	16.6 ± 1.0	-19.3 ± 1.1	22.3 ± 0.5
1-Br	3.6	11.1 ± 1.2	-38.1 ± 4.1	22.4 ± 2.4
1-I	1.8	15.8 ± 1.6	-25.1 ± 2.5	23.3 ± 2.3
2-Cl	3.8	18.1 ± 1.1	-14.5 ± 0.9	22.4 ± 1.3
3-Cl	0.1	19.2 ± 2.9	-18.3 ± 5.8	24.6 ± 3.7

^aDimerization is monitored under nitrogen atmosphere in anhydrous THF and followed by UV–vis spectroscopy. Reported standard errors are propagated from the linear least-squares analysis. ^bSecond-order rate constants for the dimerization reaction (k_D) are given at 30 °C (303 K), as no rate constant for **3-Cl** was measurable at room temperature.

§4-2.5. Dimerization Mechanistic Investigations

DFT calculations also support the decay mechanism of Ni(I)–bpy halides through dimerization. The experimental second-order decay in Ni(I) allows for a direct $2 \text{ Ni(I)}(\text{R}^{\text{bpy}})\text{X} \rightarrow [\text{Ni(I)}(\text{R}^{\text{bpy}})\text{X}]_2$ pathway (**Figure 4.7A**). We note that the experimental kinetic analysis does not rule out the inclusion of an intermediate step, $2 \text{ Ni(I)}(\text{R}^{\text{bpy}})\text{X} \rightarrow \text{Ni(0)}(\text{R}^{\text{bpy}}) + \text{Ni(II)}(\text{R}^{\text{bpy}})\text{X}_2 \rightarrow [\text{Ni(I)}(\text{R}^{\text{bpy}})\text{X}]_2$. In either case, the starting reactants are two Ni(I)(^Rbpy)X species, and the ultimate decomposition product is the [Ni(I)(^Rbpy)X]₂ dimer, making the overall reaction free energy (ΔG) the same for both pathways. We have elected to computationally examine the simpler case which does not invoke a Ni(0) species.

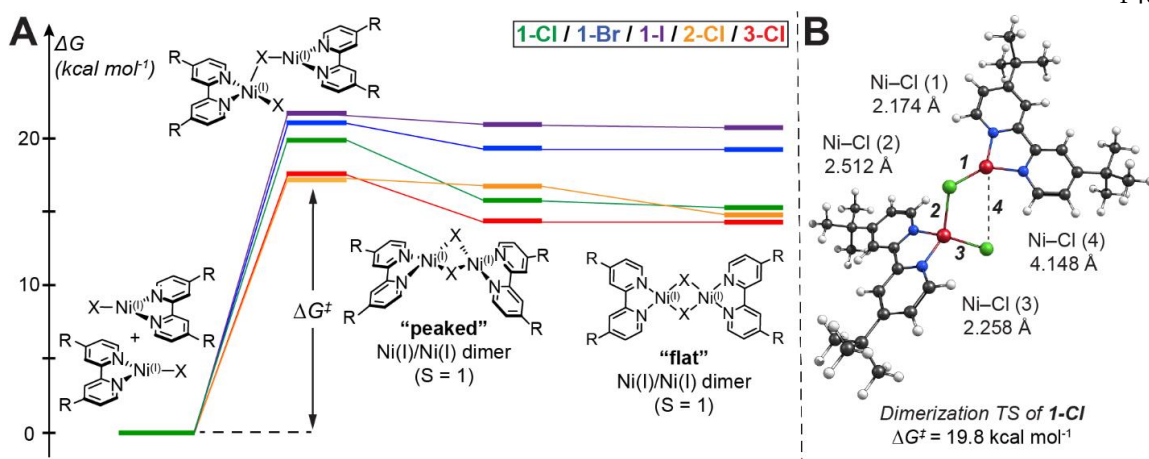


Figure 4.7. (A) Calculated energetics of the dimerization of Ni(I)-bpy halides and (B) the transition state structure for the dimerization of **1-Cl**. Relative Gibbs free energy values were computed at the B3LYP/def2-TZVP(CPCM)//BP86/def2-TZVP(CPCM) level. Computed free energies are tabulated in Table S16.

Like the oxidative addition mechanism discussed in **Section §4-2.3**, DFT finds that dimer formation is initiated by nucleophilic attack by the doubly occupied Ni $3d(z^2)$ orbital. Rather than interacting with the $C(sp^2)-X$ σ^* orbital of an aryl halide, the acceptor orbital for dimerization is an unoccupied halide p -orbital of another three-coordinate Ni(I) complex. This attack results in a transition state with a *pseudo*-tetrahedral geometry (i.e., a formal Ni(I)-bpy dihalide complex bridged via a halide to a second Ni(I)-bpy (**Figure 4.7B**)). The predicted barrier for this transformation is ~ 17 – 22 kcal mol $^{-1}$ across the complexes. Two distinct dimerization product geometries were obtained by following the downhill reaction coordinate from the transition state, both featuring two bridging halides but with different orientations (i.e., “peaked” vs. “flat” geometry in **Figure 4.7A**). At the DFT level, both dimer geometries feature two nickel sites in the Ni(I) oxidation state (Figure S68). Although both dimers are rather high in energy—alone not providing enough driving force for the dimerization—they show distinct similarities to the dimer structures obtained previously in the solid phase.^{30,32,64} Given the low solubility of the $[Ni(I)(^Rbpy)X]_2$ dimers in THF, we argue that precipitation drives the dimerization process in the forward direction and makes the dissociation of the dimer (i.e., the back-reaction) less favorable.

The free energies of activation are comparable to the experiment for **1-Cl/Br/I**; however, the DFT transition states are predicted too low in energy for **2-Cl** and **3-Cl** (orange and red data in **Figure 4.7A**). The discrepancy between experimental vs. DFT values may again be attributed to the better solubility of **1-Cl/Br** in THF, influencing the reversibility of the speciation. The higher multiconfigurational character for Ni(I)–bpy halides^{26,27} and likely for the dimeric structures (not captured by DFT) could also contribute to the differences between computed and experimental data. These should be present to a greater degree in complexes with electron-withdrawing substituents on the bpy (i.e., the electron-withdrawing trend of **3-Cl** > **2-Cl** > **1-Cl**). Therefore, it may be the case that the starting three-coordinate Ni(I)–bpy halides and their corresponding dimers are predicted to be too high in energy for **2-Cl** and **3-Cl** due to insufficient account of ligand non-innocent radical character on the bpy ligand, which may result in smaller effective barriers for dimerization. Nevertheless, computational analysis provides a plausible mechanism for Ni(I)–bpy halide dimerization.

§4-3. Discussion

Photoredox catalysis mediated by electronically excited nickel complexes, coupled to thermal reactivity pathways, can accomplish bond transformations with broad substrate versatility. Ni(I) intermediates are thought to be critical for specific bond activation steps facilitating reaction turnover (**Figure 4.1A**). Here we have demonstrated the facile photochemical generation of a library of Ni(I)(^Rbpy)X complexes (R = *t*-Bu, H, MeOOC; X = Cl, Br, I). Through experimental and computational analyses, we have evaluated their competitive reactivity with challenging C(sp²)–Cl bonds and tendency toward dimerization and have developed structure–function relationships between ligand set and reactivity.

UV–vis electronic absorption and EPR spectroscopies have provided an initial characterization of the electronic structures of the photochemically generated Ni(I)–bpy complexes. By UV–vis spectroscopy, all of the Ni(I) species exhibit relatively low-energy MLCT transitions (**Figure 4.2A**), the energies of which trend with the electronic effects of the bpy substituents. More electron-withdrawing functionalities lead to the shift of the most intense low-energy MLCT bands from ~660 nm to ~805 nm going from **1-Cl** to **3-Cl**. This

shift is attributed to the stabilization of the bpy π^* acceptor orbitals. In contrast, the variation of the halides shows a rather small influence on the MLCT energies.

EPR spectra reflect $S = 1/2$ Ni(I) ground-state electronic configurations with g_{iso} values of $\sim 2.12 - \sim 2.19$ (**Table 4.1**). The g_{iso} observed here deviate somewhat from the free electron g value (2.0023) due to the presence of ground-state orbital angular momentum. They are larger than those observed for methyl Ni(II)–terpyridine $^{\bullet-}$ ($g_{\text{iso}} = 2.02$) and mesityl Ni(II)–phenanthroline $^{\bullet-}$ ($g_{\text{iso}} = 2.01$) but smaller than observed for Ni(I)–bisoxazoline bromide ($g_{\text{iso}} = 2.24$).^{34,39,45} These g_{iso} values are consistent with greater ligand character for the terpyridine and phenanthroline alkyl complexes and greater Ni(I) character for the bisoxazoline bromide complex. While the g_{iso} of Ni(I)-bipyridine halide compounds would be consistent with Ni(I) character intermediate to these complexes, a full analysis of the aggregate g_{iso} values will require the additional assignment of the ligand field transitions that spin-orbit couple with the ground state, giving rise to orbital angular momentum.

Current efforts are underway to assign the UV–vis transitions across various isolable Ni(I) complexes to elucidate the amount of ligand vs. metal character, as well as ligand field vs. MLCT contributions to the observed g values. These may be useful to evaluate the degree of electron delocalization onto the bpy ligand. Indeed, multireference/multiconfigurational calculations predict significant multiconfigurational character (i.e., Ni(I)(bpy)X vs. Ni(II)(bpy $^{\bullet-}$)X).^{26,27} A full analysis of the Ni(I) g values will require experimental characterization of the Ni-based ligand field transitions. The g values report on the spin-orbit coupling in the ground state of Ni $3d(x^2-y^2)$ SOMO parentage. However, importantly, the electronic effects of the bpy ligand and its substituents extend beyond the Ni $3d(x^2-y^2)$ SOMO and allow for energetic tuning of the lower-energy, occupied Ni $3d$ orbitals that are actually involved in the elementary steps of oxidative addition and dimerization (as further discussed below).

When examining the Ni(I)–based reactivity toward $C(\text{sp}^2)\text{--Cl}$ oxidative addition, we find that complexes **1-Cl/Br/I**, which feature the most electron-donating *tert*-butyl substituent on

bpy, exhibit the largest rate constants for the oxidative addition of 2-chloro-toluene ($k_{\text{OA}} \sim 7.0 \times 10^{-2} \text{ M}^{-1} \text{ s}^{-1}$, **Figure 4.3** and **Table 4.2**). Changing this bpy substituent to hydrogen atoms (**2-Cl**) reduces the rate constant by twofold, while changing to the electron-withdrawing methyl ester (**3-Cl**) completely eliminates oxidative addition reactivity. Furthermore, **1-Cl** is competent towards the activation of a variety of aryl chlorides, with rate constants spanning two orders of magnitude (from $k_{\text{OA}} \sim 8.0 \times 10^{-2} \text{ M}^{-1} \text{ s}^{-1}$ to $k_{\text{OA}} \sim 6.4 \text{ M}^{-1} \text{ s}^{-1}$). Hammett relationships indicate that the mechanism of the $\text{C}(\text{sp}^2)\text{-Cl}$ bond activation proceeds by a $\text{S}_{\text{N}}\text{Ar}$ -type pathway, marking a discrete change in mechanism for the oxidative addition of aryl chlorides vs. aryl bromides or aryl iodides. These reactivity trends have been rationalized herein through analysis of the associated Ni-based $3d(z^2)$ orbital involved in the nucleophilic two-electron transfer. In particular, we find linear trends between the $3d(z^2)$ RAMO and the Hammett parameter of the bpy ligand (Figure S45), with electron donation and electron-withdrawing substituents destabilizing or stabilizing the RAMO, respectively. Interestingly, the energetic (de)stabilization is observed to occur for the entire $3d$ orbital manifold (**Figure 4.8B**). This observation is consistent with bpy-induced modifications of the Z_{eff} of the metal center; the calculated Ni(I) $1s$ and $2p(x,y,z)$ orbital energies also trend linearly with the observed rate constants (Figure S46). Increased Z_{eff} on the metal stabilizes the $3d$ orbital manifold and perturbs the overall reactivity of the complex (**Figure 4.8A**) through the kinetic barrier (ΔG^\ddagger).

The bpy and halide substituents therefore present themselves as synthetic handles by which the reactivity of Ni(I)-bpy halide complexes can be adjusted and evaluated. For example, compound **3-Cl** is selective toward the oxidative addition of $\text{C}(\text{sp}^2)\text{-Br/I}$ bonds, while **1-Cl** demonstrates robust reactivity toward even the challenging $\text{C}(\text{sp}^2)\text{-Cl}$ functionality. The relative reactivity of **1-Cl/Br/I**, **2-Cl**, and **3-Cl** allows for an estimate of the minimum energy of the Ni $3d(z^2)$ orbital required to activate the challenging $\text{C}(\text{sp}^2)\text{-Cl}$ bond (**Figure 4.8B**).

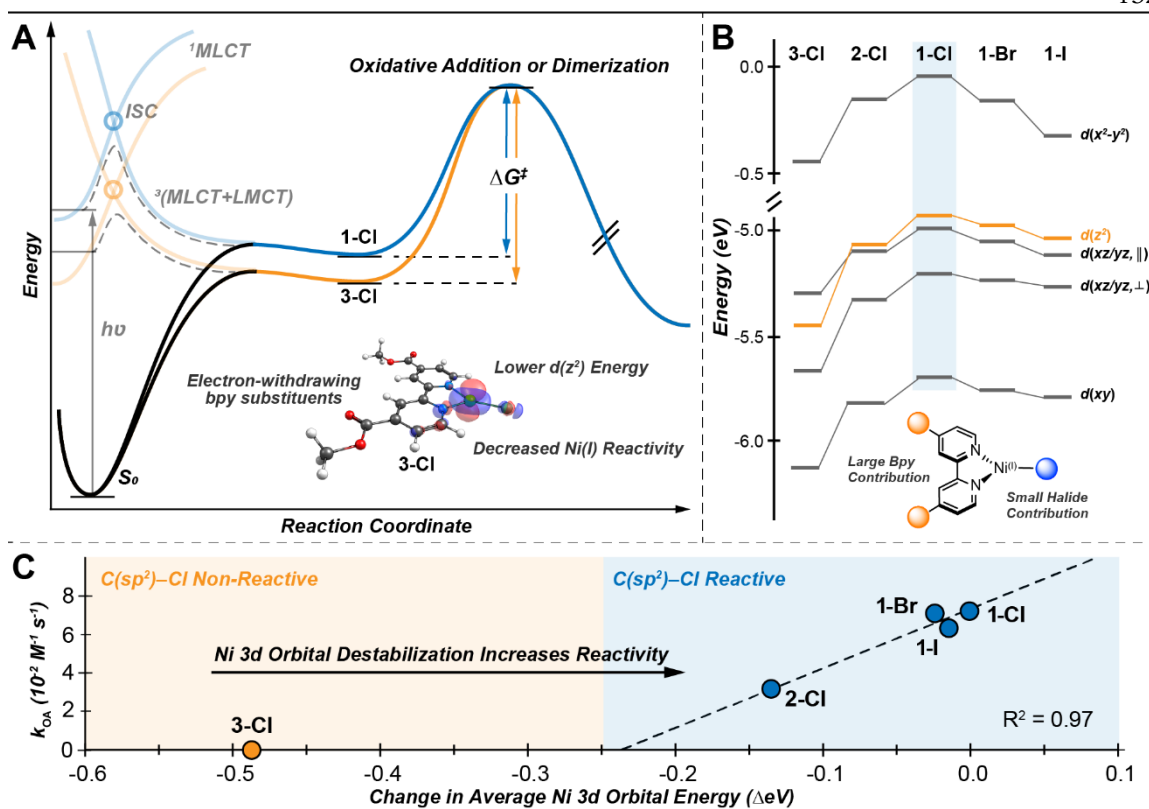


Figure 4.8. Reaction coordinate and state energy diagrams for the Ni(I)–bpy halide complexes. (A) Blue (**1-Cl**) and orange (**3-Cl**) lines depict the photoexcitation mechanism (the MLCT+LMCT ‘one-photon, two-electron’ excitation previously discussed in ref. 27) for the formation of Ni(I) complexes. Subsequent reaction coordinate diagrams for the Ni(I)-based oxidative addition (if aryl halide is present) or dimerization pathways are given for **1-Cl** (blue) and **3-Cl** (orange), highlighting the difference in kinetic barriers, ΔG^\ddagger , for the two complexes. (B) Molecular orbital diagram for the Ni(I) species, demonstrating the (de)stabilization of the β 3d orbital manifolds due to changes in Z_{eff} ; the chemically active, nucleophilic $3d(z^2)$ orbital is highlighted in orange. (C) Plot of the oxidative addition rate constants, k_{OA} , vs. the average change in Ni 3d orbital energy relative to **1-Cl**.

Furthermore, as the Ni 3d orbitals are stabilized in energy, the rate constant decreases linearly ($R^2 = 0.97$, **Figure 4.8C**). Extrapolating this correlation to the x-axis provides an approximation of the minimum orbital energy required for oxidative addition reactivity. Notably, **3-Cl**, which is not reactive toward C(sp²)-Cl bonds, falls well off the correlation

for the other complexes. Thus, from this picture, in order to activate reactivity, one would need to move the **3-Cl** point along the x-axis until it intersects with the slope for the other compounds (i.e., increase its $3d$ orbital energies). Correlations of this type over other Ni(I) species reacting with a variety of C–X bonds will be useful for generating robust reactivity predictions. It further indicates that tuning the energy of the Ni $3d$ orbitals is a key aspect for reactivity. X-ray absorption spectroscopies will prove useful to quantify ligand contributions to Z_{eff} and the $3d(z^2)$ RAMO.⁶⁵ Outside of ligand contributions, which thus far appear to be non-specific and affect all $3d$ orbitals, it may be possible to utilize other contributions such as solvent or additive effects as another handle by which to specifically target the axially accessible $3d(z^2)$ orbital and modulate the energy and reactivity (and thereby the selectivity) of these complexes toward oxidative addition. Current work is underway to further define the reactivity capabilities of these Ni(I)–bpy halide complexes.

Not only is the oxidative addition reactivity of these complexes tunable via the Ni $3d(z^2)$ orbital, but their general solution-phase stability is as well. Analysis of the temperature-dependent kinetics indicates that **3-Cl** has a markedly decreased tendency toward dimerization, with a measured room temperature free energy of activation, ΔG^\ddagger , of ~ 25 kcal mol⁻¹. Conversely, **1-Cl** readily dimerizes at room temperature suggesting that this decomposition pathway may be of concern during catalysis. These dimerization pathways also feature a nucleophilic attack by the Ni $3d(z^2)$ orbital, but in this case, the acceptor is the unoccupied p orbital of the halide on a second complex. Thus, the competitive oxidative addition and dimerization reactivity pathways are both correlated with the Ni $3d(z^2)$ orbital energy, suggesting it as a sensitive target for researchers to tune to discourage Ni(I) reactant decomposition and increase the catalytic turnover number. One can also envision similar concepts from a multiconfigurational bonding perspective. That is, increasing a ligand non-innocent Ni(II)(bpy⁺)X configuration over the metal-centered Ni(I)(bpy)X configuration will deactivate the complex toward oxidative addition and dimerization. Future studies examining additional factors (e.g., steric effects, solvent coordination, etc.) that could suppress Ni(I) dimerization without affecting its performance toward oxidative addition would be of interest.

§4-4. Conclusions

In summary, we report the straightforward photochemical generation of a series of Ni(I)–bpy halide complexes, which has allowed for detailed studies of their relative reactivity toward competitive pathways of oxidative addition and dimerization/oligomerization. Interestingly, many of the Ni(I)–bpy halide complexes studied herein are active toward oxidative addition of high-energy C(sp²)–Cl bonds. Through time-resolved UV–vis kinetic analysis, we have determined rate constants for these oxidative addition reactions. A Hammett analysis on substituted aryl chlorides elucidated the specific mechanism for the C(sp²)–Cl bond activation step as proceeding through an S_NAr-type pathway, wherein the Ni(I) complex acts as a nucleophile. Relatedly, computational studies have also supported this mechanism, well reproducing the experimental ρ value, and reveal a nucleophilic two-electron transfer from the 3d(z²) RAMO into the C_{aryl}–X σ* orbital.

While the Ni(I)-mediated reactivity is not strongly dependent on the identity of the halide ligand, we find that it is strongly influenced by the identity of the bpy substituents. Electron-withdrawing substituents increase the energetic barrier for oxidative addition and can even completely abolish reactivity with C(sp²)–Cl bonds. Electron-donating substituents, however, promote reactivity. The role of the bpy ligand in reactivity has been traced directly to substituent-induced changes in the Ni(I)-based Z_{eff}. For example, the most reactive complex, **1-Cl**, has the Z_{eff} decreased by electron donation from the *tert*-butyl substituents on the bpy. The enhanced electron density on the metal more effectively screens the nuclear charge through electron–electron Coulomb repulsion; this decrease in Z_{eff} destabilizes the entire 3d-orbital manifold. Thus, the energy of the nucleophilic 3d(z²) orbital is modulated through changes in Z_{eff}, and greater energetic destabilization results in greater reactivity due to decreases in electron binding affinities. While not evaluated here, the low coordination number and planarity of the bpy ligand also likely reduce steric contributions allowing for an ideal orbital overlap between the 3d(z²) and C_{aryl}–X σ* orbitals to be achieved.

We have additionally utilized temperature-dependent reaction kinetics to determine the thermodynamics associated with Ni(I) complex dimerization. We again find that stabilization

of the complexes is made possible via ligand effects, reporting room temperature dimerization barriers that range from moderate to untenable. Dimerization reactivity considerations parallel those of oxidative addition. Altogether, geometric changes to the ligand scaffold about the Ni(I) center in these and other catalytically relevant complexes have important implications for their relative electronic structures and reactivities. Modulation of the $3d(z^2)$ orbital (by ligand substitution or through yet-to-be explored solvent coordination) represents a tunable target by which the reactivity of Ni(I)-bpy halide complexes can be altered, potentially unveiling new ways to drive Ni-mediated photocatalytic cycles and a direct route toward stimulating reactivity with even stronger C–X bonds.

§4-5. References

- (1) Nicewicz, D. A.; MacMillan, D. W. C. Merging Photoredox Catalysis with Organocatalysis: The Direct Asymmetric Alkylation of Aldehydes. *Science* **2008**, *322* (5898), 77–80. <https://doi.org/10.1126/science.1161976>.
- (2) Shaw, M. H.; Twilton, J.; MacMillan, D. W. C. Photoredox Catalysis in Organic Chemistry. *J. Org. Chem.* **2016**, *81* (16), 6898–6926. <https://doi.org/10.1021/acs.joc.6b01449>.
- (3) Twilton, J.; Le, C.; Zhang, P.; Shaw, M. H.; Evans, R. W.; MacMillan, D. W. C. The Merger of Transition Metal and Photocatalysis. *Nat. Rev. Chem.* **2017**, *1* (7), 0052. <https://doi.org/10.1038/s41570-017-0052>.
- (4) Cavalcanti, L. N.; Molander, G. A. Photoredox Catalysis in Nickel-Catalyzed Cross-Coupling. *Top. Curr. Chem.* **2016**, *374* (4), 39. <https://doi.org/10.1007/s41061-016-0037-z>.
- (5) Larsen, C. B.; Wenger, O. S. Photoredox Catalysis with Metal Complexes Made from Earth-Abundant Elements. *Chem. Eur. J.* **2018**, *24* (9), 2039–2058. <https://doi.org/10.1002/chem.201703602>.
- (6) Welin, E. R.; Le, C.; Arias-Rotondo, D. M.; McCusker, J. K.; MacMillan, D. W. C. Photosensitized, Energy Transfer-Mediated Organometallic Catalysis through Electronically Excited Nickel(II). *Science* **2017**, *355* (6323), 380–385. <https://doi.org/10.1126/science.aal2490>.
- (7) Chan, A. Y.; Perry, I. B.; Bissonnette, N. B.; Buksh, B. F.; Edwards, G. A.; Frye, L. I.; Garry, O. L.; Lavagnino, M. N.; Li, B. X.; Liang, Y.; Mao, E.; Millet, A.; Oakley, J. V.; Reed, N. L.; Sakai, H. A.; Seath, C. P.; MacMillan, D. W. C. Metallaphotoredox: The Merger of Photoredox and Transition Metal Catalysis. *Chem. Rev.* **2021**. <https://doi.org/10.1021/acs.chemrev.1c00383>.
- (8) Dongbang, S.; Doyle, A. G. Ni/Photoredox-Catalyzed C(sp³)–C(sp³) Coupling between Aziridines and Acetals as Alcohol-Derived Alkyl Radical Precursors. *J. Am. Chem. Soc.* **2022**, *144* (43), 20067–20077. <https://doi.org/10.1021/jacs.2c09294>.
- (9) Millet, A.; Cesana, P. T.; Sedillo, K.; Bird, M. J.; Schlau-Cohen, G. S.; Doyle, A. G.; MacMillan, D. W. C.; Scholes, G. D. Bioinspired Supercharging of Photoredox Catalysis for Applications in Energy and Chemical Manufacturing. *Acc. Chem. Res.* **2022**, *55* (10), 1423–1434. <https://doi.org/10.1021/acs.accounts.2c00083>.

- (10) Kariofillis, S. K.; Doyle, A. G. Synthetic and Mechanistic Implications of Chlorine Photoelimination in Nickel/Photoredox C(sp³)–H Cross-Coupling. *Acc. Chem. Res.* **2021**, *54* (4), 988–1000. <https://doi.org/10.1021/acs.accounts.0c00694>.
- (11) Zhu, C.; Yue, H.; Chu, L.; Rueping, M. Recent Advances in Photoredox and Nickel Dual-Catalyzed Cascade Reactions: Pushing the Boundaries of Complexity. *Chem. Sci.* **2020**, *11* (16), 4051–4064. <https://doi.org/10.1039/D0SC00712A>.
- (12) Feng, Y.; Luo, H.; Zheng, W.; Matsunaga, S.; Lin, L. Light-Promoted Nickel-Catalyzed Aromatic Halogen Exchange. *ACS Catal.* **2022**, *12* (18), 11089–11096. <https://doi.org/10.1021/acscatal.2c03354>.
- (13) Speckmeier, E.; Maier, T. C. ART—An Amino Radical Transfer Strategy for C(sp²)–C(sp³) Coupling Reactions, Enabled by Dual Photo/Nickel Catalysis. *J. Am. Chem. Soc.* **2022**, *144* (22), 9997–1005. <https://doi.org/10.1021/jacs.2c03220>.
- (14) Shin, J.; Lee, J.; Suh, J.-M.; Park, K. Ligand-Field Transition-Induced C–S Bond Formation from Nickelacycles. *Chem. Sci.* **2021**, *12* (48), 15908–15915. <https://doi.org/10.1039/D1SC05113J>.
- (15) Zhang, R.; Li, G.; Wismer, M.; Vachal, P.; Colletti, S. L.; Shi, Z.-C. Profiling and Application of Photoredox C(sp³)–C(sp²) Cross-Coupling in Medicinal Chemistry. *ACS Med. Chem. Lett.* **2018**, *9* (7), 773–777. <https://doi.org/10.1021/acsmchemlett.8b00183>.
- (16) Lacker, C. R.; DeLano, T. J.; Chen, E. P.; Kong, J.; Belyk, K. M.; Piou, T.; Reisman, S. E. Enantioselective Synthesis of N-Benzylic Heterocycles by Ni/Photoredox Dual Catalysis. *J. Am. Chem. Soc.* **2022**, *144* (44), 20190–20195. <https://doi.org/10.1021/jacs.2c07917>.
- (17) Cheung, K. P. S.; Sarkar, S.; Gevorgyan, V. Visible Light-Induced Transition Metal Catalysis. *Chem. Rev.* **2022**, *122* (2), 1543–1625. <https://doi.org/10.1021/acs.chemrev.1c00403>.
- (18) Li, R.; Yang, C.-X.; Niu, B.-H.; Li, L.-J.; Ma, J.-M.; Li, Z.-L.; Jiang, H.; Cheng, W.-M. Visible Light-Induced Ni-Catalyzed C–Heteroatom Cross-Coupling of Aryl Halides via LMCT with DBU to Access a Ni(I)/Ni(III) Cycle. *Org. Chem. Front.* **2022**, *9* (14), 3847–3853. <https://doi.org/10.1039/D2QO00607C>.
- (19) Gutierrez, O.; Tellis, J. C.; Primer, D. N.; Molander, G. A.; Kozlowski, M. C. Nickel-Catalyzed Cross-Coupling of Photoredox-Generated Radicals: Uncovering a General

Manifold for Stereoconvergence in Nickel-Catalyzed Cross-Couplings. *J. Am. Chem. Soc.* **2015**, *137* (15), 4896–4899. <https://doi.org/10.1021/ja513079r>.

(20) Maity, B.; Scott, T. R.; Stroschio, G. D.; Gagliardi, L.; Cavallo, L. The Role of Excited States of $\text{LNi}^{\text{II/III}}(\text{Aryl})(\text{Halide})$ Complexes in Ni–Halide Bond Homolysis in the Arylation of $\text{Csp}^3\text{–H}$ Bonds. *ACS Catal.* **2022**, *12* (21), 13215–13224. <https://doi.org/10.1021/acscatal.2c04284>.

(21) Tang, T.; Jones, E.; Wild, T.; Hazra, A.; Minter, S. D.; Sigman, M. S. Investigating Oxidative Addition Mechanisms of Allylic Electrophiles with Low-Valent Ni/Co Catalysts Using Electroanalytical and Data Science Techniques. *J. Am. Chem. Soc.* **2022**, *144* (43), 20056–20066. <https://doi.org/10.1021/jacs.2c09120>.

(22) Almansa, A.; Jardel, D.; Massip, S.; Tassaing, T.; Schatz, C.; Domergue, J.; Molton, F.; Duboc, C.; Vincent, J.-M. Dual Photoredox Ni/Benzophenone Catalysis: A Study of the Ni^{II} Precatalyst Photoreduction Step. *J. Org. Chem.* **2022**, *87* (16), 11172–11184. <https://doi.org/10.1021/acs.joc.2c01467>.

(23) Ben-Tal, Y.; Lloyd-Jones, G. C. Kinetics of a Ni/Ir-Photocatalyzed Coupling of ArBr with RBr: Intermediacy of $\text{ArNi}^{\text{II}}(\text{L})\text{Br}$ and Rate/Selectivity Factors. *J. Am. Chem. Soc.* **2022**, *144* (33), 15372–15382. <https://doi.org/10.1021/jacs.2c06831>.

(24) Shields, B. J.; Kudisch, B.; Scholes, G. D.; Doyle, A. G. Long-Lived Charge-Transfer States of Nickel(II) Aryl Halide Complexes Facilitate Bimolecular Photoinduced Electron Transfer. *J. Am. Chem. Soc.* **2018**, *140* (8), 3035–3039. <https://doi.org/10.1021/jacs.7b13281>.

(25) Ting, S. I.; Garakyaraghi, S.; Taliaferro, C. M.; Shields, B. J.; Scholes, G. D.; Castellano, F. N.; Doyle, A. G. $^3\text{d-d}$ Excited States of Ni(II) Complexes Relevant to Photoredox Catalysis: Spectroscopic Identification and Mechanistic Implications. *J. Am. Chem. Soc.* **2020**, *142* (12), 5800–5810. <https://doi.org/10.1021/jacs.0c00781>.

(26) Cagan, D. A.; Stroschio, G. D.; Cusumano, A. Q.; Hadt, R. G. Multireference Description of Nickel–Aryl Homolytic Bond Dissociation Processes in Photoredox Catalysis. *J. Phys. Chem. A* **2020**, *124* (48), 9915–9922. <https://doi.org/10.1021/acs.jpca.0c08646>.

(27) Cagan, D. A.; Bím, D.; Silva, B.; Kazmierczak, N. P.; McNicholas, B. J.; Hadt, R. G. Elucidating the Mechanism of Excited-State Bond Homolysis in Nickel–Bipyridine Photoredox Catalysts. *J. Am. Chem. Soc.* **2022**, *144* (14), 6516–6531. <https://doi.org/10.1021/jacs.2c01356>.

- (28) Yuan, M.; Song, Z.; Badir, S. O.; Molander, G. A.; Gutierrez, O. On the Nature of C(sp³)–C(sp²) Bond Formation in Nickel-Catalyzed Tertiary Radical Cross-Couplings: A Case Study of Ni/Photoredox Catalytic Cross-Coupling of Alkyl Radicals and Aryl Halides. *J. Am. Chem. Soc.* **2020**, *142* (15), 7225–7234. <https://doi.org/10.1021/jacs.0c02355>.
- (29) Na, H.; Mirica, L. M. Deciphering the Mechanism of the Ni-Photocatalyzed C–O Cross-Coupling Reaction Using a Tridentate Pyridinophane Ligand. *Nat. Commun.* **2022**, *13* (1), 1313. <https://doi.org/10.1038/s41467-022-28948-8>.
- (30) Ting, S. I.; Williams, W. L.; Doyle, A. G. Oxidative Addition of Aryl Halides to a Ni(I)-Bipyridine Complex. *J. Am. Chem. Soc.* **2022**, *144* (12), 5575–5582. <https://doi.org/10.1021/jacs.2c00462>.
- (31) Till, N. A.; Oh, S.; MacMillan, D. W. C.; Bird, M. J. The Application of Pulse Radiolysis to the Study of Ni(I) Intermediates in Ni-Catalyzed Cross-Coupling Reactions. *J. Am. Chem. Soc.* **2021**, *143* (25), 9332–9337. <https://doi.org/10.1021/jacs.1c04652>.
- (32) Mohadjer Beromi, M.; Brudvig, G. W.; Hazari, N.; Lant, H. M. C.; Mercado, B. Q. Synthesis and Reactivity of Paramagnetic Nickel Polypyridyl Complexes Relevant to C(sp²)–C(sp³) Coupling Reactions. *Angew. Chem. Int. Ed.* **2019**, *58* (18), 6094–6098. <https://doi.org/10.1002/anie.201901866>.
- (33) Kawamata, Y.; Vantourout, J. C.; Hickey, D. P.; Bai, P.; Chen, L.; Hou, Q.; Qiao, W.; Barman, K.; Edwards, M. A.; Garrido-Castro, A. F.; deGruyter, J. N.; Nakamura, H.; Knouse, K.; Qin, C.; Clay, K. J.; Bao, D.; Li, C.; Starr, J. T.; Garcia-Irizarry, C.; Sach, N.; White, H. S.; Neurock, M.; Minter, S. D.; Baran, P. S. Electrochemically Driven, Ni-Catalyzed Aryl Amination: Scope, Mechanism, and Applications. *J. Am. Chem. Soc.* **2019**, *141* (15), 6392–6402. <https://doi.org/10.1021/jacs.9b01886>.
- (34) Jones, G. D.; Martin, J. L.; McFarland, C.; Allen, O. R.; Hall, R. E.; Haley, A. D.; Brandon, R. J.; Konovalova, T.; Desrochers, P. J.; Pulay, P.; Vicic, D. A. Ligand Redox Effects in the Synthesis, Electronic Structure, and Reactivity of an Alkyl–Alkyl Cross-Coupling Catalyst. *J. Am. Chem. Soc.* **2006**, *128* (40), 13175–13183. <https://doi.org/10.1021/ja063334i>.
- (35) Ciszewski, J. T.; Mikhaylov, D. Y.; Holin, K. V.; Kadirov, M. K.; Budnikova, Y. H.; Sinyashin, O.; Vicic, D. A. Redox Trends in Terpyridine Nickel Complexes. *Inorg. Chem.* **2011**, *50* (17), 8630–8635. <https://doi.org/10.1021/ic201184x>.

(36) Vogt, N.; Sandleben, A.; Kletsch, L.; Schäfer, S.; Chin, M. T.; Vicic, D. A.; Hörner, G.; Klein, A. Role of the X Coligands in Cyclometalated [Ni(Phbpy)X] Complexes (^HPhbpy = 6-Phenyl-2,2'-Bipyridine). *Organometallics* **2021**, *40* (11), 1776–1785. <https://doi.org/10.1021/acs.organomet.1c00237>.

(37) Kalvet, I.; Guo, Q.; Tizzard, G. J.; Schoenebeck, F. When Weaker Can Be Tougher: The Role of Oxidation State (I) in P- vs N-Ligand-Derived Ni-Catalyzed Trifluoromethylthiolation of Aryl Halides. *ACS Catal.* **2017**, *7* (3), 2126–2132. <https://doi.org/10.1021/acscatal.6b03344>.

(38) Diccianni, J. B.; Diao, T. Mechanisms of Nickel-Catalyzed Cross-Coupling Reactions. *Trends Chem.* **2019**, *1* (9), 830–844. <https://doi.org/10.1016/j.trechm.2019.08.004>.

(39) Lin, Q.; Diao, T. Mechanism of Ni-Catalyzed Reductive 1,2-Dicarbonylfunctionalization of Alkenes. *J. Am. Chem. Soc.* **2019**, *141* (44), 17937–17948. <https://doi.org/10.1021/jacs.9b10026>.

(40) Sun, R.; Qin, Y.; Rucolo, S.; Schnedermann, C.; Costentin, C.; Nocera, D. G. Elucidation of a Redox-Mediated Reaction Cycle for Nickel-Catalyzed Cross Coupling. *J. Am. Chem. Soc.* **2019**, *141* (1), 89–93. <https://doi.org/10.1021/jacs.8b11262>.

(41) Lin, C.-Y.; Power, P. P. Complexes of Ni(I): A “Rare” Oxidation State of Growing Importance. *Chem. Soc. Rev.* **2017**, *46* (17), 5347–5399. <https://doi.org/10.1039/C7CS00216E>.

(42) Yang, L.; Lu, H.-H.; Lai, C.-H.; Li, G.; Zhang, W.; Cao, R.; Liu, F.; Wang, C.; Xiao, J.; Xue, D. Light-Promoted Nickel Catalysis: Etherification of Aryl Electrophiles with Alcohols Catalyzed by a Ni^{II}-Aryl Complex. *Angew. Chem. Int. Ed.* **2020**, *59* (31), 12714–12719. <https://doi.org/10.1002/anie.202003359>.

(43) Song, G.; Li, Q.; Nong, D.-Z.; Song, J.; Li, G.; Wang, C.; Xiao, J.; Xue, D. Ni-Catalyzed Photochemical C-N Coupling of Amides with (Hetero)Aryl Chlorides. *Chem. Eur. J.* **2023**, *Accepted Article*, e202300458. <https://doi.org/10.1002/chem.202300458>.

(44) Arendt, K. M.; Doyle, A. G. Dialkyl Ether Formation by Nickel-Catalyzed Cross-Coupling of Acetals and Aryl Iodides. *Angew. Chem. Int. Ed.* **2015**, *54* (34), 9876–9880. <https://doi.org/10.1002/anie.201503936>.

- (45) Ju, L.; Lin, Q.; LiBretto, N. J.; Wagner, C. L.; Hu, C. T.; Miller, J. T.; Diao, T. Reactivity of (Bi-Oxazoline)Organonickel Complexes and Revision of a Catalytic Mechanism. *J. Am. Chem. Soc.* **2021**, *143* (36), 14458–14463. <https://doi.org/10.1021/jacs.1c07139>.
- (46) Hansch, Corwin.; Leo, A.; Taft, R. W. A Survey of Hammett Substituent Constants and Resonance and Field Parameters. *Chem. Rev.* **1991**, *91* (2), 165–195. <https://doi.org/10.1021/cr00002a004>.
- (47) Portnoy, M.; Milstein, D. Mechanism of Aryl Chloride Oxidative Addition to Chelated Palladium(0) Complexes. *Organometallics* **1993**, *12* (5), 1665–1673. <https://doi.org/10.1021/om00029a026>.
- (48) Tsou, T. T.; Kochi, J. K. Mechanism of Oxidative Addition. Reaction of Nickel(0) Complexes with Aromatic Halides. *J. Am. Chem. Soc.* **1979**, *101* (21), 6319–6332. <https://doi.org/10.1021/ja00515a028>.
- (49) Lin, Q.; Fu, Y.; Liu, P.; Diao, T. Monovalent Nickel-Mediated Radical Formation: A Concerted Halogen-Atom Dissociation Pathway Determined by Electroanalytical Studies. *J. Am. Chem. Soc.* **2021**, *143* (35), 14196–14206. <https://doi.org/10.1021/jacs.1c05255>.
- (50) Amatore, C.; Pfluger, F. Mechanism of Oxidative Addition of Palladium(0) with Aromatic Iodides in Toluene, Monitored at Ultramicroelectrodes. *Organometallics* **1990**, *9* (8), 2276–2282. <https://doi.org/10.1021/om00158a026>.
- (51) Biscoe, M. R.; Fors, B. P.; Buchwald, S. L. A New Class of Easily Activated Palladium Precatalysts for Facile C–N Cross-Coupling Reactions and the Low Temperature Oxidative Addition of Aryl Chlorides. *J. Am. Chem. Soc.* **2008**, *130* (21), 6686–6687. <https://doi.org/10.1021/ja801137k>.
- (52) Weigend, F.; Ahlrichs, R. Balanced Basis Sets of Split Valence, Triple Zeta Valence and Quadruple Zeta Valence Quality for H to Rn: Design and Assessment of Accuracy. *Phys. Chem. Chem. Phys.* **2005**, *7* (18), 3297–3305. <https://doi.org/10.1039/B508541A>.
- (53) Becke, A. D. Density-functional Thermochemistry. III. The Role of Exact Exchange. *J. Chem. Phys.* **1993**, *98* (7), 5648–5652. <https://doi.org/10.1063/1.464913>.
- (54) Lee, C.; Yang, W.; Parr, R. G. Development of the Colle-Salvetti Correlation-Energy Formula into a Functional of the Electron Density. *Phys. Rev. B* **1988**, *37* (2), 785–789. <https://doi.org/10.1103/PhysRevB.37.785>.

(55) Cramer, C. J.; Truhlar, D. G. Density Functional Theory for Transition Metals and Transition Metal Chemistry. *Phys. Chem. Chem. Phys.* **2009**, *11* (46), 10757–10816. <https://doi.org/10.1039/B907148B>.

(56) Mardirossian, N.; Head-Gordon, M. Thirty Years of Density Functional Theory in Computational Chemistry: An Overview and Extensive Assessment of 200 Density Functionals. *Mol. Phys.* **2017**, *115* (19), 2315–2372. <https://doi.org/10.1080/00268976.2017.1333644>.

(57) Tang, T.; Hazra, A.; Min, D. S.; Williams, W. L.; Jones, E.; Doyle, A. G.; Sigman, M. S. Interrogating the Mechanistic Features of Ni(I)-Mediated Aryl Iodide Oxidative Addition Using Electroanalytical and Statistical Modeling Techniques. *J. Am. Chem. Soc.* **2023**, *145* (15), 8689–8699. <https://doi.org/10.1021/jacs.3c01726>.

(58) Knizia, G.; Klein, J. E. M. N. Electron Flow in Reaction Mechanisms—Revealed from First Principles. *Angew. Chem. Int. Ed.* **2015**, *54* (18), 5518–5522. <https://doi.org/10.1002/anie.201410637>.

(59) Knizia, G. Intrinsic Atomic Orbitals: An Unbiased Bridge between Quantum Theory and Chemical Concepts. *J. Chem. Theory Comput.* **2013**, *9* (11), 4834–4843. <https://doi.org/10.1021/ct400687b>.

(60) Vermeeren, P.; Sun, X.; Bickelhaupt, F. M. Arylic C–X Bond Activation by Palladium Catalysts: Activation Strain Analyses of Reactivity Trends. *Sci. Rep.* **2018**, *8* (1), 10729. <https://doi.org/10.1038/s41598-018-28998-3>.

(61) Eyring, H. The Activated Complex in Chemical Reactions. *J. Chem. Phys.* **1935**, *3* (2), 107–115. <https://doi.org/10.1063/1.1749604>.

(62) Lente, G.; Fábrián, I.; J. Poë, A. A Common Misconception about the Eyring Equation. *New J. Chem.* **2005**, *29* (6), 759–760. <https://doi.org/10.1039/B501687H>.

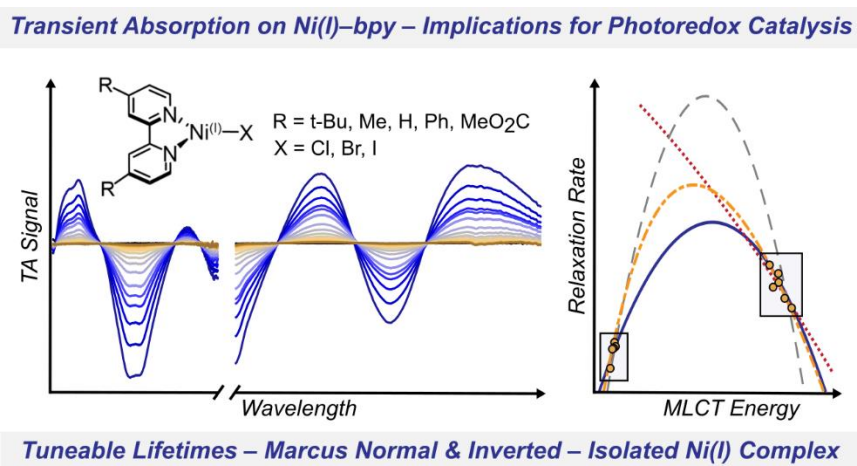
(63) Carvalho-Silva, V. H.; Coutinho, N. D.; Aquilanti, V. Temperature Dependence of Rate Processes Beyond Arrhenius and Eyring: Activation and Transitivity. *Front. Chem.* **2019**, *7* (380), 1–11. <https://doi.org/10.3389/fchem.2019.00380>.

(64) Day, C. S.; Rentería-Gómez, Á.; Ton, S. J.; Gogoi, A. R.; Gutierrez, O.; Martin, R. Elucidating Electron-Transfer Events in Polypyridine Nickel Complexes for Reductive Coupling Reactions. *Nat. Catal.* **2023**, *6* (3), 244–253. <https://doi.org/10.1038/s41929-023-00925-4>.

(65) Solomon, E. I.; Szilagy, R. K.; DeBeer George, S.; Basumallick, L. Electronic Structures of Metal Sites in Proteins and Models: Contributions to Function in Blue Copper Proteins. *Chem. Rev.* **2004**, *104* (2), 419–458. <https://doi.org/10.1021/cr0206317>.

Chapter 5

Ultrafast Photophysics of Ni(I)–Bipyridine Halide Complexes: Spanning the Marcus Normal and Inverted Regimes.



Adapted with permission from:

Sutcliffe, E.;[†] Cagan, D. A.;[†] Hadt, R. G. Ultrafast Photophysics of Ni(I)–Bipyridine Halide Complexes: Spanning the Marcus Normal and Inverted Regimes. *J. Am. Chem. Soc.* **2024**, Accepted.
[†]Co-first author.

Copyright 2024 American Chemical Society.

§5-1. Introduction

Ni(II)–bipyridine (bpy) aryl halide complexes are widely used for their ability to facilitate light-driven cross-coupling reactions.^{1–12} Excited-state Ni(II)–C(aryl) bond homolysis results in the formation of low-valent Ni(I)–bpy halide species^{13–15} that can activate aryl halides through a subsequent dark catalytic cycle. While aryl iodides and bromides can be activated with relative ease, increasing the electron-donating ability of the bpy substituents allows for activation of stronger C(sp²)–Cl bonds.^{16–24} Coupling light reactions for *in situ* Ni(I) generation to dark reactions for C–X bond activation enables Ni(I)/(III) catalytic cycles in the presence of nucleophilic coupling partners (e.g., amines, alcohols, thiols, etc., **Figure 1A**).^{25–30} Indeed, Ni(I)–bpy halide species have been shown to facilitate cross-coupling with remarkable scope, forging new C(sp²)–X bonds in good-to-excellent yields.³¹

As such, recent efforts have been made to understand the properties and reactivity profiles of Ni(I)–bpy halide complexes. However, they are prone to dimerization at elevated temperatures or high concentrations and exhibit rapid decomposition in the presence of oxygen or water, making their direct structural and spectroscopic characterization challenging.^{24,32–34} Ni(I)–bpy species can be stabilized through steric protection or backbonding to coordinating olefins.^{35,36} While these routes provided some of the first X-ray crystal structures of Ni(I)–bpy complexes, the stabilization slows or fully inhibits aryl halide oxidative addition. Alternatively, *in situ* formation of Ni(I)–bpy complexes has allowed for detailed mechanistic analysis. Pulsed radiolysis and electrochemical methods identified a Ni(I)(^{*t*}-Bu₃bpy)Br species and have provided rate constants for aryl iodide oxidative addition.^{21,37} Solid-state polynuclear Ni species (e.g., [Ni(I)(^{*Et*}O₂Cbpy)Cl]_n, n = 2 or 4) are precursors to monomeric Ni(I) and did likewise for aryl bromides.¹⁹ From Hammett analysis, both of these aryl halide classes are thought to be activated by a concerted two-electron oxidative addition. Additionally, air- and moisture-free irradiation of parent Ni(II) complexes leads to stoichiometric conversion to Ni(I)–bpy halide photoproducts, many of which activate aryl chlorides.²⁴ Analogous Hammett analysis demonstrated a nearly twofold increase in ρ-value relative to aryl bromides or iodides, suggesting a two-electron

nucleophilic aromatic substitution ($S_{\text{N}}\text{Ar}$) mechanism for the activation of the $\text{C}(\text{sp}^2)\text{--Cl}$ bond.²⁴

Interestingly, all the $\text{Ni}(\text{I})\text{--bpy}$ species observed thus far absorb light across a wide wavelength range with similar or greater extinction coefficients than their parent $\text{Ni}(\text{II})$ complexes.²⁴ More generally, many of the previously proposed metallaphotoredox reactions invoke photon absorption by specific Ni species and/or photosensitizers, indicating that *in situ* generated intermediates also absorb a significant fraction of photons during LED irradiation (**Figure 1B**).

To date, there have been no direct studies of the photophysical properties of $\text{Ni}(\text{I})$ intermediates that form as part of metallaphotoredox catalytic cycles. Given the importance of light activation for $\text{Ni}(\text{II})$, $\text{Ni}(\text{I})$ excited states may also participate in processes that could influence catalysis. Furthermore, there has been significant interest in understanding geometric and electronic structural factors that contribute to charge transfer excited-state lifetimes in first-row transition metal complexes, including recent work on $\text{Ni}(\text{II})$.^{14,18,38–40}

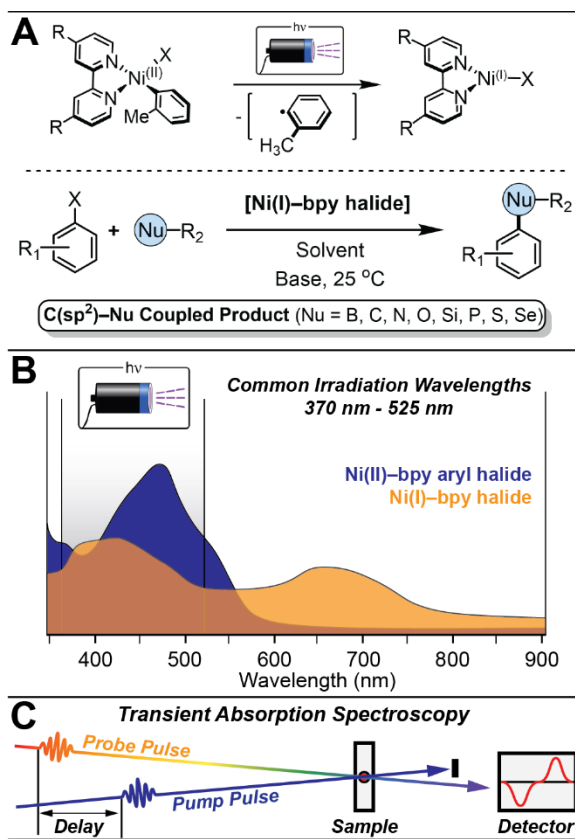


Figure 5.1. (A) Photogeneration and cross-coupling reactivity of Ni(I)-bipyridine halides. (B) Comparison of Ni(II)(*t*-Bu**py**)(*o*-tolyl)Cl and photogenerated Ni(I)(*t*-Bu**py**)Cl, illustrating their overlapping absorbance profiles. (C) Schematic of pump-probe transient absorption spectroscopy.

Herein, we have utilized ultrafast transient absorption (TA) spectroscopy (**Figure 1C**) to study a library of photogenerated Ni(I)(^Rbpy)X species (R = *t*-Bu, Me, H, Ph, MeO₂C; X = Cl, Br, I) and an independently isolated Ni(I)(MeO₂Cbpy)Cl complex, the first such photophysical study for any Ni(I) species. The TA data are consistent with the formation and decay of ²Ni(I)-to-bpy metal-to-ligand charge transfer (²MLCT) excited states with lifetimes ranging from ~10–30 ps. We also find the bpy substituent strongly influences the mechanism of ²MLCT excited-state deactivation. Tuning from electron-donating to electron-withdrawing substituents has provided a rare example of a series of related complexes whose excited-state deactivation processes span the Marcus normal and inverted regimes.

§5-2. Results

2.1. Steady-State and Ultrafast UV–vis–NIR Spectroscopy

Following our previous work,²⁴ Ni(I)(^Rbpy)X complexes were photogenerated from Ni(II)(^Rbpy)(*o*-tolyl)X parents (R = *t*-Bu, Me, Ph, H, MeO₂C; X = Cl, Br, I) (**1–5**, **Figure 2** and **Figures S7-S8**). Complete synthetic details are provided in Supporting Information Section 1.2. In general, Ni(II) complexes were dissolved in tetrahydrofuran (THF) and irradiated under air- and moisture-free conditions using purple or blue PR160L Kessil LEDs (370 or 390 nm incident light) to afford >95% Ni(II)(^Rbpy)(*o*-tolyl)X to Ni(I)(^Rbpy)X conversion.

UV–vis–NIR absorption spectra of **1–5** feature transitions with molar absorptivity on the order of 10³ M⁻¹ cm⁻¹ (**Figure 2**), with minor energy shifts upon variation of the halide; more dramatic shifts are observed upon modifications of the bpy substituents. As discussed in Supporting Information Section 1.4, the absorption bands can be assigned as Ni(I)-to-bpy MLCTs, consistent with our previous work.²⁴ DFT calculated molecular orbital diagrams are given in **Figures S34-S41**, and TDDFT predicted absorption transitions are tabulated in Supporting Information Section S2.4.

We have used ultrafast TA spectroscopy to elucidate the photophysical properties of the Ni(I) intermediates. TA spectra for all compounds were measured in THF using either 700 or 800 nm pump pulses. While some residual Ni(II) precursor can be present in solution due to the *in situ* generation of **1–5**, the precursors do not absorb light near the 700 or 800 nm excitation.^{14,15} Nevertheless, additional pump wavelengths were also used to determine the effect of pumping alternative, higher-energy transitions. Full details of the experimental setup and subsequent analysis are given in Supporting Information Section 1.1 and 1.5.

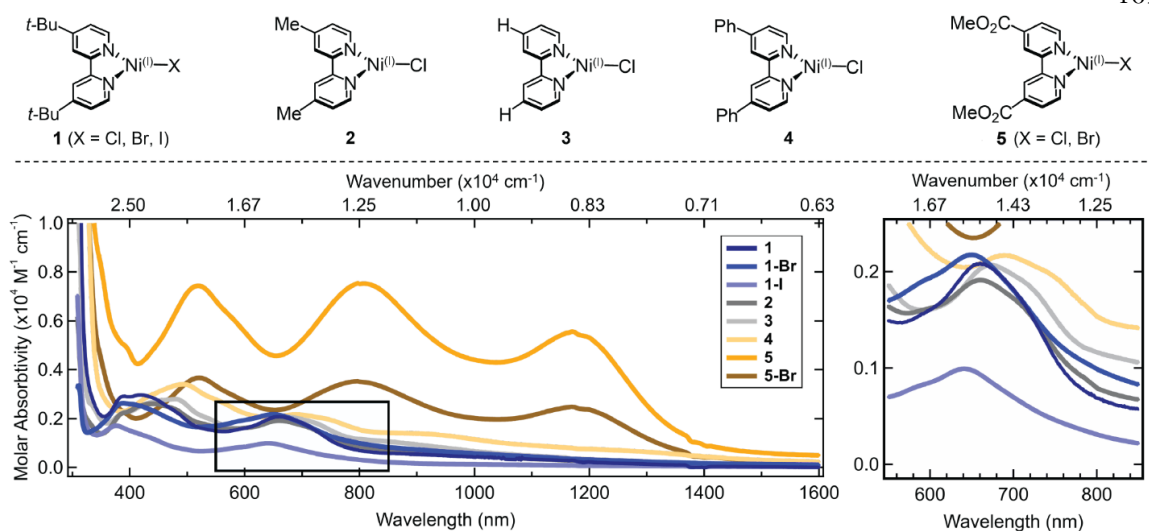


Figure 5.2. Structures and UV–vis–NIR absorption spectra of the photochemically generated Ni(I)–bpy halides in THF. Boxed section is expanded on the right. Analogous figure with wavenumber axis is given as Figure S9.

Similar to their Ni(II) precursors, all Ni(I) compounds showed a sizeable ultrafast TA response. While the Ni(II) precursors exhibit ^3d-d lifetimes of several nanoseconds,^{14,18} Ni(I) excited states decay more rapidly, with no measurable signal after a few hundred ps. Difference spectra for the longest-lived state of each compound (**Figure S32**) exhibit ground-state bleach (GSB) signals that clearly align with the MLCT bands in the Ni(I) steady-state absorption, along with significant excited-state absorption (ESA) in the UV-visible region; complexes **4** and **5** also show sizeable signal in the NIR region (**Figures S21 and S31**).

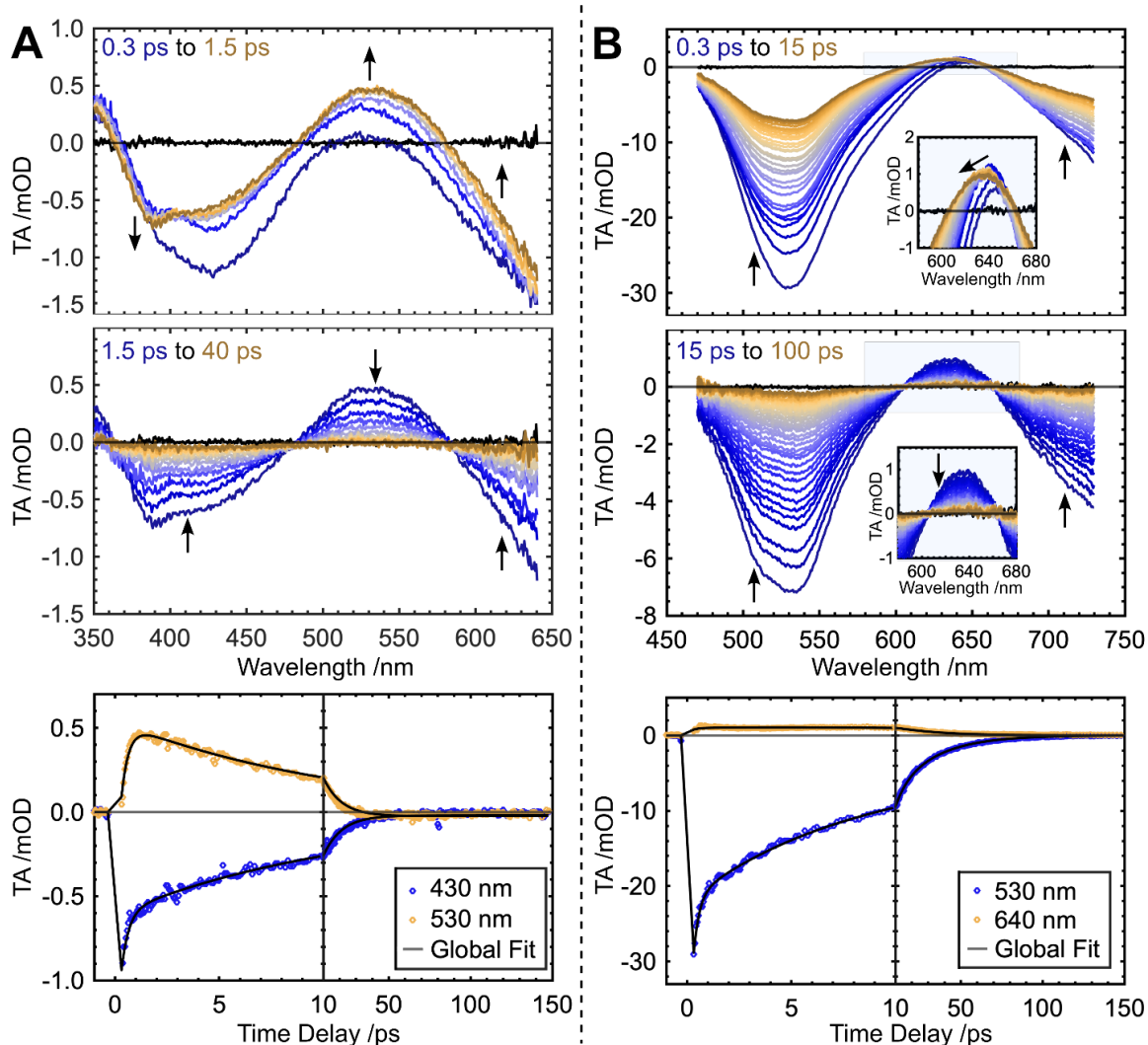


Figure 5.3. Cascaded difference spectra of (A) **1** and (B) **5**, across two time regions with TA prior to photoexcitation plotted in black. Kinetic traces at representative GSB and ESA wavelengths plotted in bottom panel alongside the fit to the data. Insets are an enlarged view of the shaded area showing the evolution of the ESA. All TA spectra, alongside their corresponding global fits, are presented in **Figures S11-S32**.

Changing the Cl ligand in **1** to Br (**1-Br**) or to I (**1-I**) slightly blue-shifts the MLCT bands in the ground-state absorption spectra ($\sim 160\text{ cm}^{-1}$ and 310 cm^{-1} , respectively). TA spectra for these halide variants were similar to **1**, but with a small increase in lifetime of the long-lived state going down the group. Substituting Cl in **5** for Br (**5-Br**) also gave a small change in

the TA spectra, but with the reverse trend; the long-lived state showed a slight decrease in lifetime for Br versus Cl. Thus, the halide has a minor but measurable impact on the relaxation kinetics. Five bpy variants were also investigated (**1–5**). Compounds **1–3** have comparable absorption spectra; these similarities are reflected in their ultrafast behavior, with all three compounds exhibiting decay pathways with similar time constants. In contrast, **4** and **5** showed a longer-lived three-component decay pathway. Notably, the lowest-energy MLCT bands of **4** and **5** extend into the NIR, while the lowest-energy MLCTs of complexes **1–3** are located in the visible. Thus, the bpy substituents significantly perturb the steady-state electronic structure and the excited-state relaxation kinetics.

The ultrafast dynamics of the eight compounds fall into two groups (**Table 1**); analysis of **1** and **5** are presented as representative compounds. Difference spectra across two ranges of time delays following photoexcitation of **1** (700 nm, 1 $\mu\text{J}/\text{pulse}$) into its lowest-energy MLCT are plotted in **Figure 3A**. Within the first picosecond, GSB and ESA peaks are observed at 390 and 540 nm, respectively, with the ESA red-shifting by $\sim 300\text{ cm}^{-1}$. Subsequently, a simultaneous decay of the whole difference spectrum occurs from 1.5 to 40 ps, as evidenced by isosbestic points at 479 and 583 nm. By 100 ps, the ground state of **1** has fully recovered. We note that there remains a small, flat, negative feature in the TA; this minor signal has no spectral features in common with the Ni(I) TA signal and is assigned to fine particulate scatter following the pump pulse (Supporting Information Section 1.5). Using global multiexponential fitting to quantify the relaxation dynamics, the TA spectrum of **1** is found to be well described by two exponentials with time constants of 0.3 and 10.9 ps, plus a small constant offset. Difference spectra for **5** following photoexcitation (800 nm, 1 $\mu\text{J}/\text{pulse}$) (**Figure 3B**) exhibit a GSB ~ 25 -fold larger than **1**, despite the comparable concentrations and pump power. The magnitude of the GSB signal of **5** is contrasted by its smaller ESA at 640 nm (**Figure 3B**, inset), which reveals an initial growth and blue shift ($\sim 380\text{ cm}^{-1}$) in the first picosecond, followed by a significant broadening and loss of intensity. Fifteen picoseconds after the excitation pulse, isosbestic points appear at 605 and 662 nm, signifying the recovery of the whole difference spectrum to the ground state. Three exponentials are required to fit to the data: the shortest time constant ($\tau_1 = 0.6\text{ ps}$) corresponds to the initial

growth of the spectrum, while the intermediate and longer time constants correspond to the blue-shift/spectral broadening ($\tau_2 = 5.6$ ps) and the relaxation of the difference spectrum to the ground state ($\tau_3 = 24.2$ ps), respectively.

Table 5.1. Lowest-energy MLCT absorption positions and relaxation time constants for all compounds in THF.

Compound	R ^b bpy / halide	MLCT λ_{max} (nm / cm ⁻¹)	τ_1 (ps) ^a	τ_2 (ps) ^a	τ_3 (ps)
1	<i>t</i> -Bu / Cl	660 / 15 150	0.3	-	10.9 ^c
1-Br	<i>t</i> -Bu / Br	653 / 15 310	0.5	-	13.9
1-I	<i>t</i> -Bu / I	640 / 15 625	0.4	1.2	15.4
2	Me / Cl	660 / 15 150	-	-	12
3	H / Cl	673 / 14 860	0.4	-	10
4	Ph / Cl	1175 ^b / 8510	0.5	5.2	22.3
5	MeO ₂ C / Cl	1178 / 8490	0.6	5.6	24.2 ^c
5'	MeO ₂ C / Cl	1178 / 8490	0.2	5.0	23.9
5-Br	MeO ₂ C / Br	1167 / 8570	0.4	5.6	23.8

^aIn the case of the quickly-relaxing compounds (**1–3**), we are only able to resolve one fast component (see Discussion Section below). ^bIdentified by using both the UV–vis–NIR absorption peak and the GSB feature in the TA spectrum (Figure S31). ^cLifetimes of 12.4 and 29.2 ps for **1** and **5** in toluene, respectively.

As discussed in Supporting Information Section 1.5, the difference in behavior between **1** and **5** is not the result of pumping different MLCT bands, solvent coordination, pump saturation, or multi-photon effects.

§5-2.2. Isolation and Characterization of Ni(I)(^{MeO₂C}bpy)Cl, **5'**

Given the disparate excited-state lifetimes for **1** and **5**, we sought their isolation and independent study. Unfortunately, this was not possible for **1**, as it was prone to dimerization, consistent with previous works.^{24,32} Compound **5**, however, does not dimerize at room temperature. Thus, we approached the synthesis of **5** photochemically. The parent Ni(II)(^{MeO₂C}bpy)(*o*-tolyl)Cl complex is only sparingly soluble in diethyl ether; we reasoned the more polar, three-coordinate Ni(I)(^{MeO₂C}bpy)Cl complex would be even less so. Indeed,

irradiation of the deep purple precursor rapidly afforded a blue precipitate, (**5'**), which was collected and analyzed.

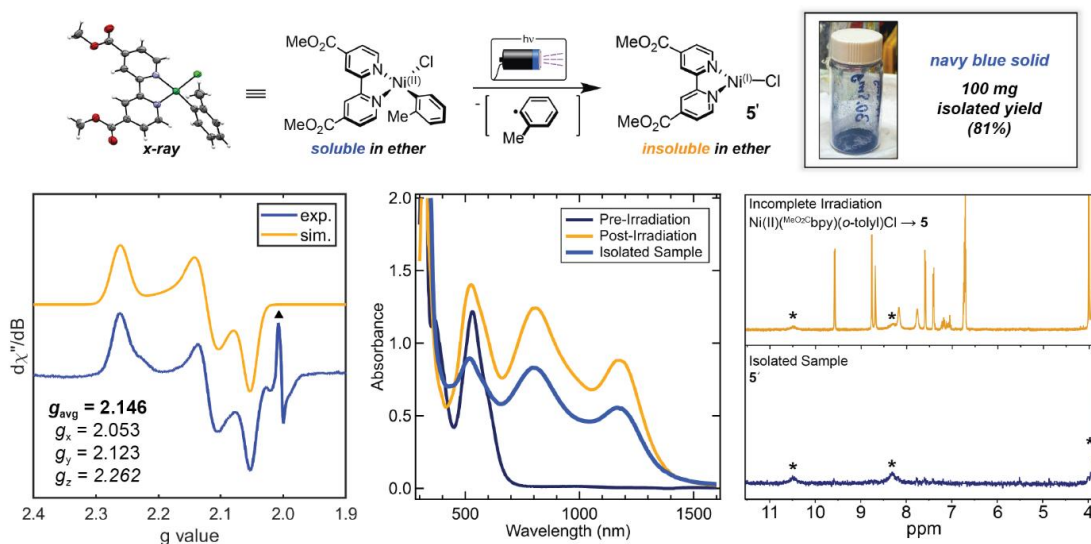


Figure 5.4. Photochemical generation and isolation of **5'**. *Top:* Synthetic route for the isolation of solid sample, **5'**. *Bottom left:* Powder X-band CW-EPR spectra of **5'** ($T = 5$ K; powder sample; frequency = 9.638 GHz; power = 2.2 mW; modulation amplitude = 8 G). Simulation parameters: $g_x = 2.053$, $g_y = 2.123$, $g_z = 2.262$, $g(\text{strain})_x = 0.025$, $g(\text{strain})_y = 0.035$, $g(\text{strain})_z = 0.033$. The sharp signal denoted with the triangle at $g = 2.003$ likely corresponds to a trace amount of an organic radical impurity (present in a $\sim 1:10\,000$ ratio relative to **5'** by spin standard measurements with TEMPO). *Bottom middle:* UV-vis-NIR spectra of **5** and **5'** in THF. *Bottom right:* ^1H NMR spectra (d_8 -THF) of a partially photolyzed sample of parent $\text{Ni}(\text{II})(\text{MeO}_2\text{C}\text{bpy})(o\text{-tolyl})\text{Cl}$ complex to generate **5** (starred peaks) compared to the isolated complex **5'**.

While small and darkly colored crystals were grown by slow evaporation of a concentrated solution of **5'** in either 2-methyl THF or toluene, they were highly air sensitive and too small for XRD analysis. We instead turned to EPR. Solid-state EPR at 5 K showed a broadened rhombic signal ($g_{\text{avg}} = 2.146$, $g_x = 2.053$, $g_y = 2.123$, $g_z = 2.262$; **Figure 4**). The g values agree well with previously reported frozen-glass solutions of Ni(I)-bpy complexes ($g_{\text{avg}} = 2.12\text{--}2.24$) and the predicted g_{avg} of the photogenerated species **5** (calculated $g_{\text{avg}} =$

2.187).^{24,35,36} Interestingly, IR spectra of solid samples exhibited a lowered carbonyl stretching frequency ($\nu_{\text{C=O}} = 1716 \text{ cm}^{-1}$) in **5'** relative to its precursor Ni(II) complex ($\nu_{\text{C=O}} = 1730 \text{ cm}^{-1}$),¹⁵ indicative of greater electron density in the bpy ligand π^* -orbital via increased back-bonding from Ni(I).

Redissolving **5'** in THF gave an identical UV–vis–NIR spectrum to **5** (**Figure 4**). Evans Method in deuterated benzene gave $\mu_{\text{eff}} = 1.9$ ($n_{\text{e}} = 1.2$), and EPR spectra of frozen solutions were consistent with a Ni(I) species (**Figures S1–S2**). Furthermore, comparison between the paramagnetic ^1H NMR spectra of *in situ* photogenerated **5** and isolated **5'** showed excellent agreement (**Figure 4**). Notably, the NMR does not match the related tetrameric sample, $[\text{Ni}(\text{I})(^{\text{EtO}_2\text{C}}\text{bpy})\text{Cl}]_4$, and we see no evidence of a redox equilibrium with Ni(0), as was seen previously for the tetramer (**Figure S55**).¹⁹ Addition of 2-bromobenzotrifluoride to a solution of **5'** gave rapid conversion to the oxidative addition product, $\text{Ni}(\text{II})(^{\text{MeO}_2\text{C}}\text{bpy})(o\text{-CF}_3\text{Ph})\text{Br}$, as confirmed by UV–vis–NIR and ^{19}F NMR spectra of the independently synthesized Ni(II) complex (**Figures S3–S4**). Finally, TA measurements on **5'** gave signals identical to **5** (**Figures S28–S29**). Altogether, **5'** is most likely monomeric $\text{Ni}(\text{I})(^{\text{MeO}_2\text{C}}\text{bpy})\text{Cl}$.

§5-3. Discussion

Given their broad absorption cross-sections and relevance for photoredox reactions, Ni(I)–bpy halide complexes are important targets for fundamental and applied photophysical investigations. Herein, we have studied a library of Ni(I)–bpy complexes, **1–5**, using ultrafast TA spectroscopy. Following excitation, relaxation proceeds through a rapid, multistep process accompanied by red- or blue-shifting of peaks and spectral broadening, characteristic of internal conversion through intermediate MLCT manifolds, vibrational cooling, and/or solvation effects.^{14,38,39,41–43} Components t_1 and t_2 are therefore assigned to relaxation into the lowest-energy MLCT manifold (**Figure 5A**). For the fastest-relaxing compounds (**1–3**), we are unable to separately resolve these components. Subsequently, ESA and GSB features recover on a longer time scale with clearly defined isosbestic points; the presence of significant ESA in the visible at all times suggests persistent reduction of the bpy ligand in an MLCT state.¹⁴ The kinetics for ground-state reformation are independent of pump

wavelength, further indicating the rate-limiting step involves nonradiative relaxation out of the lowest-energy MLCT (τ_3 in **Table 1, Figure 5A**). Overall charge transfer lifetimes span ~10–30 ps, comparable to some of the longest reported Ni(II) MLCT lifetimes only obtained through the synthetic incorporation of significant steric constraints.^{38,40} The simple three-coordinate structures of these Ni(I) intermediates may lead to limited vibrational degrees of freedom to relax to the ground state, possibly representing an alternative approach to prolonging excited-state lifetimes. Interestingly, the values of τ_3 for the eight complexes also fall into two clear classes (exemplified by **1** and **5**).

Nonradiative decay can be examined by the approach of Englman and Jortner,⁴⁴ which relates the decay rate constant ($k = \tau_3^{-1}$) and the energy gap between fully relaxed excited and ground states, ΔG° . This model considers two limiting cases of the coupling between molecular vibrations and the decay rate, namely weak or strong coupling.

The weak coupling limit applies to excited states with a small displacement from the ground state along the vibrational coordinate. This regime is found to approximately result in the energy-gap law through the interaction of the excited state with the highest vibrational mode(s) of the ground state; the decay rate constant is linearly governed by the energy gap between the relaxed ground and excited state, i.e., $\ln(k) \propto -\Delta G^\circ$. A full discussion of the weak coupling limit is given in Supporting Information Section 1.6.

In the strong coupling limit, the displacement between the ground- and excited-state potential energy surfaces is large, making their intersection thermally accessible (**Figure 5A**). This activation energy gives rise to a Gaussian dependence on the energy gap, as in Marcus theory for intermolecular electron transfer.^{45–48} For small energy gaps, an increase in ΔG° leads to a decrease in the kinetic barrier, ΔG^\ddagger , for back-electron transfer (e.g., the relaxation from the MLCT to the ground state). Accordingly, the decay rate constant increases. For large energy gaps, ΔG° and ΔG^\ddagger scale together; a larger energy gap corresponds to a reduced decay rate constant, akin to the Marcus inverted region. These two regimes of strong coupling behavior can be described by equation 1,

$$\ln(k) = \ln(A) - \frac{(\Delta G^\circ + \lambda)^2}{2\lambda\langle\hbar\omega\rangle}, \quad (5.1)$$

where λ is the reorganization energy, $\langle\hbar\omega\rangle$ the average vibrational energy, and A contains various transition-dependent parameters. Substituting $\langle\hbar\omega\rangle = 2k_B T$, where k_B is the Boltzmann constant and T is the temperature, recovers the well-known Marcus equation. This difference in denominator follows from their derivations in the classical (Marcus) and quantum limits (strong coupling). Notably, a plot of $\ln(k)$ versus $-\Delta G^\circ$ results in a parabolic shape, which captures both the Marcus normal and inverted regimes.^{49,50}

The value of the energy gap is often not easily accessible experimentally. However, λ is defined as the difference between the vertical transition energy (E_{MLCT}) and ΔG° , enabling the substitution of the energy gap for the more experimentally accessible vertical transition energy, $\Delta G^\circ = \lambda - E_{\text{MLCT}}$ ⁴⁴

$$\ln(k) = \ln(A) - \frac{(E_{\text{MLCT}} - 2\lambda)^2}{2\lambda\langle\hbar\omega\rangle}. \quad (5.2)$$

By considering the coupling of vibrations to intermolecular electron transfer, Jortner and Ulstrup developed an extended version of Marcus theory that has also seen success in modeling intramolecular electron transfer.⁵¹⁻⁵⁷ Aside from vibrational considerations, the major difference of this model is the splitting of the reorganization energy into contributions from the solvent (λ_S) and vibrational modes (λ_V), or $\lambda = \lambda_S + \lambda_V$. Making the approximation that one dominant vibronic mode (or a representative average mode) with energy $\hbar\omega$ couples to the transfer, this model simplifies to

$$k = A' \sum_{n=0}^{\infty} \frac{e^S S^n}{n!} \exp\left(-\frac{(E_{\text{MLCT}} - 2\lambda_S - \lambda_V - n\hbar\omega)^2}{4\lambda_S k_B T}\right). \quad (5.3)$$

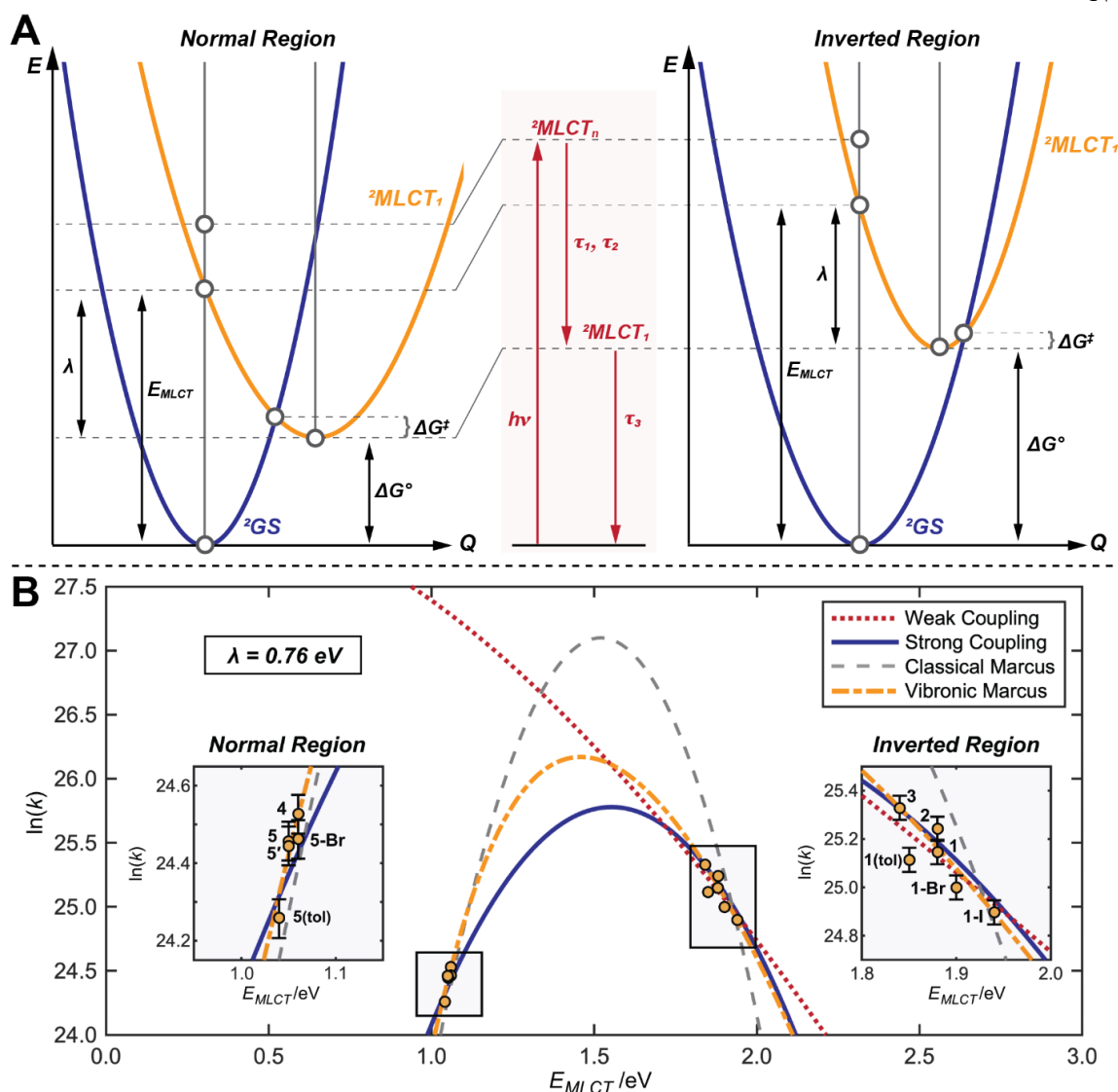


Figure 5.5. Modeling excited state relaxation dynamics of Ni(I) compounds. (A) PESs and Jablonski diagram (in red) demonstrating the relaxation pathways within the strong coupling limit, which qualitatively correspond to the Marcus normal (left) and inverted (right) regimes along the nuclear coordinate, Q . (B) A plot of the experimentally determined rate constants for relaxation from the lowest-energy MLCT back to the ground state as a function of the MLCT vertical transition energy (values taken from **Table 1**). The data reveal a clear parabolic shape and are fit to the four models discussed in the text, with vibronic Marcus giving the best fit. Error bars were extrapolated from the standard deviation of replicate measurements (see Supporting Information Section 1.1). Data were collected in THF; complexes **1** and **5** were also measured in toluene; $1 \text{ eV} = 8065 \text{ cm}^{-1}$.

Here A' is a constant defined in equation S6 and $S = \lambda_V/\hbar\omega$. We term this form of Jortner and Ulstrup's model the vibronic Marcus model to distinguish it from the simpler, classically derived Marcus theory.

To evaluate which models are most representative of the relaxation kinetics of **1–5**, we plot $\ln(k)$ against E_{MLCT} (**Figure 5B**). Two clear clusters are visible; while **1–3** appear to follow the energy gap law, **4–5** exhibit the opposite behavior. The division of the excited-state dynamics into two clusters cannot be explained solely within the weak coupling regime, which predicts a single monotonic relationship over all complexes. This is highlighted by the fit to the weak coupling model (equation S3) shown in **Figure 5B**.

On the other hand, the strong coupling and Marcus models present a simple alternative to describe the two classes of relaxation kinetics. Using equation 2 with A , λ , and $\langle\hbar\omega\rangle$ as variables, the strong coupling fit shown in **Figure 5B** is achieved. The model shows excellent agreement with the data; **1–3** and **4–5** lie in the inverted and normal regions, respectively. We find $\langle\hbar\omega\rangle = 0.13(7)$ eV and $\lambda = 0.77(3)$ eV. Perhaps coincidentally, $\langle\hbar\omega\rangle$ is comparable to the value predicted by DFT (0.14 eV, Table S4). The reorganization energy is of comparable magnitude to similar metal-to-bpy charge transfer processes.^{50,58,59} Alternatively, fitting to the classical Marcus model also gives a reasonable, but marginally worse, fit to the data with λ varying no more than the error of the original fit.

The best fit to the data is achieved by the vibronic Marcus model (equation 3), giving $\lambda = \lambda_S + \lambda_V = 0.76$ eV. This can also be roughly approximated from Gaussian fits to the widths of MLCT transitions in the absorption spectrum, which results in $\lambda \sim 0.5$ eV, in fair agreement (**Figure S10**).^{53,60} The dominant vibrational mode is fit as $\hbar\omega = 0.21$ eV. Previous studies have maintained that intramolecular charge transfer typically couples to vibrations of the ligand backbone, such as bpy breathing modes in polypyridyl-Fe complexes.^{52–54,61} These modes are predicted by DFT at ~ 0.2 eV for **1–5**, agreeing with the vibronic Marcus fit and these previous studies. The solvent and vibrational contributions to the reorganization energy are found by the fit to be $\lambda_S = 0.54$ eV and $\lambda_V = 0.22$ eV,

respectively. These individual contributions are hard to measure experimentally, but λ_V can be estimated from TD-DFT (**Figure S44**). In **1** and **5**, λ_V is ~ 0.18 and ~ 0.33 eV, respectively (average value of 0.26 eV), which is close to the value obtained from the vibronic Marcus model. We note, however, that DFT is found to have limited applicability in these systems (Supporting Information Section 2.5) and reported values of λ_V vary greatly.^{52,54,55,61} Nonetheless, the total reorganization energy found by the vibronic Marcus fit is consistent with both the classical Marcus and strong coupling models.

§5-4. Conclusions

Herein, we have examined a library of Ni(I)–bpy halide complexes, including an isolable species accessible through a simple photochemical route. To the best of our knowledge, this research represents the first ultrafast TA spectroscopic characterization of any Ni(I) complex. As such, it is also the first ultrafast characterization of a Ni(I) intermediate in metallaphotoredox catalysis. Ni(I)–bpy halide ²MLCT lifetimes are < 50 ps, prohibiting diffusion-controlled bimolecular chemistry. Varying the bpy substituents significantly influences the excited-state relaxation dynamics, with kinetics that span the Marcus normal and inverted regimes.

§5-5. References

- (1) Chan, A. Y.; Perry, I. B.; Bissonnette, N. B.; Buksh, B. F.; Edwards, G. A.; Frye, L. I.; Garry, O. L.; Lavagnino, M. N.; Li, B. X.; Liang, Y.; Mao, E.; Millet, A.; Oakley, J. V.; Reed, N. L.; Sakai, H. A.; Seath, C. P.; MacMillan, D. W. C. Metallaphotoredox: The Merger of Photoredox and Transition Metal Catalysis. *Chem. Rev.* **2021**. <https://doi.org/10.1021/acs.chemrev.1c00383>.
- (2) Tasker, S. Z.; Standley, E. A.; Jamison, T. F. Recent Advances in Homogeneous Nickel Catalysis. *Nature* **2014**, *509* (7500), 299–309. <https://doi.org/10.1038/nature13274>.
- (3) Terrett, J. A.; Cuthbertson, J. D.; Shurtleff, V. W.; MacMillan, D. W. C. Switching on Elusive Organometallic Mechanisms with Photoredox Catalysis. *Nature* **2015**, *524* (7565), 330–334. <https://doi.org/10.1038/nature14875>.
- (4) Twilton, J.; Le, C.; Zhang, P.; Shaw, M. H.; Evans, R. W.; MacMillan, D. W. C. The Merger of Transition Metal and Photocatalysis. *Nat. Rev. Chem.* **2017**, *1* (7), 0052. <https://doi.org/10.1038/s41570-017-0052>.
- (5) Welin, E. R.; Le, C.; Arias-Rotondo, D. M.; McCusker, J. K.; MacMillan, D. W. C. Photosensitized, Energy Transfer-Mediated Organometallic Catalysis through Electronically Excited Nickel(II). *Science* **2017**, *355* (6323), 380–385. <https://doi.org/10.1126/science.aal2490>.
- (6) Palkowitz, M. D.; Emmanuel, M. A.; Oderinde, M. S. A Paradigm Shift in Catalysis: Electro- and Photomediated Nickel-Catalyzed Cross-Coupling Reactions. *Acc. Chem. Res.* **2023**. <https://doi.org/10.1021/acs.accounts.3c00479>.
- (7) Kariofillis, S. K.; Doyle, A. G. Synthetic and Mechanistic Implications of Chlorine Photoelimination in Nickel/Photoredox C(sp³)-H Cross-Coupling. *Acc. Chem. Res.* **2021**, *54* (4), 988–1000. <https://doi.org/10.1021/acs.accounts.0c00694>.
- (8) Wenger, O. S. Photoactive Nickel Complexes in Cross-Coupling Catalysis. *Chem. Eur. J.* **2021**, *27* (7), 2270–2278. <https://doi.org/10.1002/chem.202003974>.
- (9) McAtee, R. C.; McClain, E. J.; Stephenson, C. R. J. Illuminating Photoredox Catalysis. *Trends Chem.* **2019**, *1* (1), 111–125. <https://doi.org/10.1016/j.trechm.2019.01.008>.
- (10) Taylor, O. R.; Saucedo, P. J.; Bahamonde, A. Leveraging the Redox Promiscuity of Nickel To Catalyze C–N Coupling Reactions. *J. Org. Chem.* **2024**. <https://doi.org/10.1021/acs.joc.3c02353>.

- (11) Yuan, M.; Gutierrez, O. Mechanisms, Challenges, and Opportunities of Dual Ni/Photoredox-Catalyzed C(sp²)-C(sp³) Cross-Couplings. *WIREs Comput. Mol. Sci.* **2022**, *12* (3), e1573. <https://doi.org/10.1002/wcms.1573>.
- (12) Larsen, C. B.; Wenger, O. S. Photoredox Catalysis with Metal Complexes Made from Earth-Abundant Elements. *Chem. Eur. J.* **2018**, *24* (9), 2039–2058. <https://doi.org/10.1002/chem.201703602>.
- (13) Cagan, D. A.; Stroschio, G. D.; Cusumano, A. Q.; Hadt, R. G. Multireference Description of Nickel–Aryl Homolytic Bond Dissociation Processes in Photoredox Catalysis. *J. Phys. Chem. A* **2020**, *124* (48), 9915–9922. <https://doi.org/10.1021/acs.jpca.0c08646>.
- (14) Ting, S. I.; Garakyaraghi, S.; Taliaferro, C. M.; Shields, B. J.; Scholes, G. D.; Castellano, F. N.; Doyle, A. G. ³d-d Excited States of Ni(II) Complexes Relevant to Photoredox Catalysis: Spectroscopic Identification and Mechanistic Implications. *J. Am. Chem. Soc.* **2020**, *142* (12), 5800–5810. <https://doi.org/10.1021/jacs.0c00781>.
- (15) Cagan, D. A.; Bím, D.; Silva, B.; Kazmierczak, N. P.; McNicholas, B. J.; Hadt, R. G. Elucidating the Mechanism of Excited-State Bond Homolysis in Nickel–Bipyridine Photoredox Catalysts. *J. Am. Chem. Soc.* **2022**, *144* (14), 6516–6531. <https://doi.org/10.1021/jacs.2c01356>.
- (16) Li, R.; Yang, C.-X.; Niu, B.-H.; Li, L.-J.; Ma, J.-M.; Li, Z.-L.; Jiang, H.; Cheng, W.-M. Visible Light-Induced Ni-Catalyzed C–Heteroatom Cross-Coupling of Aryl Halides via LMCT with DBU to Access a Ni(I)/Ni(III) Cycle. *Org. Chem. Front.* **2022**, *9* (14), 3847–3853. <https://doi.org/10.1039/D2QO00607C>.
- (17) Yang, L.; Lu, H.-H.; Lai, C.-H.; Li, G.; Zhang, W.; Cao, R.; Liu, F.; Wang, C.; Xiao, J.; Xue, D. Light-Promoted Nickel Catalysis: Etherification of Aryl Electrophiles with Alcohols Catalyzed by a Ni^{II}-Aryl Complex. *Angew. Chem. Int. Ed.* **2020**, *59* (31), 12714–12719. <https://doi.org/10.1002/anie.202003359>.
- (18) Shields, B. J.; Kudisch, B.; Scholes, G. D.; Doyle, A. G. Long-Lived Charge-Transfer States of Nickel(II) Aryl Halide Complexes Facilitate Bimolecular Photoinduced Electron Transfer. *J. Am. Chem. Soc.* **2018**, *140* (8), 3035–3039. <https://doi.org/10.1021/jacs.7b13281>.
- (19) Ting, S. I.; Williams, W. L.; Doyle, A. G. Oxidative Addition of Aryl Halides to a Ni(I)-Bipyridine Complex. *J. Am. Chem. Soc.* **2022**, *144* (12), 5575–5582. <https://doi.org/10.1021/jacs.2c00462>.

- (20) Tang, T.; Jones, E.; Wild, T.; Hazra, A.; Minter, S. D.; Sigman, M. S. Investigating Oxidative Addition Mechanisms of Allylic Electrophiles with Low-Valent Ni/Co Catalysts Using Electroanalytical and Data Science Techniques. *J. Am. Chem. Soc.* **2022**, *144* (43), 20056–20066. <https://doi.org/10.1021/jacs.2c09120>.
- (21) Till, N. A.; Oh, S.; MacMillan, D. W. C.; Bird, M. J. The Application of Pulse Radiolysis to the Study of Ni(I) Intermediates in Ni-Catalyzed Cross-Coupling Reactions. *J. Am. Chem. Soc.* **2021**, *143* (25), 9332–9337. <https://doi.org/10.1021/jacs.1c04652>.
- (22) Sun, R.; Qin, Y.; Rucolo, S.; Schnedermann, C.; Costentin, C.; Nocera, D. G. Elucidation of a Redox-Mediated Reaction Cycle for Nickel-Catalyzed Cross Coupling. *J. Am. Chem. Soc.* **2019**, *141* (1), 89–93. <https://doi.org/10.1021/jacs.8b11262>.
- (23) Goldschmid, S. L.; Soon Tay, N. E.; Joe, C. L.; Lainhart, B. C.; Sherwood, T. C.; Simmons, E. M.; Sezen-Edmonds, M.; Rovis, T. Overcoming Photochemical Limitations in Metallaphotoredox Catalysis: Red-Light-Driven C–N Cross-Coupling. *J. Am. Chem. Soc.* **2022**, *144* (49), 22409–22415. <https://doi.org/10.1021/jacs.2c09745>.
- (24) Cagan, D. A.; Bím, D.; McNicholas, B. J.; Kazmierczak, N. P.; Oyala, P. H.; Hadt, R. G. Photogenerated Ni(I)–Bipyridine Halide Complexes: Structure–Function Relationships for Competitive C(sp²)–Cl Oxidative Addition and Dimerization Reactivity Pathways. *Inorg. Chem.* **2023**, *62* (24), 9538–9551. <https://doi.org/10.1021/acs.inorgchem.3c00917>.
- (25) Qin, Y.; Sun, R.; Gianoulis, N. P.; Nocera, D. G. Photoredox Nickel-Catalyzed C–S Cross-Coupling: Mechanism, Kinetics, and Generalization. *J. Am. Chem. Soc.* **2021**, *143* (4), 2005–2015. <https://doi.org/10.1021/jacs.0c11937>.
- (26) Till, N. A.; Tian, L.; Dong, Z.; Scholes, G. D.; MacMillan, D. W. C. Mechanistic Analysis of Metallaphotoredox C–N Coupling: Photocatalysis Initiates and Perpetuates Ni(I)/Ni(III) Coupling Activity. *J. Am. Chem. Soc.* **2020**, *142* (37), 15830–15841. <https://doi.org/10.1021/jacs.0c05901>.
- (27) Chrisman, C. H.; Kudisch, M.; Puffer, K. O.; Stewart, T. K.; Lamb, Y. M. L.; Lim, C.-H.; Escobar, R.; Thordarson, P.; Johannes, J. W.; Miyake, G. M. Halide Noninnocence and Direct Photoreduction of Ni(II) Enables Coupling of Aryl Chlorides in Dual Catalytic, Carbon–Heteroatom Bond-Forming Reactions. *J. Am. Chem. Soc.* **2023**, *145* (22), 12293–12304. <https://doi.org/10.1021/jacs.3c02784>.
- (28) Lin, C.-Y.; Power, P. P. Complexes of Ni(I): A “Rare” Oxidation State of Growing Importance. *Chem. Soc. Rev.* **2017**, *46* (17), 5347–5399. <https://doi.org/10.1039/C7CS00216E>.

- (29) Li, Y.; Zou, L.; Bai, R.; Lan, Y. Ni(I)–Ni(III) vs. Ni(II)–Ni(IV): Mechanistic Study of Ni-Catalyzed Alkylation of Benzamides with Alkyl Halides. *Org. Chem. Front.* **2018**, *5* (4), 615–622. <https://doi.org/10.1039/C7QO00850C>.
- (30) Shin, J.; Lee, J.; Suh, J.-M.; Park, K. Ligand-Field Transition-Induced C–S Bond Formation from Nickelacycles. *Chem. Sci.* **2021**, *12* (48), 15908–15915. <https://doi.org/10.1039/D1SC05113J>.
- (31) Ghosh, I.; Shlapakov, N.; Karl, T. A.; Düker, J.; Nikitin, M.; Burykina, J. V.; Ananikov, V. P.; König, B. General Cross-Coupling Reactions with Adaptive Dynamic Homogeneous Catalysis. *Nature* **2023**, *619* (7968), 87–93. <https://doi.org/10.1038/s41586-023-06087-4>.
- (32) Mohadjer Beromi, M.; Brudvig, G. W.; Hazari, N.; Lant, H. M. C.; Mercado, B. Q. Synthesis and Reactivity of Paramagnetic Nickel Polypyridyl Complexes Relevant to C(sp²)–C(sp³) Coupling Reactions. *Angew. Chem. Int. Ed.* **2019**, *58* (18), 6094–6098. <https://doi.org/10.1002/anie.201901866>.
- (33) Na, H.; Mirica, L. M. Deciphering the Mechanism of the Ni-Photocatalyzed C–O Cross-Coupling Reaction Using a Tridentate Pyridinophane Ligand. *Nat. Commun.* **2022**, *13* (1), 1313. <https://doi.org/10.1038/s41467-022-28948-8>.
- (34) Huang, H.; Alvarez-Hernández, J. L.; Hazari, N.; Mercado, B. Q.; Uehling, M. R. Effect of 6,6'-Substituents on Bipyridine-Ligated Ni Catalysts for Cross-Electrophile Coupling. *ACS Catal.* **2024**, 6897–6914. <https://doi.org/10.1021/acscatal.4c00827>.
- (35) Newman-Stonebraker, S. H.; Raab, T. J.; Roshandel, H.; Doyle, A. G. Synthesis of Nickel(I)–Bromide Complexes via Oxidation and Ligand Displacement: Evaluation of Ligand Effects on Speciation and Reactivity. *J. Am. Chem. Soc.* **2023**, *145* (35), 19368–19377. <https://doi.org/10.1021/jacs.3c06233>.
- (36) Dawson, G. A.; Lin, Q.; Neary, M. C.; Diao, T. Ligand Redox Activity of Organonickel Radical Complexes Governed by the Geometry. *J. Am. Chem. Soc.* **2023**. <https://doi.org/10.1021/jacs.3c07031>.
- (37) Tang, T.; Hazra, A.; Min, D. S.; Williams, W. L.; Jones, E.; Doyle, A. G.; Sigman, M. S. Interrogating the Mechanistic Features of Ni(I)-Mediated Aryl Iodide Oxidative Addition Using Electroanalytical and Statistical Modeling Techniques. *J. Am. Chem. Soc.* **2023**, *145* (15), 8689–8699. <https://doi.org/10.1021/jacs.3c01726>.

- (38) Ogawa, T.; Sinha, N.; Pfund, B.; Prescimone, A.; Wenger, O. S. Molecular Design Principles to Elongate the Metal-to-Ligand Charge Transfer Excited-State Lifetimes of Square-Planar Nickel(II) Complexes. *J. Am. Chem. Soc.* **2022**, *144* (48), 21948–21960. <https://doi.org/10.1021/jacs.2c08838>.
- (39) Ogawa, T.; Wenger, O. S. Nickel(II) Analogues of Phosphorescent Platinum(II) Complexes with Picosecond Excited-State Decay. *Angew. Chem. Int. Ed.* **2023**, *62* (46), e202312851. <https://doi.org/10.1002/anie.202312851>.
- (40) Bím, D.; Luedecke, K. M.; Cagan, D. A.; Hadt, R. G. Light Activation and Photophysics of a Structurally Constrained Nickel(II)–Bipyridine Aryl Halide Complex. *Inorg. Chem.* **2024**, *63* (9), 4120–4131. <https://doi.org/10.1021/acs.inorgchem.3c03822>.
- (41) Yu, H.-Z.; Baskin, J. S.; Zewail, A. H. Ultrafast Dynamics of Porphyrins in the Condensed Phase: II. Zinc Tetraphenylporphyrin. *J. Phys. Chem. A* **2002**, *106* (42), 9845–9854. <https://doi.org/10.1021/jp0203999>.
- (42) Tan, J.; Zhang, J.; Li, C.; Luo, Y.; Ye, S. Ultrafast Energy Relaxation Dynamics of Amide I Vibrations Coupled with Protein-Bound Water Molecules. *Nat. Commun.* **2019**, *10* (1), 1010. <https://doi.org/10.1038/s41467-019-08899-3>.
- (43) Monni, R.; Capano, G.; Auböck, G.; Gray, H. B.; Vlček, A.; Tavernelli, I.; Chergui, M. Vibrational Coherence Transfer in the Ultrafast Intersystem Crossing of a Diplatinum Complex in Solution. *Proc. Natl. Acad. Sci.* **2018**, *115* (28), E6396–E6403. <https://doi.org/10.1073/pnas.1719899115>.
- (44) Englman, R.; Jortner, J. The Energy Gap Law for Radiationless Transitions in Large Molecules. *Mol. Phys.* **1970**, *18* (2), 145–164. <https://doi.org/10.1080/00268977000100171>.
- (45) Marcus, R. A. Chemical and Electrochemical Electron-Transfer Theory. *Annu. Rev. Phys. Chem.* **1964**, *15* (1), 155–196. <https://doi.org/10.1146/annurev.pc.15.100164.001103>.
- (46) Marcus, R. A. Theoretical Relations among Rate Constants, Barriers, and Broensted Slopes of Chemical Reactions. *J. Phys. Chem.* **1968**, *72* (3), 891–899. <https://doi.org/10.1021/j100849a019>.
- (47) Marcus, R. A.; Sutin, N. Electron Transfers in Chemistry and Biology. *Biochim. Biophys. Acta BBA—Rev. Bioenerg.* **1985**, *811* (3), 265–322. [https://doi.org/10.1016/0304-4173\(85\)90014-X](https://doi.org/10.1016/0304-4173(85)90014-X).

- (48) Marcus, R. A. On the Theory of Oxidation-Reduction Reactions Involving Electron Transfer. I. *J. Chem. Phys.* **2004**, *24* (5), 966–978. <https://doi.org/10.1063/1.1742723>.
- (49) Fox, L. S.; Kozik, M.; Winkler, J. R.; Gray, H. B. Gaussian Free-Energy Dependence of Electron-Transfer Rates in Iridium Complexes. *Science* **1990**, *247* (4946), 1069–1071. <https://doi.org/10.1126/science.247.4946.1069>.
- (50) Chan, A. Y.; Ghosh, A.; Yarranton, J. T.; Twilton, J.; Jin, J.; Arias-Rotondo, D. M.; Sakai, H. A.; McCusker, J. K.; MacMillan, D. W. C. Exploiting the Marcus Inverted Region for First-Row Transition Metal-Based Photoredox Catalysis. *Science* **2023**, *382* (6667), 191–197. <https://doi.org/10.1126/science.adj0612>.
- (51) Ulstrup, J.; Jortner, J. The Effect of Intramolecular Quantum Modes on Free Energy Relationships for Electron Transfer Reactions. *J. Chem. Phys.* **1975**, *63* (10), 4358–4368. <https://doi.org/10.1063/1.431152>.
- (52) Closs, G. L.; Miller, J. R. Intramolecular Long-Distance Electron Transfer in Organic Molecules. *Science* **1988**, *240* (4851), 440–447. <https://doi.org/10.1126/science.240.4851.440>.
- (53) Kunnus, K.; Li, L.; Titus, C. J.; Lee, S. J.; Reinhard, M. E.; Koroidov, S.; Kjær, K. S.; Hong, K.; Ledbetter, K.; Doriese, W. B.; O’Neil, G. C.; Swetz, D. S.; Ullom, J. N.; Li, D.; Irwin, K.; Nordlund, D.; Cordones, A. A.; Gaffney, K. J. Chemical Control of Competing Electron Transfer Pathways in Iron Tetracyano-Polypyridyl Photosensitizers. *Chem. Sci.* **2020**, *11* (17), 4360–4373. <https://doi.org/10.1039/C9SC06272F>.
- (54) Mataga, N.; Chosrowjan, H.; Shibata, Y.; Yoshida, N.; Osuka, A.; Kikuzawa, T.; Okada, T. First Unequivocal Observation of the Whole Bell-Shaped Energy Gap Law in Intramolecular Charge Separation from S₂ Excited State of Directly Linked Porphyrin–Imide Dyads and Its Solvent-Polarity Dependencies. *J. Am. Chem. Soc.* **2001**, *123* (49), 12422–12423. <https://doi.org/10.1021/ja010865s>.
- (55) Asahi, T.; Ohkohchi, M.; Matsusaka, R.; Mataga, N.; Zhang, R. P.; Osuka, A.; Maruyama, K. Intramolecular Photoinduced Charge Separation and Charge Recombination of the Product Ion Pair States of a Series of Fixed-Distance Dyads of Porphyrins and Quinones: Energy Gap and Temperature Dependences of the Rate Constants. *J. Am. Chem. Soc.* **1993**, *115* (13), 5665–5674. <https://doi.org/10.1021/ja00066a036>.

- (56) Miller, J. R.; Calcaterra, L. T.; Closs, G. L. Intramolecular Long-Distance Electron Transfer in Radical Anions. The Effects of Free Energy and Solvent on the Reaction Rates. *J. Am. Chem. Soc.* **1984**, *106* (10), 3047–3049. <https://doi.org/10.1021/ja00322a058>.
- (57) Heitele, H.; Poellinger, F.; Haerberle, T.; Michel-Beyerle, M. E.; Staab, H. A. Energy Gap and Temperature Dependence of Photoinduced Electron Transfer in Porphyrin-Quinone Cyclophanes. *J. Phys. Chem.* **1994**, *98* (30), 7402–7410. <https://doi.org/10.1021/j100081a028>.
- (58) Endicott, J. F.; Jamal Uddin, M. Correlations of Optical and Thermal Charge Transfer. *Coord. Chem. Rev.* **2001**, *219–221*, 687–712. [https://doi.org/10.1016/S0010-8545\(01\)00363-0](https://doi.org/10.1016/S0010-8545(01)00363-0).
- (59) Carey, M. C.; Adelman, S. L.; McCusker, J. K. Insights into the Excited State Dynamics of Fe(II) Polypyridyl Complexes from Variable-Temperature Ultrafast Spectroscopy. *Chem. Sci.* **2018**, *10* (1), 134–144. <https://doi.org/10.1039/C8SC04025G>.
- (60) Tominaga, K.; Kliner, D. A. V.; Johnson, A. E.; Levinger, N. E.; Barbara, P. F. Femtosecond Experiments and Absolute Rate Calculations on Intervalence Electron Transfer of Mixed-valence Compounds. *J. Chem. Phys.* **1993**, *98* (2), 1228–1243. <https://doi.org/10.1063/1.464344>.
- (61) Häberle, T.; Hirsch, J.; Pöllinger, F.; Heitele, H.; Michel-Beyerle, M. E.; Anders, C.; Döhling, A.; Krieger, C.; Rückemann, A.; Staab, H. A. Ultrafast Charge Separation and Driving Force Dependence in Cyclophane-Bridged Zn–Porphyrin–Quinone Molecules. *J. Phys. Chem.* **1996**, *100* (46), 18269–18274. <https://doi.org/10.1021/jp960423g>.

Appendix A

Supporting Information for Chapter 2: Multireference Description Of Nickel–Aryl Homolytic Bond Dissociation Processes in Photoredox Catalysis

The Supporting Information is available free of charge at <https://pubs.acs.org/doi/10.1021/acs.jpca.0c08646> and includes the tabulation of TDDFT and CASSCF/QD-NEVPT2 energetics; tabulation of CASSCF/QD-NEVPT2 CI vectors; plotted data for **2** analogous to data for **1** presented in the manuscript; and DFT-optimized structures.

A p p e n d i x B

Supporting Information for Chapter 3: Elucidating The Mechanism of Excited-State Bond Homolysis in Nickel–Bipyridine Photoredox Catalysts

The Supporting Information is available free of charge at <https://pubs.acs.org/doi/10.1021/jacs.2c01356> and includes the experimental and computational methods, UV–vis/photochemical data, X-ray crystallography, NMR spectra, calculated spectra/properties, global analysis modeling, and additional comments.

Appendix C

Supporting Information for Chapter 4: Photogenerated Ni(I)–Bipyridine Halide Complexes: Structure-Function Relationships for Competitive C(sp²)–Cl Oxidative Addition and Dimerization Reactivity Pathways

The Supporting Information is available free of charge at <https://pubs.acs.org/doi/10.1021/acs.inorgchem.3c00917> and includes the experimental and computational methods; UV–vis/photochemical data; NMR and EPR spectra; calculated spectra/properties; additional comments; and DFT-optimized XYZ files of all structures.

A p p e n d i x D

Supporting Information for Chapter 5: Ultrafast Photophysics of
Ni(I)–Bipyridine Halide Complexes: Spanning the Marcus Normal and
Inverted Regimes

S1. Experimental Section.

S1.1. General Considerations.

All purchased compounds were used as received unless otherwise noted. Bis-(1,5-cyclooctadiene) nickel(0) was purchased from Strem Chemicals. Ligands N,N,N',N'-tetramethyl ethylenediamine (TMEDA), 4,4'-di-*tert*-butyl-2,2'-bipyridine (^{*t*}-Bu₂bpy), 4,4'-dimethyl-2,2'-bipyridine (^{Me}bpy), 2,2'-bipyridine (bpy), 4,4'-diphenyl-2,2'-bipyridine (^{Ph}bpy), and dimethyl-2,2'-bipyridine-4,4'-dicarboxylate (^{MeO₂C}bpy) were purchased from Sigma-Aldrich. Aryl halide compounds, 2-*chloro*-toluene, 2-*bromo*-toluene, 2-*iodo*-toluene, and 2-*bromo*- α,α,α -trifluorotoluene were also obtained from Sigma-Aldrich. Solids were dried under vacuum and brought into a nitrogen-atmosphere glove box; liquids (including aryl halides) were sparged (N₂) and degassed via freeze-pump-thaw techniques, brought into the glove box, and stored over 3 Å molecular sieves. All solvents were air-free and collected from a solvent purification system (SPS), then stored in the glove box over 3 Å molecular sieves in amber jars. Tetrahydrofuran (THF), 2-methyl tetrahydrofuran (2-MeTHF), and *d*₈-tetrahydrofuran (*d*₈-THF) were inhibitor-free. All deuterated solvents were purchased from Cambridge Isotope Laboratories, Inc. and also dried and stored over activated 3 Å molecular sieves in a nitrogen-filled glove box for at least three days before use. All synthesized compounds were made using air-free Schlenk techniques or made in the glove box. All synthesized complexes are considered air and moisture sensitive. Light sensitivity was also seen even in the solid state if left exposed for extended time.

UV-vis spectra of the complexes were obtained on a Varian Cary 500 spectrophotometer or a StellarNet, Inc., Black Comet UV-vis spectrophotometer. Starna Cells 6-Q 2- or 10-mm path length cuvettes fitted with air-tight seals were used. Proton nuclear magnetic resonance (¹H NMR) and fluorine nuclear magnetic resonance (¹⁹F NMR) spectra were recorded on a 400 MHz Varian Spectrometer with broadband auto-tune OneProbe. ¹⁹F NMR were externally referenced to neat fluorobenzene ($\delta = -113.15$ ppm). ¹³C NMR spectra were collected on a Bruker AV-III HD 400 MHz spectrometer and were ¹H decoupled. Chemical shifts are reported in parts per million (δ in ppm, s: singlet, d: doublet, t: triplet, m: multiplet) and are referenced to residual solvent signal (THF-*d*₈ = 3.58 ppm). NMR samples were prepared in the glove box into Norell J-Young tubes. IR measurements were performed on a Bruker Alpha Platinum ATR spectrometer. Samples were analyzed with high resolution mass spectrometry (HRMS) by Field Desorption ionization using a JEOL AccuTOF GC-Alpha (JMS-T2000GC) mass spectrometer interfaced with an Agilent 8890 GC system. Electron paramagnetic resonance (EPR) spectroscopy was collected on a Bruker EMX X-band CW-EPR Spectrometer using either an Oxford ESR 900 liquid helium/nitrogen flow-through cryostat or a liquid nitrogen immersion dewar for experiments at a fixed temperature of 77 K. The recorded spectra were simulated in EasySpin for MATLAB.¹ EPR samples were prepared in the glove box into Wilmad quartz low pressure/vacuum EPR tubes fitted with a with air-tight PTFE piston.

Ultrafast laser pulses used for the transient absorption (TA) measurements originate from a Coherent Astrella Ti:Sapphire amplifier system, which generates 5 mJ, 40 fs pulses centered on 800 nm at a 1 kHz repetition rate. These pulses were passed into an Ultrafast Systems Helios spectrometer system to carry out the transient absorption spectroscopy measurements. Pulses from the Astrella were attenuated and then delayed by the Helios' built-in 7 ns delay stage before undergoing supercontinuum generation to generate a white-light probe. Three different non-linear optical media were used to generate white light across the UV to the NIR as needed: CaF₂ (330–650 nm), Sapphire (470–750 nm), YAG (850–1600 nm). The majority of the beam was focused onto the sample and then subsequently into a fiber spectrometer, while the remaining portion of the beam bypassed the sample and was focused into a second fiber spectrometer to act as a reference.

Pump pulses were generated through various means using a stronger portion of the Astrella output than that of the probe. To generate 560, 700 and 1200 nm pump pulses, a Coherent OPerA optical parametric amplifier was used in various configurations. For pumping at 800nm, the fundamental output of the Astrella was used and for 400 nm the fundamental was frequency doubled in a β -barium borate (BBO) crystal (EKsMA Optics, 10 mm x 10 mm x 0.2 mm, $\theta = 29.2^\circ$, $\phi = 90^\circ$, P/P@400–800 nm) crystal. After wavelength manipulation, the pump was chopped, attenuated with a variable neutral density filter, focused onto the sample, and subsequently blocked.

TA samples were prepared in a nitrogen-filled glovebox using 2 mm quartz cuvettes fitted with air-tight PTFE piston seals (Schlenk cuvettes). Concentration varied between measurements but was chosen to maximize absorbance while minimizing the dimerization occurring at high concentrations. Thus, typical absorbances at the pumped wavelength were around 0.1–0.3 OD. Some compounds were especially prone to dimerization and the resultant precipitate caused significant scattered pump light in the results. This was minimized through the use of spectral filters (ThorLabs FELH0450, FESH0650, FESH0750) to block the pump wavelengths, but these also blocked wavelengths shorter than 400 nm so were only used when necessary. A magnetic stirrer was also used to stir the sample over the course of the measurement.

Data were acquired using the Helios control software and subsequently exported to a custom MATLAB script for processing. Each datapoint was averaged for 2 s (1000 total pump-probe cycles) and an exponentially spaced time array was used to capture the decay of the signal. Each scan was repeated five times. Background points collected before time-zero where no signal was present were subtracted from the remaining data to remove pump scatter and other unwanted effects. Following this, the chirp in the data was corrected by tracking the position of the center of the cross-phase modulation (XPM) feature across the first picosecond of the spectrum and resampling the data with the original time array to remove the chirp. The data were then globally fit through nonlinear least-squares to a series of exponentials convoluted

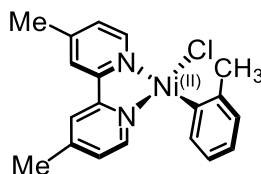
with a Gaussian instrument response function. Since the true pulse length at the sample is unknown, the width of the response function was set to 70 fs to best fit the data. In most cases, the XPM was many times larger than the actual signal and so greatly biased the fit. In this work our interest lies with the dynamics after the first picosecond so the signal between -0.3 and 0.3 ps (0.5 ps for toluene due to a wider XPM) was excluded from the fit. The fitting procedure yields several fitted time constants alongside the decay-associated spectrum (DAS) corresponding to each exponential decay. For some cases, the least-squared algorithm would not converge so coarse manual tuning of the parameters was necessary to provide a good fit. Further processing can convert the DAS into evolution- or species-associated spectra but the presence of significant vibrational cooling violates the assumption of bilinearity required by the global fitting procedure making subsequent postprocessing of the spectrum questionable. However, the time constants are still valid and the DAS can still be used to understand the origin of each component.

Errors on the fitted parameters can be estimated through the residuals and numerical Jacobian matrix outputted by the fitting algorithm. The errors on the time constants calculated this way ranged from around 0.1 to 1%. However, errors calculated this way notoriously underestimate the true uncertainty and more accurate errors can only be garnered from more complex statistical methods such as bootstrapping.^{2,3} Therefore, we adopt a compromise here. Across all compounds, **1** and **5** were studied most thoroughly so the standard deviation of τ_3 across many different samples and measurements was taken as the error and found to be 5 and 4%, respectively. Such a large number of individual measurements were not possible for all compounds, so instead several permutations of repeats of the noisiest, **4**, were fitted and their standard deviation found to also be around 5%. Therefore, we approximate the error on τ_3 to be 5% for all compounds. The shorter time constants typically correspond to a much smaller change in the signal and so have larger uncertainty. However, these components are of less relevance to the study as a whole and thus a detail consideration of their corresponding errors is considered beyond the scope of this work.

S1.2. Synthetic Details.

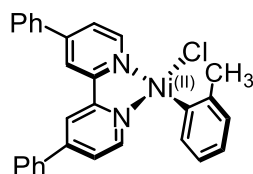
The parent four-coordinate complexes, Ni(II)(^t-Bu**bpy**)(*o*-tolyl)Cl, Ni(II)(^t-Bu**bpy**)(*o*-tolyl)Br, Ni(II)(^t-Bu**bpy**)(*o*-tolyl)I, Ni(II)(bpy)(*o*-tolyl)Cl, and Ni(II)(MeO₂Cbpy)(*o*-tolyl)Cl, were synthesized according to previous reports.⁴⁻⁶ Their spectroscopic properties were identical to those described prior. The precatalyst, Ni(II)TMEDA(*o*-tolyl)Br, and the parent complexes, Ni(II)(Me**bpy**)(*o*-tolyl)Cl, Ni(II)(Ph**bpy**)(*o*-tolyl)Cl, and Ni(II)(MeO₂Cbpy)(*o*-tolyl)Br were prepared as given below.

Preparation of Parent Ni(II)-bpy Aryl Halide Complexes.



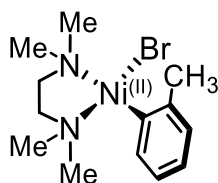
Ni(Me₂bpy)(*o*-tolyl)Cl. In a nitrogen-filled glove box, a 20 mL scintillation vial was charged with a Teflon coated stir bar, bis-(1,5-cyclooctadiene) nickel(0) (0.240 g, 0.870 mmol, 1.00 eq.), and 4,4'-dimethyl-2-2'-bipyridine (0.165 g, 0.896 mmol, 1.03 eq.). To this vial, 5.0 mL THF was added, and the mixture was stirred for 90 minutes affording a deep purple solution. Subsequently, 1.5 mL of 2-*chloro*-toluene (excess) was added dropwise, while stirring. An orange solid precipitated after 3.5 hours alongside a gray-black solid. Pentane (10 mL) were added to the mixture to complete precipitation. The crude solid mixture was then collected by filtration, washed with pentane and heptane (3x5 mL each), and the filtrate discarded. Into a second, clean filter flask, the solid mixture was rinsed with diethyl ether, affording a red/orange filtrate; the insoluble solids were discarded. To this filtrate, pentane was added to precipitate an orange solid. This solid was collected by filtration, washed again with pentane and heptane (3x5 mL each) then dried under vacuum (0.075 g, 23% yield). *Note:* The solid product is prone to decomposition over the course of days/weeks, even in the glove box, becoming an orange/brown solid. Sample should be stored at low temperature, if possible. Solutions decompose at room temperature over the course of several hours to days. Solutions should be used immediately to avoid insoluble decomposition products.

UV-vis (THF): $\lambda_{\text{MLCT}} = 477 \text{ nm} / 20,964 \text{ cm}^{-1}$ ($\epsilon_{\text{MLCT}} = 4530 \text{ cm}^{-1} \text{ M}^{-1}$). ¹H NMR (400 MHz, CD₂Cl₂): δ 8.97 (d, $J = 6.0 \text{ Hz}$, 1H), 7.71 (d, $J = 1.6 \text{ Hz}$, 1H), 7.67 (d, $J = 1.5 \text{ Hz}$, 1H), 7.54 – 7.48 (m, 1H), 7.35 (dd, $J = 5.2, 1.6 \text{ Hz}$, 1H), 7.10 (d, $J = 5.7 \text{ Hz}$, 1H), 6.91 (dd, $J = 5.5, 1.9 \text{ Hz}$, 1H), 6.83–6.74 (m, 3H), 3.04 (s, 3H), 2.49 (s, 3H), 2.37 (s, 3H). ¹³C{¹H}NMR (100 MHz, CD₂Cl₂) δ 156.1, 151.3, 150.5, 149.2, 142.7, 135.8, 127.5, 127.2, 123.3, 123.2, 122.8, 121.8, 121.0, 25.2, 21.7, 21.5. FT-IR (ATR, cm⁻¹): 3036, 2977, 1615, 1556, 1478, 1445, 1418, 1024, 1018, 921, 846, 827, 733, 650, 556, 515. HRMS (FD-MS): calculated for [C₁₉H₁₉N₂NiCl]⁺: 368.0590 found: 368.0584.



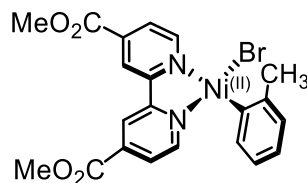
Ni(Phbpy)(*o*-tolyl)Cl. Synthetic procedure was adapted from a literature method.⁵ In a nitrogen-filled glove box, a 4 mL vial with air-tight septa cap was charged with a Teflon coated stir bar and Ni(TMEDA)(*o*-tolyl)Cl (0.024 g, 0.080 mmol, 1.00 eq.). To this vial, 4,4'-diphenyl-2,2'-bipyridine (0.026 g, 0.085 mmol, 1.06 eq.) was added along with 1.6 mL of benzene. The vial was capped and sealed with three turns of electrical tape, removed from the glove box, and stirred at 45 °C for 4 hours affording a dark red solution with precipitate. After allowing the vial to cool, it was brought back into the glove box where the red solid was collected by vacuum filtration, washed with benzene (2x2 mL), diethyl ether (2x2 mL), and pentane (4x2 mL), then was dried under vacuum (0.028 g, 73% yield). Spectroscopic properties were identical to those reported previously.

UV-vis (THF): $\lambda_{\text{MLCT}} = 500 \text{ nm} / 20,000 \text{ cm}^{-1}$ ($\epsilon_{\text{MLCT}} = 5300$). $^1\text{H NMR}$ (400 MHz, CD_2Cl_2): δ 9.25 (d, $J = 5.7 \text{ Hz}$, 1H), 8.20 (s, 1H), 8.15 (s, 1H), 7.83–7.76 (m, 3H), 7.73–7.68 (m, 2H), 7.63–7.49 (m, 7H), 7.36 (d, $J = 3.0 \text{ Hz}$, 2H), 6.89–6.78 (m, 3H), 3.09 (s, 3H). HRMS (FD-MS): calculated for $[\text{C}_{29}\text{H}_{23}\text{N}_2\text{NiCl}]^+$: 492.0903 found: 492.0923.



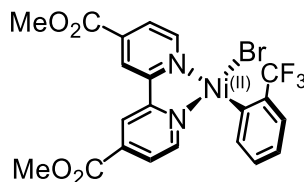
Ni(TMEDA)(*o*-tolyl)Br. In a nitrogen-filled glove box, a 20 mL scintillation vial was charged with a Teflon coated stir bar and bis-(1,5-cyclooctadiene) nickel(0) (0.250 g, 0.909 mmol, 1 eq.). Via micro syringe, 0.175 mL (1.182 mmol, 1.3 eq.) of N,N,N',N'-tetramethyl ethylenediamine was added along with 3.25 mL of 2-bromo-toluene (excess). A red/orange solid began precipitating in the vial. After 5 hours stirring at room temperature, hexanes was added (10 mL) to further precipitate the solid; the mixture was left overnight. The red/orange solid was collected by vacuum filtration where it was rinsed thoroughly with hexane and pentane, and dried (290 mg, 92% yield).

$^1\text{H NMR}$ (400 MHz, CD_2Cl_2): δ 7.38 (dd, $J = 7.3, 1.4 \text{ Hz}$, 1H), 6.70–6.62 (m, 2H), 6.61–6.53 (m, 1H), 3.41 (s, 4H), 2.79–2.31 (m, 12H), 2.17 (d, $J = 10.4 \text{ Hz}$, 2H), 1.78 (s, 2H). $^{13}\text{C}\{^1\text{H}\}\text{NMR}$ (100 MHz, CD_2Cl_2) δ 144.8, 143.7, 136.2, 126.5, 122.5, 121.9, 61.4, 57.3, 50.1, 49.1, 47.7, 47.0, 26.7. FT-IR (ATR, cm^{-1}): 3037, 2971, 2893, 2840, 2784, 1558, 1456, 1277, 1123, 1047, 1018, 1010, 953, 806, 772, 749, 648, 605. HRMS (FD-MS): calculated for $[\text{C}_{13}\text{H}_{23}\text{N}_2\text{NiBr}]^+$: 344.0398 found: 344.0396.



Ni^(MeO₂Cbpy)(*o*-tolyl)Br. In a nitrogen-filled glove box, a 100 mL Schlenk flask was charged with a Teflon coated stir bar and Ni(TMEDA)(*o*-tolyl)Br (0.250 g, 0.723 mmol, 1.00 eq.). To this vial, dimethyl-2,2'-bipyridine-4,4'-dicarboxylate (0.240 g, 0.881 mmol, 1.22 eq.) was added along with 24 mL of heptane and 4 mL toluene (7:1 heptane/toluene). Upon removal from the glove box, the flask was sonicated to promote solubilization of the reagents. The flask was attached to the nitrogen Schlenk line, covered in aluminum foil, and stirred at 60 °C for 24 hours affording a deep purple solution with purple precipitate. Orange starting material was still seen in the flask after inspection, so the temperature was then increased to 65 °C and the reaction continued for an additional 48 hours. After allowing the Schlenk flask to cool, it was brought back into the glove box. A purple solid had precipitated; it was collected by vacuum filtration, washed copiously with heptane, diethyl ether (3x2 mL), and excess pentane, then was dried under vacuum (0.255 g, 70% yield).

UV-vis (THF): $\lambda_{\text{MLCT}} = 538 \text{ nm} / 18,587 \text{ cm}^{-1}$ ($\epsilon_{\text{MLCT}} = 5100 \text{ M}^{-1} \text{ cm}^{-1}$). ¹H NMR (400 MHz, CD₂Cl₂): δ 9.73 (d, $J = 5.0 \text{ Hz}$, 1H), 8.58 (d, $J = 2.5 \text{ Hz}$, 1H), 8.51 (d, $J = 1.4 \text{ Hz}$, 1H), 8.11 (dd, $J = 5.7, 1.7 \text{ Hz}$, 1H), 7.71 (dd, $J = 6.0, 1.8 \text{ Hz}$, 1H), 7.48 (dd, $J = 6.9, 1.8 \text{ Hz}$, 1H), 7.43 (d, $J = 6.1 \text{ Hz}$, 1H), 6.88 – 6.76 (m, 3H), 4.03 (s, 3H), 3.97 (s, 3H), 2.96 (s, 3H). ¹³C{¹H}NMR (100 MHz, CD₂Cl₂) δ 164.1, 163.9, 155.8, 153.0, 152.2, 151.6, 147.4, 142.1, 139.7, 138.3, 135.6, 127.8, 126.3, 125.8, 123.5, 122.9, 120.8, 120.1, 25.1. FT-IR (ATR, cm⁻¹): 3028, 2950, 1725, 1556, 1433, 1398, 1322, 1250, 1232, 1121, 1012, 962, 884, 841, 840, 766, 737, 715, 649. HRMS (FD-MS): calculated for [C₂₁H₁₉N₂O₄NiBr]⁺: 499.9882 found: 499.9899.



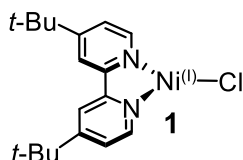
Ni^(MeO₂Cbpy)(*o*-CF₃Ph)Br. In a nitrogen-filled glove box, a 20 mL scintillation vial was charged with a Teflon coated stir bar, bis-(1,5-cyclooctadiene) nickel(0) (0.220 g, 0.800 mmol, 1.00 eq.), and dimethyl-2,2'-bipyridine-4,4'-dicarboxylate (0.225 g, 0.826 mmol, 1.03 eq.). To this vial, 5.0 mL THF was added, and the mixture was stirred for 90 minutes affording a deep purple solution. Subsequently, 2.0 mL of 2-bromobenzotrifluoride (excess) was added while stirring. The product solid precipitated after 4 hours. Hexane (10 mL) was added to the mixture to complete precipitation, and the mixture was placed in the glovebox freezer (-35 °C) for 60 hours. The solid was finally collected by filtration, washed thoroughly with hexane, diethyl ether (3x2 mL), and excess pentane, then dried under vacuum (0.405 g, 91% yield).

UV-vis (THF): $\lambda_{\text{MLCT}} = 499 \text{ nm} / 20,040 \text{ cm}^{-1}$ ($\epsilon_{\text{MLCT}} = 4370 \text{ M}^{-1} \text{ cm}^{-1}$). ¹H NMR (400 MHz, *d*₈-toluene): δ 9.74 (d, *J* = 5.7 Hz, 1H), 7.96–7.92 (m, 1H), 7.91 (s, 1H), 7.74 (s, 1H), 7.65 (s, 1H), 7.37 (d, *J* = 8.3 Hz, 2H), 7.22 (t, *J* = 5.2 Hz, 2H), 6.55 (d, *J* = 5.4 Hz, 1H), 3.40 (s, 3H), 3.36 (s, 3H). ¹⁹F NMR (400 MHz, CD₂Cl₂) δ -58.6 ppm; (400 MHz, *d*₈-THF) δ -58.4 ppm. ¹³C{¹H}NMR (100 MHz, CD₂Cl₂) δ 163.8, 155.8, 152.8, 152.1, 146.1, 137.9, 137.1, 128.3, 126.0, 125.7, 123.0, 120.8, 120.3, 120.2. Low signal to noise precluded the resolution of the *J*_{C-F} coupling values for the trifluorotoluene peak. FT-IR (ATR, cm⁻¹): 3061, 2960, 1723, 1558, 1435, 1398, 1311, 1232, 1148, 1092, 1020, 967, 883, 842, 764, 735, 702, 675, 638. HRMS (FD-MS): calculated for [C₂₁H₁₆N₂O₄F₃NiBr]⁺: 553.9599 found: 553.9594.

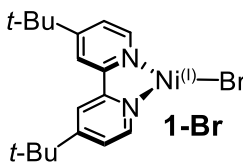
Photochemical Preparation of Ni(I)–bpy Halide Complexes.

Following our previous report,⁶ the Ni(I)(^Rbpy)X (R = *t*-Bu, Me, Ph, H, MeO₂C; X = Cl, Br, I) compounds studied herein were accessed directly from their parent Ni(II)–bpy aryl halide precursors by air- and moisture-free irradiation (370 nm or 390 nm).

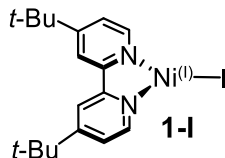
Stock solutions of parent Ni(II)–bpy aryl halide complexes (0.5–1 mM) were prepared in a nitrogen-filled glove box and distributed into separate spectroscopic cuvettes (Starna Cells, 2- or 10-mm path length) fitted with air-tight PTFE piston seals (Schlenk cuvettes). Solutions were prepared fresh daily for analysis. Each cuvette was placed 5 cm away from either a Gen 2 Kessil PR160L 370 nm LED or Kessil PR160L 390 nm LED on highest setting. A cooling fan was used to maintain room-temperature irradiation during the experiment. *Note:* Kessil LEDs may auto-shut off if left on for extended periods without the external fan due to overheating. Typical irradiation times, *t*, were ~60 minutes, but these varied with each complex and are listed below.



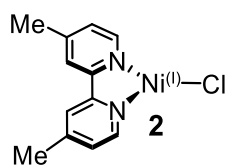
Ni(I)(^{*t*-Bu}bpy)Cl, **1**. Air- and moisture-free irradiation of the parent Ni(II) compound, Ni(II)(^{*t*-Bu}bpy)(*o*-tolyl)Cl, for 60 minutes using a Gen 2 Kessil PR160L 370 nm LED afforded the title compound. UV–vis (THF): $\lambda_1 = 660$ nm (15,152 cm⁻¹), $\lambda_2 = 422$ nm, (23,700 cm⁻¹). Spectroscopic properties were identical to those reported previously.



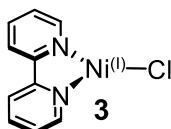
Ni(I)(^{*t*-Bu}bpy)Br, **1-Br**. Air- and moisture-free irradiation of the parent Ni(II) compound, Ni(II)(^{*t*-Bu}bpy)(*o*-tolyl)Br, for 45 minutes using a Kessil PR160L 390 nm LED afforded the title compound. UV–vis (THF): $\lambda_1 = 653$ nm (15,314 cm⁻¹), $\lambda_2 = 386$ nm, (25,906 cm⁻¹). Spectroscopic properties were identical to those reported previously.



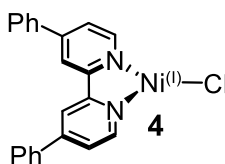
Ni(I)(^{*t*-Bu}bpy)I, **1-I**. Air- and moisture-free irradiation of the parent Ni(II) compound, Ni(II)(^{*t*-Bu}bpy)(*o*-tolyl)I, for 60 minutes using a Kessil PR160L 390 nm LED afforded the title compound. UV–vis (THF): $\lambda_1 = 640$ nm (15,625 cm⁻¹), $\lambda_2 = 382$ nm, (26,178 cm⁻¹). Spectroscopic properties were identical to those reported previously.



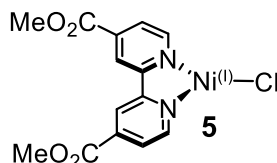
Ni(I)(^{Me}bpy)Cl, 2. Air- and moisture-free irradiation of the parent Ni(II) compound, Ni(II)(^{Me}bpy)(*o*-tolyl)Cl, for 60 minutes using a Kessil PR160L 390 nm LED afforded the title compound. UV-vis (THF): $\lambda_1 = 660$ nm ($15,152$ cm⁻¹), $\lambda_2 = 440$ nm, ($22,727$ cm⁻¹).



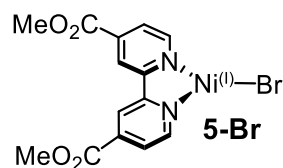
Ni(I)(^Hbpy)Cl, 3. Air- and moisture-free irradiation of the parent Ni(II) compound, Ni(II)(^Hbpy)(*o*-tolyl)Cl, for 75 minutes using a Kessil PR160L 390 nm LED afforded the title compound. Precipitation can occur after extended irradiation; it can be filtered off in a glove box to yield a homogenous filtrate solution of the Ni(I) complex. UV-vis (THF): $\lambda_1 = 673$ nm ($15,625$ cm⁻¹), $\lambda_2 = 431$ nm, ($23,200$ cm⁻¹). Spectroscopic properties were identical to those reported previously.



Ni(I)(^{Ph}bpy)Cl, 4. Air- and moisture-free irradiation of the parent Ni(II) compound, Ni(II)(^{Ph}bpy)(*o*-tolyl)Cl, for 75 minutes using a Gen 2 Kessil PR160L 370 nm LED afforded the title compound. UV-vis (THF): $\lambda_1 = 1175$ nm ($8,510$ cm⁻¹), $\lambda_2 = 915$ nm, ($10,929$ cm⁻¹), $\lambda_3 = 690$ nm, ($14,493$ cm⁻¹), $\lambda_4 = 485$ nm, ($20,619$ cm⁻¹).



Ni(I)(^{MeO₂C}bpy)Cl, 5. Air- and moisture-free irradiation of the parent Ni(II) compound, Ni(II)(^{MeO₂C}bpy)(*o*-tolyl)Cl, for 45 minutes using a Gen 2 Kessil PR160L 370 nm LED afforded the title compound. UV-vis (THF): $\lambda_1 = 1178$ nm ($8,490$ cm⁻¹), $\lambda_2 = 805$ nm ($12,422$ cm⁻¹), $\lambda_3 = 523$ nm ($19,120$ cm⁻¹). Spectroscopic properties were identical to those reported previously.



Ni(I)(^{MeO₂C}bpy)Br, 5-Br. Air- and moisture-free irradiation of the parent Ni(II) compound, Ni(II)(^{MeO₂C}bpy)(*o*-tolyl)Br, for 45 minutes using a Gen 2 Kessil PR160L 370 nm LED afforded the title compound. UV–vis (THF): $\lambda_1 = 1167$ nm (8,570 cm⁻¹), $\lambda_2 = 785$ nm (12,739 cm⁻¹), $\lambda_3 = 520$ nm (19,231 cm⁻¹).

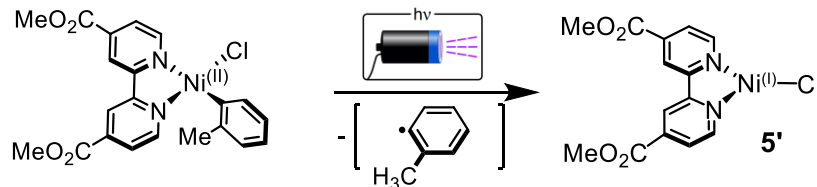
Table S1. Summary of the photochemical parameters used to generate the Ni(I)–bpy halide complexes from their Ni(II)–bpy aryl halide parents (Ar = *o*-tolyl) alongside their photochemical properties. MLCT peak positions and molar extinction coefficients are given for the lowest-energy MLCT transition seen in the UV–vis–NIR data. Solvent = THF; *t* = irradiation time.

Parent Ni(II) Complex	Ni(II) MLCT (nm / cm ⁻¹)	Ni(II) ϵ_{MLCT} (M ⁻¹ cm ⁻¹)	LED (nm)	<i>t</i> (min)
Ni(II)(^{<i>t</i>-Bu} bpy)(Ar)Cl	475 / 21 053	4970	370	60
Ni(II)(^{<i>t</i>-Bu} bpy)(Ar)Br	479 / 20 877	3100	390	45
Ni(II)(^{<i>t</i>-Bu} bpy)(Ar)I	488 / 20 492	2200	390	60
Ni(II)(^{Me} bpy)(Ar)Cl	465 / 21 505	4540	390	60
Ni(II)(^H bpy)(Ar)Cl	483 / 20 704	4070	390	75
Ni(II)(^{Ph} bpy)(Ar)Cl	501 / 19 960	5400 ^b	370	75
Ni(II)(^{MeO₂C} bpy)(Ar)Cl	532 / 18 797	6100	370	45
Ni(II)(^{MeO₂C} bpy)(Ar)Br	538 / 18 587	5100	370	45
Parent Ni(II) Complex	Ni(I) Complex	Ni(I) MLCT (nm / cm ⁻¹)	Ni(I) ϵ_{MLCT} (M ⁻¹ cm ⁻¹) ^a	
Ni(II)(^{<i>t</i>-Bu} bpy)(Ar)Cl	1	660 / 15 150	2000	
Ni(II)(^{<i>t</i>-Bu} bpy)(Ar)Br	1-Br	653 / 15 310	2100	
Ni(II)(^{<i>t</i>-Bu} bpy)(Ar)I	1-I	640 / 15 625	1000	
Ni(II)(^{Me} bpy)(Ar)Cl	2	660 / 15 150	1900	
Ni(II)(^H bpy)(Ar)Cl	3	673 / 14 860	2100	
Ni(II)(^{Ph} bpy)(Ar)Cl	4	1175 ^c / 8510	800	
Ni(II)(^{MeO₂C} bpy)(Ar)Cl	5	1178 / 8490	5500	
Ni(II)(^{MeO₂C} bpy)(Ar)Br	5-Br	1167 / 8570	2500	

^aValues obtained following complete photolysis of parent Ni(II) complexes and may be underestimated.

^bReference value⁵. ^cIdentified by using both the UV–vis–NIR absorption peak and the GSB feature in the TA spectrum (Figure S31).

Isolation of a Ni(I)–bpy Halide Complex.



Ni(I)(MeO₂Cbpy)Cl, 5' In a nitrogen-filled glove box Ni(II)(MeO₂Cbpy)(*o*-tolyl)Cl⁶ (0.160 g, 0.350 mmol) was dissolved in 175.0 mL of diethyl ether. This purple solution was filtered to ensure homogeneity and transferred to a 350 mL Schlenk flask with a Teflon coated stir bar. The flask was sealed and removed from the glovebox. The flask was attached to a nitrogen Schlenk line and allowed to stir. Two Gen 2 Kessil PR160L 370 nm LEDs were pointed at the flask (one on either side); a fan was pointed at the entire setup to ensure room-temperature irradiation. The LEDs were allowed to irradiate the solution on their maximum setting for 48 hours. During the course of the irradiation, a dark precipitate could be seen evolving from the solution. The flask was then returned to the glovebox, and the solid collected by vacuum filtration (fraction 1). The purple filtrate was transferred back into the Schlenk flask, removed from the glovebox, and reattached to the nitrogen line. Irradiation of the solution was continued in the same manner as before for an additional 24 hours, affording more precipitated solid. The flask was again returned to the glovebox, and the new solid collected by vacuum filtration (fraction 2); the filtrate was discarded. The collected navy blue solid was washed with excess diethyl ether, 2-methyl tetrahydrofuran (5x1 mL), hexane (3x2 mL), and pentane (3x2 mL), then dried under reduced pressure (fraction 1: 0.072 g, fraction 2: 0.029 g, combined fractions: 0.101 g, 81% yield).

Note: The title compound is highly air and moisture sensitive. It is insoluble in pentane, hexane, heptane, and ether. It is sparingly soluble in 2-MeTHF and is soluble in benzene, toluene, and THF. The compound reacts readily with dichloromethane (affording a red solution) and decomposes in acetonitrile (becoming a black solution). The compound readily reacts with aryl bromides.

Powder sample X-band CW-EPR ($T = 5$ K; frequency = 9.638 GHz; power = 2.2 mW; modulation amplitude = 8 G): $g_{\text{avg}} = 2.146$ ($g_x = 2.053$, $g_y = 2.123$, $g_z = 2.262$; $g(\text{strain})_x = 0.025$, $g(\text{strain})_y = 0.035$, $g(\text{strain})_z = 0.033$). FT-IR solid sample (ATR, cm^{-1}): 3073, 2957, 1716, 1567, 1511, 1435, 1398, 1316, 1277, 1224, 1102, 1014, 992, 885, 836, 751, 726, 698, 542.

Frozen solution (toluene) X-band CW-EPR ($T = 5$ K; frequency = 9.639 GHz; power = 2.2 mW; modulation amplitude = 8 G): $g_{\text{iso}} = 2.2011$; $g(\text{strain}) = 0.5$. Frozen solution (THF) X-band CW-EPR ($T = 5$ K; frequency = 9.639 GHz; power = 2.2 mW; modulation amplitude = 8 G): $g_{1,\text{iso}} = 2.2011$; $g_1(\text{strain}) = 0.5$; $g_{2,\text{iso}} = 2.1870$; $g_2(\text{strain}) = 0.0902$. UV-vis (THF):

$\lambda_1 = 1178 \text{ nm}$ ($8,490 \text{ cm}^{-1}$), $\lambda_2 = 805 \text{ nm}$ ($12,422 \text{ cm}^{-1}$), $\lambda_3 = 523 \text{ nm}$ ($19,120 \text{ cm}^{-1}$). UV-vis (Benzene): $\lambda_2 = 1181 \text{ nm}$ ($8,490 \text{ cm}^{-1}$), $\lambda_2 = 820 \text{ nm}$ ($12,422 \text{ cm}^{-1}$), $\lambda_3 = 526 \text{ nm}$ ($19,120 \text{ cm}^{-1}$). Paramagnetic ^1H NMR (400 MHz, $d_8\text{THF}$): δ 10.51 (br s, 1H), 8.31 (br s, 2H), 3.81 (br s, 3H). Effective magnetic moment (Evans method, 298 K, C_6D_6): $1.9 \mu\text{B}$.

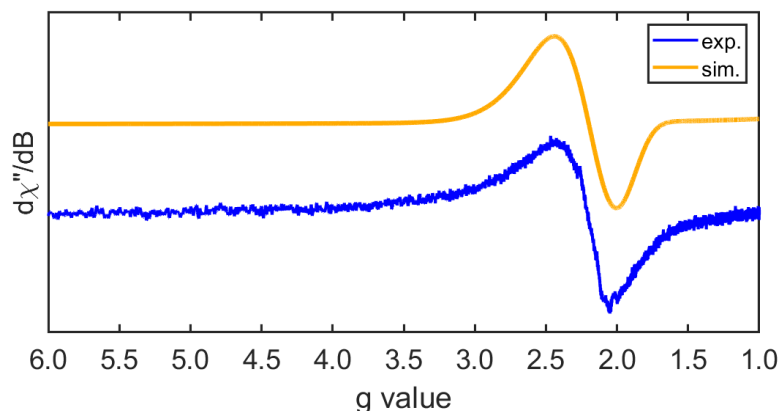


Figure S1. Frozen solution (toluene) X-band CW-EPR spectrum and fit (blue and orange lines, respectively) of $5'$ ($T = 5 \text{ K}$; frequency = 9.639 GHz; power = 2.2 mW; modulation amplitude = 8 G). Anisotropy in the signal could not be resolved due to line broadening, likely arriving from suspended particles of the complex which precipitated upon freezing or were not fully solvated. Simulation values: $g_{\text{iso}} = 2.201$; $g(\text{strain}) = 0.5$.

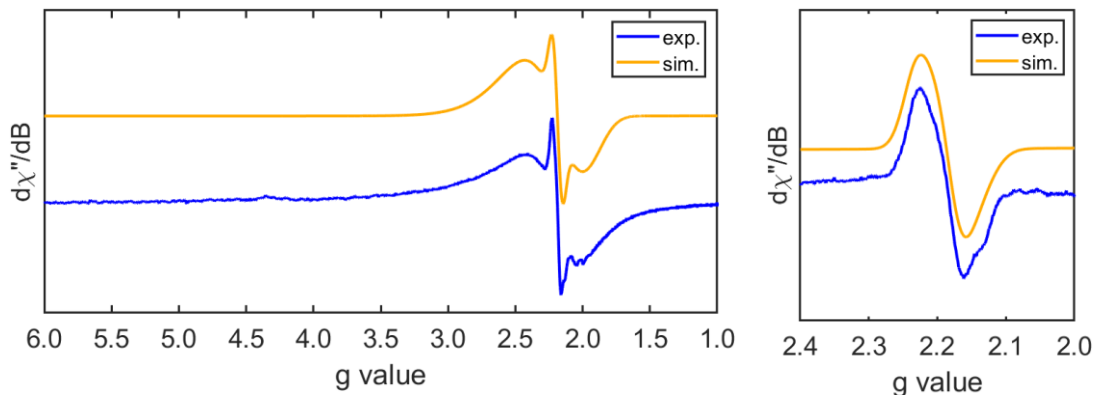


Figure S2. Frozen solution (THF) X-band CW-EPR spectrum and fit (blue and orange lines, respectively) of $5'$ ($T = 5 \text{ K}$; frequency = 9.639 GHz; power = 2.2 mW; modulation amplitude = 8 G). (Left) Full spectrum plotted showing two species; anisotropy in the signal could not be resolved due to line broadening, likely arising from suspended particles of the complex which precipitated upon freezing or were not fully solvated. The second feature in the spectrum (labeled as g_2) is attributed to a small fraction of the species coordinating to THF, which may occur during freezing of the sample. Dual spin simulation values: $g_{1,\text{iso}} = 2.201$; $g_1(\text{strain}) = 0.5$; $g_{2,\text{iso}} = 2.187$; $g_2(\text{strain}) = 0.090$. (Right) Spectrum after subtraction of the broad signal corresponding to g_1 . Simulation values: $g_z = 2.230$, $g_x = 2.180$, $g_y = 2.146$, $g_{\text{avg}} = 2.185$; $g_z(\text{strain}) = 0.043$, $g_x(\text{strain}) = 0.043$, $g_y(\text{strain}) = 0.065$.

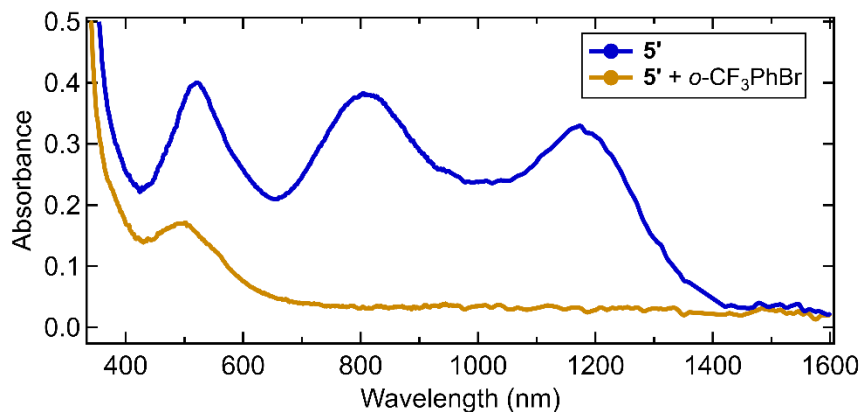


Figure S3. UV-vis-NIR spectra of **5'** pre- and post-addition (blue and orange lines, respectively) of 100 μL of 2-bromobenzotrifluoride.

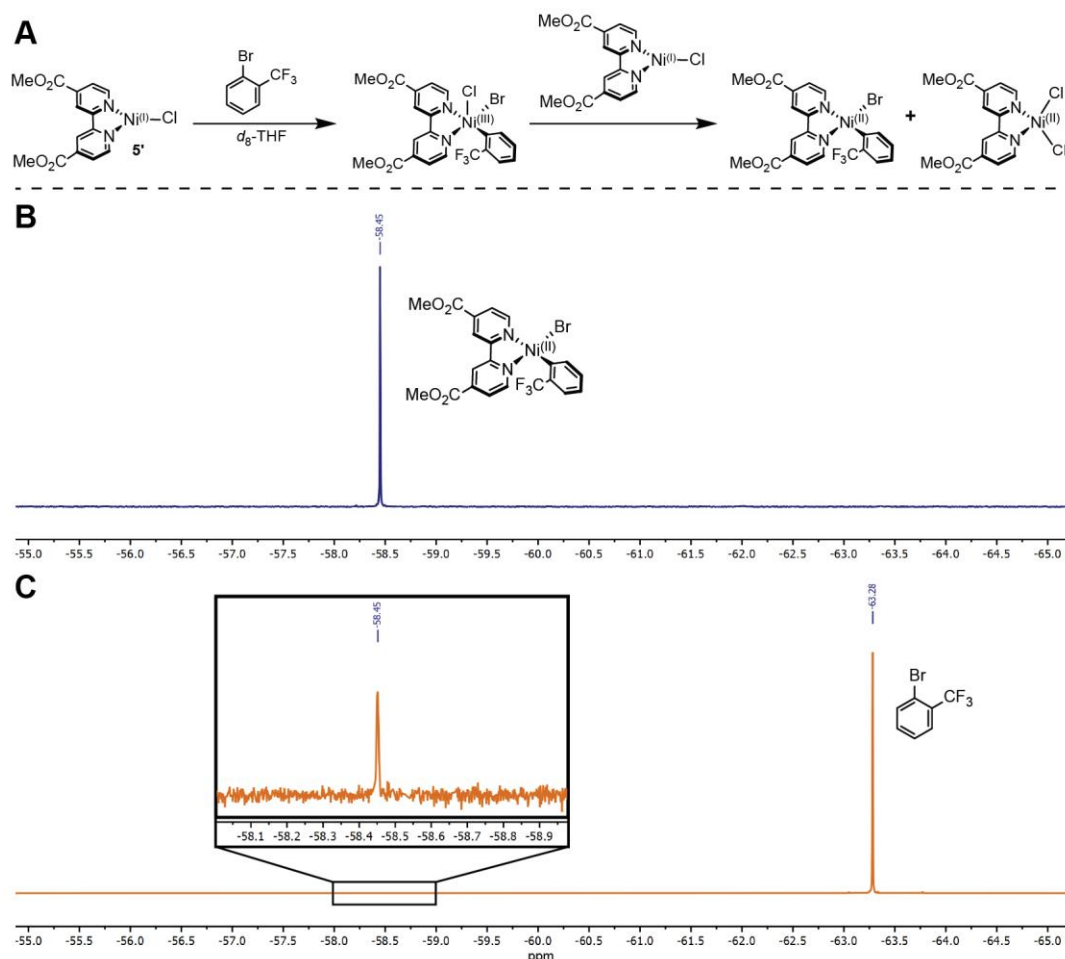


Figure S4. Aryl bromide reactivity analysis of **5'** by ^{19}F NMR (d_8 -THF). (A) Reaction scheme for the oxidative addition of the aryl bromide by Ni(I), forming Ni(II)(MeO_2Cbpy)(o - CF_3Ph)Br and paramagnetic Ni(II)(MeO_2Cbpy) Cl_2 .^{6,7} (B) ^{19}F NMR spectrum of independently synthesized Ni(MeO_2Cbpy)(o - CF_3Ph)Br. (C) ^{19}F NMR spectrum of **5'** post-addition of 100 μL of 2-bromobenzotrifluoride.

S1.3. X-ray Crystallography.

Collection and Refinement Details for Ni(II)(^{MeO₂C}bpy)(*o*-tolyl)Cl.

Ni(II)(^{MeO₂C}bpy)(*o*-tolyl)Cl was crystallized by slow evaporation in diethyl ether. Low-temperature diffraction data (ϕ - and ω -scans) were collected on a Bruker AXS D8 VENTURE KAPPA diffractometer coupled to a PHOTON II CPAD detector with Mo $K\alpha$ radiation ($\lambda = 0.71073 \text{ \AA}$) from an I μ S micro-source for the structure of compound V23337. The structure was solved by direct methods using SHELXS⁸ and refined against F^2 on all data by full-matrix least-squares with SHELXL-2019⁹ using established refinement techniques.¹⁰ All non-hydrogen atoms were refined anisotropically. All hydrogen atoms were included into the model at geometrically calculated positions and refined using a riding model. The isotropic displacement parameters of all hydrogen atoms were fixed to 1.2 times the U value of the atoms they are linked to (1.5 times for methyl groups). All disordered atoms were refined with the help of similarity restraints on the 1,2- and 1,3-distances and displacement parameters as well as enhanced rigid bond restraints for anisotropic displacement parameters. Ni(II)(^{MeO₂C}bpy)(*o*-tolyl)Cl crystallizes in the monoclinic space group $P2_1/n$ with one molecule in the asymmetric unit. The *o*-tolyl group was modeled as a two-component disorder. These data are provided free of charge from The Cambridge Crystallographic Data Centre by The Cambridge Crystallographic Data Centre.

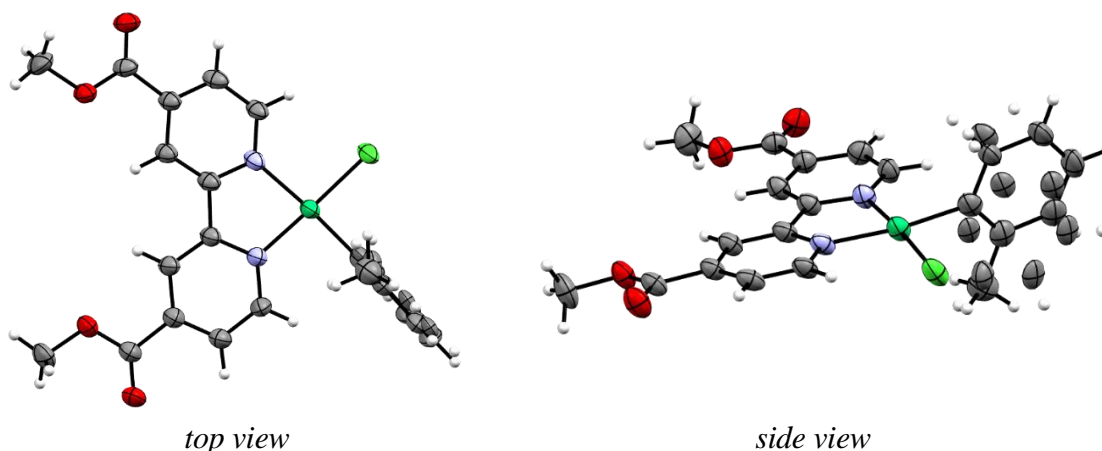


Figure S5. Top down and side views of the refined crystal structure of Ni(II)(^{MeO₂C}bpy)(*o*-tolyl)Cl. The *o*-tolyl group was modeled as a two-component disorder, with one conformer pointing up and the other pointing down.

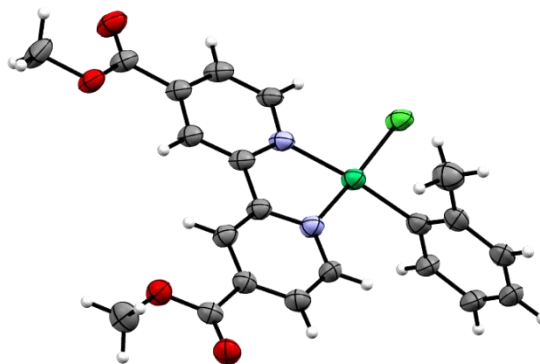


Figure S6. The refined crystal structure of Ni(II)(^{MeO₂C}bpy)(*o*-tolyl)Cl showing only one aryl ligand conformer for clarity.

Compound	Ni(II)(^{MeO₂C}bpy)(<i>o</i>-tolyl)Cl	
Empirical formula	C ₂₁ H ₁₉ ClN ₂ NiO ₄	
Formula weight	457.54 g mol ⁻¹	
Temperature	100(2) K	
Wavelength	1.54178 Å	
Crystal system	Monoclinic	
Space group	P2 ₁ /n	
Unit cell dimensions	a = 7.1614(11) Å	a = 90°
	b = 22.156(2) Å	b = 102.715(10)°
	c = 12.972(3) Å	g = 90°
Volume	2007.8(6) Å ³	
Z	4	
Density (calculated)	1.514 Mg/m ³	
Absorption coefficient	2.881 mm ⁻¹	
F(000)	944	
Crystal size	0.150 x 0.100 x 0.050 mm ³	
Theta range for data collection	3.990 to 74.733°.	
Index ranges	-8 ≤ h ≤ 8, -27 ≤ k ≤ 27, -16 ≤ l ≤ 12	
Reflections collected	23344	
Independent reflections	4086 [R(int) = 0.1627]	
Completeness to theta = 67.679°	99.9 %	
Absorption correction	Semi-empirical from equivalents	
Max. and min. transmission	0.7538 and 0.5432	
Refinement method	Full-matrix least-squares on F ²	
Data / restraints / parameters	4086 / 384 / 330	
Goodness-of-fit on F ²	1.073	
Final R indices [I > 2σ(I)]	R1 = 0.0699, wR2 = 0.1544	
R indices (all data)	R1 = 0.1140, wR2 = 0.1754	
Extinction coefficient	n/a	
Largest diff. peak and hole	0.674 and -0.450 e.Å ⁻³	

S1.4. Steady-State UV–vis–NIR Spectroscopy. Steady-State Spectra

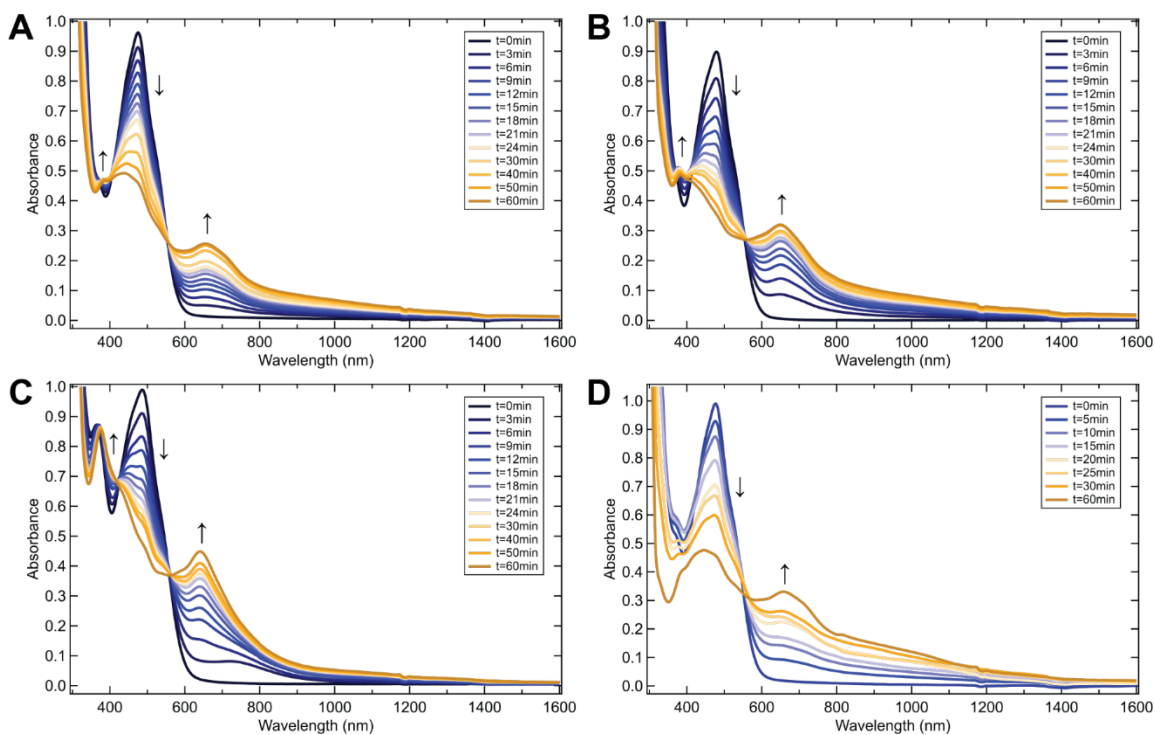


Figure S7. Time-course UV–vis–NIR spectra in THF of the parent Ni(II)–bpy aryl halide compounds (blue line) being photogenerated to the Ni(I)–bpy halide complexes (orange line) examined in this work. (A) Photochemical conversion of Ni(II)(*t*-Bu**bpy**)(*o*-tolyl)Cl to Ni(I)(*t*-Bu**bpy**)Cl, **1**. (B) Photochemical conversion of Ni(II)(*t*-Bu**bpy**)(*o*-tolyl)Br to Ni(I)(*t*-Bu**bpy**)Br, **1-Br**. (C) Photochemical conversion of Ni(II)(*t*-Bu**bpy**)(*o*-tolyl)I to Ni(I)(*t*-Bu**bpy**)I, **1-I**. (D) Photochemical conversion of Ni(II)(Me**bpy**)(*o*-tolyl)Cl to Ni(I)(Me**bpy**)Cl, **2**.

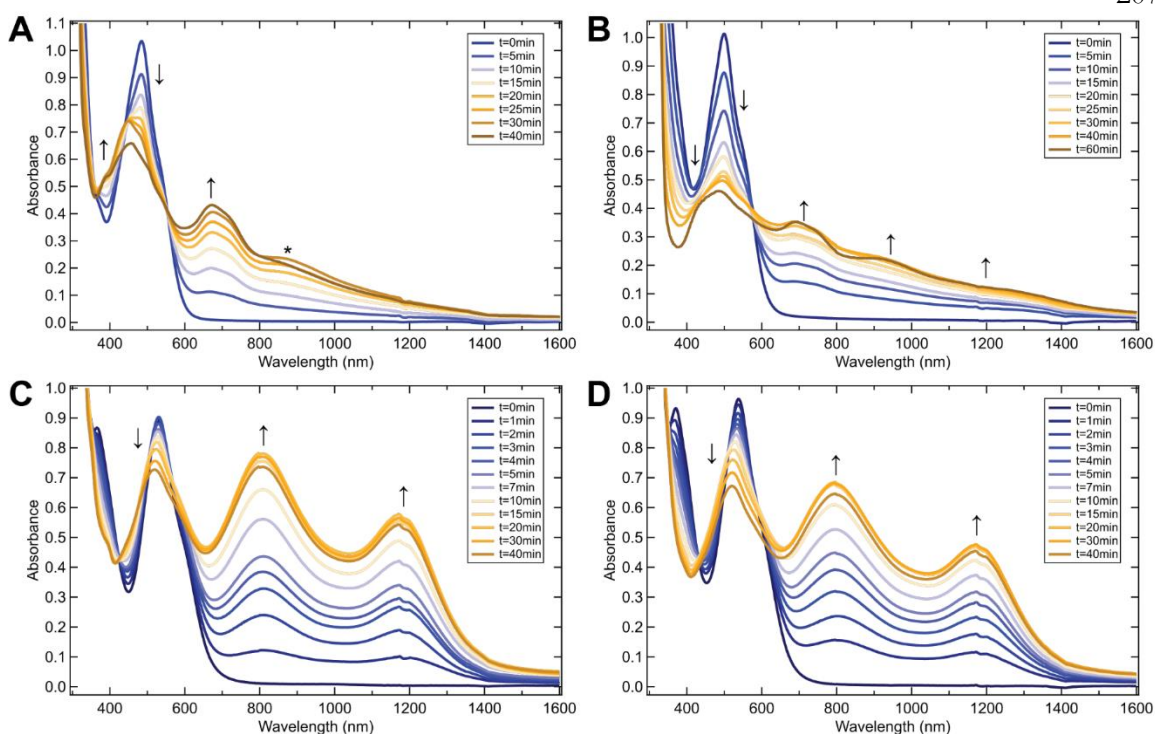


Figure S8. Time-course UV-vis-NIR spectra in THF of the parent Ni(II)-bpy aryl halide compounds (blue line) being photogenerated to the Ni(I)-bpy halide complexes (orange line) examined in this work. (A) Photochemical conversion of Ni(II)(^Hbpy)(*o*-tolyl)Cl to Ni(I)(^Hbpy)Cl, **3**. Starred peak corresponds to an aggregation between Ni(II) and Ni(I) which is seen at low Ni(II) conversion.⁶ (B) Photochemical conversion of Ni(II)(^{Ph}bpy)(*o*-tolyl)Cl to Ni(I)(^{Ph}bpy)Cl, **4**. (C) Photochemical conversion of Ni(II)(^{MeO₂C}bpy)(*o*-tolyl)Cl to Ni(I)(^{MeO₂C}bpy)Cl, **5**. (D) Photochemical conversion of Ni(II)(^{MeO₂C}bpy)(*o*-tolyl)Br to Ni(I)(^{MeO₂C}bpy)Br, **5-Br**.

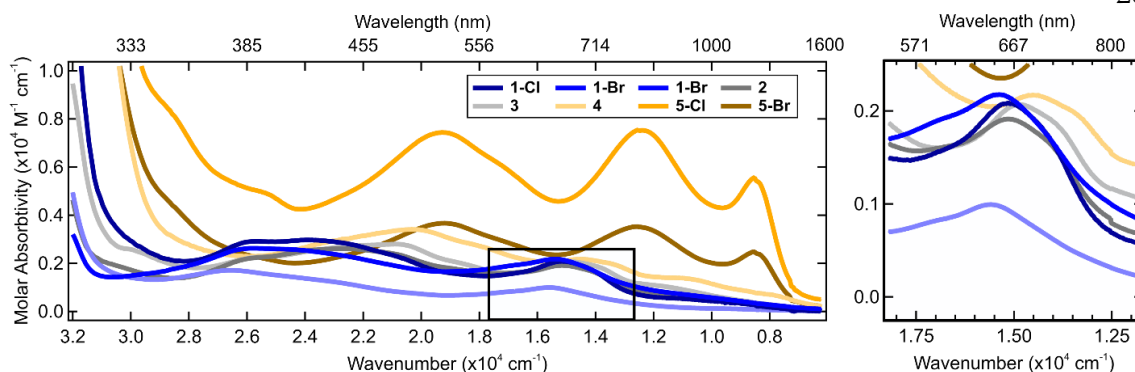


Figure S9. UV-vis-NIR absorption spectra of the photochemically generated Ni(I)-bpy halides in THF. Boxed section is expanded on the right. Analogous figure with wavelength axis is given as Figure 2.

The electronic structure of **1-5** and related compounds have been assigned by EPR and quantum chemical calculations as having a $[d(xy)]^2, [d(yz)]^2, [d(xz)]^2, [d(z^2)]^2, [d(x^2-y^2)]^1$ ground state.¹¹⁻¹⁴ The four β - β ligand field transitions are predicted by TDDFT to require only ~ 0.5 – 1.1 eV (~ 4050 – 8900 cm^{-1}) of photonic energy, placing them all in the IR to NIR region (~ 2500 – 1100 nm, see Supporting Information Section 2.4). Given the formal electric dipole forbidden nature of these transitions, their intensities would be much lower than those seen here. Contrastingly, the bpy π^* orbitals lie energetically between the metal-based HOMO and LUMO (β - $3d(x^2-y^2)$), allowing for numerous spin- and orbitally-allowed d - π^* transitions across the full wavelength range shown. From these observations, the absorption bands can be assigned as Ni(I)-to-bpy MLCTs, consistent with our previous work.¹¹

Fitting of Steady-State Spectra

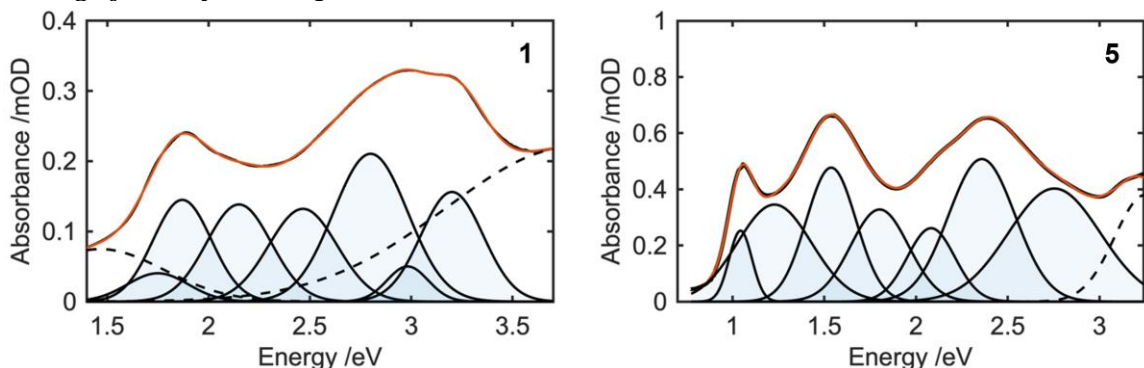


Figure S10. Fits to absorption spectra (red) alongside the raw spectrum (solid black) for compound **1** (left) and **5** (right) and the components to the fit as individual Gaussians underneath. The data were fit only in the wavelength region shown; components required to satisfy the boundaries are shown as dotted lines and not included in the fit.

We focus here on compounds **1** and **5** as representative examples. Given the number of transitions expected in these compounds and the inaccuracy of the TD-DFT, we cannot fit the data to a series of vibronic progressions. This would provide the best comparison to the values obtained from equation 3, but the number of unknowns would severely limit the reliability of the fit. Therefore, we instead approximate the lineshape of each transition as a simple Gaussian and the absorption spectrum can be fitted to estimate the contributions of each transition to the absorption spectrum, $A(E)$. Mathematically, we fit to

$$A(E) = \sum_{i=1}^N a_i \exp\left(-\frac{(E - b_i)^2}{2c_i^2}\right), \quad (\text{S1})$$

where E is photon energy, and a_i , b_i and c_i are fitting parameters which describe the amplitude, center, and width of each transition. Excellent fits to the data with only minor deviations are achieved using $N = 9$ for **1** and $N = 8$ for **5** with all parameters shown in Table S2; these are plotted in Figure S10. The dashed Gaussians are used to account for the boundaries of the fit and are not included the subsequent analysis. The total reorganization energy, λ , can be approximated from the peak widths as

$$\lambda \sim \frac{c^2}{2k_B T} \quad (\text{S2})$$

Averaging over λ and taking the error on the mean gives $\lambda = 0.47(5)$ eV and $\lambda = 0.6(1)$ eV for **1** and **5**, respectively. Given the number of fitting parameters used, the overlapping nature of the peaks, and the assumed lineshape as a perfect Gaussian (no vibronic considerations) this fit is unlikely to be unique and constitutes an underestimate of the true

λ . Despite this, all fitted peaks have similar widths suggesting that this is a reasonable approximation.

Table S2. Parameters for the fits shown in Figure S10 for complexes **1** and **5**. Components not included in the average are underneath the dotted line.

1			5		
<i>a</i> (OD)	<i>b</i> (eV)	<i>c</i> (eV)	<i>a</i> (OD)	<i>b</i> (eV)	<i>c</i> (eV)
0.040	1.75	0.15	0.25	1.04	0.06
0.14	1.87	0.14	0.35	1.23	0.20
0.14	2.15	0.16	0.48	1.53	0.14
0.13	2.47	0.17	0.33	1.80	0.16
0.050	2.98	0.10	0.26	2.08	0.13
0.16	3.2	0.15	0.51	2.35	0.18
0.21	2.80	0.18	0.40	2.75	0.25
<i>0.075</i>	<i>1.46</i>	<i>0.31</i>	<i>0.38</i>	<i>3.25</i>	<i>0.17</i>
<i>0.22</i>	<i>3.81</i>	<i>0.64</i>	-	-	-

S1.5 Time-Resolved Spectroscopy Transient Absorption Spectra

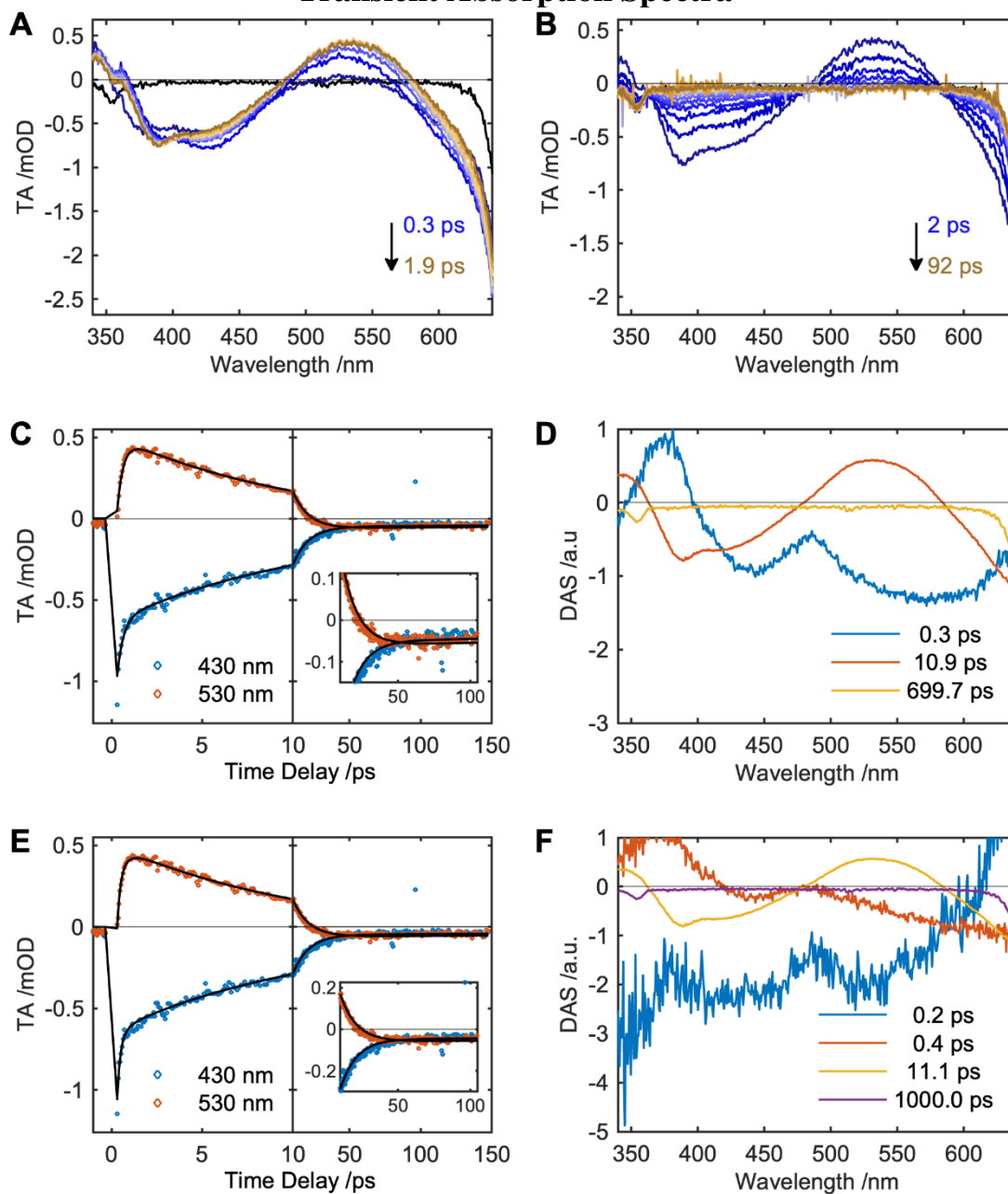


Figure S11. TA data for **1** in THF following 700 nm, 1 μ J photoexcitation. (A,B) Cascaded difference spectra across the two time regions indicated. (C,D) and (E,F) show results of three and four component global fits, respectively. (C,E) Kinetic traces at indicative wavelengths across two time regions. Inset is an enlarged view of the traces at long times. (D,F) DAS corresponding to the time constants indicated in the legend.

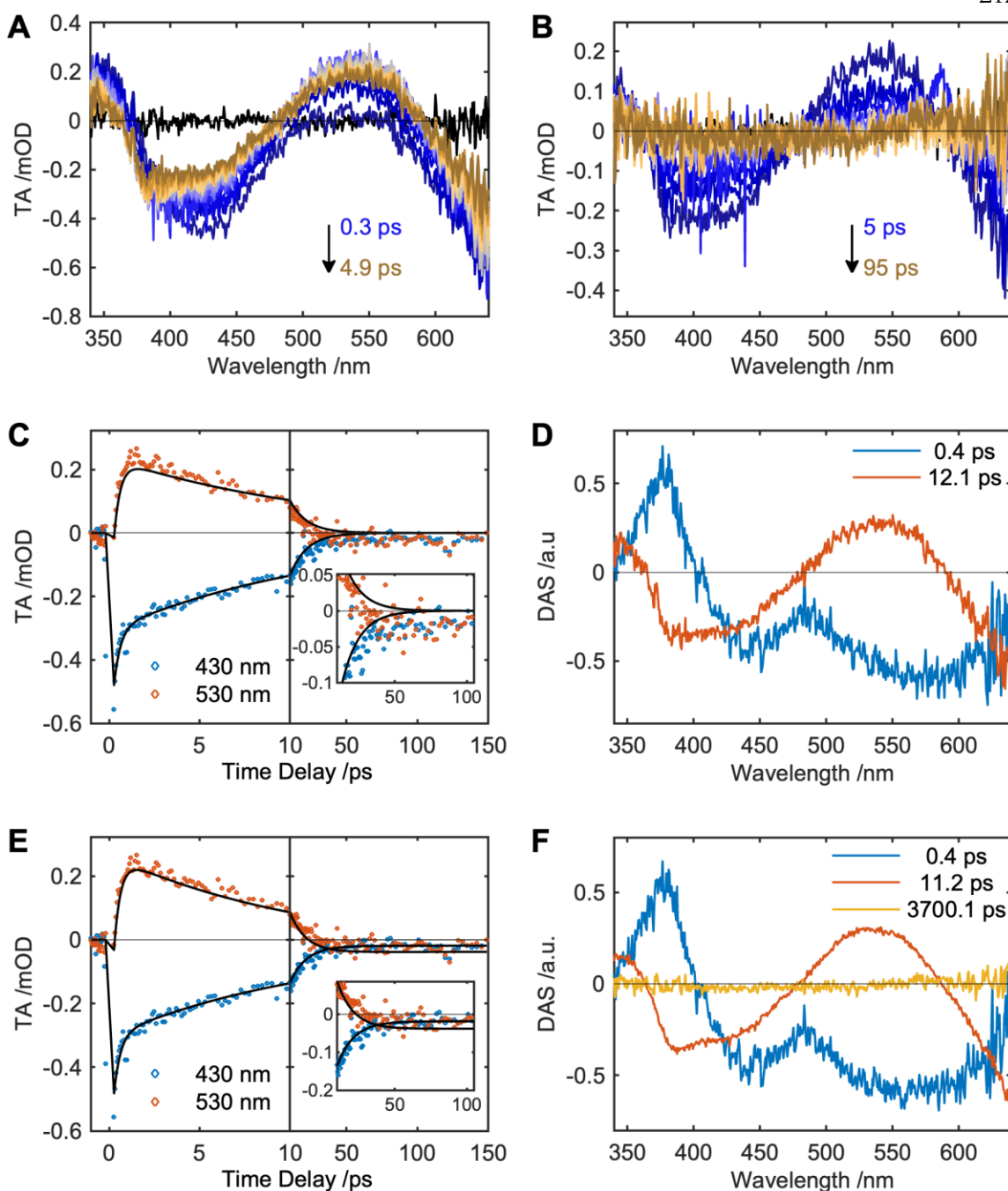


Figure S12. TA data for **1** in THF following 700 nm, 0.3 μJ photoexcitation. (A,B) Cascaded difference spectra across the two time regions indicated. (C,D) and (E,F) show results of three and four component global fits, respectively. (C,E) Kinetic traces at indicative wavelengths across two time regions. Inset is an enlarged view of the traces at long times. (D,F) DAS corresponding to the time constants indicated in the legend.

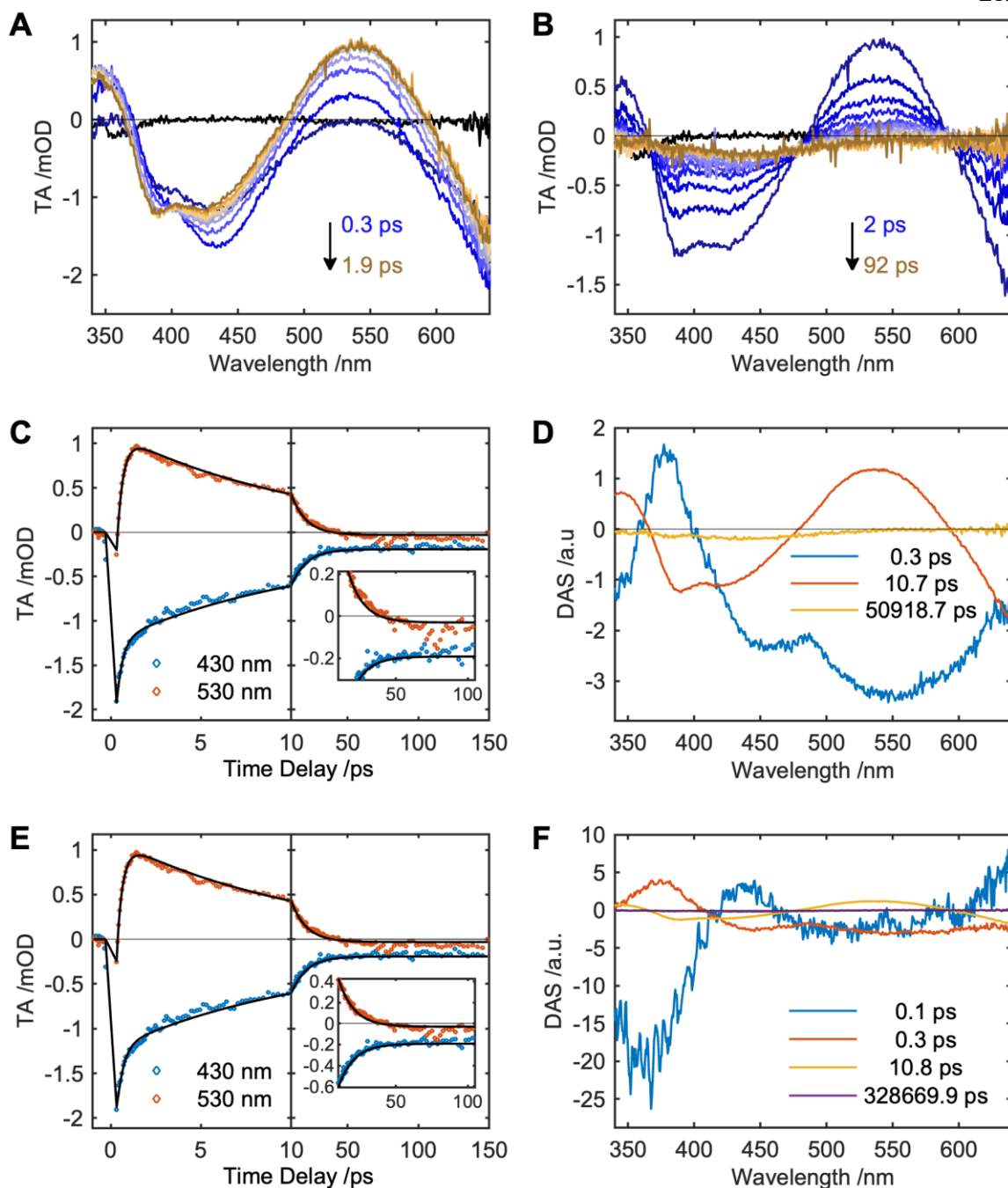


Figure S13. TA data for **1** in THF following 700 nm, 1.5 μJ photoexcitation. (A,B) Cascaded difference spectra across the two time regions indicated. (C,D) and (E,F) show results of three and four component global fits, respectively. (C,E) Kinetic traces at indicative wavelengths across two time regions. Inset is an enlarged view of the traces at long times. (D,F) DAS corresponding to the time constants indicated in the legend.

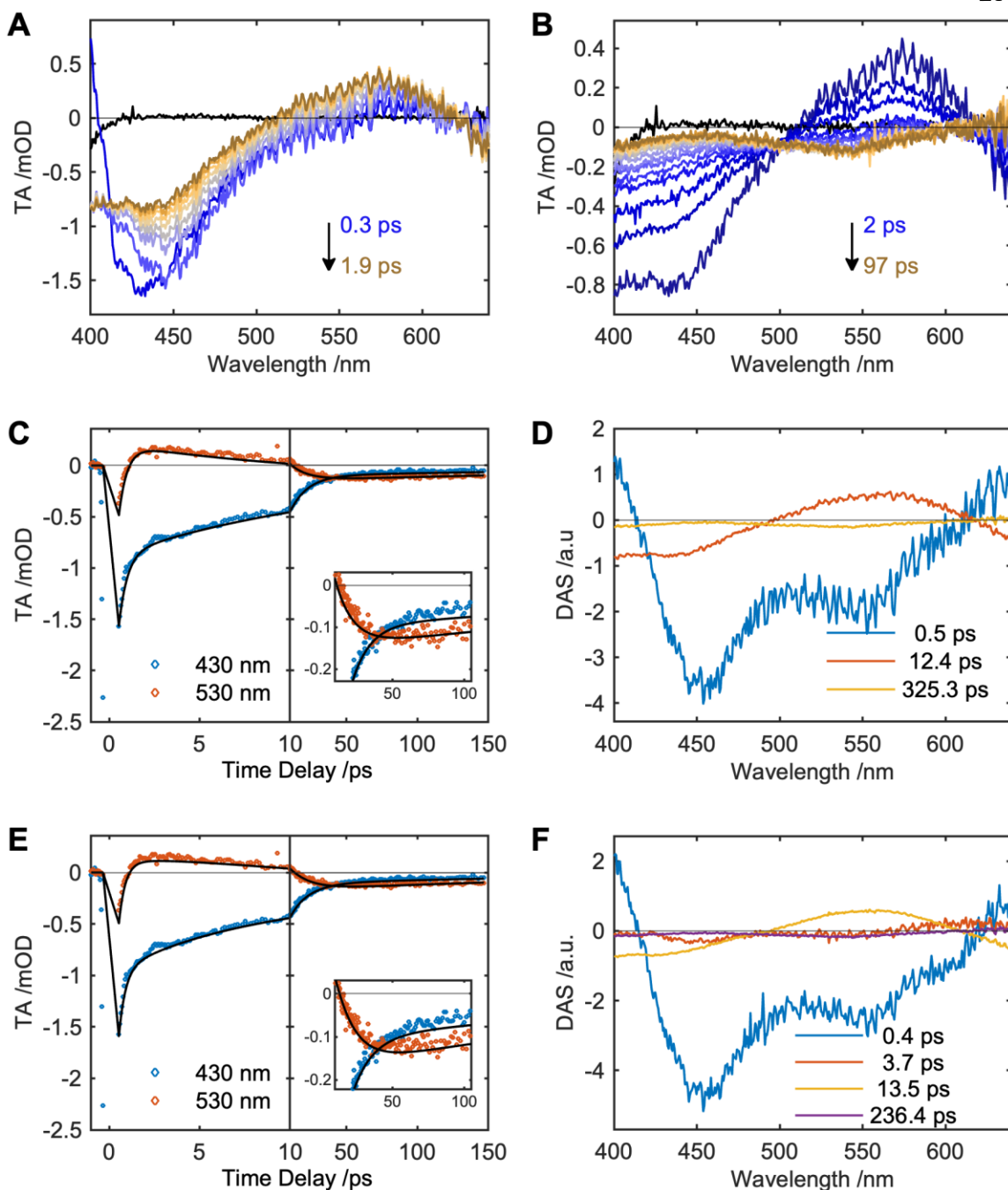


Figure S14. TA data for **1** in toluene following 700 nm, 1 μJ photoexcitation. (A,B) Cascaded difference spectra across the two time regions indicated. (C,D) and (E,F) show results of three and four component global fits, respectively. (C,E) Kinetic traces at indicative wavelengths across two time regions. Inset is an enlarged view of the traces at long times. (D,F) DAS corresponding to the time constants indicated in the legend.

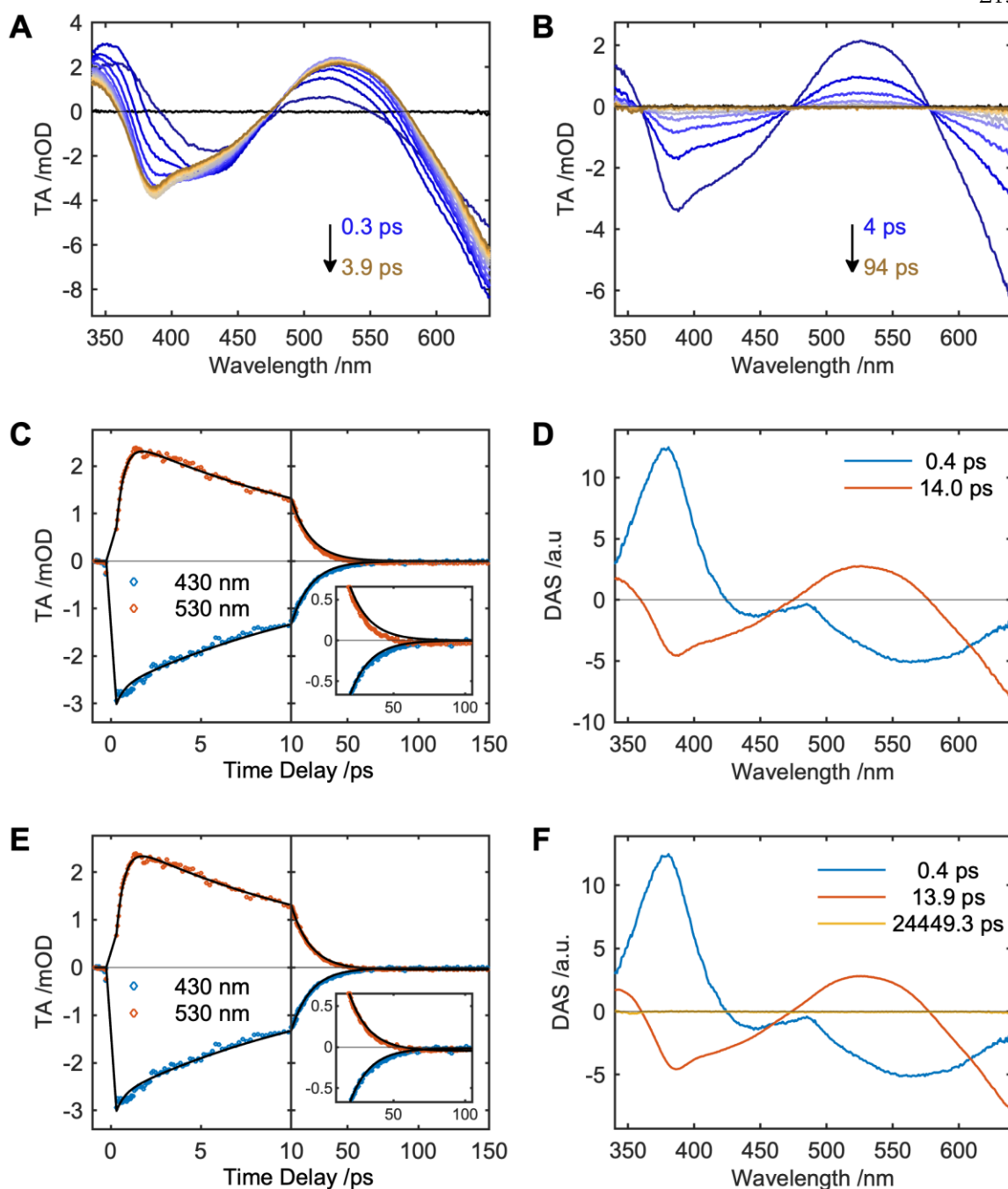


Figure S15. TA data for **1-Br** in THF following 700 nm, 1 μ J photoexcitation. (A,B) Cascaded difference spectra across the two time regions indicated. (C,D) and (E,F) show results of three and four component global fits, respectively. (C,E) Kinetic traces at indicative wavelengths across two time regions. Inset is an enlarged view of the traces at long times. (D,F) DAS corresponding to the time constants indicated in the legend.

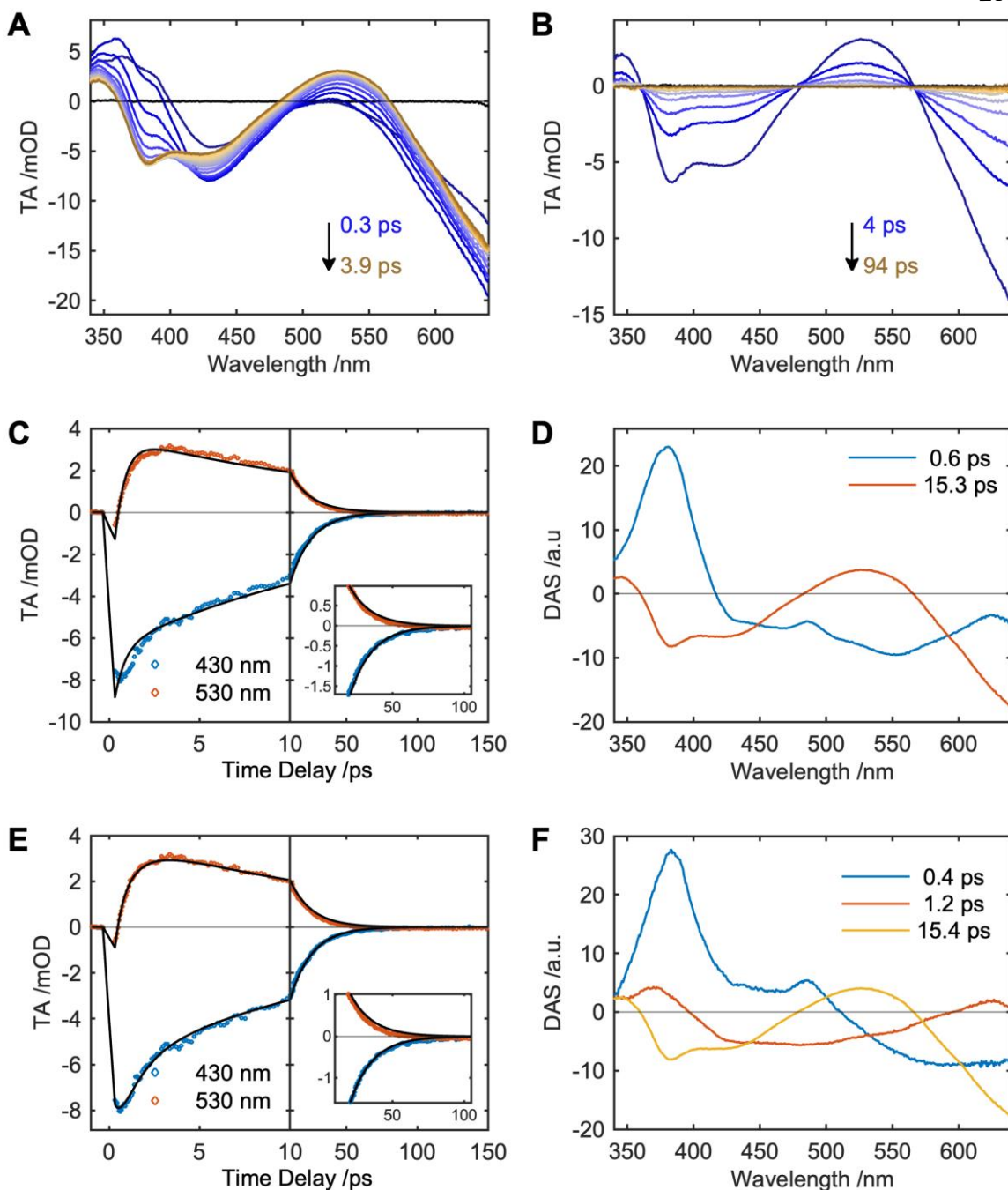


Figure S16. TA data for **1-I** in THF following 700 nm, 1 μJ photoexcitation. (A,B) Cascaded difference spectra across the two time regions indicated. (C,D) and (E,F) show results of three and four component global fits, respectively. (C,E) Kinetic traces at indicative wavelengths across two time regions. Inset is an enlarged view of the traces at long times. (D,F) DAS corresponding to the time constants indicated in the legend.

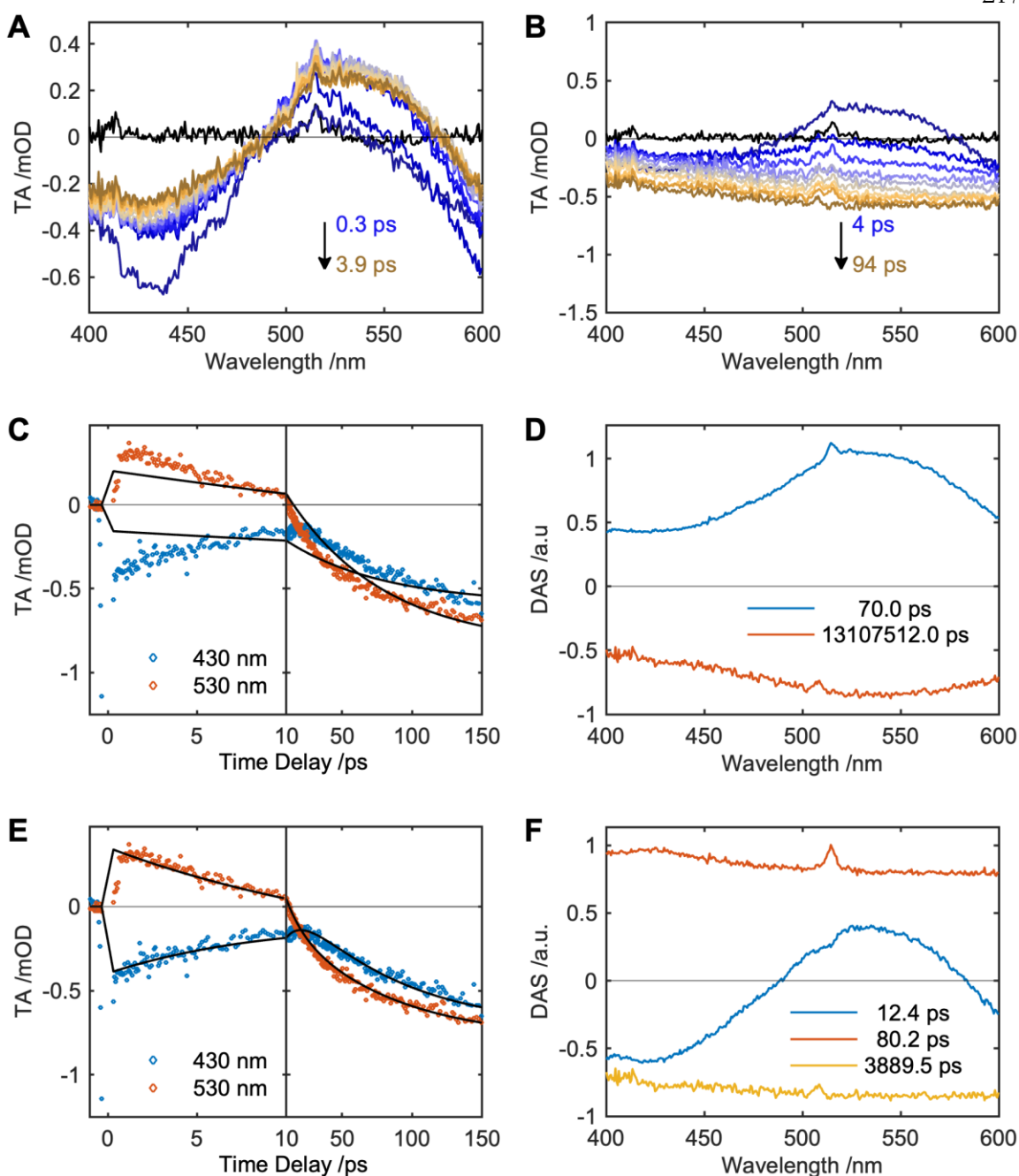


Figure S17. TA data for **2** in THF following 700 nm, 1 μ J photoexcitation. (A,B) Cascaded difference spectra across the two time regions indicated. (C,D) and (E,F) show results of three and four component global fits, respectively. (C,E) Kinetic traces at indicative wavelengths across two time regions. Inset is an enlarged view of the traces at long times. (D,F) DAS corresponding to the time constants indicated in the legend. Peak at 510 nm is a result of pump scatter.

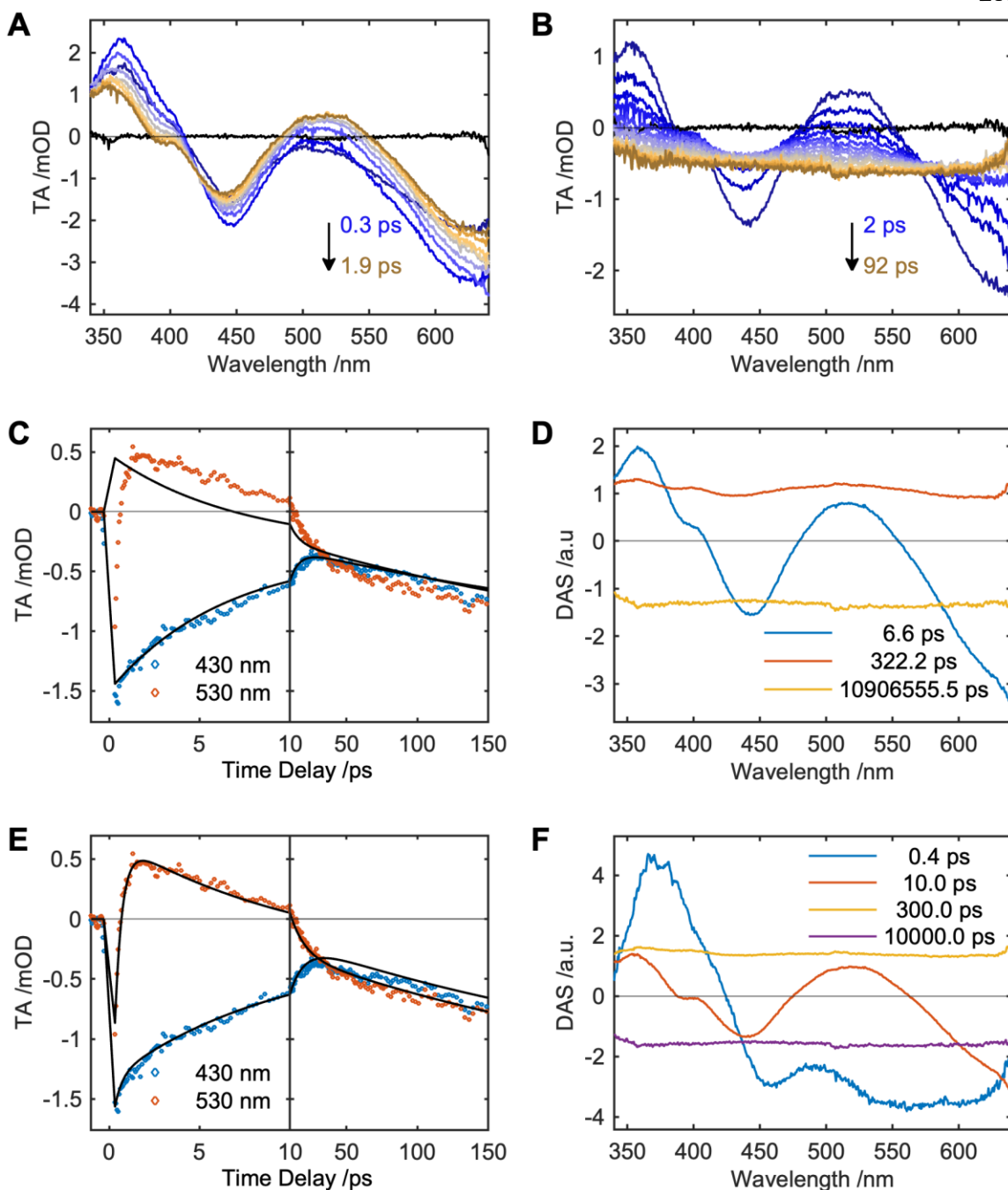


Figure S18. TA data for **3** in THF following 700 nm, 1 μ J photoexcitation. (A,B) Cascaded difference spectra across the two time regions indicated. (C,D) and (E,F) show results of three and four component global fits, respectively. (C,E) Kinetic traces at indicative wavelengths across two time regions. Inset is an enlarged view of the traces at long times. (D,F) DAS corresponding to the time constants indicated in the legend.

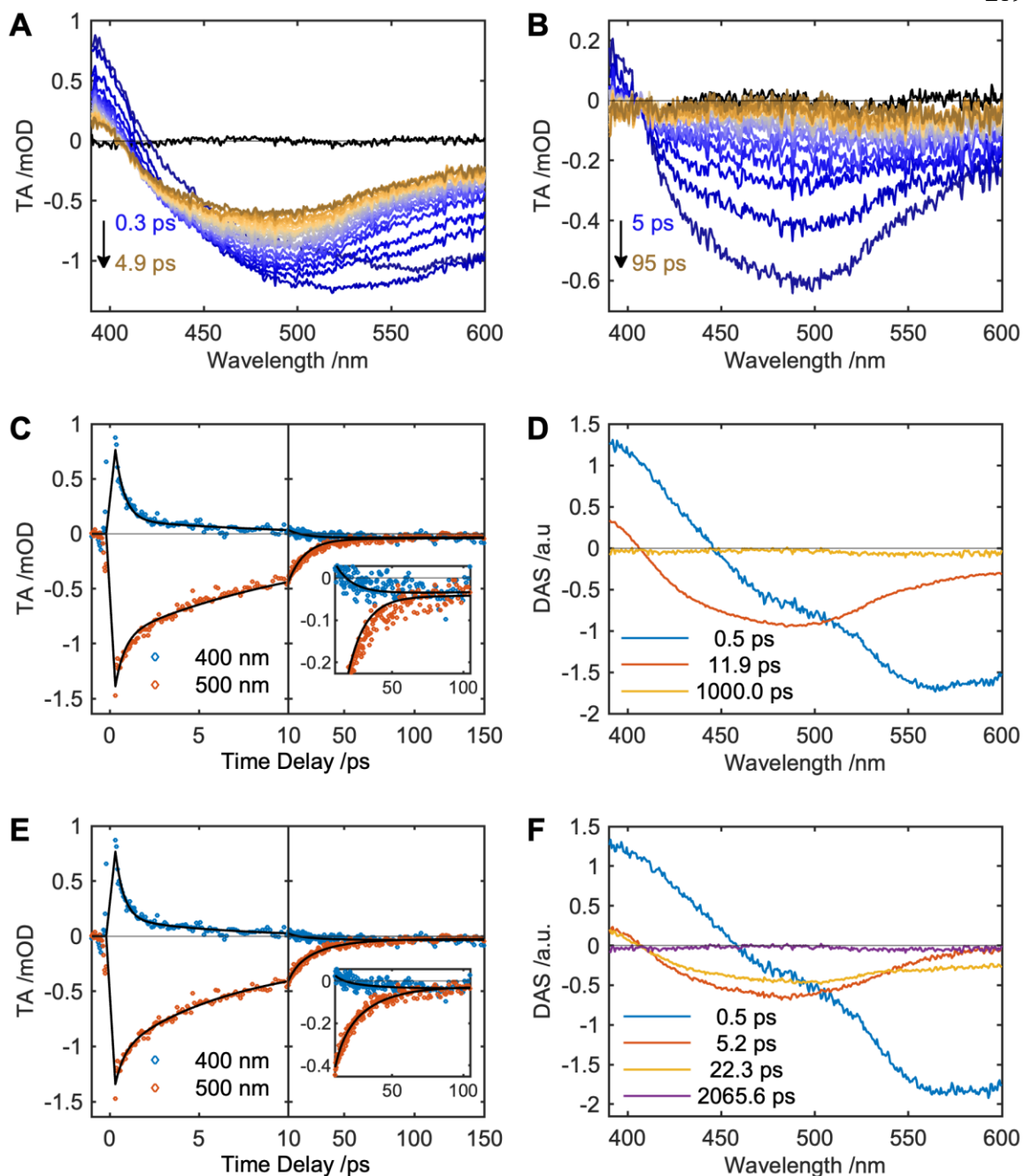


Figure S19. TA data for **4** in THF following 700 nm, 1 μ J photoexcitation. (A,B) Cascaded difference spectra across the two time regions indicated. (C,D) and (E,F) show results of three and four component global fits, respectively. (C,E) Kinetic traces at indicative wavelengths across two time regions. Inset is an enlarged view of the traces at long times. (D,F) DAS corresponding to the time constants indicated in the legend.

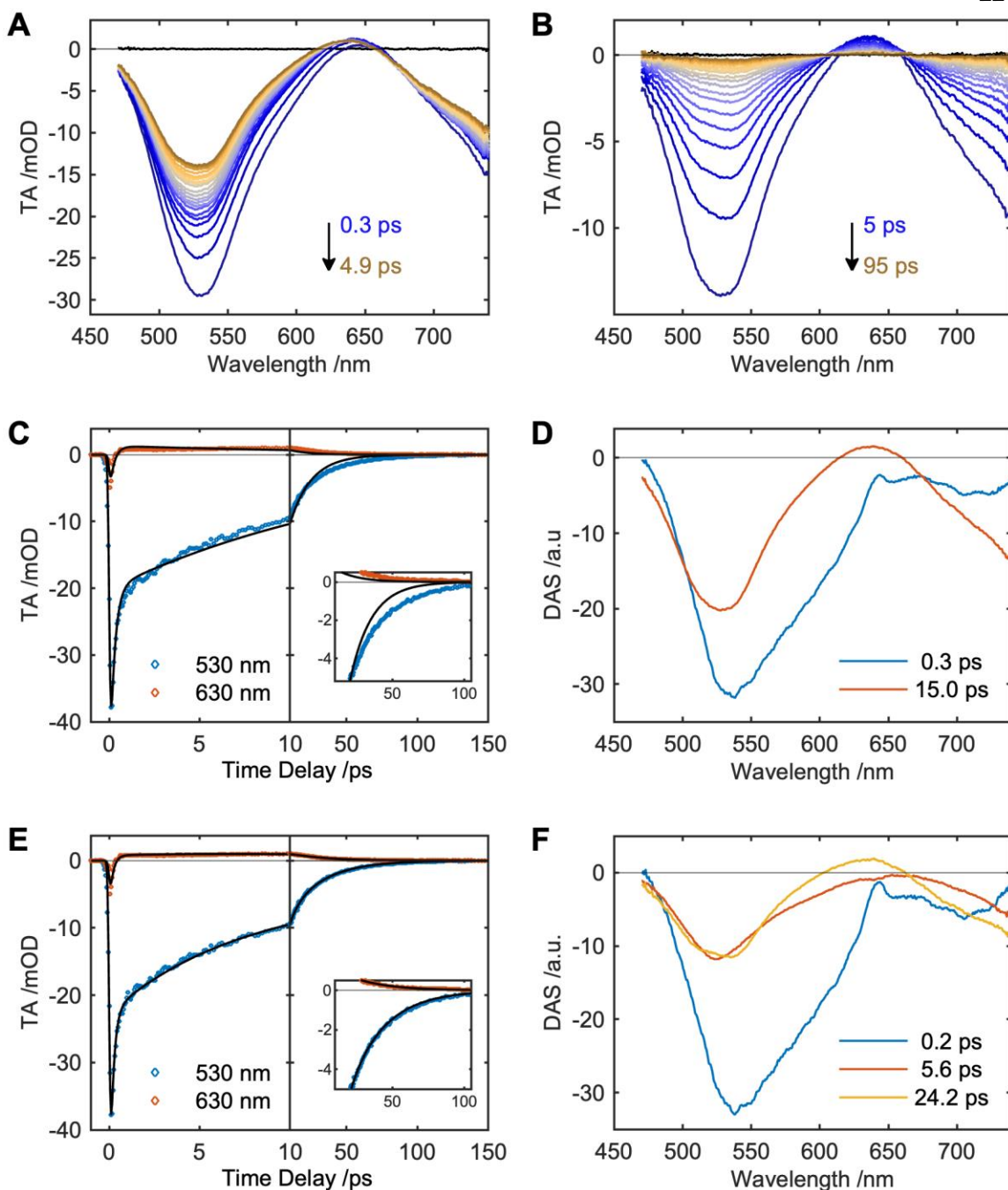


Figure S20. TA data for **5** in THF following 800 nm, 1 μ J photoexcitation. (A,B) Cascaded difference spectra across the two time regions indicated. (C,D) and (E,F) show results of three and four component global fits, respectively. (C,E) Kinetic traces at indicative wavelengths across two time regions. Inset is an enlarged view of the traces at long times. (D,F) DAS corresponding to the time constants indicated in the legend.

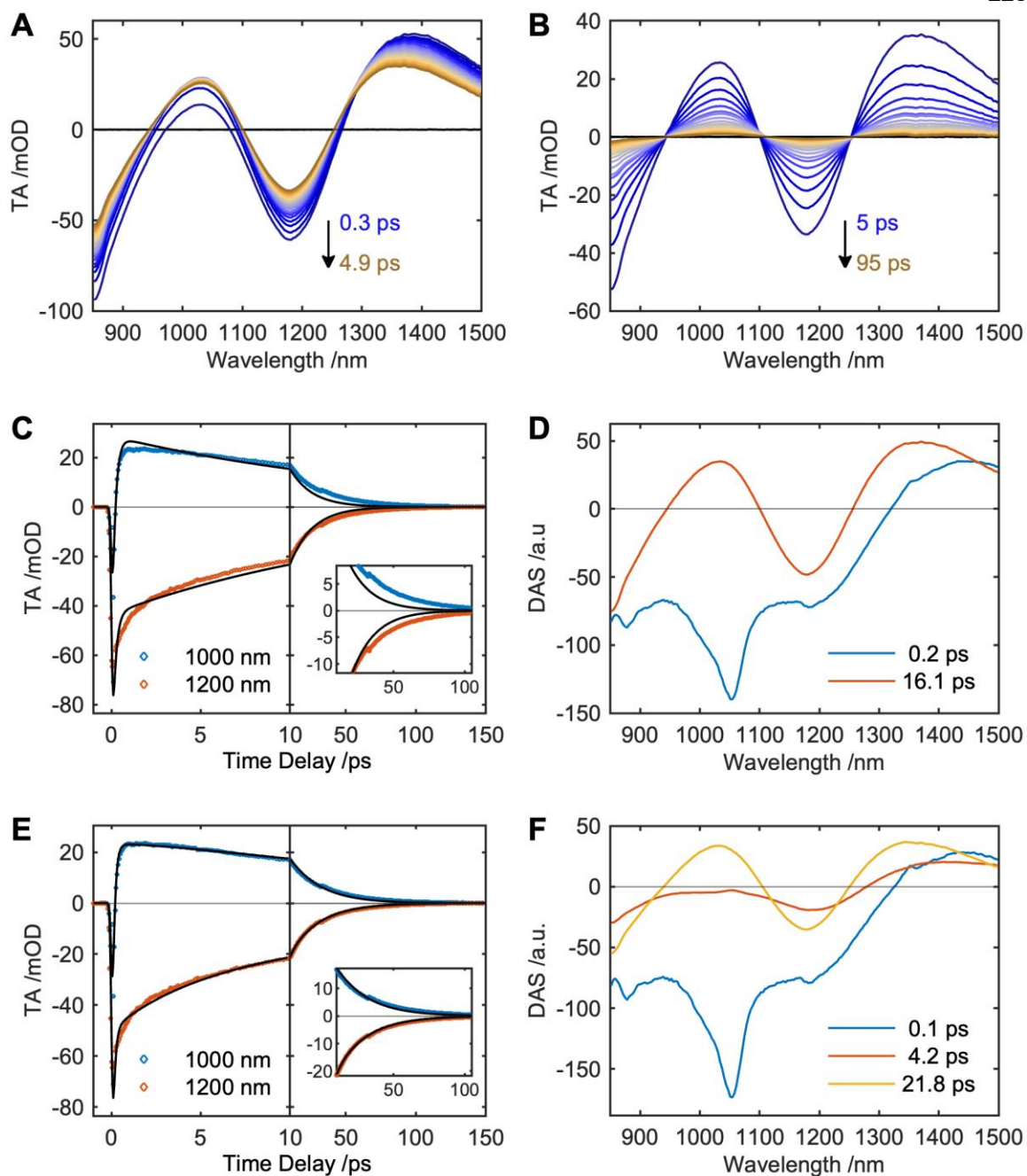


Figure S21. TA data for **5** in THF following 800 nm, 1 μ J photoexcitation. (A,B) Cascaded difference spectra across the two time regions indicated. (C,D) and (E,F) show results of three and four component global fits, respectively. (C,E) Kinetic traces at indicative wavelengths across two time regions. Inset is an enlarged view of the traces at long times. (D,F) DAS corresponding to the time constants indicated in the legend.

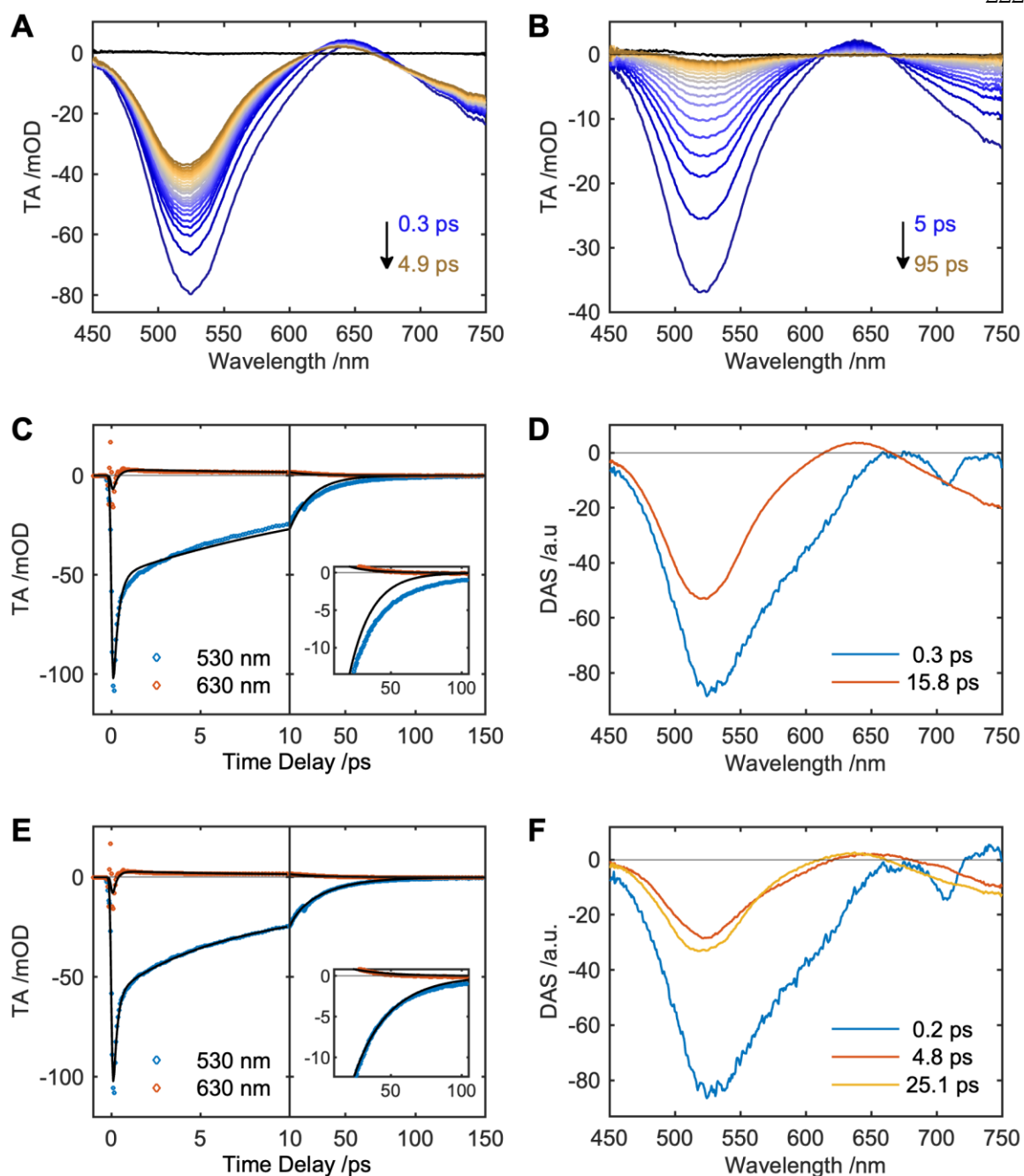


Figure S22. TA data for **5** in THF following 1200 nm photoexcitation. (A,B) Cascaded difference spectra across the two time regions indicated. (C,D) and (E,F) show results of three and four component global fits, respectively. (C,E) Kinetic traces at indicative wavelengths across two time regions. Inset is an enlarged view of the traces at long times. (D,F) DAS corresponding to the time constants indicated in the legend.

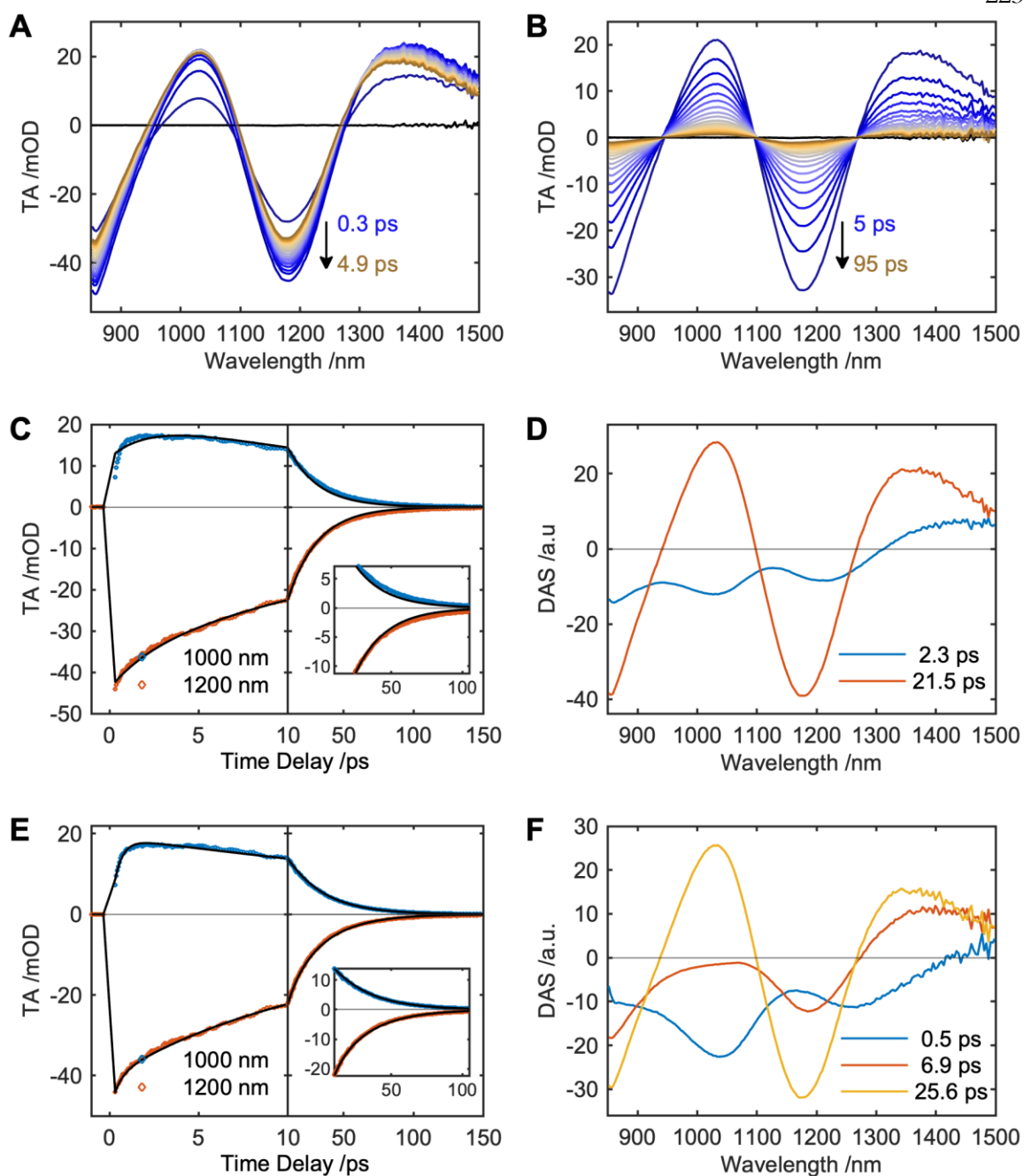


Figure S23. TA data for **5** in THF following 560 nm, 1 μ J photoexcitation. (A,B) Cascaded difference spectra across the two time regions indicated. (C,D) and (E,F) show results of three and four component global fits, respectively. (C,E) Kinetic traces at indicative wavelengths across two time regions. Inset is an enlarged view of the traces at long times. (D,F) DAS corresponding to the time constants indicated in the legend. The peak at \sim 1120 nm is due to scattered pump light.

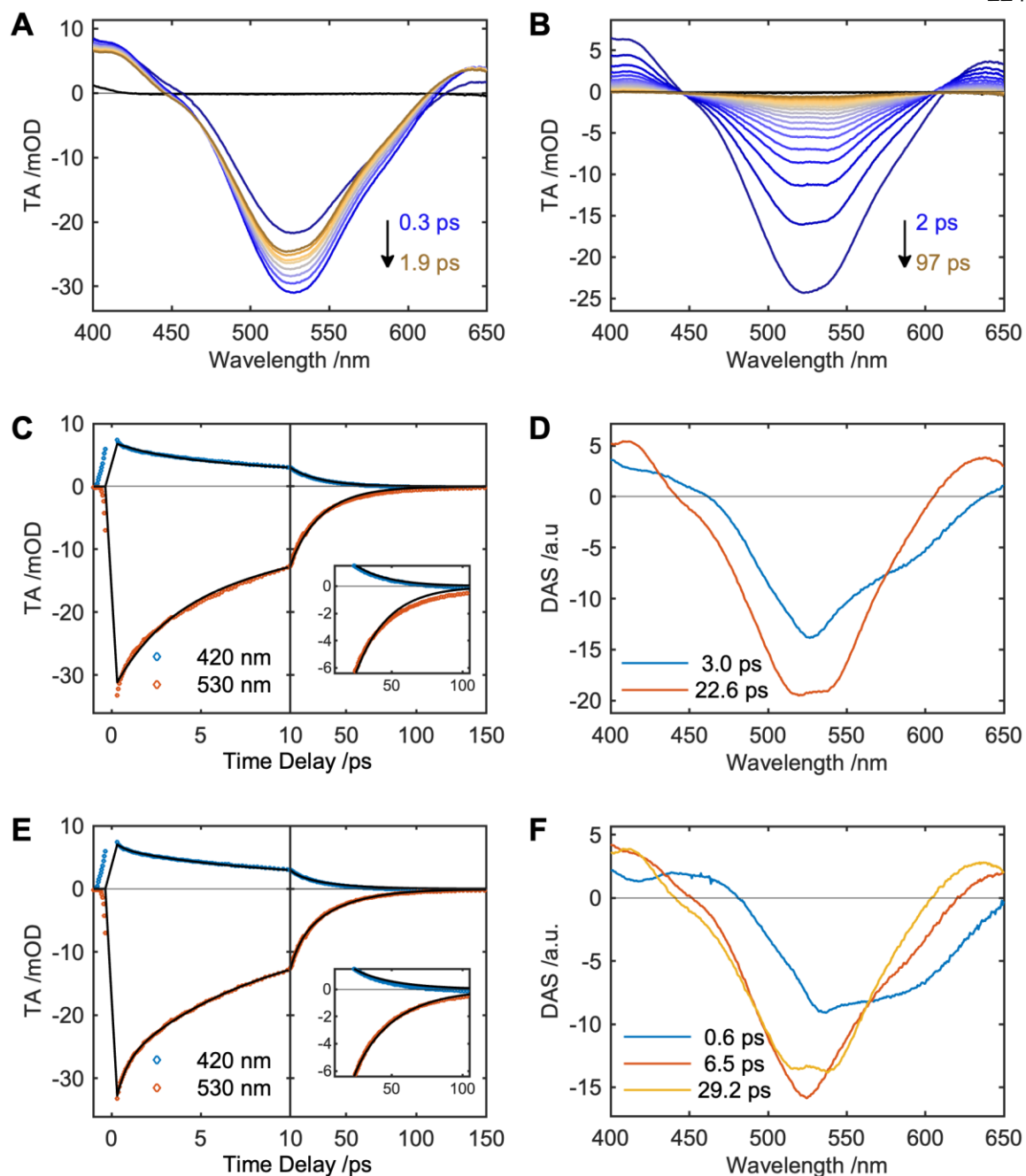


Figure S24. TA data for **5** in toluene following 800 nm, 1 μ J photoexcitation. (A,B) Cascaded difference spectra across the two time regions indicated. (C,D) and (E,F) show results of three and four component global fits, respectively. (C,E) Kinetic traces at indicative wavelengths across two time regions. Inset is an enlarged view of the traces at long times. (D,F) DAS corresponding to the time constants indicated in the legend.

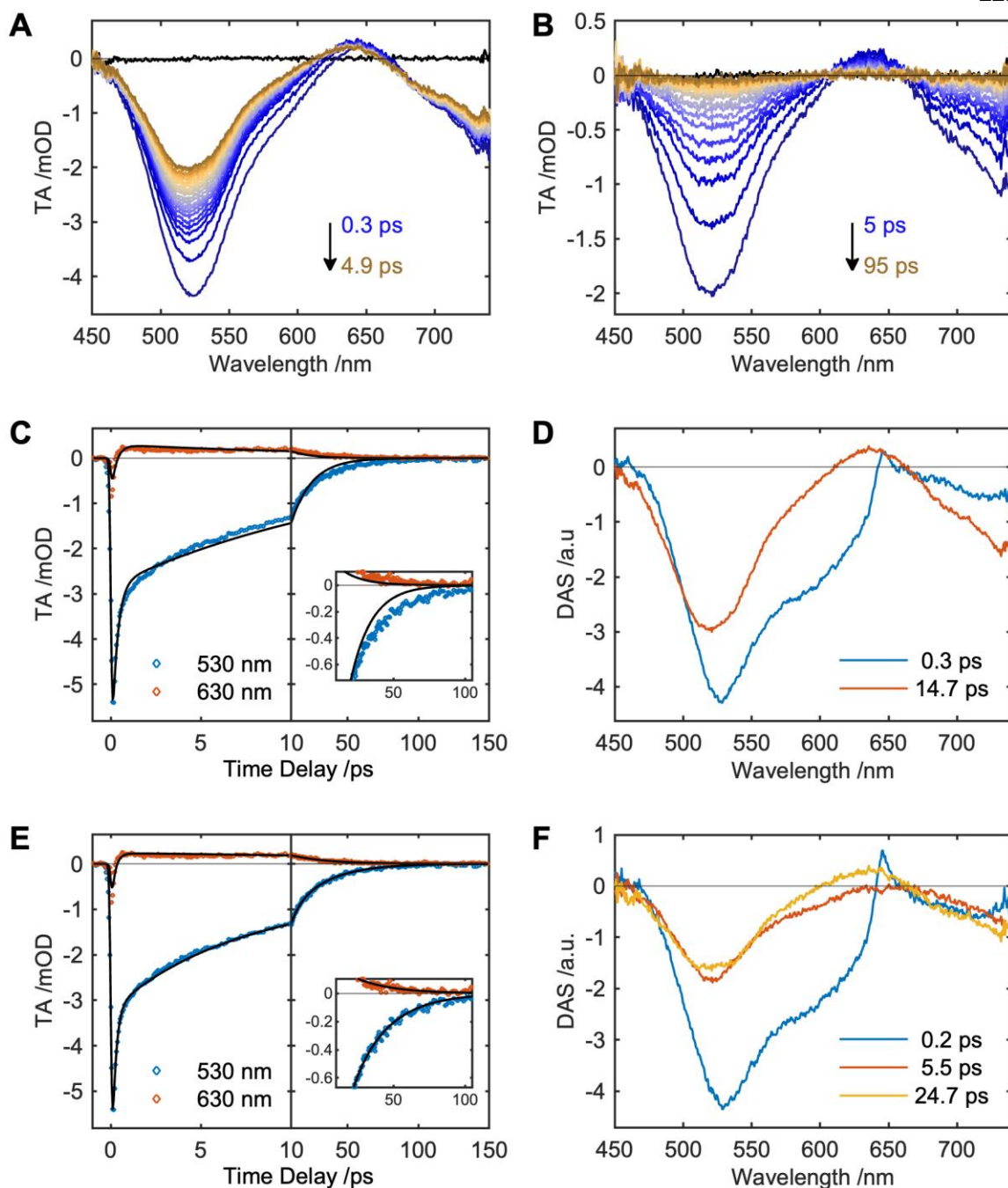


Figure S25. TA data for **5** in THF following 800 nm, 0.15 μJ photoexcitation. (A,B) Cascaded difference spectra across the two time regions indicated. (C,D) and (E,F) show results of three and four component global fits, respectively. (C,E) Kinetic traces at indicative wavelengths across two time regions. Inset is an enlarged view of the traces at long times. (D,F) DAS corresponding to the time constants indicated in the legend.

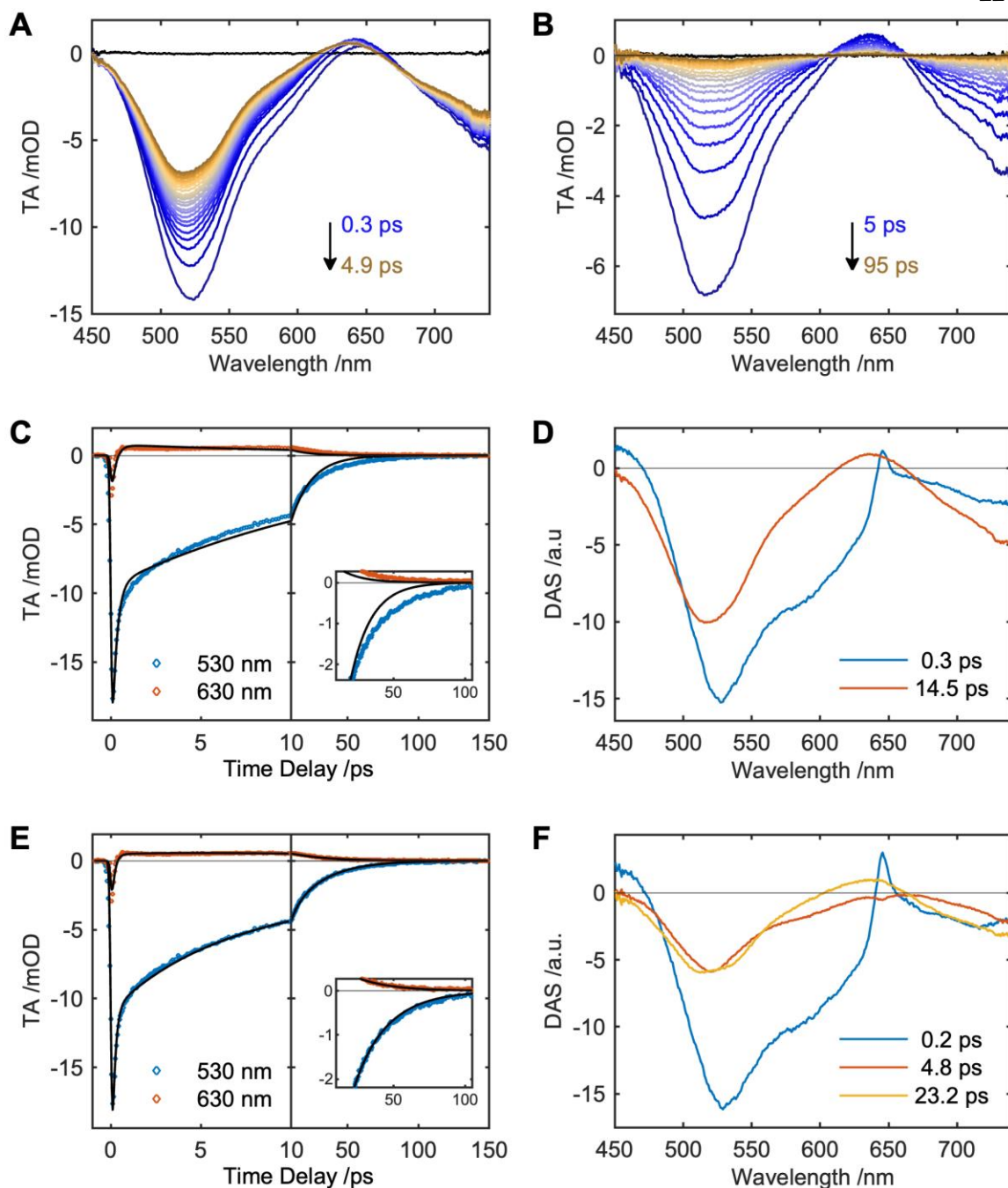


Figure S26. TA data for **5** in THF following 800 nm, 0.3 μJ photoexcitation. (A,B) Cascaded difference spectra across the two time regions indicated. (C,D) and (E,F) show results of three and four component global fits, respectively. (C,E) Kinetic traces at indicative wavelengths across two time regions. Inset is an enlarged view of the traces at long times. (D,F) DAS corresponding to the time constants indicated in the legend.

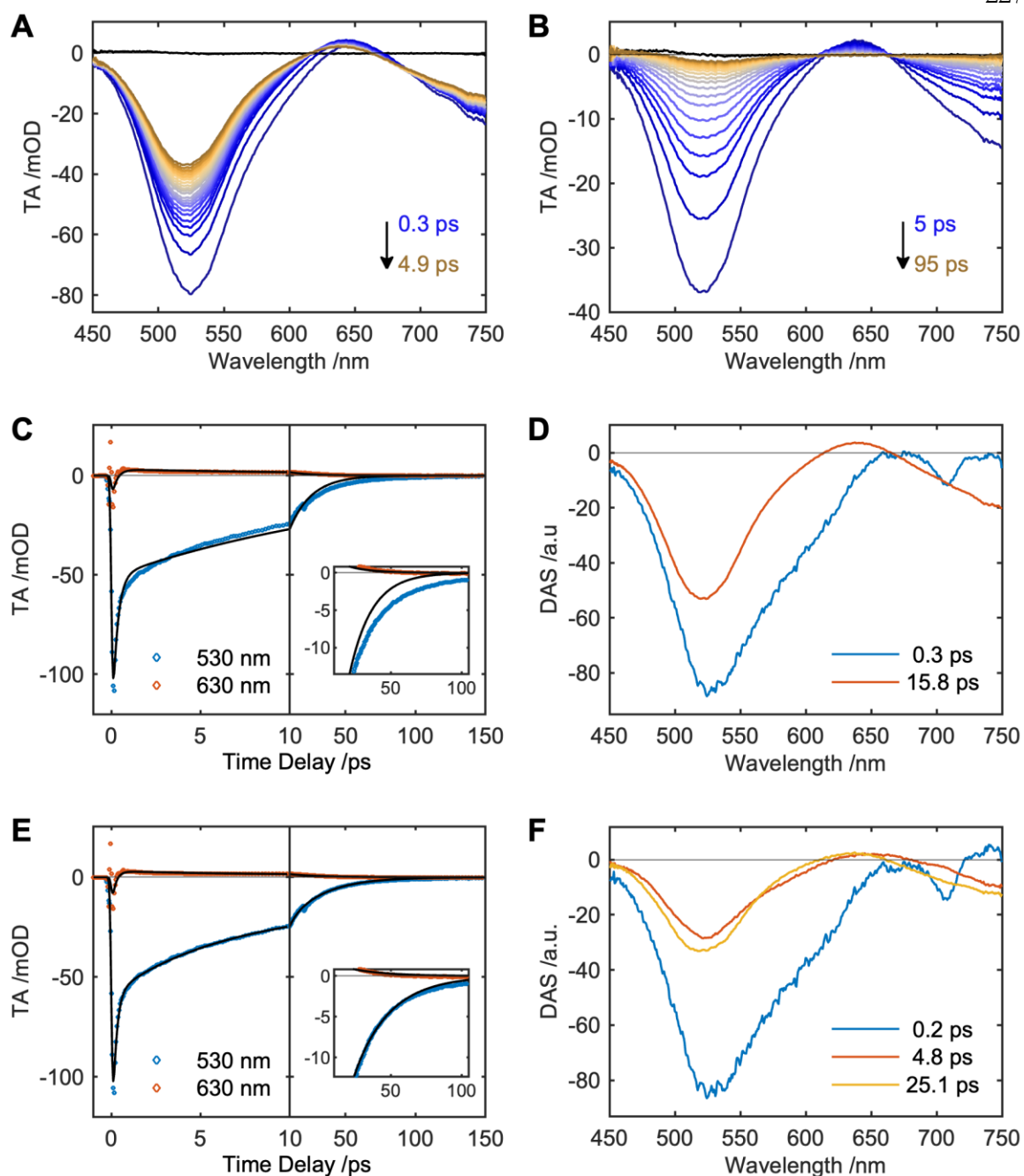


Figure S27. TA data for **5** in THF following 800 nm, 2 μ J photoexcitation. (A,B) Cascaded difference spectra across the two time regions indicated. (C,D) and (E,F) show results of three and four component global fits, respectively. (C,E) Kinetic traces at indicative wavelengths across two time regions. Inset is an enlarged view of the traces at long times. (D,F) DAS corresponding to the time constants indicated in the legend.

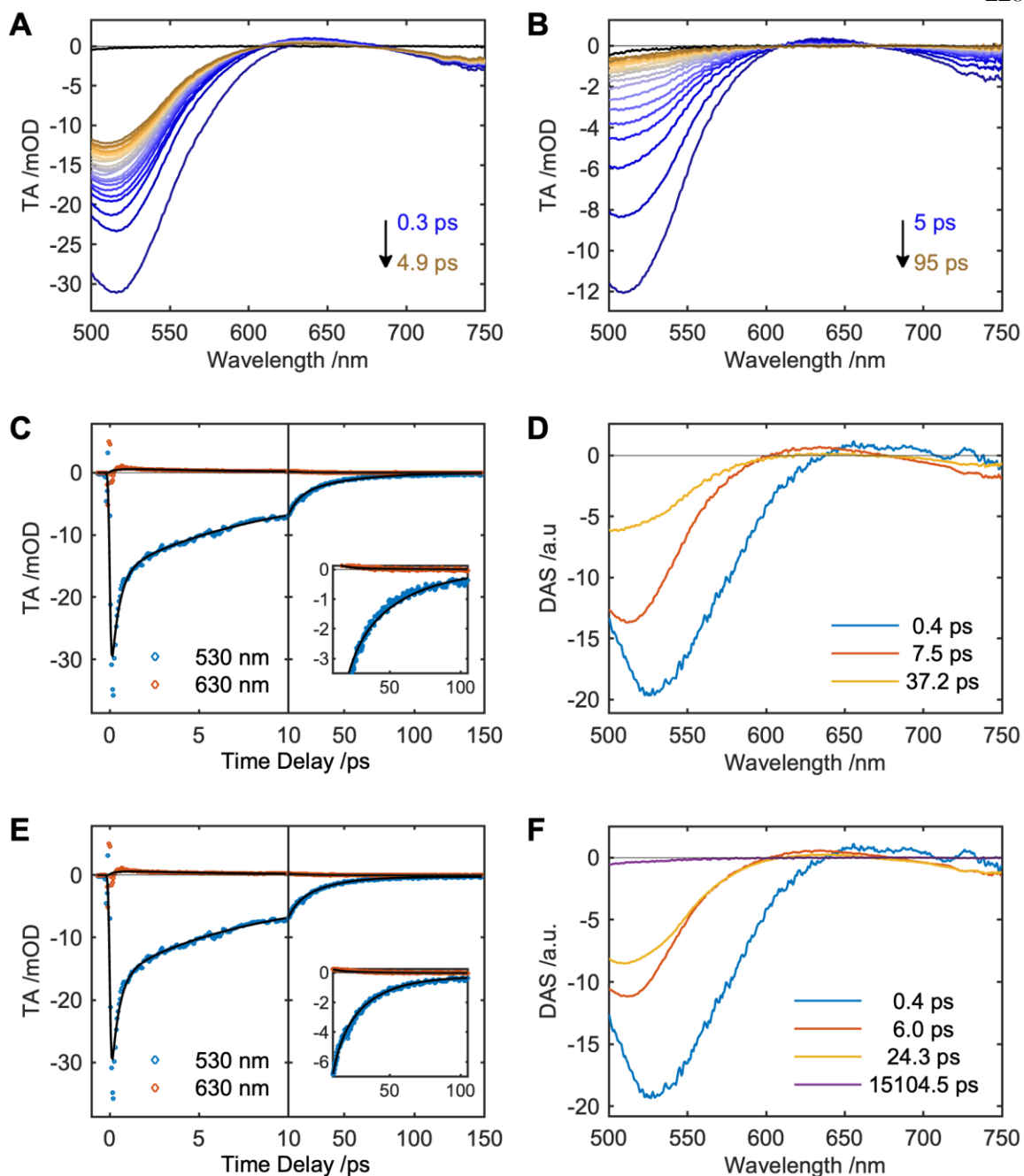


Figure S28. TA data for 5' in THF following 1200 nm photoexcitation. (A,B) Cascaded difference spectra across the two time regions indicated. (C,D) and (E,F) show results of three and four component global fits, respectively. (C,E) Kinetic traces at indicative wavelengths across two time regions. Inset is an enlarged view of the traces at long times. (D,F) DAS corresponding to the time constants indicated in the legend.

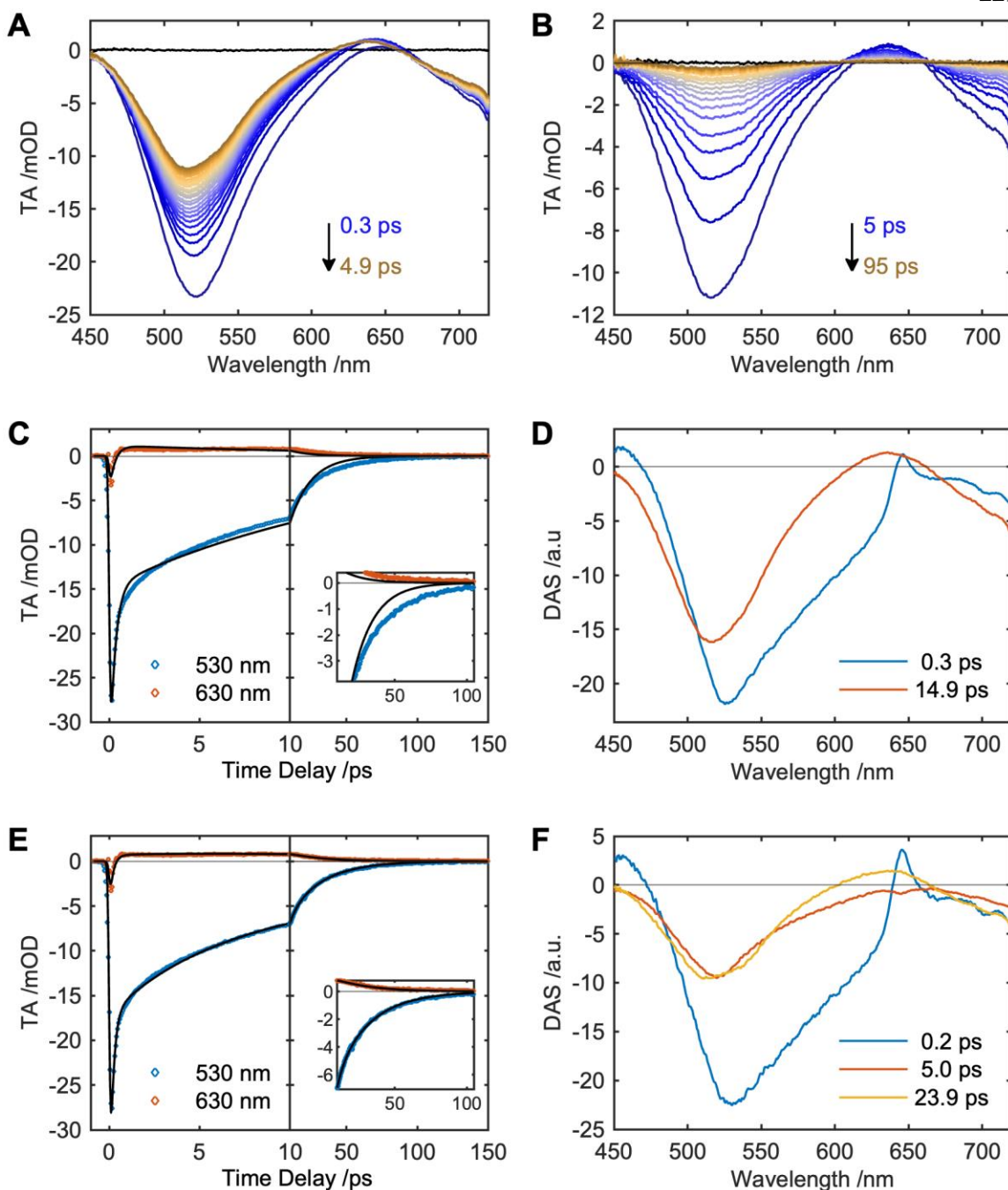


Figure S29. TA data for $5'$ in THF following 800 nm, 1 μ J photoexcitation. (A,B) Cascaded difference spectra across the two time regions indicated. (C,D) and (E,F) show results of three and four component global fits, respectively. (C,E) Kinetic traces at indicative wavelengths across two time regions. Inset is an enlarged view of the traces at long times. (D,F) DAS corresponding to the time constants indicated in the legend.

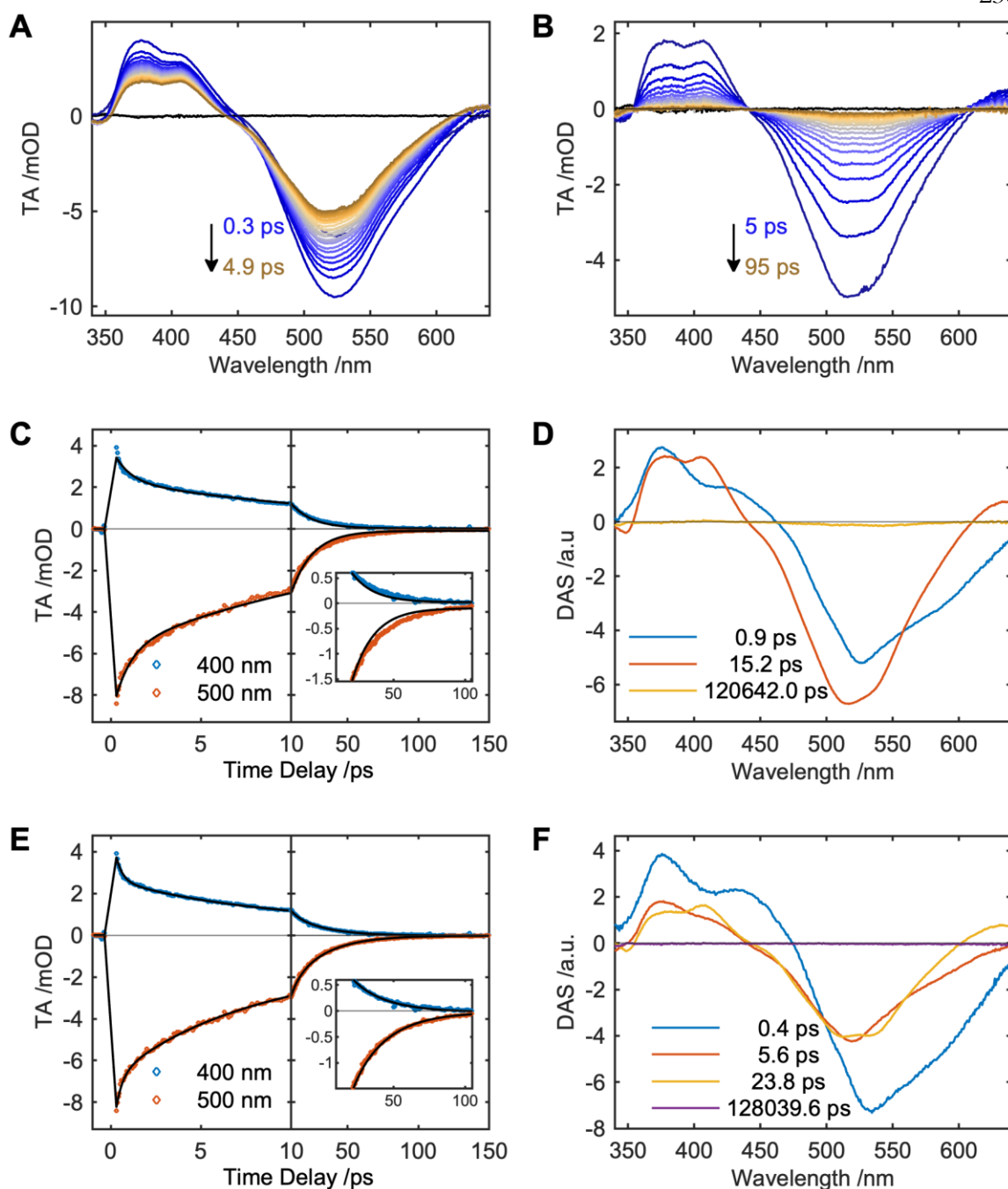


Figure S30. TA data for **5-Br** in THF following 800 nm, 1 μJ photoexcitation. (A,B) Cascaded difference spectra across the two time regions indicated. (C,D) and (E,F) show results of three and four component global fits, respectively. (C,E) Kinetic traces at indicative wavelengths across two time regions. Inset is an enlarged view of the traces at long times. (D,F) DAS corresponding to the time constants indicated in the legend.

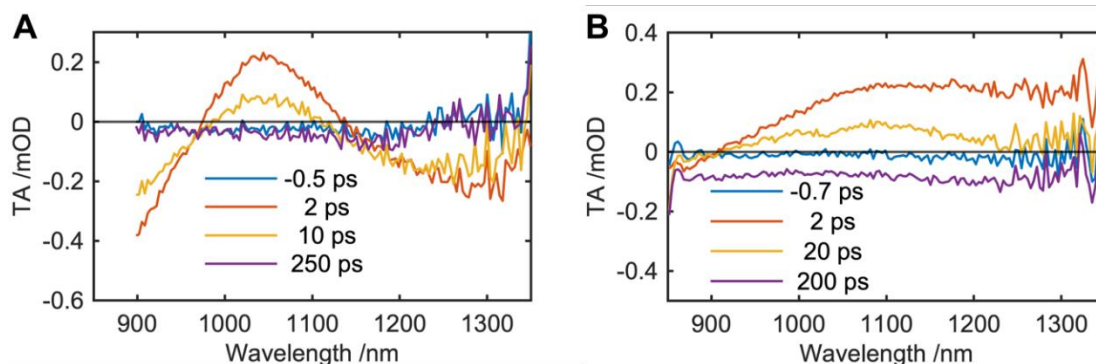


Figure S31. NIR difference spectra for (A) **4** and (B) **5-Br** at selected time delays following 700 nm and 800nm, 1 μ J photoexcitation, respectively. The GSB is partially obscured by the overlapping ESA in **4**. Noise precluded reliable fitting, but the features are shown for comparison to other measurements.

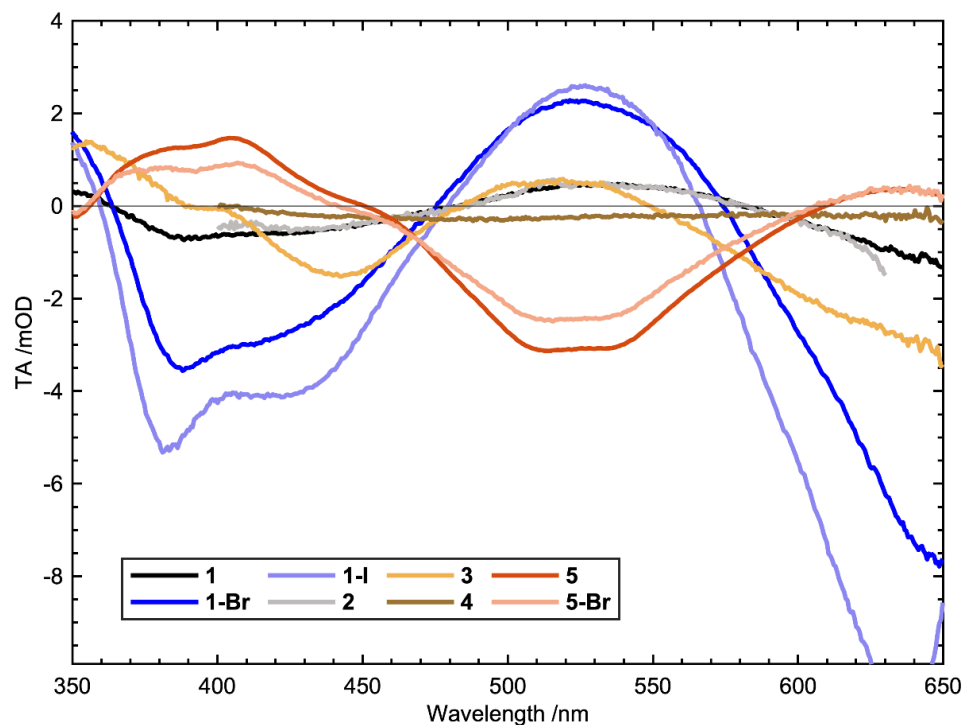


Figure S32. Difference spectra for all compounds overlaid following 1 μ J photoexcitation at either 700 or 800 nm. Time delays chosen to represent difference spectrum of rate-limiting process: compounds **1**, **1-Br**, **2** and **3** are shown at 2 ps, **1-I** at 5 ps, and **4**, **5** and **5-Br** at 15 ps. The spectrum for **5** has been scaled by 0.1 to fit on the same y-axis as the other compounds.

In this section, we have presented TA spectra measured for each compound (Figures S11-S31) using the procedure described in Section S1. Where possible, each dataset is shown

with fits to two kinetic models. The parameters obtained from the better of these two fits are given in Table S3 below.

TA spectra were also measured for **5** following photoexcitation into its MLCT bands at 1200 and 560 nm (Figures S22-S23). The resulting spectra and time constants agree well with the results for 800 nm photoexcitation, indicating the difference in behavior between **1** and **5** is not the result of pumping different MLCT bands; the lowest-energy MLCT dictates the overall ultrafast behavior.

We additionally questioned if solvent coordination to Ni obfuscated the comparison between **1** and **5**. Thus, TA spectra were also measured in toluene. The spectral and kinetic profiles of **1** and **5** were largely unchanged (still requiring two- and three-component fits, respectively) and both exhibited slightly slower relaxation to the ground state (12.4 ps in **1** and 29.2 ps in **5**). The difference in kinetic behavior between **1** and **5** is therefore not due to solvent coordination; we do not observe any evidence of a difference in relaxation pathway between solvents.

Finally, we repeated the above TA measurements on **1** and **5** at a range of pump powers to ensure the observed differences in dynamics were not due to saturation or multi-photon effects. For both **1** and **5**, the kinetics were independent of pump power from 0.15 to 2 mW (Table S3).

Table S3. Table of relaxation time constants for all compounds in THF.

Compound	Pump Wavelength (nm)	Pump Power (μJ)	Solvent	τ_1 (ps)	τ_2 (ps)	τ_3 (ps)	τ_4 (ps) ^a	τ_5 (ps) ^a
1	700	1.0	THF	0.3	-	10.9	-	∞
1	700	0.3	THF	0.4	-	11.2	-	∞
1	700	1.5	THF	0.3	-	10.7	-	∞
1	700	1.0	Toluene	0.5	-	12.4	-	∞
1-Br	700	1.0	THF	0.4	-	13.9	-	∞
1-I	700	1.0	THF	0.4	1.2	15.4	-	-
2	700	1.0	THF	-	-	12	80	∞
3	700	1.0	THF	0.4	-	10	300	∞
4	800	1.0	THF	0.5	5.2	22.3	-	∞
5	800	1.0	THF	0.6	5.6	24.2	-	-
5^b	800	1.0	THF	0.1	4.2	21.8	-	-
5	1200	n.d ^c	THF	0.2	4.8	25.1	-	-
5^b	560	1.0	THF	0.5	6.9	25.6	-	-
5	800	1.0	Toluene	0.6	6.5	29.2	-	-
5	800	0.15	THF	0.2	5.5	24.7	-	-
5	800	0.3	THF	0.2	4.8	23.2	-	-
5	800	2.0	THF	0.2	4.8	25.1	-	-
5'	1200	n.d ^c	THF	0.4	6.0	24.3	-	∞
5'	800	1.0	THF	0.2	5.0	23.9	-	-
5-Br	800	1.0	THF	0.4	5.6	23.8	-	∞

^aTime constants correspond to growth of long-lived feature discussed below, with those much longer than the time window considered infinite. ^bSpectra recorded with NIR probe.

^cNot determined due to lack of a suitable NIR power meter.

Discussion of Anomalous Long-lived Feature

As noted in the main text, a long-lived feature is observed in some spectra. This feature is negative and flat with little-to-no shape and appears to increase in magnitude as time-delay increases. The DAS corresponding to the shortest time constants show signals that clearly correspond to the growth or decay of the GSB and ESA of interest. Given the overlap of the positions of the GSB with the peaks in the static absorbance spectrum, these features must correspond to the Ni(I) species. In contrast, the final time constant corresponds to a constant offset which does not decay on the timescale of the experiment. The lack of any GSB features in the DAS corresponding to the static Ni(I) absorbance show that this signal does not arise from the Ni(I) species. For most compounds, this long-lived signal is very small and has minimal impact on the results other than necessitating an extra constant-offset component in the fitting procedure. However, in the samples containing **3** (Figure S18), this long-lived feature is non-negligible, and four components are needed for a reasonable fit to the data.

To better understand the kinetics of **3**, we turn again to the DAS. The shortest two components clearly correspond to the Ni(I) complex, due to GSB peaks with the same positions as peaks in the steady-state absorbance spectrum. The near-UV band (~350 nm) in the 10 ps DAS is often diagnostic of the presence of reduced bpy (an MLCT state). In contrast, the other two DAS are largely flat, and as such are not included in the analysis in the rest of this work. These latter two time components correspond to the slow growth of the flat feature and persist beyond the experimental timescale. Notably, consecutive repeats of this TA (Figure S33A) overlap exactly, showing that the signal is not due to sample degradation over the course of the experiment. Thus, we find a strong Ni(I) signal which decays alongside a slowly growing, broad, negative feature.

Given that the long-lived signal is largest in **3**, we investigated it in more depth using **3** as a model system. Photogeneration of **3** from its parent Ni(II) complex resulted in the formation of some precipitate. We brought the sample into the glove box, filtered the cuvette solution through a Kimwipe, and returned the filtrate for TA analysis. TA on this solution did not exhibit a noticeable change to the unfiltered sample. We further questioned if this signal was from a Ni(I) complex. Ni(I) species are known to react quickly with aryl halides. In the glove box, aryl bromide was added to the solution. Doing so removed the TA signal originating from the Ni(I) species, but the long-lived signal was still present in the sample (Figure S33B). Therefore, we find that the short-lived signals assigned to **3** do indeed arise from the Ni(I)–bpy halide complex, but that the long-lived signal does not.

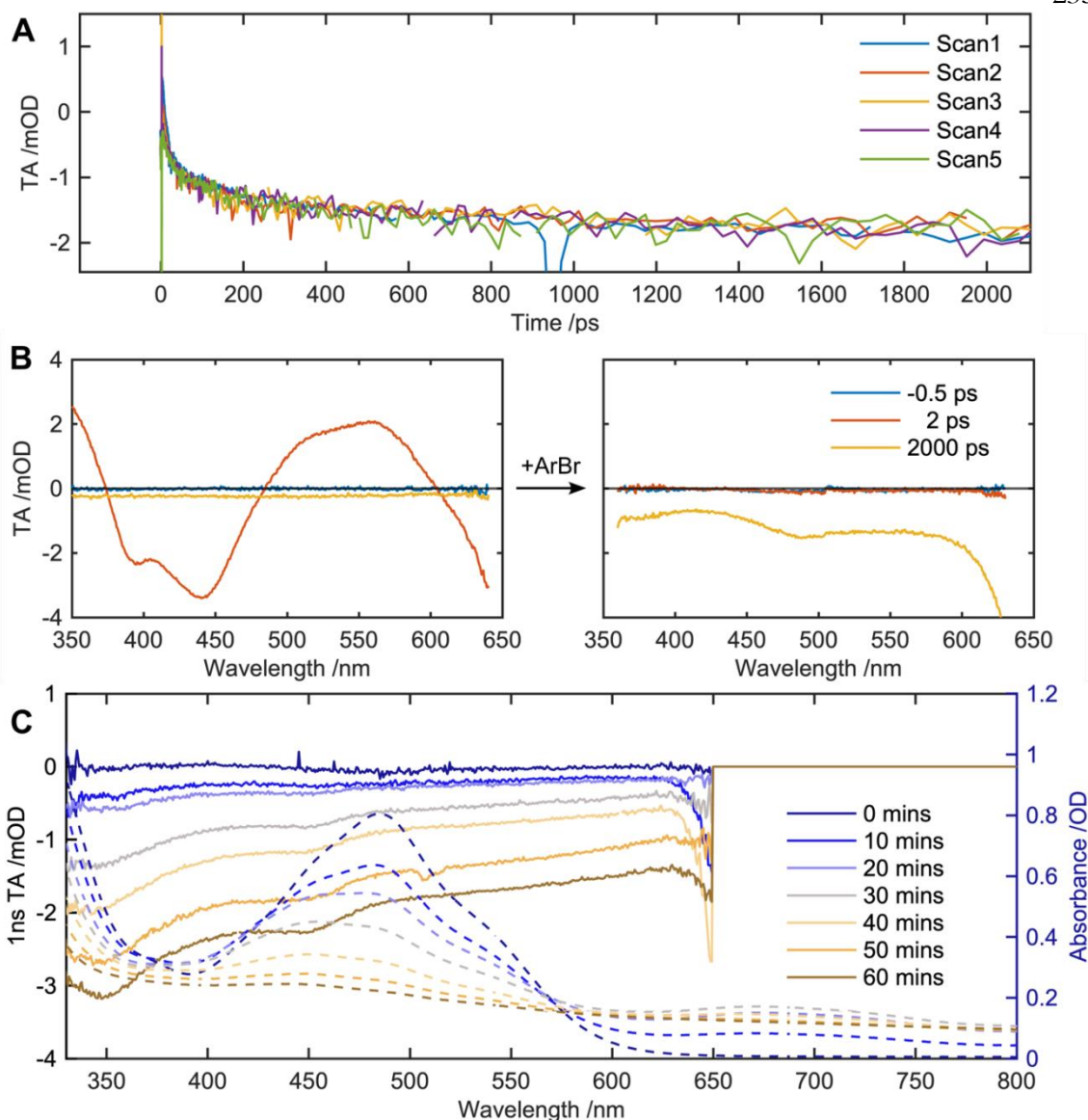


Figure S33. TA spectra for sample containing **3** under various conditions following 700 nm, 1 μJ photoexcitation. (A) Consecutive scans of the TA measurement showing the reproducibility of the long-lived feature. (B) Difference spectra before and after addition of aryl bromide showing disappearance of Ni(I) signal. (C) Difference spectra at 1 ns (solid lines) recorded at different irradiation times alongside the corresponding absorption spectra (dotted lines).

We next turned to a photogeneration time-course experiment to try to identify the origin of the signal. A solution of the Ni(II) parent complex for **3** was irradiated for different lengths of time and the TA signal at 1 ns was plotted alongside the UV-vis data (Figure S33C). Pumping the compound at 700 nm avoids exciting any parent Ni(II) left in solution. Furthermore, by looking at only the TA signal at a long time delay (1 ns) wherein all

photoexcited **3** will be back in the ground state, we can select for only the long-lived feature. From the absorbance data, the Ni(II) peak (~480 nm) decreases monotonically with time, while the peak around 670 nm grows in and then decreases. This lower-energy peak is indicative of the formation and then subsequent thermal degradation of **3**. In the corresponding TA, a monotonic growth of the signal magnitude with increasing irradiation time is observed. The signal presents as a broad feature that slowly grows towards the blue with two small peaks around 350 and 450 nm.

From comparison to Figure S18, it is clear that the shape of the long-lived feature varies between samples but is reproducible for multiple measurements of the same solution. The dependence of the long-lived TA signal on irradiation time is markedly different than that of the steady-state Ni(I) peak at 670 nm, further supporting the idea that this long-lived feature does not originate from **3**.

While we can conclude that the long-lived feature originates from neither photoexcited **3** nor its Ni(II) parent, its true identity is unknown. Previous studies into the speciation which occurs when Ni(II)-bpy aryl halide complexes are irradiated present three potential other candidates: Ni(II)/Ni(I) bimetallic aggregates,^{6,16} Ni(I)/Ni(I) dimers,^{6,17,18} or high-spin Ni(II)-bpy dihalide.^{6,7} The first of these require there be significant Ni(II) parent in solution, which does not fit with the above kinetic observations. Most likely for our case is the insoluble (or sparingly soluble) Ni(I)/Ni(I) dimer which forms irreversibly and depends only on the Ni(I) concentration (formation of the dimer is expected to be the main thermal degradation pathway for **3**)⁶ or further downstream decomposition resulting in the high-spin Ni(II)-bpy dihalide.

Therefore, we tentatively postulate that the pump pulse deposits a significant amount of thermal energy into the system causing dissolved dimers or high-spin Ni species to precipitate. The newly formed precipitate at the focus of the light would then slowly diffuse outwards, scattering a greater proportion of light as the delay time increases. This would be evidenced by a growing GSB in the TA signal, such as what we observe. Then, over the subsequent microseconds, the precipitate would diffuse far enough away from the focused light as to not affect the transmitted signal (or the precipitate could redissolve), thereby making the TA repeatable. Whatever the origin of the signal, it arises from neither photoexcited parent Ni(II) nor the Ni(I) complexes studied herein.

S1.6 Fits to Alternative Relaxation Models

In an attempt to rationalize the differences between **1-3** and **4-5**, we considered the possibility of alternative decay pathways, including relaxation through the intermediacy of an optically dark metal-centered state (^2d-d) or a 4MLCT state accessed by intersystem crossing (ISC). Rate-limiting decay of a dark ^2d-d state can be excluded by considering that the relaxation proceeds through simultaneous recovery of the ESA and GSB with isosbestic points for all compounds and the presence of strong ESA in the visible. Therefore, if a dark ^2d-d state is formed, it must relax much faster than the 2MLCT . The $^2d-d \rightarrow ^2GS$ transition has an energy gap similar to that of the MLCT state and is formally orbitally forbidden, making it unlikely that it is significantly faster than a rate-limiting $^2MLCT \rightarrow ^2d-d$ step (Figure S44). Conversely, optical TA is not sensitive to state multiplicity, allowing for the possibility of relaxation from $^2MLCT \rightarrow ^4MLCT$ by fast ISC followed by spin-forbidden relaxation to the ground state ($^4MLCT \rightarrow ^2GS$, Figure S42). Albeit not completely unprecedented, the observed values for τ_3 would constitute very short time constants for reverse ISC to the ground state.⁵ We further find that the relaxation kinetics of this step show no dependence on pump wavelength (Table S3). As such, we propose that all compounds relax from the same MLCT excited state (Figure 5A).

Several models have been presented for intramolecular electron transfer (ET) over the past decades; in this section we discuss four of these to understand the data presented in main text Figure 5B. These models all rely on the same four approximations:

1. The series of compounds relax from the same MLCT excited state.
2. E_{MLCT} is an accurate reflection of the lowest MLCT state.
3. The electronic coupling is roughly the same along the series.
4. The series of compounds show roughly the same reorganization energies between ground and excited states.

That all compounds in the series relax from the same MLCT state is discussed above, and the association of this state to E_{MLCT} is supported by the TD-DFT assignments (Tables S5-S12) of the absorption spectra presented in Section S1.4. The lowest MLCT transition energy is only slightly lower than that of the lowest high-absorbance MLCT, justifying this approximation. The latter two are assumed for almost all literature examples of Marcus theory discussed below, and we see them as equally valid in this case. Only the bpy substituents or the halide change between compounds; the bpy coordination sites that have most influence on the MLCT character are mostly unchanged by these modifications. Therefore, we expect that the electronic coupling and reorganization energies are similar across all compounds. Any additional model-specific assumptions are discussed where relevant in the following paragraphs.

Weak Coupling Model

Jortner and co-workers^{19,20} developed one such model to describe the non-radiative relaxation of excited states. Their framework relates the rate of relaxation to the deformation of the excited state relative to the ground state. If the deformation is relatively small—the so-called weak coupling limit—then the intersection between the ground- and excited-state PESs lies at very high energy. Therefore, relaxation proceeds through coupling of the excited state to high-energy vibronic modes of the ground state. At room temperature, this leads to Eq. (S3).

$$k = \frac{V^2}{\hbar} \sqrt{\frac{2\pi}{\hbar\omega_M\Delta G^\circ}} \exp\left(-\frac{\Delta G^\circ}{\hbar\omega_M} \left[\log\left(\frac{\Delta G^\circ}{d\lambda}\right) - 1\right]\right) \quad (\text{S3})$$

Here $\hbar\omega_M$ is the energy of the highest vibrational mode with degeneracy, d . V is the matrix element for the transition, and ΔG° is the energy gap between the relaxed excited and ground states. Given the explicit dependence on the maximum vibrational frequency, the rate is expected to show a strong dependence on the character of this transition. To derive Eq. (S4), it is assumed that the reorganizational energy is small such that $\left[\log\left(\frac{\Delta G^\circ}{d\lambda}\right) - 1\right] > 0$. This results in a slightly stronger than exponential dependence on ΔG° and thus recovers the empirical energy gap law. Our main interest here lies with the dependence on ΔG° so we can simplify to

$$k = \frac{A}{\sqrt{E_{MLCT} - \lambda}} \exp\left(-\frac{E_{MLCT} - \lambda}{\hbar\omega_M} \left[\log\left(\frac{E_{MLCT} - \lambda}{d\lambda}\right) - 1\right]\right), \quad (\text{S4})$$

where the pre-factors have been condensed into A . The same assumption as in the main text that $\Delta G^\circ = \lambda - E_{MLCT}$ is also made to relate the model back to the experimentally accessible vertical transition energies. For all compounds, the highest vibrational modes are C–H stretches on the bpy at around 0.39 eV (Table S4); six of these are in common to all **1–5**. While not strictly degenerate, these are similar in energy so we follow literature precedent^{19,21} in setting $d = 6$ and fit for the remaining parameters. This results in the fit shown in Figure 5B, with $\lambda = 0.09$ eV, $\hbar\omega_M = 0.41$ eV and $A = 0.26$ eV^{1/2} ps⁻¹. While it can describe the high-energy results well, the monotonically increasing function cannot account for the slower relaxation of the lower-energy compounds. Despite this, it does seem to recover the energy of the C–H stretches, suggesting that there may be some merit to the fit in the high-energy region. Observation of a large change in rate upon deuteration of the bpy could interrogate this experimentally, as the energy change from C–H to C–D vibrational modes ($\hbar\omega_M(\text{C–D}) \sim 0.28$ eV)¹⁹ are expected to result in sizable changes to the coupling between the ground and excited states.

Importantly, a globally poor fit to our data is to be expected from the weak coupling model given the assumptions taken in its derivation. Here we observe MLCT transitions where there will, by definition, be a significant redistribution of charge. Therefore, unlike a $\pi \rightarrow \pi^*$ transition, for example, the reorganization energy here is relatively large, as is observed in the absorption spectra in Figure S10. Thus, again we find that our system most likely does not lie within the weak coupling limit.

Strong Coupling and Classical Marcus Models

When the excited-state deformation is large enough, the intersection between the surfaces becomes thermally accessible. The system will instead move along the vibrational coordinate with a small activation energy into the ground-state PES through the intersection. This behavior is shown schematically in the main text Figure 5A and corresponds to the strong coupling limit presented by Jortner *et al.*¹⁹ and given mathematically by main text Eq. (1). As ΔG° decreases, excited- and ground-state PESs transition from nested to displaced, and the resulting change in activation energy yields a parabolic dependence on ΔG° . In deriving Eq. (1), it is approximated that probability of surmounting the energy barrier is determined by the mean vibrational energy. Here we again relate back to E_{MLCT} to get Eq. (2) and then fit this to the observed rate constants. A good fit is achieved (Figure 5B) with fitting parameters: $\lambda = 0.77(3)$ eV, $\ln(A) = 25.7(6)$, $\langle \hbar\omega \rangle = 0.13(7)$ eV. As discussed in the main text, $\langle \hbar\omega \rangle$ is indeed close to the calculated average vibrational energy; the reorganizational energy is larger than that obtained from fitting the steady-state spectra, but of similar magnitude.

The most successful theory of electron transfer (ET) is Marcus theory.²²⁻²⁴ However, this was developed for ET between two relatively independent species rather than the non-radiative relaxation we observe here.²⁵ These could be different molecules in the case of intermolecular ET or even a large molecule with well-separated donor and acceptor. This places limits on the applicability of the model to intramolecular systems. Despite this fact, we can still utilize Marcus theory to approximate the dynamics of charge transfer transitions. Making the same assumption that $\Delta G^\circ = \lambda - E_{MLCT}$ leads to Eq. (S5)

$$\ln(k) = \ln(A'') - \frac{(E_{MLCT} - 2\lambda)^2}{4\lambda k_B T}. \quad (\text{S5})$$

Fitting this to the data in Figure 5B and fixing T to 298 K, yields $\lambda = 0.76(1)$ eV, $\ln(A) = 27.1(2)$. This fit is plotted alongside the other three models in Figure 5B, where it is clearly worse than that of Eq. (2) yet still captures the main features of the data; the reorganization energy is consistent between the two models. The worse fit is to be expected given that the ET in question is short-range and intramolecular, and there is one fewer fitted parameter.

Likewise, the consistency in λ likely only reflects the very similar functional forms of the models.

Nonetheless, the loose applicability of classical Marcus theory here is borne out by the similarities between the Marcus equation and the strong coupling model discussed in the main text and Eq. (2). Both the classical Marcus theory and strong coupling models have the same form, save for the substitution $\langle \hbar\omega \rangle = 2k_B T$, which physically corresponds to the charge transfer being driven by vibrational modes rather than thermal energy. This difference follows from their derivation in classical and quantum regimes, respectively. Accordingly, the semiclassical derivation of Marcus theory leads to the same dependence on $\langle \hbar\omega \rangle$.²⁶

Vibronic Marcus Model

Classical Marcus theory can be extended into a quantum regime by considering coupling of the electron transfer with vibronic modes.²⁷ Summation over all vibronic modes is not practical for fitting experimental data, so this can be simplified by assuming quantum coupling to just one mode—either one dominant mode, or a representative average mode—while low frequency modes are treated classically.²⁸ This semiclassical vibronic Marcus model was first applied in the context of long-distance intramolecular electron transfer²⁹ and splits the reorganization energy into contributions from the solvent and vibrations, λ_S and λ_V , respectively. Mathematically, this gives rate constants of

$$k = V^2 \sqrt{\frac{\pi}{\hbar^2 \lambda_S k_B T}} \sum_{w=0}^{\infty} \frac{e^S S^n}{n!} \exp\left(-\frac{(\Delta G^\circ + \lambda_S + n\hbar\omega)^2}{4\lambda_S k_B T}\right), \quad (\text{S6})$$

where $S = \lambda_V / \hbar\omega$ and $\hbar\omega$ is the energy of the mode to which the ET couples. The sum over w accounts for transitions into each of the ground-state vibronic modes and the weighting of the exponential corresponds to the Franck-Condon factor for each transition. Substituting $\Delta G^\circ = \lambda - E_{MLCT} = (\lambda_S + \lambda_V) - E_{MLCT}$ results in

$$k = A' \sum_{n=0}^{\infty} \frac{e^S S^n}{n!} \exp\left(-\frac{(E_{MLCT} - 2\lambda_S - \lambda_V - n\hbar\omega)^2}{4\lambda_S k_B T}\right), \quad (\text{S7})$$

where the pre-factors are again collated into A . This constitutes the fourth model we fit to our data, resulting in parameters $A = 0.044 \text{ ps}^{-1}$, $\hbar\omega = 0.21 \text{ eV}$, $\lambda_S = 0.54 \text{ eV}$, $\lambda_V = 0.22 \text{ eV}$; the fit to this vibronic Marcus model is plotted in Figure 5B. Accurate estimates of errors on these values could not be obtained due to the infinite sum requiring a more involved fit. Given the explicit dependence on solvent, we exclude the toluene datapoints from the fit here, but their inclusion has a negligible impact on the fitted parameters. The Franck-Condon weighted sum results in an asymmetric, near-parabolic dependence that gives the best fit to

the data out of all models considered here (albeit with the greatest number of fitted parameters).

Previous studies on Fe–polypyridyl complexes¹⁵ supposed that bpy breathing modes couple to MLCT transitions. Vibronic coupling to a particular mode is typically accompanied by corresponding vibronic progressions into the absorption spectrum. However, given the linewidth and number of transitions expected in the spectra for **1–5**, we are not able to say whether significant vibronic transitions are present. Despite this, the 0.21 eV value obtained from the fit does lie within the range of bpy breathing modes of **1–5**, which are predicted by DFT to be ~0.2 eV. It is also often assumed that ET along organic spacers is coupled to general skeletal modes in the region of 0.19 eV,^{29–31} further corroborating the fitted value. Only the solvent contribution to the reorganization energy affects the linewidths of the peaks in the absorption spectrum. Indeed, λ matches the widths obtained from Section S1.4. This value is also identical to that observed for Zn porphyrin complexes in THF.³⁰ The vibrational reorganization energy is much harder to determine experimentally, but it can be approximated through calculations of the PESs in Figure S44. These calculations (with implicit solvation model, CPCM) do not account for reorganization of the solvent, reducing the predicted contribution of λ_S . Consequently, they should roughly correspond to λ_V and are found to be 0.18 eV and 0.33 in **1** and **5**, respectively, which is close to the 0.22 eV given by the fit. However, as discussed in Section S2.5, there are several limitations to DFT in these systems. Literature values for λ_V are found in the range 0.15–0.6 eV,^{29–32} reflecting the dependence on excited-state distortion, which can vary greatly between compounds. The total reorganization energy $\lambda = \lambda_S + \lambda_V = 0.76$ eV found by the vibronic Marcus fit is consistent with the classical Marcus and strong coupling models.

Comparing Eqs. S6 and S7, $V = 1.4$ meV $\ll k_B T$, indicating that the relaxation is nonadiabatic, which is assumed by the Marcus model and implies that crossing the PES is the rate-determining step.²⁹

Despite being developed for longer-range ET, the vibronic Marcus model still appears to provide a self-consistent description of the data here. The model has also been applied with success to short-range intramolecular charge transfer transitions in both inorganic and organic systems, suggesting that its semiclassical nature is not a significant limitation.^{15,30–35} Both strong coupling and vibronic Marcus models appear to give good descriptions of the data, and both of these arise from considering the intersection of displaced PESs.

Therefore, while Marcus theory was initially developed for long-distance charge transfer, it is functionally the same as strong coupling in this case. In compounds **1–3** with their larger E_{MLCT} , the ground-state and MLCT PESs are nested (known as “inverted” in the language

of Marcus theory) and so behave in a manner reminiscent of the energy gap law. For ~~4~~**5**, which have smaller E_{MLCT} , the PES are displaced (normal) so the energy gap law behavior is effectively reversed.

S2. Computational Section.

S2.1. General Computational Details.

All the computations were performed using ORCA 5.0.3 software.^{36,37} Molecular structures were optimized with DFT using the BP86 functional^{38,39} with the def2-TZVP basis set⁴⁰ on all atoms except Ni which received def2-TZVPP. The Weigend auxiliary basis set, def2/J was used.⁴¹ The calculations were expedited by employing the resolution-of-identity (RI) approximation. The D3BJ dispersion correction^{42,43} was applied; the conductor-like polarizable continuum (CPCM) solvation model^{44,45} was used for implicit solvation.

Single point calculations with the hybrid B3LYP functional^{46,47} and def2-TZVP+def2-TZVPP(Ni) basis set were used to refine the electronic energies and molecular properties. Again, def2/J was used as auxiliary basis, alongside D3BJ and CPCM for dispersion correction and solvation modeling, respectively. The chain-of-spheres approximation, RIJCOSX,⁴⁸ was utilized as is default for hybrid-DFT in ORCA 5.

For equilibrium geometries, the terms contributing to Gibbs free energy were calculated as follows:

$$G = E_{\text{el}} + G_{\text{solv}} + [E_{\text{ZPVE}} + RT - RT \ln(Q)], \quad (\text{S8})$$

where, *i*) E_{el} is the *in vacuo* electronic energy; calculated using RI-B3LYP-D3 method as above, *ii*) G_{solv} is the free energy of solvation; calculated using CPCM, *iii*) $[E_{\text{ZPVE}} + RT - RT \ln(Q)]$ corresponds to the thermal enthalpic and entropic contributions to the solute energy with E_{ZPVE} and Q being the zero-point vibrational energy and the molecular partition function, respectively; obtained from frequency calculations with the rigid rotor/harmonic oscillator approximation (for $p = 1$ bar, $T = 298$ K).

The spin states considered in our computational analysis of **1-5** were all doublets ($S = 1/2$), taken following experimental data. For **1** and **5**, ISC to a quartet ($S = 3/2$) was also considered.

On top of the DFT-optimized geometries, TDDFT was used to predict the excited states and compare the computational absorption patterns with experimental UV–vis–NIR spectra. For each TDDFT calculation, 100 roots were considered. Relaxed excited-state geometries were also found using TDDFT via the iRoot keyword in ORCA.

The XYZ coordinate system used for labeling orbitals throughout the manuscript was selected according to the parent Ni(II) complexes to maintain consistency with the previous studies,^{4,6,49} i.e., the x and y axes are oriented along the Ni–N(bpy) axes, making the singly occupied orbital to be the $3d(x^2-y^2)$. By this, the orbitals parallel and perpendicular to the Ni–

halide axis are the mixtures of $d(xz)$ and $d(yz)$ orbitals. To distinguish them, we thus label the orbitals as $d(xz/yz, \parallel)$ and $d(xz/yz, \perp)$ according to their parallel and perpendicular orientation to the Ni–halide axis.

S2.2. Sample ORCA Inputs.

Example DFT Geometry Optimization	Example DFT Single Point Calculation
<pre>! UKS BP86 def2-TZVP def2/J RI D3BJ ! TightSCF CPCM(THF) SlowConv ! OPT FREQ %basis newgto Ni "def2-TZVPP" end end *xyzfile 0 2 structure.xyz</pre>	<pre>! UKS B3LYP def2-TZVP def2/J RIJCOSX ! D3BJ CPCM(THF) SlowConv ! MOREAD ! SP %moinp "optimization.gbw" %basis newgto Ni "def2-TZVPP" end end *xyzfile 0 2 optimized-structure.xyz</pre>
Example TDDFT Calculation	Example TDDFT Excited State Optimization
<pre>! UKS B3LYP def2-TZVP def2/J RIJCOSX ! D3BJ CPCM(THF) SlowConv %basis newgto Ni "def2-TZVPP" end end %tddft nroots 100 maxdim 5 end *xyzfile 0 2 optimized-structure.xyz</pre>	<pre>! UKS B3LYP def2-TZVP def2/J RIJCOSX ! D3BJ CPCM(THF) SlowConv ! OPT Keepdens %basis newgto Ni "def2-TZVPP" end end %tddft nroots 5 maxdim 5 IRoot 1 end * xyzfile 0 2 optimized-structure.xyz</pre>

S2.3. DFT Molecular Orbital Diagrams and Vibrational Energies

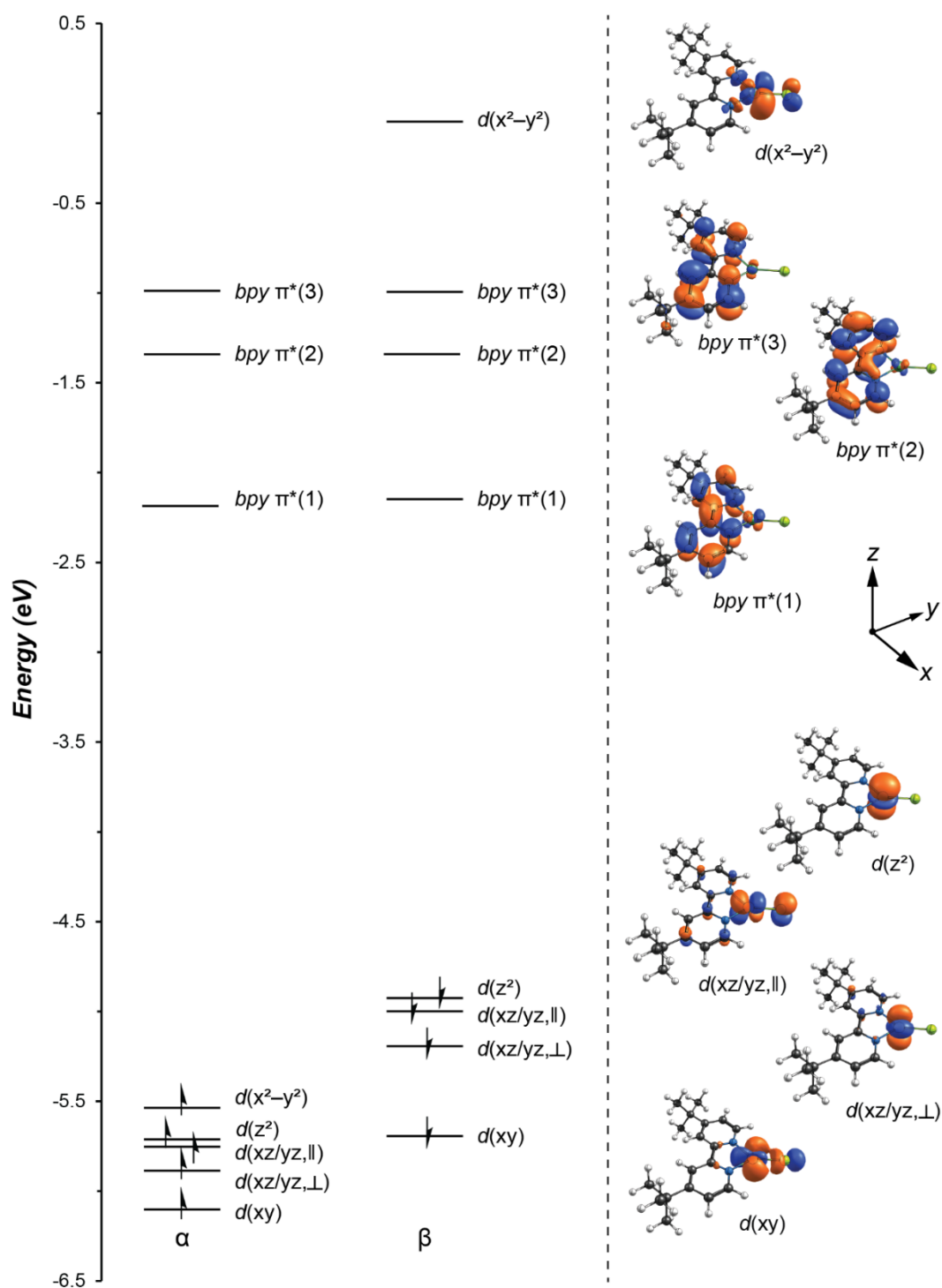


Figure S34. Molecular orbital diagram for **1** at the DFT(B3LYP) level.

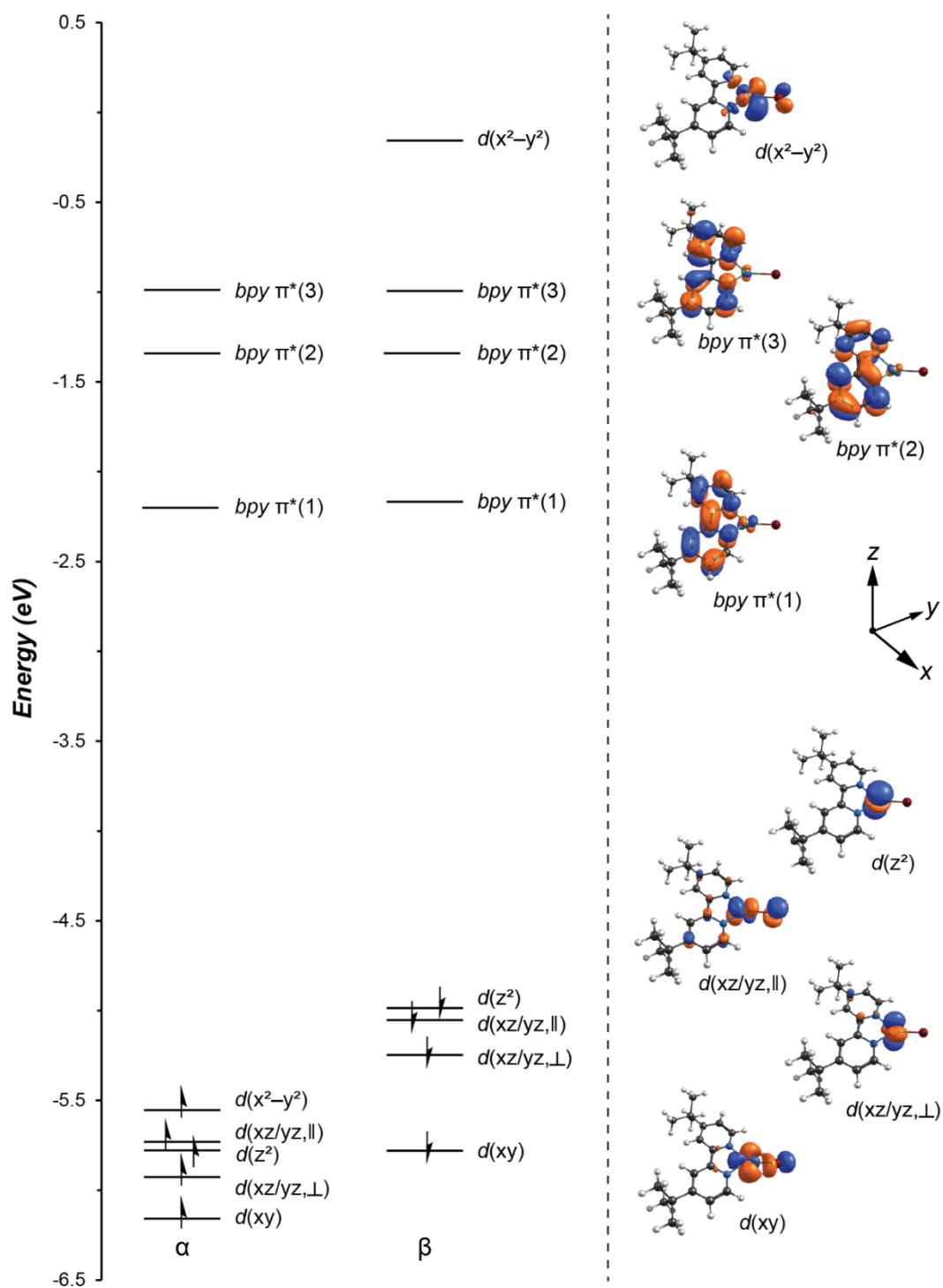


Figure S35. Molecular orbital diagram for **1-Br** at the DFT(B3LYP) level.

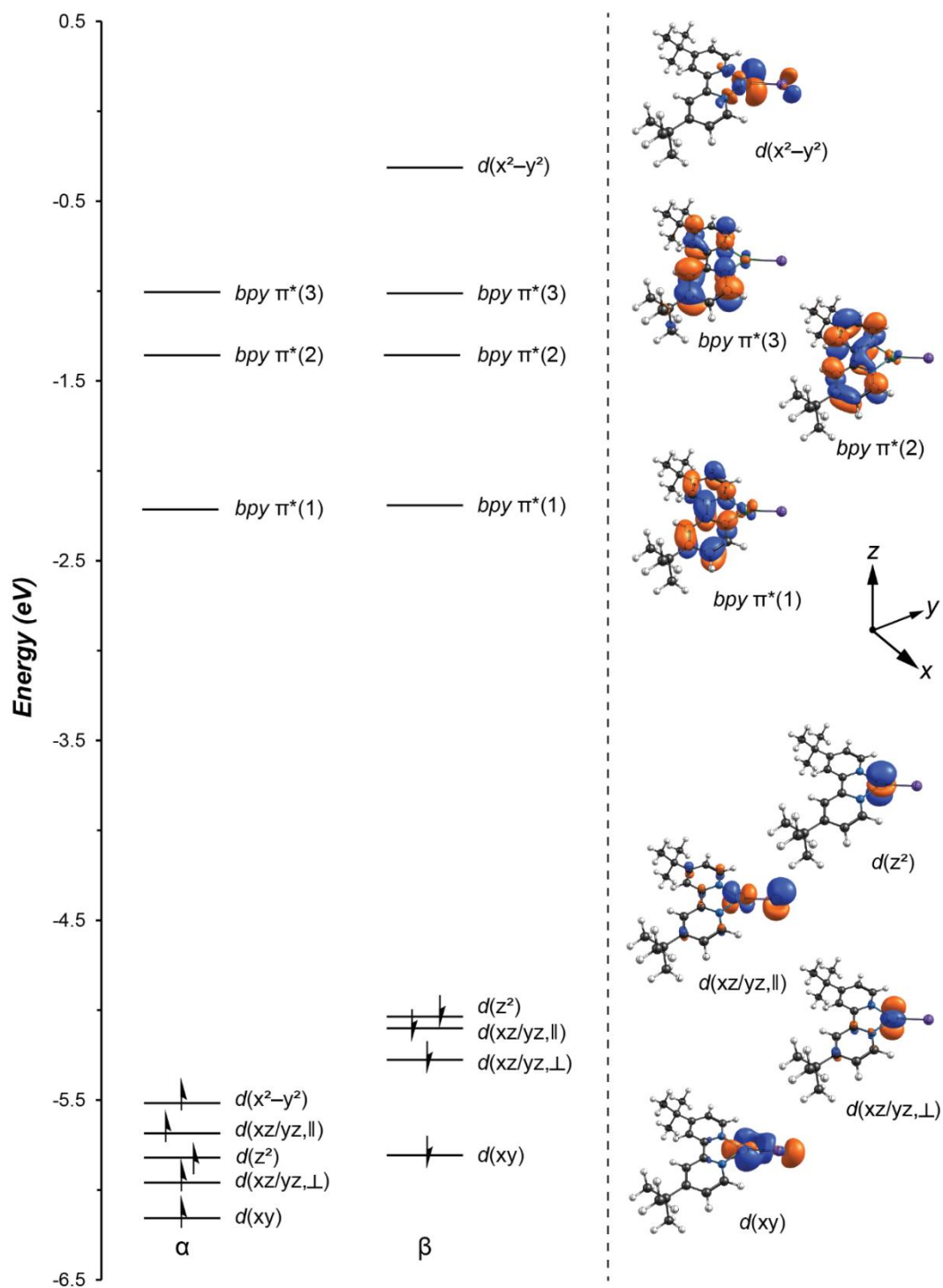


Figure S36. Molecular orbital diagram for **1-I** at the DFT(B3LYP) level.

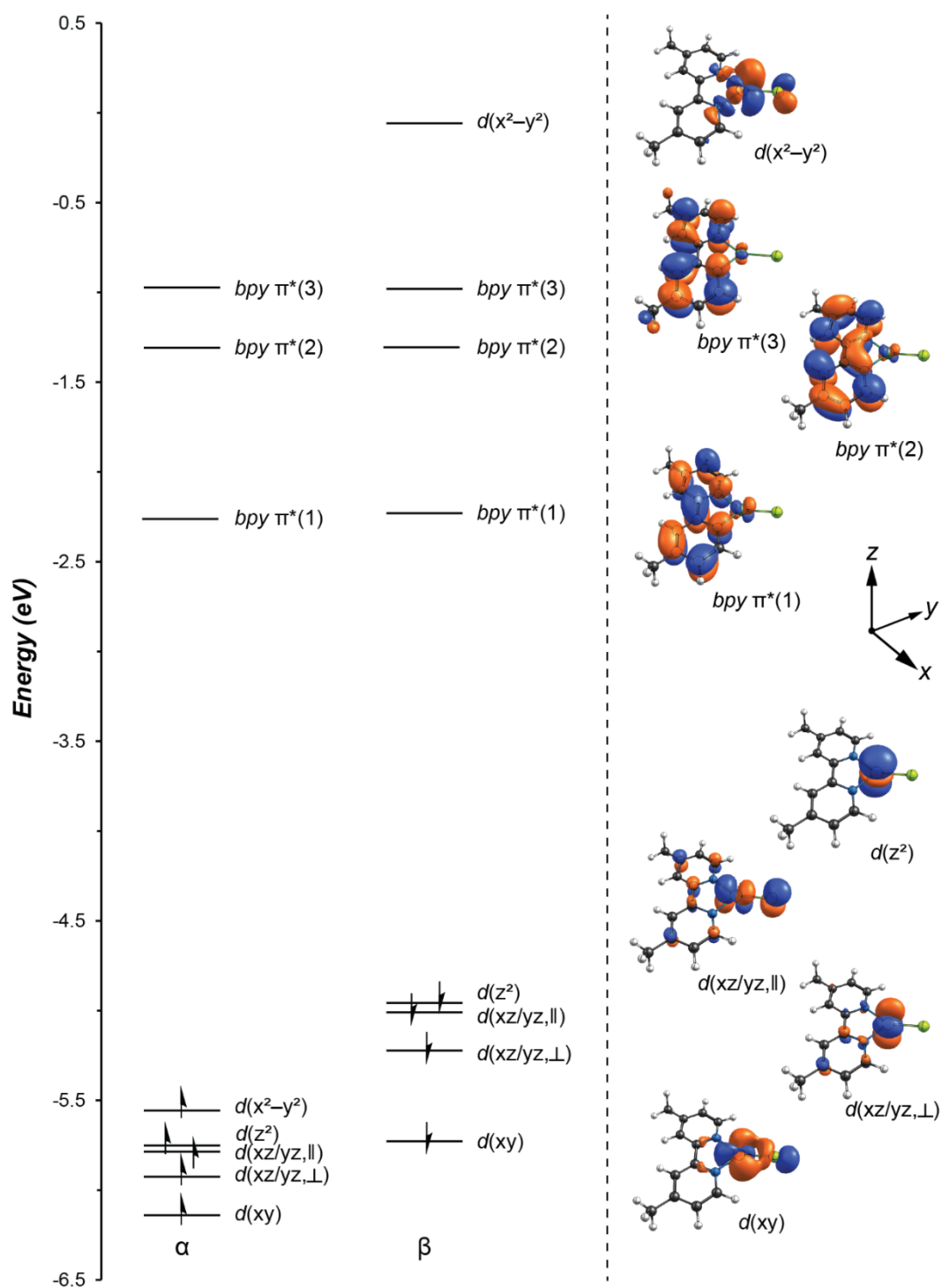


Figure S37. Molecular orbital diagram for **2** at the DFT(B3LYP) level.

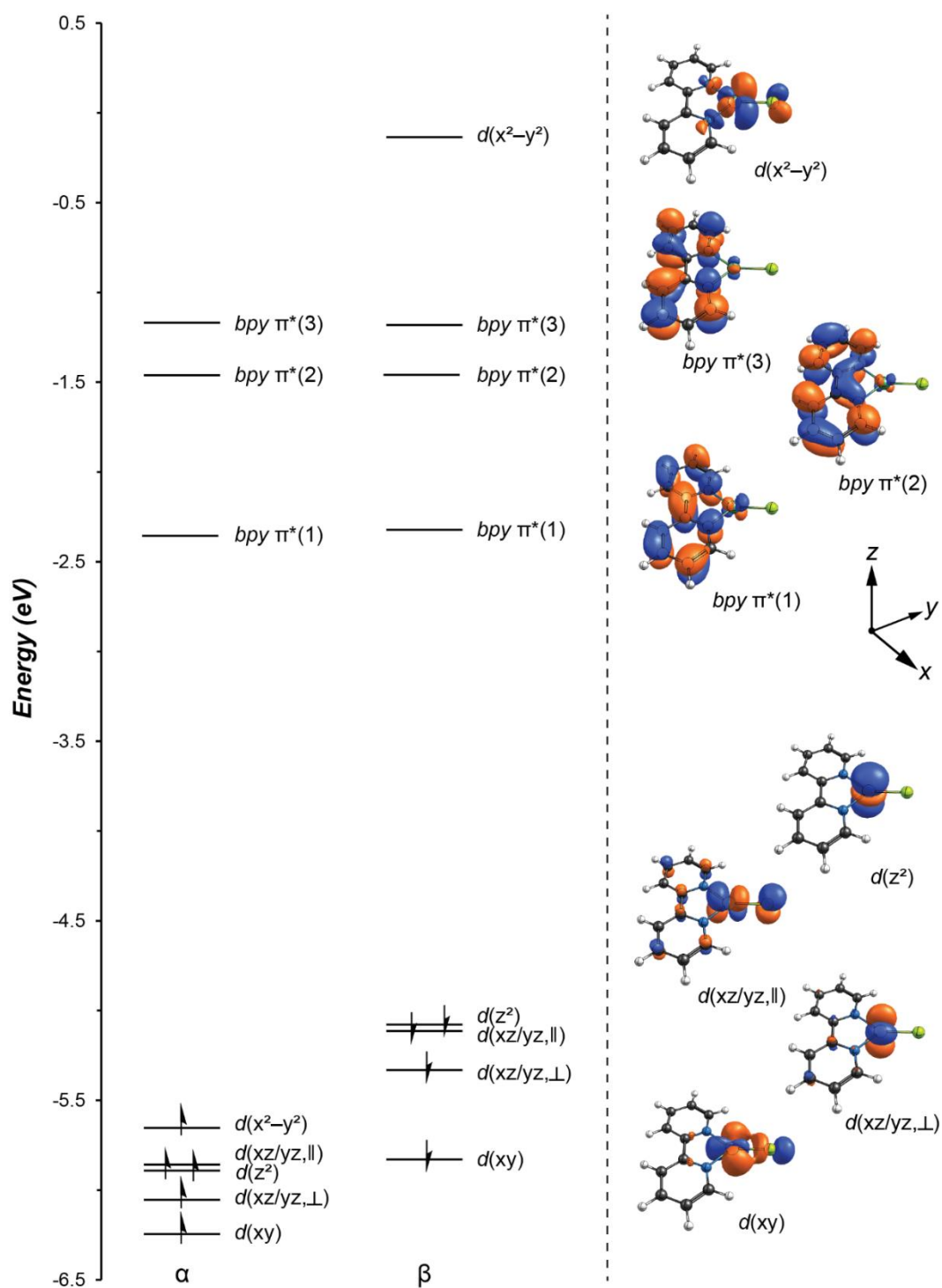


Figure S38. Molecular orbital diagram for **3** at the DFT(B3LYP) level.

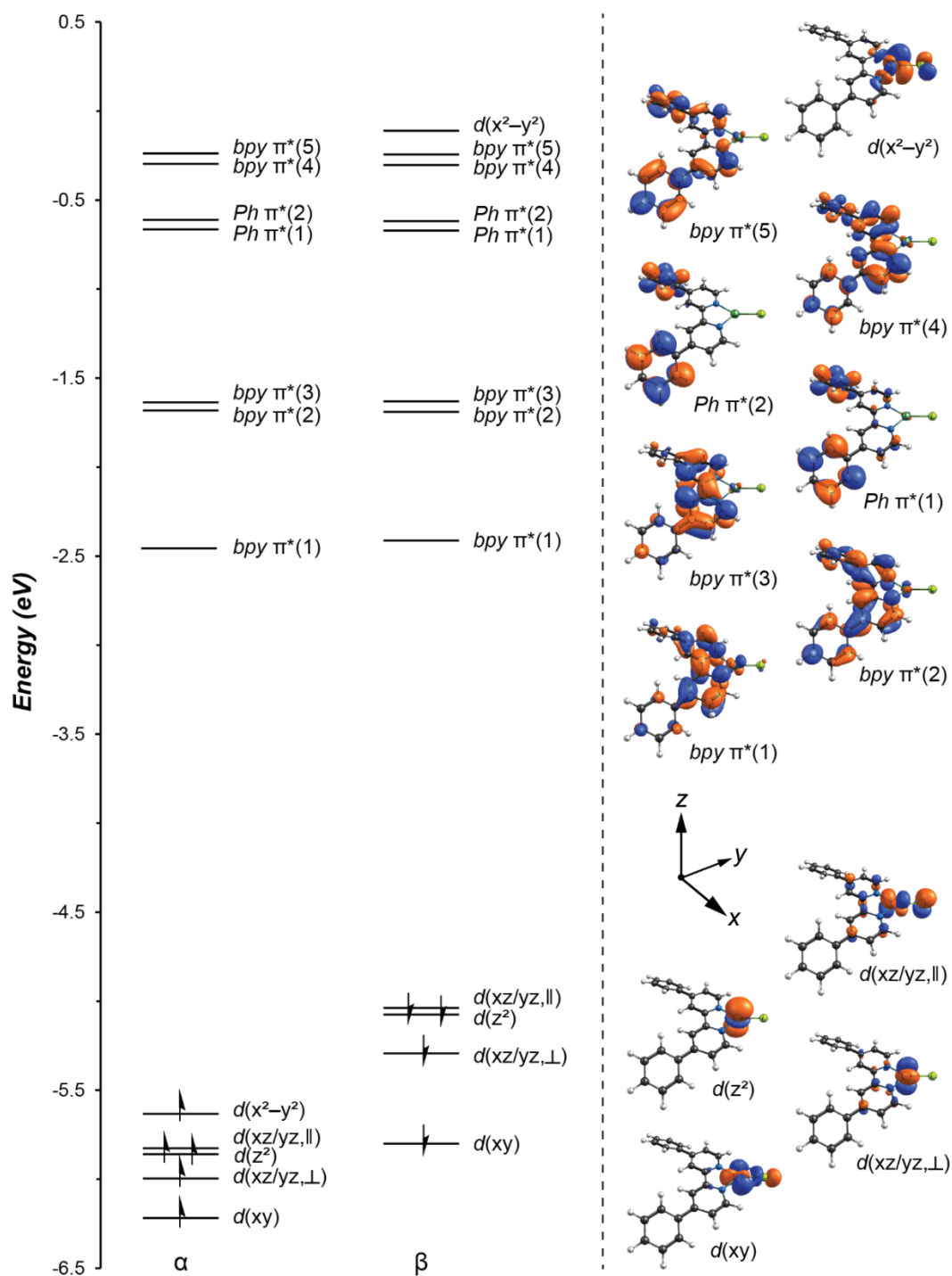


Figure S39. Molecular orbital diagram for **4** at the DFT(B3LYP) level.

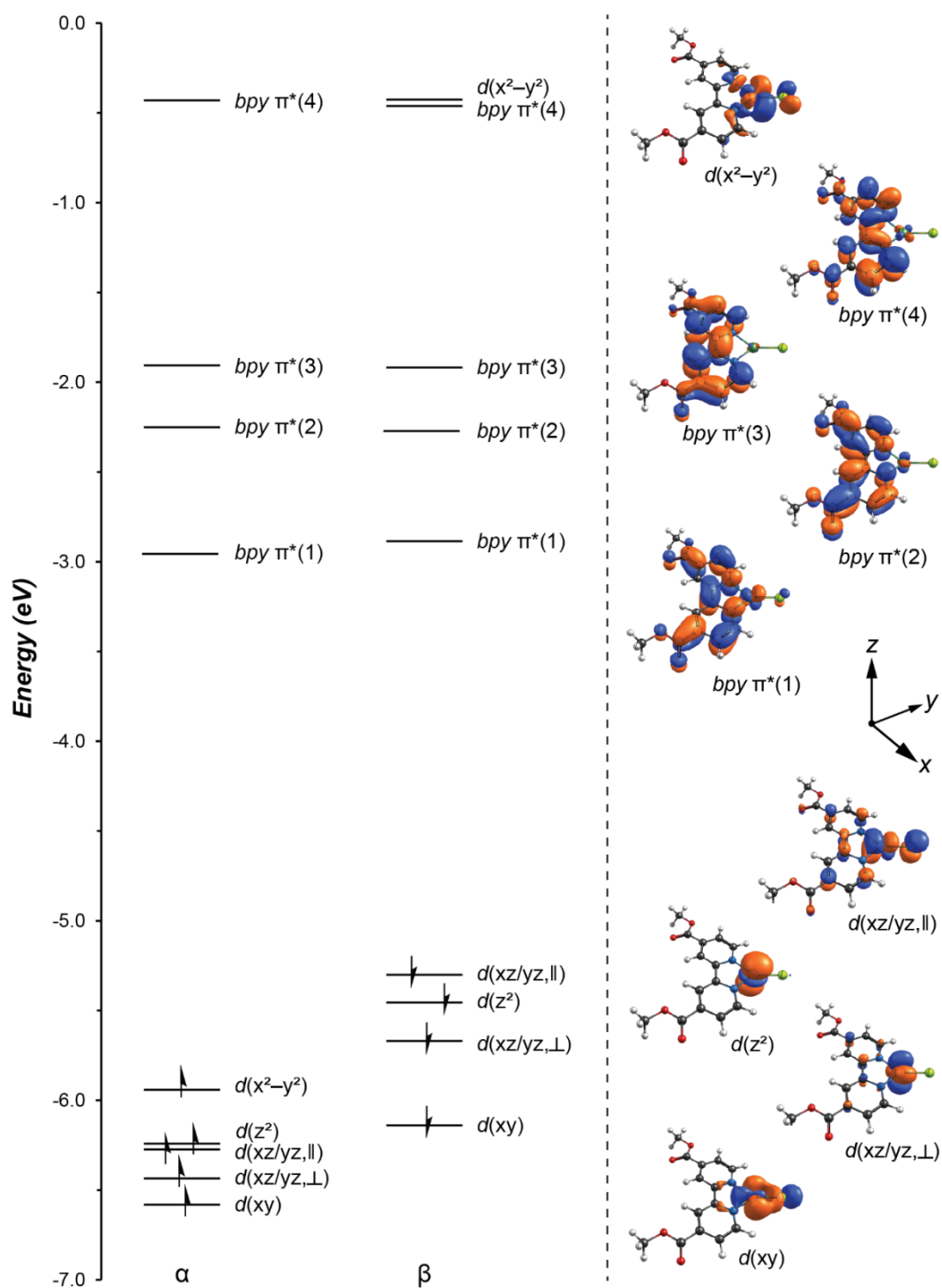


Figure S40. Molecular orbital diagram for **5** at the DFT(B3LYP) level.

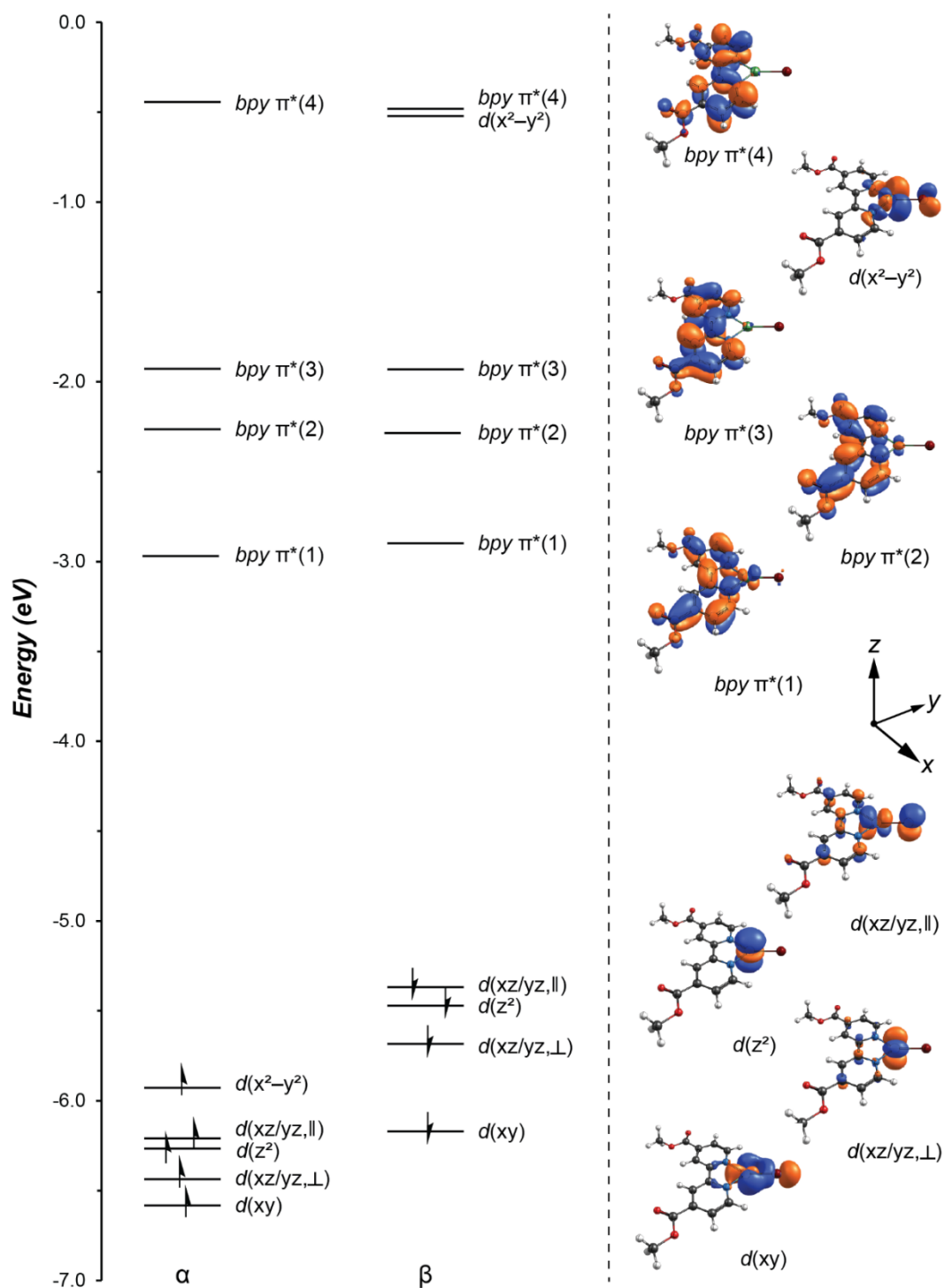
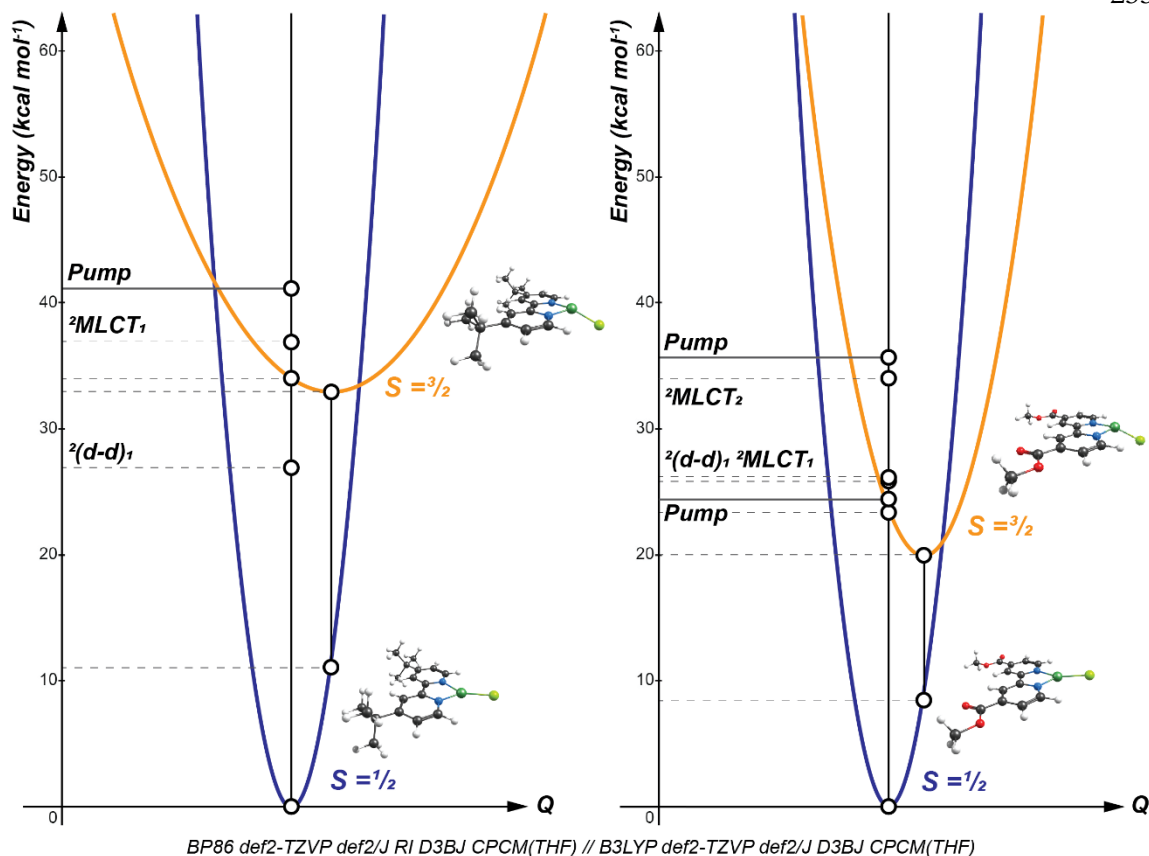


Figure S41. Molecular orbital diagram for **5-Br** at the DFT(B3LYP) level.

Table S4. Vibrational energies for complexes **1-5** computed at the DFT (BP86) level. The highest vibrational level for all the complexes is a C–H stretching frequency on the bipyridine ligand.

Compound	Average Vibrational Energy, $\langle \hbar\omega \rangle$ (cm ⁻¹ / eV)	Highest Vibrational Energy (cm ⁻¹ / eV)
1	1241.1 / 0.154	3145.3 / 0.390
1-Br	1240.0 / 0.154	3145.1 / 0.390
1-I	1239.9 / 0.154	3148.1 / 0.390
2	1175.9 / 0.146	3124.6 / 0.387
3	1142.8 / 0.142	3141.4 / 0.389
4	1145.1 / 0.142	3135.7 / 0.389
5	1087.4 / 0.135	3155.3 / 0.391
5-Br	1086.3 / 0.135	3155.4 / 0.391
Average	1169.8 / 0.145	3143.9 / 0.390



BP86 def2-TZVP def2/J RI D3BJ CPCM(THF) // B3LYP def2-TZVP def2/J D3BJ CPCM(THF)

Figure S42. Computed PESs for **1** (left) and **5** (right) showing the positions of the calculated TD-DFT transitions (see below) relative to the TA pump (800 or 1200 nm). Relaxed structures computed at the DFT BP86 level for the doublet ground state (blue surface) and relaxed quartet excited state (orange surface) are shown. Open circles indicate computed values and correspond to the energy markers on the y-axis. Calculations were performed to investigate the possibility of ISC to a quartet state (see Supporting Information Section 1.6; Fits to Alternative Relaxation Models for more details). Since both quartets are nested in the doublet surface (energy gap law behavior/Marcus inverted region), one would expect **5** to relax more quickly than **1** given its lower energy (a result opposite of that to the experiment). Thus, DFT suggests that a rate-limiting $^4\text{MLCT} \rightarrow ^2\text{GS}$ is unlikely. We note, however, that accurate computed displacements are precluded without the use of an explicit solvation model to account for outer sphere reorganization energy. Vertical and relaxed excited-state energies of **5** are likely to be overestimated (see Supporting Information Section 2.5; Limitations of DFT/TDDFT for more details).

S2.4. TDDFT Spectra and Tabulated Transitions

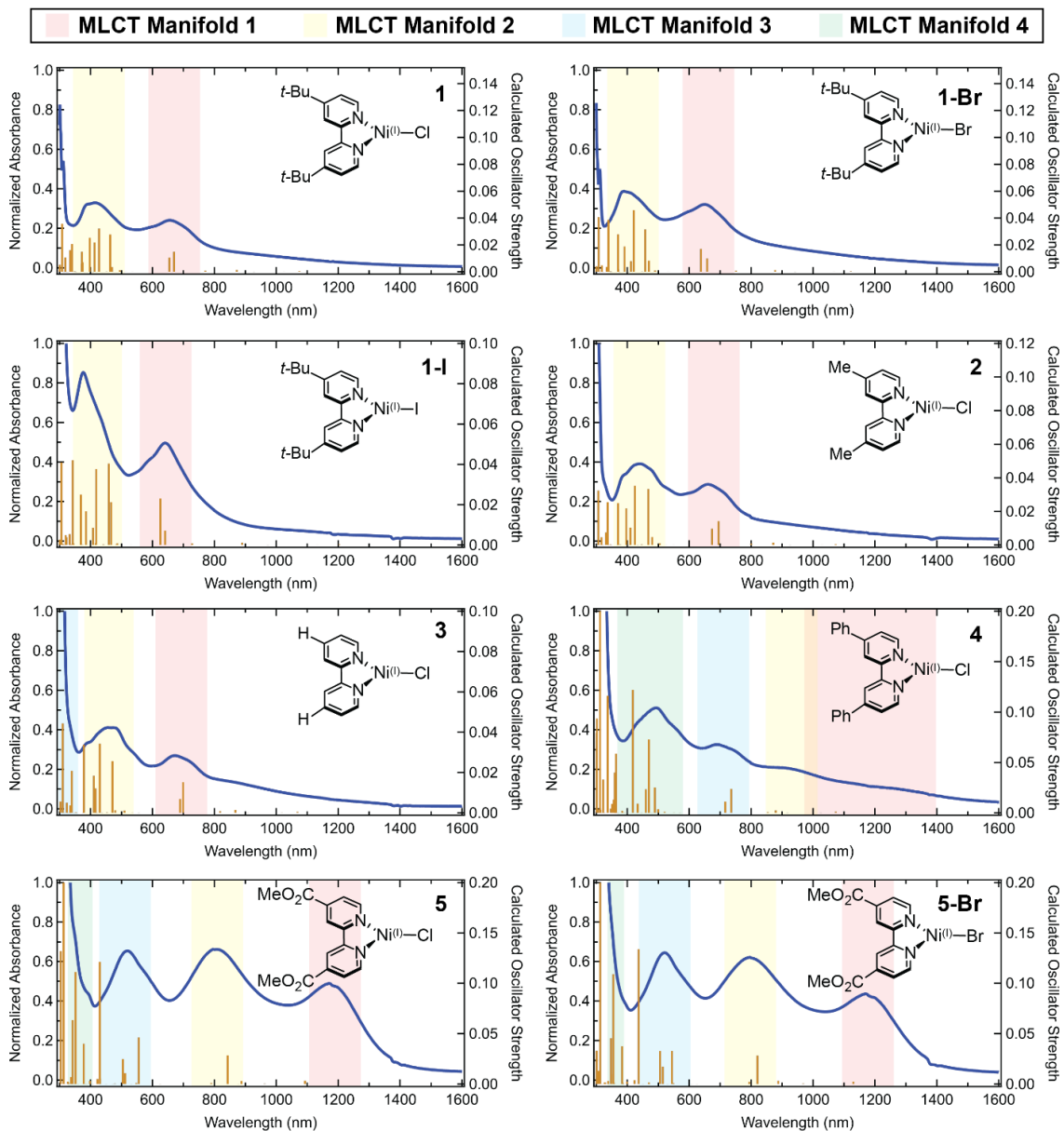


Figure S43. Experimental UV-vis-NIR spectra of complexes **1-5** (blue lines) and their predicted excited-state transitions (orange sticks) using TDDFT (B3LYP) with the CPCM(THF) solvation model. MLCT Manifolds are labeled from lowest to highest energy and are denoted by the highlighted regions (Manifold 1 = magenta, 2 = yellow, 3 = cyan, 4 = green). Complexes **4**, **5**, and **5-Br** are not well modeled by TDDFT (note the absence of the low-energy MLCT Manifold 1).

Table S5. Absorption transitions for the equilibrium structure of **1** at the TDDFT(B3LYP) level with the CPCM(THF) solvation model.

State	E (cm ⁻¹)	E (nm)	f_{osc}	Transition Assignment	
1	9305	1075	0.0004300	β -Ni 3d(z ²)	→ β -Ni 3d(x ² -y ²)
2	9758	1025	0.0000523	β -Ni 3d(xz/yz,⊥)	→ β -Ni 3d(x ² -y ²)
3	10781	928	0.0000023	β -Ni 3d(xz/yz,∥)	→ β -Ni 3d(x ² -y ²)
4	11462	873	0.0014185	β -Ni 3d(xy)	→ β -Ni 3d(x ² -y ²)
5	12973	771	0.0008758	β -Ni 3d(z ²)	→ β - π^* (1)
6	14931	670	0.0148499	β -Ni 3d(xz/yz,∥)	→ β - π^* (1)
7	15269	655	0.0105068	β -Ni 3d(xz/yz,⊥)	→ β - π^* (1)
8	18675	536	0.0000537	α -Ni 3d(x ² -y ²)	→ α - π^* (1)
9	19490	513	0.0000902	β -Ni 3d(xy)	→ β - π^* (1)
10	20225	494	0.0010854	α -Ni 3d(z ²)	→ α - π^* (1)
11	21293	470	0.0035294	α -Ni 3d(xz/yz,⊥)	→ α - π^* (1)
12	21575	464	0.0276969	α -Ni 3d(xz/yz,∥)	→ α - π^* (1)
13	22119	452	0.0002490	β -Ni 3d(z ²)	→ β - π^* (2)
14	23376	428	0.0321762	β -Ni 3d(xz/yz,∥)	→ β - π^* (2)
15	23483	426	0.0000779	α -Ni 3d(xy)	→ α - π^* (1)
16	24201	413	0.0217040	β -Ni 3d(xz/yz,⊥)	→ β - π^* (2)
17	24448	409	0.0000061	β -Ni 3d(z ²)	→ β - π^* (3)
18	25159	398	0.0253318	β -Ni 3d(xz/yz,∥)	→ β - π^* (3)
19	26720	374	0.0069969	α/β - π	→ α/β - π^* (1)
20	26879	372	0.0148811	β -Ni 3d(xz/yz,⊥)	→ β - π^* (2)
21	26899	372	0.0060159	α -Ni 3d(x ² -y ²)	→ α - π^* (2)
22	28373	352	0.0000002	β -Ni 3d(xy)	→ β - π^* (2)
23	28664	349	0.0002781	α -Ni 3d(z ²)	→ α - π^* (2)
24	29219	342	0.0000696	α -Ni 3d(x ² -y ²)	→ α - π^* (3)
25	29386	340	0.0208177	α -Ni 3d(xz/yz,∥)	→ α - π^* (2)
26	29945	334	0.0160776	α -Ni 3d(xz/yz,⊥)	→ α - π^* (2)
27	30712	326	0.0000008	β -Ni 3d(xy)	→ β - π^* (3)
28	31189	321	0.0000156	α -Ni 3d(z ²)	→ α - π^* (3)
29	31378	319	0.0105837	α -Ni 3d(xz/yz,∥)	→ α - π^* (3)
30	31867	314	0.0000012	α -Ni 3d(xy)	→ α - π^* (2)
31	32464	308	0.0356698	α -Ni 3d(xz/yz,⊥)	→ α - π^* (3)
32	33280	301	0.0052250	α/β - π	→ α/β - π^* (2)

Table S6. Absorption transitions for the equilibrium structure of **1-Br** at the TDDFT(B3LYP) level with the CPCM(THF) solvation model.

State	E (cm ⁻¹)	E (nm)	f_{osc}	Transition Assignment	
1	8910	1122	0.0003991	β -Ni 3d(z ²)	→ β -Ni 3d(x ² -y ²)
2	9364	1068	0.0000572	β -Ni 3d(xz/yz,⊥)	→ β -Ni 3d(x ² -y ²)
3	10612	942	0.0000099	β -Ni 3d(xz/yz,∥)	→ β -Ni 3d(x ² -y ²)
4	11396	878	0.0012884	β -Ni 3d(xy)	→ β -Ni 3d(x ² -y ²)
5	13312	751	0.0008388	β -Ni 3d(z ²)	→ β - π^* (1)
6	15204	658	0.0098469	β -Ni 3d(xz/yz,⊥)	→ β - π^* (1)
7	15677	638	0.0169887	β -Ni 3d(xz/yz,∥)	→ β - π^* (1)
8	18794	532	0.0001154	α -Ni 3d(x ² -y ²)	→ α - π^* (1)
9	20078	498	0.0002039	β -Ni 3d(xy)	→ β - π^* (1)
10	20432	489	0.0009542	α -Ni 3d(z ²)	→ α - π^* (1)
11	21288	470	0.0082070	α -Ni 3d(xz/yz,⊥)	→ α - π^* (1)
12	21841	458	0.0316036	α -Ni 3d(xz/yz,∥)	→ α - π^* (1)
13	22335	448	0.0002508	β -Ni 3d(z ²)	→ β - π^* (2)
14	23755	421	0.0457485	β -Ni 3d(xz/yz,∥)	→ β - π^* (2)
15	23832	420	0.0000714	α -Ni 3d(xy)	→ α - π^* (1)
16	24292	412	0.0079633	β -Ni 3d(xz/yz,⊥)	→ β - π^* (2)
17	24722	405	0.0000136	β -Ni 3d(z ²)	→ β - π^* (3)
18	25572	391	0.0187942	β -Ni 3d(xz/yz,∥)	→ β - π^* (3)
19	26754	374	0.0000144	α/β - π	→ α/β - π^* (1)
20	26952	371	0.0017301	α -Ni 3d(x ² -y ²)	→ α - π^* (2)
21	27024	370	0.0279220	β -Ni 3d(xz/yz,⊥)	→ β - π^* (2)
22	28843	347	0.0000016	β -Ni 3d(xy)	→ β - π^* (2)
23	28893	346	0.0002863	α -Ni 3d(z ²)	→ α - π^* (2)
24	29363	341	0.0002532	α -Ni 3d(x ² -y ²)	→ α - π^* (3)
25	29497	339	0.0386636	α -Ni 3d(xz/yz,∥)	→ α - π^* (2)
26	29991	333	0.0036054	α -Ni 3d(xz/yz,⊥)	→ α - π^* (2)
27	31259	320	0.0000037	β -Ni 3d(xy)	→ β - π^* (3)
28	31360	319	0.0000669	α -Ni 3d(z ²)	→ α - π^* (3)
29	31468	318	0.0047503	α -Ni 3d(xz/yz,∥)	→ α - π^* (3)
30	32167	311	0.0000001	α -Ni 3d(xy)	→ α - π^* (2)
31	32539	307	0.0407090	α -Ni 3d(xz/yz,⊥)	→ α - π^* (3)
32	33281	301	0.0040320	α/β - π	→ α/β - π^* (2)

Table S7. Absorption transitions for the equilibrium structure of **1-I** at the TDDFT(B3LYP) level with the CPCM(THF) solvation model.

State	E (cm ⁻¹)	E (nm)	f_{osc}	Transition Assignment	
1	8308	1204	0.0003008	β -Ni 3d(z ²)	→ β -Ni 3d(x ² -y ²)
2	8829	1133	0.0000591	β -Ni 3d(xz/yz, \perp)	→ β -Ni 3d(x ² -y ²)
3	10281	973	0.0000098	β -Ni 3d(xz/yz, \parallel)	→ β -Ni 3d(x ² -y ²)
4	11238	890	0.0011694	β -Ni 3d(xy)	→ β -Ni 3d(x ² -y ²)
5	13731	728	0.0007837	β -Ni 3d(z ²)	→ β - π^* (1)
6	15603	641	0.0071086	β -Ni 3d(xz/yz, \perp)	→ β - π^* (1)
7	15983	626	0.0229720	β -Ni 3d(xz/yz, \parallel)	→ β - π^* (1)
8	18840	531	0.0001058	α -Ni 3d(x ² -y ²)	→ α - π^* (1)
9	20550	487	0.0008454	β -Ni 3d(xy)	→ β - π^* (1)
10	20661	484	0.0003566	α -Ni 3d(z ²)	→ α - π^* (1)
11	21430	467	0.0212783	α -Ni 3d(xz/yz, \perp)	→ α - π^* (1)
12	21779	459	0.0404195	α -Ni 3d(xz/yz, \parallel)	→ α - π^* (1)
13	22648	442	0.0002552	β -Ni 3d(z ²)	→ β - π^* (2)
14	23905	418	0.0376620	β -Ni 3d(xz/yz, \parallel)	→ β - π^* (2)
15	23985	417	0.0008700	α -Ni 3d(xy)	→ α - π^* (1)
16	24509	408	0.0085618	β -Ni 3d(xz/yz, \perp)	→ β - π^* (2)
17	25028	400	0.0000163	β -Ni 3d(z ²)	→ β - π^* (3)
18	25953	385	0.0167115	β -Ni 3d(xz/yz, \parallel)	→ β - π^* (3)
19	26754	374	0.0001335	α/β - π	→ α/β - π^* (1)
20	26919	372	0.0001459	α -Ni 3d(x ² -y ²)	→ α - π^* (2)
21	27132	369	0.0250047	β -Ni 3d(xz/yz, \perp)	→ β - π^* (2)
22	29026	345	0.0008326	α -Ni 3d(z ²)	→ α - π^* (2)
23	29179	343	0.0007470	β -Ni 3d(xy)	→ β - π^* (2)
24	29219	342	0.0420723	α -Ni 3d(xz/yz, \parallel)	→ α - π^* (2)
25	29398	340	0.0003774	α -Ni 3d(x ² -y ²)	→ α - π^* (3)
26	29821	335	0.0000016	β -Br p(x/y, \perp)	→ β - π^* (1)
27	30087	332	0.0053483	α -Ni 3d(xz/yz, \perp)	→ α - π^* (2)
28	31007	323	0.0038798	β -Br 3p(z)	→ β - π^* (1)
29	31270	320	0.0049428	β -Ni 3d(xz/yz, \parallel)	→ β - π^* (3)
30	31478	318	0.0000444	α -Ni 3d(z ²)	→ α - π^* (3)
31	31624	316	0.0000028	β -Ni 3d(xy)	→ α - π^* (3)
32	31796	315	0.0000026	α -Br 3p(x/y, \perp)	→ α - π^* (1)
33	32222	310	0.0000639	α -Br 3p(x/y, \parallel)	→ α - π^* (2)
34	32239	310	0.0005966	α -Br 3p(z)	→ α - π^* (1)
35	32707	306	0.0410170	α -Ni 3d(xz/yz, \perp)	→ α - π^* (3)
36	33242	301	0.0026747	α/β - π	→ α/β - π^* (2)

Table S8. Absorption transitions for the equilibrium structure of **2** at the TDDFT(B3LYP) level with the CPCM(THF) solvation model.

State	E (cm ⁻¹)	E (nm)	f_{osc}	Transition Assignment	
1	9316	1073	0.0004425	β -Ni 3d(z^2)	\rightarrow β -Ni 3d(x^2-y^2)
2	9715	1029	0.0000437	β -Ni 3d(xz/yz, \perp)	\rightarrow β -Ni 3d(x^2-y^2)
3	10799	926	0.0000010	β -Ni 3d(xz/yz, \parallel)	\rightarrow β -Ni 3d(x^2-y^2)
4	11474	872	0.0013918	β -Ni 3d(xy)	\rightarrow β -Ni 3d(x^2-y^2)
5	12493	801	0.0008308	β -Ni 3d(z^2)	\rightarrow β - $\pi^*(1)$
6	14396	695	0.0141462	β -Ni 3d(xz/yz, \parallel)	\rightarrow β - $\pi^*(1)$
7	14840	674	0.0096912	β -Ni 3d(xz/yz, \perp)	\rightarrow β - $\pi^*(1)$
8	18193	550	0.0000616	α -Ni 3d(x^2-y^2)	\rightarrow α - $\pi^*(1)$
9	19026	526	0.0000801	β -Ni 3d(xy)	\rightarrow β - $\pi^*(1)$
10	19810	505	0.0010316	α -Ni 3d(z^2)	\rightarrow α - $\pi^*(1)$
11	20808	481	0.0047675	α -Ni 3d(xz/yz, \perp)	\rightarrow α - $\pi^*(1)$
12	21373	468	0.0333436	α -Ni 3d(xz/yz, \parallel)	\rightarrow α - $\pi^*(1)$
13	22397	447	0.0002836	β -Ni 3d(z^2)	\rightarrow β - $\pi^*(2)$
14	23062	434	0.0000109	α -Ni 3d(xy)	\rightarrow α - $\pi^*(1)$
15	23560	425	0.0351858	β -Ni 3d(xz/yz, \parallel)	\rightarrow β - $\pi^*(2)$
16	24395	410	0.0103361	β -Ni 3d(xz/yz, \perp)	\rightarrow β - $\pi^*(2)$
17	24653	406	0.0000010	β -Ni 3d(z^2)	\rightarrow β - $\pi^*(3)$
18	25222	397	0.0217931	β -Ni 3d(xz/yz, \parallel)	\rightarrow β - $\pi^*(3)$
19	26536	377	0.0002506	α/β - π	\rightarrow α/β - $\pi^*(1)$
20	27022	370	0.0248685	β -Ni 3d(xz/yz, \perp)	\rightarrow β - $\pi^*(3)$
21	27136	369	0.0000233	α -Ni 3d(x^2-y^2)	\rightarrow α - $\pi^*(2)$
22	28672	349	0.0000001	β -Ni 3d(xy)	\rightarrow β - $\pi^*(2)$
23	28956	345	0.0003385	α -Ni 3d(z^2)	\rightarrow α - $\pi^*(2)$
24	29420	340	0.0000264	α -Ni 3d(x^2-y^2)	\rightarrow α - $\pi^*(3)$
25	29714	337	0.0254983	α -Ni 3d(xz/yz, \parallel)	\rightarrow α - $\pi^*(2)$
26	30185	331	0.0074432	α -Ni 3d(xz/yz, \perp)	\rightarrow α - $\pi^*(2)$
27	30928	323	0.0000002	β -Ni 3d(xy)	\rightarrow β - $\pi^*(3)$
28	31403	318	0.0000074	α -Ni 3d(z^2)	\rightarrow α - $\pi^*(3)$
29	31574	317	0.0046334	α -Ni 3d(xz/yz, \parallel)	\rightarrow α - $\pi^*(3)$
30	32170	311	0.0000011	α -Ni 3d(xy)	\rightarrow α - $\pi^*(2)$
31	32618	307	0.0323619	α -Ni 3d(xz/yz, \perp)	\rightarrow α - $\pi^*(3)$

Table S9. Absorption transitions for the equilibrium structure of **3** at the TDDFT(B3LYP) level with the CPCM(THF) solvation model.

State	E (cm ⁻¹)	E (nm)	f_{osc}	Transition Assignment	
1	9360	1068	0.0005099	β -Ni 3d(z ²)	→ β -Ni 3d(x ² -y ²)
2	9822	1018	0.0000331	β -Ni 3d(xz/yz,⊥)	→ β -Ni 3d(x ² -y ²)
3	11017	908	0.0000012	β -Ni 3d(xz/yz,∥)	→ β -Ni 3d(x ² -y ²)
4	11518	868	0.0014098	β -Ni 3d(xy)	→ β -Ni 3d(x ² -y ²)
5	12214	819	0.0008277	β -Ni 3d(z ²)	→ β - π^* (1)
6	14304	699	0.0152190	β -Ni 3d(xz/yz,∥)	→ β - π^* (1)
7	14507	689	0.0068829	β -Ni 3d(xz/yz,⊥)	→ β - π^* (1)
8	17984	556	0.0000108	α -Ni 3d(x ² -y ²)	→ α - π^* (1)
9	18676	536	0.0000766	β -Ni 3d(xy)	→ β - π^* (1)
10	19629	510	0.0011378	α -Ni 3d(xz/yz,∥)	→ α - π^* (1)
11	20849	480	0.0012266	α -Ni 3d(xz/yz,⊥)	→ α - π^* (1)
12	21240	471	0.0256761	α -Ni 3d(z ²)	→ α - π^* (1)
13	22078	453	0.0001954	β -Ni 3d(z ²)	→ β - π^* (2)
14	22873	437	0.0000108	α -Ni 3d(xy)	→ α - π^* (1)
15	23254	430	0.0342562	β -Ni 3d(xz/yz,∥)	→ β - π^* (2)
16	23809	420	0.0000003	β -Ni 3d(z ²)	→ β - π^* (3)
17	24018	416	0.0120753	β -Ni 3d(xz/yz,⊥)	→ β - π^* (2)
18	24352	411	0.0183904	β -Ni 3d(xz/yz,∥)	→ β - π^* (3)
19	26411	379	0.0336622	β -Ni 3d(xz/yz,⊥)	→ β - π^* (3)
20	26464	378	0.0008086	α/β - π	→ α/β - π^* (1)
21	26658	375	0.0000053	α -Ni 3d(x ² -y ²)	→ α - π^* (2)
22	28207	355	0.0000234	β -Ni 3d(xy)	→ β - π^* (2)
23	28322	353	0.0002583	α -Ni 3d(x ² -y ²)	→ α - π^* (3)
24	28756	348	0.0000260	α -Ni 3d(xz/yz,∥)	→ α - π^* (2)
25	29489	339	0.0208373	α -Ni 3d(z ²)	→ α - π^* (2)
26	29918	334	0.0036422	α -Ni 3d(xz/yz,⊥)	→ α - π^* (2)
27	29965	334	0.0000001	β -Ni 3d(xy)	→ β - π^* (3)
28	30568	327	0.0000013	α -Ni 3d(xz/yz,∥)	→ α - π^* (3)
29	30928	323	0.0049812	α -Ni 3d(z ²)	→ α - π^* (3)
30	31742	315	0.0000018	α -Ni 3d(xy)	→ α - π^* (2)
31	32255	310	0.0443949	α -Ni 3d(xz/yz,⊥)	→ α - π^* (3)
32	33020	303	0.0055649	α/β - π	→ α/β - π^* (2)

Table S10. Absorption transitions for the equilibrium structure of **4** at the TDDFT(B3LYP) level with the CPCM(THF) solvation model.

State	E (cm ⁻¹)	E (nm)	f_{osc}	Transition Assignment	
1	9315	1074	0.0012938	β -Ni 3d(z ²)	→ β -Ni 3d(x ² -y ²)
2	9757	1025	0.0000222	β -Ni 3d(xz/yz, \perp)	→ β -Ni 3d(x ² -y ²)
3	10904	917	0.0000046	β -Ni 3d(xz/yz, \parallel)	→ β -Ni 3d(x ² -y ²)
4	11368	880	0.0023779	β -Ni 3d(xy)	→ β -Ni 3d(x ² -y ²)
5	11712	854	0.0007462	β -Ni 3d(z ²)	→ β - π^* (1)
6	13592	736	0.0236330	β -Ni 3d(xz/yz, \parallel)	→ β - π^* (1)
7	13959	716	0.0110160	β -Ni 3d(xz/yz, \perp)	→ β - π^* (1)
8	17543	570	0.0000432	α -Ni 3d(x ² -y ²)	→ α - π^* (1)
9	18154	551	0.0000570	β -Ni 3d(xy)	→ β - π^* (1)
10	19220	520	0.0010219	α -Ni 3d(z ²)	→ α - π^* (1)
11	20014	500	0.0036455	α -Ni 3d(xz/yz, \perp)	→ α - π^* (1)
12	20455	489	0.0250978	α -Ni 3d(xz/yz, \parallel)	→ α - π^* (1)
13	20888	479	0.0000001	β -Ni 3d(z ²)	→ β - π^* (2)
14	21296	470	0.0728130	β -Ni 3d(xz/yz, \parallel)	→ β - π^* (2)
15	21315	469	0.0001460	β -Ni 3d(z ²)	→ β - π^* (3)
16	21742	460	0.0233042	β -Ni 3d(xz/yz, \parallel)	→ β - π^* (3)
17	22418	446	0.0000110	α -Ni 3d(xy)	→ α - π^* (1)
18	23073	433	0.0091206	β -Ni 3d(xz/yz, \perp)	→ β - π^* (3)
19	23927	418	0.1216611	β -Ni 3d(xz/yz, \perp)	→ β - π^* (2)
20	25614	390	0.0002358	α -Ni 3d(x ² -y ²)	→ α - π^* (2)
21	25808	388	0.0000905	α -Ni 3d(x ² -y ²)	→ α - π^* (3)
22	26063	384	0.0019861	α/β - π (1)	→ α/β - π^* (1)
23	27039	370	0.0000042	β -Ni 3d(xy)	→ β - π^* (2)
24	27418	365	0.0000243	β -Ni 3d(xy)	→ β - π^* (3)
25	27492	364	0.0585519	α -Ni 3d(xz/yz, \parallel)	→ α - π^* (2)
26	27685	361	0.0000517	α -Ni 3d(z ²)	→ α - π^* (2)
27	27815	360	0.0398972	α/β - π (2)	→ α/β - π^* (1)
28	27900	358	0.0000528	α -Ni 3d(z ²)	→ α - π^* (3)
29	28080	356	0.0130280	α -Ni 3d(xz/yz, \parallel)	→ α - π^* (3)
30	28518	351	0.0088201	α -Ni 3d(xz/yz, \parallel)	→ α - π^* (2)
31	28828	347	0.0041067	α -Ni 3d(xz/yz, \perp)	→ α - π^* (3)
32	29706	337	0.1162010	α -Ni 3d(xz/yz, \perp)	→ α - π^* (2)
33	30679	326	0.0000027	α -Ni 3d(xy)	→ α - π^* (2)
34	30909	324	0.0000251	α -Ni 3d(xy)	→ α - π^* (3)
35	31051	322	0.0330242	β -Ni 3d(xz/yz, \parallel)	→ β -Ph π^* (1)
36	31471	318	0.0000043	β -Ni 3d(z ²)	→ β -Ph π^* (1)
37	31940	313	0.0028909	α/β - π (1)	→ α/β - π^* (3)
38	32016	312	0.0042637	β -Ni 3d(xz/yz, \parallel)	→ β -Ph π^* (2)
39	32078	312	0.4313805	α - π (3)	→ α - π^* (1)
40	32318	309	0.0000060	α -Ph π^* (1)	→ α - π^* (1)

Table S11. Absorption transitions for the equilibrium structure of **5** at the TDDFT(B3LYP) level with the CPCM(THF) solvation model.

State	E (cm ⁻¹)	E (nm)	f_{osc}	Transition Assignment	
1	9091	1100	0.0002290	β -Ni 3d(z^2)	\rightarrow β - $\pi^*(1)$
2	9151	1093	0.0033827	β -Ni 3d(z^2)	\rightarrow β -Ni 3d(x^2-y^2)
3	10389	963	0.0004404	β -Ni 3d(xz/yz, \perp)	\rightarrow β -Ni 3d(x^2-y^2)
4	11264	888	0.0030372	β -Ni 3d(xy)	\rightarrow β -Ni 3d(x^2-y^2)
5	11392	878	0.0000812	β -Ni 3d(xz/yz, \parallel)	\rightarrow β -Ni 3d(x^2-y^2)
6	11860	843	0.0284356	β -Ni 3d(xz/yz, \parallel)	\rightarrow β - $\pi^*(1)$
7	12658	790	0.0009997	β -Ni 3d(xz/yz, \perp)	\rightarrow β - $\pi^*(1)$
8	15983	626	0.0000290	β -Ni 3d(xy)	\rightarrow β - $\pi^*(1)$
9	16030	624	0.0000045	α -Ni 3d(x^2-y^2)	\rightarrow α - $\pi^*(1)$
10	17987	556	0.0463427	β -Ni 3d(xz/yz, \parallel)	\rightarrow β - $\pi^*(2)$
11	18260	548	0.0009906	α -Ni 3d(z^2)	\rightarrow α - $\pi^*(1)$
12	18809	532	0.0000022	β -Ni 3d(z^2)	\rightarrow β - $\pi^*(2)$
13	19552	512	0.0106762	β -Ni 3d(xz/yz, \perp)	\rightarrow β - $\pi^*(2)$
14	19828	504	0.0246655	α -Ni 3d(xz/yz, \perp)	\rightarrow α - $\pi^*(1)$
15	20886	479	0.0003944	β -Ni 3d(xz/yz, \parallel)	\rightarrow β - $\pi^*(3)$
16	21168	472	0.0000018	α -Ni 3d(xy)	\rightarrow α - $\pi^*(1)$
17	22193	451	0.0000033	β -Ni 3d(z^2)	\rightarrow β - $\pi^*(3)$
18	23219	431	0.0054451	α -Ni 3d(x^2-y^2)	\rightarrow α - $\pi^*(2)$
19	23248	430	0.1213548	α -Ni 3d(xz/yz, \parallel)	\rightarrow α - $\pi^*(1)$
20	23662	423	0.0050371	β -Ni 3d(xz/yz, \perp)	\rightarrow β - $\pi^*(3)$
21	24509	408	0.0000006	β -Ni 3d(xy)	\rightarrow β - $\pi^*(2)$
22	25113	398	0.0032781	α/β - π	\rightarrow α/β - $\pi^*(1)$
23	25853	387	0.0000009	α -Ni 3d(z^2)	\rightarrow α - $\pi^*(2)$
24	26043	384	0.0000004	α -Ni 3d(x^2-y^2)	\rightarrow α - $\pi^*(3)$
25	26468	378	0.0399679	α -Ni 3d(xz/yz, \parallel)	\rightarrow α - $\pi^*(2)$
26	27775	360	0.0000103	β -Ni 3d(xy)	\rightarrow β - $\pi^*(3)$
27	28457	351	0.1106965	α -Ni 3d(xz/yz, \perp)	\rightarrow α - $\pi^*(2)$
28	28589	350	0.0000012	α -Ni 3d(xy)	\rightarrow α - $\pi^*(2)$
29	28780	348	0.0000007	α -Ni 3d(z^2)	\rightarrow α - $\pi^*(3)$
30	29229	342	0.0634764	α -Ni 3d(xz/yz, \parallel)	\rightarrow α - $\pi^*(3)$
31	29675	337	0.0070271	α -Ni 3d(xz/yz, \perp)	\rightarrow α - $\pi^*(3)$
32	30412	329	0.0012561	α/β - π	\rightarrow α/β - $\pi^*(2)$
33	30628	327	0.0023853	α/β - π	\rightarrow α/β - $\pi^*(3)$
34	31416	318	0.0000132	α -Ni 3d(xy)	\rightarrow α - $\pi^*(3)$
35	31968	313	0.3709734	β -Ni 3p(z)	\rightarrow β - $\pi^*(1)$
36	32798	305	0.0000048	β -Ni 3p(x/y, \perp)	\rightarrow β - $\pi^*(1)$
37	32920	304	0.1317423	β -Ni 3d(xz/yz, \parallel)	\rightarrow β - $\pi^*(3)$

Table S12. Absorption transitions for the equilibrium structure of **5-Br** at the TDDFT(B3LYP) level with the CPCM(THF) solvation model.

State	E (cm ⁻¹)	E (nm)	f_{osc}	Transition Assignment	
1	8849	1130	0.0024990	β -Ni 3d(z ²)	→ β -Ni 3d(x ² -y ²)
2	9135	1095	0.0000423	β -Ni 3d(xz/yz,⊥)	→ β -Ni 3d(x ² -y ²)
3	10326	969	0.0005262	β -Ni 3d(z ²)	→ β - π^* (1)
4	11131	898	0.0000184	β -Ni 3d(xz/yz,)	→ β -Ni 3d(x ² -y ²)
5	11266	888	0.0033695	β -Ni 3d(xy)	→ β -Ni 3d(x ² -y ²)
6	12189	820	0.0281527	β -Ni 3d(xz/yz,)	→ β - π^* (1)
7	12595	794	0.0020666	β -Ni 3d(xz/yz,⊥)	→ β - π^* (1)
8	16002	625	0.0000073	α -Ni 3d(x ² -y ²)	→ α - π^* (1)
9	16481	607	0.0000518	β -Ni 3d(xy)	→ β - π^* (1)
10	18208	549	0.0009511	α -Ni 3d(z ²)	→ α - π^* (1)
11	18375	544	0.0328136	β -Ni 3d(xz/yz,)	→ β - π^* (2)
12	18871	530	0.0000601	β -Ni 3d(z ²)	→ β - π^* (2)
13	19437	515	0.0172895	β -Ni 3d(xz/yz,⊥)	→ β - π^* (2)
14	19764	506	0.0326760	α -Ni 3d(xz/yz,⊥)	→ α - π^* (1)
15	21205	472	0.0000214	α -Ni 3d(xy)	→ α - π^* (1)
16	21301	470	0.0014812	β -Ni 3d(xz/yz,)	→ β - π^* (3)
17	22197	451	0.0001503	β -Ni 3d(z ²)	→ β - π^* (3)
18	22899	437	0.1336416	α -Ni 3d(xz/yz,)	→ α - π^* (1)
19	23179	431	0.0001572	α -Ni 3d(x ² -y ²)	→ α - π^* (2)
20	23632	423	0.0038845	β -Ni 3d(xz/yz,⊥)	→ β - π^* (3)
21	24849	402	0.0000008	β -Ni 3d(xy)	→ β - π^* (2)
22	25045	399	0.0022873	α/β - π	→ α/β - π^* (1)
23	25798	388	0.0001838	α -Ni 3d(z ²)	→ α - π^* (2)
24	25982	385	0.0010291	α -Ni 3d(x ² -y ²)	→ α - π^* (3)
25	26096	383	0.0375426	α -Ni 3d(xz/yz,)	→ α - π^* (2)
26	28025	357	0.0010304	β -Ni 3d(xy)	→ β - π^* (3)
27	28171	355	0.1092840	α -Ni 3d(xz/yz,⊥)	→ α - π^* (2)
28	28615	350	0.0000006	α -Ni 3d(xy)	→ α - π^* (2)
29	28719	348	0.0095568	α -Ni 3d(z ²)	→ α - π^* (3)
30	28794	347	0.0453802	α -Ni 3d(xz/yz,)	→ α - π^* (3)
31	29330	341	0.0000008	β -Ni 3p(x/y,⊥)	→ β - π^* (1)
32	29561	338	0.0029779	α -Ni 3d(xz/yz,⊥)	→ α - π^* (3)
33	30407	329	0.0010950	α/β - π	→ α/β - π^* (2)
34	30567	327	0.0000111	β -Ni 3p(z)	→ β - π^* (1)
35	30605	327	0.0015624	α/β - π	→ α/β - π^* (3)
36	31202	321	0.0000006	α -Ni 3p(x/y,⊥)	→ α - π^* (1)
37	31406	318	0.0000256	α -Ni 3d(xy)	→ α - π^* (3)
38	32009	312	0.4327586	β - π	→ β - π^* (1)
39	32588	307	0.0130867	α -Ni 3p(z)	→ α - π^* (1)
40	33226	301	0.0321215	β -Ni 3d(xz/yz,)	→ β - π^* (3)

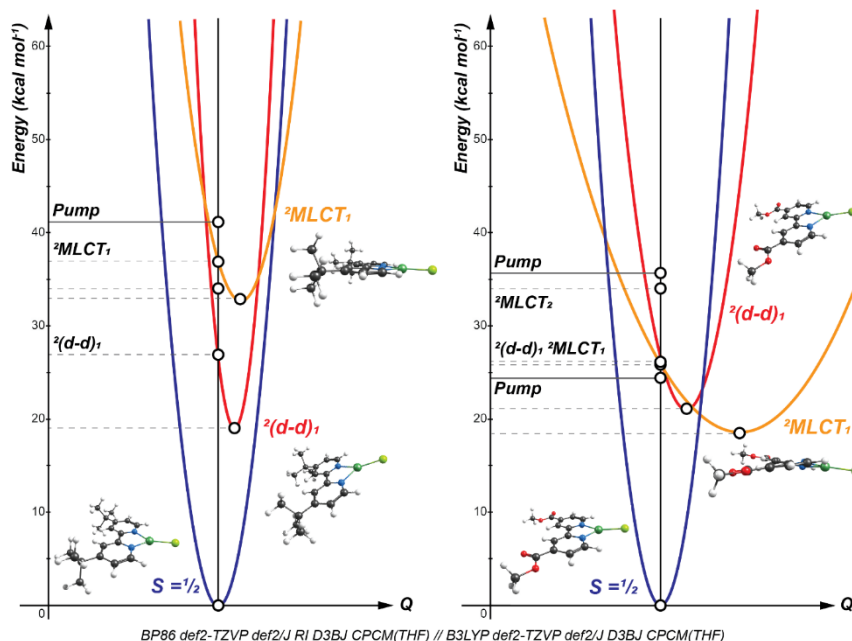


Figure S44. Computed PESs for **1** (left) and **5** (right) showing the positions of the calculated transitions relative to the TA pump (800 or 1200 nm). Relaxed structures computed at the DFT BP86 level for the ground state. Lowest-energy excited states corresponding to β -Ni $3d(z^2) \rightarrow \beta$ -Ni $3d(x^2-y^2)$ for the metal-centered state (red surface) and β -Ni $3d(z^2) \rightarrow \text{bpy } \pi^*(1)$ for the MLCT state (orange surface) were optimized using TDDFT at the B3LYP level; structures are shown. Open circles indicate computed values and correspond to the energy markers on the y-axis. Calculations were performed to investigate the possibility surface crossing into a ligand field excited state and to interrogate the relative geometries of the $^2\text{MLCT}$ excited states vs. the ground-state structures (see Supporting Information Section 1.6; Fits to Alternative Relaxation Models for more details). We find that only in **1** is there a $^2\text{d-d}$ state lower than the MLCT. Given the similar energies of the $^2\text{d-d}$ in **1** and the $^2\text{MLCT}$ in **5** (the lowest-energy surfaces are both $\sim 19 \text{ kcal mol}^{-1}$ above the ground state by TD-DFT), one would expect their relaxation times to be similar under energy gap law behavior (a result opposite of that to the experiment). Thus, DFT/TD-DFT suggests that a rate-limiting $^2\text{d-d} \rightarrow ^2\text{GS}$ is unlikely; relaxation is from the $^2\text{MLCT}$ (a point better emphasized by the experimental TA spectra). The $^2\text{MLCT}$ geometry of **5** is more distorted than for the $^2\text{MLCT}$ of **1**, indicative of an excited-state surface that is nested with the ground state in **1** (Marcus inverted) but a displaced excited-state surface in **5** (Marcus normal). We note, however, that the relative widths and displacements along Q of the excited-state surfaces are qualitative; accurate computed displacements are precluded without the use of an explicit solvation model to account for outer sphere reorganization energy. Vertical and relaxed excited-state energies of **5** are likely to be overestimated (see Supporting Information Section 2.5; Limitations of DFT/TDDFT).

S2.5 Limitations of DFT/TDDFT

As can be noted in the experimental versus computed absorption spectra (Figure S43 and Tables S5-S12), TDDFT well simulates the Ni(I) complexes with electron-rich bpy ligands, particularly those with electron-rich substituents (i.e., **1-3**). However, it quickly fails to adequately stabilize the charge transfer excited states of those with an electron poor bpy ligand or with an extended π -system (i.e., **4-5**). The lowest-energy MLCTs of these complexes (labeled Manifold 1 in Figure S43) are either substantially blue-shifted in energy or not accounted for at all.

Taking complex **5** as an example, we attempted to better model the experiment by adjusting the functional used in the TDDFT calculations⁵⁰ and thereby tuning the amount of exact exchange (which can favor open-shell electronic configurations)^{51,52} from 20% in B3LYP^{46,47} to 10% in meta-hybrid TPSSh⁵³⁻⁵⁵ and 0% in the standard generalized gradient approximation (GGA) functional, BP86.^{38,39} However, in none of these cases were we able to reproduce the experimental spectrum of **5** well (Figure S45).

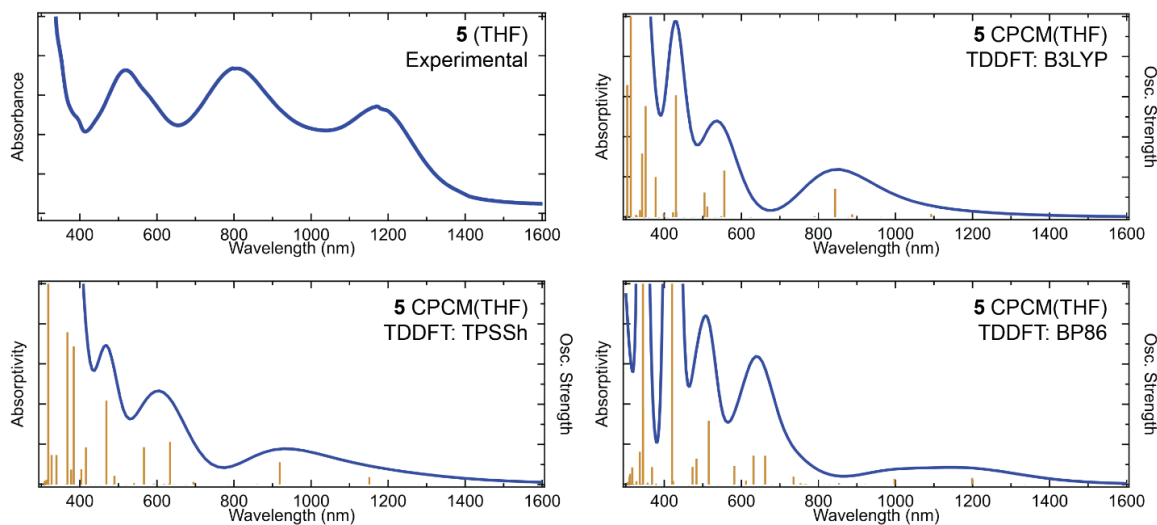


Figure S45. Comparison of the experimental absorption spectrum of **5** in THF (*top left*) and the computed spectra of the same using TDDFT at the B3LYP (*top right*), TPSSh (*bottom left*), and BP86 (*bottom right*) levels. Although the electronic transitions red-shift, their positions and intensities are still poor models of the experiment.

Excited-state optimizations using TDDFT, particularly those of the MLCT transitions, would similarly suffer. Relaxed MLCT geometries of **4-5** are likely computed too high in energy. Additionally, an implicit solvation model CPCM is used to simulate THF, but it cannot adequately describe outer sphere reorganization energies and related effects that contributing to the experimental value of λ presented in the manuscript.

A detailed computational analysis of these electron-deficient bpy-ligated Ni(I) complexes is needed, likely employing multireference calculations (which have been previously demonstrated to reveal substantial bpy ligand non-innocence effects)^{4,49} and/or excited-state molecular dynamics, both of which are beyond the scope of this work. As such, the analysis of **1-5** given in the manuscript main text rests on the experimental data; computational analysis of **4-5** is provided here for completeness.

S3. NMR and IR Spectra.

Proton nuclear magnetic resonance (^1H NMR) and fluorine nuclear magnetic resonance (^{19}F NMR) spectra were recorded on a 400 MHz Varian Spectrometer with broadband auto-tune OneProbe. Fluorine NMR were externally referenced to neat fluorobenzene ($\delta = -113.15$ ppm). All ^{13}C NMR spectra were collected on a Bruker AV-III HD 400 MHz spectrometer and were ^1H decoupled. Chemical shifts are reported in parts per million and are referenced to residual solvent signal.

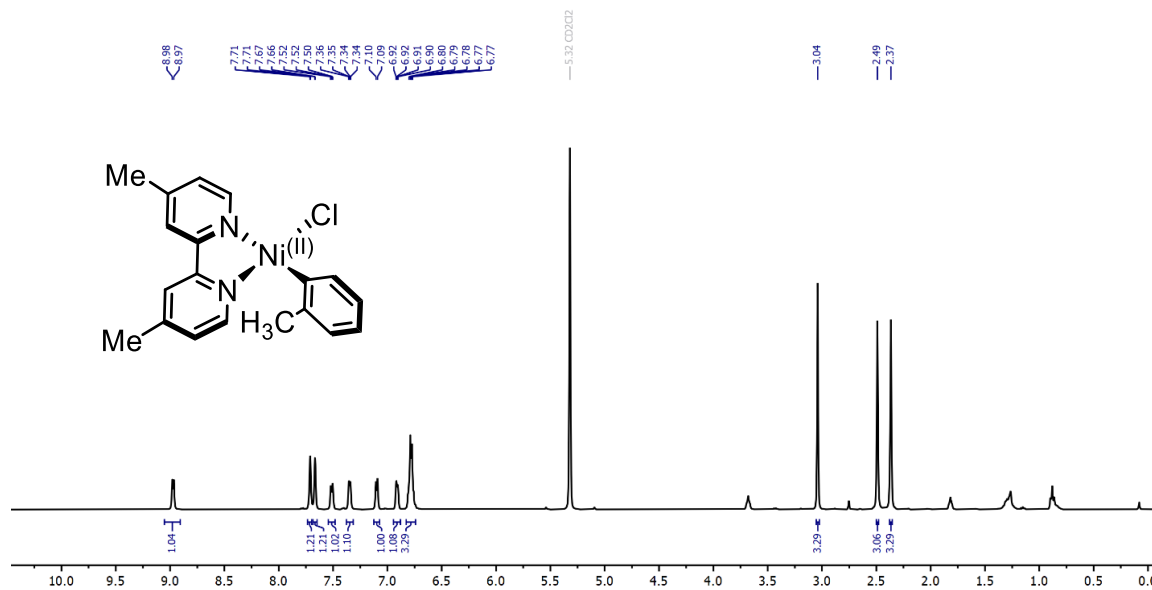


Figure S46. ^1H NMR (400 MHz, CD_2Cl_2) spectra of $\text{Ni}(\text{Me}_2\text{bpy})(o\text{-tolyl})\text{Cl}$, parent compound for **2**.

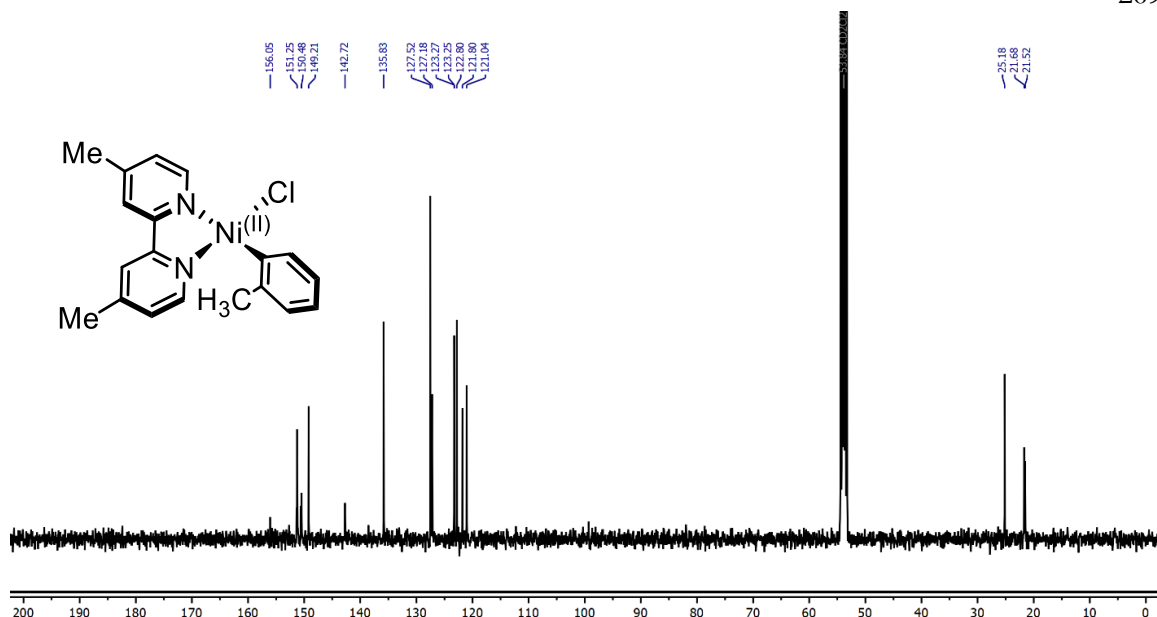


Figure S47. ^{13}C NMR (100 MHz, CD_2Cl_2) spectra of $\text{Ni}(\text{Me}^2\text{bpy})(o\text{-tolyl})\text{Cl}$, parent compound for **2**.

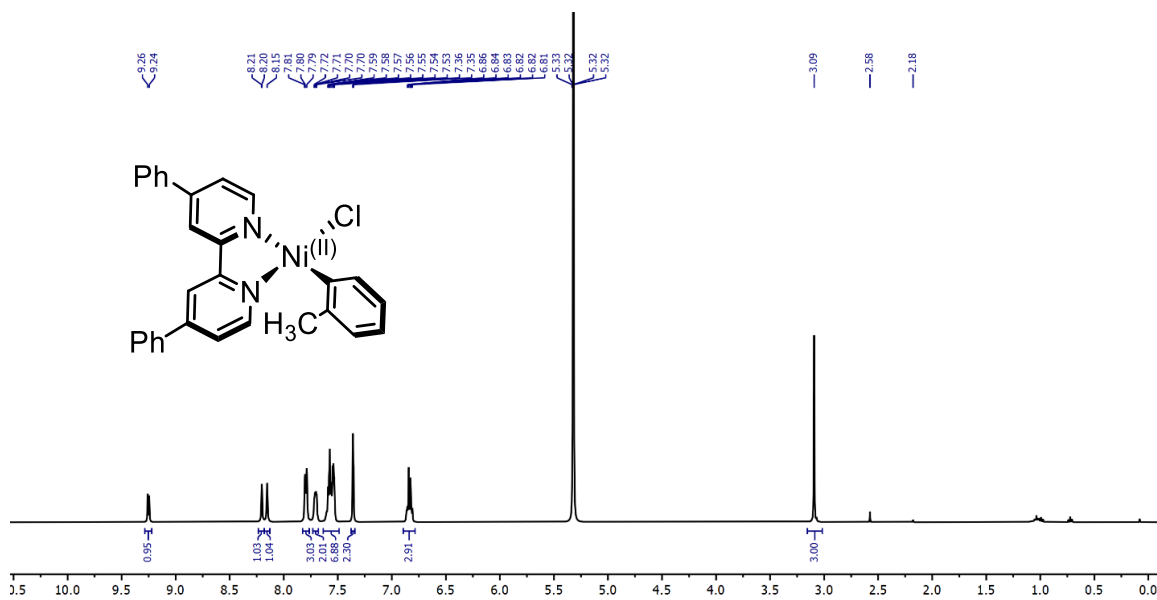


Figure S48. ^1H NMR (400 MHz, CD_2Cl_2) spectra of $\text{Ni}(\text{Ph}^2\text{bpy})(o\text{-tolyl})\text{Cl}$, parent compound for **4**. Proton NMR agrees with previous report.⁵

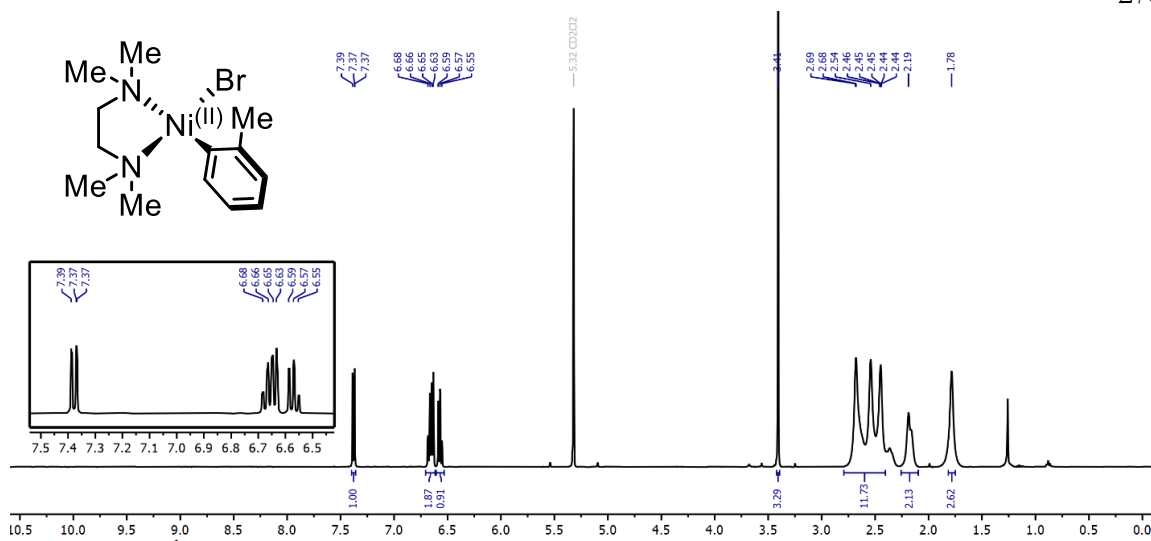


Figure S49. ¹H NMR (400 MHz, CD₂Cl₂) spectra of Ni(TMEDA)(*o*-tolyl)Br.

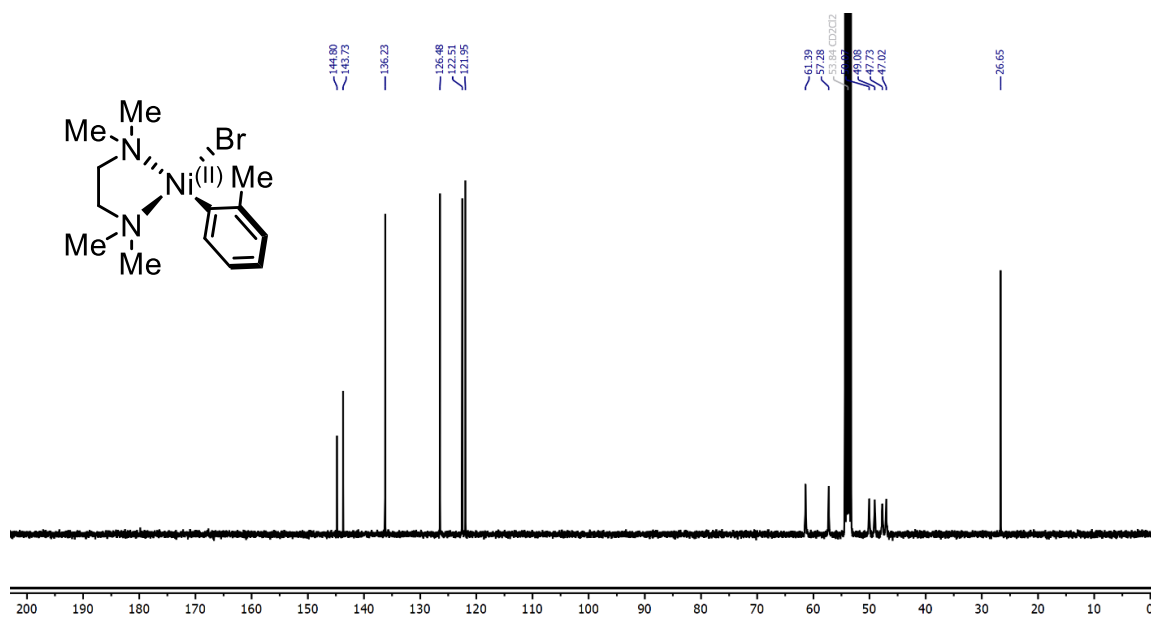
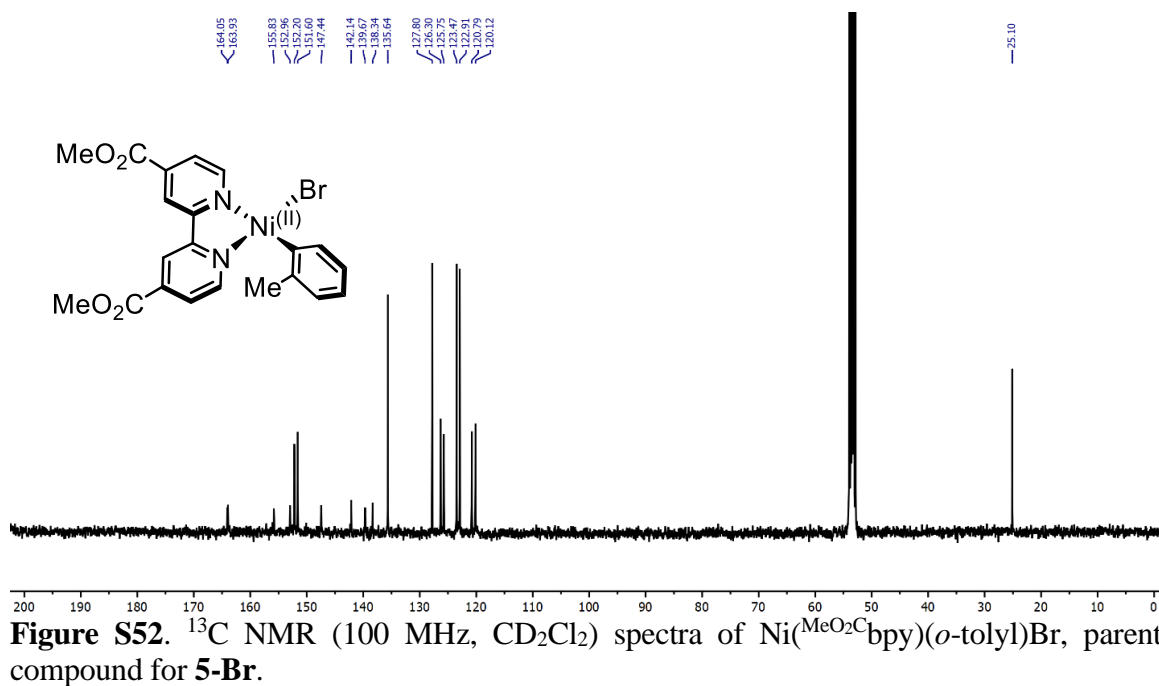
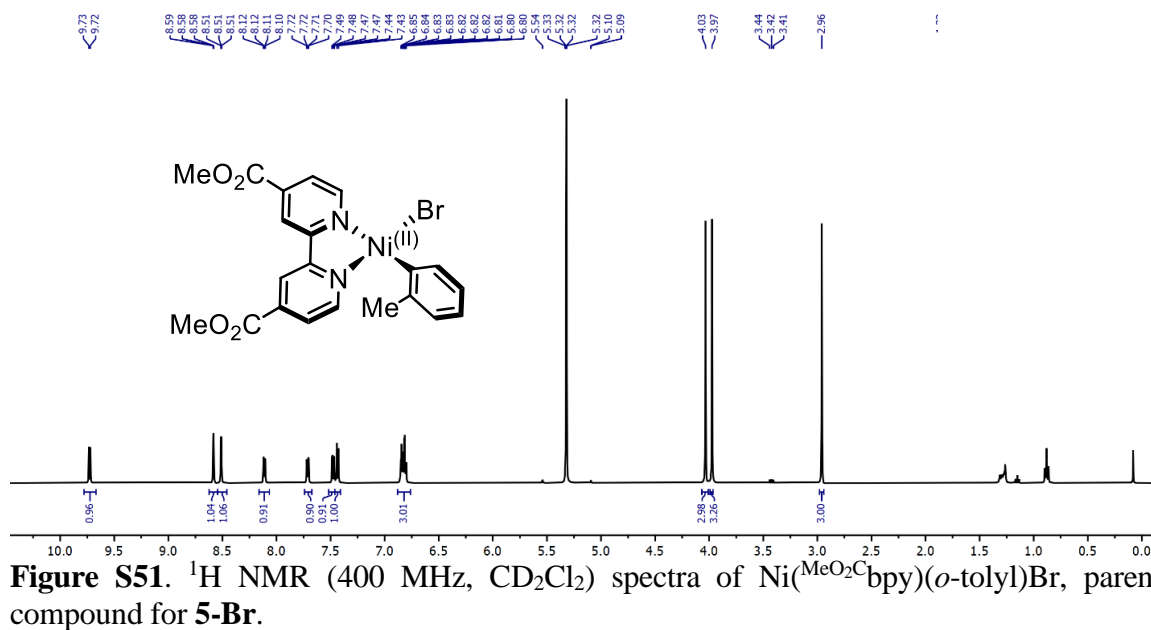


Figure S50. ¹³C NMR (100 MHz, CD₂Cl₂) spectra of Ni(TMEDA)(*o*-tolyl)Br.



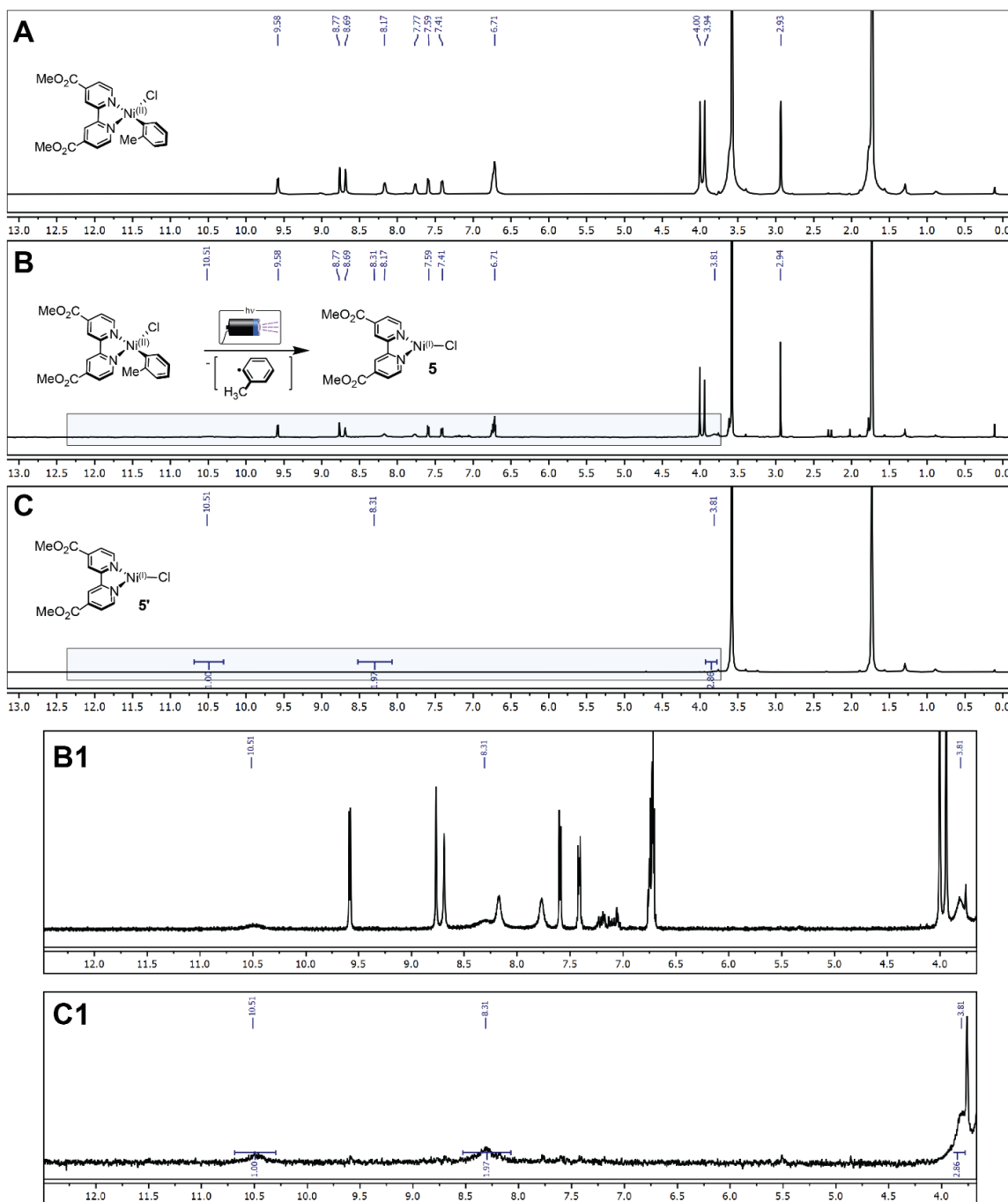


Figure S55. ^1H NMR (400 MHz, d_8 -THF) spectra of (A) $\text{Ni}(\text{MeO}_2\text{Cbpy})(o\text{-tolyl})\text{Cl}$, (B) the photochemical conversion of $\text{Ni}(\text{MeO}_2\text{Cbpy})(o\text{-tolyl})\text{Cl}$ to **5**, and (C) paramagnetic, isolated **5'**. Boxed insets in (B) and (C) are shown in panels (B1) and (C1), respectively. Assignments for $\text{Ni}(\text{MeO}_2\text{Cbpy})(o\text{-tolyl})\text{Cl}$ are as described previously.⁴

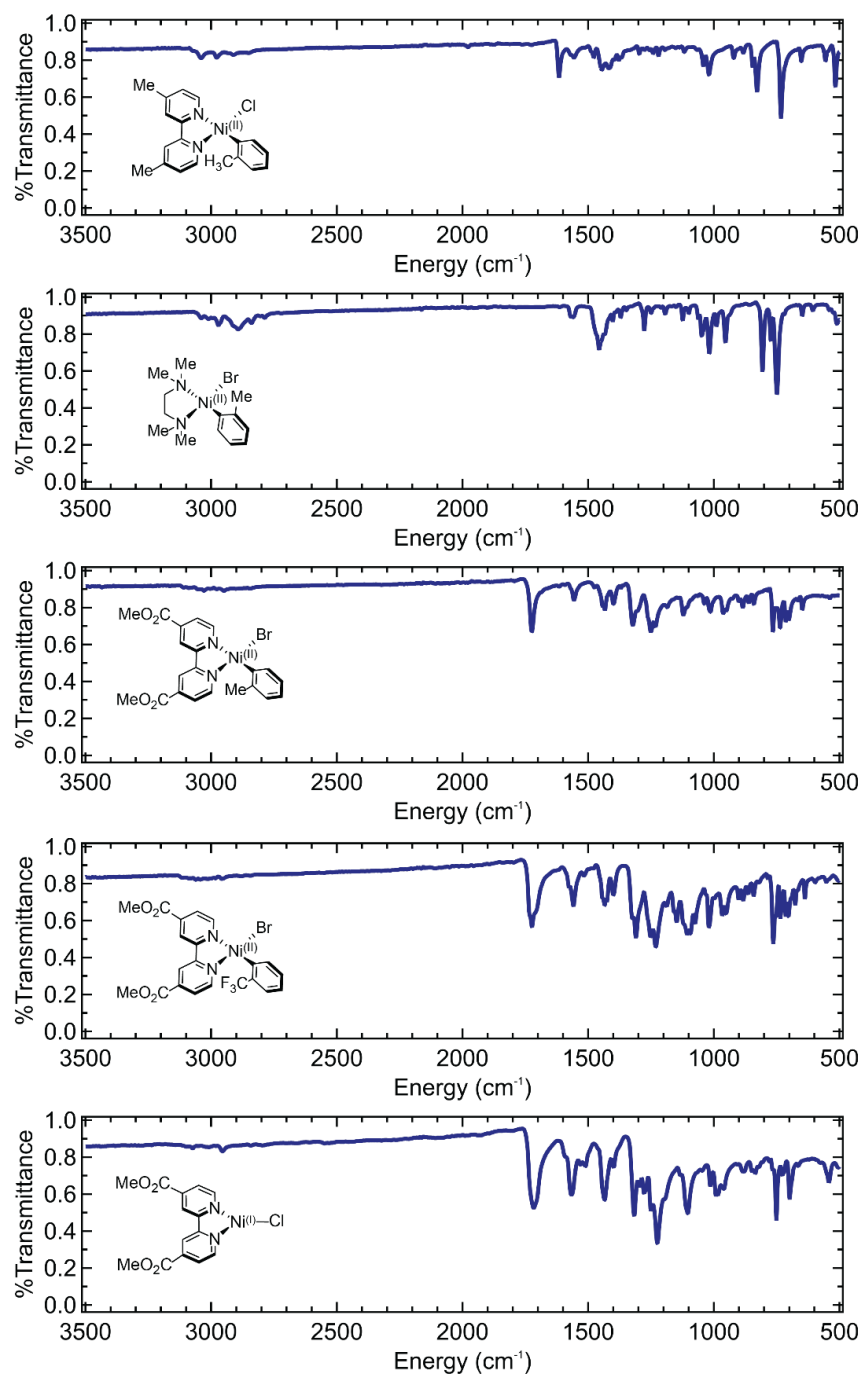
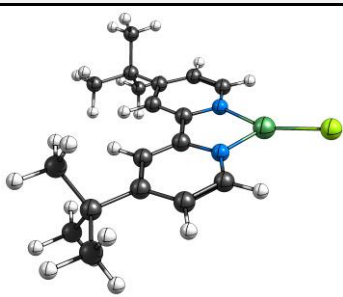
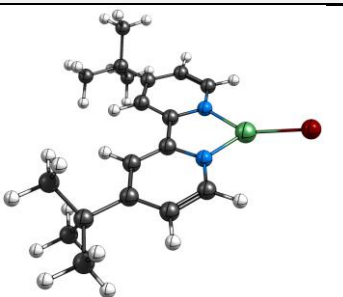
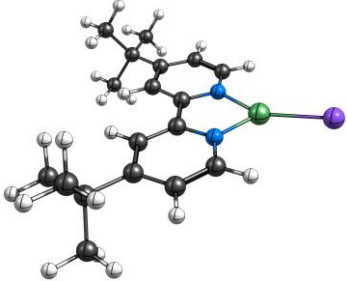



Figure S56. Solid-state IR spectra of the Ni(II) complexes newly synthesized in this work and the isolated complex, **5'**. From top to bottom: Ni(II)(Me₁bpy)(*o*-tolyl)Cl, Ni(II)(TMEDA)(*o*-tolyl)Cl, Ni(II)(MeO₂Cbpy)(*o*-tolyl)Br, Ni(II)(MeO₂Cbpy)(*o*-CF₃Ph)Br, Ni(II)(MeO₂Cbpy)Cl. Structures shown on each spectrum.

S4. Appendix.

1			1-Br				
							
C	-2.029767481	-5.482378378	0.242513014	C	0.659321000	-2.259714000	0.041788000
N	-2.993320211	-4.541935687	0.229603853	N	-0.397352000	-1.428101000	0.119515000
C	-4.295276591	-4.956603212	0.200439005	C	-1.649222000	-1.968507000	0.012015000
C	-4.630774991	-6.307361731	0.186192007	C	-1.840237000	-3.333722000	-0.178781000
C	-3.635290044	-7.296086104	0.202279473	C	-0.746495000	-4.209229000	-0.260353000
C	-2.306945286	-6.846340471	0.230069863	C	0.526474000	-3.632789000	-0.142727000
C	-5.261779440	-3.849662986	0.190029655	C	-2.727948000	-0.975037000	0.116787000
C	-6.648934787	-4.006354925	0.151789945	C	-4.091702000	-1.272852000	0.071256000
C	-7.493591358	-2.892159547	0.143655115	C	-5.047239000	-0.257758000	0.181630000
C	-6.868329156	-1.631051876	0.179230886	C	-4.557068000	1.053054000	0.333112000
C	-5.485454487	-1.534413023	0.215901240	C	-3.191298000	1.290266000	0.376550000
N	-4.677959590	-2.617770489	0.220269810	N	-2.278114000	0.301427000	0.274279000
C	-9.016340381	-3.002867842	0.098655540	C	-6.550778000	-0.522399000	0.143140000
C	-9.601934114	-2.328966391	1.359270503	C	-7.183911000	-0.000721000	1.452255000
Ni	-2.752347324	-2.623508518	0.259827385	Ni	-0.358827000	0.480878000	0.358578000
Cl	-1.059195981	-1.305289447	0.317631596	Br	1.053673000	2.255198000	0.638329000
C	-4.022766266	-8.773587920	0.191453470	C	-0.974933000	-5.704285000	-0.474611000
C	-4.891752963	-9.069960068	1.434425899	C	-1.869149000	-6.245857000	0.662745000
C	-9.489648427	-4.463198015	0.051075312	C	-6.873605000	-2.016991000	0.001797000
C	-9.532749178	-2.273372247	-1.161574862	C	-7.156813000	0.234846000	-1.059583000
C	-2.793524766	-9.693511954	0.216089041	C	0.342297000	-6.493501000	-0.483851000
C	-4.838551620	-9.067196224	-1.087289670	C	-1.689293000	-5.906205000	-1.829868000
H	-7.065085163	-5.010934268	0.127776804	H	-4.402007000	-2.308624000	-0.046145000
H	-7.454021382	-0.712160239	0.178081633	H	-5.235811000	1.900709000	0.421825000
H	-4.984029087	-0.566301298	0.242288659	H	-2.791397000	2.297545000	0.498717000
H	-5.681886650	-6.592145825	0.165020124	H	-2.854691000	-3.720427000	-0.267245000
H	-1.472701894	-7.544815970	0.242795152	H	1.429217000	-4.238110000	-0.193174000
H	-1.003355313	-5.113796749	0.264629404	H	1.641470000	-1.794106000	0.132408000
H	-3.125386762	-10.741100459	0.204986446	H	0.124197000	-7.560941000	-0.627315000
H	-2.189664978	-9.541107276	1.122413974	H	0.884848000	-6.384022000	0.466347000
H	-2.149507033	-9.535050064	-0.661128316	H	1.004616000	-6.172965000	-1.301145000
H	-10.587640101	-4.487448094	0.014460344	H	-7.964180000	-2.150816000	-0.012640000
H	-9.170794673	-5.023994300	0.941803493	H	-6.474049000	-2.599403000	0.844773000
H	-9.111098939	-4.982162212	-0.841603077	H	-6.471514000	-2.435361000	-0.932513000
H	-9.123131571	-2.731811081	-2.073275273	H	-6.718811000	-0.118922000	-2.004097000
H	-9.255802893	-1.210271219	-1.156192434	H	-6.984190000	1.317268000	-0.983942000
H	-10.629749085	-2.339348662	-1.203057528	H	-8.242662000	0.064168000	-1.095596000
H	-4.243248926	-8.857561688	-1.987679478	H	-1.074874000	-5.521211000	-2.656492000
H	-5.753897280	-8.461049022	-1.131336205	H	-2.660069000	-5.391982000	-1.853258000
H	-5.131020694	-10.127257327	-1.104148959	H	-1.866678000	-6.978306000	-1.999478000
H	-4.332046802	-8.868430762	2.359199251	H	-1.388861000	-6.100021000	1.641047000
H	-5.190577441	-10.128344393	1.433356604	H	-2.040007000	-7.322462000	0.517547000
H	-5.804367177	-8.458291521	1.443432679	H	-2.847755000	-5.747024000	0.681522000
H	-9.250452573	-2.833680152	2.270759038	H	-6.762950000	-0.522027000	2.324143000
H	-10.700034884	-2.384748993	1.333256842	H	-8.269275000	-0.177178000	1.433738000
H	-9.316120791	-1.269916189	1.419775304	H	-7.016833000	1.077236000	1.581444000

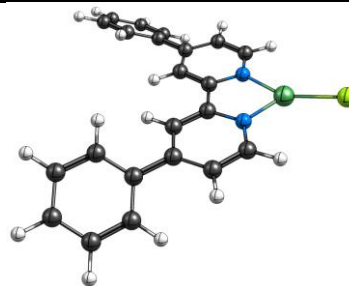
1-I				2			
							
C	-0.751175000	2.863174000	0.039848000	C	-0.710483000	2.863308000	0.180761000
N	0.216287000	1.927032000	0.046683000	N	0.262518000	1.931301000	0.097130000
C	1.517527000	2.346358000	0.066315000	C	1.559679000	2.351214000	0.045922000
C	1.846986000	3.698260000	0.074519000	C	1.890582000	3.706989000	0.080218000
C	0.847183000	4.683179000	0.064787000	C	0.888165000	4.678474000	0.166719000
C	-0.479159000	4.228310000	0.048675000	C	-0.441423000	4.224544000	0.216764000
C	2.491693000	1.244221000	0.070050000	C	2.527817000	1.250223000	-0.044628000
C	3.877410000	1.409261000	0.118877000	C	3.913083000	1.408225000	-0.114486000
C	4.728096000	0.299192000	0.113278000	C	4.750709000	0.291287000	-0.196705000
C	4.112406000	-0.965072000	0.055949000	C	4.133307000	-0.971932000	-0.205470000
C	2.729961000	-1.070136000	0.016149000	C	2.750849000	-1.068540000	-0.134968000
N	1.918915000	0.008728000	0.024492000	N	1.947017000	0.014365000	-0.055631000
C	6.249761000	0.417804000	0.159594000	Ni	0.023437000	0.013952000	0.046003000
C	6.778836000	-0.367947000	1.379607000	Cl	-1.691356000	-1.276324000	0.095598000
Ni	-0.009358000	0.014083000	0.017072000	H	4.348734000	2.407504000	-0.105601000
I	-1.757424000	-1.706865000	0.005504000	H	4.730038000	-1.882751000	-0.267441000
C	1.227408000	6.162348000	0.068929000	H	2.247241000	-2.035856000	-0.140650000
C	2.055040000	6.462742000	1.338405000	H	2.935772000	4.014392000	0.040845000
C	6.713712000	1.877312000	0.273631000	H	-1.268961000	4.931670000	0.284708000
C	6.831188000	-0.191122000	-1.136123000	H	-1.731723000	2.482348000	0.219264000
C	-0.008786000	7.073668000	0.057297000	C	6.243486000	0.429869000	-0.272213000
C	2.077925000	6.462862000	-1.185246000	H	6.724932000	-0.087009000	0.571548000
H	4.287757000	2.415278000	0.163858000	H	6.630314000	-0.031285000	-1.193411000
H	4.705457000	-1.878916000	0.043982000	H	6.548672000	1.483447000	-0.255454000
H	2.232167000	-2.039731000	-0.022912000	C	1.213724000	6.143338000	0.203972000
H	2.896881000	3.988782000	0.084580000	H	0.817025000	6.607006000	1.119609000
H	-1.316660000	4.922644000	0.041484000	H	2.296930000	6.312533000	0.168362000
H	-1.776107000	2.490317000	0.025775000	H	0.750804000	6.665870000	-0.646746000
H	0.314596000	8.123904000	0.060367000				
H	-0.639190000	6.912120000	0.943558000				
H	-0.622112000	6.912334000	-0.840898000				
H	7.811562000	1.907254000	0.312162000				
H	6.331195000	2.353487000	1.188210000				
H	6.392446000	2.476063000	-0.591113000				
H	6.470584000	0.355448000	-2.019487000				
H	6.550799000	-1.247781000	-1.246572000				
H	7.929022000	-0.129330000	-1.114004000				
H	1.507143000	6.256388000	-2.102118000				
H	2.995528000	5.858824000	-1.208574000				
H	2.368469000	7.523581000	-1.189549000				
H	1.467437000	6.256957000	2.244712000				
H	2.346227000	7.523249000	1.347555000				
H	2.971510000	5.857978000	1.378164000				
H	6.371029000	0.041487000	2.315115000				
H	7.875457000	-0.295007000	1.418533000				
H	6.511232000	-1.431864000	1.323651000				

3

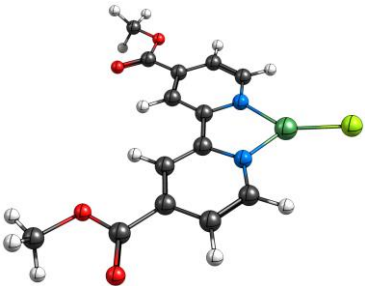
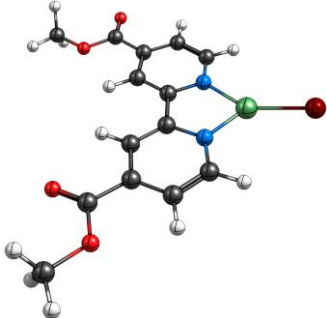


C	0.473042000	-2.474101000	0.301340000
N	-0.621213000	-1.686728000	0.241593000
C	-1.820768000	-2.247454000	-0.095944000
C	-1.933067000	-3.610491000	-0.379539000
C	-0.798133000	-4.417499000	-0.316330000
C	0.426311000	-3.837966000	0.030900000
C	-2.929113000	-1.285073000	-0.124235000
C	-4.254095000	-1.595831000	-0.438432000
C	-5.214232000	-0.585292000	-0.427954000
C	-4.822396000	0.717024000	-0.101945000
C	-3.487035000	0.963078000	0.200276000
N	-2.551375000	-0.010033000	0.191995000
Ni	-0.679100000	0.210618000	0.584668000
Cl	0.725756000	1.738839000	1.122454000
H	-4.532733000	-2.618318000	-0.689887000
H	-6.252626000	-0.810518000	-0.670461000
H	-5.539336000	1.537014000	-0.081022000
H	-3.133022000	1.961473000	0.459119000
H	-2.898610000	-4.037241000	-0.647427000
H	-0.868067000	-5.482974000	-0.534779000
H	1.337867000	-4.431333000	0.092479000
H	1.403530000	-1.976099000	0.575931000

4



C	-0.303121000	2.357166000	-1.786324000
N	0.370314000	1.197550000	-1.632083000
C	1.340992000	0.888638000	-2.542159000
C	1.643905000	1.733652000	-3.605965000
C	0.948392000	2.941798000	-3.774420000
C	-0.049372000	3.239870000	-2.825965000
C	2.002125000	-0.397495000	-2.277626000
C	3.017789000	-0.943208000	-3.057500000
C	3.583328000	-2.184070000	-2.722633000
C	3.070632000	-2.829197000	-1.580223000
C	2.057866000	-2.233660000	-0.843102000
N	1.520684000	-1.038404000	-1.170501000
Ni	0.120011000	-0.109760000	-0.235981000
Cl	-1.159087000	-0.274252000	1.478289000
H	3.359026000	-0.413421000	-3.945518000
H	3.475143000	-3.784416000	-1.247827000
H	1.652308000	-2.709981000	0.050026000
H	2.409633000	1.443726000	-4.323622000
H	-0.614348000	4.169553000	-2.880582000
H	-1.064154000	2.569899000	-1.034839000
C	1.252568000	3.851686000	-4.894780000
C	0.244798000	4.652755000	-5.464168000
C	2.556277000	3.937364000	-5.419065000
C	0.531524000	5.508562000	-6.527592000
C	2.842500000	4.797980000	-6.478636000
C	1.831232000	5.585590000	-7.038813000
H	-0.776753000	4.584838000	-5.087682000
H	3.358085000	3.345468000	-4.975335000
H	-0.264922000	6.113522000	-6.963318000
H	3.861054000	4.859297000	-6.864606000
H	2.055069000	6.256808000	-7.869049000
C	4.663419000	-2.778875000	-3.532174000
C	4.790750000	-4.176191000	-3.645886000
C	5.590001000	-1.962084000	-4.207824000
C	5.809841000	-4.738031000	-4.414914000
C	6.611721000	-2.525698000	-4.971884000
C	6.725020000	-3.915699000	-5.080299000
H	4.070040000	-4.826883000	-3.148912000
H	5.526701000	-0.877222000	-4.111536000
H	5.886107000	-5.822953000	-4.500356000
H	7.327196000	-1.877112000	-5.479460000
H	7.523016000	-4.355894000	-5.679758000

5				5-Br			
							
C	0.568503000	-2.394588000	0.316547000	C	0.764158000	-2.191930000	0.350402000
N	-0.519621000	-1.595903000	0.306684000	N	-0.323481000	-1.393036000	0.341233000
C	-1.753839000	-2.162453000	0.148607000	C	-1.558559000	-1.957846000	0.184071000
C	-1.908807000	-3.537154000	-0.001582000	C	-1.714520000	-3.332451000	0.034530000
C	-0.779763000	-4.362047000	0.010679000	C	-0.586011000	-4.158180000	0.046305000
C	0.483694000	-3.773251000	0.173273000	C	0.677975000	-3.570739000	0.207383000
C	-2.850198000	-1.186377000	0.156934000	C	-2.655609000	-0.981640000	0.191745000
C	-4.199573000	-1.503469000	0.021577000	C	-4.004795000	-1.300035000	0.057076000
C	-5.149743000	-0.476662000	0.047900000	C	-4.955627000	-0.273731000	-0.081623000
C	-4.707806000	0.844794000	0.209841000	C	-4.515313000	1.048328000	0.240264000
C	-3.349024000	1.092138000	0.339974000	C	-3.156501000	1.297154000	0.370217000
N	-2.427774000	0.104205000	0.316439000	N	-2.235630000	0.309625000	0.348946000
C	-6.612290000	-0.734410000	-0.088046000	C	-6.418504000	-0.533285000	-0.052459000
O	-6.882910000	-2.048339000	-0.229848000	O	-6.687937000	-1.847857000	-0.187666000
C	-8.286502000	-2.386728000	-0.365605000	C	-8.091449000	-2.188373000	-0.320409000
Ni	-0.529882000	0.317468000	0.498309000	Ni	-0.337623000	0.517928000	0.540196000
Cl	0.960350000	1.824056000	0.786525000	C	-0.785026000	-5.628340000	-0.112243000
C	-0.977021000	-5.831976000	-0.149263000	O	0.381935000	-6.301605000	-0.075498000
O	0.190825000	-6.504183000	-0.112213000	C	0.278198000	-7.741378000	-0.218972000
C	0.088721000	-7.943740000	-0.257699000	O	-7.269897000	0.343453000	-0.040063000
O	-7.463500000	0.142614000	-0.071618000	O	-1.878068000	-6.156553000	-0.256796000
O	-2.069176000	-6.361714000	-0.295546000	H	-4.320438000	-2.333754000	-0.064544000
H	-4.515737000	-2.536785000	-0.102283000	H	-5.231610000	1.867955000	0.262336000
H	-5.423238000	1.665127000	0.233770000	H	-2.770426000	2.308504000	0.497451000
H	-2.962519000	2.103126000	0.468761000	H	-2.698855000	-3.780523000	-0.091230000
H	-2.892830000	-3.985669000	-0.128370000	H	1.582467000	-4.174833000	0.221837000
H	1.388707000	-4.376553000	0.188369000	H	1.723792000	-1.690908000	0.478182000
H	1.527777000	-1.892921000	0.444695000	H	-8.643445000	-1.862308000	0.569907000
H	-8.839144000	-2.065172000	0.525972000	H	-8.512503000	-1.709724000	-1.213329000
H	-8.706483000	-1.902810000	-1.256203000	H	-8.114985000	-3.277492000	-0.415395000
H	-8.311075000	-3.475297000	-0.466662000	H	-0.328688000	-8.157626000	0.594718000
H	-0.519047000	-8.361820000	0.554406000	H	-0.175988000	-7.991643000	-1.185777000
H	-0.363635000	-8.193319000	-1.225558000	H	1.306252000	-8.110018000	-0.165190000
H	1.117044000	-8.311511000	-0.202772000	Br	1.211822000	2.149558000	0.887246000

S5. References

- (1) Stoll, S.; Schweiger, A. EasySpin, a Comprehensive Software Package for Spectral Simulation and Analysis in EPR. *J. Magn. Reson.* **2006**, *178* (1), 42–55. <https://doi.org/10.1016/j.jmr.2005.08.013>.
- (2) Kazmierczak, N. P.; Chew, J. A.; Vander Griend, D. A. Bootstrap Methods for Quantifying the Uncertainty of Binding Constants in the Hard Modeling of Spectrophotometric Titration Data. *Anal. Chim. Acta* **2022**, *1227*, 339834. <https://doi.org/10.1016/j.aca.2022.339834>.
- (3) Shields, B. J.; Kudisch, B.; Scholes, G. D.; Doyle, A. G. Long-Lived Charge-Transfer States of Nickel(II) Aryl Halide Complexes Facilitate Bimolecular Photoinduced Electron Transfer. *J. Am. Chem. Soc.* **2018**, *140* (8), 3035–3039. <https://doi.org/10.1021/jacs.7b13281>.
- (4) Cagan, D. A.; Bím, D.; Silva, B.; Kazmierczak, N. P.; McNicholas, B. J.; Hadt, R. G. Elucidating the Mechanism of Excited-State Bond Homolysis in Nickel–Bipyridine Photoredox Catalysts. *J. Am. Chem. Soc.* **2022**, *144* (14), 6516–6531. <https://doi.org/10.1021/jacs.2c01356>.
- (5) Ting, S. I.; Garakyaraghi, S.; Taliaferro, C. M.; Shields, B. J.; Scholes, G. D.; Castellano, F. N.; Doyle, A. G. ³d-d Excited States of Ni(II) Complexes Relevant to Photoredox Catalysis: Spectroscopic Identification and Mechanistic Implications. *J. Am. Chem. Soc.* **2020**, *142* (12), 5800–5810. <https://doi.org/10.1021/jacs.0c00781>.
- (6) Cagan, D. A.; Bím, D.; McNicholas, B. J.; Kazmierczak, N. P.; Oyala, P. H.; Hadt, R. G. Photogenerated Ni(I)–Bipyridine Halide Complexes: Structure-Function Relationships for Competitive C(sp²)–Cl Oxidative Addition and Dimerization Reactivity Pathways. *Inorg. Chem.* **2023**, *62* (24), 9538–9551. <https://doi.org/10.1021/acs.inorgchem.3c00917>.
- (7) Ting, S. I.; Williams, W. L.; Doyle, A. G. Oxidative Addition of Aryl Halides to a Ni(I)-Bipyridine Complex. *J. Am. Chem. Soc.* **2022**, *144* (12), 5575–5582. <https://doi.org/10.1021/jacs.2c00462>.
- (8) Sheldrick, G. M. Phase Annealing in SHELX-90: Direct Methods for Larger Structures. *Acta Crystallogr. A* **1990**, *46* (6), 467–473. <https://doi.org/10.1107/S0108767390000277>.
- (9) Sheldrick, G. M. Crystal Structure Refinement with SHELXL. *Acta Crystallogr. Sect. C Struct. Chem.* **2015**, *71* (1), 3–8. <https://doi.org/10.1107/S2053229614024218>.

- (10) Müller, P. Practical Suggestions for Better Crystal Structures. *Crystallogr. Rev.* **2009**, *15* (1), 57–83. <https://doi.org/10.1080/08893110802547240>.
- (11) Cagan, D. A.; Bím, D.; McNicholas, B. J.; Kazmierczak, N. P.; Oyala, P. H.; Hadt, R. G. Photogenerated Ni(I)–Bipyridine Halide Complexes: Structure–Function Relationships for Competitive C(sp²)–Cl Oxidative Addition and Dimerization Reactivity Pathways. *Inorg. Chem.* **2023**, *62* (24), 9538–9551. <https://doi.org/10.1021/acs.inorgchem.3c00917>.
- (12) Newman-Stonebraker, S. H.; Raab, T. J.; Roshandel, H.; Doyle, A. G. Synthesis of Nickel(I)–Bromide Complexes via Oxidation and Ligand Displacement: Evaluation of Ligand Effects on Speciation and Reactivity. *J. Am. Chem. Soc.* **2023**, *145* (35), 19368–19377. <https://doi.org/10.1021/jacs.3c06233>.
- (13) Dawson, G. A.; Lin, Q.; Neary, M. C.; Diao, T. Ligand Redox Activity of Organonickel Radical Complexes Governed by the Geometry. *J. Am. Chem. Soc.* **2023**. <https://doi.org/10.1021/jacs.3c07031>.
- (14) Diccianni, J. B.; Diao, T. Mechanisms of Nickel-Catalyzed Cross-Coupling Reactions. *Trends Chem.* **2019**, *1* (9), 830–844. <https://doi.org/10.1016/j.trechm.2019.08.004>.
- (15) Kunnus, K.; Li, L.; Titus, C. J.; Lee, S. J.; Reinhard, M. E.; Koroidov, S.; Kjær, K. S.; Hong, K.; Ledbetter, K.; Doriese, W. B.; O’Neil, G. C.; Swetz, D. S.; Ullom, J. N.; Li, D.; Irwin, K.; Nordlund, D.; Cordones, A. A.; Gaffney, K. J. Chemical Control of Competing Electron Transfer Pathways in Iron Tetracyano-Polypyridyl Photosensitizers. *Chem. Sci.* **2020**, *11* (17), 4360–4373. <https://doi.org/10.1039/C9SC06272F>.
- (16) Sun, R.; Qin, Y.; Ruccolo, S.; Schnedermann, C.; Costentin, C.; Daniel G. Nocera. Elucidation of a Redox-Mediated Reaction Cycle for Nickel-Catalyzed Cross Coupling. *J. Am. Chem. Soc.* **2019**, *141* (1), 89–93. <https://doi.org/10.1021/jacs.8b11262>.
- (17) Mohadjer Beromi, M.; Brudvig, G. W.; Hazari, N.; Lant, H. M. C.; Mercado, B. Q. Synthesis and Reactivity of Paramagnetic Nickel Polypyridyl Complexes Relevant to C(sp²)–C(sp³) Coupling Reactions. *Angew. Chem. Int. Ed.* **2019**, *58* (18), 6094–6098. <https://doi.org/10.1002/anie.201901866>.
- (18) Till, N. A.; Oh, S.; MacMillan, D. W. C.; Bird, M. J. The Application of Pulse Radiolysis to the Study of Ni(I) Intermediates in Ni-Catalyzed Cross-Coupling Reactions. *J. Am. Chem. Soc.* **2021**, *143* (25), 9332–9337. <https://doi.org/10.1021/jacs.1c04652>.

- (19) Englman, R.; Jortner, J. The Energy Gap Law for Radiationless Transitions in Large Molecules. *Mol. Phys.* **1970**, *18* (2), 145–164. <https://doi.org/10.1080/00268977000100171>.
- (20) Freed, K. F.; Jortner, J. Multiphonon Processes in the Nonradiative Decay of Large Molecules. *J. Chem. Phys.* **1970**, *52* (12), 6272–6291. <https://doi.org/10.1063/1.1672938>.
- (21) Byrne, J. P.; McCoy, E. F.; Ross, I. G. Internal Conversion in Aromatic and N-Heteroaromatic Molecules. *Aust. J. Chem.* **1965**, *18* (10), 1589–1603. <https://doi.org/10.1071/ch9651589>.
- (22) Marcus, R. A. Chemical and Electrochemical Electron-Transfer Theory. *Annu. Rev. Phys. Chem.* **1964**, *15* (1), 155–196. <https://doi.org/10.1146/annurev.pc.15.100164.001103>.
- (23) Marcus, R. A. On the Theory of Oxidation-Reduction Reactions Involving Electron Transfer. I. *J. Chem. Phys.* **1956**, *24* (5), 966–978. <https://doi.org/10.1063/1.1742723>.
- (24) Marcus, R. A. Theoretical Relations among Rate Constants, Barriers, and Broensted Slopes of Chemical Reactions. *J. Phys. Chem.* **1968**, *72* (3), 891–899. <https://doi.org/10.1021/j100849a019>.
- (25) Marcus, R. A.; Sutin, N. Electron Transfers in Chemistry and Biology. *Biochim. Biophys. Acta BBA—Rev. Bioenerg.* **1985**, *811* (3), 265–322. [https://doi.org/10.1016/0304-4173\(85\)90014-X](https://doi.org/10.1016/0304-4173(85)90014-X).
- (26) Siders, P.; Marcus, R. A. Quantum Effects for Electron-Transfer Reactions in the “Inverted Region”. *J. Am. Chem. Soc.* **1981**, *103* (4), 748–752. <https://doi.org/10.1021/ja00394a004>.
- (27) Ulstrup, J.; Jortner, J. The Effect of Intramolecular Quantum Modes on Free Energy Relationships for Electron Transfer Reactions. *J. Chem. Phys.* **1975**, *63* (10), 4358–4368. <https://doi.org/10.1063/1.431152>.
- (28) Kumpulainen, T.; Lang, B.; Rosspeintner, A.; Vauthey, E. Ultrafast Elementary Photochemical Processes of Organic Molecules in Liquid Solution. *Chem. Rev.* **2017**, *117* (16), 10826–10939. <https://doi.org/10.1021/acs.chemrev.6b00491>.
- (29) Closs, G. L.; Miller, J. R. Intramolecular Long-Distance Electron Transfer in Organic Molecules. *Science* **1988**, *240* (4851), 440–447. <https://doi.org/10.1126/science.240.4851.440>.

- (30) Mataga, N.; Chosrowjan, H.; Shibata, Y.; Yoshida, N.; Osuka, A.; Kikuzawa, T.; Okada, T. First Unequivocal Observation of the Whole Bell-Shaped Energy Gap Law in Intramolecular Charge Separation from S₂ Excited State of Directly Linked Porphyrin–Imide Dyads and Its Solvent-Polarity Dependencies. *J. Am. Chem. Soc.* **2001**, *123* (49), 12422–12423. <https://doi.org/10.1021/ja010865s>.
- (31) Häberle, T.; Hirsch, J.; Pöllinger, F.; Heitele, H.; Michel-Beyerle, M. E.; Anders, C.; Döhling, A.; Krieger, C.; Rückemann, A.; Staab, H. A. Ultrafast Charge Separation and Driving Force Dependence in Cyclophane-Bridged Zn–Porphyrin–Quinone Molecules. *J. Phys. Chem.* **1996**, *100* (46), 18269–18274. <https://doi.org/10.1021/jp960423g>.
- (32) Asahi, T.; Ohkohchi, M.; Matsusaka, R.; Mataga, N.; Zhang, R. P.; Osuka, A.; Maruyama, K. Intramolecular Photoinduced Charge Separation and Charge Recombination of the Product Ion Pair States of a Series of Fixed-Distance Dyads of Porphyrins and Quinones: Energy Gap and Temperature Dependences of the Rate Constants. *J. Am. Chem. Soc.* **1993**, *115* (13), 5665–5674. <https://doi.org/10.1021/ja00066a036>.
- (33) Poronik, Y. M.; Sadowski, B.; Szychta, K.; Quina, F. H.; Vullev, V. I.; Gryko, D. T. Revisiting the Non-Fluorescence of Nitroaromatics: Presumption *versus* Reality. *J. Mater. Chem. C* **2022**, *10* (8), 2870–2904. <https://doi.org/10.1039/D1TC05423F>.
- (34) Miller, J. R.; Calcaterra, L. T.; Closs, G. L. Intramolecular Long-Distance Electron Transfer in Radical Anions. The Effects of Free Energy and Solvent on the Reaction Rates. *J. Am. Chem. Soc.* **1984**, *106* (10), 3047–3049. <https://doi.org/10.1021/ja00322a058>.
- (35) Heitele, H.; Poellinger, F.; Haeberle, T.; Michel-Beyerle, M. E.; Staab, H. A. Energy Gap and Temperature Dependence of Photoinduced Electron Transfer in Porphyrin–Quinone Cyclophanes. *J. Phys. Chem.* **1994**, *98* (30), 7402–7410. <https://doi.org/10.1021/j100081a028>.
- (36) Neese, F. The ORCA Program System. *WIREs Comput. Mol. Sci.* **2012**, *2* (1), 73–78. <https://doi.org/10.1002/wcms.81>.
- (37) Neese, F. Software Update: The ORCA Program System—Version 5.0. *WIREs Comput. Mol. Sci.* **2022**, *12* (5), e1606. <https://doi.org/10.1002/wcms.1606>.
- (38) Perdew, J. P. Density-Functional Approximation for the Correlation Energy of the Inhomogeneous Electron Gas. *Phys. Rev. B* **1986**, *33* (12), 8822–8824. <https://doi.org/10.1103/PhysRevB.33.8822>.

- (39) Becke, A. D. Density-Functional Exchange-Energy Approximation with Correct Asymptotic Behavior. *Phys. Rev. A* **1988**, *38* (6), 3098–3100. <https://doi.org/10.1103/PhysRevA.38.3098>.
- (40) Weigend, F.; Ahlrichs, R. Balanced Basis Sets of Split Valence, Triple Zeta Valence and Quadruple Zeta Valence Quality for H to Rn: Design and Assessment of Accuracy. *Phys. Chem. Chem. Phys.* **2005**, *7* (18), 3297–3305. <https://doi.org/10.1039/B508541A>.
- (41) Eichkorn, K.; Treutler, O.; Öhm, H.; Häser, M.; Ahlrichs, R. Auxiliary Basis Sets to Approximate Coulomb Potentials. *Chem. Phys. Lett.* **1995**, *240* (4), 283–290. [https://doi.org/10.1016/0009-2614\(95\)00621-A](https://doi.org/10.1016/0009-2614(95)00621-A).
- (42) Grimme, S.; Antony, J.; Ehrlich, S.; Krieg, H. A Consistent and Accurate Ab Initio Parametrization of Density Functional Dispersion Correction (DFT-D) for the 94 Elements H-Pu. *J. Chem. Phys.* **2010**, *132* (15), 154104. <https://doi.org/10.1063/1.3382344>.
- (43) Grimme, S.; Ehrlich, S.; Goerigk, L. Effect of the Damping Function in Dispersion Corrected Density Functional Theory. *J. Comput. Chem.* **2011**, *32* (7), 1456–1465. <https://doi.org/10.1002/jcc.21759>.
- (44) Klamt, A.; Schüürmann, G. COSMO: A New Approach to Dielectric Screening in Solvents with Explicit Expressions for the Screening Energy and Its Gradient. *J. Chem. Soc. Perkin Trans. 2* **1993**, No. 5, 799–805. <https://doi.org/10.1039/P29930000799>.
- (45) Barone, V.; Cossi, M. Quantum Calculation of Molecular Energies and Energy Gradients in Solution by a Conductor Solvent Model. *J. Phys. Chem. A* **1998**, *102* (11), 1995–2001. <https://doi.org/10.1021/jp9716997>.
- (46) Lee, C.; Yang, W.; Parr, R. G. Development of the Colle-Salvetti Correlation-Energy Formula into a Functional of the Electron Density. *Phys. Rev. B* **1988**, *37* (2), 785–789. <https://doi.org/10.1103/PhysRevB.37.785>.
- (47) Becke, A. D. Density-functional Thermochemistry. III. The Role of Exact Exchange. *J. Chem. Phys.* **1993**, *98* (7), 5648–5652. <https://doi.org/10.1063/1.464913>.
- (48) Neese, F.; Wennmohs, F.; Hansen, A.; Becker, U. Efficient, Approximate and Parallel Hartree-Fock and Hybrid DFT Calculations. A ‘Chain-of-Spheres’ Algorithm for the Hartree-Fock Exchange. *Chem. Phys.* **2009**, *356* (1), 98–109. <https://doi.org/10.1016/j.chemphys.2008.10.036>.

- (49) Cagan, D. A.; Strocio, G. D.; Cusumano, A. Q.; Hadt, R. G. Multireference Description of Nickel–Aryl Homolytic Bond Dissociation Processes in Photoredox Catalysis. *J. Phys. Chem. A* **2020**, *124* (48), 9915–9922. <https://doi.org/10.1021/acs.jpca.0c08646>.
- (50) Jensen, K. P.; Roos, B. O.; Ryde, U. Performance of Density Functionals for First Row Transition Metal Systems. *J. Chem. Phys.* **2007**, *126* (1), 014103. <https://doi.org/10.1063/1.2406071>.
- (51) Neese, F. A Critical Evaluation of DFT, Including Time-Dependent DFT, Applied to Bioinorganic Chemistry. *JBIC J. Biol. Inorg. Chem.* **2006**, *11* (6), 702–711. <https://doi.org/10.1007/s00775-006-0138-1>.
- (52) Jensen, K. P. Bioinorganic Chemistry Modeled with the TPSSh Density Functional. *Inorg. Chem.* **2008**, *47* (22), 10357–10365. <https://doi.org/10.1021/ic800841t>.
- (53) Perdew, J. P.; Kurth, S.; Zupan, A.; Blaha, P. Accurate Density Functional with Correct Formal Properties: A Step Beyond the Generalized Gradient Approximation. *Phys. Rev. Lett.* **1999**, *82* (12), 2544–2547. <https://doi.org/10.1103/PhysRevLett.82.2544>.
- (54) Perdew, J. P.; Tao, J.; Staroverov, V. N.; Scuseria, G. E. Meta-Generalized Gradient Approximation: Explanation of a Realistic Nonempirical Density Functional. *J. Chem. Phys.* **2004**, *120* (15), 6898–6911. <https://doi.org/10.1063/1.1665298>.
- (55) Staroverov, V. N.; Scuseria, G. E.; Tao, J.; Perdew, J. P. Comparative Assessment of a New Nonempirical Density Functional: Molecules and Hydrogen-Bonded Complexes. *J. Chem. Phys.* **2003**, *119* (23), 12129–12137. <https://doi.org/10.1063/1.1626543>.